②

FUNDAMENTAL PROPERTIES OF SOILS FOR
COMPLEX DYNAMIC LOADINGS

FINAL REPORT

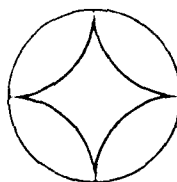"Development of a Three Invariant Constitutive Mo

Appendices A through W

DTIC
S **:LECTE** **D**
FEB 1 1 1986
D

DISTRIBUTION STATEMENT A

Approved for public release;
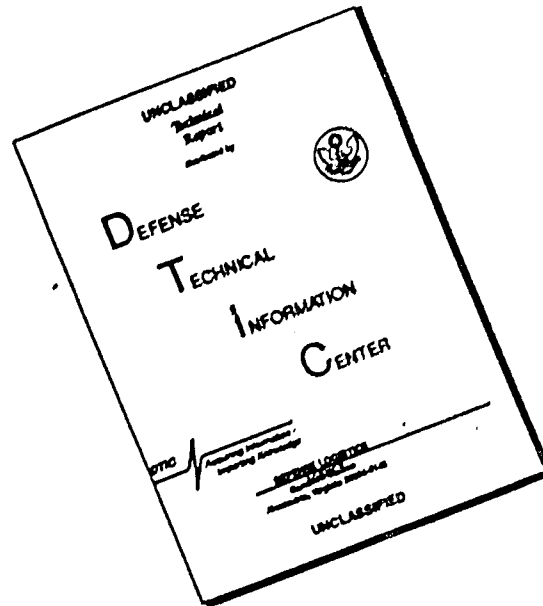Distribution Unlimited

APPLIED
RESEARCH
ASSOCIATES, INC.

Engineering and Applied Science

86   2   11   032

DISCLAIMER NOTICE

THIS DOCUMENT IS BEST QUALITY AVAILABLE. THE COPY FURNISHED TO DTIC CONTAINED A SIGNIFICANT NUMBER OF PAGES WHICH DO NOT REPRODUCE LEGIBLY.

FUNDAMENTAL PROPERTIES OF SOILS FOR
COMPLEX DYNAMIC LOADINGS

FINAL REPORT

"Development of a Three Invariant Constitutive Model"

Appendices A through W

by

Douglas H. Merkle
William C. Dass

22 April 1985

Applied Research Associates, Inc.
4300 San Mateo NE,   Suite A220
Albuquerque, NM 87110

Prepared for

Air Force Office of Scientific Research
Bolling Air Force Base
Washington, DC   20332

Contract No. F49620-80-C-0088

AD-A146207

REPORT DOCUMENTATION PAGE

Form Approved
OMB No 0704-0188
Exp Date Jun 30, 1986

1a REPORT SECURITY CLASSIFICATION	1b RESTRICTIVE MARKINGS
UNCLASSIFIED	

2a SECURITY CLASSIFICATION AUTHORITY	3 DISTRIBUTION / AVAILABILITY OF REPORT
2b DECLASSIFICATION · DOWNGRADING SCHEDULE	Approved for public release; distribution unlimited

4 PERFORMING ORGANIZATION REPORT NUMBER(S)	5 MONITORING ORGANIZATION REPORT NUMBER(S)
5230	AFOSR-TR· 85-1232

6a NAME OF PERFORMING ORGANIZATION	6b OFFICE SYMBOL (If applicable)	7a NAME OF MONITORING ORGANIZATION
Applied Research Associates, Inc.		Air Force Office of Scientific Research/NA

6c ADDRESS (City, State, and ZIP Code)	7b ADDRESS (City, State, and ZIP Code)
4300 San Mateo Blvd. NE Suite A220 Albuquerque, NM 87110	Bolling AFB, DC 20332

8a NAME OF FUNDING SPONSORING ORGANIZATION	8b OFFICE SYMBOL (If applicable)	9 PROCUREMENT INSTRUMENT IDENTIFICATION NUMBER
AFOSR	NA	Contract F49620-80-C-0088

8c ADDRESS (City, State, and ZIP Code)	10 SOURCE OF FUNDING NUMBERS			
	PROGRAM ELEMENT NO	PROJECT NO	TASK NO	WORK UNIT ACCESSION NO
Bolling AFB, DC 20332	61102F	2307	C1	

11 TITLE (Include Security Classification)
FUNDAMENTAL PROPERTIES OF SOILS FOR COMPLEX DYNAMIC LOADINGS:
Development of a Three Invariant Constitutive Model (U)

12 PERSONAL AUTHOR(S)
Merkle, Douglas Hall; and Dass, William Christopher

13a TYPE OF REPORT	13b TIME COVERED	14 DATE OF REPORT (Year, Month, Day)	15 PAGE COUNT
Final	FROM 800801 TO 840731	850422	609

16 SUPPLEMENTARY NOTATION

	COSATI CODES		18 SUBJECT TERMS (Continue on reverse if necessary and identify by block number)
FIELD	GROUP	SUB-GROUP	effective stress, soil dynamics, stress-strain behavior, shear strength, material modeling

19 ABSTRACT (Continue on reverse if necessary and identify by block number)

The objective of the study reported herein was to develop a general soil stress-strain model which can be used to solve a wide range of soil dynamics problems of interest to the Air Force. The approach used was to review existing soil constitutive models used to predict the response of soil masses to complex dynamic loads, and then formulate a new model for that purpose. Eight existing soil dynamic stress-strain models were studied, including exercising them along common stress and strain paths for comparison. The models were: linear elastic, linear viscoelastic, hyperbolic, Pyke cyclic simple shear, elastic-perfectly plastic, modified AFWL engineering, effective stress cap, and Lade. Each model is discussed and reviewed. The discussion of each model includes: motivation, assumptions, basic equations, parameter determination, and computed behavior. Based on the above review, the Lade model was selected as the best point of departure for developing a new soil stress-strain model for complex dynamic loading, because of its accuracy and flexibility in representing soil stress-strain behavior, ease of parameter determination, and ease of developing intuition for parameter

20 DISTRIBUTION / AVAILABILITY OF ABSTRACT	21 ABSTRACT SECURITY CLASSIFICATION
☐ UNCLASSIFIED/UNLIMITED ☒ SAME AS RPT ☐ DTIC USERS	UNCLASSIFIED

22a NAME OF RESPONSIBLE INDIVIDUAL	22b TELEPHONE (Include Area Code)	22c OFFICE SYMBOL
Lt. Col. Lawrence D. Hokanson	(202) 767-4935	AFOSR/NA

DD FORM 1473, 84 MAR
83 APR edition may be used until exhausted
All other editions are obsolete

ABSTRACT (continued)

physical significance and accuracy. The same five attributes discussed for each existing model were examined for the new ARA conic model, so called because its principal mathematical surfaces are conic sections. The computer code used to exercise all nine soil constitutive models under eleven stress and strain paths is called the Soil Element Model (SEM). It can be incorporated in large finite difference or finite element codes for analyzing the response of soil masses to complex dynamic loads.

The ARA conic model performs well over a wide range of loading conditions, many departing considerably from those used to determine the model parameters. The parameters are determined in a straightforward manner, and the model reflects the influence of the intermediate principal stress on shear strength through a shear failure surface involving three independent stress invariants: the first total stress invariant and the second and third deviator stress invariants. For this reason the model is also called a three invariant model. Measured shear strengths in both compression and extension can be matched exactly, and the mathematical formulation of the shear failure surface is such that the shear strength for any value of the intermediate principal stress can be computed directly without trial and error. The ARA conic model also exhibits dilatancy, generates only positive plastic work, and has a provision for strain softening in shear.

APPENDIX A

ANALYSIS OF STRESS

Stress Transformation Equations

Consider plane ABC of tetrahedron OABC in Figure (A.1), having the outward unit normal vector:

$$\bar{n} = \alpha_{1n}\bar{e}_1 + \alpha_{2n}\bar{e}_2 + \alpha_{3n}\bar{e}_3 = \begin{Bmatrix} \alpha_{1n} \\ \alpha_{2n} \\ \alpha_{3n} \end{Bmatrix} \tag{A.1}$$

Line OP is the shortest line from the coordinate origin to plane ABC, and is therefore normal to the plane, so that the unit normal vector $\bar{n}$ can be drawn along OP. Let the distance OP be h, and let the coordinates of any point, R, in plane ABC be (x_1, x_2, x_3), so that the position vector of point R is:

$$\overline{OR} = x_1\bar{e}_1 + x_2\bar{e}_2 + x_3\bar{e}_3 \tag{A.2}$$

Then since line OP is normal to the plane, the projection of $\overline{OR}$ on $\bar{n}$ must be of magnitude h, i.e.:

$$\bar{n}\cdot\overline{OR} = \alpha_{1n}x_1 + \alpha_{2n}x_2 + \alpha_{3n}x_3 = \alpha_{in}x_i = h \tag{A.3}$$

Equation (A.3) is the equation of a plane in rectangular Cartesian coordinates, and by considering the intersections of the plane with the three coordinate axes we obtain:

$$|\overline{OA}| = a = \frac{h}{\alpha_{1n}} \tag{A.4a}$$

97

$$|\overline{OB}| = b = \frac{h}{\alpha_{2n}} \qquad (A.4b)$$

$$|\overline{OC}| = c = \frac{h}{\alpha_{3n}} \qquad (A.4c)$$

Because the area of a pyramid cross section taken parallel to the base is proportional to the square of the perpendicular distance to the cross section from the apex, the volume of a pyramid is given by the well known formula:

$$\text{volume} = \frac{\text{height}}{3} \times \text{base area}$$

Therefore, the volume of tetrahedron OABC can be expressed in any of four ways:

$$V = \frac{h}{3} \text{ (area ABC)} = \frac{a}{3} \text{ (area BOC)} = \frac{b}{3} \text{ (area AOC)} = \frac{c}{3} \text{ (area AOB)} \qquad (A.5)$$

from which it follows that, using Equations (A.4),

$$\frac{\text{area BOC}}{\text{area ABC}} = \frac{h}{a} = \alpha_{1n} \qquad (A.6a)$$

$$\frac{\text{area AOC}}{\text{area ABC}} = \frac{h}{b} = \alpha_{2n} \qquad (A.6b)$$

$$\frac{\text{area AOB}}{\text{area ABC}} = \frac{h}{c} = \alpha_{3n} \qquad (A.6c)$$

Consider now the stresses exerted on tetrahedron OABC by the surrounding material, shown in Figure (A.2). The stress vectors $\overline{\sigma}_n$, $-\overline{\sigma}_1$, $-\overline{\sigma}_2$ and $-\overline{\sigma}_3$ are equal to the resultant forces acting on faces ABC, BOC, AOC and AOB, respectively, divided by the area of the face on which they act. In the limit, as the dimensions of the tetrahedron approach zero, the stress vectors each represent a uniformly distributed force per

98

unit area. Equilibrium considerations dictate that the vector sum of all
forces acting on the tetrahedron be zero. Body forces, such as those due
to gravity and inertia, need not be included in the vector equilibrium
equation for an infinitesimal tetrahedron, since their magnitudes are
proportional to h^3, whereas the magnitudes of surface forces are
proportional to h^2. The body forces therefore approach zero more
rapidly than do the surface forces as the tetrahedron dimensions approach
zero. Therefore, the following development is as applicable to problems
of wave propagation as it is to static problems. The vector equilibrium
equation for the infinitesimal tetrahedron is:

$$\overline{\sigma}_n \text{ (area ABC)} - \overline{\sigma}_1 \text{ (area BOC)} - \overline{\sigma}_2 \text{ (area AOC)} - \overline{\sigma}_3 \text{ (area AOB)} = \overline{0} \qquad (A.7)$$

Dividing both sides of Equation (A.7) by (area ABC) and using
Equations (A.6) yields

$$\overline{\sigma}_n = \overline{\sigma}_1 \alpha_{1n} + \overline{\sigma}_2 \alpha_{2n} + \overline{\sigma}_3 \alpha_{3n} = \overline{\sigma}_j \alpha_{jn} \qquad (A.8)$$

Equation (A.8) is commonly referred to as Cauchy's equation.

Each of the stress vectors in Figure (A.2) can be written in
component form, so that

$$\overline{\sigma}_1 = \sigma_{11}\overline{e}_1 + \sigma_{21}\overline{e}_2 + \sigma_{31}\overline{e}_3 \qquad (A.9a)$$

$$\overline{\sigma}_2 = \sigma_{12}\overline{e}_1 + \sigma_{22}\overline{e}_2 + \sigma_{32}\overline{e}_3 \qquad (A.9b)$$

$$\overline{\sigma}_3 = \sigma_{13}\overline{e}_1 + \sigma_{23}\overline{e}_2 + \sigma_{33}\overline{e}_3 \qquad (A.9c)$$

where

99

σ_{ij} = stress acting in direction $\bar{e}_i$, on the face with outward unit normal $\bar{e}_j$.

Equations (A.9) can be written concisely in the form:

$$\bar{\sigma}_j = \sigma_{ij}\bar{e}_i \tag{A.10}$$

Substitution of Equation (A.10) into Equation (A.8) yields:

$$\bar{\sigma}_n = \bar{\sigma}_j\alpha_{jn} = (\sigma_{ij}\bar{e}_i)\alpha_{jn} = (\sigma_{ij}\alpha_{jn})\bar{e}_i \tag{A.11}$$

or, in matrix form:

$$\{\sigma_n\} = \underline{\sigma}\,\{\alpha_n\} \tag{A.12}$$

The component of $\bar{\sigma}_n$ in the direction of the unit vector $\bar{m}$ in Figure (A.2) is:

$$\sigma_{mn} = \bar{m}\,\bar{\sigma}_n = \{\alpha_m\}^T\{\sigma_n\} = \{\alpha_m\}^T\underline{\sigma}\{\alpha_n\} = \alpha_{im}\sigma_{ij}\alpha_{jn} \tag{A.13}$$

Consider now two rectangular Cartesian coordinate systems having a common origin, as shown in Figure (A.3), and let

σ_{ij} = stress component defined in the 1,2,3 coordinate system

σ'_{ij} = stress component defined in the 1',2',3' coordinate system

α_{ij} = cosine of the angle between $\bar{e}_i$ and $\bar{e}'_j$

Then Equation (A.13) gives

$$\sigma'_{mn} = \alpha_{im}\sigma_{ij}\alpha_{jn} = \alpha_{mi}^T\sigma_{ij}\alpha_{jn} \tag{A.14}$$

or

$$\underline{\sigma}' = \underline{a}^T \underline{\sigma} \underline{a} \tag{A.15}$$

From Equation (A.13) it also follows that the normal component of $\overline{\sigma}_n$ in Figure (A.2), denoted σ_{nn}, is simply

$$\sigma_{nn} = \overline{n} \cdot \overline{\sigma}_n = \{\alpha_n\}^T \underline{\sigma} \{\alpha_n\} \tag{A.16}$$

Principal Stresses

It is of interest to investigate the change in σ_{nn} in Equation (A.16) due to an infinitesimal change in $\overline{n}$. Figure (A.4) shows that since $\overline{n}$ must remain a unit vector, it can only change direction, so that

$$\{d\alpha_n\} = d\lambda \{\alpha_t\} \tag{A.17}$$

where

$$\{\alpha_t\}^T \{\alpha_n\} = 0 \tag{A.18}$$

Equations (A.17) and A.18) merely state that an infinitesimal change in the unit vector $\overline{n}$ must lie in the plane normal to $\overline{n}$. The increment in σ_{nn} due to $\overline{dn}$ can now be obtained by differentiating Equation (A.16), which yields

$$d\sigma_{nn} = \{d\alpha_n\}^T \underline{\sigma} \{\alpha_n\} + \{\alpha_n\}^T \underline{\sigma} \{d\alpha_n\} = \{d\alpha_n\}^T (\underline{\sigma} + \underline{\sigma}^T) \{\alpha_n\} \tag{A.19}$$

However, because there are assumed to be no distributed torques, the stress matrix is symmetric, i.e.:

$$\underline{\sigma}^T = \underline{\sigma} \tag{A.20}$$

Therefore, substitution of Equations (A.17) and (A.20) into Equation (A.19), taking account of Equation (A.13), yields

$$d\sigma_{nn} = 2d\lambda \{\alpha_t\}^T \underline{\sigma} \{\alpha_n\} = 2d\lambda\sigma_{tn} \tag{A.21}$$

where σ_{tn} is the shearing component of $\overline{\sigma}_n$ in the direction of $\overline{t}$. From Equation (A.21) it follows that stationary values of normal stress occur on planes of zero shear. Therefore, to locate stationary values of normal stress, one seeks those directions for which the stress vector, $\overline{\sigma}_n$, has no component normal to $\overline{n}$, and is therefore parallel to $\overline{n}$. For such a "principal" direction,

$$\overline{\sigma}_n = \sigma\overline{n} \tag{A.22}$$

Using Equation (A.12), Equation (A.22) can be written in matrix form as

$$\{\sigma_n\} = \underline{\sigma}\{\alpha_n\} = \sigma\{\alpha_n\} \tag{A.23}$$

or, in homogeneous form

$$(\underline{\sigma} - \sigma\underline{I})\{\alpha_n\} = \{0\} \tag{A.24}$$

The expanded form of Equation (A.24) is

$$\begin{bmatrix} \sigma_{11} - \sigma & \sigma_{12} & \sigma_{13} \\ \sigma_{21} & \sigma_{22} - \sigma & \sigma_{23} \\ \sigma_{31} & \sigma_{32} & \sigma_{33} - \sigma \end{bmatrix} \begin{Bmatrix} \alpha_{1n} \\ \alpha_{2n} \\ \alpha_{3n} \end{Bmatrix} = \begin{Bmatrix} 0 \\ 0 \\ 0 \end{Bmatrix} \tag{A.25}$$

and since Equations (A.25) are a set of homogeneous linear equations, they possess a unique solution if and only if the determinant of the coefficient matrix, in this case referred to as the *characteristic determinant*, is zero. The equation expressing this condition is the *characteristic equation*:

$$\begin{vmatrix} \sigma_{11} - \sigma & \sigma_{12} & \sigma_{13} \\ \sigma_{21} & \sigma_{22} - \sigma & \sigma_{23} \\ \sigma_{31} & \sigma_{32} & \sigma_{33} - \sigma \end{vmatrix} = 0 \qquad (A.26)$$

Expansion of Equation (A.26) yields

$$(\sigma_{11} - \sigma)(\sigma_{22} - \sigma)(\sigma_{33} - \sigma) + \sigma_{12}\sigma_{23}\sigma_{31} + \sigma_{13}\sigma_{21}\sigma_{32}$$

$$- (\sigma_{11} - \sigma)\sigma_{23}\sigma_{32} - \sigma_{12}\sigma_{21}(\sigma_{33} - \sigma) - \sigma_{13}(\sigma_{22} - \sigma)\sigma_{31}$$

$$= - \sigma^3 + (\sigma_{11} + \sigma_{22} + \sigma_{33})\sigma^2 - \left(\begin{vmatrix} \sigma_{11} & \sigma_{12} \\ \sigma_{21} & \sigma_{22} \end{vmatrix} + \begin{vmatrix} \sigma_{22} & \sigma_{23} \\ \sigma_{32} & \sigma_{33} \end{vmatrix} \right.$$

$$\left. + \begin{vmatrix} \sigma_{33} & \sigma_{31} \\ \sigma_{13} & \sigma_{11} \end{vmatrix} \right) \sigma + \begin{vmatrix} \sigma_{11} & \sigma_{12} & \sigma_{13} \\ \sigma_{21} & \sigma_{22} & \sigma_{23} \\ \sigma_{31} & \sigma_{32} & \sigma_{33} \end{vmatrix} = 0$$

or

$$-(\sigma^3 - I_1\sigma^2 - I_2\sigma - I_3) = -(\sigma - \sigma_1)(\sigma - \sigma_2)(\sigma - \sigma_3) = 0 \qquad (A.27)$$

where σ_1, σ_2, and σ_3 are the three real roots of the cubic characteristic equation, called the principal stresses, and the stress invariants, I_1, I_2 and I_3 are defined as follows:

$$I_1 = \sigma_{11} + \sigma_{22} + \sigma_{33} = \sigma_1 + \sigma_2 + \sigma_3 \qquad (A.28)$$

103

$$I_2 = -\left(\begin{vmatrix} \sigma_{11} & \sigma_{12} \\ \sigma_{21} & \sigma_{22} \end{vmatrix} + \begin{vmatrix} \sigma_{22} & \sigma_{23} \\ \sigma_{32} & \sigma_{33} \end{vmatrix} + \begin{vmatrix} \sigma_{33} & \sigma_{31} \\ \sigma_{13} & \sigma_{11} \end{vmatrix} \right)$$

$$= -(\sigma_1\sigma_2 + \sigma_2\sigma_3 + \sigma_3\sigma_1) \tag{A.29}$$

$$I_3 = \begin{vmatrix} \sigma_{11} & \sigma_{12} & \sigma_{13} \\ \sigma_{21} & \sigma_{22} & \sigma_{23} \\ \sigma_{31} & \sigma_{32} & \sigma_{33} \end{vmatrix} = \sigma_1\sigma_2\sigma_3 \tag{A.30}$$

Cardan's classic solution of Equation (A.27) [USPENSKY (1948:84)] begins by setting

$$\sigma = s + \frac{I_1}{3} \tag{A.31}$$

which causes Equation (A.26) to take the form

$$\begin{vmatrix} (\sigma_{11} - \frac{I_1}{3}) - s & \sigma_{12} & \sigma_{13} \\ \sigma_{21} & (\sigma_{22} - \frac{I_1}{3}) - s & \sigma_{23} \\ \sigma_{31} & \sigma_{32} & (\sigma_{33} - \frac{I_1}{3}) - s \end{vmatrix} = 0 \tag{A.32}$$

or

$$\begin{vmatrix} s_{11} - s & s_{12} & s_{13} \\ s_{21} & s_{22} - s & s_{23} \\ s_{31} & s_{32} & s_{33} - s \end{vmatrix} = 0 \tag{A.33}$$

where the deviator stress matrix, $\underline{s}$, is defined by the equation

$$\underline{s} = \underline{\sigma} - \frac{I_1}{3} \underline{I} \tag{A.34}$$

104

Expansion of Equation (A.33) yields

$$- (s^3 - J_2 s - J_3) = - (s - s_1)(s - s_2)(s - s_3) = 0 \qquad (A.35)$$

where s_1, s_2, s_3 are the three real roots (principal deviator stresses), and the deviator stress invariants, J_1, J_2, and J_3 are defined as follows:

$$J_1 = s_{11} + s_{22} + s_{33} = s_1 + s_2 + s_3 = 0 \qquad (A.36)$$

$$J_2 = - \left(\begin{vmatrix} s_{11} & s_{12} \\ s_{21} & s_{22} \end{vmatrix} + \begin{vmatrix} s_{22} & s_{23} \\ s_{32} & s_{33} \end{vmatrix} + \begin{vmatrix} s_{33} & s_{31} \\ s_{13} & s_{11} \end{vmatrix} \right)$$

$$= - (s_1 s_2 + s_2 s_3 + s_3 s_1) \qquad (A.37)$$

$$J_3 = \begin{vmatrix} s_{11} & s_{12} & s_{13} \\ s_{21} & s_{22} & s_{23} \\ s_{31} & s_{32} & s_{33} \end{vmatrix} = s_1 s_2 s_3 \qquad (A.38)$$

The s^2 term is absent from Equation (A.35) because J_1 is zero, and Equation (A.35) is therefore referred to as the reduced characteristic or reduced cubic equation.

The solution to Equation (A.35) is assumed to be of the form

$$s = A + B \qquad (A.39)$$

so that

$$s^3 = A^3 + 3A^2 B + 3AB^2 + B^3$$

$$= A^3 + B^3 + 3AB(A + B)$$

$$= A^3 + B^3 + 3ABs$$

or

$$s^3 - 3ABs - (A^3 + B^3) = 0 \qquad (A.40)$$

105

Comparison of Equations (A.40) and (A.35) shows that

$$3AB = J_2 \qquad\qquad (A.41)$$

or

$$A^3 B^3 = \left(\frac{J_2}{3}\right)^3 \qquad\qquad (A.42)$$

and

$$A^3 + B^3 = J_3 \qquad\qquad (A.43)$$

Thus, the sum and product of A^3 and B^3 are specified, which means that A^3 and B^3 are the roots of a quadratic equation. To obtain the quadratic equation we first obtain an expression for B^3 from Equation (A.43).

$$B^3 = J_3 - A^3 \qquad\qquad (A.44)$$

Substitution of Equation (A.44) into Equation (A.42) then yields

$$A^3(J_3 - A^3) = J_3 A^3 - (A^3)^2 = \left(\frac{J_2}{3}\right)^3$$

or

$$(A^3)^2 - J_3 A^3 + \left(\frac{J_2}{3}\right)^3 = 0 \qquad\qquad (A.45)$$

Because of the symmetry of Equations (A.42) and (A.43), B^3 also satisfies Equation (A.45). Therefore, the solutions for A^3 and B^3 are

$$A^3 = \frac{J_3}{2} + \sqrt{\left(\frac{J_3}{2}\right)^2 - \left(\frac{J_2}{3}\right)^3} \qquad\qquad (A.46a)$$

106

and

$$B^3 = \frac{J_3}{2} - \sqrt{\left(\frac{J_3}{2}\right)^2 - \left(\frac{J_2}{3}\right)^3} \qquad \text{(A.46b)}$$

The quantities A^3 and B^3 are real or complex, depending upon whether the quantity under the radical in Equations (A.46) is non-negative or negative, which can be determined by evaluating the ratio

$$\frac{\dfrac{J_3}{2}}{\left(\dfrac{J_2}{3}\right)^{3/2}}$$

Now the three roots of Equation (A.35) are physical quantities, and are therefore real. Thus, we can assume that:

$$s_1 \geq s_2 \geq s_3 \qquad \text{(A.47)}$$

In addition, if we set

$$\frac{s_1 + s_3}{2} = r \qquad \text{(A.48)}$$

$$\frac{s_1 - s_3}{2} = q \qquad \text{(A.49)}$$

and define Lode's parameter by the relation

$$\mu = \frac{s_2 - r}{q} = \frac{s_2 - \dfrac{s_1 + s_3}{2}}{\dfrac{s_1 - s_3}{2}} = \frac{2s_2 - s_1 - s_3}{s_1 - s_3} \qquad \text{(A.50)}$$

then

$$s_1 = r + q \qquad \text{(A.51)}$$

107

$$s_2 = r + \mu q \tag{A.52}$$

$$s_3 = r - q \tag{A.53}$$

In addition, Equation (A.36) requires that

$$s_1 + s_2 + s_3 = 3r + \mu q = 0 \tag{A.54}$$

so that the deviator stress paramenters r and q are related by the expression

$$r = -\frac{\mu}{3} q \tag{A.55}$$

and therefore the principal deviator stresses can all be expressed in terms of the parameters μ and q as follows:

$$s_1 = (1 - \frac{\mu}{3})q \tag{A.56}$$

$$s_2 = \frac{2\mu}{3}q \tag{A.57}$$

$$s_3 = -(1 + \frac{\mu}{3})q \tag{A.58}$$

Substitution of Equation (A.56-58) into the ratio in question reduces it to a function of μ only, as follows:

$$\frac{J_3}{2} = -\frac{\mu}{3}(1 - \frac{\mu^2}{9})q^3 = -\frac{\mu(9 - \mu^2)}{27}q^3 \tag{A.59}$$

$$\frac{J_2}{3} = -\frac{q^2}{27}[2\mu(3 - \mu) - 2\mu(3 + \mu) - (9 - \mu^2)]$$

$$= \frac{3 + \mu^2}{9}q^2 \tag{A.60}$$

$$\frac{\frac{J_3}{2}}{\left(\frac{J_2}{3}\right)^{3/2}} = -\frac{\mu(3 + \mu)(3 - \mu)}{(3 + \mu^2)^{3/2}} \tag{A.61}$$

According to Equation (A.50) the parameter μ varies between -1 (when $s_2 = s_3$) and $+1$ (when $s_2 = s_1$). The ratio in Equation (A.61) therefore also varies between $+1$ and -1, as can be verified by direct calculation, and therefore the radicand in Equations (A.46) is nonpositive. This being the case, the quantities A^3 and B^3 are complex, and can therefore be represented by an Argand diagram as shown in Figure (A.5).

The expressions for A^3 and B^3, shown in Figure (A.5) are:

$$A^3 = \frac{J_3}{2} + i\sqrt{\left(\frac{J_2}{3}\right)^3 - \left(\frac{J_3}{2}\right)^2} = \left(\frac{J_2}{3}\right)^{3/2} e^{i3\omega} \tag{A.62a}$$

$$B^3 = \frac{J_3}{2} - i\sqrt{\left(\frac{J_2}{3}\right)^3 - \left(\frac{J_3}{2}\right)^2} = \left(\frac{J_2}{3}\right)^{3/2} e^{-i3\omega} \tag{A.62b}$$

where

$$\cos 3\omega = \frac{\frac{J_3}{2}}{\left(\frac{J_2}{3}\right)^{3/2}} = -\frac{\mu(3 + \mu)(3 - \mu)}{(3 + \mu^2)^{3/2}} \tag{A.63}$$

Equation (A.63) is plotted in Figure A.6.

The desired values of A and B are therefore the complex cube roots of the expressions in Equations (A.62), i.e.:

$$A = \sqrt{\frac{J_2}{3}} \, e^{i\omega_j} \quad (j = 1,2,3) \tag{A.64a}$$

$$B = \sqrt{\frac{J_2}{3}} \, e^{-i\omega_k} \quad (k = 1,2,3) \tag{A.64b}$$

where

$$\omega_1 = \omega - \frac{2\pi}{3} \tag{A.65a}$$

$$\omega_2 = \omega \tag{A.65b}$$

$$\omega_3 = \omega + \frac{2\pi}{3} \tag{A.65c}$$

and

$$\omega = \frac{1}{3}\cos^{-1}\left[\frac{\frac{J_3}{2}}{\left(\frac{J_2}{3}\right)^{3/2}}\right] \tag{A.66}$$

Now Equation (A.39) states that each of the three roots, s_1, s_2, and s_3 is the sum of two quantities, A and B, whose product is real according to Equation (A.41). Therefore, the values of A and B used to form s_j ($j = 1,2,3$) must be complex conjugates, which requires that $k = j$ in Equations (A.64). Equation (A.39) therefore takes the form:

$$s_j = \sqrt{\frac{J_2}{3}} \, (e^{i\omega_j} + e^{-i\omega_j}) = 2\sqrt{\frac{J_2}{3}} \cos \omega_j \quad (j = 1,2,3) \tag{A.67}$$

or

$$s_1 = 2\sqrt{\frac{J_2}{3}} \cos \omega_1 \tag{A.68a}$$

$$s_2 = 2\sqrt{\frac{J_2}{3}} \cos \omega_2 \tag{A.68b}$$

$$s_3 = 2\sqrt{\frac{J_2}{3}} \cos \omega_3 \tag{A.68c}$$

110

so that Equation (A.31) takes the form:

$$\sigma_1 = s_1 + \frac{I_1}{3} = 2\sqrt{\frac{J_2}{3}} \cos \omega_1 + \frac{I_1}{3} \tag{A.69a}$$

$$\sigma_2 = s_2 + \frac{I_1}{3} = 2\sqrt{\frac{J_2}{3}} \cos \omega_2 + \frac{I_1}{3} \tag{A.69b}$$

$$\sigma_3 = s_3 + \frac{I_1}{3} = 2\sqrt{\frac{J_2}{3}} \cos \omega_3 + \frac{I_1}{3} \tag{A.69c}$$

Principal Stress Directions

Once the principal stresses have been calculated, the direction cosines associated with each principal stress can be obtained from three separate solutions of Equation (A.25) in which σ is successively set equal to σ_1, σ_2 and σ_3. In each solution at least one of the equations will be redundant, so that a corresponding number of the direction cosines will be arbitrary. The directions thus obtained are those of the principal stress axes, and can be shown to be orthogonal as follows. Let

$$\underline{\alpha} = \left[\{\alpha_1\} \mid \{\alpha_2\} \mid \{\alpha_3\} \right] \tag{A.70}$$

where $\{\alpha_1\}$, $\{\alpha_2\}$ and $\{\alpha_3\}$ are the three principal directions. Then Equation (A.23) can be written in the form:

$$\underline{\sigma}\,\underline{\alpha} = \underline{\alpha}\,\ulcorner\sigma_{p\lrcorner} \tag{A.71}$$

where

$$\ulcorner\sigma_{p\lrcorner} = \begin{bmatrix} \sigma_1 & 0 & 0 \\ 0 & \sigma_2 & 0 \\ 0 & 0 & \sigma_3 \end{bmatrix} \tag{A.72}$$

111

Premultiplying both sides of Equation (A.71) by $\underline{\alpha}^T$, then transposing the result and taking account of Equation (A.20) yields

$$\underline{\alpha}^T \, \underline{\sigma} \, \underline{\alpha} = \underline{\alpha}^T \, \underline{\alpha} \, \lceil \sigma_{p} \rfloor$$

$$\underline{\alpha}^T \, \underline{\sigma}^T \, \underline{\alpha} = \lceil \sigma_{p} \rfloor \, \underline{\alpha}^T \, \underline{\alpha}$$

$$\underline{\alpha}^T \underline{\sigma} \, \underline{\alpha} = \lceil \sigma_{p} \rfloor \, \underline{\alpha}^T \, \underline{\alpha}$$

$$(\underline{\alpha}^T \, \underline{\alpha}) \lceil \sigma_{p} \rfloor = \lceil \sigma_{p} \rfloor (\underline{\alpha}^T \, \underline{\alpha}) \tag{A.73}$$

The only way Equation (A.73) can be satisfied is for the matrix $\underline{\alpha}^T \, \underline{\alpha}$ to be diagonal, which means the columns of $\underline{\alpha}$ are orthogonal (perpendicular). Since the $\{\alpha_j\}$ are unit vectors, we have

$$\underline{\alpha}^T \, \underline{\alpha} = \underline{I} \tag{A.74}$$

so that Equation (A.71) yields

$$\underline{\alpha}^T \, \underline{\sigma} \, \underline{\alpha} = \lceil \sigma_{p} \rfloor \tag{A.75}$$

and

$$\underline{\alpha} \, \lceil \sigma_{p} \rfloor \, \underline{\alpha}^T = \underline{\sigma} \tag{A.76}$$

112
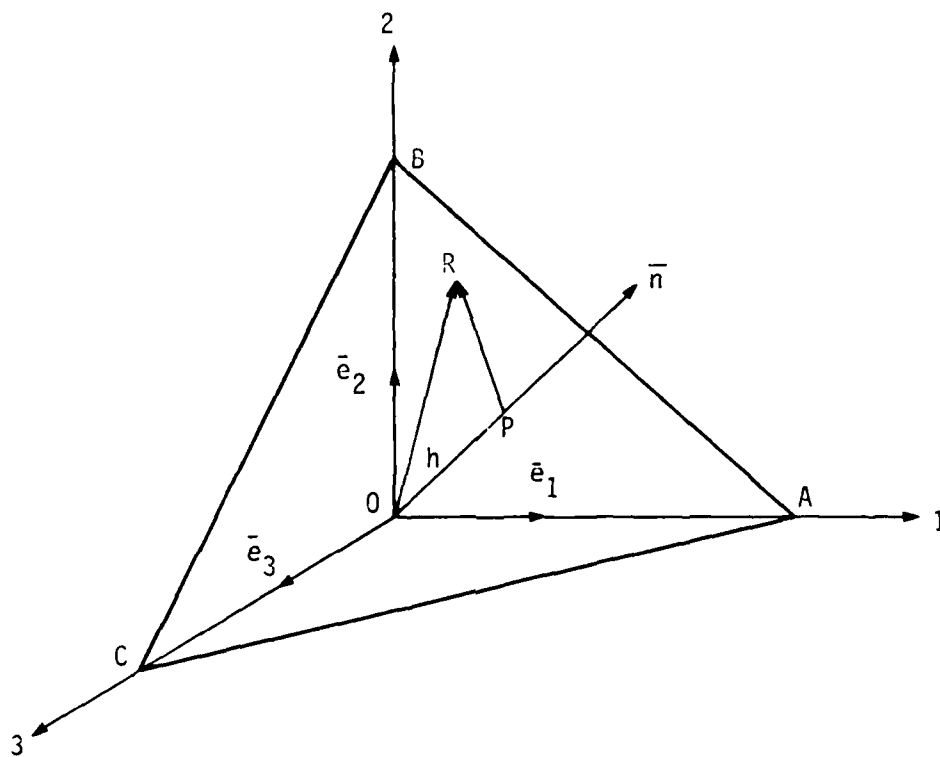
Figure A.1.   Tetrahedron OABC.

Figure A.2. Stresses exerted on tetrahedron OABC by the surrounding material.
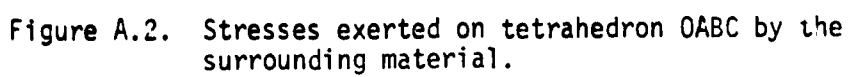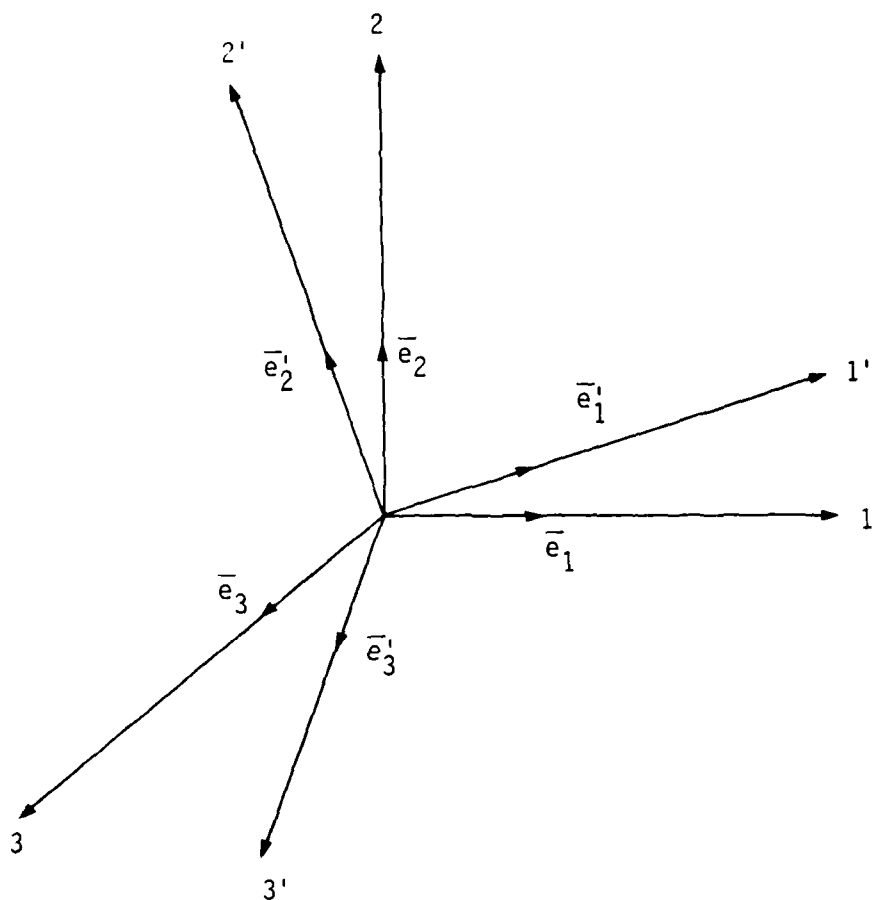
Figure A.3. Rotation of rectangular Cartesian coordinates.

$$\overline{t}$$

$$d\overline{n} = d\lambda\overline{t}$$

$$\overline{n} + d\overline{n}$$

$$\overline{n}$$
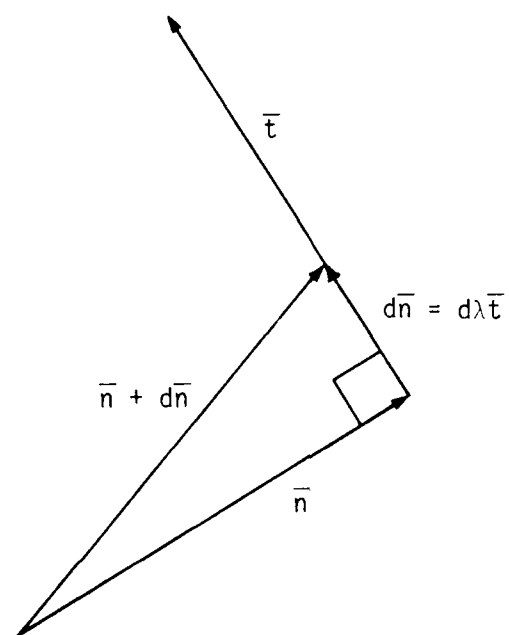
Figure A.4.   Infinitesimal change in a unit vector.

$(\frac{J_2}{3})^{3/2}$

A^3

$\sqrt{(\frac{J_2}{3})^3 - (\frac{J_3}{2})^2}$

3ω $\frac{J_3}{2}$

x

3ω

$\sqrt{(\frac{J_2}{3})^3 - (\frac{J_3}{2})^2}$

B^3

y
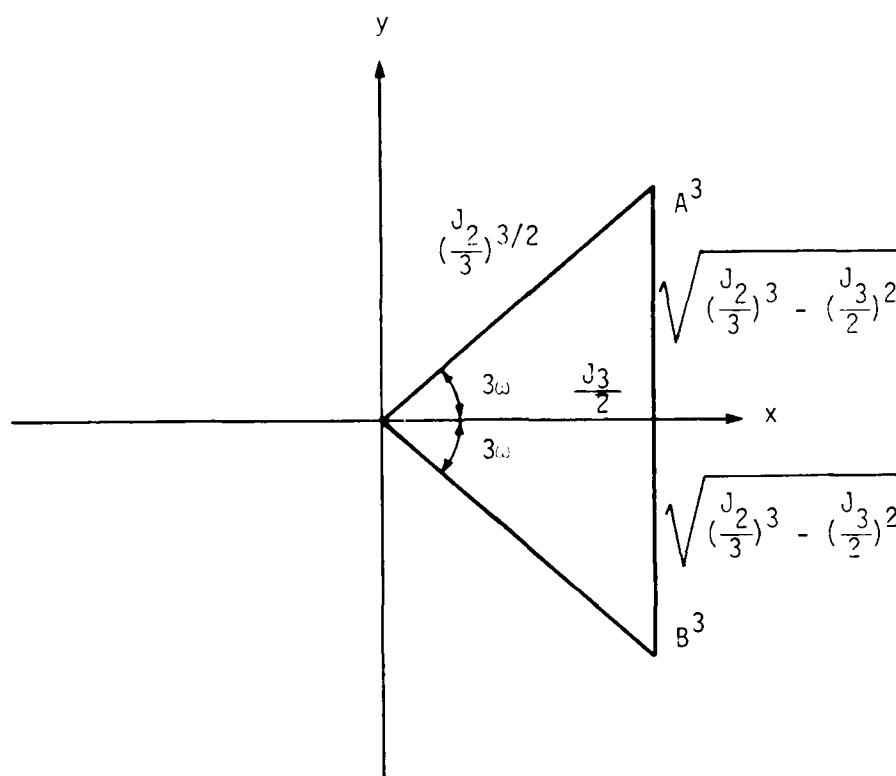
Figure A.5. Representation of the roots of Equation (A.45) in an Argand diagram.

117
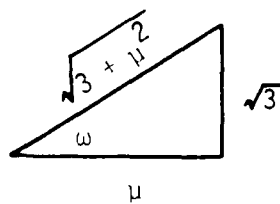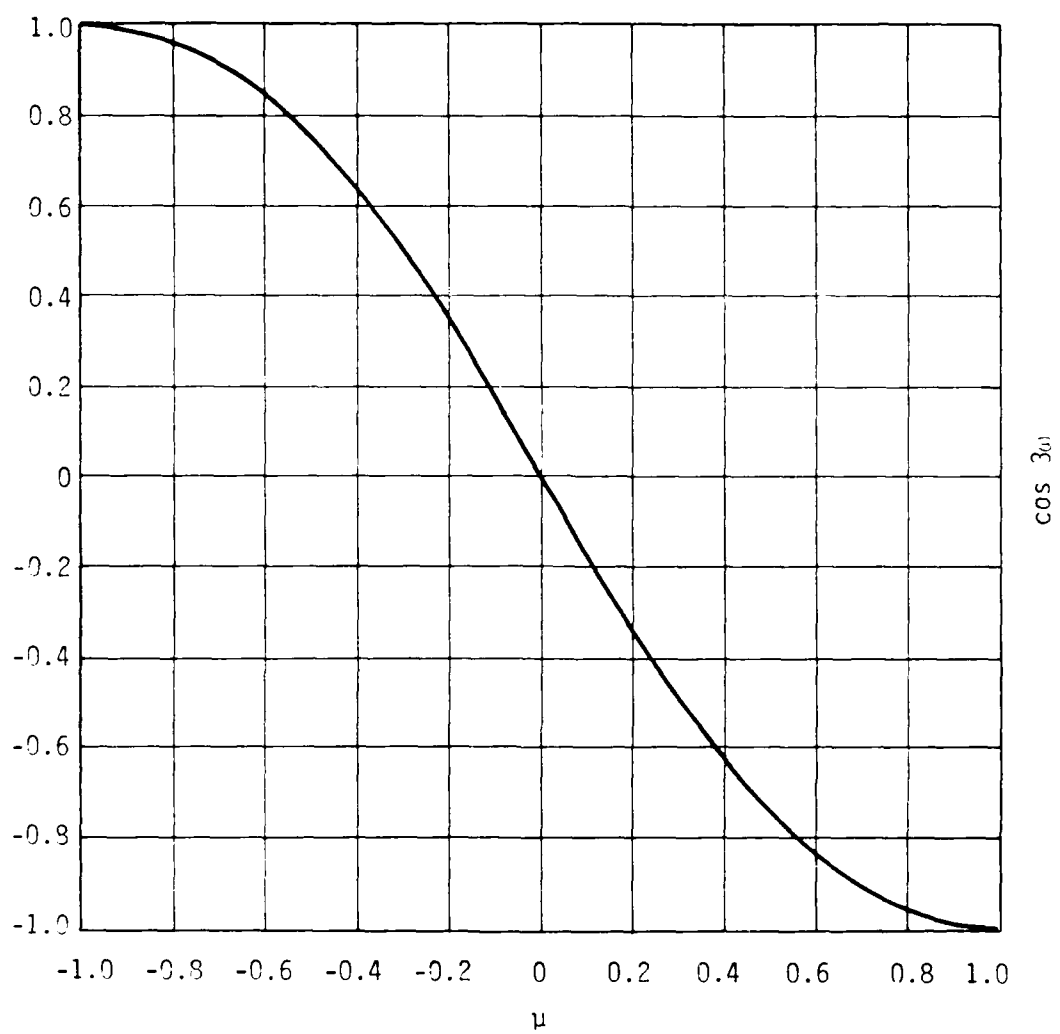
Figure A.6.   Relation between μ and ω.

118

APPENDIX B

CAYLEY-HAMILTON INVARIANT FORMULATIONS

If $\underline{a}$ is the 3 x 3 matrix containing the column vectors of direction cosines of unit vectors in the three principal stress directions of the stress matrix, $\underline{\sigma}$, and $\ulcorner\sigma_p\urcorner$ is the diagonal matrix of corresponding principal stresses, then Equations (A.74-76) give

$$\underline{a}^T \, \underline{a} = \underline{I} \tag{A.74}$$

$$\underline{a}^T \, \underline{\sigma} \, \underline{a} = \ulcorner\sigma_p\urcorner \tag{A.75}$$

$$\underline{a} \, \ulcorner\sigma_p\urcorner \, \underline{a}^T = \underline{\sigma} \tag{A.76}$$

It is easy to generalize Equation (A.76) for higher powers of σ_p and $\underline{\sigma}$. For example,

$$\underline{a} \, \ulcorner\sigma_p\urcorner^2 \, \underline{a}^T = (\underline{a} \, \ulcorner\sigma_p\urcorner \, \underline{a}^T)(\underline{a} \, \ulcorner\sigma_p\urcorner \, \underline{a}^T) = \underline{\sigma}^2 \tag{B.1}$$

and, in general,

$$\underline{a} \, \ulcorner\sigma_p\urcorner^n \, \underline{a}^T = (\underline{a} \, \ulcorner\sigma_p\urcorner \, \underline{a}^T)^n = \underline{\sigma}^n \quad \text{(n an integer)} \tag{B.2}$$

Now if Equation (A.27) is written for each of the three principal stresses, and the result put in diagonal matrix form, we obtain

$$\ulcorner\sigma_p\urcorner^3 - I_1 \, \ulcorner\sigma_p\urcorner^2 - I_2 \, \ulcorner\sigma_p\urcorner - I_3\underline{I} = \ulcorner0\urcorner \tag{B.3}$$

Premultiplication of Equation (B.3) by $\underline{a}$ and postmultiplication by $\underline{a}^T$ then yields

119

$$\underline{\sigma}^3 - I_1\underline{\sigma}^2 - I_2\underline{\sigma} - I_3\underline{I} = \underline{0} \tag{B.4}$$

Equation (B.4) states that the stress matrix, $\underline{\sigma}$, satisfies the matrix form of its own characteristic equation. This is a particular example of the Cayley-Hamilton theorem, and leads to useful expressions for the invariants I_1, I_2, I_3, J_1, J_2, and J_3, as shown below.

Recall that the inverse of a square matrix equals its adjoint (the transpose of its matrix of cofactors), divided by its determinant. Thus,

$$\underline{\sigma}^{-1} = \frac{\underline{\sigma}^{\star}}{|\underline{\sigma}|} = \frac{\underline{\Sigma}^T}{|\underline{\sigma}|} \tag{B.5}$$

Now

$$I_2 = -\,\mathrm{Tr}(\underline{\Sigma}) = -\,\mathrm{Tr}(\underline{\Sigma}^T) \tag{B.6}$$

and

$$I_3 = |\underline{\sigma}| \tag{B.7}$$

so that

$$\mathrm{Tr}(\underline{\sigma}^{-1}) = \frac{\mathrm{Tr}(\underline{\Sigma}^T)}{|\underline{\sigma}|} = -\frac{I_2}{I_3} \tag{B.8}$$

Now first note that

$$I_1 = \mathrm{Tr}(\underline{\sigma}) \tag{B.9}$$

Next, premultiply Equation (B.4) by $\underline{\sigma}^{-1}$ to obtain

$$\underline{\sigma}^2 - I_1\underline{\sigma} - I_2\underline{I} - I_3\underline{\sigma}^{-1} = \underline{0} \tag{B.10}$$

Taking the trace of Equation (B.10) then yields

120

$$Tr(\underline{\sigma}^2) - I_1^2 - 3I_2 - I_3(-\frac{I_2}{I_3})$$

$$= Tr(\underline{\sigma}^2) - I_1^2 - 2I_2 = 0 \tag{B.11}$$

so that

$$I_2 = \frac{1}{2}[Tr(\underline{\sigma}^2) - I_1^2] \tag{B.12}$$

Finally, taking the trace of Equation (B.4) yields

$$Tr(\underline{\sigma}^3) - I_1 Tr(\underline{\sigma}^2) - I_2 I_1 - 3I_3$$

$$= Tr(\underline{\sigma}^3) - I_1 Tr(\underline{\sigma}^2) - \frac{I_1}{2}[Tr(\underline{\sigma}^2) - I_1^2] - 3I_3$$

$$= Tr(\underline{\sigma}^3) - \frac{3}{2}I_1 Tr(\underline{\sigma}^2) + \frac{I_1^3}{2} - 3I_3 = 0 \tag{B.13}$$

so that

$$I_3 = \frac{1}{6}[2Tr(\underline{\sigma}^3) - 3I_1 Tr(\underline{\sigma}^2) + I_1^3] \tag{B.14}$$

Since the deviator stress matrix, $\underline{s}$, can be viewed as a particular type of stress matrix whose trace (first invariant) is zero, Equations (B.9), (B.12), and (B.14) yield

$$J_1 = Tr(\underline{s}) = 0 \tag{B.15}$$

$$J_2 = \frac{1}{2}Tr(\underline{s}^2) \tag{B.16}$$

$$J_3 = \frac{1}{3}Tr(\underline{s}^3) \tag{B.17}$$

For machine computation, the following invariant expressions are convenient because they do not require calculation of principal stresses:

$$I_1 = \sigma_{11} + \sigma_{22} + \sigma_{33} \tag{B.18}$$

$$J_2 = \frac{(s_{11}^2 + s_{22}^2 + s_{33}^2) + 2(s_{12}^2 + s_{23}^2 + s_{31}^2)}{2} \tag{B.19}$$

$$J_3 = s_{11}s_{22}s_{33} + s_{12}s_{23}s_{31} + s_{32}s_{21}s_{13} \tag{B.20}$$

$$- (s_{11}s_{23}^2 + s_{22}s_{31}^2 + s_{33}s_{12}^2)$$

Equation (B.18) is identical to Equation (A.28); Equation (B.19) is an expansion of Equation (B.16); and Equation (B.20) is an expansion of Equation (A.38).

Another useful expression for J_2 is obtained by setting

$$J_2 = J_2 - \frac{J_1^2}{6}$$

$$= \frac{3(s_{11}^2 + s_{22}^2 + s_{33}^2) - (s_{11} + s_{22} + s_{33})^2}{6} + (s_{12}^2 + s_{23}^2 + s_{31}^2)$$

$$= \frac{2(s_{11}^2 + s_{22}^2 + s_{33}^2 - s_{11}s_{22} - s_{22}s_{33} - s_{33}s_{11})}{6} + (s_{12}^2 + s_{23}^2 + s_{31}^2)$$

$$= \frac{(s_{11} - s_{22})^2 + (s_{22} - s_{33})^2 + (s_{33} - s_{11})^2}{6} + (s_{12}^2 + s_{23}^2 + s_{31}^2)$$

$$= \frac{(\sigma_{11} - \sigma_{22})^2 + (\sigma_{22} - \sigma_{33})^2 + (\sigma_{33} - \sigma_{11})^2}{6} + (\sigma_{12}^2 + \sigma_{23}^2 + \sigma_{31}^2) \tag{B.21}$$

By using Equation (A.34) in the form

$$\underline{\sigma} = \underline{s} + \frac{I_1}{3}\underline{I} \tag{B.22}$$

Equations (B.12) and (B.14) can be made to yield

$$I_2 = \frac{1}{2}\lfloor Tr(\underline{\sigma}^2) - I_1^2 \rfloor = \frac{1}{2}\left\{ Tr[(\underline{s} + \frac{I_1}{3}\underline{I})^2] - I_1^2 \right\}$$

$$= \frac{1}{2}[Tr(\underline{s}^2 + \frac{2I_1}{3}\underline{s} + \frac{I_1^2}{9}\underline{I}) - I_1^2]$$

$$= J_2 - \frac{I_1^2}{3} \tag{B.23}$$

and

$$I_3 = \frac{1}{6}[2Tr(\underline{\sigma}^3) - 3I_1 Tr(\underline{\sigma}^2) + I_1^3]$$

$$= \frac{1}{6}\left\{ 2Tr[(\underline{s} + \frac{I_1}{3}\underline{I})^3] - 3I_1 Tr[(\underline{s} + \frac{I_1}{3}\underline{I})^2] + I_1^3 \right\}$$

$$= \frac{1}{6}[2Tr(\underline{s}^3 + I_1\underline{s}^2 + \frac{I_1^2}{3}\underline{s} + \frac{I_1^3}{27}\underline{I}) - 3I_1 Tr(\underline{s}^2 + \frac{2I_1}{3}\underline{s} + \frac{I_1^2}{9}\underline{I}) + I_1^3]$$

$$= J_3 + \frac{2I_1}{3}J_2 + \frac{I_1^3}{27} - I_1 J_2 - \frac{I_1^3}{6} + \frac{I_1^3}{6}$$

$$= J_3 - \frac{I_1 J_2}{3} + \frac{I_1^3}{27} \tag{B.24}$$

so that

$$J_2 = I_2 + \frac{I_1^2}{3} \tag{B.25}$$

123

and

$$J_3 = I_3 + \frac{I_1}{3}(I_2 + \frac{I_1^2}{3}) - \frac{I_1^3}{27} = I_3 + \frac{I_1 I_2}{3} + \frac{2I_1^3}{27} \qquad (B.26)$$

Equations (B.23), (B.24), (B.25) and (B.26) show how any function of I_1, I_2, and I_3 can also be written as a function of I_1, J_2, and J_3, and vice versa.

124

APPENDIX C

OCTAHEDRAL PLANE PLOTS

The positive directions of the orthogonal principal stress axes, defined by Equation (A.70), are arbitrary. Thus, the principal stress axes define eight octants within which the stress vector repeats itself in a symmetrical fashion. It is convenient to use the principal stress axes as coordinate axes, as shown in Figure (C.1). The principal stress axes define the principal stress space, and in that coordinate system the stress matrix reduces to the diagonal matrix of principal stresses.

$$\underline{\sigma} = \lceil \sigma_{p_{\rfloor}} = \begin{bmatrix} \sigma_1 & 0 & 0 \\ 0 & \sigma_2 & 0 \\ 0 & 0 & \sigma_3 \end{bmatrix} \tag{C.1}$$

The hydrostatic axis in principal stress space has the equation

$$\sigma_1 = \sigma_2 = \sigma_3 \tag{C.2}$$

and the unit vector pointing away from the origin along the hydrostatic axis, having equal positive components along each of the three principal stress axes, is the octahedral unit normal,

$$\overline{n}_{OCT} = \frac{1}{\sqrt{3}} (\overline{e}_1 + \overline{e}_2 + \overline{e}_3) \tag{C.3}$$

The plane through a stressed point for which n_{OCT} is the unit normal vector is called the octrahedral plane. Referring to Equations (A.8) or (A.12), the octahedral stress vector, i.e., the stress vector acting on the octahedral plane, is

$$\overline{\sigma}_{OCT} = \frac{1}{\sqrt{3}} (\sigma_1 \overline{e}_1 + \sigma_2 \overline{e}_2 + \sigma_3 \overline{e}_3) \tag{C.4}$$

125

The normal component of the octahedral stress vector, called the octahedral normal stress, is

$$\sigma_{OCT} = \overline{\sigma}_{OCT} \cdot \overline{n}_{OCT} = \frac{\sigma_1 + \sigma_2 + \sigma_3}{3} = \frac{I_1}{3} \tag{C.5}$$

and the tangential or in-plane component of $\overline{\sigma}_{OCT}$, called the octahedral shear stress vector, is

$$\overline{\tau}_{OCT} = \overline{\sigma}_{OCT} - (\overline{\sigma}_{OCT} \cdot \overline{n}_{OCT}) \, \overline{n}_{OCT}$$

$$= \frac{1}{\sqrt{3}} (\sigma_1 \overline{e}_1 + \sigma_2 \overline{e}_2 + \sigma_3 \overline{e}_3) - \frac{\sigma_{OCT}}{\sqrt{3}} (\overline{e}_1 + \overline{e}_2 + \overline{e}_3)$$

$$= \frac{1}{\sqrt{3}} (s_1 \overline{e}_1 + s_2 \overline{e}_2 + s_3 \overline{e}_3) \tag{C.6}$$

The magnitude of the octahedral shear stress vector, called the octahedral shear stress, is

$$\tau_{OCT} = \sqrt{\overline{\tau}_{OCT} \cdot \overline{\tau}_{OCT}} = \sqrt{\frac{s_1^2 + s_2^2 + s_3^2}{3}} = \sqrt{\frac{2J_2}{3}} \tag{C.7}$$

so that Equations (A.68) can be written in the form

$$s_1 = \sqrt{2} \, \tau_{OCT} \cos \omega_1 \tag{C.8a}$$

$$s_2 = \sqrt{2} \, \tau_{OCT} \cos \omega_2 \tag{C.8b}$$

$$s_3 = \sqrt{2} \, \tau_{OCT} \cos \omega_3 \tag{C.8c}$$

When plotting triaxial stress data it is convenient to work with a mathematical vector, $\overline{\sigma}$, called the principal stress vector, shown in Figure (C.2), the components of which are the principal stresses, i.e.

126

$$\overline{\sigma} = \sqrt{3}\,\overline{\sigma}_{OCT} = \sigma_1\overline{e}_1 + \sigma_2\overline{e}_2 + \sigma_3\overline{e}_3 \tag{C.9}$$

It is also convenient to define a second set of mutually orthogonal, right-handed unit vectors, called the octahedral unit vectors, according to the relations

$$\overline{n}_3 = \overline{n}_{OCT} = \frac{1}{\sqrt{3}}\,(\,\overline{e}_1 + \overline{e}_2 + \overline{e}_3) \tag{C.10}$$

$$\overline{n}_1 = \frac{1}{\sqrt{2}}\,(\,\overline{e}_1 - \overline{e}_3) \tag{C.11}$$

$$\overline{n}_2 = \overline{n}_3 \times \overline{n}_1 = \frac{1}{\sqrt{6}}\,\begin{vmatrix} \overline{e}_1 & \overline{e}_2 & \overline{e}_3 \\ 1 & 1 & 1 \\ 1 & 0 & -1 \end{vmatrix}$$

$$= \frac{-\overline{e}_1 + 2\overline{e}_2 - \overline{e}_3}{\sqrt{6}} \tag{C.12}$$

The unit vectors $\overline{n}_1$ and $\overline{n}_2$ are both normal to $\overline{n}_{OCT}$ and therefore both lie in the octahedral plane. The unit vector $\overline{n}_1$ has a positive $\overline{e}_1$ component, an equal and opposite $\overline{e}_3$ component, and no $\overline{e}_2$ component. The $\overline{n}_1$, $\overline{n}_2$, and $\overline{n}_3$ components of the principal stress vector are

$$x = \overline{\sigma} \cdot \overline{n}_1 = \frac{\sigma_1 - \sigma_3}{\sqrt{2}} = \frac{s_1 - s_3}{\sqrt{2}} \tag{C.13}$$

$$y = \overline{\sigma} \cdot \overline{n}_2 = \frac{2\sigma_2 - \sigma_1 - \sigma_3}{\sqrt{6}} = \frac{2s_2 - s_1 - s_3}{\sqrt{6}} = \sqrt{\frac{3}{2}}\,s_2 \tag{C.14}$$

$$z = \overline{\sigma} \cdot \overline{n}_3 = \frac{\sigma_1 + \sigma_2 + \sigma_3}{\sqrt{3}} = \sqrt{3}\,\sigma_{OCT} \tag{C.15}$$

127

The octahedral plane component of the principal stress vector is

$$\overline{R} = \overline{\sigma} - (\overline{\sigma} \cdot \overline{n}_3) \, \overline{n}_3$$

$$= (\sigma_1 \overline{e}_1 + \sigma_2 \overline{e}_2 + \sigma_3 \overline{e}_3) - \sqrt{3} \, \tau_{OCT} \cdot \frac{1}{\sqrt{3}} \, (\overline{e}_1 + \overline{e}_2 + \overline{e}_3)$$

$$= s_1 \overline{e}_1 + s_2 \overline{e}_2 + s_3 \overline{e}_3 \qquad (C.16)$$

and the magnitude of the octahedral plane component of the principal stress vector is

$$R = \sqrt{\overline{R} \cdot \overline{R}} = \sqrt{s_1^2 + s_2^2 + s_3^2} = \sqrt{2J_2} = \sqrt{3} \, \tau_{OCT} \qquad (C.17)$$

It can easily be verified by direct expansion, using Equations (C.13) and (C.14), that

$$x^2 + y^2 = \frac{s_1^2 - 2s_1 s_3 + s_3^2}{2} + \frac{3s_2^2}{2}$$

$$= \frac{s_1^2 - 2s_1 s_3 + s_3^2 + 2s_2^2 + (-s_1 - s_3)^2}{2}$$

$$= s_1^2 + s_2^2 + s_3^2 = R^2 = 2J_2 = 3 \, \tau_{OCT}^2 \qquad (C.18)$$

Now Equations (C.13) and (C.14) also yield

$$\frac{y}{x} = \frac{1}{\sqrt{3}} \left(\frac{2\sigma_2 - \sigma_1 - \sigma_3}{\sigma_1 - \sigma_3} \right) = \frac{1}{\sqrt{3}} \left(\frac{2s_2 - s_1 - s_3}{s_1 - s_3} \right) = \frac{\mu}{\sqrt{3}} \qquad (C.19)$$

where μ is Lode's parameter, defined by Equation (A.50), so that, referring to Figure (C.3),

$$y = R \left(\frac{\mu}{\sqrt{3 + \mu^2}} \right) \qquad (C.20)$$

128

or

$$\sqrt{\frac{3}{2}} \, s_2 = \sqrt{3} \, \tau_{OCT} \left(\frac{\mu}{\sqrt{3 + \mu^2}} \right)$$

or

$$s_2 = \sqrt{2} \, \tau_{OCT} \left(\frac{\mu}{\sqrt{3 + \mu^2}} \right) \qquad (C.21)$$

Comparison of Equations (C.8b) and (C.21) shows that

$$\cos \omega_2 = \frac{\mu}{\sqrt{3 + \mu^2}} \qquad (C.22)$$

which can be checked, since

$$\cos 3\omega_2 = 4 \cos^3 \omega_2 - 3 \cos \omega_2$$

$$= \frac{4\mu^3}{(3 + \mu^2)^{3/2}} - \frac{3\mu}{(3 + \mu^2)^{1/2}}$$

$$= \frac{4\mu^3 - 3\mu (3 + \mu^2)}{(3 + \mu^2)^{3/2}} = \frac{\mu^3 - 9\mu}{(3 + \mu^2)^{3/2}}$$

$$= - \frac{\mu(3 + \mu)(3 - \mu)}{(3 + \mu^2)^{3/2}} \qquad (C.23)$$

which agrees with Equation (A.63). Thus, Equations (C.13) and (C.14) can be written in the form

$$x = \sqrt{3} \, \tau_{OCT} \sin \omega_2 \qquad (C.24)$$

$$y = \sqrt{3} \, \tau_{OCT} \cos \omega_2 \qquad (C.25)$$

A common equation for soil shear strength is the Mohr-Coulomb equation, which can be written in the form

$$q = (d + p) \sin \bar{\phi} \qquad \text{(C.26)}$$

where the friction angle, $\bar{\phi}$, may depend on μ; d is a constant material parameter; and

$$p = \frac{\sigma_1 + \sigma_3}{2} \qquad \text{(C.27)}$$

$$q = \frac{\sigma_1 - \sigma_3}{2} \qquad \text{(C.28)}$$

Now Equations (C.13) and (C.14) can also be written in the form

$$x = \sqrt{2}\, q \qquad \text{(C.29)}$$

$$y = \frac{2(\sigma_1 + \sigma_2 + \sigma_3) - 3(\sigma_1 - \sigma_3)}{\sqrt{6}} = \sqrt{6}\, (\sigma_{OCT} - p) \qquad \text{(C.30)}$$

Substituting Equation (C.26) into Equation (C.29), then solving for p yields

$$x = \sqrt{2}\, (d + p) \sin \bar{\phi} \qquad \text{(C.31)}$$

$$p = \frac{x}{\sqrt{2} \sin \bar{\phi}} - d \qquad \text{(C.32)}$$

and substituting Equation (C.32) into Equation (C.30) yields

$$y = \sqrt{6} \left(d + \sigma_{OCT} - \frac{x}{\sqrt{2} \sin \bar{\phi}} \right)$$

$$= \sqrt{6}\, (d + \sigma_{OCT}) - \frac{\sqrt{3}}{\sin \bar{\phi}}\, x \qquad \text{(C.33)}$$

Finally, if we set

$$x' = \frac{x}{d + \sigma_{OCT}} \qquad \text{(C.34)}$$

130

$$y' = \frac{y}{d + \sigma_{OCT}} \tag{C.35}$$

then Equations (C.19) and (C.33) yield

$$\frac{y'}{x'} = \frac{\mu}{\sqrt{3}} \tag{C.36}$$

$$y' = \sqrt{6} - \frac{3}{\sin \overline{\phi}} \ x' \tag{C.37}$$

where, when d = 0,

$$\sin \overline{\phi} = \frac{1 - 3}{2 + 3} \tag{C.38}$$

. . . . show a rapid method for plotting triaxial
. . . . plane, based on Equations (C.36) and (C.37),
. . . . that equation (C.26) applies [Merkle (1971:346)].
. . . . soil shear failure criterion than the
. . . . in which the octahedral shear stress is a
. . . . normal stress and the octahedral polar angle,
. . . . . .

$$\cdots \cdots \cdots \tag{C.39}$$

In this case a unique octahedral cross section can be obtained by
plotting

$$\frac{R}{P(\sigma_{OCT})} = \frac{\sqrt{3} \ \sigma_{OCT}}{P(\sigma_{OCT})} = \sqrt{3} \ Q(3\omega) \tag{C.40}$$

131
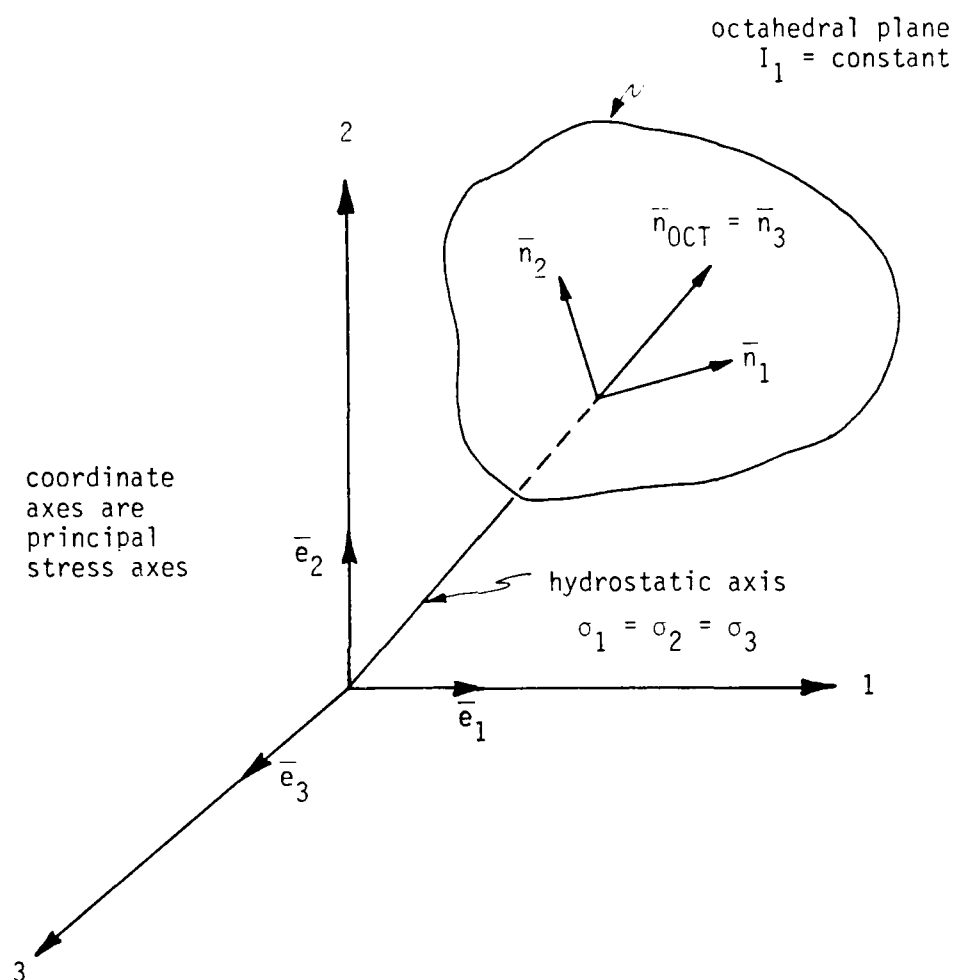
Figure C.1. Octahedral unit vectors in principal
stress space.
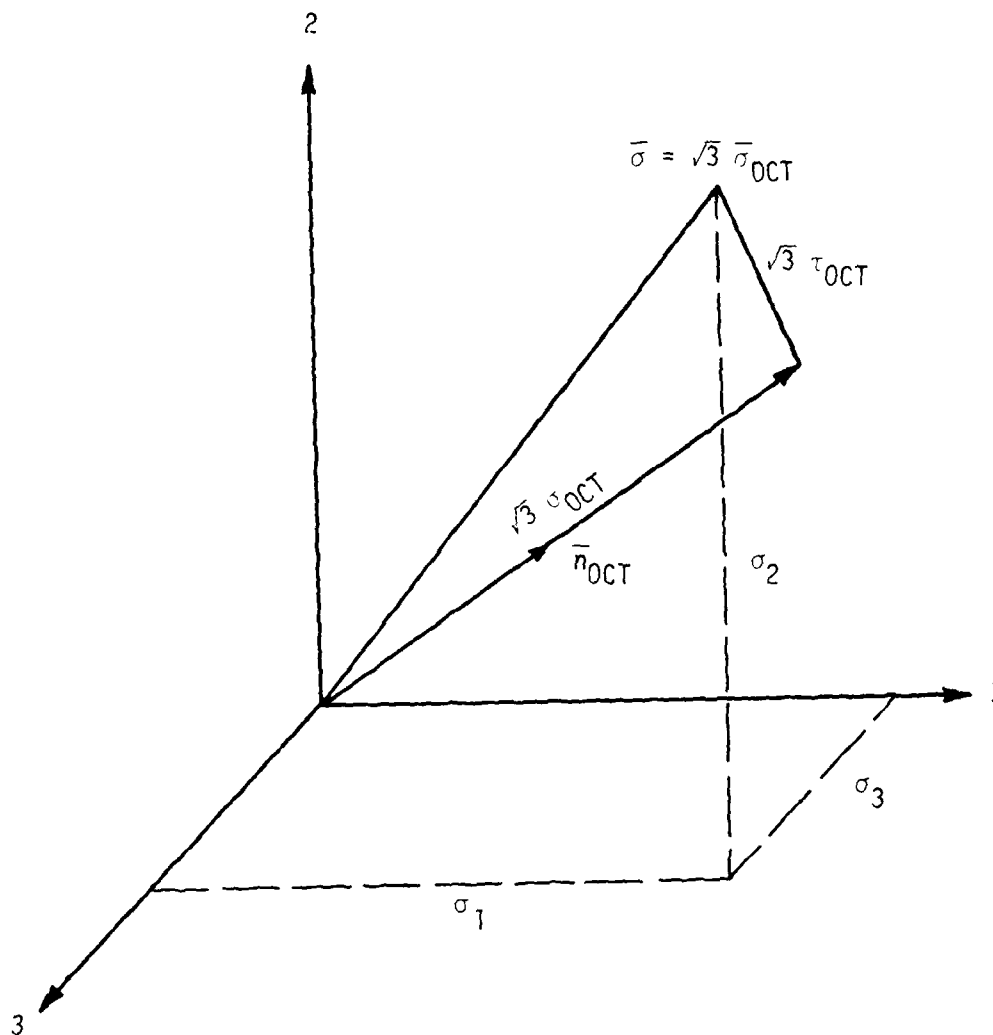
Figure C.2. Principal stress vector in principal
stress s, ce.

133
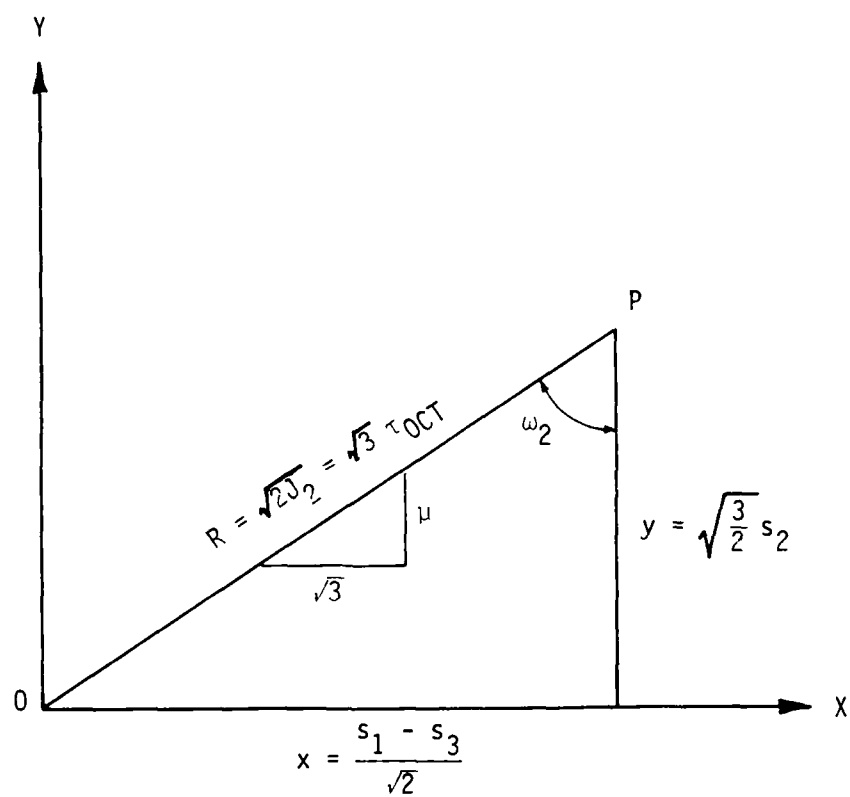
Figure C.3. Octahedral Plane Geometry.
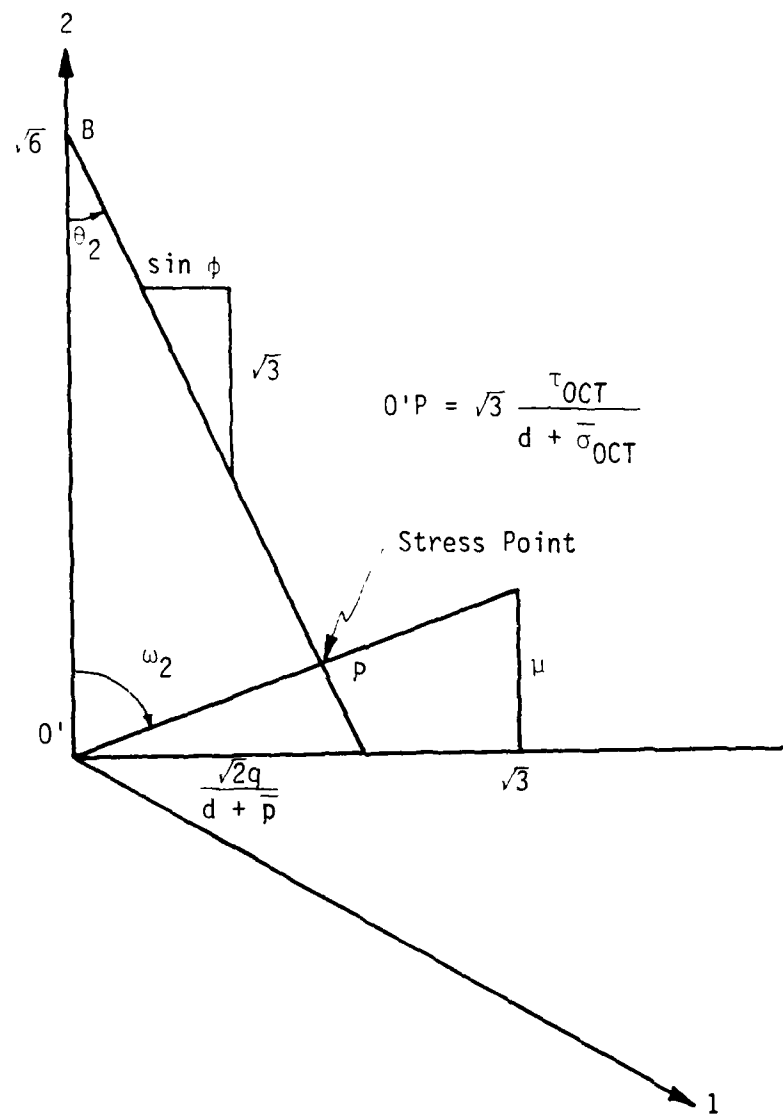
Figure C.4. Location of a Stress Point in the Octahedral Plane.

$$O'P = \sqrt{3} \; \frac{\tau_{OCT}}{d + \overline{\sigma}_{OCT}}$$

135
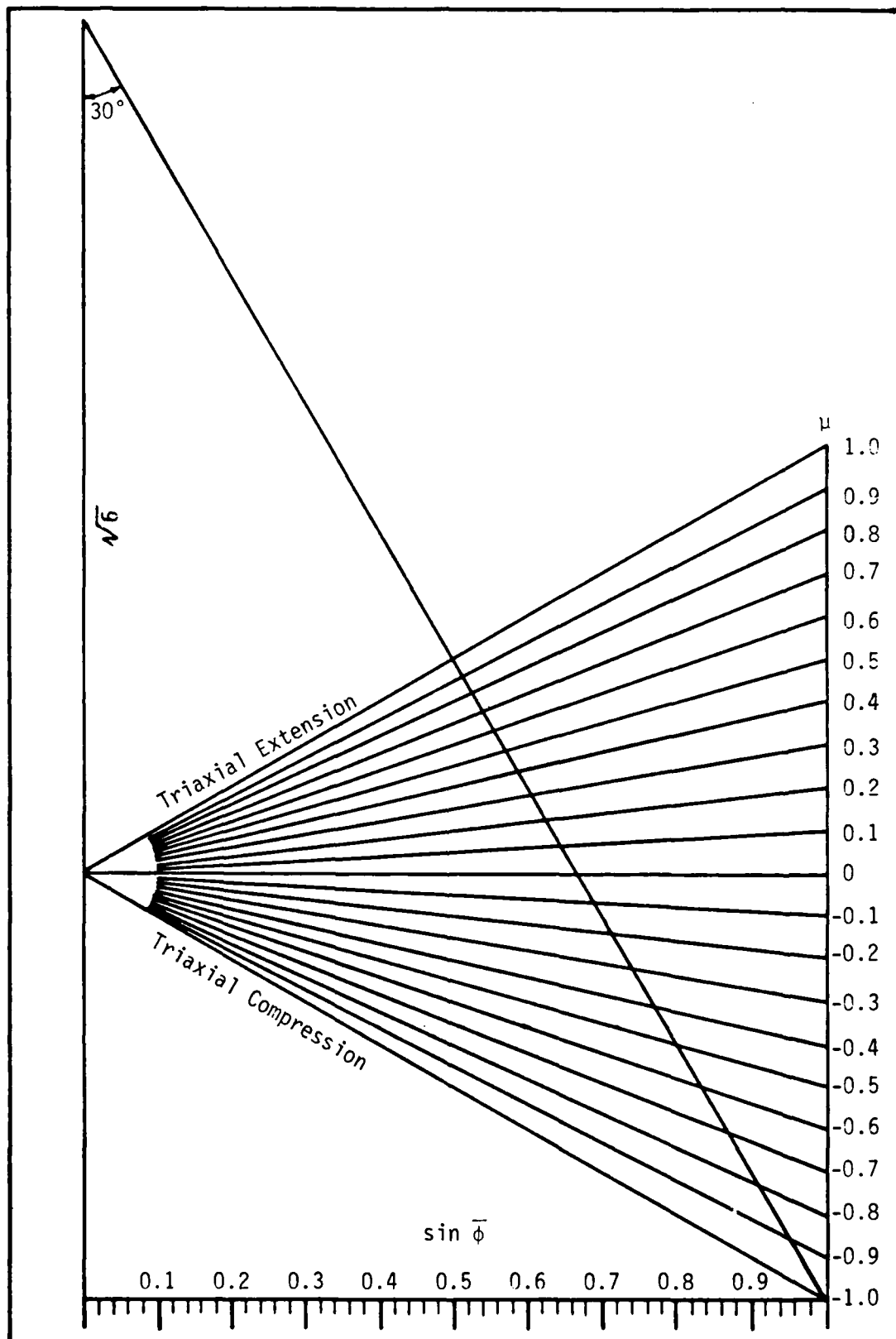
Figure C.5.   Form for plotting strength data in the octahedral plane.

APPENDIX D

BASIC EQUATIONS OF ELASTOPLASTICITY

If a cylindrical soil specimen is consolidated under an isotropic stress $(\bar{\sigma}_{1c} = \bar{\sigma}_{2c} = \bar{\sigma}_{3c})$, then subjected to drained compressive loading, unloading, and reloading under constant confining stress $(\bar{\sigma}_2 = \bar{\sigma}_3 = \bar{\sigma}_{3c}; \bar{\sigma}_1 \geq \bar{\sigma}_{3c})$, the stress-strain curve appears as shown in Figure (D.1). Several important features are shown in Figure (D.1):

1. The stress-strain curve is nonlinear, even for small stresses and strains.

2. Upon unloading from point A, some of the total strain is recoverable (BE), but the remainder is irrecoverable (OB).

3. Reloading occurs along a path (BC) somewhat different from the unloading path (AB), until nearing the previous maximum stress. At this point additional loading approaches and proceeds along what appears to be a continuation of the virgin compression curve (OA), with little apparent further influence of previous unloading or reloading.

4. Unloading and reloading occur along paths whose secant from zero to maximum stress has a slope very close to that of the initial tangent to the stress-strain curve. This means that the irrecoverable portion of any strain increment is essentially the difference between the total strain increment and the strain increment associated with a straight line stress-strain curve having a slope equal to that of the initial tangent to the actual stress-strain curve.

By convention, recoverable strains are called elastic, and irrecoverable strains are called plastic. If the unloading and reloading curves in Figure (D.1) both retraced the virgin loading curve (OA) instead of following curves (AB) and (BC) the stress-strain behavior would be called nonlinearly elastic. As it is, the linear portion of the stress-strain behavior shown in Figure (D.1) is elastic, and the nonlinear portion is plastic. Since some of the stress-strain behavior is elastic

137

and the rest is plastic, the overall stress-strain behavior is called elastoplastic.

Multiaxial elastoplasticity theory extrapolates the above one-dimensional stress-strain observations, and assumes that plastic strains are superimposed on elastic strains. Thus

$$\epsilon_{ij} = \epsilon_{ij}^e + \epsilon_{ij}^p \qquad (D.1)$$

with a similar relation holding for each strain increment.

$$d\epsilon_{ij} = d\epsilon_{ij}^e + d\epsilon_{ij}^p \qquad (D.2)$$

When the elastic behavior is isotropic, the stress increments are related to the elastic strain increments by the equations

$$d\sigma_{ij} = C_{ijkl}^e \; d\epsilon_{kl}^e \qquad (D.3)$$

where the elastic incremental stiffness tensor is given by the expression

$$C_{ijkl}^e = MK_0 \delta_{ij} \delta_{kl} + M(1-K_0) \; \delta_{ik} \delta_{jl} \qquad (D.4)$$

and M = constrained elastic modulus

K_0 = coefficient of elastic lateral stress at rest.

The parameters M and K_0 are sometimes assumed to be constant, independent of strain, and are sometimes assumed to vary in a prescribed manner.

Once the possibility of plastic strains is recognized, four questions arise:

1. Can plastic strains occur?

2. If they occur, what will be their relative algebraic values?

138

3. If they occur, what will be their actual algebraic values?

4. Will they occur?

Obviously, Question 2 is a subset of Question 3. The reasons for listing the two questions separately are the mathematical and physical conditions used to answer them, which are explained below.

The mathematical theory of elastoplasticity presented here contains four parts, each needed to answer one of the above four questions:

1. A yield criterion, assumed to be of the form

$$f(\sigma_{ij}, \varepsilon_{ij}^p) = 0 \qquad (D.5)$$

satisfaction of which is a necessary condition for the occurrence of additional plastic strain at a point.

2. A plastic potential function, $g(\sigma_{ij})$, for which

$$d\varepsilon_{ij}^p = d\lambda \frac{\partial g}{\partial \sigma_{ij}} \qquad (D.6)$$

which gives the relative algebraic values of the plastic strain increments, i.e. the direction of the plastic strain increment vector in stress space. Equation (D.6) is called a flow rule, and the scalar constant $d\lambda$ is determined by the next condition.

3. The requirement that Equation (D.5) be satisfied not only at the beginning of yielding, but throughout yielding as well, so that

$$df = \frac{\partial f}{\partial \sigma_{ij}} d\sigma_{ij} + \frac{\partial f}{\partial \varepsilon_{ij}^p} d\varepsilon_{ij}^p = 0 \qquad (D.7)$$

Equation (D.7) is called the consistency condition, and yields the value of $d\lambda$ in Equation (D.6). It therefore permits calculation of the actual algebraic values of the plastic strain increments.

4. The requirement that the calculated plastic strain increments lead to a positive plastic work increment,

$$dW^p = \sigma_{ij} d\varepsilon_{ij}^p > 0 \qquad (D.8)$$

139

Equation (D.8) is called the dissipation condition. If it is not satisfied, then additional plastic strain does not occur at a point, in which case all strain increments are elastic.

Equations (D.5), (D.6), (D.7), and (D.8) have been written assuming one yield criterion (or yield surface), and one plastic potential function. There can, however, be more than one yield surface, and an equal number of corresponding plastic potential functions. If this happens, then the above four equations apply to each active yield surface. Thus, if m yield surfaces are active, there will be a set of plastic strain increments for each active yield surface, the values of which are determined by 4m equations (counting Equation (D.6) as one tensor equation.)

The stress tensor σ_{ij} contains nine elements,

$$\sigma_{ij} = \begin{bmatrix} \sigma_{11} & \sigma_{12} & \sigma_{13} \\ \sigma_{21} & \sigma_{22} & \sigma_{23} \\ \sigma_{31} & \sigma_{32} & \sigma_{33} \end{bmatrix} \qquad (D.9)$$

but only six are independent because

$$\sigma_{ji} = \sigma_{ij} \qquad (D.10)$$

Each stress component, σ_{ij}, can be expressed as a function of the three principal stresses, σ_1, σ_2, σ_3, and the nine direction cosines of the three principal stress axes with respect to the arbitrary Cartesian axes used to define the σ_{ij}. However, if a unit vector pointing in the direction of the ith principal stress axis is $\overline{e}_i$, then because the three principal stress axes are orthogonal, we have

$$\overline{e}_i \cdot \overline{e}_j = \delta_{ij} \qquad (D.11)$$

Equation (D.11) represents six independent scalar equations involving the nine principal stress axis direction cosines. Thus, there are only three independent principal stress axis direction cosines. Let them be α_1, α_2, and α_3. Then we can write

$$\sigma_{ij} = \sigma_{ij}(\sigma_1, \sigma_2, \sigma_3; \alpha_1, \alpha_2, \alpha_3) \tag{D.12}$$

If a material is isotropic, the dependencies of the yield function, f, in Equation (D.5) and of the plastic potential function, g, in Equation (D.6) on the principal stresses σ_1, σ_2, and σ_3 are independent of the orientation of the principal stress axes with respect to the coordinate axes. This means that not only do α_1, α_2, and α_3 not appear in the expressions for f or g, but also the stress functions which do appear in those expressions are insensitive to subscript interchanges, i.e., they are symmetric functions of σ_1, σ_2 and σ_3. The total stress invariants I_1, I_2, and I_3 satisfy the required conditions of symmetry. They are, from Appendix A:

$$I_1 = \sigma_{11} + \sigma_{22} + \sigma_{33} \tag{A.28}$$

$$I_2 = -\left(\begin{vmatrix} \sigma_{11} & \sigma_{12} \\ \sigma_{21} & \sigma_{22} \end{vmatrix} + \begin{vmatrix} \sigma_{22} & \sigma_{23} \\ \sigma_{32} & \sigma_{33} \end{vmatrix} + \begin{vmatrix} \sigma_{33} & \sigma_{31} \\ \sigma_{13} & \sigma_{11} \end{vmatrix} \right) \tag{A.29}$$

$$I_3 = \begin{vmatrix} \sigma_{11} & \sigma_{12} & \sigma_{13} \\ \sigma_{21} & \sigma_{22} & \sigma_{23} \\ \sigma_{31} & \sigma_{32} & \sigma_{33} \end{vmatrix} \tag{A.30}$$

Equation (D.6) gives the relative values of the plastic strain increments, from which the relative values of the principal plastic strain

141

increments and the orientation of the principal plastic strain increment
axes can be determined. Since the plastic potential function, g, is a
function of the three total stress invariants, I_1, I_2, and I_3, given
by Equations (A.28), (A.29), and (A.30), we have

$$g = g(I_1, I_2, I_3) \tag{D.13}$$

so that Equation (D.6) can be written in the form

$$d\varepsilon_{ij}^p = d\lambda \frac{\partial g}{\partial \sigma_{ij}} = d\lambda \left(\frac{\partial g}{\partial I_1} \frac{\partial I_1}{\partial \sigma_{ij}} + \frac{\partial g}{\partial I_2} \frac{\partial I_2}{\partial \sigma_{ij}} + \frac{\partial g}{\partial I_3} \frac{\partial I_3}{\partial \sigma_{ij}} \right) \tag{D.14}$$

Now Equations (A.28) and (A.29) yield

$$\frac{\partial I_1}{\partial \sigma_{ij}} = \begin{bmatrix} 1 & 0 & 0 \\ 0 & 1 & 0 \\ 0 & 0 & 1 \end{bmatrix} = \delta_{ij} \tag{D.15}$$

$$\frac{\partial I_2}{\partial \sigma_{ij}} = \begin{bmatrix} -(\sigma_{22} + \sigma_{33}) & \sigma_{21} & \sigma_{31} \\ \sigma_{12} & -(\sigma_{33} + \sigma_{11}) & \sigma_{32} \\ \sigma_{13} & \sigma_{23} & -(\sigma_{11} + \sigma_{22}) \end{bmatrix}$$

$$= \sigma_{ji} - I_1 \delta_{ij} = \sigma_{ij} - I_1 \delta_{ij} \tag{D.16}$$

To obtain the derivatives $\partial I_3 / \partial \sigma_{ij}$ we first expand the expression for
I_3 in Equation (A.30). Referring to the development of Equation (A.27),
we obtain

$$\tag{D.17}$$

$$I_3 = |\underline{\sigma}| = \begin{vmatrix} \sigma_{11} & \sigma_{12} & \sigma_{13} \\ \sigma_{21} & \sigma_{22} & \sigma_{23} \\ \sigma_{31} & \sigma_{32} & \sigma_{33} \end{vmatrix} = \begin{array}{l} \sigma_{11}\sigma_{22}\sigma_{33} + \sigma_{12}\sigma_{23}\sigma_{31} + \sigma_{13}\sigma_{21}\sigma_{32} \\ - \sigma_{11}\sigma_{23}\sigma_{32} - \sigma_{12}\sigma_{21}\sigma_{33} - \sigma_{13}\sigma_{22}\sigma_{31} \end{array}$$

142

Differentiation of Equation (D.17) now yields

$$\frac{\partial I_3}{\partial \sigma_{11}} = \sigma_{22}\sigma_{33} - \sigma_{23}\sigma_{32} = \Sigma_{11} \tag{D.18a}$$

$$\frac{\partial I_3}{\partial \sigma_{12}} = -(\sigma_{21}\sigma_{33} - \sigma_{23}\sigma_{31}) = \Sigma_{12} \tag{D.18b}$$

$$\frac{\partial I_3}{\partial \sigma_{13}} = \sigma_{21}\sigma_{32} - \sigma_{22}\sigma_{31} = \Sigma_{13} \tag{D.18c}$$

$$\frac{\partial I_3}{\partial \sigma_{21}} = -(\sigma_{12}\sigma_{33} - \sigma_{13}\sigma_{32}) = \Sigma_{21} \tag{D.18d}$$

$$\frac{\partial I_3}{\partial \sigma_{22}} = \sigma_{11}\sigma_{33} - \sigma_{13}\sigma_{31} = \Sigma_{22} \tag{D.18e}$$

$$\frac{\partial I_3}{\partial \sigma_{23}} = -(\sigma_{11}\sigma_{32} - \sigma_{12}\sigma_{31}) = \Sigma_{23} \tag{D.18f}$$

$$\frac{\partial I_3}{\partial \sigma_{31}} = \sigma_{12}\sigma_{23} - \sigma_{13}\sigma_{22} = \Sigma_{31} \tag{D.18g}$$

$$\frac{\partial I_3}{\partial \sigma_{32}} = -(\sigma_{11}\sigma_{23} - \sigma_{13}\sigma_{21}) = \Sigma_{32} \tag{D.18h}$$

$$\frac{\partial I_3}{\partial \sigma_{33}} = \sigma_{11}\sigma_{22} - \sigma_{12}\sigma_{21} = \Sigma_{33} \tag{D.18i}$$

where Σ_{ij} = cofactor or signed minor of σ_{ij}, arising in the Laplace expansion of $|\underline{\sigma}|$, which is

$$|\underline{\sigma}| = I_3 = \frac{1}{3} \sigma_{ij} \Sigma_{ij} = \frac{1}{3} \text{Tr} (\underline{\sigma} \ \underline{\Sigma}) \tag{D.19}$$

The compact form of Equations (D.18) is

$$\frac{\partial I_3}{\partial \sigma_{ij}} = \Sigma_{ij} \tag{D.20}$$

Substitution of Equations (D.15), (D.16), and (D.20) into Equation (D.14) yields

$$d\epsilon^p_{ij} = d\lambda [\frac{\partial g}{\partial I_1} \delta_{ij} + \frac{\partial g}{\partial I_2}(\sigma_{ij} - I_1 \delta_{ij}) + \frac{\partial g}{\partial I_3} \Sigma_{ij}] \tag{D.21}$$

Since $\underline{\Sigma}$ has the same principal axes as does $\underline{\sigma}$, it follows from Equation (D.21) that $\underline{d\epsilon}^p$ also has the same principal axes as does $\underline{\sigma}$. This condition is a consequence of the assumption of material isotropy, and not an independent assumption.

A convenient assumption concerning the dependence of the yield function, f, in Equation (D.5) on plastic strain is that f is a function of stress, σ_{ij}, and plastic work, W^p, where plastic work is in turn a function of plastic strain [Malvern (1969:367)].

$$f(\sigma_{ij}, \epsilon^p_{ij}) = f[\sigma_{ij}, W^p(\epsilon^p_{ij})] \tag{D.22}$$

The plastic work increment in Equation (D.8) can be written in the form

$$dW^p = \frac{\partial W^p}{\partial \epsilon^p_{ij}} d\epsilon^p_{ij} = \sigma_{ij} d\epsilon^p_{ij} \tag{D.23}$$

so that

$$\frac{\partial W^p}{\partial \epsilon^p_{ij}} = \sigma_{ij} \tag{D.24}$$

144

Substitution of Equation (D.21) into Equation (D.23) yields

$$dW^p = \sigma_{ij} d\varepsilon^p_{ij} = d\lambda \left\{ \frac{\partial g}{\partial I_1} \text{Tr}(\underline{\sigma}) + \frac{\partial g}{\partial I_2} \left[\text{Tr}(\underline{\sigma}^2) - I_1^2 \right] + \frac{\partial g}{\partial I_3} I_3 \text{Tr}(\underline{\sigma}\,\underline{\sigma}) \right\}$$

$$= d\lambda \left[\frac{\partial g}{\partial I_1} I_1 + 2 \frac{\partial g}{\partial I_2} I_2 + 3 \frac{\partial g}{\partial I_3} I_3 \right] = h d\lambda \qquad (D.25)$$

where

$$h = \frac{\partial g}{\partial I_1} I_1 + 2 \frac{\partial g}{\partial I_2} I_2 + 3 \frac{\partial g}{\partial I_3} I_3 \qquad (D.26)$$

The above expression for h agrees with Euler's theorem, since the invariants I_1, I_2, and I_3 are homogeneous functions of degree 1, 2, and 3, respectively [Sokolnikoff and Redheffer (1966:325)].

Equation (D.13), which assumes the plastic potential function depends explicitly on the total stress invariants, I_1, I_2, and I_3, gives reasonably good results for stress or strain paths involving mainly *volumetric compression*. However, *shear strength data*, plotted in the octahedral plane as described in Appendix C, suggest that a plastic potential function for stress or strain paths involving significant shear deformation is better assumed to depend explicitly on the first total stress invariant, I_1, and the second and third deviator stress invariants, J_2, and J_3, so that

$$g = g(I_1, J_2, J_3) \qquad (D.27)$$

Equation (D.6) then yields

$$d\varepsilon^p_{ij} = d\lambda \frac{\partial g}{\partial \sigma_{ij}} = d\lambda \left[\frac{\partial g}{\partial I_1} \frac{\partial I_1}{\partial \sigma_{ij}} + \frac{\partial g}{\partial J_2} \frac{\partial J_2}{\partial s_{kl}} \frac{\partial s_{kl}}{\partial \sigma_{ij}} + \frac{\partial g}{\partial J_3} \frac{\partial J_3}{\partial s_{kl}} \frac{\partial s_{kl}}{\partial \sigma_{ij}} \right]$$
$$(D.28)$$

145

where

$$\frac{\partial I_1}{\partial \sigma_{ij}} = \delta_{ij} \tag{D.15}$$

and by analogy with Equations (D.16) and (D.20)

$$\frac{\partial J_2}{\partial s_{kl}} = s_{kl} \tag{D.29}$$

$$\frac{\partial J_3}{\partial s_{kl}} = S_{kl} \tag{D.30}$$

and since Equation (A.34) can be written in the form

$$s_{kl} = \sigma_{kl} - \frac{I_1}{3} \delta_{kl} \tag{D.31}$$

we have

$$\frac{\partial s_{kl}}{\partial \sigma_{ij}} = \delta_{ik}\delta_{jl} - \frac{1}{3} \delta_{ij}\delta_{kl} \tag{D.32}$$

Substitution of Equations (D.15), (D.29), (D.30), and (D.32) into Equation (D.28) now yields

$$
\begin{aligned}
d\varepsilon_{ij}^p &= d\lambda \left[\frac{\partial g}{\partial I_1} \delta_{ij} + \frac{\partial g}{\partial J_2} s_{kl} \left(\delta_{ik}\delta_{jl} - \frac{1}{3} \delta_{ij}\delta_{kl} \right) \right. \\
&\qquad\qquad \left. + \frac{\partial g}{\partial J_3} S_{kl} \left(\delta_{ik}\delta_{jl} - \frac{1}{3} \delta_{ij}\delta_{kl} \right) \right] \\
&= d\lambda \left[\frac{\partial g}{\partial I_1} \delta_{ij} + \frac{\partial g}{\partial J_2} s_{ij} + \frac{\partial g}{\partial J_3} \left(S_{ij} + \frac{J_2}{3} \delta_{ij} \right) \right] \tag{D.33}
\end{aligned}
$$

146

The plastic work increment in Equations (D.8) or (D.23) is therefore

$$dW^P = \sigma_{ij}d\epsilon^P_{ij} = \left(\frac{I_1}{3}\delta_{ij} + s_{ij} \quad d\epsilon^P_{ij}\right)$$

$$= d\lambda\left[\frac{\partial g}{\partial I_1}\frac{I_1}{3}\text{Tr}(\underline{I}) + \frac{\partial g}{\partial J_2}\text{Tr}(\underline{s}^2) + \frac{\partial g}{\partial J_3}\text{Tr}(\underline{s}\,\underline{S})\right]$$

$$= d\lambda\left[\frac{\partial g}{\partial I_1}I_1 + 2\frac{\partial g}{\partial J_2}J_2 + 3\frac{\partial g}{\partial J_3}J_3\right] = hd\lambda \tag{D.34}$$

where

$$h = \frac{\partial g}{\partial I_1}I_1 + 2\frac{\partial g}{\partial J_2}J_2 + 3\frac{\partial g}{\partial J_3}J_3 \tag{D.35}$$

Comparison of Equations (D.26) and (D.35) shows that

$$2\frac{\partial g}{\partial I_2}I_2 + 3\frac{\partial g}{\partial I_3}I_3 = 2\frac{\partial g}{\partial J_2}J_2 + 3\frac{\partial g}{\partial J_3}J_3 \tag{D.36}$$

Finally, the plastic work increment, dW^P, can be expressed as the sum of a volumetric term and a deviatoric or distortional term. This is done by expressing the stress components, σ_{ij}, and plastic strain increments, $d\epsilon^P_{ij}$, as the sums of their volumetric and deviatoric components.

$$\sigma_{ij} = \frac{\sigma_{kk}}{3}\delta_{ij} + s_{ij} \tag{D.37}$$

$$d\epsilon^P_{ij} = \frac{d\epsilon^P_{mm}}{3}\delta_{ij} + de^P_{ij} \tag{D.38}$$

The expression for the plastic work increment can now be written in the form

$$dW^P = \sigma_{ij}d\epsilon^P_{ij} = \left(\frac{\sigma_{kk}}{3}\delta_{ij} + s_{ij}\right)\left(\frac{d\epsilon^P_{mm}}{3}\delta_{ij} + de^P_{ij}\right)$$

$$= \frac{\sigma_{kk}}{3}d\epsilon^P_{mm} + s_{ij}de^P_{ij} \tag{D.39}$$

The first term in Equation (D.39) is the volumetric plastic work increment; the second term is the deviatoric or distortional plastic work increment.

147
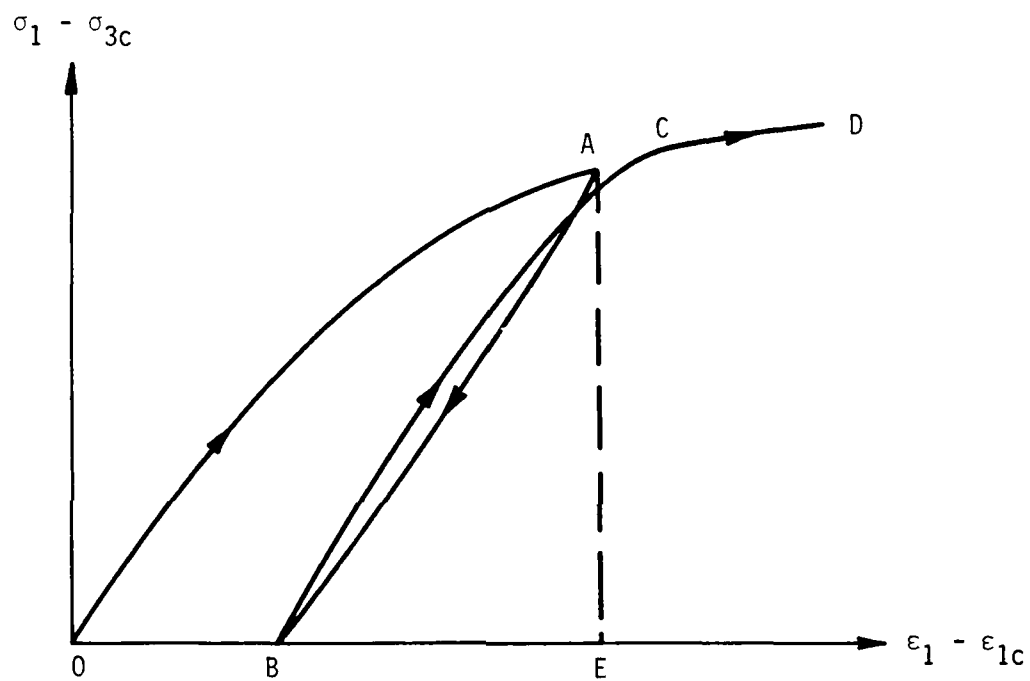
Figure D.1. Drained triaxial compression stress-strain curve.

APPENDIX E

VECTOR REPRESENTATION OF A GENERAL STRESS OR STRAIN STATE

Consider the two-dimensional rectangular Cartesian coordinate system (X,Y) shown in Figure (E.1a). The X and Y axes define a two-dimensional vector space, and the line $x = y$ is a one-dimensional vector subspace. Point P in the one-dimensional subspace can be located by the single coordinate $s = \sqrt{2}\, x$.

In three dimensions a similar situation exists, as shown in Figure (E.1b). The X,Y, and Z axes define a three-dimensional vector space, and the plane $x = y$ containing the Z axis is a two-dimensional vector subspace. Point P in the two-dimensional subspace can be located by the two coordinates $(s = \sqrt{2}\, x, z)$.

Generalization of the above analysis for an n-dimensional vector space is straightforward. If an n-dimensional vector space is defined by the coordinates x_i $(i = 1,n)$, then the hyperplane $x_i = x_j$ $(i \neq j)$ is an (n-1)-dimensional vector subspace. A point in that subspace can be located by the coordinates

$$(x_1, x_2, \ldots x_{i-1}, \sqrt{2x_i}, x_{i+1}, \ldots x_{j-1}, x_{j+1}, \ldots x_n)$$

Now consider a general stress tensor, or matrix,

$$\underline{\sigma} = \left[\sigma_{ij}\right] = \begin{bmatrix} \sigma_{11} & \sigma_{12} & \sigma_{13} \\ \sigma_{21} & \sigma_{22} & \sigma_{23} \\ \sigma_{31} & \sigma_{32} & \sigma_{33} \end{bmatrix} \tag{E.1}$$

149

which has nine components. The nine stress components can be used to define a nine-dimensional vector space, in which the location of a point is specified by a vector having nine components.

$$\{\sigma_9\} = \begin{Bmatrix} \sigma_{11} \\ \sigma_{22} \\ \sigma_{33} \\ \sigma_{12} \\ \sigma_{23} \\ \sigma_{31} \\ \sigma_{21} \\ \sigma_{32} \\ \sigma_{13} \end{Bmatrix} \tag{E.2}$$

However, only six stress components in Equations (E.1) and (E.2) are independent because the stress matrix is symmetric according to Equation (A.20), i.e.,

$$\sigma_{ji} = \sigma_{ij} \tag{E.3}$$

so that

$$\sigma_{21} = \sigma_{12} \tag{E.4a}$$

$$\sigma_{32} = \sigma_{23} \tag{E.4b}$$

$$\sigma_{13} = \sigma_{31} \tag{E.4c}$$

Therefore, only the six-dimensional vector subspace defined by Equations (E.4), of the nine-dimensional vector space defined by Equation (E.2) will ever be needed. Thus, a general stress state can be specified by the six-dimensional vector

$$\{\sigma\} = \{\sigma_6\} = \begin{Bmatrix} \sigma_1 \\ \sigma_2 \\ \sigma_3 \\ \sigma_4 \\ \sigma_5 \\ \sigma_6 \end{Bmatrix} = \begin{Bmatrix} \sigma_{11} \\ \sigma_{22} \\ \sigma_{33} \\ \sqrt{2}\,\sigma_{12} \\ \sqrt{2}\,\sigma_{23} \\ \sqrt{2}\,\sigma_{31} \end{Bmatrix} \qquad (E.5)$$

Note carefully that σ_1, σ_2, and σ_3 in Equation (E.5) are not necessarily principal stresses, but simply the first three elements of the column vector $\{\sigma\}$, which represent the normal stresses σ_{11}, σ_{22}, and σ_{33}.

Expressions for the total and deviator stress invariants can be developed using the notation of Equation (E.5). The total stress invariants, I_1, I_2, and I_3, are

$$I_1 = \sigma_1 + \sigma_2 + \sigma_3 \qquad (E.6)$$

$$I_2 = -(\sigma_1\sigma_2 + \sigma_2\sigma_3 + \sigma_3\sigma_1) + \frac{1}{2}(\sigma_4^2 + \sigma_5^2 + \sigma_6^2) \qquad (E.7)$$

$$I_3 = \sigma_1\sigma_2\sigma_3 + \frac{1}{\sqrt{2}}\sigma_4\sigma_5\sigma_6 - \frac{1}{2}(\sigma_1\sigma_5^2 + \sigma_2\sigma_6^2 + \sigma_3\sigma_4^2) \qquad (E.8)$$

and if we set

$$\{m\} = \begin{Bmatrix} 1 \\ 1 \\ 1 \\ 0 \\ 0 \\ 0 \end{Bmatrix} \qquad (E.9)$$

then the deviator stress vector can be written in the form

151

$$\{s\} = \{\sigma\} - \frac{I_1}{3} \{m\} \qquad (E.10)$$

so that the deviator stress invariants, J_1, J_2, and J_3, are

$$J_1 = s_1 + s_2 + s_3 = 0 \qquad (E.11)$$

$$J_2 = \frac{s_1^2 + s_2^2 + s_3^2 + s_4^2 + s_5^2 + s_6^2}{2} \qquad (E.12)$$

$$J_3 = s_1 s_2 s_3 + \frac{1}{\sqrt{2}} s_4 s_5 s_6 - \frac{1}{2}(s_1 s_5^2 + s_2 s_6^2 + s_3 s_4^2) \qquad (E.13)$$

The derivatives of the total stress invariants are

$$\left\{\frac{\partial I_1}{\partial \sigma}\right\} = \{m\} \qquad (E.14)$$

$$\left\{\frac{\partial I_2}{\partial \sigma}\right\} = \{\sigma\} - I_1 \{m\} \qquad (E.15)$$

$$\left\{\frac{\partial I_3}{\partial \sigma}\right\} = \{\Sigma\} \qquad (E.16)$$

where

$$\{\Sigma\} = \begin{Bmatrix} \Sigma_1 \\ \Sigma_2 \\ \Sigma_3 \\ \Sigma_4 \\ \Sigma_5 \\ \Sigma_6 \end{Bmatrix} = \begin{Bmatrix} \Sigma_{11} \\ \Sigma_{22} \\ \Sigma_{33} \\ \sqrt{2}\ \Sigma_{12} \\ \sqrt{2}\ \Sigma_{23} \\ \sqrt{2}\ \Sigma_{31} \end{Bmatrix} \qquad (E.17)$$

The derivatives of the deviator stress vector are

$$\left[\frac{\partial s}{\partial \sigma}\right] = \underline{I} - \frac{1}{3} \{m\}\{m\}^T \qquad (E.18)$$

152

and the derivatives of the deviator stress invariants are

$$\left\{ \frac{\partial J_2}{\partial s} \right\} = \{s\} \tag{E.19}$$

$$\left\{ \frac{\partial J_3}{\partial s} \right\} = \{S\} \tag{E.20}$$

where

$$\{S\} = \left\{ \begin{array}{c} S_1 \\ S_2 \\ S_3 \\ S_4 \\ S_5 \\ S_6 \end{array} \right\} = \left\{ \begin{array}{c} S_{11} \\ S_{22} \\ S_{33} \\ \sqrt{2}\, S_{12} \\ \sqrt{2}\, S_{23} \\ \sqrt{2}\, S_{31} \end{array} \right\} \tag{E.21}$$

so that

$$\left\{ \frac{\partial J_2}{\partial \sigma} \right\} = \left[\frac{\partial s}{\partial \sigma} \right] \left\{ \frac{\partial J_2}{\partial s} \right\} = (\underline{I} - \frac{1}{3} \{m\} \{m\}^T) \{s\} = \{s\} \tag{E.22}$$

$$\left\{ \frac{\partial J_3}{\partial \sigma} \right\} = \left[\frac{\partial s}{\partial \sigma} \right] \left\{ \frac{\partial J_3}{\partial s} \right\} = (\underline{I} - \frac{1}{3} \{m\} \{m\}^T) \{S\} = \{S\} + \frac{J_2}{3} \{m\} \tag{E.23}$$

In a similar manner, a general strain state can be represented by a six-dimensional column vector. The total strain vector is

$$\{\epsilon\} = \left\{ \begin{array}{c} \epsilon_1 \\ \epsilon_2 \\ \epsilon_3 \\ \epsilon_4 \\ \epsilon_5 \\ \epsilon_6 \end{array} \right\} = \left\{ \begin{array}{c} \epsilon_{11} \\ \epsilon_{22} \\ \epsilon_{33} \\ \sqrt{2}\, \epsilon_{12} \\ \sqrt{2}\, \epsilon_{23} \\ \sqrt{2}\, \epsilon_{31} \end{array} \right\} \tag{E.24}$$

and the deviator strain vector is

$$\{e\} = \{\varepsilon\} - \frac{\varepsilon_{kk}}{3} \{m\} \qquad (E.25)$$

Stress and strain increment vectors can be defined in the same way

$$\{d\sigma\} = \begin{Bmatrix} d\sigma_1 \\ d\sigma_2 \\ d\sigma_3 \\ d\sigma_4 \\ d\sigma_5 \\ d\sigma_6 \end{Bmatrix} = \begin{Bmatrix} d\sigma_{11} \\ d\sigma_{22} \\ d\sigma_{33} \\ \sqrt{2}\ d\sigma_{12} \\ \sqrt{2}\ d\sigma_{23} \\ \sqrt{2}\ d\sigma_{31} \end{Bmatrix} \qquad (E.26)$$

$$\{d\varepsilon\} = \begin{Bmatrix} d\varepsilon_1 \\ d\varepsilon_2 \\ d\varepsilon_3 \\ d\varepsilon_4 \\ d\varepsilon_5 \\ d\varepsilon_6 \end{Bmatrix} = \begin{Bmatrix} d\varepsilon_{11} \\ d\varepsilon_{22} \\ d\varepsilon_{33} \\ \sqrt{2}\ d\varepsilon_{12} \\ \sqrt{2}\ d\varepsilon_{23} \\ \sqrt{2}\ d\varepsilon_{31} \end{Bmatrix} \qquad (E.27)$$
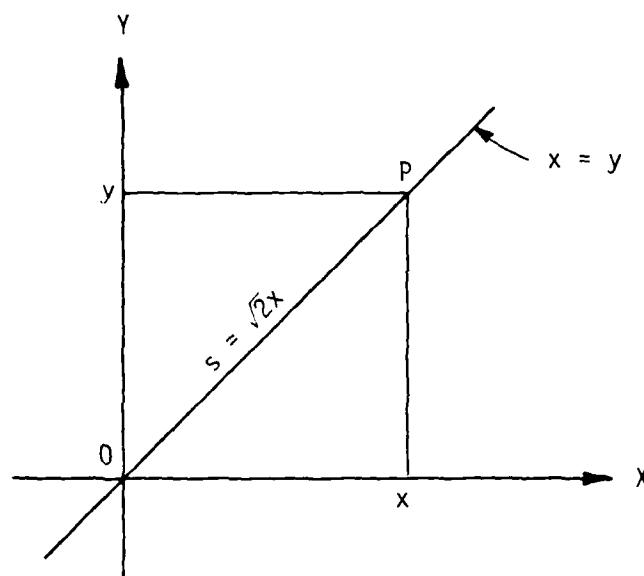
E.1a
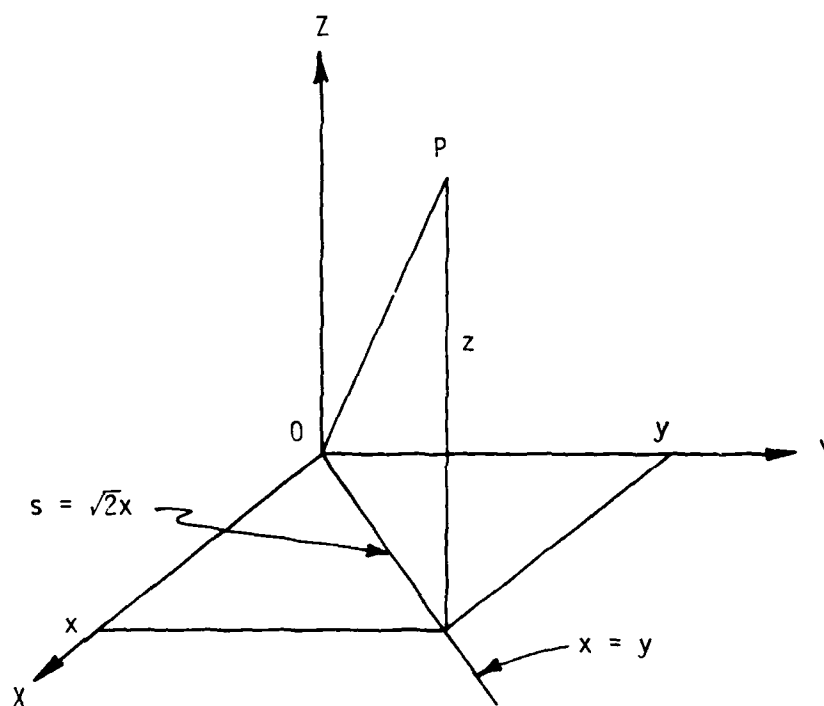
E.1b

Figure E.1.   Vector subspaces corresponding to two equal
Cartesian coordinates.

APPENDIX F

INCREMENTAL FLEXIBILITY MATRIX FOR
STRESS CONTROL

Consider a rate independent elastoplastic model having two
independent, strain hardening yield surfaces and two corresponding plastic
potential functions. Using nomenclature similar to Lade's, one yield
surface will be called the compressive yield surface and the other the
expansive yield surface. Four incremental deformation modes are possible
for such a model:

1. Both yield surfaces active, which implies both compressive (C)
   and expansive (P) yielding, plus elastic (E) response (the ECP
   mode).

2. Only the compressive yield surface active, which implies
   compressive yielding plus elastic response (the EC mode).

3. Only the expansive yield surface active, which implies expansive
   yielding plus elastic response (the EP mode).

4. Only elastic response (the E mode).

For such a model a plastic strain increment has two components:
compressive and expansive.

$$d\epsilon_{ij}^{p} = d\epsilon_{ij}^{pc} + d\epsilon_{ij}^{pp} \tag{F.1}$$

Thus, a total strain increment is the sum of three components:
elastic, compressive plastic, and expansive plastic.

$$d\epsilon_{ij} = d\epsilon_{ij}^{e} + d\epsilon_{ij}^{p} = d\epsilon_{ij}^{e} + d\epsilon_{ij}^{pc} + d\epsilon_{ij}^{pp} \tag{F.2}$$

The compressive and expansive plastic work functions are

$$W_c = \int \sigma_{ij} \; d\epsilon_{ij}^{pc} \tag{F.3}$$

156

$$W_p = \int \tau_{ij} \, d\varepsilon_{ij}^{pp} \tag{F.4}$$

Both the compressive and expansive yield criteria are assumed to have a particularly simple form, based on that of Equation (D.22).

$$\text{compressive:} \quad f_c = f_c' \, (\underline{\sigma}) - f_c'' \, (W_c) = 0 \tag{F.5}$$

$$\text{expansive:} \quad f_p = f_p' \, (\underline{\sigma}) - f_p'' \, (W_p) = 0 \tag{F.6}$$

When the ECP mode is active, the two consistency Equations (D.7) are

$$df_c = \left\{ \frac{\partial f_c'}{\partial \sigma} \right\}^T \{d\sigma\} - \frac{df_c''}{dW_c} \, dW_c = 0 \tag{F.7}$$

$$df_p = \left\{ \frac{\partial f_p'}{\partial \sigma} \right\}^T \{d\sigma\} - \frac{df_p''}{dW_p} \, dW_p = 0 \tag{F.8}$$

Now Equation (D.25) yields

$$dW_c = h_c d\lambda_c \tag{F.9}$$

$$dW_p = h_p d\lambda_p \tag{F.10}$$

where

$$h_c = \{\sigma\}^T \left\{ \frac{\partial g_c}{\partial \sigma} \right\} \tag{F.11}$$

$$h_p = \{\sigma\}^T \left\{ \frac{\partial g_p}{\partial \sigma} \right\} \tag{F.12}$$

When the compressive and expansive plastic potential functions are convex, h_c and h_p will both be positive, so that $d\lambda_c$ and $d\lambda_p$ must both be positive for dW_c and dW_p to both be positive. Substitution of

157

Equation (F.9) into Equation (F.7), and Equation (F.10) into
Equation (F.8) yields

$$df_c = \left\{\frac{\partial f'_c}{\partial \sigma}\right\}^T \{d\sigma\} - \frac{df''_c}{dW_c} h_c d\lambda_c = 0 \qquad (F.13)$$

$$df_p = \left\{\frac{\partial f'_p}{\partial \sigma}\right\}^T \{d\sigma\} - \frac{df''_p}{dW_p} h_p d\lambda_p = 0 \qquad (F.14)$$

Equations (F.13) and (F.14) can be written together in the form

$$\{df\} = \underline{F}^T \{d\sigma\} - \ulcorner D \lrcorner \{d\lambda\} = \{0\} \qquad (F.15)$$

where

$$\underline{F} = \left[\left\{\frac{\partial f'_c}{\partial \sigma}\right\} \middle| \left\{\frac{\partial f'_p}{\partial \sigma}\right\}\right] \qquad (F.16)$$

$$\ulcorner D \lrcorner = \begin{bmatrix} \dfrac{df''_c}{dW_c} h_c & 0 \\ 0 & \dfrac{df''_p}{dW_p} h_p \end{bmatrix} \qquad (F.17)$$

$$\{d\sigma\} = \begin{Bmatrix} d\sigma_{11} \\ d\sigma_{22} \\ d\sigma_{33} \\ \sqrt{2}\, d\sigma_{12} \\ \sqrt{2}\, d\sigma_{23} \\ \sqrt{2}\, d\sigma_{31} \end{Bmatrix} \qquad (E.26)$$

$$\{d\lambda\} = \begin{Bmatrix} d\lambda_c \\ d\lambda_p \end{Bmatrix} \qquad (F.18)$$

The solution of Equation (F.15) is

$$\{d\lambda\} = \ulcorner D \lrcorner^{-1} \underline{F}^T \{d\sigma\} \tag{F.19}$$

Provided $d\lambda_c$ and $d\lambda_p$ are both positive, so that dW_c and dW_p are both positive, the total strain increment is, according to Equation (F.1)

$$\{d\varepsilon\} = \{d\varepsilon^e\} + \{d\varepsilon^p\} \tag{F.20}$$

Now the elastic strain increment is related to the stress increment by the equation

$$\{d\varepsilon^e\} = \underline{H}^e \{d\sigma\} \tag{F.21}$$

where

$\underline{H}^e$ = elastic incremental flexibility matrix, defined by
Equation (J.23)

and the plastic strain increment is given by the flow rule, Equation (D.6), as

$$\{d\varepsilon^p\} = \underline{G} \{d\lambda\} \tag{F.22}$$

where

$$\underline{G} = \left[\left\{ \frac{\partial g_c}{\partial \sigma} \right\} \middle| \left\{ \frac{\partial g_p}{\partial \sigma} \right\} \right] \tag{F.23}$$

Substitution of Equations (F.21) and (F.22) into Equation (F.20) yields

$$
\begin{aligned}
\{d\varepsilon\} &= \underline{H}^e \{d\sigma\} + \underline{G} \{d\lambda\} \\
&= \underline{H}^e \{d\sigma\} + \underline{G} \ulcorner D \lrcorner^{-1} \underline{F}^T \{d\sigma\} \\
&= (\underline{H}^e + \underline{G} \ulcorner D \lrcorner^{-1} \underline{F}^T) \{d\sigma\} \\
&= \underline{H}^{ep} \{d\sigma\}
\end{aligned} \tag{F.24}
$$

159

where the elastoplastic incremental flexibility matrix, $\underline{H}^{ep}$, is given by the expression

$$\underline{H}^{ep} = \underline{H}^{e} + \underline{G} \ \ulcorner D \lrcorner^{-1} \ \underline{F}^{T} \qquad (F.25)$$

Now Equations (F.13) and (F.14) are uncoupled when $\{d\sigma\}$ is known, so that

$$d\lambda_{c} = \frac{\left\{\dfrac{\partial f'_{c}}{\partial \sigma}\right\}^{T} \{d\sigma\}}{D_{11}} \qquad (F.26)$$

$$d\lambda_{p} = \frac{\left\{\dfrac{\partial f'_{p}}{\partial \sigma}\right\}^{T} \{d\sigma\}}{D_{22}} \qquad (F.27)$$

which is the same result obtained by expanding Equation (F.19). Equation (F.25) can thus be written in the form

$$\underline{H}^{ep} = \underline{H}^{e} + \frac{1}{D_{11}} \left\{\frac{\partial g_{c}}{\partial \sigma}\right\} \left\{\frac{\partial f'_{c}}{\partial \sigma}\right\}^{T} + \frac{1}{D_{22}} \left\{\frac{\partial g_{p}}{\partial \sigma}\right\} \left\{\frac{\partial f'_{p}}{\partial \sigma}\right\}^{T} \qquad (F.28)$$

When the EC mode is active, $d\lambda_{p}$ is set equal to zero and $d\lambda_{c}$ is calculated by Equation (F.26), as before. When that result is positive the elastoplastic incremental flexibility matrix is obtained by deleting the expansive term from Equation (F.28), which yields

$$\underline{H}^{ep} = \underline{H}^{e} + \frac{1}{D_{11}} \left\{\frac{\partial g_{c}}{\partial \sigma}\right\} \left\{\frac{\partial f'_{c}}{\partial \sigma}\right\}^{T} \qquad (F.29)$$

When the EP mode is active, $d\lambda_{c}$ is set equal to zero and $d\lambda_{p}$ is calculated by Equation (F.27) as before. When that result is positive the elastoplastic incremental flexibility matrix is obtained by deleting the compressive term from Equation (F.28), which yields

$$\underline{H}^{ep} = \underline{H}^e + \frac{1}{D_{22}} \left\{ \frac{\partial g_p}{\partial \sigma} \right\} \left\{ \frac{\partial f'_p}{\partial \sigma} \right\}^T \qquad (F.30)$$

When the E mode is active, both $d\lambda_c$ and $d\lambda_p$ are set equal to zero, and the elastic incremental flexibility matrix is obtained by deleting both the compressive and expansive terms from Equation (F.28), which yields

$$\underline{H}^{ep} = \underline{H}^e \qquad (F.31)$$

The logic for deciding which incremental deformation mode is active, under stress control, is discussed in Appendix H.

APPENDIX G

INCREMENTAL STIFFNESS MATRIX FOR
STRAIN CONTROL

The material in this appendix builds on the development in Appendix F.

When the ECP mode is active, the consistency equations for a two

yield surface model take the form of Equation (F.15).

$$\{df\} = \underline{F}^T \{d\sigma\} - \ulcorner D_\lrcorner \{d\lambda\} = \{0\} \tag{F.15}$$

However, under strain control what is known is not the stress

increment, $\{d\sigma\}$, but the total strain increment, $\{d\varepsilon\}$. Thus, in place of

Equation (F.21) we write

$$\{d\sigma\} = \underline{C}^e \{d\varepsilon^e\} \tag{G.1}$$

where

$\underline{C}^e$ = elastic incremental stiffness matrix, defined by

Equation (J.32).

In addition, we write Equation (F.20) in the form

$$\{d\varepsilon^e\} = \{d\varepsilon\} - \{d\varepsilon^p\} \tag{G.2}$$

and again use the flow rule to obtain an expression for the plastic strain

increment.

$$\{d\varepsilon^p\} = \underline{G} \{d\lambda\} \tag{F.22}$$

Substitution of Equations (G.1), (G.2), and (F.22) into

Equation (F.15) yields

$$\{df\} = \underline{F}^T \underline{C}^e \left\{\{d\varepsilon\} - \underline{G} \{d\lambda\}\right\} - \ulcorner D_\lrcorner \{d\lambda\} = \{0\} \tag{G.3}$$

or

$$(\underline{F}^T \underline{C}^e \underline{G} + \ulcorner D_\lrcorner)\{d\lambda\} = \underline{F}^T \underline{C}^e \{d\varepsilon\} \tag{G.4}$$

162

Solving Equation (G.4) for $\{d\lambda\}$ yields

$$\{d\lambda\} = (\underline{F}^T\underline{c}^e\underline{G} + \ulcorner D_J)^{-1}\underline{F}^T\underline{c}^e\{d\epsilon\} \tag{G.5}$$

Provided $d\lambda_c$ and $d\lambda_p$ are both positive, we substitute
Equations (G.2), (F.22) and (G.5) into Equation (G.1) to obtain an
expression for the stress increment, $\{d\sigma\}$, in terms of the prescribed
total strain increment, $\{d\epsilon\}$.

$$
\begin{aligned}
\{d\sigma\} = \underline{c}^e\{d\epsilon^e\} &= \underline{c}^e\left\{\{d\epsilon\} - \underline{G}\{d\lambda\}\right\} \\
&= \underline{c}^e\left\{\{d\epsilon\} - \underline{G}(\underline{F}^T\underline{c}^e\underline{G} + \ulcorner D_J)^{-1}\underline{F}^T\underline{c}^e\{d\epsilon\}\right\} \\
&= [\underline{c}^e - \underline{c}^e\underline{G}(\underline{F}^T\underline{c}^e\underline{G} + \ulcorner D_J)^{-1}\underline{F}^T\underline{c}^e]\{d\epsilon\} \\
&= \underline{c}^{ep}\{d\epsilon\} \tag{G.6}
\end{aligned}
$$

where the elastoplastic incremental stiffness matrix for the ECP mode is
defined by the expression

$$\underline{c}^{ep} = \underline{c}^e - \underline{c}^e\underline{G}(\underline{F}^T\underline{c}^e\underline{G} + \ulcorner D_J)^{-1}\underline{F}^T\underline{c}^e \tag{G.7}$$

The fact that $\underline{H}^{ep}$ as defined by Equation (F.25) and $\underline{c}^{ep}$ as
defined by Equation (G.7) are the inverse of one another can be proven by
showing that

$$\underline{H}^{ep}\underline{c}^{ep} = \underline{c}^{ep}\underline{H}^{ep} = \underline{I} \tag{G.8}$$

In verifying Equation (G.8) use is made of the fact that

$$\underline{H}^e\underline{c}^e = \underline{c}^e\underline{H}^e = \underline{I} \tag{J.31}$$

When the EC mode is active, $d\lambda_p$ is set equal to zero so that
Equation (G.3) reduces to

$$df_c = \left\{\frac{\partial f'_c}{\partial\sigma}\right\}^T \underline{c}^e\left\{\{d\epsilon\} - \left\{\frac{\partial g_c}{\partial\sigma}\right\}d\lambda_c\right\} - D_{11}\,d\lambda_c = 0 \tag{G.9}$$

163

or

$$\left(\left\{ \frac{\partial f'_c}{\partial \sigma} \right\}^T \underline{C}^e \left\{ \frac{\partial g_c}{\partial \sigma} \right\} + D_{11} \right) d\lambda_c = \left\{ \frac{\partial f'_c}{\partial \sigma} \right\}^T \underline{C}^e \{d\varepsilon\} \qquad (G.10)$$

Solving Equation (G.10) for $d\lambda_c$ yields

$$d\lambda_c = \frac{\left\{ \frac{\partial f'_c}{\partial \sigma} \right\}^T \underline{C}^e \{d\varepsilon\}}{\left\{ \frac{\partial f'_c}{\partial \sigma} \right\}^T \underline{C}^e \left\{ \frac{\partial g_c}{\partial \sigma} \right\} + D_{11}} \qquad (G.11)$$

Provided $d\lambda_c$ is positive, we substitute Equations (G.2), (F.22), and (G.11) into Equation (G.1) to obtain an expression for the stress increment, $\{d\sigma\}$, in terms of the prescribed total strain increment, $\{d\varepsilon\}$.

$$\{d\sigma\} = \underline{C}^e\{d\varepsilon^e\} = \underline{C}^e \left\{ \{d\varepsilon\} - \left\{ \frac{\partial g_c}{\partial \sigma} \right\} d\lambda_c \right\}$$

$$= \underline{C}^e \left\{ \{d\varepsilon\} - \frac{\left\{ \frac{\partial g_c}{\partial \sigma} \right\} \left\{ \frac{\partial f'_c}{\partial \sigma} \right\}^T \underline{C}^e \{d\varepsilon\}}{\left\{ \frac{\partial f'_c}{\partial \sigma} \right\}^T \underline{C}^e \left\{ \frac{\partial g_c}{\partial \sigma} \right\} + D_{11}} \right\}$$

$$= \left(\underline{C}^e - \frac{\underline{C}^e \left\{ \frac{\partial g_c}{\partial \sigma} \right\} \left\{ \frac{\partial f'_c}{\partial \sigma} \right\}^T \underline{C}^e}{\left\{ \frac{\partial f'_c}{\partial \sigma} \right\}^T \underline{C}^e \left\{ \frac{\partial g_c}{\partial \sigma} \right\} + D_{11}} \right) \{d\varepsilon\}$$

$$= \underline{C}^{ep} \{d\varepsilon\} \qquad (G.12)$$

where the elastoplastic incremental stiffness matrix for the EC mode is defined by the expression

$$\underline{C}^{ep} = \underline{C}^e - \frac{\underline{C}^e \left\{ \frac{\partial g_c}{\partial \sigma} \right\} \left\{ \frac{\partial f'_c}{\partial \sigma} \right\}^T \underline{C}^e}{\left\{ \frac{\partial f'_c}{\partial \sigma} \right\}^T \underline{C}^e \left\{ \frac{\partial g_c}{\partial \sigma} \right\} + D_{11}} \qquad (G.13)$$

164

The fact that $\underline{H}^{ep}$ as defined by Equation (F.29) and $\underline{C}^{ep}$ as defined by Equation (G.13) are the inverse of one another can be proven by showing that

$$\underline{H}^{ep}\underline{C}^{ep} = \underline{C}^{ep}\underline{H}^{ep} = \underline{I} \tag{G.8}$$

again using Equation (J.31).

When the EP mode is active, $d\lambda_c$ is set equal to zero so that Equation (G.3) reduces to

$$df_p = \left\{\frac{\partial f_p'}{\partial \sigma}\right\}^T \underline{C}^e \left\{\{d\varepsilon\} - \left\{\frac{\partial g_p}{\partial \sigma}\right\} d\lambda_p\right\} - D_{22} \, d\lambda_p = 0 \tag{G.14}$$

or

$$\left(\left\{\frac{\partial f_p'}{\partial \sigma}\right\}^T \underline{C}^e \left\{\frac{\partial g_p}{\partial \sigma}\right\} + D_{22}\right) d\lambda_p = \left\{\frac{\partial f_p'}{\partial \sigma}\right\}^T \underline{C}^e \{d\varepsilon\} \tag{G.15}$$

Solving Equation (G.15) for $d\lambda_p$ yields

$$d\lambda_p = \frac{\left\{\frac{\partial f_p'}{\partial \sigma}\right\}^T \underline{C}^e \{d\varepsilon\}}{\left\{\frac{\partial f_p'}{\partial \sigma}\right\}^T \underline{C}^e \left\{\frac{\partial g_p}{\partial \sigma}\right\} + D_{22}} \tag{G.16}$$

Provided $d\lambda_p$ is positive, we substitute Equations (G.2), (F.22), and (G.16) into Equation (G.1) to obtain an expression for the stress increment, $\{d\sigma\}$, in terms of the prescribed total strain increment, $\{d\varepsilon\}$.

$$\{d\sigma\} = \underline{C}^e \{d\varepsilon^e\} = \underline{C}^e \left\{\{d\varepsilon\} - \left\{\frac{\partial g_p}{\partial \sigma}\right\} d\lambda_p\right\}$$

$$= \underline{C}^e \left\{\{d\varepsilon\} - \frac{\left\{\frac{\partial g_p}{\partial \sigma}\right\}\left\{\frac{\partial f_p'}{\partial \sigma}\right\}^T \underline{C}^e \{d\varepsilon\}}{\left\{\frac{\partial f_p'}{\partial \sigma}\right\}^T \underline{C}^e \left\{\frac{\partial g_p}{\partial \sigma}\right\} + D_{22}}\right\}$$

165

$$= \left(\underline{C}^e - \frac{\underline{C}^e \left\{ \frac{\partial g_p}{\partial \sigma} \right\} \left\{ \frac{\partial f'_p}{\partial \sigma} \right\}^T \underline{C}^e}{\left\{ \frac{\partial f'_p}{\partial \sigma} \right\}^T \underline{C}^e \left\{ \frac{\partial g_p}{\partial \sigma} \right\} + D_{22}} \right) \{ d\epsilon \}$$

$$= \underline{C}^{ep} \{ d\epsilon \} \tag{G.17}$$

where the elastoplastic incremental stiffness matrix for the EP mode is defined by the expression

$$\underline{C}^{ep} = \underline{C}^e - \frac{\underline{C}^e \left\{ \frac{\partial g_p}{\partial \sigma} \right\} \left\{ \frac{\partial f'_p}{\partial \sigma} \right\}^T \underline{C}^e}{\left\{ \frac{\partial f'_p}{\partial \sigma} \right\}^T \underline{C}^e \left\{ \frac{\partial g_p}{\partial \sigma} \right\} + D_{22}} \tag{G.18}$$

The fact that $\underline{H}^{ep}$ as defined by Equation (F.30) and $\underline{C}^{ep}$ as defined by Equation (G.18) are the inverse of one another can be proven by showing that

$$\underline{H}^{ep} \underline{C}^{ep} = \underline{C}^{ep} \underline{H}^{ep} = \underline{I} \tag{G.8}$$

again, using Equation (J.31).

When the E mode is active, both $d\lambda_c$ and $d\lambda_p$ are set equal to zero, so that Equation (G.2) reduces to

$$\{ d\epsilon^e \} = \{ d\epsilon \} \tag{G.19}$$

and therefore Equation (G.1) takes the form

$$\{ d\sigma \} = \underline{C}^e \{ d\epsilon \} = \underline{C}^{ep} \{ d\epsilon \} \tag{G.20}$$

where the elastoplastic incremental stiffness matrix for the E mode is simply the elastic incremental stiffness matrix.

$$\underline{C}^{ep} = \underline{C}^e \tag{G.21}$$

The logic for deciding which incremental deformation mode is active, under strain control, is discussed in Appendix I.

167

APPENDIX H

INCREMENTAL DEFORMATION MODE LOGIC FOR STRESS CONTROL

The material in this appendix builds on the development in Appendix F.
Equations (F.26) and (F.27) can be written in the form

$$d\lambda_c = \frac{df'_c}{D_{11}} \qquad (H.1)$$

$$d\lambda_p = \frac{df'_p}{D_{22}} \qquad (H.2)$$

where

$$df'_c = \left\{ \frac{\partial f'_c}{\partial \sigma} \right\}^T \{d\sigma\} \qquad (H.3)$$

$$df'_p = \left\{ \frac{\partial f'_p}{\partial \sigma} \right\}^T \{d\sigma\} \qquad (H.4)$$

When D_{11} is positive, implying strain hardening behavior of the
compressive yield surface, df'_c must be positive for $d\lambda_c$ to be
positive. The same argument applies to D_{22}, df'_p, and $d\lambda_p$.
Therefore, in view of Equations (F.9), (F.10), (F.11), and (F.12), and the
dissipation condition as stated in Equation (D.8), the incremental
deformation mode logic for a strain hardening material under stress
control is as shown in Table (H.1).

When both the compressive and expansive yield criteria are satisfied,
i.e., when the stress point lies at the intersection of the compressive
and expansive yield surfaces (the corner conditions $f_c = f_p = 0$) the above
incremental deformation mode logic can also be represented graphically, as

168

shown in Figure (H.1). The figure is drawn in the plane of principal stress space containing the yield surface gradient vectors $\overline{\nabla}f_c'$ and $\overline{\nabla}f_p'$, because Equations (H.1), (H.2), (H.3), and (H.4) show that the quantities $d\lambda_c$ and $d\lambda_p$ are proportional to the dot products of $d\sigma$ with $\overline{\nabla}f_c'$ and $\overline{\nabla}f_p'$, respectively. It follows that $d\lambda_c$ and $d\lambda_p$ are determined by the component of $\overline{d\sigma}$ in the plane containing $\overline{\nabla}f_c'$ and $\overline{\nabla}f_p'$. Thus if we set

$$\overline{n} = \frac{\overline{\nabla}f_c' \times \overline{\nabla}f_p'}{\left|\overline{\nabla}f_c' \times \overline{\nabla}f_p'\right|} \tag{H.5}$$

then $\overline{n}$ will be a unit vector perpendicular to the plane containing $\overline{\nabla}f_c'$ and $\overline{\nabla}f_p'$. And if we set

$$\overline{d\sigma}^* = \overline{d\sigma} - (\overline{d\sigma} \cdot \overline{n})\overline{n} \tag{H.6}$$

then $\overline{d\sigma}^*$ will be the component of $\overline{d\sigma}$ in the plane containing $\overline{\nabla}f_c'$ and $\overline{\nabla}f_p'$. It is $\overline{d\sigma}^*$ which determines $d\lambda_c$ and $d\lambda_p$ *for the corner condition,* as shown in Figure (H.1). The component of $\overline{d\sigma}$ normal to the plane containing $\overline{\nabla}f_c'$ and $\overline{\nabla}f_p'$, i.e., $(\overline{\sigma} \cdot \overline{n})\overline{n}$, causes only elastic deformation.

The equations of Appendix F can now be generalized for the corner condition by using the ramp function, R(x), defined in Figure (H.2) as

$$R(x) = \int_{-\infty}^{x} \int_{-\infty}^{y} \delta(z) \, dz \, dy = x \qquad (x > 0) \tag{H.7}$$
$$= 0 \qquad (x \leq 0)$$

so that one incremental flexibility equation yields the total strain increment *for any stress increment at the corner.* The generalization of Equation (F.24) is

$$\{d\epsilon\} = \underline{H}^e \{d\sigma\} + \frac{1}{D_{11}} \left\{\frac{\partial g_c}{\partial\sigma}\right\} R(df_c') + \frac{1}{D_{22}} \left\{\frac{\partial g_p}{\partial\sigma}\right\} R (df_p') \qquad (H.8)$$

Equation (H.8) applies for all four incremental deformation modes at the corner.

Negative values of D_{11} or D_{22}, implying strain softening, result in lack of uniqueness under stress control. For example, if D_{22} is negative a stress change for which df_p' is negative can be caused either by expansive yielding or elastic unloading, and there is no way to distinguish between the two under stress control.

A computational problem which needs to be addressed is how to avoid violation of a yield surface which is inactive at the start of a stress increment. If the stress point lies beneath a yield surface at the start of a stress increment, what assurance is there that the stress increment will not be so large (or the distance to the inactive yield surface so small) that the stress increment "punches through" the inactive yield surface The answer is "none" unless a restriction on the magnitude of the stress increment vector is established to prevent yield surface violation in the EC, EP, and E modes. When the compressive yield surface is inactive, the restriction on $\{d\sigma\}$ is

$$df_c' = \left\{\frac{\partial f_c'}{\partial\sigma}\right\}^T \{d\sigma\} \leq f_c'' - f_c' = - f_c \qquad (H.9)$$

and when the expansive yield surface is inactive, the restriction on $\{d\sigma\}$ is

$$df_p' = \left\{\frac{\partial f_p'}{\partial\sigma}\right\}^T \{d\sigma\} \leq f_p'' - f_p' = - f_p \qquad (H.10)$$

170

Table (H.2) shows that for each combination of initial conditions and incremental deformation mode a distinct set of four conditions must be satisfied to ensure positive energy dissipation and prevent yield surface violation. Each set is a subset of the following four general conditions:

$$df_c \leq - f_c \qquad (H.11)$$

$$df_p \leq - f_p \qquad (H.12)$$

$$d\lambda_c \geq 0 \qquad (H.13)$$

$$d\lambda_p \geq 0 \qquad (H.14)$$

Expressions (H.11) and (H.12) ensure that f_c and f_p are nonpositive, and Expressions (H.13) and (H.14) require that $d\lambda_c$ and $d\lambda_p$ be nonnegative.

The restrictions on the magnitude of the stress increment vector defined by Equations (H.9) and (H.10) are implemented as follows. Assume the expansive yield surface to be inactive and the compressive yield surface active at the start of a stress increment, i.e., $f_c = 0$ and $f_p < 0$. Then if the ratio

$$\zeta_p = \frac{df_p'}{-f_p} \qquad (H.15)$$

exceeds 1.0, the expansive yield surface will be violated unless the stress increment is reduced. This is done by splitting the stress increment into two parts by setting

$$\{d\sigma\} = \{d\sigma\}_1 + \{d\sigma\}_2 \qquad (H.16)$$

where

171

$$\{d\sigma\}_1 = \frac{1}{\zeta_p} \{d\sigma\} \tag{H.17}$$

$$\{d\sigma\}_2 = (1 - \frac{1}{\zeta_p}) \{d\sigma\} \tag{H.18}$$

The stress subincrement $\{d\sigma\}_1$, is just sufficient to bring the stress point into contact with the expansive yield surface. The remaining stress subincrement, $\{d\sigma\}_2$, is then applied assuming the expansive yield surface to be active (ECP or EP mode).

A similar procedure is used when the compressive yield surface is inactive and the expansive yield surface active at the start of a stress increment, i.e., $f_c < 0$ and $f_p = 0$, using the ratio

$$\zeta_c = \frac{df'_c}{-f_c} \tag{H.19}$$

When both yield surfaces are inactive at the start of a stress increment, i.e., $f_c < 0$ and $f_p < 0$, compute both ζ_c and ζ_p. Unless both ratios are less than 1.0, set

$$\{d\sigma\} = \{d\sigma\}_1 + \{d\sigma\}_2 \tag{H.16}$$

where

$$\{d\sigma\}_1 = \frac{1}{\zeta} \{d\sigma\} \tag{H.20}$$

$$\{d\sigma\}_2 = (1 - \frac{1}{\zeta})\{d\sigma\} \tag{H.21}$$

$$\zeta = \text{larger of } \zeta_c \text{ and } \zeta_p \tag{H.22}$$

The stress subincrement $\{d\sigma\}_1$, will bring the stress point into contact with one yield surface, at which point one of the first two tests

must be applied to see whether $\{d\sigma\}_2$ should be split to avoid violation of the other yield surface.

When both ζ_c and ζ_p are greater than 1.0, e.g., when $\zeta_c > \zeta_p > 1.0$, we could set

$$\{d\sigma\} = \frac{1}{\zeta_c} \{d\sigma\} + (\frac{1}{\zeta_p} - \frac{1}{\zeta_c}) \{d\sigma\} + (1 - \frac{1}{\zeta_p}) \{d\sigma\}$$

and apply each stress subincrement in succession without recomputing the initial conditions at the start of the second and third stress subincrements. However, this is not recommended because it is numerically less accurate than recomputing a new set of initial conditions at the start of each new stress increment.

INCREMENTAL DEFORMATION MODE LOGIC FOR A
STRAIN HARDENING, TWO YIELD SURFACE ELASTOPLASTIC
MODEL UNDER STRESS CONTROL

				f_p		
				$= 0$		< 0
				df_p'		
				> 0	≤ 0	
f_c	$= 0$	df_c'	> 0	$\underline{E}CP$	EC	
			≤ 0	EP	E	
	< 0					

RESTRICTIONS IMPOSED FOR EACH INITIAL CONDITION
AND INCREMENTAL DEFORMATION MODE

Initial Conditions		Incremental Deformation Mode			
f_c	f_p	ECP	EC	EP	E
0	0	$df_c = 0$ $df_p = 0$ $d\lambda_c > 0$ $d\lambda_p > 0$	$df_c = 0$ $df_p' \leq 0$ $d\lambda_c > 0$ $d\lambda_p = 0$	$df_c' \leq 0$ $df_p = 0$ $d\lambda_c = 0$ $d\lambda_p > 0$	$df_c' \leq 0$ $df_p' \leq 0$ $d\lambda_c = 0$ $d\lambda_p = 0$
0	< 0	n/a	$df_c = 0$ $df_p' \leq -f_p$ $d\lambda_c > 0$ $d\lambda_p = 0$	n/a	$df_c' \leq 0$ $df_p' \leq -f_p$ $d\lambda_c = 0$ $d\lambda_p = 0$
< 0	0	n/a	n/a	$df_c' \leq -f_c$ $df_p = 0$ $d\lambda_c = 0$ $d\lambda_p > 0$	$df_c' \leq -f_c$ $df_p' \leq 0$ $d\lambda_c = 0$ $d\lambda_p = 0$
< 0	< 0	n/a	n/a	n/a	$df_c' \leq -f_c$ $df_p' \leq -f_p$ $d\lambda_c = 0$ $d\lambda_p = 0$
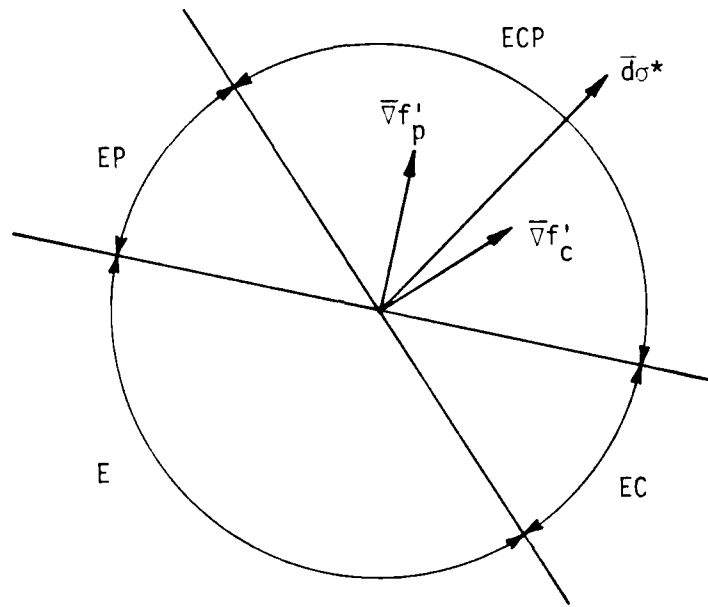
Figure H.1. Incremental deformation mode logic for a strain
hardening, two yield surface elastoplastic model
under stress control, at the corner.

176
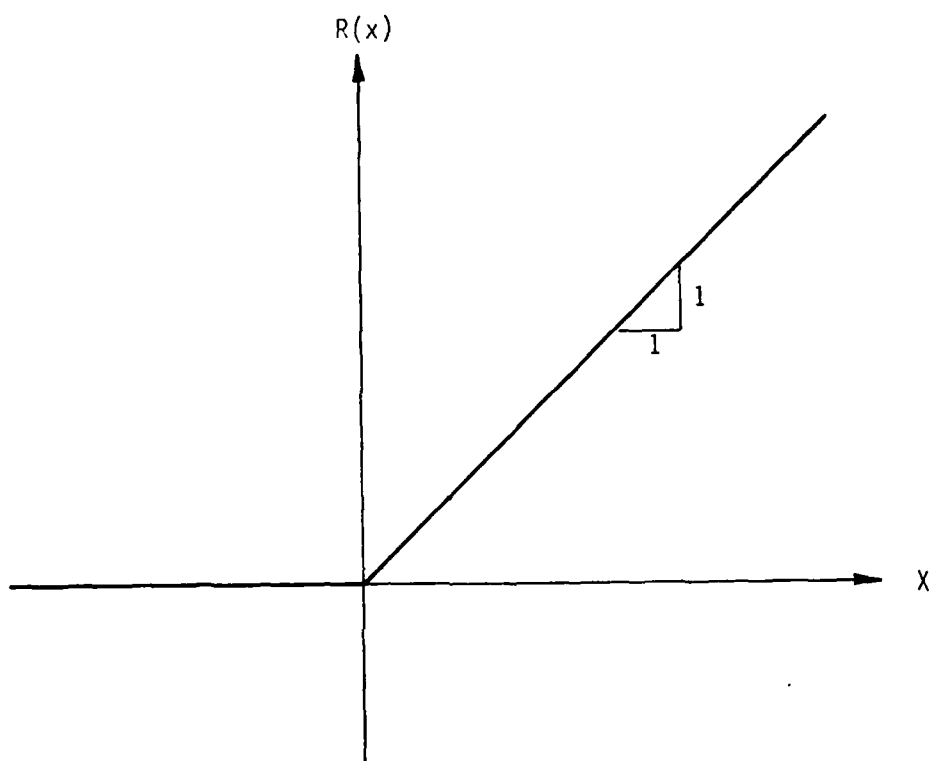
$$R(x) = \int\limits_{-\infty}^{x} \int\limits_{-\infty}^{y} \delta(z) \; dzdy = x \qquad (x > 0)$$
$$= 0 \qquad (x \leq 0)$$

Figure H.2. The ramp function.

177

APPENDIX I

INCREMENTAL DEFORMATION MODE LOGIC FOR STRAIN CONTROL

The incremental deformation mode logic for a strain hardening, two yield surface elastoplastic model under stress control, as presented in Appendix H, is simple because the two yield criteria are defined in stress space. For the corner condition, the incremental deformation mode is determinded by the component of $\overline{d}\sigma$ in the plane containing $\overline{V}f_c'$ and $\overline{V}f_p'$. All stress increment vectors are possible, and each stress increment vector leads to one and only one strain increment vector, as indicated by Equation (H.8).

$$\{d\epsilon\} = \underline{H}^e \{d\sigma\} + \frac{1}{D_{11}} \left\{\frac{\partial g_c}{\partial \sigma}\right\} R (df_c') + \frac{1}{D_{22}} \left\{\frac{\partial g_p}{\partial \sigma}\right\} R (df_p') \qquad (H.8)$$

However, it remains to be seen whether there are some strain increment vectors not produced by any stress increment vector, or whether two different stress increment vectors can produce the same strain increment vector.

The situation under strain control is more complicated than that under stress control, because each incremental deformation mode has a different incremental stiffness matrix. However, the conditions listed in Table (H.2) also apply under strain control, and what must be done is to express those conditions in terms of a prescribed strain increment rather than a prescribed stress increment.

The conditions $df_c = 0$ and $df_p = 0$, when they apply, are taken care of by the consistency conditions, Equations (F.7) and (F.8). The

178

conditions $d\lambda_c = 0$ and $d\lambda_p = 0$, when they apply, are taken care of arbitrarily. It is the conditions $d\lambda_c > 0$, $d\lambda_p > 0$, $df_c' \leq -f_c$, and $df_p' \leq -f_p$ which require further discussion.

First, consider the corner conditions $f_c = f_p = 0$. For the ECP mode, Equation (G.5) can be written in the form

$$\{d\lambda\} = \underline{L}^{-1} \{df_e'\} \tag{I.1}$$

where

$$\underline{L} = \begin{bmatrix} \begin{Bmatrix} L_{11} \\ L_{21} \end{Bmatrix} \Big| \begin{Bmatrix} L_{12} \\ L_{22} \end{Bmatrix} \end{bmatrix} = \begin{bmatrix} \{L_1\} \Big| \{L_2\} \end{bmatrix} = \underline{F}^T \underline{C}^e \underline{G} + \ulcorner D \lrcorner$$

$$= \begin{bmatrix} \left\{ \begin{Bmatrix} \dfrac{\partial f_c'}{\partial \sigma} \end{Bmatrix}^T \underline{C}^e \begin{Bmatrix} \dfrac{\partial g_c}{\partial \sigma} \end{Bmatrix} + D_{11} \right\} & \Bigg| & \left\{ \begin{Bmatrix} \dfrac{\partial f_c'}{\partial \sigma} \end{Bmatrix}^T \underline{C}^e \begin{Bmatrix} \dfrac{\partial g_p}{\partial \sigma} \end{Bmatrix} \right\} \\[4ex] \left\{ \begin{Bmatrix} \dfrac{\partial f_p'}{\partial \sigma} \end{Bmatrix}^T \underline{C}^e \begin{Bmatrix} \dfrac{\partial g_c}{\partial \sigma} \end{Bmatrix} \right\} & \Bigg| & \left\{ \begin{Bmatrix} \dfrac{\partial f_p'}{\partial \sigma} \end{Bmatrix}^T \underline{C}^e \begin{Bmatrix} \dfrac{\partial g_p}{\partial \sigma} \end{Bmatrix} + D_{22} \right\} \end{bmatrix} \tag{I.2}$$

D_{11} and D_{22} are defined by Equations (F.11), (F.12), and (F.17), and the elastic trial matrix, $\{df_e'\}$, is defined as

$$\{df_e'\} = \begin{Bmatrix} df_{ce}' \\ df_{pe}' \end{Bmatrix} = \underline{F}^T \underline{C}^e \{d\varepsilon\} \tag{I.3}$$

The two columns of the vertically partitioned $\underline{L}$ matrix in Equation (I.2) can each be interpreted as a two component vector, and can be represented graphically in the plane containing both of them (the L plane), as shown in Figure (I.1). The lengths of the column vectors, $\overline{L}_1$ and $\overline{L}_2$ are

$$L_1 = \sqrt{L_{11}^2 + L_{21}^2} \tag{I.4}$$

179

$$L_2 = \sqrt{L_{12}^2 + L_{22}^2} \tag{I.5}$$

and the acute or obtuse angle between them can be found by computing their cross product,

$$\overline{L}_1 \times \overline{L}_2 = \begin{vmatrix} \overline{e}_1 & L_{11} & L_{12} \\ \overline{e}_2 & L_{21} & L_{22} \\ \overline{e}_3 & 0 & 0 \end{vmatrix} = (L_{11}L_{22} - L_{21}L_{12})\overline{e}_3$$

$$= L\overline{e}_3 = L_1L_2 \sin \phi \; \overline{e}_3 \tag{I.6}$$

where

$$L = L_{11}L_{22} - L_{21}L_{12} = \begin{vmatrix} L_{11} & L_{12} \\ L_{21} & L_{22} \end{vmatrix} = |\underline{L}| \tag{I.7}$$

Therefore, if $L > 0$ the acute or obtuse angle from $\overline{L}_1$ to $\overline{L}_2$ is nonzero and counterclockwise.

Now, consider the inverse of $\underline{L}$, which appears in Equation (I.1), and set

$$\underline{L}^{-1} = \underline{M} = \left[\begin{array}{c|c} M_{11} & M_{12} \\ \hline M_{21} & M_{22} \end{array} \right] = \left[\begin{array}{c} M_1 \\ \hline M_2 \end{array} \right]$$

$$= \frac{1}{L} \left[\begin{array}{c|c} L_{22} & -L_{12} \\ \hline -L_{21} & L_{11} \end{array} \right] \tag{I.8}$$

The relation between the row vectors of the horizontally partitioned $\underline{M}$ matrix and the column vectors of the vertically partitioned $\underline{L}$ matrix is

shown in Figure (I.2). In order for $\underline{M}$ to be the inverse of $\underline{L}$, it must be that

$$\overline{M}_1 \cdot \overline{L}_1 = 1 \qquad\qquad (I.9)$$

$$\overline{M}_1 \cdot \overline{L}_2 = 0 \qquad\qquad (I.10)$$

$$\overline{M}_2 \cdot \overline{L}_1 = 0 \qquad\qquad (I.11)$$

$$\overline{M}_2 \cdot \overline{L}_2 = 1 \qquad\qquad (I.12)$$

which dictates the slopes of the vectors $\overline{M}_1$ and $\overline{M}_2$ in Figure (I.2), as well as their lengths

$$M_1 = \frac{1}{L} \sqrt{L_{22}^2 + L_{12}^2} = \frac{L_2}{L} \qquad\qquad (I.13)$$

$$M_2 = \frac{1}{L} \sqrt{L_{21}^2 + L_{11}^2} = \frac{L_1}{L} \qquad\qquad (I.14)$$

Equation (I.1) can now be expanded to yield

$$d\lambda_c = \overline{M}_1 \cdot \overline{df}_e' > 0 \qquad\qquad (I.15)$$

$$d\lambda_p = \overline{M}_2 \cdot \overline{df}_e' > 0 \qquad\qquad (I.16)$$

Equations (I.15) and (I.16) will be satisfied if and only if the vector $\overline{df}_e'$ lies between the vectors $\overline{L}_1$ and $\overline{L}_2$ in Figure (I.2). That zone is labelled ECP in Figure (I.3).

When $\overline{df}_e'$ is parallel to $\overline{L}_1$, Equation (I.16) gives

$$d\lambda_p = \overline{M}_2 \cdot \overline{df}_e' = 0 \qquad\qquad (I.17)$$

Also, in that case

$$\frac{df'_e}{L_1} = \frac{df'_{ce}}{L_{11}} \qquad (I.18)$$

so that

$$d\lambda_c = \overline{M}_1 \cdot \overline{df}'_e = \overline{M}_1 \cdot \left(\frac{df'_{ce}}{L_{11}} \overline{L}_1\right) = \frac{df'_{ce}}{L_{11}} \qquad (I.19)$$

Similarly, when $\overline{df}'_e$ is parallel to $\overline{L}_2$, we have

$$d\lambda_c = 0 \qquad (I.20)$$

$$\frac{df'_e}{L_2} = \frac{df'_{pe}}{L_{22}} \qquad (I.21)$$

$$d\lambda_p = \overline{M}_2 \cdot \overline{df}'_e = \frac{df'_{pe}}{L_{22}} \qquad (I.22)$$

For the EC mode Equation (G.11) can be written in the form

$$d\lambda_c = \frac{df'_{ce}}{L_{11}} > 0 \qquad (I.19)$$

which is the same as the expression obtained when $\overline{df}'_e$ is parallel to $\overline{L}_1$ in the ECP mode. When $L_{11} > 0$, Equation (I.19) requires that

$$df'_{ce} > 0 \qquad (I.23)$$

In addition, when $d\lambda_p = 0$, Equations (H.4), (G.1), (G.2), and (F.22) yield

$$df'_p = \left\{\frac{\partial f'_p}{\partial \sigma}\right\}^T \{d\sigma\} = \left\{\frac{\partial f'_p}{\partial \sigma}\right\}^T \underline{C}^e \left\{\{d\varepsilon\} - \left\{\frac{\partial g_c}{\partial \sigma}\right\} d\lambda_c\right\}$$

182

$$= df'_{pe} - L_{21} d\lambda_c$$

$$= df'_{pe} - L_{21} \frac{df'_{ce}}{L_{11}} \leq 0 \qquad (I.24)$$

When $L_{11} > 0$, Equation (I.24) yields

$$L_{11} \, df'_p = L_{11} \, df'_{pe} - L_{21} \, df'_{ce} = \overline{M}_2 \cdot \overline{df'_e} \leq 0 \qquad (I.25)$$

The zone of the L plane in which both Equations (I.23) and (I.25) are satisfied is the EC zone in Figure (I.3).

For the EP mode, Equation (G.16) can be written in the form

$$d\lambda_p = \frac{df'_{pe}}{L_{22}} > 0 \qquad (I.22)$$

which is the same as the expression obtained when $\overline{df'_e}$ is parallel to $\overline{L}_2$ in the ECP mode. When $L_{22} > 0$, Equation (I.22) requires that

$$df'_{pe} > 0 \qquad (I.26)$$

In addition, when $d\lambda_c = 0$, Equations (H.3), (G.1), (G.2), and (F.22) yield

$$df'_c = \left\{\frac{\partial f'_c}{\partial \sigma}\right\}^T \{d\sigma\} = \left\{\frac{\partial f'_c}{\partial \sigma}\right\}^T \underline{C}^e \left\{\{d\epsilon\} - \left\{\frac{\partial g_p}{\partial \sigma}\right\} d\lambda_p\right\}$$

$$= df'_{ce} - L_{12} \, d\lambda_p$$

$$= df'_{ce} - \frac{L_{12}}{L_{22}} \, df'_{pe} \leq 0 \qquad (I.27)$$

When $L_{22} > 0$, Equation (I.27) yields

$$L_{22} \, df'_c = L_{22} \, df'_{ce} - L_{12} \, df'_{pe} = \overline{M}_1 \cdot \overline{df'_e} \leq 0 \qquad (I.28)$$

183

The zone of the L plane in which both Equations (I.26) and (I.28) are satisfied is the EP zone in Figure (I.3).

For the E mode,

$$\{d\lambda\} = \begin{Bmatrix} d\lambda_c \\ d\lambda_p \end{Bmatrix} = \{0\} \tag{I.29}$$

so that Equations (H.3), (H.4), (G.1), (G.2), and (F.22) yield

$$df'_c = \left\{ \frac{\partial f'_c}{\partial \sigma} \right\}^T \{d\sigma\} = \left\{ \frac{\partial f'_c}{\partial \sigma} \right\}^T \underline{C}^e \{d\varepsilon\} = df'_{ce} \leq 0 \tag{I.30}$$

and

$$df'_p = \left\{ \frac{\partial f'_p}{\partial \sigma} \right\}^T \{d\sigma\} = \left\{ \frac{\partial f'_p}{\partial \sigma} \right\}^T \underline{C}^e \{d\varepsilon\} = df'_{pe} \leq 0 \tag{I.31}$$

The zone of the L plane in which both Equations (I.30) and (I.31) are satisfied is the E zone in Figure (I.3).

Figure (I.3), which is called a polar mode check, shows both the vectors $\overline{L}_1$ and $\overline{L}_2$ in the first quadrant, with a counterclockwise acute angle between $\overline{L}_1$ and $\overline{L}_2$. However, there are other possibilities. If we assume the compressive yield surface to be always strain hardening so that $L_{11} > 0$, but admit the possibility of strain softening for the expansive yield surface so that L_{22} might be negative, then there are twelve possible relative angular positions for $\overline{L}_1$ and $\overline{L}_2$. Because $L_{11} > 0$, $\overline{L}_1$ must lie in the first or fourth quadrant. But $\overline{L}_2$ can lie in any quadrant, and when $\overline{L}_2$ lies in the quadrant opposite (i.e., not adjacent to) the quadrant containing $\overline{L}_1$ the obtuse angle between $\overline{L}_1$ and $\overline{L}_2$ can be either counterclockwise or clockwise. The twelve relative angular possibilities for $\overline{L}_1$ and $\overline{L}_2$, together with their

184

impact on both uniqueness and completeness of the incremental deformation
mode solution are tabulated below:

	QUADRANT		ANGLE		
CASE	$\overline{L}_1$	$\overline{L}_2$	$\overline{L}_1$ to $\overline{L}_2$	UNIQUE	COMPLETE
1	1	2	CCW	Yes	Yes
2	1	1	CCW	Yes	Yes
3	1	1	CW	Yes	No
4	1	4	CW	No	No
5	1	3	CW	No	No
6	1	3	CCW	No	Yes
7	4	2	CCW	Yes	Yes
8	4	1	CCW	Yes	Yes
9	4	4	CCW	No	No
10	4	4	CW	No	No
11	4	3	CW	No	No
12	4	2	CW	No	Yes

In the above table a unique solution is one having no overlap between
incremental deformation mode zones, and a complete solution is one for
which no angular zones are prohibited. It turns out that the only cases
for which the incremental deformation mode solution is both unique and
complete are those for which

$$L_{11} > 0 \tag{I.32}$$

$$L_{22} > 0 \tag{I.33}$$

$$L = L_{11}L_{22} - L_{12}L_{21} > 0 \tag{I.34}$$

Now consider the case in which the stress point lies on the
compressive yield surface but below the expansive yield surface, so that
$f_c = 0$ but $f_p < 0$. Equation (I.19) still applies, so that

$$d\lambda_c = \frac{df'_{ce}}{L_{11}} > 0 \tag{I.19}$$

185

There is no danger of the stress point punching through the compressive yield surface, because if $d\lambda_c > 0$ the consistency condition $df_c = 0$ prevents punch through; and if $d\lambda_c \leq 0$ it is because $df'_{ce} \leq 0$, so that the stress point stays on or pulls away from the compressive yield surface. However, a restriction is needed to avoid violation of the expansive yield surface. Equation (I.24) can be generalized to give

$$df'_p = df'_{pe} - \frac{L_{21}}{L_{11}} R(df'_{ce})$$ (I.35)

Then if the ratio

$$\zeta_p = \frac{df'_p}{-f_p}$$ (I.36)

exceeds 1.0, the expansive yield surface will be violated unless the strain increment is reduced. This is done by splitting the strain increment into two parts by setting

$$\{d\varepsilon\} = \{d\varepsilon\}_1 + \{d\varepsilon\}_2$$ (I.37)

where

$$\{d\varepsilon\}_1 = \frac{1}{\zeta_p} \{d\varepsilon\}$$ (I.38)

$$\{d\varepsilon\}_2 = (1 - \frac{1}{\zeta_p}) \{d\varepsilon\}$$ (I.39)

The strain subincrement $\{d\varepsilon\}_1$ is just sufficient to bring the stress point into contact with the expansive yield surface. The remaining strain subincrement, $\{d\varepsilon\}_2$, is then applied assuming the expansive yield surface to be active (ECP or EP mode).

186

A similar procedure is used when the compressive yield surface is inactive and the expansive yield surface active at the start of a strain increment, i.e., $f_c < 0$ and $f_p = 0$, using Equation (I.22)

$$d\lambda_p = \frac{df'_{pe}}{L_{22}} > 0 \tag{I.22}$$

a generalization of Equation (I.27),

$$df'_c = df'_{ce} - \frac{L_{12}}{L_{22}} R(df'_{pe}) \tag{I.40}$$

and the ratio

$$\zeta_c = \frac{df'_c}{-f_c} \tag{I.41}$$

When both yield surfaces are inactive at the start of a strain increment, i.e., $f_c < 0$ and $f_p < 0$, compute both

$$\zeta_c = \frac{df'_{ce}}{-f_c} \tag{I.42}$$

and

$$\zeta_p = \frac{df'_{pe}}{-f_p} \tag{I.43}$$

Unless both ratios are less than 1.0, set

$$\{d\epsilon\} = \{d\epsilon\}_1 + \{d\epsilon\}_2 \tag{I.44}$$

where

$$\{d\epsilon\}_1 = \frac{1}{\zeta} \{d\epsilon\} \tag{I.45}$$

187

$$\{d\varepsilon\}_2 = (1 - \frac{1}{\zeta}) \{d\varepsilon\} \qquad\qquad (I.46)$$

$$\zeta = \text{larger of } \zeta_c \text{ and } \zeta_p \qquad\qquad (I.47)$$

The strain subincrement $\{d\varepsilon\}_1$ will bring the stress point into contact with one yield surface, at which point one of the first two tests must be applied to see whether $\{d\varepsilon\}_2$ should be split to avoid violation of the other yield surface.
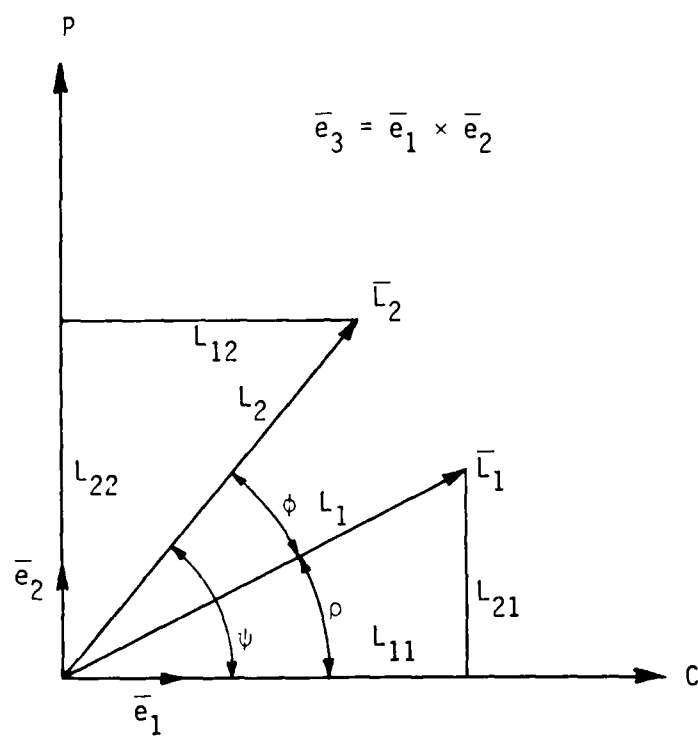
Figure I.1. The partitioned column vectors $\overline{L}_1$ and $\overline{L}_2$.

189
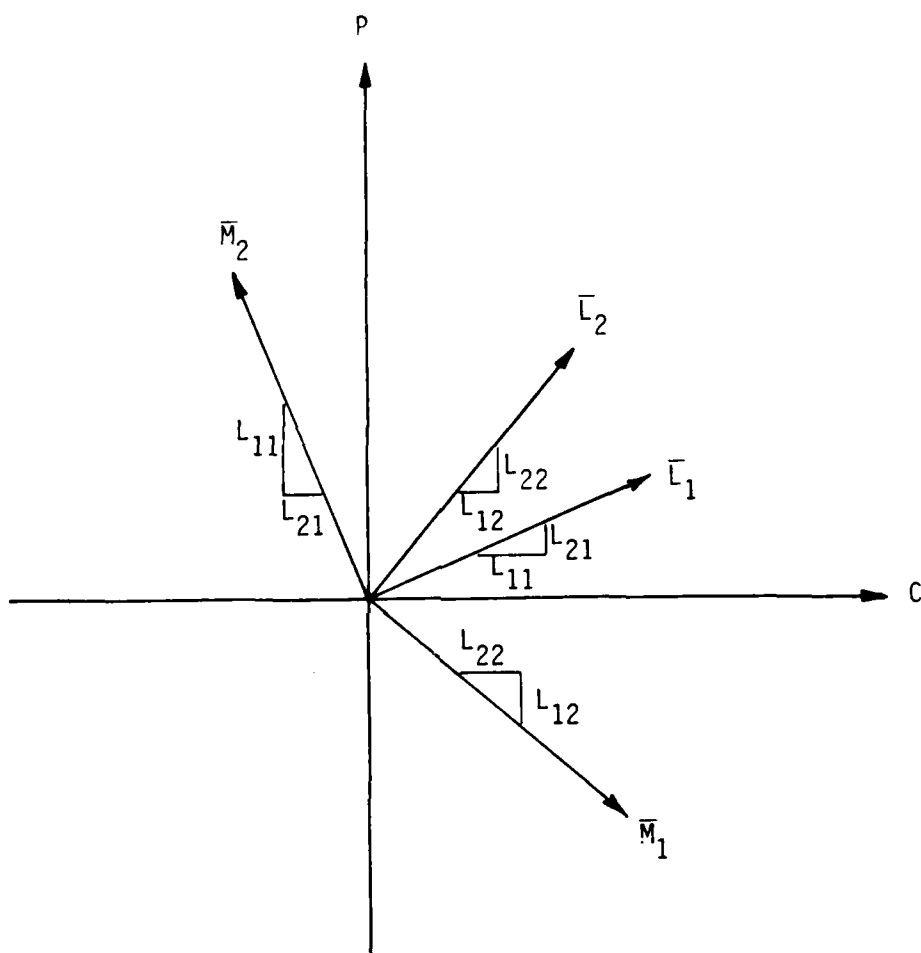
Figure I.2. Relation between the row vectors of $\underline{M}$ and the
column vectors of $\underline{L}$.
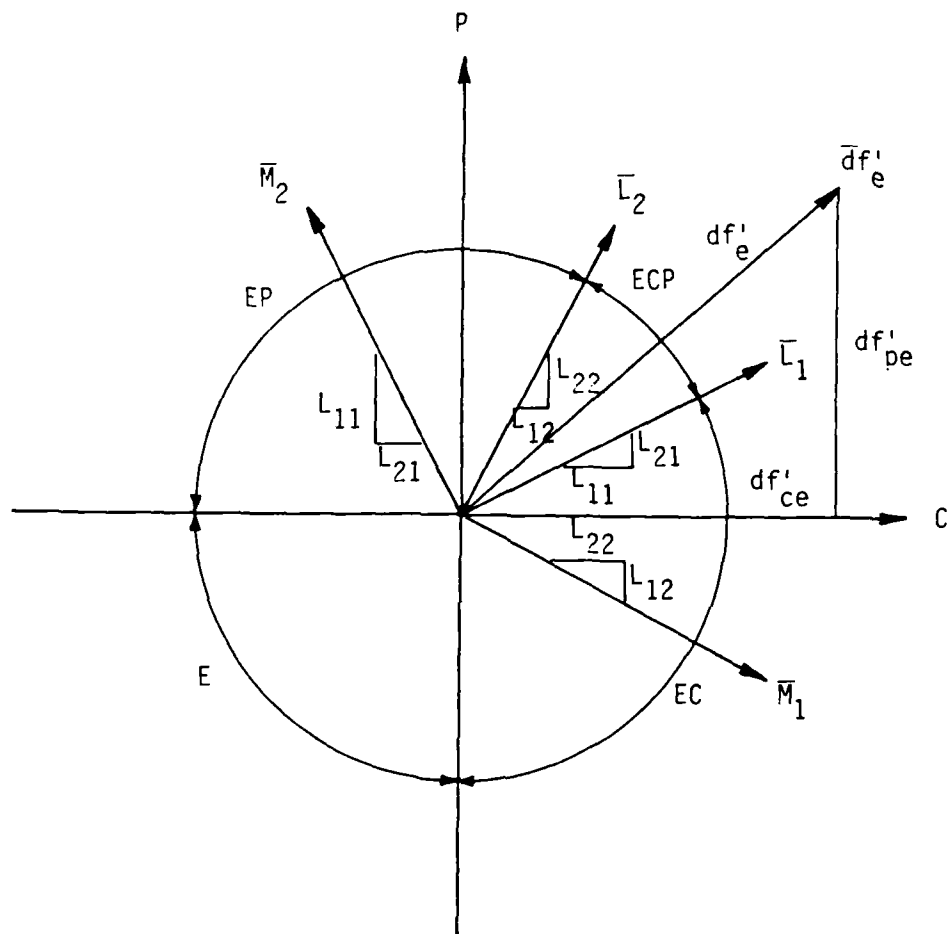
Figure I.3. Incremental deformation mode logic for a strain
hardening, two yield surface elastoplastic model
under strain control, at the corner.

191

APPENDIX J

ELASTIC STRESS-STRAIN EQUATIONS

The theory of linear elasticity assumes the stress vector $\{\sigma\}$ in Equation (E.5) and the strain vector $\{\epsilon\}$ in Equation (E.24) are related by a set of linear equations of the form

$$\{\epsilon\} = \underline{H}^e \{\sigma\} \tag{J.1}$$

where the elements of the elastic flexibility matrix, $\underline{H}^e$, are constant.

First consider the work done when two successive stress increments, $\{d\sigma\}_1$ and $\{d\sigma\}_2$, are added to an existing stress, $\{\sigma\}$. The increment of work must be independent of the order of application of the stress increments, so that

$$dW = \{\sigma\}^T \{d\epsilon\}_1 + \left(\left[\{\sigma\} + \{d\sigma\}_1 \right]^T \{d\epsilon\}_2 \right)$$

$$= \{\sigma\}^T \{d\epsilon\}_2 + \left(\left[\{\sigma\} + \{d\sigma\}_2 \right]^T \{d\epsilon\}_1 \right) \tag{J.2}$$

Equation (J.2) yields

$$\{d\sigma\}_1^T \{d\epsilon\}_2 = \{d\sigma\}_2^T \{d\epsilon\}_1 = \{d\epsilon\}_1^T \{d\sigma\}_2 \tag{J.3}$$

and from Equation (J.1) we have

$$\{d\epsilon\}_1 = \underline{H}^e \{d\sigma\}_1 \tag{J.4}$$

$$\{d\epsilon\}_2 = \underline{H}^e \{d\epsilon\}_2 \tag{J.5}$$

Substitution of Equations (J.4) and (J.5) into Equation (J.3) yields

$$\{d\sigma\}_1^T \underline{H}^e \{d\sigma\}_2 = \{d\sigma\}_1^T \underline{H}^{e,T} \{d\sigma\}_2 \qquad (J.6)$$

and Equation (J.6) will be satisfied if and only if the elastic flexibility matrix, $\underline{H}^e$, is symmetric, i.e.,

$$\underline{H}^{e,T} = \underline{H}^e \qquad (J.7)$$

Next consider what happens when the positive direction of one of the coordinate axes, say X_1, is reversed. Because the positive direction of the corresponding particle displacement is also reversed, the two strain elements

$$\varepsilon_4 = \sqrt{2}\, \varepsilon_{12} = \frac{1}{\sqrt{2}} \left(\frac{\partial u_1}{\partial x_2} + \frac{\partial u_2}{\partial x_1} \right) \qquad (J.8)$$

and

$$\varepsilon_6 = \sqrt{2}\, \varepsilon_{31} = \frac{1}{\sqrt{2}} \left(\frac{\partial u_3}{\partial x_1} + \frac{\partial u_1}{\partial x_3} \right) \qquad (J.9)$$

change sign, but the other four strain elements remain unchanged. Similarly, the two stress elements $\sigma_4 = \sqrt{2}\, \sigma_{12}$ and $\sigma_6 = \sqrt{2}\, \sigma_{31}$ change sign, but the other four stress elements remain unchanged.

The only way for the above two conditions (symmetry and independence of stress axis reversal) to be satisfied is for $\underline{H}^e$ to be of the form

$$\underline{H}^e = \begin{bmatrix} a & b & c & 0 & 0 & 0 \\ b & d & e & 0 & 0 & 0 \\ c & e & f & 0 & 0 & 0 \\ 0 & 0 & 0 & g & 0 & 0 \\ 0 & 0 & 0 & 0 & h & 0 \\ 0 & 0 & 0 & 0 & 0 & i \end{bmatrix} \qquad (J.10)$$

193

In addition, if the material is isotropic, then the relationship between each normal stress and the corresponding extensional strain, each normal stress and the two orthogonal normal strains, and each shear stress and the corresponding shear strain must be the same. Thus, Equation (J.10) reduces to

$$\underline{H}^e = \begin{bmatrix} a & b & b & 0 & 0 & 0 \\ b & a & b & 0 & 0 & 0 \\ b & b & a & 0 & 0 & 0 \\ 0 & 0 & 0 & g & 0 & 0 \\ 0 & 0 & 0 & 0 & g & 0 \\ 0 & 0 & 0 & 0 & 0 & g \end{bmatrix} \tag{J.11}$$

With $\underline{H}^e$ defined by Equation (J.11), the first, second and fourth of Equations (J.1) take the form

$$\varepsilon_1 = a\sigma_1 + b\sigma_2 + b\sigma_3 \tag{J.12}$$

$$\varepsilon_2 = b\sigma_1 + a\sigma_2 + b\sigma_3 \tag{J.13}$$

$$\varepsilon_4 = g\sigma_4 \tag{J.14}$$

so that

$$\frac{\varepsilon_1 - \varepsilon_2}{2} = (a - b)\left(\frac{\sigma_1 - \sigma_2}{2}\right) \tag{J.15}$$

If the X_1 and X_2 axes are now rotated until the shear strain, ε_4', and the shear stress, σ_4', reach a maximum, a Mohr circle analysis shows that Equation (J.14) would take the form

$$\sqrt{\left(\frac{\varepsilon_1 - \varepsilon_2}{2}\right)^2 + \frac{\varepsilon_4^2}{2}} = g\sqrt{\left(\frac{\sigma_1 - \sigma_2}{2}\right)^2 + \frac{\sigma_4^2}{2}} \tag{J.16}$$

194

Substitution of Equations (J.14) and (J.15) into the left hand side of Equation (J.16) yields

$$\sqrt{(a - b)^2 \left(\frac{\sigma_1 - \sigma_2}{2}\right)^2 + g^2 \frac{\sigma_4^2}{2}} = g \sqrt{\left(\frac{\sigma_1 - \sigma_2}{2}\right)^2 + \frac{\sigma_4^2}{2}} \qquad (J.17)$$

and Equation (J.17) will be satisfied if and only if

$$a - b = g \qquad (J.18)$$

Therefore, if we set

$$a = \frac{1}{E} \qquad (J.19)$$

$$b = -\frac{\nu}{E} \qquad (J.20)$$

$$g = \frac{1}{2G} \qquad (J.21)$$

then Equation (J.18) yields

$$\frac{1}{2G} = \frac{1 + \nu}{E}$$

or

$$E = 2G (1 + \nu) \qquad (J.22)$$

so that the final form of Equation (J.11) is

$$\underline{H}^e = \frac{1}{E} \begin{bmatrix} 1 & -\nu & -\nu & 0 & 0 & 0 \\ -\nu & 1 & -\nu & 0 & 0 & 0 \\ -\nu & -\nu & 1 & 0 & 0 & 0 \\ 0 & 0 & 0 & 1+\nu & 0 & 0 \\ 0 & 0 & 0 & 0 & 1+\nu & 0 \\ 0 & 0 & 0 & 0 & 0 & 1+\nu \end{bmatrix} \qquad (J.23)$$

195

With $\underline{H}^e$ defined by Equation (J.23), the tensor stress-strain equations represented by Equation (J.1) can be written in the form

$$\varepsilon_{ij} = \frac{1}{E} [(1 + \nu)\sigma_{ij} - \nu\sigma_{kk}\delta_{ij}] \tag{J.24}$$

so that the volumetric strain is

$$\varepsilon_{kk} = \frac{1 - 2\nu}{E} \sigma_{kk} \tag{J.25}$$

and therefore the deviator strains are

$$e_{ij} = \varepsilon_{ij} - \frac{\varepsilon_{kk}}{3} \delta_{ij} = \frac{1}{E}[(1 + \nu)\sigma_{ij} - \nu\sigma_{kk}\delta_{ij}] - \frac{1 - 2\nu}{E} \frac{\sigma_{kk}}{3} \delta_{ij}$$

$$= \frac{1 + \nu}{E} \left(\sigma_{ij} - \frac{\sigma_{kk}}{3} \delta_{ij}\right) = \frac{1 + \nu}{E} s_{ij} \tag{J.26}$$

Equations (J.25) and (J.26) can be inverted in the form

$$s_{ij} = \frac{E}{1 + \nu} e_{ij} \tag{J.27}$$

$$\sigma_{kk} = \frac{E}{1 - 2\nu} \varepsilon_{kk} \tag{J.28}$$

so that

$$\sigma_{ij} = s_{ij} + \frac{\sigma_{kk}}{3} \delta_{ij} = \frac{E}{1 + \nu} \left(\varepsilon_{ij} - \frac{\varepsilon_{kk}}{3} \delta_{ij}\right) + \frac{E}{3(1 - 2\nu)} \varepsilon_{kk}\delta_{ij}$$

$$= \frac{E}{1 + \nu} \left[\varepsilon_{ij} + \left(\frac{\nu}{1 - 2\nu}\right) \varepsilon_{kk}\delta_{ij}\right] \tag{J.29}$$

which means that the elastic stiffness matrix, $\underline{C}^e$, in the equations

$$\{\sigma\} = \underline{C}^e\{\varepsilon\} \tag{J.30}$$

where

$$\underline{H}^e\underline{C}^e = \underline{C}^e\underline{H}^e = \underline{I} \tag{J.31}$$

196

is

$$\underline{C}^e = \frac{E(1-\nu)}{(1+\nu)(1-2\nu)} \begin{bmatrix} 1 & \frac{\nu}{1-\nu} & \frac{\nu}{1-\nu} & 0 & 0 & 0 \\ \frac{\nu}{1-\nu} & 1 & \frac{\nu}{1-\nu} & 0 & 0 & 0 \\ \frac{\nu}{1-\nu} & \frac{\nu}{1-\nu} & 1 & 0 & 0 & 0 \\ 0 & 0 & 0 & \frac{1-2\nu}{1-\nu} & 0 & 0 \\ 0 & 0 & 0 & 0 & \frac{1-2\nu}{1-\nu} & 0 \\ 0 & 0 & 0 & 0 & 0 & \frac{1-2\nu}{1-\nu} \end{bmatrix} \qquad (J.32)$$

Equation (J.31) can be written in terms of two quantities familar in soil mechanics, viz.

$$M = \frac{E(1-\nu)}{(1+\nu)(1-2\nu)} = \text{constrained modulus} \qquad (J.33)$$

$$K_0 = \frac{\nu}{1-\nu} = \text{coefficient of lateral stress at rest} \qquad (J.34)$$

so that

$$\underline{C}^e = M \begin{bmatrix} 1 & K_0 & K_0 & 0 & 0 & 0 \\ K_0 & 1 & K_0 & 0 & 0 & 0 \\ K_0 & K_0 & 1 & 0 & 0 & 0 \\ 0 & 0 & 0 & 1-K_0 & 0 & 0 \\ 0 & 0 & 0 & 0 & 1-K_0 & 0 \\ 0 & 0 & 0 & 0 & 0 & 1-K_0 \end{bmatrix} \qquad (J.35)$$

In an elastoplastic model, Equations (J.1) and (J.29) are written in incremental form.

$$\{d\varepsilon^e\} = \underline{H}^e \{d\sigma\} \qquad (J.36)$$

$$\{d\sigma\} = \underline{C}^e \{d\varepsilon^e\} \qquad (J.37)$$

197

The elastic incremental flexibility and stiffness matrixes, $\underline{H}^e$ and $\underline{C}^e$, are still written in the form of Equations (J.23), (J.31) or (J.35), but the elastic constants may be assumed to vary with stress and/or strain.

APPENDIX K

SPECIAL EQUATIONS FOR THE TRIAXIAL TEST

In the triaxial test the normal stresses are principal stresses, and the lateral principal stresses are equal. Consequently, the stress matrix and its matrix of cofactors reduces to

$$\underline{\sigma} = \begin{bmatrix} \sigma_a & 0 & 0 \\ 0 & \sigma_r & 0 \\ 0 & 0 & \sigma_r \end{bmatrix} \tag{K.1}$$

$$\underline{\Sigma} = \sigma_r \begin{bmatrix} \sigma_r & 0 & 0 \\ 0 & \sigma_a & 0 \\ 0 & 0 & \sigma_a \end{bmatrix} \tag{K.2}$$

and the total stress invariants are

$$I_1 = \sigma_a + 2\sigma_r \tag{K.3}$$

$$I_2 = -\sigma_r(2\sigma_a + \sigma_r) \tag{K.4}$$

$$I_3 = \sigma_a \sigma_r^2 \tag{K.5}$$

The deviator stress matrix and its matrix of cofactors are

$$\underline{s} = \left(\frac{\sigma_a - \sigma_r}{3}\right) \begin{bmatrix} 2 & 0 & 0 \\ 0 & -1 & 0 \\ 0 & 0 & -1 \end{bmatrix} \tag{K.6}$$

$$\underline{S} = \left(\frac{\sigma_a - \sigma_r}{3}\right)^2 \begin{bmatrix} 1 & 0 & 0 \\ 0 & -2 & 0 \\ 0 & 0 & -2 \end{bmatrix} \tag{K.7}$$

199

and the deviator stress invariants are

$$J_1 = 0 \tag{K.8}$$

$$J_2 = \frac{(\sigma_a - \sigma_r)^2}{3} \tag{K.9}$$

$$J_3 = 2\left(\frac{\sigma_a - \sigma_r}{3}\right)^3 \tag{K.10}$$

Also,

$$\sigma_{oct} = \frac{\sigma_a + 2\sigma_r}{3} \tag{K.11}$$

$$\sigma_{oct}^2 = \frac{2}{3} J_2 = 2\left(\frac{\sigma_a - \sigma_r}{3}\right)^2 \tag{K.12}$$

$$\tau_{oct} = \frac{\sqrt{2}}{3} \left| \sigma_a - \sigma_r \right| \tag{K.13}$$

$$\cos 3\theta = \frac{\dfrac{J_3}{2}}{\left(\dfrac{J_2}{3}\right)^{3/2}} = \frac{\left(\dfrac{\sigma_a - \sigma_r}{3}\right)^3}{\left|\dfrac{\sigma_a - \sigma_r}{3}\right|^3} = \operatorname{sgn}(\sigma_a - \sigma_r) \tag{K.14}$$

Because of axial symmetry, the orientation of the coordinate axes, and isotropy the 3 x 3 elastoplastic incremental stiffness matrix, $\underline{C}^{ep}$, has the property that

$$C_{12}^{ep} = C_{13}^{ep} \tag{K.15}$$

$$C_{22}^{ep} = C_{33}^{ep} \tag{K.16}$$

$$C_{21}^{ep} = C_{31}^{ep} \tag{K.17}$$

$$C_{23}^{ep} = C_{32}^{ep} \tag{K.18}$$

200

The 3 x 3 elastoplastic incremental flexibility matrix, $\underline{H}^{ep}$, has the same properties.

For hydrostatic compression

$$\sigma_a = \sigma_r = \sigma_{OCT} \tag{K.19}$$

$$\epsilon_a = \epsilon_r = \frac{\epsilon_{KK}}{3} \tag{K.20}$$

and the 3 x 3 incremental stiffness matrix has the additional property that

$$C_{11}^{ep} = C_{22}^{ep} = C_{33}^{ep} \tag{K.21}$$

$$C_{12}^{ep} = C_{13}^{ep} = C_{21}^{ep} = C_{23}^{ep} = C_{31}^{ep} = C_{32}^{ep} \tag{K.22}$$

Therefore, the octahedral normal stress increment is

$$d\sigma_{OCT} = d\sigma_a = (C_{11}^{ep} + 2C_{12}^{ep})\, d\epsilon_a = \left(\frac{C_{11}^{ep} + 2C_{12}^{ep}}{3}\right) d\epsilon_{KK} = B^{ep} d\epsilon_{KK} \tag{K.23}$$

where the elastoplastic incremental bulk modulus for pure hydrostatic compression, B^{ep}, is

$$B^{ep} = \frac{C_{11}^{ep} + 2C_{12}^{ep}}{3} \tag{K.24}$$

As long as the octahedral normal stress increases monotonically, the incremental deformation mode is the EC mode. Unloading and reloading are elastic.

For triaxial compression at constant cell pressure, starting from isotropic consolidation, the ECP mode is active as long as $(\sigma_a - \sigma_r)$ is increasing. Since

$$d\sigma_r = 0 \tag{K.25}$$

201

the incremental flexibility equations take the form

$$d\varepsilon_a = H_{11}^{ep} \, d\sigma_a = \frac{d\sigma_a}{E^{ep}} \qquad (K.26)$$

$$d\varepsilon_r = H_{21}^{ep} \, d\sigma_a = \frac{H_{21}^{ep}}{H_{11}^{ep}} \, d\varepsilon_a = -\nu^{ep} d\varepsilon_a \qquad (K.27)$$

where the elastoplastic incremental Young's modulus, E^{ep}, is

$$E^{ep} = \frac{1}{H_{11}^{ep}} \qquad (K.28)$$

and the elastoplastic incremental Poisson's ratio, ν^{ep}, is

$$\nu^{ep} = - \frac{H_{21}^{ep}}{H_{11}^{ep}} \qquad (K.29)$$

If the calculation is performed under axial strain control, then Equation (K.26) is written in the form

$$d\sigma_a = \frac{d\varepsilon_a}{H_{11}^{ep}} = E^{ep} \, d\varepsilon_a \qquad (K.30)$$

The above equations can be written in incremental stiffness form as well, by setting

$$d\sigma_a = C_{11}^{ep} \, d\varepsilon_a + 2C_{12}^{ep} \, d\varepsilon_r \qquad (K.31)$$

$$d\sigma_r = 0 = C_{21}^{ep} \, d\varepsilon_a + (C_{22}^{ep} + C_{23}^{ep}) \, d\varepsilon_r \qquad (K.32)$$

Equation (K.32) yields

$$d\epsilon_r = -\left(\frac{C_{21}^{ep}}{C_{22}^{ep} + C_{23}^{ep}}\right) d\epsilon_a = -\nu^{ep} d\epsilon_a \tag{K.33}$$

where

$$\nu^{ep} = \frac{C_{21}^{ep}}{C_{22}^{ep} + C_{23}^{ep}} \tag{K.34}$$

Substitution of Equation (K.33) into Equation (K.31) yields

$$d\sigma_a = (C_{11}^{ep} - 2\nu^{ep} C_{12}^{ep}) d\epsilon_a = E^{ep} d\epsilon_a \tag{K.35}$$

where

$$E^{ep} = C_{11}^{ep} - \frac{2C_{12}^{ep} C_{21}^{ep}}{C_{22}^{ep} + C_{23}^{ep}} \tag{K.36}$$

Comparison of Equations (K.29) and (K.34), and (K.28) and (K.36) shows that

$$\nu^{ep} = -\frac{H_{21}^{ep}}{H_{11}^{ep}} = \frac{C_{21}^{ep}}{C_{22}^{ep} + C_{23}^{ep}} \tag{K.37}$$

$$E^{ep} = \frac{1}{H_{11}^{ep}} = C_{11}^{ep} - \frac{2C_{12}^{ep} C_{21}^{ep}}{C_{22}^{ep} + C_{23}^{ep}} \tag{K.38}$$

which is confirmed by forming the inverse of the 2 x 2 matrix of coefficients of Equations (K.31) and (K.32).

For a general triaxial stress path test in which

$$d\sigma_r = \alpha d\sigma_a \tag{K.39}$$

so that

$$\frac{dq}{dp} = \frac{d\sigma_a - d\sigma_r}{d\sigma_a + d\sigma_r} = \frac{1 - \alpha}{1 + \alpha} \qquad (K.40)$$

the incremental deformation mode is determined by the methods of Appendix H, since

$$df'_c = \left\{\frac{\partial f'_c}{\partial \sigma}\right\}^T \{d\sigma\} \qquad (K.41)$$

$$df'_p = \left\{\frac{\partial f'_p}{\partial \sigma}\right\}^T \{d\sigma\} \qquad (K.42)$$

where

$$\{d\sigma\} = d\sigma_a \begin{Bmatrix} 1 \\ \alpha \\ \alpha \end{Bmatrix} \qquad (K.43)$$

The methods of Appendix H apply no matter whether the calculations are performed under axial stress or strain control, because the stress path is prescribed by Equation (K.39).

The incremental flexibility equations take the form

$$d\varepsilon_a = (H_{11}^{ep} + 2\alpha\, H_{12}^{ep})\, d\sigma_a \qquad (K.44)$$

$$d\varepsilon_r = \left[H_{21}^{ep} + \alpha(H_{22}^{ep} + H_{23}^{ep}) \right] d\sigma_a \qquad (K.45)$$

If the calculation is performed under axial strain control, Equations (K.44) and (K.45) are written in the form

$$d\sigma_a = \frac{d\varepsilon_a}{H_{11}^{ep} + 2\alpha\, H_{12}^{ep}} \qquad (K.46)$$

204

$$d\epsilon_r = \left[\frac{H_{21}^{ep} + \alpha(H_{22}^{ep} + H_{23}^{ep})}{H_{11}^{ep} + 2\alpha H_{12}^{ep}}\right] d\epsilon_a = -\beta d\epsilon_a \qquad (K.47)$$

where

$$\beta = -\frac{H_{21}^{ep} + \alpha(H_{22}^{ep} + H_{23}^{ep})}{H_{11}^{ep} + 2\alpha H_{12}^{ep}} \qquad (K.48)$$

The corresponding incremental stiffness equations take the form

$$d\sigma_a = C_{11}^{ep} d\epsilon_a + 2C_{12}^{ep} d\epsilon_r \qquad (K.49)$$

$$d\sigma_r = \alpha d\sigma_a = C_{21}^{ep} d\epsilon_a + (C_{22}^{ep} + C_{23}^{ep}) d\epsilon_r \qquad (K.50)$$

Elimination of $d\sigma_r$ between Equations (K.49) and (K.50) yields

$$d\sigma_r = C_{21}^{ep} d\epsilon_a + (C_{22}^{ep} + C_{23}^{ep}) d\epsilon_r$$

$$= \alpha C_{11}^{ep} d\epsilon_a + 2\alpha C_{12}^{ep} d\epsilon_r \qquad (K.51)$$

so that

$$(C_{22}^{ep} + C_{23}^{ep} - 2\alpha C_{12}^{ep}) d\epsilon_r = (\alpha C_{11}^{ep} - C_{21}^{ep}) d\epsilon_a$$

or

$$d\epsilon_r = -\left(\frac{C_{21}^{ep} - \alpha C_{11}^{ep}}{C_{22}^{ep} + C_{23}^{ep} - 2\alpha C_{12}^{ep}}\right) d\epsilon_a = -\beta d\epsilon_a \qquad (K.52)$$

where

$$\beta = \frac{C_{21}^{ep} - \alpha C_{11}^{ep}}{C_{22}^{ep} + C_{23}^{ep} - 2\alpha C_{12}^{ep}} \qquad (K.53)$$

Substitution of Equation (K.52) into Equation (K.49) yields

$$d\sigma_a = (C_{11}^{ep} + 2\beta C_{12}^{ep}) d\varepsilon_a \qquad (K.54)$$

If the calculation is performed under axial stress control, Equation (K.54) is written in the form

$$d\varepsilon_a = \frac{d\sigma_a}{C_{11}^{ep} + 2\beta C_{12}^{ep}} \qquad (K.55)$$

For constrained (one-dimensional) compression

$$d\varepsilon_r = 0 \qquad (K.56)$$

A constrained compression test is a particular strain path test, so that the incremental deformation mode is determined by the methods of Appendix I. The incremental stiffness equations take the form

$$d\sigma_a = C_{11}^{ep} d\varepsilon_a = M^{ep} d\varepsilon_a \qquad (K.57)$$

$$d\sigma_r = C_{21}^{ep} d\varepsilon_a = \frac{C_{21}^{ep}}{C_{11}^{ep}} d\sigma_a = K_0^{ep} d\sigma_a \qquad (K.58)$$

where the incremental elastoplastic constrained modulus, M^{ep}, is

$$M^{ep} = C_{11}^{ep} \qquad (K.59)$$

206

and the incremental elastoplastic coefficient of lateral stress, K_0^{ep}, is

$$K_0^{ep} = \frac{C_{21}^{ep}}{C_{11}^{ep}} \qquad (K.60)$$

For constant volume compression

$$d\epsilon_a + 2d\epsilon_r = 0 \qquad (K.61)$$

so that

$$d\epsilon_r = -\frac{1}{2} d\epsilon_a \qquad (K.62)$$

A constant volume test is also a particular strain path test, so that the incremental deformation mode is again determined by the methods of Appendix I. The incremental stiffness equations take the form

$$d\sigma_a = (C_{11}^{ep} - C_{12}^{ep}) \, d\epsilon_a \qquad (K.63)$$

$$d\sigma_r = \left[C_{21}^{ep} - \frac{1}{2} (C_{22}^{ep} + C_{23}^{ep}) \right] d\epsilon_a \qquad (K.64)$$

so that

$$d\sigma_r = \alpha \, d\sigma_a \qquad (K.65)$$

where

$$\alpha = \frac{C_{21}^{ep} - \frac{1}{2} (C_{22}^{ep} - C_{23}^{ep})}{C_{11}^{ep} - C_{12}^{ep}} \qquad (K.66)$$

If the calculation is performed under axial stress control, Equation (K.63) is written in the form

$$d\epsilon_a = \frac{d\sigma_a}{C_{11}^{ep} - C_{12}^{ep}} \qquad (K.67)$$

207

For a general triaxial strain path test in which

$$d\varepsilon_r = -\beta\, d\varepsilon_a \qquad (K.68)$$

the incremental deformation mode is determined by the methods of Appendix I. The incremental stiffness equations take the form

$$d\sigma_a = (C_{11}^{ep} - 2\beta\, C_{12}^{ep})\, d\varepsilon_a \qquad (K.69)$$

$$d\sigma_r = \left[C_{21}^{ep} - \beta\,(C_{22}^{ep} + C_{23}^{ep}) \right] d\varepsilon_a \qquad (K.70)$$

so that

$$d\sigma_r = \alpha\, d\sigma_a \qquad (K.71)$$

where

$$\alpha = \frac{C_{21}^{ep} - \beta(C_{22}^{ep} + C_{23}^{ep})}{C_{11}^{ep} - 2\beta\, C_{12}^{ep}} \qquad (K.72)$$

If the calculation is performed under axial stress control, Equation (K.69) is written in the form

$$d\varepsilon_a = \frac{d\sigma_a}{C_{11}^{ep} - 2\beta\, C_{12}^{ep}} \qquad (K.73)$$

APPENDIX L

TRANSIENT RESPONSE OF A THREE ELEMENT
VISCOELASTIC MODEL

Consider the three element viscoelastic model shown in Figure (L.1).

The basic equations governing the model response are [Bland (1960:3)].

$$F_1 = F_2 = F \tag{L.1}$$

$$x_1 + x_2 = x \tag{L.2}$$

$$F_1 = k_1 x_1 \tag{L.3}$$

$$F_2 = k_2 x_2 + \eta_2 \frac{dx_2}{dt} \tag{L.4}$$

Substitution of Equations (L.1), (L.2), and (L.3) into Equation (L.4) yields

$$F = k_2 \left(x - \frac{F}{k_1} \right) + \eta_2 \frac{d}{dt} \left(x - \frac{F}{k_1} \right)$$

or

$$F = k_2 x - \frac{k_2}{k_1} F + \eta_2 \frac{dx}{dt} - \frac{\eta_2}{k_1} \frac{dF}{dt}$$

or

$$\frac{dF}{dt} + \left(\frac{k_1 + k_2}{\eta_2} \right) F = k_1 \frac{dx}{dt} + \frac{k_1 k_2}{\eta_2} x \tag{L.5}$$

Equation (L.5) can be written in the form

$$\frac{dF}{dt} + aF = g(t) \tag{L.6}$$

209

where

$$a = \frac{k_1 + k_2}{n_2} \tag{L.7}$$

$$g = k_1 \left(\frac{dx}{dt} + \frac{k_2}{n_2} x \right) \tag{L.8}$$

Assuming that

$$x(0-) = F(0-) = 0 \tag{L.9}$$

the solution to Equation (L.6) is

$$F(t) = \int_0^t g(\gamma) e^{-a(t-\gamma)} d\gamma \tag{L.10}$$

Substitution of Equation (L.8) into Equation (L.10) yields

$$F(t) = k_1 \left[\int_0^t \frac{dx}{d\gamma} e^{-a(t-\gamma)} d\gamma + \frac{k_2}{n_2} \int_0^t x(\gamma) e^{-a(t-\gamma)} d\gamma \right] \tag{L.11}$$

The second integral on the RHS of Equation (L.11) can be integrated by parts by setting

$$U = x(\gamma) \tag{L.12}$$

$$dU = \frac{dx}{d\gamma} d\gamma \tag{L.13}$$

$$dV = e^{-a(t-\gamma)} d\gamma \tag{L.14}$$

$$V = \frac{1}{a} e^{-a(t-\gamma)} \tag{L.15}$$

so that

$$\int_0^t x(\gamma)e^{-a(t-\gamma)}\, d\gamma = \frac{1}{a}\left[x(\gamma)e^{-a(t-\gamma)}\Big|_0^t - \int_0^t \frac{dx}{d\gamma}\, e^{-a(t-\gamma)}d\gamma \right]$$

$$= \frac{1}{a}\left[x(t) - \int_0^t \frac{dx}{d\gamma}\, e^{-a(t-\gamma)}d\gamma \right] \qquad (L.16)$$

and substitution of Equation (L.16) into Equation (L.11) yields

$$F(t) = \frac{k_1 k_2}{r_2 a}\, x(t) + \left(k_1 - \frac{k_1 k_2}{n_2 a} \right) \int_0^t \frac{dx}{d\gamma}\, e^{-a(t-\gamma)}d\gamma$$

$$= \frac{k_1 k_2}{k_1 + k_2}\, \int_0^t \left[1 + \frac{k_2}{k_1}\, e^{-a(t-\gamma)} \right] \frac{dx}{d\gamma}\, d\gamma \qquad (L.17)$$

If the displacement, $x(\gamma)$, is a Heaviside step pulse, so that $dx/d\gamma$ is a Dirac-delta function, i.e.

$$x(\gamma) = XH(\gamma) \qquad (L.18)$$

$$\frac{dx}{d\gamma} = X\, \delta(\gamma) \qquad (L.19)$$

where

$$X = \text{constant} \qquad (L.20)$$

$$H(\gamma) = 0 \qquad (\gamma < 0)$$
$$= \frac{1}{2} \qquad (\gamma = 0) \qquad (L.21)$$
$$= 1 \qquad (\gamma > 0)$$

$$\delta(\gamma) = 0 \qquad (\gamma \neq 0) \qquad (L.22)$$

211

$$\int_{-\epsilon}^{\epsilon} f(\gamma)\, \delta(\gamma)\, d\gamma = f(0) \qquad (\epsilon > 0) \tag{L.23}$$

then Equation (L.17) yields the relaxation response

$$\frac{F_R(t)}{X} = R(t) = \frac{k_1 k_2}{k_1 + k_2}\left(1 + \frac{k_1}{k_2} e^{-at}\right) \tag{L.24}$$

and differentiation of Equation (L.23) yields

$$\frac{dR}{dt} = \dot{R} = -\frac{k_1^2 a}{k_1 + k_2} e^{-at} = -\frac{k_1^2}{\eta_2} e^{-at} \tag{L.25}$$

Equation (L.24) yields

$$R(0^+) = k_1 \tag{L.26}$$

$$R(\infty) = \frac{k_1 k_2}{k_1 + k_2} = k_1\left(\frac{k_2}{k_1 + k_2}\right) \tag{L.27}$$

and Equation (L.25) yields

$$\dot{R}(0^+) = -\frac{k_1^2}{\eta_2} \tag{L.28}$$

Referring to Figure (L.2) we define

$$t^\star = \frac{R(0^+) - R(\infty)}{\dot{R}(0^+)} = \frac{k_1\left(1 - \dfrac{k_2}{k_1 + k_2}\right)}{\dfrac{k_1^2}{\eta_2}} = \frac{\eta_2}{k_1 + k_2} \tag{L.29}$$

so that the parameters k_1, k_2, and n_2 can be calculated from the equations

$$k_1 = R(0+) \tag{L.30}$$

$$k_2 = \frac{R(0+) \cdot R(\infty)}{R(0+) - R(\infty)} \tag{L.31}$$

$$n_2 = \frac{R^2(0+)}{\dot{R}(0+)} \tag{L.32}$$

Note that Figure (L.1) shows only one of two possible viscoelastic models containing two springs and one dashpot [Bland (1960:3)], and that the determination of the parameter values, k_1, k_2, and n_2 is configuration dependent and therefore not unique.

213

$F(t)$

k_1

η_2

k_2

$l_1 + x_1(t)$

$l_2 + x_2(t)$

$l_1 + l_2 + x(t)$

$F(t)$
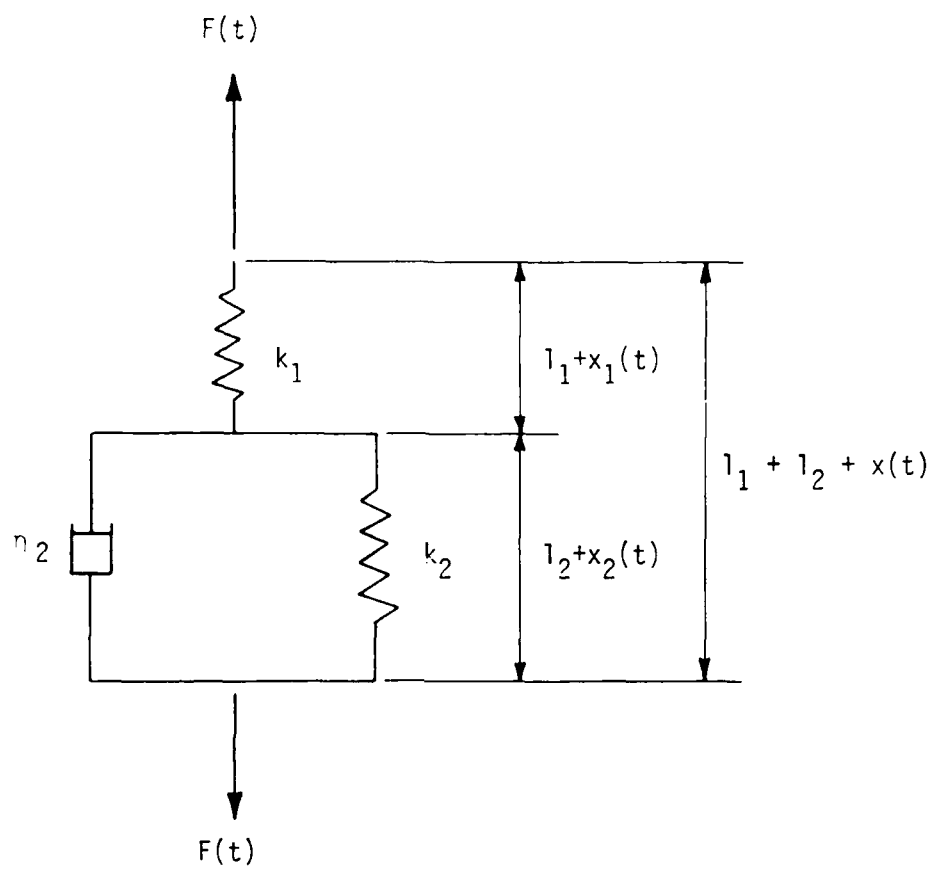
Figure L.1. Three element viscoelastic model.

214
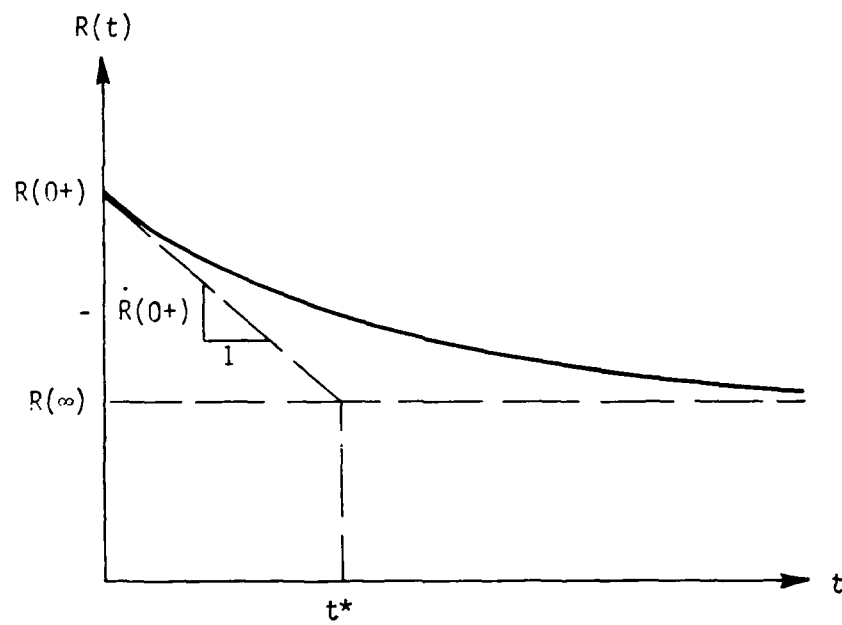
Figure L.2. Relaxation response of a three element
viscoelastic model.

215

APPENDIX M

YOUNG'S MODULUS FOR A HYPERBOLIC STRESS-STRAIN CURVE

The fact that a hyperbolic equation of the form

$$y = \frac{x}{a + bx} \tag{M.1}$$

can be written in the linear form

$$\frac{x}{y} = a + bx \tag{M.2}$$

has long been used to obtain an empirical formula for data originating at the origin and rising with steadily decreasing slope to approach a horizontal asymptote [Saxelby (1913:138); Running (1917:39,53)]. Southwell used the method in 1932 to determine the critical load of an elastic column with initial curvature; Gregory used it in 1959 to study structural stability; Kondner and Krizek used it in 1962 to fit a hyperbola to footing load--settlement data; Kondner and Zelasko used it in 1963 and 1964 to fit a hyperbola to triaxial compression data for both sand and clay; and Duncan and Chang used it in 1970, also to fit a hyperbola to triaxial compression data for soil, as a means of obtaining a general expression for the tangent Young's modulus to use in a finite element computer code [Southwell (1932); Southwell (1936); Gregory (1959); Gregory (1960); Timoshenko and Gere (1961); Kondner and Krizek (1962); Kondner (1963); Kondner and Zelasko (1963); Kondner and Zelasko (1964); Duncan and Chang (1970)].

For the case of cylindrical compression under constant confining (radial) stress, the intermediate and minor principal stresses are equal and constant, so that

$$\sigma_2 = \sigma_3 = \sigma_{3C} \tag{M.3}$$

Equation (J.23) therefore yields

$$\sigma_{\epsilon_1} = \frac{d\sigma_1}{E_T} = \frac{d(\sigma_1 - \sigma_{3C})}{E_T} \tag{M.4}$$

where

E_T = tangent Young's modulus for a nonlinear stress-strain curve

and, therefore

$$E_T = \frac{d(\sigma_1 - \sigma_{3C})}{d\epsilon_1} \tag{M.5}$$

If the relation between principal stress difference and axial strain is assumed to be of the hyperbolic form

$$\sigma_1 - \sigma_{3C} = \frac{\epsilon_1}{a + b\epsilon_1} \tag{M.6}$$

then it follows that

$$\lim_{\epsilon_1 \to 0} \left(\frac{\sigma_1 - \sigma_{3C}}{\epsilon_1} \right) = E_i = \frac{1}{a} \tag{M.7}$$

and

$$\lim_{\epsilon_1 \to \infty} (\sigma_1 - \sigma_{3C}) = (\sigma_1 - \sigma_{3C})_{ult} = \frac{1}{b} \tag{M.8}$$

217

Thus, the parameter a in Equation (M.6) is the reciprocal of the initial slope of the stress-strain curve, and the parameter b is the reciprocal of the upper asymptotic limit of the principal stress difference. The parameters a and b are commonly estimated by plotting $\varepsilon_1/(\sigma_1 - \sigma_{3C})$ against ε_1 and fitting a straight line to that plot, as shown in Figure (M.1), because Equation (M.6) has the linear form

$$\frac{\varepsilon_1}{\sigma_1 - \sigma_{3C}} = a + b\varepsilon_1 \qquad\qquad (M.9)$$

Note, however, that the values of the parameters a and b obtained by linear regression for Equation (M.9) are not the same as those obtained by nonlinear regression for Equation (M.6), or even those obtained by linear regression for the equation

$$\frac{1}{\sigma_1 - \sigma_{3C}} = a\left(\frac{1}{\varepsilon_1}\right) + b \qquad\qquad (M.10)$$

because the error functions to be minimized in each case are different.

Note also that if we set

$$\frac{(\sigma_1 - \sigma_{3C})\text{ult}}{E_i} = \frac{a}{b} = \varepsilon_{10} \qquad\qquad (M.11)$$

then Equation (M.6) can be written in the form

$$\frac{(\sigma_1 - \sigma_{3C})}{(\sigma_1 - \sigma_{3C})\text{ult}} = \frac{\dfrac{\varepsilon_1}{\varepsilon_{10}}}{1 + \dfrac{\varepsilon_1}{\varepsilon_{10}}} \qquad\qquad (M.12)$$

218

Duncan and Chang used Janbu's empirical relation between E_i and σ_{3C} [Janbu (1963)], which is

$$E_i = \frac{1}{a} = Kp_a \left(\frac{\sigma_{3C}}{p_a}\right)^n \tag{M.13}$$

where

p_a = atmospheric pressure

and K and n are dimensionless constants often obtained by fitting a straight line to a plot of

$\log_{10}\left(\frac{E_i}{p_a}\right)$ versus $\log_{10}\left(\frac{\sigma_{3C}}{p_a}\right)$ because Equation (M.13) has the linear form

$$\log_{10}\left(\frac{E_i}{p_a}\right) = \log_{10} K + n \log_{10}\left(\frac{\sigma_{3C}}{p_a}\right) \tag{M.14}$$

Again note, however, that the values of the parameters K and n obtained by linear regression for Equation (M.14) are not the same as those obtained by nonlinear regression for Equation (M.13).

Duncan and Chang also used the Mohr-Coulomb failure criterion to relate measured strength, $(\sigma_1 - \sigma_{3C})_f$, to cell pressure, σ_{3C}, as shown in Figure (M.2).

$$(\sigma_1 - \sigma_{3C})_f = \frac{2(c \cos \phi + \sigma_{3C} \sin \phi)}{1 - \sin \phi} \tag{M.15}$$

They found that the measured strength, $(\sigma_1 - \sigma_{3C})_f$, fell below the fitted asymptotic strength, $(\sigma_1 - \sigma_{3C})_{ult}$, by a factor R_f, so that

$$(\sigma_1 - \sigma_{3C})_f = R_f (\sigma_1 - \sigma_{3C})_{ult} = \frac{R_f}{b} \qquad (0.75 \le R_f \le 1.00) \tag{M.16}$$

However, the above observation is not consistent with much of Kondner's published data, and may be affected by the hyperbolic curve fitting procedure used.

To obtain an expression for E_T as a function of $\sigma_1 - \sigma_{3C}$, we write Equation (M.6) in the form

$$\frac{\epsilon_1}{\epsilon_{10}} = \frac{\dfrac{(\sigma_1 - \sigma_{3C})}{(\sigma_1 - \sigma_{3C})_{ult}}}{1 - \dfrac{(\sigma_1 - \sigma_{3C})}{(\sigma_1 - \sigma_{3C})_{ult}}} \tag{M.17}$$

Differentiation of Equation (M.17) with respect to $\sigma_1 - \sigma_{3C}$ then yields

$$\frac{d\epsilon_1}{d(\sigma_1 - \sigma_{3C})} = \frac{1}{E_T} = \frac{1}{E_i \left[1 - \dfrac{(\sigma_1 - \sigma_{3C})}{(\sigma_1 - \sigma_{3C})}\right]^2} \tag{M.18}$$

so that

$$\frac{d(\sigma_1 - \sigma_{3C})}{d\epsilon_1} = E_T = E_i \left[1 - \frac{(\sigma_1 - \sigma_{3C})}{(\sigma_1 - \sigma_{3C})_{ult}}\right]^2 \tag{M.19}$$

Substitution of Equations (M.13), (M.15), and (M.16) into Equation (M.19) therefore yields

$$E_T = Kp_a \left(\frac{\sigma_{3C}}{p_a}\right)^n \left[1 - \frac{R_f (1 - \sin\phi)(\sigma_1 - \sigma_{3C})}{2 (c \cos\phi + \sigma_{3C} \sin\phi)}\right]^2 \tag{M.20}$$

What Duncan and Chang did to obtain a general expression for E_T for finite element code use was assume that for any stress path, even when σ_3 is not constant, the relation between E_T, σ_1, and σ_3 is that obtained by replacing σ_{3C} in Equation (M.20) by σ_3, to obtain

220

$$E_T = Kp_a \left(\frac{\sigma_3}{p_a}\right)^n \left[1 - \frac{R_f (1 - \sin \phi)(\sigma_1 - \sigma_3)}{2(c \cos \phi + \sigma_3 \sin \phi)}\right]^2 \qquad (M.21)$$

Equation (M.21) does not take full account of the stress path dependence of triaxial compressive strength for a Mohr-Coulomb material, as illustrated by Figure (M.3). If the current stress point is point B, Equation (M.21) assumes the stress path to failure is BD, even though the actual stress path may be ABC. The difference in compressive strengths for the two stress paths is considerable, although admittedly that difference will decrease as the stress point approaches the failure line.
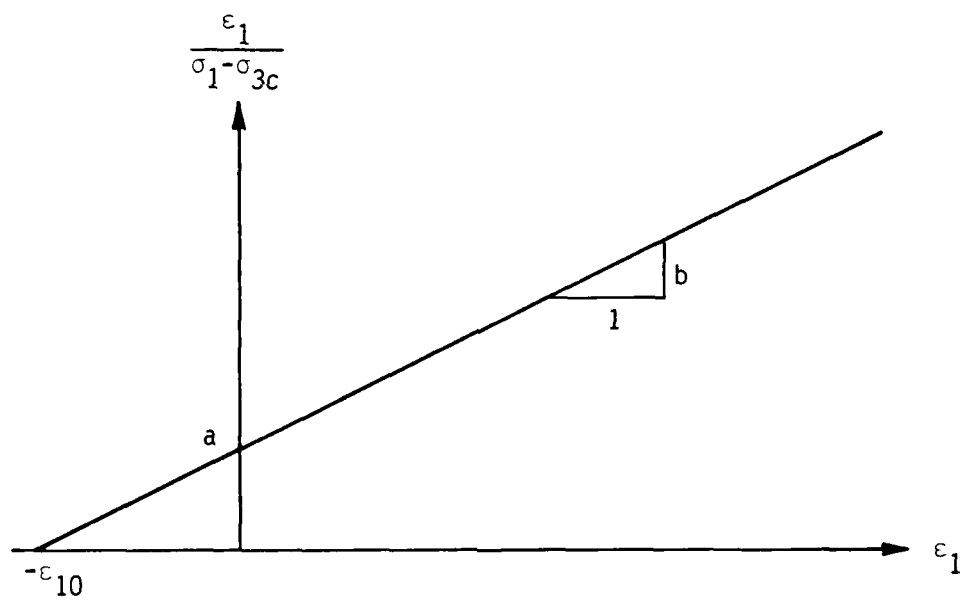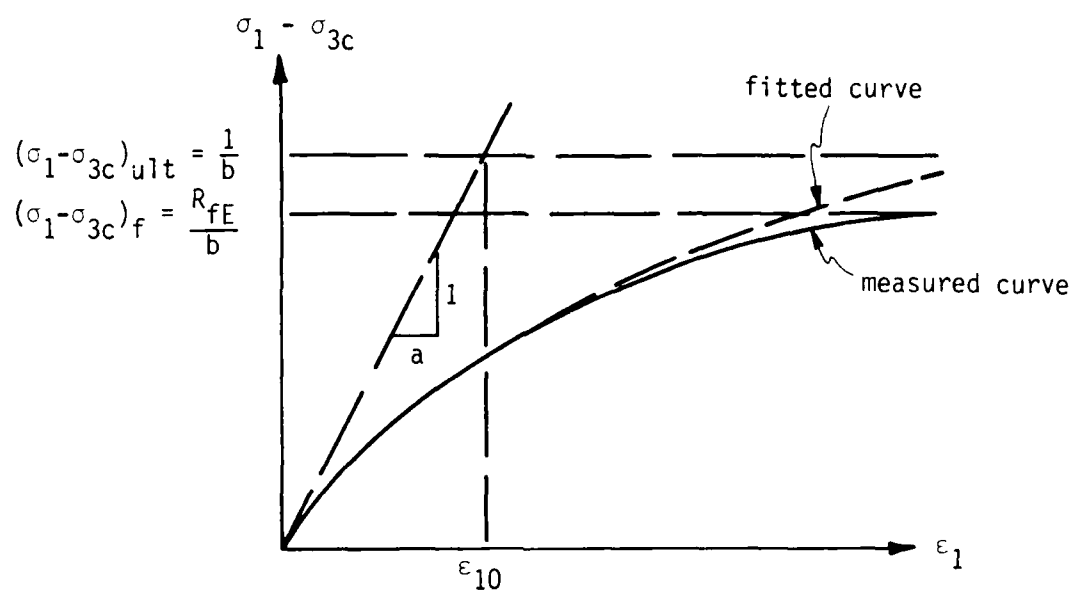
Figure M.1. Linear determination of hyperbolic parameters.
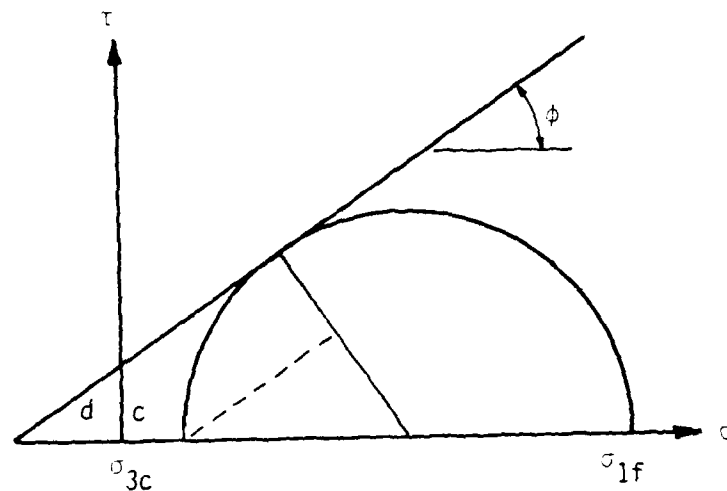
$$\frac{(\sigma_1 - \sigma_{3c})_f}{2} = (d + \sigma_{3c})\sin \phi + \frac{(\sigma_1 - \sigma_{3c})_f}{2} \sin \phi$$

$$\therefore (\sigma_1 - \sigma_{3c})_f = \frac{2(c \cos \phi + \sigma_{3c} \sin \phi)}{1 - \sin \phi}$$

Figure M.2. Mohr-Coulomb strength equation for constant
minor principal effective stress.

223
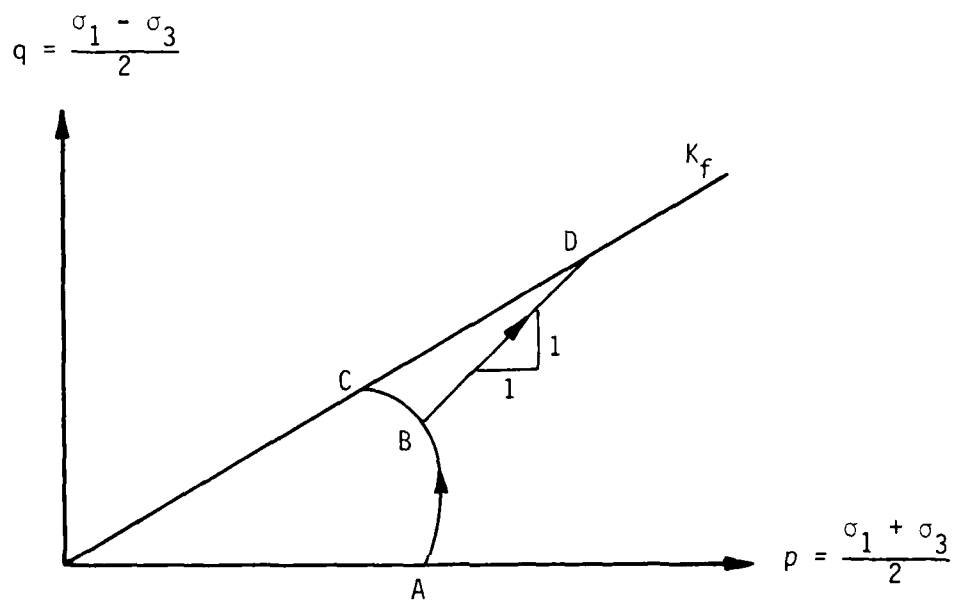
Figure M.3. Stress path dependence of triaxial compressive strength for a Mohr-Coulomb material.

APPENDIX N

A HYPERBOLIC EXPRESSION FOR POISSON'S RATIO

In a triaxial compression test at constant cell pressure, a plot of axial strain versus radial strain for stress levels well below the failure level might appear as shown in Figure (N.1) [cf Desai and Abel (1972:323)]. Such a plot suggests the possibility of a hyperbolic fit, of the form

$$\varepsilon_1 = \frac{-\varepsilon_3}{f - d\varepsilon_3} \tag{N.1}$$

which means that

$$\varepsilon_3 = \frac{-f\varepsilon_1}{1 - d\varepsilon_1} \tag{N.2}$$

and therefore

$$\nu_T = - \frac{d\varepsilon_3}{d\varepsilon_1} = \frac{f}{(1 - d\varepsilon_1)^2} = \frac{\nu_i}{(1 - d\varepsilon_1)^2} \tag{N.3}$$

where, from test data [Kulhawy, Duncan and Seed (1969)] found that

$$\nu_i = f = G - F \log_{10} \left(\frac{\sigma_{3c}}{P_a} \right) \tag{N.4}$$

The parameter d is obtained as the slope of a plot of $-\varepsilon_3/\varepsilon_1$ versus $-\varepsilon_3$, since Equation (N.1) has the linear form

$$\frac{-\varepsilon_3}{\varepsilon_1} = f + d (-\varepsilon_3) \tag{N.5}$$

225

The parameters F and G are obtained from a semilogarithmic plot of ν_i versus $\log_{10}(\sigma_{3C}/p_a)$.

Substitution of Equations (M.17), (M.13), (M.16), and (M.15) into Equation (N.3) yields

$$\nu_T = \frac{G - F \log_{10}\left(\dfrac{\sigma_{3C}}{p_a}\right)}{\left\{1 - \dfrac{d(\sigma_1 - \sigma_{3C})}{Kp_a\left(\dfrac{\sigma_{3C}}{p_a}\right)^n \left[1 - \dfrac{R_f(1 - \sin\phi)(\sigma_1 - \sigma_{3C})}{2(c\cos\phi + \sigma_{3C}\sin\phi)}\right]}\right\}^2} \quad (N.6)$$

The assumption that σ_{3C} can be replaced by σ_3 for an arbitrary stress path leads to the expression

$$\nu_T = \frac{G - F \log_{10}\left(\dfrac{\sigma_3}{p_a}\right)}{(1 - A)^2} \quad (N.7)$$

where

$$A = \frac{d(\sigma_1 - \sigma_3)}{Kp_a\left(\dfrac{\sigma_3}{p_a}\right)^n \left[\dfrac{R_f(1 - \sin\phi)(\sigma_1 - \sigma_3)}{2(c\cos\phi + \sigma_3\sin\phi)}\right]} \quad (N.8)$$

Although Equation (N.1) implies an upper asymptotic limit on ε_1 equal to 1/d, there is obviously no reason why the axial strain in a triaxial compression test should be limited, and it was not the authors' intent that Equations (N.7) and (N.8) be used at stress levels approaching failure [Kulhawy (1984)]. More complete relations between ε_1 and ε_3 for triaxial compression tests at constant cell pressure on a loose and a dense sand would have the shapes shown in Figure (N.2). Obviously, neither curve is hyperbolic in the strain range approaching a constant volume critical state, and the authors' intent was to use the hyperbolic

226

fit only for the early upturning portions of these curves. Consequently, when Equations (N.7) and (N.8) are used in a computer program to handle problems involving possibly large strains, an arbitrary upper limit on ν_T may need to be established.
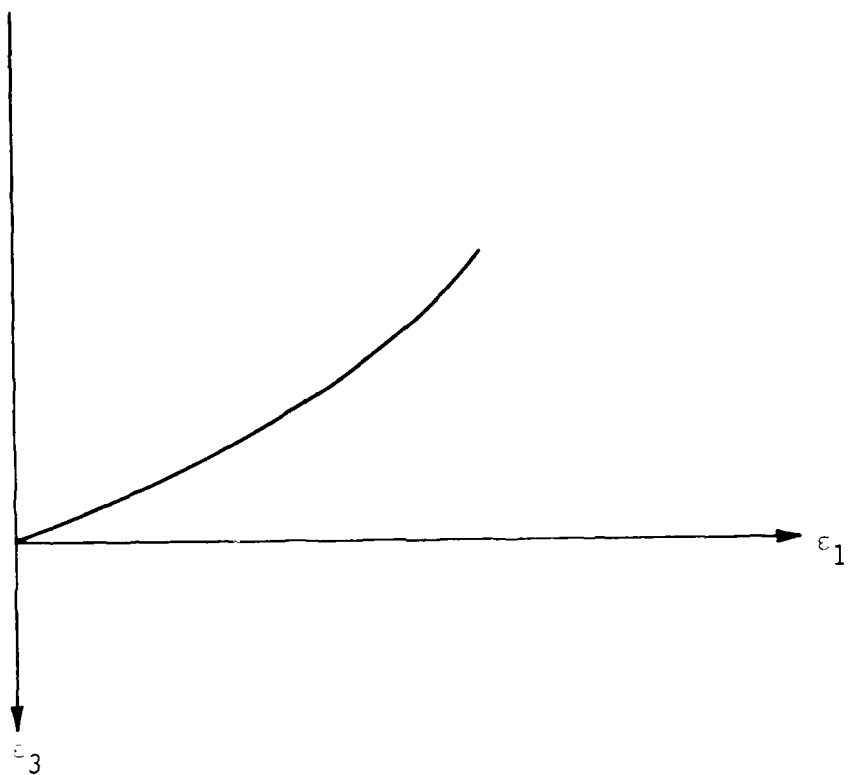
Figure N.1. Relation between major (axial) and minor
(radial) principal strains in the early
phase of a triaxial compression test at
constant cell pressure.

228
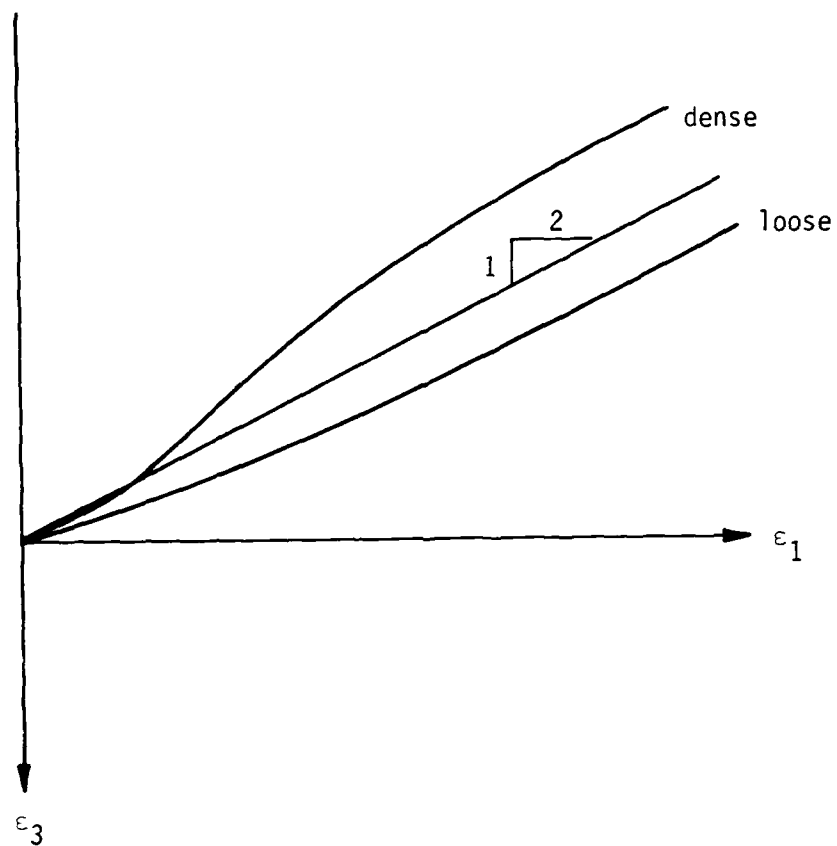
Figure N.2. More complete relation between major (axial) and minor (radial) principal strains in a triaxial compression test at constant cell pressure.

APPENDIX O

HYPERBOLIC MODEL FOR CYCLIC SIMPLE SHEAR

[Pyke (1979:721)] proposed a variation of the hyperbolic shear model for irregular cyclic loading, in which the simple shear stress-strain curve, starting at the latest point of strain reversal, (γ_c, τ_c), is a hyperbola with fixed initial slope, G_{MAX}, and fixed upper and lower asymptotes, τ_y and $-\tau_y$, as shown in Figure (O.1). If $d\gamma > 0$ after reversal, hyperbola PQ applies, having the equation

$$\tau - \tau_c = \frac{G_{MAX}(\gamma - \gamma_c)}{1 + \left(\dfrac{G_{MAX}}{\tau_y - \tau_c}\right)(\gamma - \gamma_c)} \qquad (d\gamma > 0) \qquad (O.1)$$

and if $d\gamma < 0$ after reversal, hyperbola PR applies, having the equation

$$\tau_c - \tau = \frac{G_{MAX}(\gamma_c - \gamma)}{1 + \left(\dfrac{G_{MAX}}{\tau_y + \tau_c}\right)(\gamma_c - \gamma)} \qquad (d\gamma < 0) \qquad (O.2)$$

Equation (O.2) can be written in the form

$$\tau - \tau_c = \frac{G_{MAX}(\gamma - \gamma_c)}{1 + \left(\dfrac{G_{MAX}}{-\tau_y - \tau_c}\right)(\gamma - \gamma_c)} \qquad (d\gamma < 0) \qquad (O.3)$$

which is identical to Equation (O.1) except for the sign of the τ_y term. Therefore, Equations (O.1) and (O.3) can be combined in the form

$$\tau - \tau_c = \frac{G_{MAX}(\gamma - \gamma_c)}{1 + \left(\dfrac{G_{MAX}}{\tau_y^* - \tau_c}\right)(\gamma - \gamma_c)} \qquad (O.4)$$

where

$$\tau_y^* = \tau_y \, \text{sgn} \, (d\gamma) \tag{0.5}$$

Differentiation of Equation (0.4) yields the tangent shear modulus,

$$\frac{d(\tau - \tau_c)}{d(\gamma - \gamma_c)} = G_T = \frac{G_{MAX}}{\left[1 + \left(\dfrac{G_{MAX}}{\tau_y^* - \tau_c} \right) (\gamma - \gamma_c) \right]^2} \tag{0.6}$$

The parameters τ_y and G_{MAX} can be obtained from a simple shear test, in which the relation between τ and γ is assumed to be hyperbolic $(\gamma_c = \tau_c = 0)$, so that Equation (0.1) reduces to

$$\tau = \frac{G_{MAX} \, \gamma}{1 + \dfrac{G_{MAX}}{\tau_y} \gamma} \tag{0.7}$$

A plot of τ/γ versus τ should then follow the linear form

$$\frac{\tau}{\gamma} = G_{MAX} \left(1 - \frac{\tau}{\tau_y} \right) \tag{0.8}$$

231
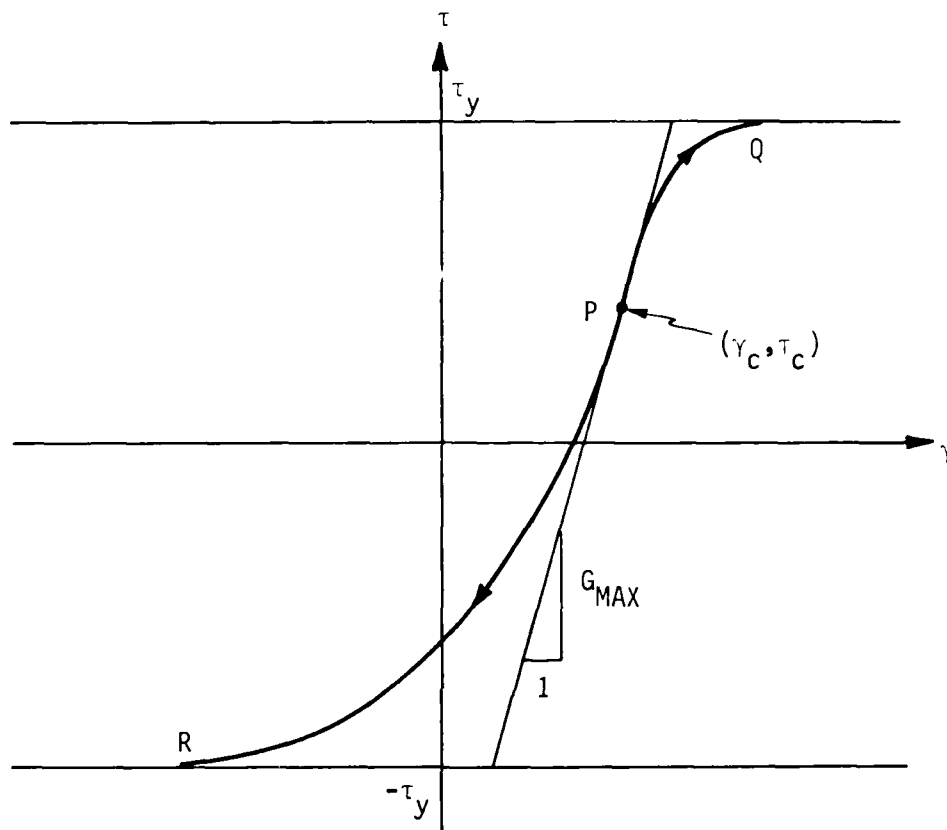
Figure 0.1. Pyke hyperbolic shear model.
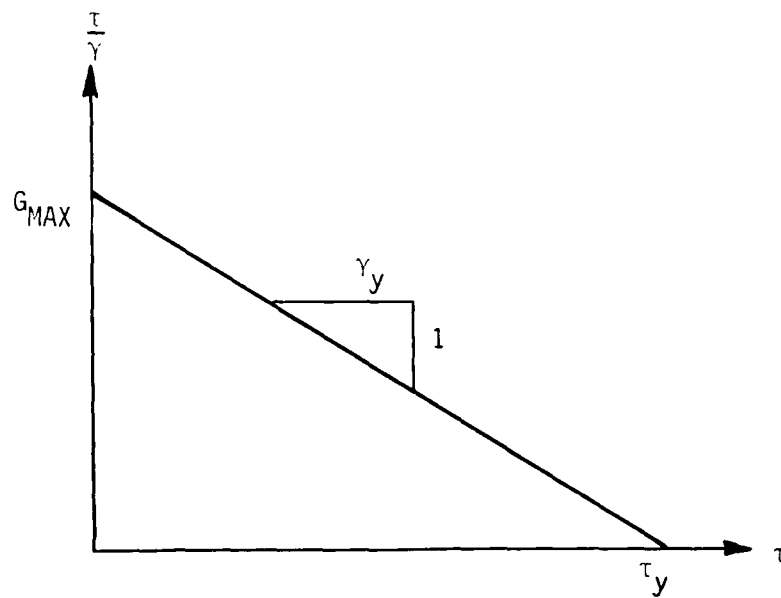
Figure 0.2. Linear plot for determining hyperbolic model
parameters for cyclic simple shear.

APPENDIX P

YIELD SURFACE VIOLATION CORRECTION FOR AN ELASTIC-PERFECTLY PLASTIC MODEL

An elastic-perfectly plastic model does not strain harden. Instead the yield surface remains fixed, and so it is often called a failure surface. The failure surface is concave with respect to the origin in stress space, and its intersection with any octahedral plane is a closed curve, with its center on the hydrostatic axis and having six-fold angular symmetry. When the stress point lies inside the failure surface, i.e., when the shortest line from the stress point to the hydrostatic axis does not intersect the failure surface, the material responds entirely elastically. Plastic strains occur only when the stress point lies on the failure surface; and the stress point is prohibited from going beyond the failure surface by a correction procedure which will now be explained.

Consider a failure surface having the equation

$$f\left(I_1, \sqrt{J_2}\right) = 0 \tag{P.1}$$

Its octahedral cross-section is a circle with its center on the hydrostatic axis; and its intersection with any plane containing the hydrostatic axis is a scaled plot of Equation (P.1), shown in Figure (P.1). Assume that a strain-controlled elastic trial calculation starting from Point 1 in Figure (P.1) has moved the stress point to Point 3, passing through the failure surface at Point 2. The objective of the correction procedure is to bring the stress point back to the failure surface at constant total strain. This is done by using the consistency

234

condition starting from Point 2, and a (possibly nonassociative) flow rule to find that portion of the total strain increment which is: plastic, normal to the plastic potential surface at Point 4, and just sufficient so that the remaining elastic strain increment causes the stress increment to terminate in the failure surface (at Point 5).

The consistency condition without strain hardening reduces from Equation (D.7) to simply

$$df = \left\{\frac{\partial f}{\partial \sigma}\right\}^T \left\{d\sigma\right\} = 0 \tag{P.2}$$

where

$$\left\{\frac{\partial f}{\partial \sigma}\right\} = \frac{\partial f}{\partial I_1} \left\{\frac{\partial I_1}{\partial \sigma}\right\} + \frac{\partial f}{\partial \sqrt{J_2}} \left\{\frac{\partial \sqrt{J_2}}{\partial \sigma}\right\} \tag{P.3}$$

and

$$\frac{\partial f}{\partial I_1} = f_I \tag{P.4}$$

$$\left\{\frac{\partial I_1}{\partial \sigma}\right\} = \{m\} \tag{E.14}$$

$$\frac{\partial f}{\partial \sqrt{J_2}} = f_{II} \tag{P.5}$$

$$\left\{\frac{\partial \sqrt{J_2}}{\partial \sigma}\right\} = \frac{1}{2\sqrt{J_2}} \{s\} \quad [\text{cf Equation (E.22)}] \tag{P.6}$$

so that Equation (P.3) takes the form

$$\left\{\frac{\partial f}{\partial \sigma}\right\} = f_I \{m\} + \frac{f_{II}}{2\sqrt{J_2}} \{s\} \tag{P.7}$$

235

In addition, if the plastic potential function is of the same form as the failure criterion, i.e.,

$$g = g(I_1, \sqrt{J_2}) \tag{P.8}$$

and if

$$\frac{\partial g}{\partial I_1} = g_I \tag{P.9}$$

$$\frac{\partial g}{\partial \sqrt{J_2}} = g_{II} \tag{P.10}$$

then

$$\left\{ \frac{\partial g}{\partial \sigma} \right\} = g_I \{m\} + \frac{g_{II}}{2\sqrt{J_2}} \{s\} \tag{P.11}$$

Now if, in Equations (J.27) and (J.28), we set

$$\frac{E}{3(1-2\nu)} = K \tag{P.12}$$

$$\frac{E}{1+\nu} = 2G \tag{P.13}$$

where K and G are the elastic bulk and shear moduli, respectively, then Equation (J.30) can be written in the form

$$\underline{C}^e = K \{m\} \{m\}^T + 2G \left(\underline{I} - \frac{1}{3} \{m\} \{m\}^T \right)$$

$$= \left(K - \frac{2G}{3} \right) \{m\} \{m\}^T + 2G \, \underline{I} \tag{P.14}$$

Then with a view toward evaluating Equation (G.16), Equations (P.7) and (P.14) yield

$$\left\{\frac{\partial f}{\partial \sigma}\right\}^T \underline{C}^e = 3Kf_I \{m\}^T + \frac{Gf_{II}}{\sqrt{J_2}} \{s\}^T \qquad (P.15)$$

so that Equations (P.11) and (P.15) yield

$$\left\{\frac{\partial f}{\partial \sigma}\right\}^T \underline{C}^e \left\{\frac{\partial g}{\partial \sigma}\right\} = 9Kf_I g_I + Gf_{II} g_{II} \qquad (P.16)$$

Setting D_{22} equal to zero because of the absence of strain hardening, Equation (G.16) therefore yields

$$d\lambda = \frac{df_E}{9Kf_I g_I + Gf_{II} g_{II}} = \frac{f_3}{9Kf_I g_I + Gf_{II} g_{II}} \qquad (P.17)$$

Note that the elastic trial calculation is assumed to start from Point 2, rather than Point 1. This is why the value of the yield function, f, at Point 3 (f_3) is substituted for the differential df_E in the numerator of the first form of Equation (P.17). It is f_3 which is needed, and that can be found from the equation

$$f_3 = f\left[(I_1)_3, \left(\sqrt{J_2}\right)_3\right] \qquad (P.18)$$

where

$$(I_1)_3 = (I_1)_1 + 3K \{m\}^T \{d\epsilon\} \qquad (P.19)$$

$$\left(\sqrt{J_2}\right)_3 = \sqrt{\frac{1}{2} \{s\}_3^T \{s\}_3} \qquad (P.20)$$

$$\{s\}_3 = \{s\}_1 + 2G \{de\} \qquad (P.21)$$

and

$$\{de\} = \left(\underline{I} - \frac{1}{3} \{m\} \{m\}^T\right) \{d\epsilon\} \qquad (J.26)$$

237

Having $d\lambda$, the adjustments to I_1 and $\sqrt{J_2}$ can be calculated from the equations

$$\{d\epsilon^P\} = d\lambda \left\{\frac{\partial g}{\partial \sigma}\right\} = d\lambda \left\{g_I\{m\} + \frac{g_{II}}{2\sqrt{J_2}}\{s\}\right\} \qquad (P.22)$$

$$d\epsilon_{KK}^P = \{m\}^T\{d\epsilon^P\} = 3g_I\, d\lambda \qquad (P.23)$$

$$\{de^P\} = \left(\underline{I} - \frac{1}{3}\{m\}\{m\}^T\right)\{d\epsilon^P\} = \frac{g_{II}\, d\lambda}{2\sqrt{J_2}}\{s\} \qquad (P.24)$$

$$(dI_1)_p = -3K\, d\epsilon_{KK}^P = -9Kg_I\, d\lambda \qquad (P.25)$$

$$\left(d\sqrt{J_2}\right)_p = -\frac{1}{2\sqrt{J_2}}\{s\}^T \cdot 2G\,\{de^P\} = -Gg_{II}\, d\lambda \qquad (P.26)$$

and therefore the values of I_1, $\sqrt{J_2}$, and $\{s\}$ at Point 5 in Figure (P.1) are

$$(I_1)_5 = (I_1)_3 - 9Kg_I\, d\lambda \qquad (P.27)$$

$$\left(\sqrt{J_2}\right)_5 = \left(\sqrt{J_2}\right)_3 - Gg_{II}\, d\lambda \qquad (P.28)$$

$$\{s\}_5 = \sqrt{\frac{(J_2)_5}{(J_2)_3}}\,\{s\}_3 \qquad (P.29)$$

Note that the derivatives f_I, f_{II}, g_I, and g_{II} are evaluated at Point 4 and not Point 5. Therefore, the values of I_1 and $\sqrt{J_2}$ calculated by Equations (P.27) and (P.28) may still define a stress point lying slightly outside the yield surface. Therefore, if

$$f_5 > \epsilon > 0 \qquad (P.30)$$

where ϵ is a specified tolerance, then repeat the correction procedure by treating Point 5 as a new Point 3, and defining a new Point 4.

238

Equation (G.18) can be used to evaluate the incremental stiffness matrix for a point on the failure surface. Equations (P.11) and (P.14) yield

$$\underline{C}^e \left\{\frac{\partial g}{\partial \sigma}\right\} = 3Kg_I \{m\} + \frac{Gg_{II}}{\sqrt{J_2}} \{s\} \tag{P.31}$$

Substitution of Equations (P.15), (P.16) and (P.31) into Equation (G.18) yields

$$\underline{C}^{ep} = \underline{C}^e - \frac{\underline{C}^e \left\{\frac{\partial g}{\partial \sigma}\right\} \left\{\frac{\partial f}{\partial \sigma}\right\}^T \underline{C}^e}{\left\{\frac{\partial f}{\partial \sigma}\right\}^T \underline{C}^e \left\{\frac{\partial g}{\partial \sigma}\right\}}$$

$$= \underline{C}^e - \frac{\left\{3Kg_I\{m\} + \frac{Gg_{II}}{\sqrt{J_2}} \{s\}\right\} \left\{3Kf_I\{m\} + \frac{Gf_{II}}{\sqrt{J_2}} \{s\}\right\}^T}{9Kf_Ig_I + Gf_{II}g_{II}} \tag{P.32}$$

239
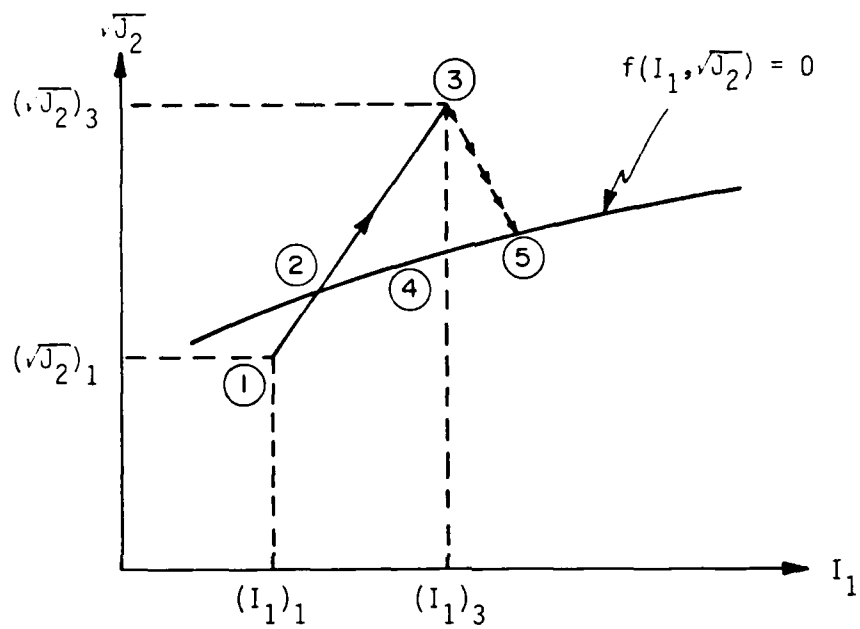
Figure P.1. Correction procedure for elastic-perfectly plastic failure surface violation.

APPENDIX Q

AFWL ENGINEERING MODEL INCREMENTAL PLASTIC RESPONSE

Figure (Q.1) shows the shear failure and plastic potential surfaces, and hysteretic hydrostat which partially define a modified version of the AFWL engineering model in use at Applied Research Associates. Each segment of the failure surface has an equation of the form

$$f(I_1, \sqrt{J_2}) = \sqrt{J_2} - (a + bI_1) = 0 \qquad (Q.1)$$

and the von Mises plastic potential function has the equation

$$g(I_1, \sqrt{J_2}) = \sqrt{J_2} \qquad (Q.2)$$

so that Equations (P.4), (P.5), (P.9), and (P.10) yield

$$f_I = -b \qquad (Q.3)$$

$$f_{II} = 1 \qquad (Q.4)$$

$$g_I = 0 \qquad (Q.5)$$

$$g_{II} = 1 \qquad (Q.6)$$

and, therefore, Equation (P.32) yields

$$\underline{c}^{ep} = \underline{c}^e - \frac{\dfrac{G}{\sqrt{J_2}} \{s\} \left\{ -3Kb\{m\} + \dfrac{G}{\sqrt{J_2}} \{s\} \right\}^T}{G}$$

$$= \underline{c}^e + \frac{3Kb}{\sqrt{J_2}} \{s\}\{m\}^T - \frac{G}{J_2} \{s\}\{s\}^T \qquad (Q.7)$$

241

Substitution of Equation (P.14) into Equation (Q.7) yields

$$\underline{C}^{ep} = \left(K - \frac{2G}{3}\right)\{m\}\{m\}^T + 2G\underline{I} + \frac{3Kb}{\sqrt{J_2}}\{s\}\{m\}^T - \frac{G}{J_2}\{s\}\{s\}^T \qquad (Q.8)$$

Now the total strain increment can be written in the form

$$\{d\varepsilon\} = \frac{1}{3}\{m\}\{m\}^T\{d\varepsilon\} + \{de\} \qquad (Q.9)$$

so that Equations (Q.8) and (Q.9) yield

$$\{d\sigma\} = \underline{C}^{ep}\{d\varepsilon\} = \left(K - \frac{2G}{3}\right)\{m\}\{m\}^T\{d\varepsilon\} + \frac{2G}{3}\{m\}\{m\}^T\{d\varepsilon\}$$

$$+ \frac{3Kb}{\sqrt{J_2}}\{s\}\{m\}^T\{d\varepsilon\} + 2G\{de\}$$

$$- \frac{G}{J_2}\{s\}\{s\}^T\{de\}$$

$$= K\{m\}\{m\}^T\{d\varepsilon\} + \frac{3Kb}{\sqrt{J_2}}\{s\}\{m\}^T\{d\varepsilon\}$$

$$+ 2G\{de\} - \frac{G}{J_2}\{s\}\{s\}^T\{de\} \qquad (Q.10)$$

so that

$$dI_1 = \{m\}^T\{d\sigma\} = 3K\{m\}^T\{d\varepsilon\} \qquad (Q.11)$$

$$d\sqrt{J_2} = \frac{1}{2\sqrt{J_2}}\{s\}^T\{d\sigma\} = 3Kb\{m\}^T\{d\varepsilon\} + \frac{G}{\sqrt{J_2}}\{s\}^T\{de\}$$

$$- \frac{G}{\sqrt{J_2}}\{s\}^T\{de\}$$

$$= 3Kb\{m\}^T\{d\varepsilon\} \qquad (Q.12)$$

242

Comparison of Equations (Q.11) and (Q.12) shows that

$$d\sqrt{J_2} = b(dI_1) \qquad\qquad (Q.13)$$

which means that if the stress increment starts in the failure surface it ends in the same failure surface.

Notice that the last two terms on the RHS of Equation (Q.10) for $\{d\sigma\}$ contribute nothing to either dI_1 or $d\sqrt{J_2}$. They do, however, contribute to dJ_3, and represent components of a circular stress path increment in the octahedral plane. The first term on the RHS of Equation (Q.10) is an incremental vector pointing along the hydrostatic axis. The second and fourth terms are incremental vectors pointing in the current radial direction, and the third term is an incremental vector which returns the stress point to the same circle on which the second incremental vector terminates. The relation between these incremental vectors is shown in Figure (Q.2).
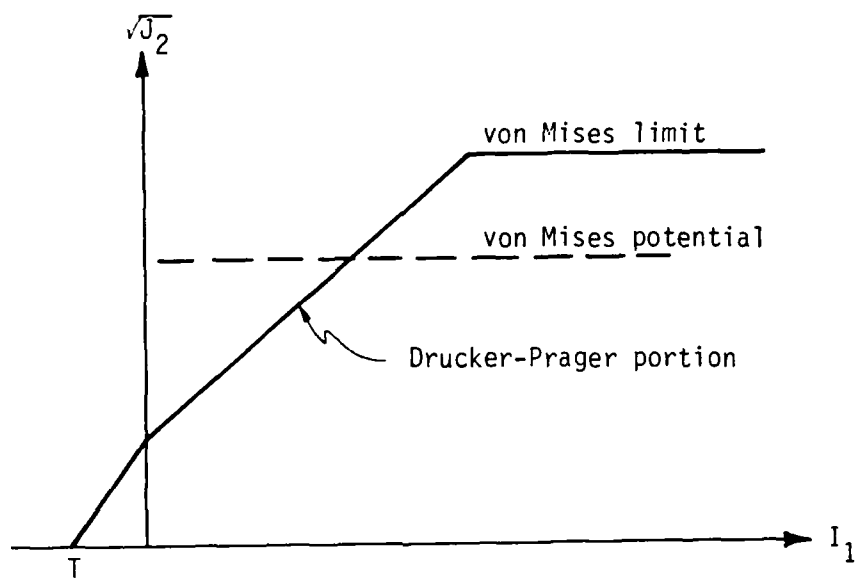
a) Shear failure and plastic potential surfaces

b) hydrostat
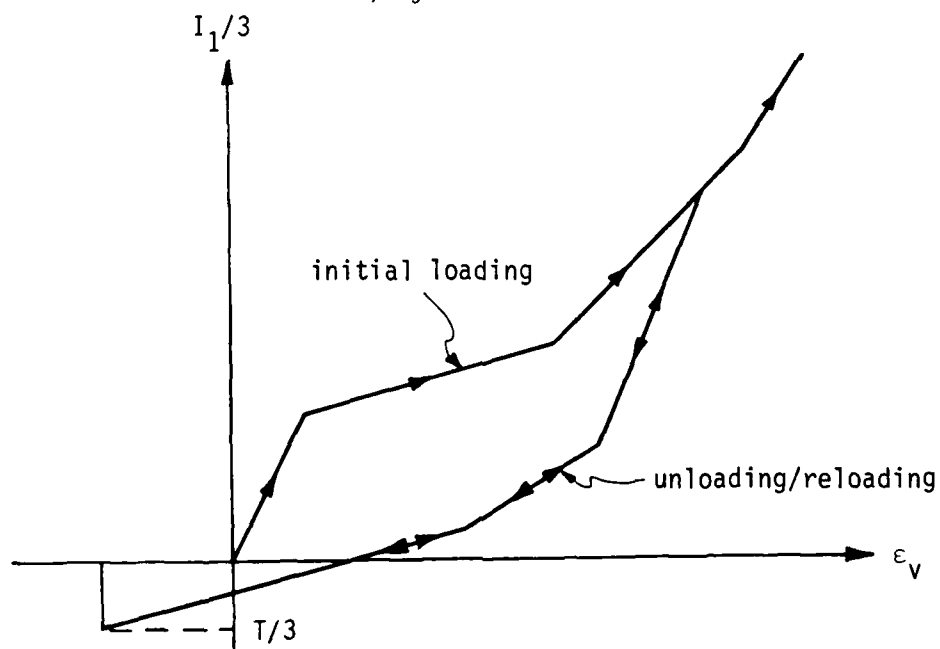
Figure Q.1. Modified AFWL Engineering Model.

244
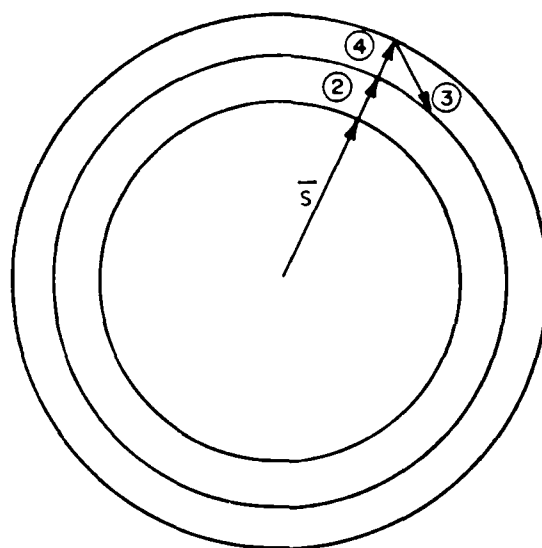
Figure Q.2.   Physical significance of terms 2, 3, and four
on the RHS of Equation (Q.10).

245

APPENDIX R

DRAINED CAP MODEL AND COMPUTATIONAL ALGORITHM

The cap model is an isotropic, rate independent, elastoplastic model with two yield surfaces. The shear yield surface does not strain harden, and is called the shear failure surface. The cap yield surface both hardens and softens in response to plastic volumetric strain. Both yield surfaces are associative. Figure (R.1) shows the two cap model yield surfaces, which intersect at the corner point, $I_1 = k$.

The shear failure surface has the equation

$$\sqrt{J_2} = f(I_1) \qquad (I_1 \geq T) \qquad (R.1)$$

$$= 0 \qquad (I_1 < T) \qquad (R.2)$$

where T is the tension cutoff, and

$$\frac{\partial f}{\partial I_1} > 0 \qquad (R.3)$$

The cap yield surface has the equation

$$\sqrt{J_2} = F(I_1,k) \quad \begin{Bmatrix} \geq 0 \\ \leq f(I_1) \end{Bmatrix} \quad (L \leq I_1 \leq X) \qquad (R.4)$$

where

$$k = k(\epsilon_{KK}^p) \qquad (R.5)$$

$$X = X(\epsilon_{KK}^p) \qquad (R.6)$$

$$\frac{dX}{d\epsilon_{KK}^P} \geq 0 \qquad\qquad\qquad (R.7)$$

$$L = k \qquad (k \geq 0) \atop = 0 \qquad (k < 0) \Bigg\} \qquad (R.8)$$

$$F(X,k) = 0 \qquad\qquad\qquad (R.9)$$

$$F(L,k) = f(k) \qquad\qquad\qquad (R.10)$$

$$\frac{\partial F}{\partial I_1} \leq 0 \qquad\qquad (L \leq I_1 \leq X) \qquad\qquad (R.11)$$

$$\frac{\partial F}{\partial k} > 0 \qquad\qquad (L \leq I_1 \leq X) \qquad\qquad (R.12)$$

When $k < 0$ a von Mises cap transition surface is defined by the equation

$$\sqrt{J_2} = F(0,k) = f(k) \qquad\qquad (k \leq I_1 < 0) \qquad (R.13)$$

and therefore when $I_1 < 0$, *the yield criterion is the lesser of the*
shear failure criterion and the von Mises transition, i.e.,

$$\sqrt{J_2} = F_e (I_1,k) = \min \left\{ f(I_1); \; f(k) \right\} \qquad (T \leq I_1 < 0) \qquad (R.14)$$

Within the yield surfaces the material is hypoelastic without
hysteresis, with incremental bulk and shear unloading/reloading moduli
defined by the equations

$$K_s = K_s (I_1,k) \qquad\qquad\qquad (R.15)$$

$$G = G(\sqrt{J_2}, k) \qquad\qquad\qquad (R.16)$$

The particular cap model discussed here is that presented by Baladi
and Akers (1981), except that the shear failure criterion has the equation

$$\sqrt{J_2} = f(I_1) = (C_s + \alpha I_1) + C(1 - e^{-BI_1}) \qquad (R.17)$$

The ellipsoidal, strain hardening cap yield surface has the equation

$$\left(\frac{I_1 - L}{X - L}\right)^2 + \left(\frac{\sqrt{J_2}}{f(k)}\right)^2 = 1 \qquad (L \leq I_1 \leq X) \qquad (R.18)$$

so that

$$\sqrt{J_2} = F(I_1, k) = f(k) \sqrt{1 - \left(\frac{I_1 - L}{X - L}\right)^2}$$

$$= \frac{f(k)}{X-L} \sqrt{(X-L)^2 - (I_1-L)^2} = \frac{1}{R} \sqrt{(X-L)^2 - (I_1-L)^2} \qquad (R.19)$$

where

$$R = \frac{X-L}{f(k)} \qquad (R.20)$$

R is the ratio of the cap ellipse principal axes, but it is not obvious which is the major and which the minor principal axis until the model parameters have been determined. The relation between plastic volumetric strain, ε_{KK}^p, and peak hydrostatic effective stress, σ_{OCT}, determined by hydrostatic unloading, is

$$\varepsilon_{KK}^p = W \left[1 - e^{-3D(\sigma_{OCT} - G_r)}\right] \qquad (R.21)$$

where W and D are material constants, and G_r is the hydrostatic component of the geostatic effective stress tensor. This relation is shown in Figure (R.2). The relation between X, the value of I_1 at which the ellipsoidal cap meets the I_1 axis, is patterned after Equation (R.21). However, a mathematical device is inserted to prevent further shrinking of the cap due to dilatancy on the shear failure surface

248

when the corner has shrunk to the $\sqrt{J_2}$ axis. This means k cannot be negative. The relation between X and ε_{KK}^p is constructed by defining an auxiliary plastic volumetric strain variable, z, for which

$$dz = 0 \qquad\qquad (k \le 0 \text{ and } d\varepsilon_{KK}^p < 0) \left.\vphantom{\begin{array}{c} \\ \\ \end{array}}\right\}$$
$$\quad = d\varepsilon_{KK}^p \qquad\quad (\text{otherwise}) \qquad\qquad\qquad (R.22)$$

so that z will decrease due to dilatancy on the shear failure surface only when k > 0. Then z is related to X by the equation

$$z = \int dz = W \left[1 - e^{-D(X - 3G_r)} \right] \qquad\qquad (R.23)$$

Inversion of Equation (R.23) yields

$$X = 3G_r + \frac{1}{D} \ln \left(\frac{1}{1 - \frac{z}{W}} \right) \qquad\qquad (R.24)$$

The parameters W and D in Equations (R.21), (R.23), and (R.24) can be obtained from a drained isotropic compression test in which ε_{KK}^p increases continuously so that ε_{KK}^p and z are identical.

The relations between X, k = L, R, and z can be obtained by combining the results of drained isotropic compression tests and drained triaxial compression tests at constant cell pressure. For drained triaxial compression tests at constant cell pressure, Equations (K.3) and (K.9) yield

$$I_1 = \sigma_1 + 2\sigma_{3C} = (\sigma_1 - \sigma_{3C}) + 3\sigma_{3C} \qquad\qquad (R.25)$$

and

$$\sqrt{J_2} = \frac{\sigma_1 - \sigma_{3C}}{\sqrt{3}} \qquad\qquad (R.26)$$

249

so that

$$I_1 = 3\sigma_{3C} + \sqrt{3J_2}$$ (R.27)

Figure (R.3) shows the hypothetical results of such a test. Figure (R.3a) shows the loading stress path, with slope $1/\sqrt{3}$. When the stress point is at P, the flow rule predicts the plastic strain increment, $\overline{d\varepsilon}P$, will be normal to the cap surface passing through P, and therefore $d\varepsilon_{KK}^p > 0$ at all points on the stress path until failure occurs at Point S on the shear failure surface. Only then does dilatancy suddenly occur, according to the theory of the cap model. Figure (R.3b) shows the stress-strain response, assuming strain control. Failure occurs at Point S, at which $(\sigma_1 - \sigma_{3C})$ is a maximum. From unloading data a curve showing the plastic volumetric strain, ε_{KK}^p, corresponding to a given value of $\sigma_1 - \sigma_{3C}$ on the loading stress-strain curve can be constructed, and from that curve the plastic volumetric strain at failure, $\varepsilon_{KK,f}^p$, can be found. The triaxial compressive strength, $(\sigma_1 - \sigma_{3C})_f$, is the ordinate at Point S on the stress-strain curve, so that Equations (R.25) and (R.26) yield

$$I_{1f} = (\sigma_1 - \sigma_{3C})_f + 3\sigma_{3C}$$ (R.28)

$$\sqrt{J_{2f}} = \frac{(\sigma_1 - \sigma_{3C})_f}{\sqrt{3}}$$ (R.29)

Figure (R.4) shows how the results of isotropic and triaxial compression tests can be combined on a three-axis plot which yields X, k = L, and R as functions of ε_{KK}^p. For computational purposes ε_{KK}^p is replaced by z to prevent excessive shrinking of the cap. The

250

above discussion is conceptual. Cap model users often determine or refine the model parameters by trial and error.

The drained hypoelastic incremental unloading/reloading bulk modulus is defined by the equation

$$K_s = \frac{K_{is}}{1 - K_{1S}} \left[1 - K_{1S} e^{-K_{2S}(I_1 - 3G_r)} \right] \tag{R.30}$$

and the hypoelastic incremental unloading/reloading shear modulus, which applies to both drained and undrained conditions, is defined by an equation of the same form

$$G = \frac{G_i}{1 - G_1} \left(1 - G_1 e^{-G_2 \sqrt{J_2}} \right) \tag{R.31}$$

The parameters K_{is}, K_{1S}, K_{2S}, G_i, G_1, and G_2 are material constants. The shear modulus is obtained from the unloading/reloading portion of a plot of $(\sigma_1 - \sigma_3)$ against $(\epsilon_1 - \epsilon_3)$, measured during a triaxial compression test with both axial and radial or volumetric strain measurements.

Equations (R.17), (R.21), (R.30), and (R.31) are all of the form

$$y = a + bx - ce^{-dx} \tag{R.32}$$

the parameters of which can be determined as follows:

1. Plot $\frac{y}{x}$ against $\frac{1}{x}$. The value of $\frac{y}{x}$ extrapolated to $\frac{1}{x} \rightarrow 0$ is b. See Figure (R.5a).

2. Plot $y - bx$ against $\frac{1}{x}$. The value of $y - bx$ extrapolated to $\frac{1}{x} \rightarrow 0$ is a. See Figure (R.5b).

251

3. Plot $\ln(a + bx - y)$ against x. The y intercept is $\ln c$ and the slope is $-d$, since Equation (R.32) yields

$$\ln(a + bx - y) = \ln(ce^{-dx}) = \ln c - dx \tag{R.33}$$

See Figure (R.5c).

The cap model response to prescribed strain inputs is hypoelastic, provided the stress point lies within the yield surfaces. In this case Equations (R.15) and (R.16) yield

$$dI_1 = 3K_s d\epsilon_{KK} \tag{R.34}$$

and

$$ds_{ij} = 2G\, de_{ij} \tag{R.35}$$

If the assumed hypoelastic stress increment (the elastic trial) violates the tension cutoff the first stress invariant is set equal to $-T$, and all deviator stresses are set equal to zero. In this case the plastic volumetric strain increment is calculated from the equation

$$I_1^{n+1} = T = I_1^E - 3K\, d\epsilon_{KK}^p \tag{R.36}$$

so that

$$d\epsilon_{KK}^p = \frac{I_1^E - T}{3K} \tag{P.37}$$

If the elastic trial point lies to the left of the corner and violates the shear failure surface, the stress point is corrected back to the shear failure surface using the method of Appendix P for a perfectly plastic material. Since the cap model is entirely associative, Equations (P.17), (P.23), and (P.27) yield

252

$$d\lambda = \frac{af_e^E}{9K\left(\frac{dF_e}{dI_1}\right)^2 + G} \tag{R.38}$$

$$d\varepsilon_{KK}^p = -3 \frac{dF_e}{dI_1} d\lambda \tag{R.39}$$

$$I_1^{n+1} = I_1^E - 3K \, d\varepsilon_{KK}^p \tag{R.40}$$

and

$$\sqrt{J_2^{n+1}} = f(I_1^{n+1}) \tag{R.41}$$

The cap shrinks (if possible) in response to the dilatant plastic volumetric strain given by Equation (R.39).

Equations (R.40) and (R.41) define a point on the shear failure surface (extended beyond the corner, if necessary), but that point will violate the cap if the point lies to the right of the shrunken corner. This situation is shown in Figure (R.6), where N is the initial stress point, E the elastic trial point, T the shear failure surface correction point assuming the plastic strain increment to be directed along normal PQ to the shear failure surface, C the initial corner, and D the shrunken corner (which may coincide with C). If the shear failure surface correction point had been taken as P instead of T, implying a plastic strain increment lying along vertical PR, the corner would have remained at C and cap violation would not have occurred. As the assumed shear failure surface correction point moves from P toward T along the shear failure surface the direction of the plastic strain increment shifts from PR toward PQ and the corner point shrinks (if it can) from C toward D. Eventually the assumed corrected stress point meets the shrunken corner

(somewhere between C and D) and that is the final corrected stress point. If $k^n = 0$ so the cap cannot shrink, then D coincides with C and therefore C must be the final corrected stress point. Then

$$I_1^{n+1} = k^n = 0 \tag{R.42}$$

and

$$\sqrt{J_2^{n+1}} = f(k^n) = f(0) \tag{R.43}$$

If $k^n > 0$ so the cap can shrink, then the hardening relation between the amount of dilatant plastic volumetric strain on the shear failure surface and the shrinking of the cap must be satisfied. This relation and the elastic bulk stress-strain equation take the form

$$I_1^{n+1} = I_1^E - 3K \, d\epsilon_{KK}^p = k^{n+1} = k^n + \left(\frac{dk}{d\epsilon_{KK}^p}\right)_n d\epsilon_{KK}^p \tag{R.44}$$

which yields

$$d\epsilon_{KK}^p = \frac{I_1^E - k^{n+1}}{3K} = \frac{k^{n+1} - k^n}{\left(\dfrac{dk}{d\epsilon_{KK}^p}\right)_n} \tag{R.45}$$

so that

$$k^{n+1} = \frac{I_1^E \left(\dfrac{dk}{d\epsilon_{KK}^p}\right)_n + 3K \, k^n}{\left(\dfrac{dK}{d\epsilon_{KK}^p}\right)_n + 3K} = L^{n+1} = I_1^{n+1} \tag{R.46}$$

254

The derivative $dk/d\epsilon_{KK}^p$ is determined empirically. (See Figure (R.4).) The final deviator stresses, after all the above corrections have been applied, are given by the equation

$$s_{ij}^{n+1} = \sqrt{\frac{J_2^{n+1}}{J_2^E}} \; s_{ij}^E \qquad\qquad (R.47)$$

If the elastic trial point lies to the right of the corner and violates the cap, a trial and error correction is used (in place of the incremental equations of Appendix G). The correction places the final stress point on the expanded cap and also satisfies a secant flow rule. The expanded yield surface has the equation

$$\sqrt{J_2^{n+1}} = F(I_1^{n+1}, k^{n+1}) = \frac{1}{R^{n+1}} \sqrt{(X^{n+1} - L^{n+1})^2 - (I_1^{n+1} - L^{n+1})^2}$$

$$(L^{n+1} \leq I_1^{n+1} \leq X^{n+1}) \qquad (R.48)$$

and the flow rule takes the form

$$d\epsilon_{ij}^p = d\lambda \frac{\partial}{\partial \sigma_{ij}} \left[\sqrt{J_2} - F(I_1, k) \right] = d\lambda \left(\frac{s_{ij}}{2\sqrt{J_2}} + a \, \delta_{ij} \right) \qquad (R.49)$$

where

$$a = - \frac{\partial F}{\partial I_1} = \frac{(I_1 - L)}{R \sqrt{(X - L)^2 - (I_1 - L)^2}} \qquad (L \leq I_1 \leq X) \qquad (R.50)$$

Note that

$$\left. \begin{array}{ll} a = 0 & (I_1 = L) \\[2mm] = \infty & (I_1 = X) \end{array} \right\} \qquad (R.51)$$

255

Equation (R.49) yields

$$d\epsilon_{KK}^{P} = 3a\ d\lambda \tag{R.52}$$

and Equations (R.49) and (R.52) yield

$$de_{ij} = \frac{s_{ij}}{2\sqrt{J_2}}\ d\lambda \tag{R.53}$$

Now

$$I_1^{n+1} = I_1^E - 3K\ d\epsilon_{KK}^{P} = I_1^E - 9Ka d\lambda \tag{R.54}$$

and

$$s_{ij}^{n+1} = s_{ij}^n - 2G\ de_{ij}^P = s_{ij}^{n+1} - \frac{Gs_{ij}^{n+1}}{\sqrt{J_2^{n+1}}}\ d\lambda \tag{R.55}$$

and Equation (R.55) yields

$$\left(1 + \frac{Gd\lambda}{\sqrt{J_2^{n+1}}}\right)\ s_{ij}^{n+1} = s_{ij}^E \tag{R.56}$$

and taking the square root of one-half the trace of Equation (R.56) yields

$$\sqrt{J_2^{n+1}} + Gd\lambda = \sqrt{J_2^E} \tag{R.57}$$

Eliminating $d\lambda$ between Equations (R.54) and (R.57) yields

$$d\lambda = \frac{I_1^E - I_1^{n+1}}{9Ka} = \frac{\sqrt{J_2^E} - \sqrt{J_2^{n+1}}}{G} \tag{R.58}$$

256

so that

$$\sqrt{J_2^{n+1}} = \sqrt{J_2^E} - \frac{G}{9Ka} (I_1^E - I_1^{n+1})$$ (R.59)

Equations (R.48) and (R.59) are the two equations which the final stress point must satisfy.

Figure (R.7) illustrates the trial and error solution process, which proceeds (conceptually) as follows:

1. Assume $k(= L)$.

2. Determine $d\varepsilon_{KK}^P$, R, and X from empirical relations. [See Figure (R.4)].

3. Compute I_1 from Equation (R.54).

4. Compute a from Equation (R.50).

5. Compute $\sqrt{J_2}$ from Equation (R.59). Steps 3 and 5 locate a point on the flow path in Figure (R.7).

6. Compute $\sqrt{J_2}$ from Equation (R.48). Steps 3 and 6 locate a point on the yield path in Figure (R.7).

7. The flow path and yield path eventually intersect at $\left(I_1^{n+1}, \sqrt{J_2^{n+1}}\right)$.

The flow path cannot pass to the left of the expanded corner and miss the yield surface altogether, because Equations (R.51) and (R.59) show that the flow path would have a vertical secant if I_1 were equal to L. Therefore, the flow path will always intersect the yield path (or the expanded cap) to the right of the expanded corner. Also, since Equations (R.51) and (R.59) show that the flow path has a horizontal secant when $I_1 = X$, it is convenient to (conceptually) set

$$a = \infty$$ $(I_1 > X)$ (R.60)

257

so that the flow path will be a horizontal straight line until $I_1 < X$. Based on the above analysis, it is apparent that

$$k^O \leq k \leq I_1^E \qquad (R.61)$$

so that the range of k to be tested in the trial and error solution of Equations (R.48) and (R.59) is bounded.

Simultaneous solution of Equations (R.48) and (R.59) actually consists of finding the value of $k = k^{n+1}$ for which

$$k^n \leq k \leq I_1^E$$

$$L \leq I_1 \leq X$$

and

$$\sqrt{J_2} = \sqrt{J_2^E} - \frac{G}{9Ka} (I_1^E - I_1) = f(I_1,k) \qquad (R.62)$$

or

$$\sqrt{J_2^E} - b = 0 \qquad (L \leq I_1 \leq X) \qquad (R.63)$$

where

$$b = f(I_1,k) + \frac{G}{9Ka} (I_1^E - I_1) \geq 0 \qquad (R.64)$$

The function on the LHS of Equation (R.63) is not bounded, so it is convenient to work with the bounded function

$$P(k) = \frac{\sqrt{J_2^E} - b}{\sqrt{J_2^E} + b} \qquad (L \leq I_1 \leq X) \qquad (R.65)$$

258

for which $-1 \leq P(k) \leq 1$, and which has the same root as Equation (R.63) because the denominator is always positive. The function $P(k)$ decreases steadily as k increases. Because it is possible to have $I_1^E > X^n$, it is desirable to also define

$$P(k) = \frac{I_1 - L}{X - L} \qquad (I_1 > X) \qquad (R.66)$$

so that $P(k)$ will decrease steadily as k increases (and I_1 decreases) even if $I_1 \geq X$, and will be equal to 1 when $I_1 = X$ and therefore never less than the upper bound on $P(k)$ for the range $(L \leq I_1 \leq X)$. And because it is possible to have $I_1 < L$ during the trial and error process, it is desirable to define

$$P(k) = \frac{I_1 - X}{X - L} \qquad (I_1 < L) \qquad (R.67)$$

so that $P(k)$ will also decrease steadily as k increases (and I_1 decreases) even if $I_1 \leq L$, and will be equal to -1 when $I_1 = L$ and therefore never greater than the lower bound on $P(k)$ for the range $(L \leq I_1 \leq X)$. Equations (R.66) and (R.67) ensure that the final value of I_1^{n+1} will lie in the interval $L^{n+1} \leq I_1^{n+1} \leq X^{n+1}$, and also that Equation (R.60) will not be needed because the quantity a will be used to calculate $P(k)$ only when I_1 lies in the desired interval. Once $k^{n+1} = L^{n+1}$ is found, $d\varepsilon_{KK}^p$, X^{n+1}, and R^{n+1} are determined empirically, I_1^{n+1} is calculated by Equation (R.54), $\sqrt{J_2^{n+1}}$ by Equation (R.48), and the deviator stress components by Equation (R.47).

When dealing with finite stress or strain differences during unloading/reloading, or during any phase of isotropic compression, direct

259

integration of Equations (R.30) and (R.31) is sometimes advantageous.

Both are of the general form

$$\frac{dy}{dx} = A - Be^{-Cy} \qquad (R.68)$$

so that

$$dx = \frac{dy}{A - Be^{-Cy}} = \frac{e^{Cy}dy}{Ae^{Cy} - B}$$

or

$$AC\ dx = \frac{ACe^{Cy}dy}{Ae^{Cy} - B} = d\ [\ln(Ae^{Cy} - B)] \qquad (R.69)$$

and therefore

$$x_2 - x_1 = \frac{1}{AC} \ln \left(\frac{e^{Cy_2} - \frac{B}{A}}{e^{Cy_1} - \frac{B}{A}} \right) \qquad (R.70)$$

Also

$$y_2 = \frac{1}{C} \ln \left[\frac{B}{A} + \left(e^{Cy_1} - \frac{B}{A} \right) e^{AC\ (x_2 - x_1)} \right] \qquad (R.71)$$

For drained hydrostatic unloading/reloading

$$x = \epsilon_{KK}^e \qquad (R.72)$$

$$y = I_1 - 3G_r \qquad (R.73)$$

$$A = \frac{3K_{1s}}{1 - K_{1s}} \qquad (R.74)$$

260

$$B = \frac{3K_{1s}K_{1s}}{1 - K_{1s}} \tag{R.75}$$

$$C = K_{2S} \tag{R.76}$$

$$AC = \frac{3K_{is}K_{2S}}{1 - K_{1s}} \tag{R.77}$$

$$\frac{B}{A} = K_{1s} \tag{R.78}$$

so that Equation (R.70) yields

$$\varepsilon^e_{KK,2} - \varepsilon^e_{KK,1} = \frac{1 - K_{1s}}{3K_{is}K_{2S}} \ln \left[\frac{e^{K_{2S}(I_{1,2} - 3G_r)} - K_{1s}}{e^{K_{2S}(I_{1,1} - 3G_r)} - K_{1s}} \right] \tag{R.79}$$

and Equation (R.71) yields

$$I_{1,2} = 3G_r + \frac{1}{K_{2S}} \ln \left\{ K_{1S} + \left[e^{K_{2S}(I_{1,1} - 3G_r)} - K_{1S} \right] \cdot \right.$$

$$\left. e^{\frac{3K_{is}K_{2S}}{1 - K_{1S}}(\varepsilon^e_{KK,2} - \varepsilon^e_{KK,1})} \right\} \tag{R.80}$$

Equation (R.21) also has the general form

$$\varepsilon^p_{KK,2} - \varepsilon^p_{KK,1} = W \left[e^{-D(I_{1,1} - 3G_r)} - e^{-D(I_{1,2} - 3G_r)} \right] \tag{R.81}$$

the inverse of which is

$$I_{1,2} = 3G_r + \frac{1}{D} \ln \left[\frac{1}{e^{-D(I_{1,1} - 3G_r)} - \frac{\varepsilon^p_{KK,2} - \varepsilon^p_{KK,1}}{W}} \right] \tag{R.82}$$

261

Equations (R.79) and (R.81) combined give an expression for the increase in total volumetric strain between any two stress points on the drained loading hydrostat. The inverse calculation can be accomplished graphically, as follows:

1. Stipulate $I_{1,1}$, and $\varepsilon^p_{KK,1} = \varepsilon^e_{KK,1} = 0$.

2. Assume $\varepsilon^p_{KK,2}$.

3. Calculate $I_{1,2}$ by Equation (R.82).

4. Calculate $\varepsilon^e_{KK,2}$ by Equation (R.79).

5. Plot $\varepsilon^p_{KK,2}$ against $\varepsilon^e_{KK,2}$ as in Figure (R.8), and find $\varepsilon_{KK,2}$ as shown.

6. For a given ε_{KK}, enter the figure backward and find ε^e_{KK}, and ε^p_{KK}, either of which can be used to find I_1.
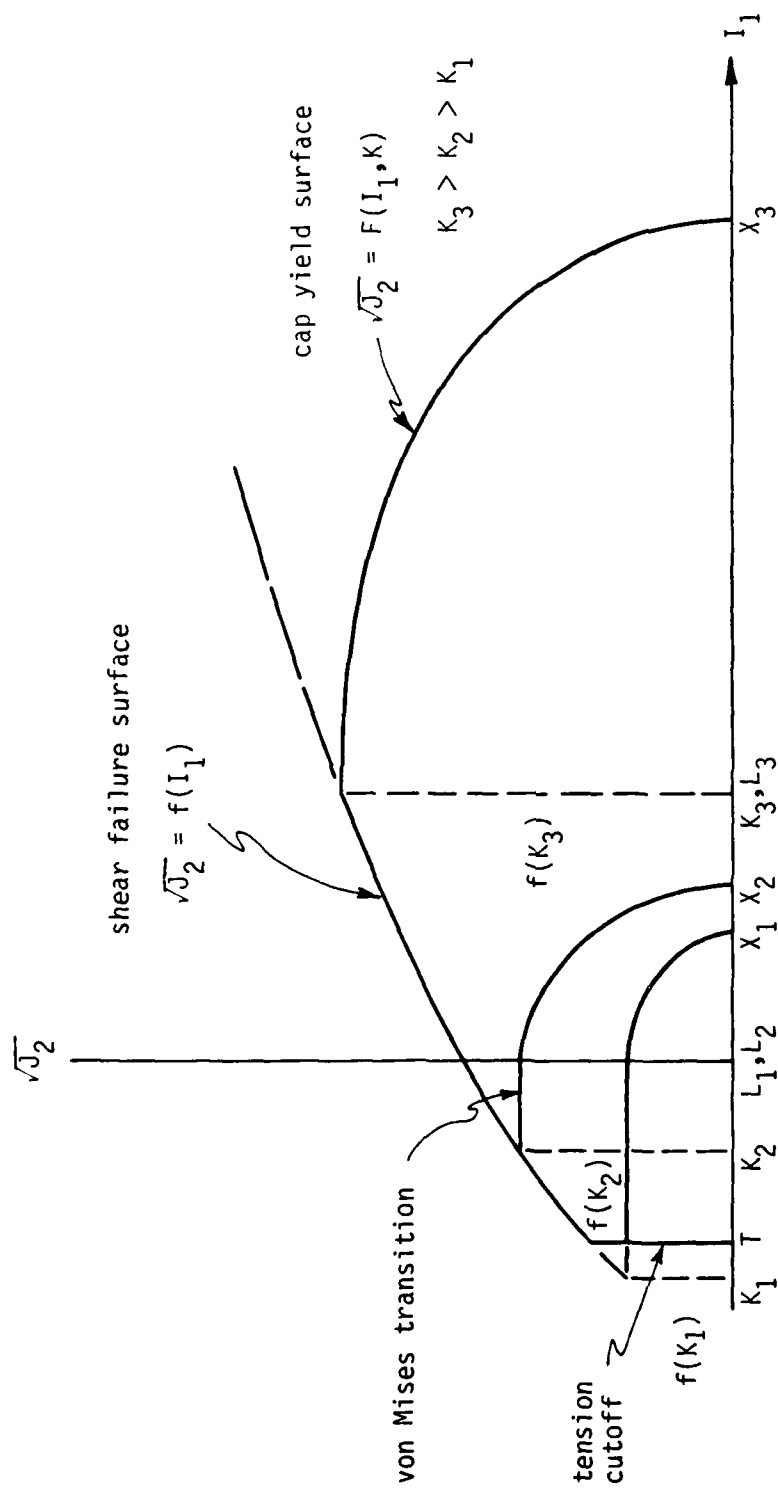
Figure R.1. Cap model yield surfaces.

263
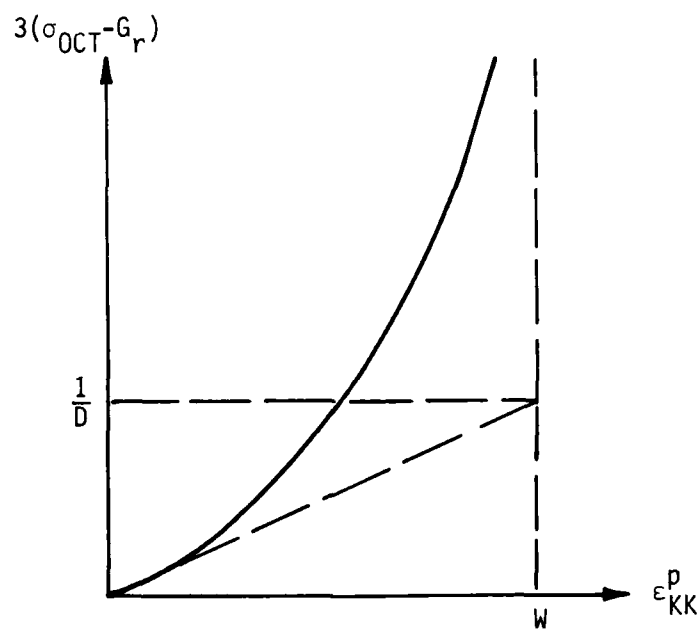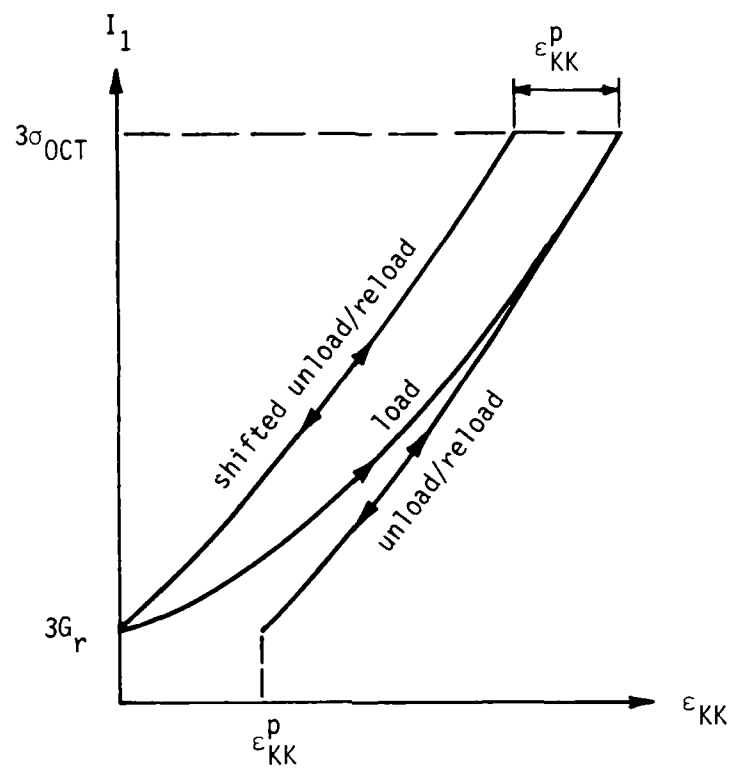
Figure R.2. Relation between peak hydrostatic effective stress and plastic volumetric strain.

$\sqrt{J_2}$

shear failure surface

$\overline{d\varepsilon}^p$

P

S

stress
path

1

$\sqrt{3}$

$3\sigma_{3c}$

I_1

(a) Stress Path

$\sigma_1 - \sigma_{3c}$

S

$(\sigma_1 - \sigma_{3c})_f$

ε_1

$\varepsilon_{KK,f}^p$

ε_{KK}^p

ε_{KK}

ε_{KK}
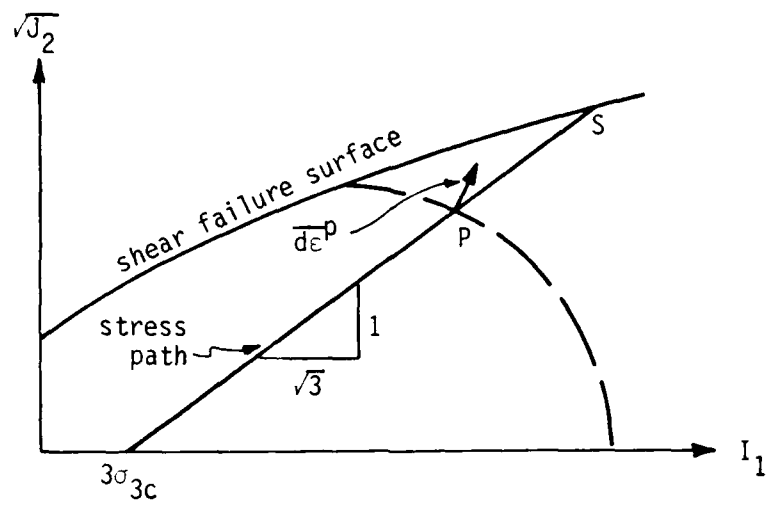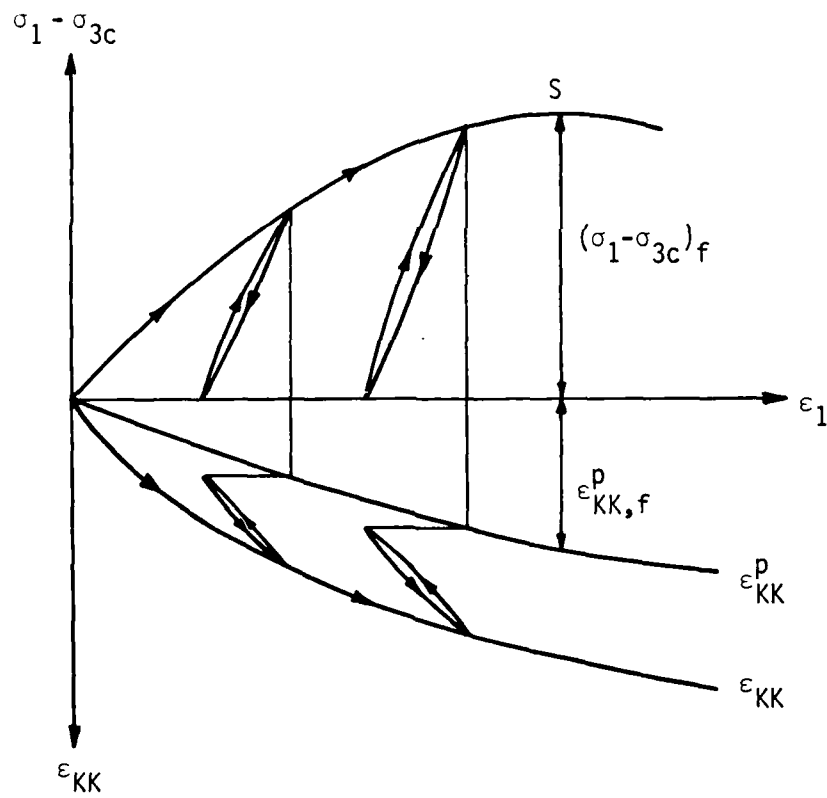
(b) Stress-Strain Response

Figure R.3.   Results of a drained triaxial compression test at
constant cell pressure with unloading/reloading.

265
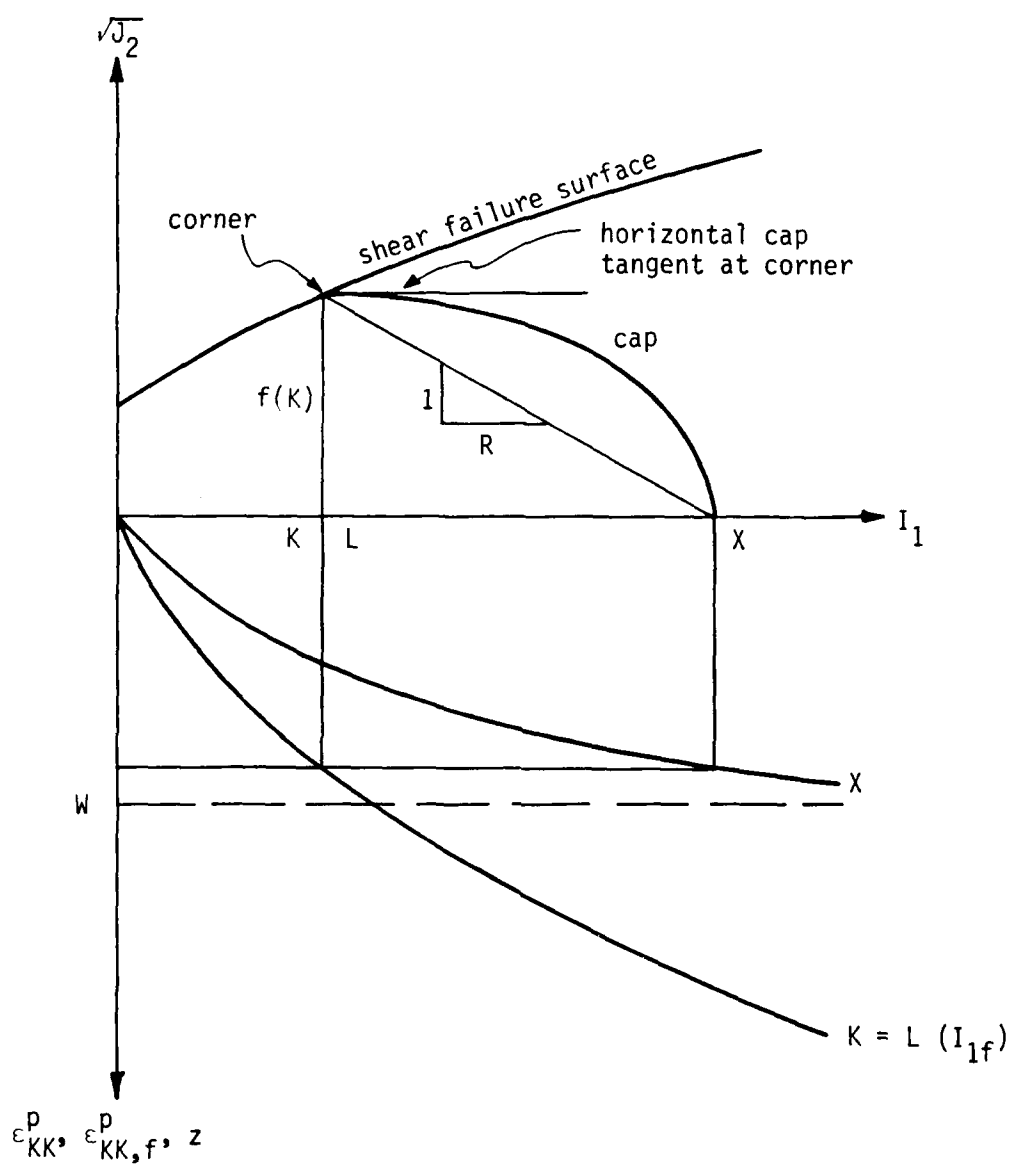
Figure R.4. Relations between cap parameters and plastic volumetric strain.
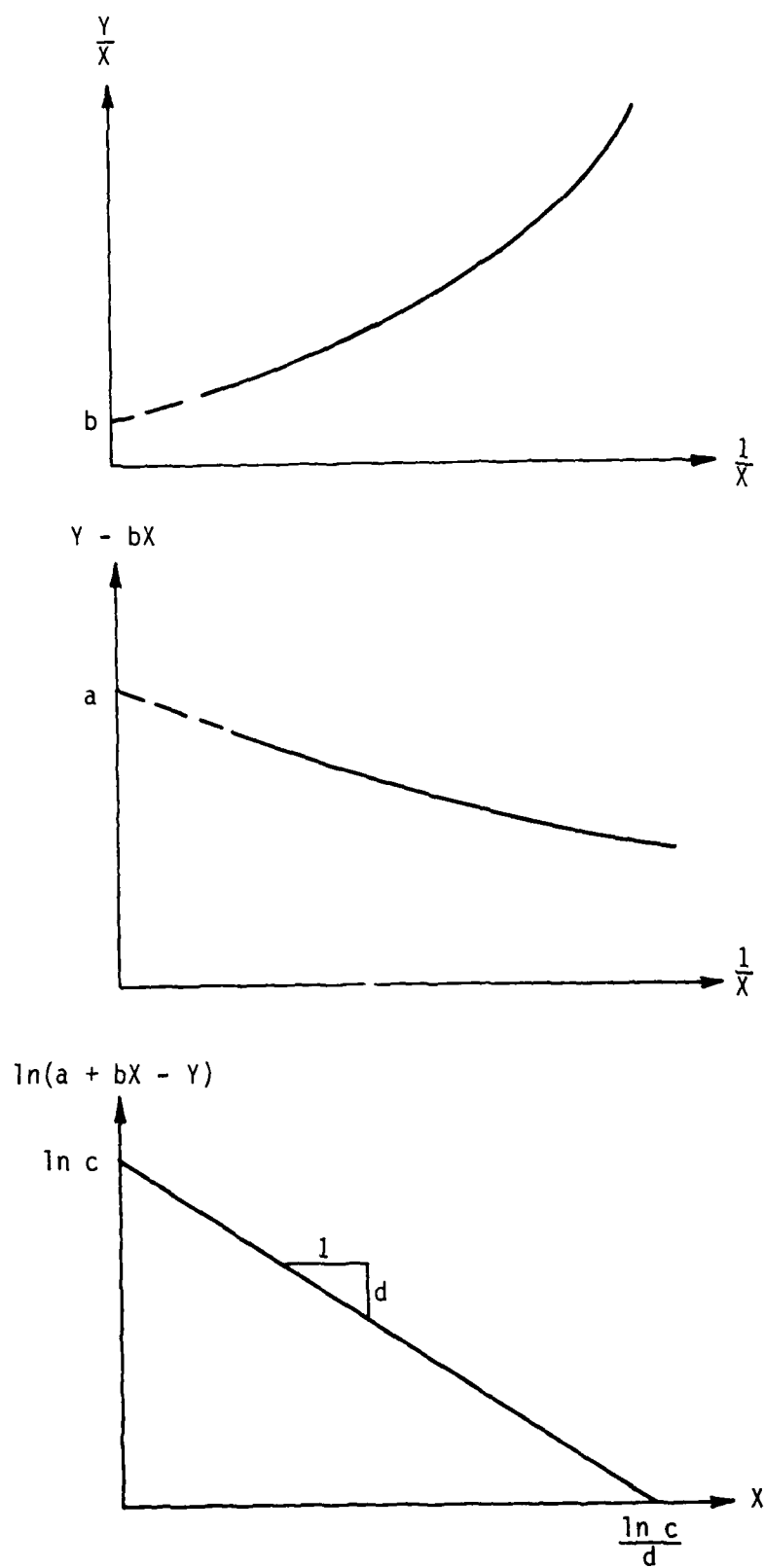
Figure R.5. Decaying exponential parameter determination.
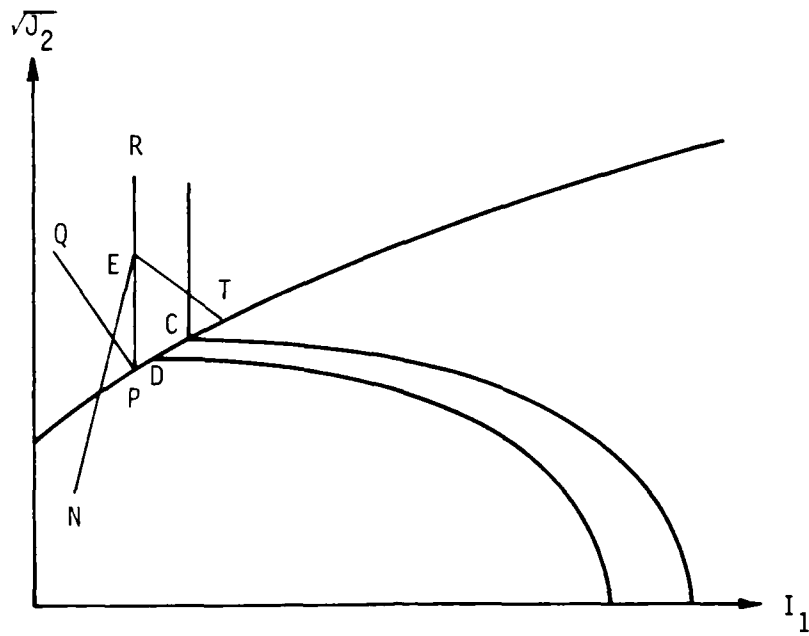
Figure R.6.   Cap violation caused by shear failure
            surface correction.

$\sqrt{J_2}$

$\sqrt{J_2^E}$

$\sqrt{J_2^{n+1}}$

flow path

solution point

yield path

$K^n \rightarrow$ I_1^{n+1} $\leftarrow I_1^E X^n \rightarrow$ I_1
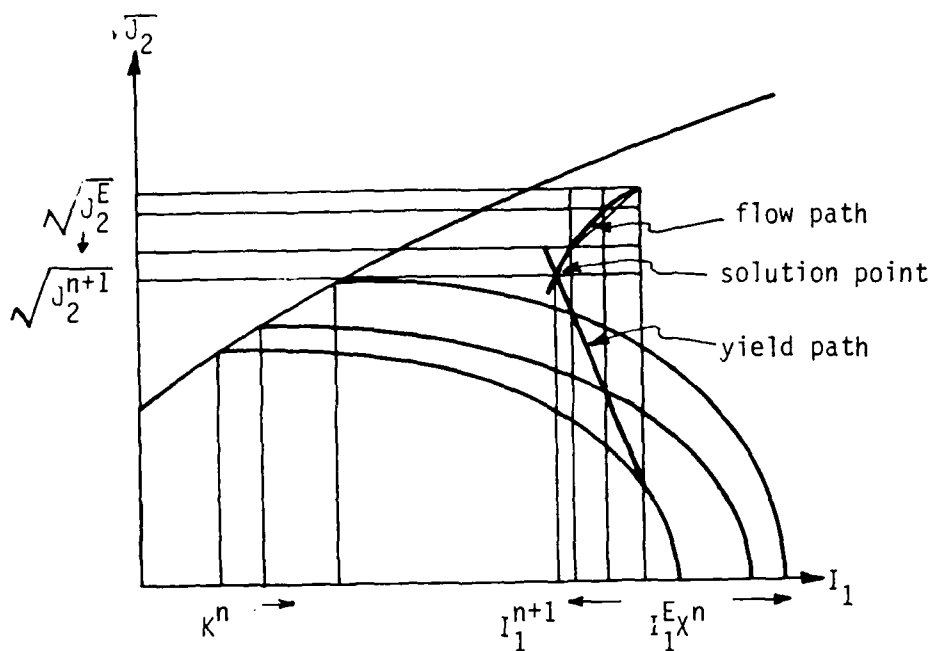
(a) Flow path, yield path and solution point.

$\sqrt{J_2}$

$\sqrt{J_2^E}$

$\dfrac{G}{3a}\, d\varepsilon_{KK}^p$

(R.59)

(R.48)

$f(I_1^E, K^n)$

K^n K^{n+1} I_1^E K
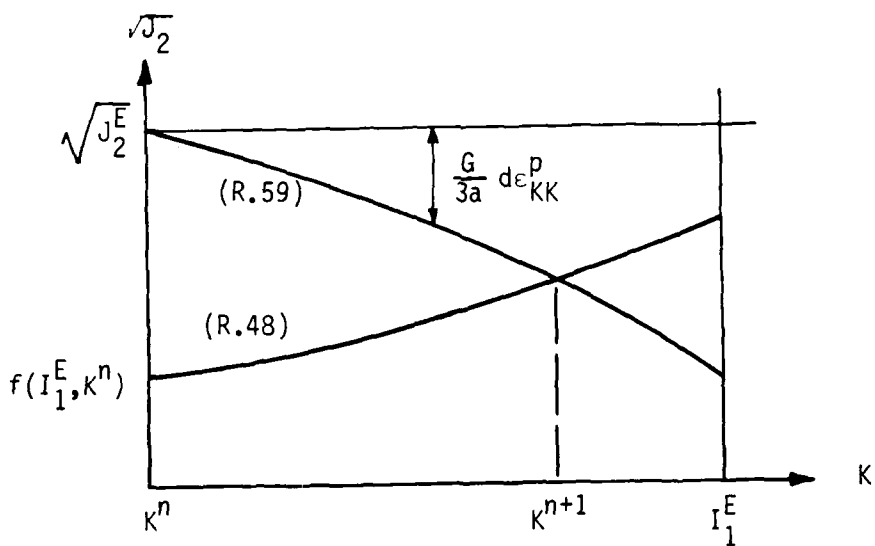
(b) Functions to be equalized by trial and error.

Figure R.7. Cap violation correction.
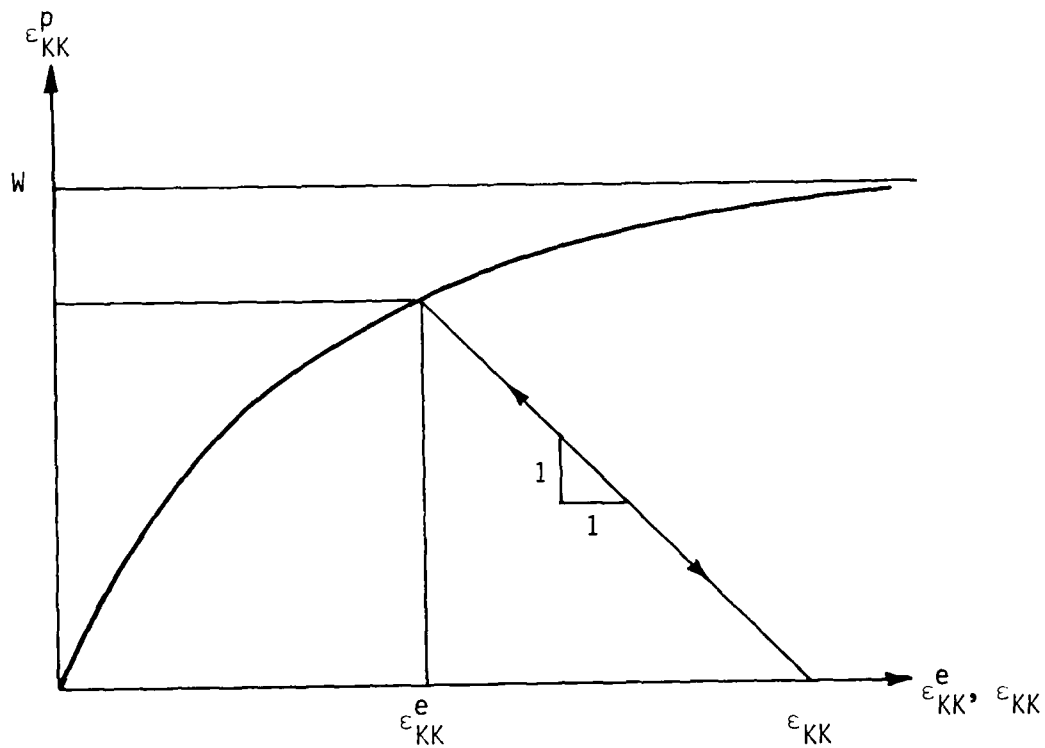
Figure R.8. Relation between plastic, elastic and total
volumetric strain in drained isotropic
compression.

270

APPENDIX S

UNDRAINED CAP MODEL AND COMPUTATIONAL ALGORITHM

During undrained isotropic compressive loading the measured total stress incremental bulk modulus is assumed to have the same form as Equation (R.30).

$$K_m = \frac{K_{im}}{1 - K_{1m}} \left[1 - K_{1m} e^{-K_{2m}(I_1 - 3G_r)} \right] \qquad (S.1)$$

so that, by analogy with Equations (R.79) and (R.80),

$$\varepsilon_{KK,2} - \varepsilon_{KK,1} = \frac{1 - K_{1m}}{3K_{im}K_{2m}} \ln \left[\frac{e^{K_{2m}(I_{1,2} - 3G_r)} - K_{1m}}{e^{K_{2m}(I_{1,1} - 3G_r)} - K_{1m}} \right] \qquad (S.2)$$

$$I_{1,2} = 3G_r + \frac{1}{K_{2m}} \ln \left\{ K_{1m} + \left[e^{K_{2m}(I_{1,1} - 3G_r)} - K_{1m} \right] \cdot \right.$$

$$\left. e^{\frac{3K_{im}K_{2m}}{1 - K_{1m}} (\varepsilon_{KK,2} - \varepsilon_{KK,1})} \right\} \qquad (S.3)$$

During undrained isotropic compression Equations (R.79), (R.80), (R.81), and (R.82) apply to the effective stresses, so that

$$\varepsilon^e_{KK,2} - \varepsilon^e_{KK,1} = \frac{1 - K_{1s}}{3K_{is}K_{2S}} \ln \left[\frac{e^{K_{2S}(I'_{1,2} - 3G'_r)} - K_{1S}}{e^{K_{2S}(I'_{1,1} - 3G'_r)} - K_{1S}} \right] \qquad (S.4)$$

$$I'_{1,2} = 3G'_r + \frac{1}{K_{2S}} \ln \left\{ K_{1S} + \left[e^{K_{2S}(I'_{1,1} - 3G'_r)} - K_{1S} \right] \cdot \right.$$

$$\left. e^{\frac{3K_{is}K_{2S}}{1 - K_{1S}} (\varepsilon^e_{KK,2} - \varepsilon^e_{KK,1})} \right\} \qquad (S.5)$$

271

$$\varepsilon_{KK,2}^{p} - \varepsilon_{KK,1}^{p} = W \left[e^{-D(I'_{1,1}-3G'_r)} - e^{-D(I'_{1,2}-3G'_r)} \right] \tag{S.6}$$

$$I'_{1,2} = 3G'_r + \frac{1}{D} \ln \left[\frac{1}{e^{-D(I'_{1,1}-3G'_r)} - \dfrac{\varepsilon_{KK,2}^{p} - \varepsilon_{KK,1}^{p}}{W}} \right] \tag{S.7}$$

The value of $I'_{1,2}$ corresponding to a given total volumetric strain increment, $\varepsilon_{KK,2} - \varepsilon_{KK,1}$, can be calculated using Figure (R.8), and either Equation (S.5) or (S.7).

For undrained triaxial compression at constant cell pressure the slope of the total stress path in $(I_1, \sqrt{J_2})$ space is $1/\sqrt{3}$, so that

$$I_1 = 3\sigma_{3C} + \sqrt{3J_2} = 3\sigma_{3C} + \sqrt{3J'_2} \tag{S.8}$$

since

$$\sqrt{J_2} = \sqrt{J'_2} \tag{S.9}$$

The procedure for calculating an effective stress path increment is as follows:

1. Stipulate $\Delta\varepsilon_1$ and assume $\Delta\varepsilon_3$.

2. Calculate the effective stresses σ'_1, σ'_3, I'_1, and $\sqrt{J'_2}$ using the drained (effective stress) model.

3. Calculate I_1 by Equation (S.3).

4. Calculate the excess pore pressure by the equation

$$u = \frac{I_1 - I'_1}{3} \tag{S.10}$$

5. Calculate the total radial stress by the equation

$$\sigma_3 = \sigma'_3 + u \tag{S.11}$$

6. If $\sigma_3 \neq \sigma_{3C}$ select a new value of $\Delta\varepsilon_3$ and repeat steps 2-6.

272

7. When $\sigma_3 = \sigma_{3C}$, calculate the total axial stress by the equation

$$\sigma_1 = \sigma_1' + u \qquad (S.12)$$

Equation (S.8) will be satisfied because it takes the form of Equation (R.25).

Strain-controlled undrained response is calculated as follows:

1. Stipulate $\Delta\varepsilon_{ij}$.
2. Caculate σ_{ij}' and I_1' using the drained (effective stress) model.
3. Calculate I_1 by Equations (S.3).
4. Calculate the excess pore pressure by Equation (S.10).
5. Calculate the total stresses by the equation

$$\sigma_{ij} = \sigma_{ij}' + u\delta_{ij} \qquad (S.11)$$

Notice that this approach recognizes dilatancy in the effective stress model, but not in the total stress model.

273

APPENDIX T

LADE MODEL CROSS SECTIONS AND PARAMETER DETERMINATION

Lade's failure criterion (the expansive yield surface at its maximum extent) has the equation

$$f'_p = \left(\frac{I_1^3}{I_3} - 27\right)\left(\frac{I_1}{P_a}\right)^m = \eta_1 \tag{T.1}$$

or

$$\frac{I_3}{I_1^3} = \frac{\left(\frac{I_1}{P_a}\right)^m}{\eta_1 + 27\left(\frac{I_1}{P_a}\right)^m} = r \tag{T.2}$$

Now Equation (C.5) yields

$$I_1 = 3\sigma_{OCT} \tag{T.3}$$

Equation (B.24) gives

$$I_3 = J_3 - \frac{I_1 J_2}{3} + \frac{I_1^3}{27} \tag{B.24}$$

Equation (A.63) yields

$$J_3 = 2 \cos 3\omega \left(\frac{J_2}{3}\right)^{3/2} \tag{T.4}$$

and Equation (C.7) yields

$$\frac{J_2}{3} = \frac{\tau_{OCT}^2}{2} \tag{T.5}$$

274

Substitution of Equations (T.3), (B.24), (T.4), and (T.5) into Equation (T.2) yields

$$\frac{2 \cos 3\omega \left(\frac{\tau_{OCT}^2}{2}\right)^{\frac{3}{2}} - \sigma_{OCT}\left(\frac{3\ \tau_{OCT}^2}{2}\right) + \sigma_{OCT}^3}{27\sigma_{OCT}^3} =$$

$$\frac{\frac{\cos 3\omega}{\sqrt{2}}\left(\frac{\tau_{OCT}}{\sigma_{OCT}}\right)^3 - \frac{3}{2}\left(\frac{\tau_{OCT}}{\sigma_{OCT}}\right)^2 + 1}{27} = r \tag{T.6}$$

or

$$\frac{\cos 3\omega}{\sqrt{2}}\left(\frac{\tau_{OCT}}{\sigma_{OCT}}\right)^3 - \frac{3}{2}\left(\frac{\tau_{OCT}}{\sigma_{OCT}}\right)^2 + (1 - 27r) = 0 \tag{T.7}$$

If we set

$$h = \left(\frac{I_1}{P_a}\right)^m / n_1 \tag{T.8}$$

$$z = \frac{\tau_{OCT}}{\sigma_{OCT}} \tag{T.9}$$

$$A = \frac{\cos 3\omega}{\sqrt{2}} \tag{T.10}$$

$$B = 1 - 27r = 1 - \frac{27h}{1 + 27h} = \frac{1}{1 + 27h} \tag{T.11}$$

then Equation (T.7) can be written in the form

$$Az^3 - 1.5z^2 + B = 0 \tag{T.12}$$

or

$$z^2(1.5 - Az) = B$$

275

or

$$z = \sqrt{\frac{B}{1.5 - Az}} \quad \text{(iterate)} \tag{T.13}$$

By fixing ω and therefore A in Equation (T.10), and varying h and therefore B in Equation (T.11), Equation (T.13) will yield a longitudinal cross section of the failure surface. By fixing h and therefore B, and varying ω and therefore A, Equation (T.13) will yield a transverse (octahedral) cross section. For triaxial compression

$$\sigma_1 > \sigma_2 = \sigma_3 \tag{T.14}$$

so that if

$$\frac{\sigma_1}{\sigma_3} = N_\phi = \frac{1 + \sin \phi}{1 - \sin \phi} \tag{T.15}$$

where ϕ is the compression angle of obliquity, then

$$I_1 = \sigma_1 + 2\sigma_3 = \sigma_3 (N_\phi + 2) \tag{T.16}$$

$$I_3 = \sigma_1 \sigma_3^2 = \sigma_3^3 N_\phi \tag{T.17}$$

and therefore Equation (T.2) yields

$$\frac{I_3}{I_1^3} - \frac{N_\phi}{(N_\phi + 2)^3} = r \tag{T.18}$$

where Equation (T.11) yields

$$B = 1 - 27r \tag{T.11}$$

and also

$$h = \frac{\frac{1}{B} - 1}{27} \tag{T.19}$$

276

Values of r, B, and h corresponding to compression angles of obliquity of 30, 35, 40, 45, and 50 degrees are tabulated below:

ø DEG	r ----	B ---	h ---
30	0.02400	0.35200	0.06818
35	0.02003	0.45920	0.04362
40	0.01600	0.56788	0.02818
45	0.01215	0.67199	0.01808
50	0.00867	0.76590	0.01132

Values of z for Lade's failure criterion are tabulated in Table (T.1). The rows show longitudinal cross section values for a given ω, and the columns show octahedral cross section values for a given h.

The determination of Lade's model parameters proceeds as follows. The unloadng/reloading elastic modulus, E_{ur}, is measured on plots of $(\sigma_1 - \sigma_{3C})$ against ϵ_1 from drained triaxial compression tests at constant cell pressure, and is assumed to be an exponential function of cell pressure of the form

$$E_{ur} = K_{ur} \left(\frac{\sigma_{3C}}{P_a}\right)^n \tag{T.20}$$

Taking the logarithm of both sides of Equation (T.20) yields

$$\log_{10} E_{ur} = \log_{10} K_{ur} + n \log_{10} \left(\frac{\sigma_{3C}}{P_a}\right) \tag{T.21}$$

so that the parameters K_{ur} and n can be obtained from a log log plot of E_{ur} against σ_{3C}/P_a, which should appear as a straight line.

277

The unloading/reloading bulk modulus, B_{ur}, can be obtained from drained isotropic compression tests with unloading, and since

$$B_{ur} = \frac{E_{ur}}{3(1 - 2\nu_{ur})} \tag{T.22}$$

where ν_{ur} is Poisson's ratio for unloading/reloading, the value of ν_{ur} can be found from the expression

$$\nu_{ur} = \frac{1}{2} \left(1 - \frac{E_{ur}}{3B_{ur}}\right) \tag{T.23}$$

Frequently, ν_{ur} is found to be relatively insensitive to σ_{3C}, and is therefore assumed constant.

Drained isotropic compression activates only the collapse yield surface, so W_c can be determined from drained isotropic compression tests with unloading as the area under a plot of octahedral normal stress against plastic volumetric strain. For isotropic compressive primary loading Equations (3.8.1), (3.8.2) and (3.8.3) yield

$$f_c' = 3\sigma_{OCT}^2 = f_c'' = p_a^2 \left(\frac{W_c}{Cp_a}\right)^{1/p} \tag{T.24}$$

so that

$$\frac{W_c}{p_a} = C \left[3 \left(\frac{\sigma_{OCT}}{p_a}\right)^2\right]^p \tag{T.25}$$

Taking the logarithm of both sides of Equation (T.25) yields

$$\log_{10}\left(\frac{W_c}{p_a}\right) = \log_{10} C + p \log_{10} \left[3 \left(\frac{\sigma_{OCT}}{p_a}\right)^2\right] \tag{T.26}$$

so that the parameters C and p can be obtained from a log log plot of W_c/p_a against $3(\sigma_{OCT}/p_a)^2$, which should appear as a straight line.

Shear failure in a strain-controlled drained triaxial compression test at constant cell pressure is defined as attainment of the maximum value of $(\sigma_1 - \sigma_{3C})$. At this point Equation (3.8.8) yields

$$(f_p')_f = f_{p,MAX}' = \left[\left(\frac{I_1^3}{I_3} - 27\right)\left(\frac{I_1}{p_a}\right)^m\right]_f = \eta_1 \tag{T.27}$$

so that

$$\left(\frac{I_1^3}{I_3} - 27\right)_f = \eta_1 \left(\frac{p_a}{I_1}\right)^m_f \tag{T.28}$$

Taking the logarithm of both sides of Equation (T.28) yields

$$\log_{10}\left(\frac{I_1^3}{I_3} - 27\right)_f = \log_{10}\eta_1 - m \log_{10}\left(\frac{I_1}{p_a}\right)_f \tag{T.29}$$

so that the parameters η_1 and m can be obtained from a log log plot of

$$\left(\frac{I_1^3}{I_3} - 27\right)_f \text{ against } \left(\frac{I_1}{p_a}\right)_f, \text{ which should appear as a straight line.}$$

Having the parameters E_{ur}, ν_{ur}, C, and p, the elastic and collapse plastic strains can be computed throughout a triaxial compression test at constant cell pressure. The elastic and collapse plastic axial and volumetric strain increments are

$$d\epsilon_1^e = \frac{d\sigma_1}{E_{ur}} \tag{T.30}$$

279

$$d\varepsilon_v^e = \left(\frac{1 - 2\nu_{ur}}{E_{ur}}\right) d\sigma_1 \tag{T.31}$$

and

$$d\varepsilon_1^C = \frac{2\sigma_1^2 \, d\sigma_1}{\dfrac{p_a^3}{Cp} \left(\dfrac{\sigma_1^2 + 2\sigma_{3C}^2}{p_a^2}\right)^{2-p}} \tag{T.32}$$

$$d\varepsilon_v^C = \frac{2\sigma_1(\sigma_1 + 2\sigma_{3C}) \, d\sigma_1}{\dfrac{p_a^3}{Cp} \left(\dfrac{\sigma_1^2 + 2\sigma_{3C}^2}{p_a^2}\right)^{2-p}} \tag{T.33}$$

and the expansive axial and volumetric strain increments are

$$d\varepsilon_1^p = d\varepsilon_1 - (d\varepsilon_1^e + d\varepsilon_1^C) \tag{T.34}$$

$$d\varepsilon_v^p = d\varepsilon_v - (d\varepsilon_v^e + d\varepsilon_v^C) \tag{T.35}$$

The expansive plastic work is

$$W_p = \int \sigma_1 d\varepsilon_1^p + 2\sigma_{3C}\varepsilon_3^p = \int (\sigma_1 - \sigma_{3C})d\varepsilon_1^p + \sigma_{3C}\varepsilon_v^p \tag{T.36}$$

The values of W_P corresponding to $f_p' = \eta_1$ and $f_p' = 0.60 \, \eta_1$, respectively, are called $W_{P,PEAK}$ and $W_{P,60}$.

The assumption is that $W_{P,PEAK}$ is related to σ_{3C} by the expression

$$W_{P,PEAK} = \overline{P}p_a \left(\frac{\sigma_{3C}}{P_a}\right)^1 \tag{T.37}$$

Taking the logarithm of both sides of Equation (T.37) yields

$$\log_{10}\left(\frac{W_{P,PEAK}}{P_a}\right) = \log_{10}\overline{P} + 1 \log_{10}\left(\frac{\sigma_{3C}}{P_a}\right) \tag{T.38}$$

280

so that the parameters $\overline{P}$ and l can be obtained from a log log plot of

$$\frac{W_{P,PEAK}}{P_a} \text{ against } \frac{\sigma_{3C}}{P_a}, \text{ which should appear as a straight line.}$$

Now because f'_p and f''_p are equal as long as $(\sigma_1 - \sigma_{3C})$ is increasing, and f''_p is a function of W_p according to Equation (3.8.9), let $W_{P,PEAK}$ be the value of W_p which maximizes f''_p (or f'_p) at the value η_1. Then Equation (3.8.9) yields

$$\frac{df''_p}{dW_p} = -abe^{-bW_p}\left(\frac{W_p}{P_a}\right)^{1/q} + \frac{a}{qP_a}e^{-bW_p}\left(\frac{W_p}{P_a}\right)^{1/q-1}$$

$$= f''_p\left(\frac{1}{qW_p} - b\right) \qquad (T.39)$$

so that at failure

$$\left(\frac{df''_p}{dW_p}\right)_f = \eta_1\left(\frac{1}{qW_{P,PEAK}}\right) - b = 0 \qquad (T.40)$$

and therefore since η_1 is not zero,

$$b = \frac{1}{qW_{P,PEAK}} \qquad (T.41)$$

Substitution of Equation (T.41) into Equation (3.8.9) yields

$$f''_p = a\left(\frac{W_p e^{-\frac{W_p}{W_{P,PEAK}}}}{P_a}\right)^{1/q} \qquad (T.42)$$

so that according to the definitions of $W_{P,PEAK}$ and $W_{P,60}$,

$$\eta_1 = a\left(\frac{W_{P,PEAK}\ e^{-1}}{P_a}\right)^{1/q} \qquad (T.43)$$

281

and

$$0.60 \, \eta_1 = a \left(\frac{W_{P,60} \, e^{-\frac{W_{P,60}}{W_{P,PEAK}}}}{P_a} \right)^{1/q} \qquad \text{(T.44)}$$

Note that $W_{P,60}$ must be measured as a function of σ_{3C}, but no empirical formula relating $W_{P,60}$ to σ_{3C} is needed. Dividing Equation (T.44) by Equation (T.43) yields

$$0.60 = \left[\left(\frac{W_{P,60}}{W_{P,PEAK}} \right) e^{\left(1 - \frac{W_{P,60}}{W_{P,PEAK}} \right)} \right]^{1/q} \qquad \text{(T.45)}$$

so that

$$q = \frac{\ln \left(\frac{W_{P,60}}{W_{P,PEAK}} \right) + \left(1 - \frac{W_{P,60}}{W_{P,PEAK}} \right)}{\ln 0.60} \qquad \text{(T.46)}$$

The assumption is that q is related to σ_{3C} by a linear equation of the form

$$q = \alpha + \beta \left(\frac{\sigma_{3C}}{P_a} \right) \qquad \text{(T.47)}$$

so that the parameters α and β can be obtained from an arithmetic plot of q against σ_{3C}/P_a, which should appear as a straight line.

Having both $W_{P,PEAK}$ and q as functions of σ_{3C}, the parameter b can be obtained as a function of σ_{3C} by Equation (T.41), and the parameter a can be obtained as a function of σ_{3C} by writing Equation (T.43) in the form

$$a = \frac{n_1}{\left(\dfrac{W_{P,PEAK}}{e p_a}\right)^{1/q}} \qquad (T.48)$$

The parameter n_2 in Equation (3.8.11) can be determined from the expansive plastic Poisson's ratio,

$$\nu^P = - \frac{d\varepsilon_3^P}{d\varepsilon_1^P} \qquad (T.49)$$

obtained from a drained triaxial compression test at constant cell pressure, where using the results of Equations (T.34) and (T.35) yields

$$d\varepsilon_3^P = \frac{1}{2}(d\varepsilon_v^P - d\varepsilon_1^P) \qquad (T.50)$$

so that

$$\nu^P = - \frac{d\varepsilon_3^P}{d\varepsilon_1^P} = \frac{1}{2}\left(1 - \frac{d\varepsilon_v^P}{d\varepsilon_1^P}\right) \qquad (T.51)$$

Using the flow rule and Equation (3.8.11) yields

$$\nu^P = \frac{G n_2 - J}{K - H n_2} \qquad (T.52)$$

where

$$G = \left(\frac{p_a}{I_1}\right)^m \left[\sigma_1 \sigma_{3C} - m I_1^2 \left(\frac{I_3}{I_1^3}\right)\right] \qquad (T.53)$$

$$H = \left(\frac{p_a}{I_1}\right)^m \left[\sigma_{3C}^2 - m I_1^2 \left(\frac{I_3}{I_1^3}\right)\right] \qquad (T.54)$$

283

$$J = 3I_1^2 - 27 \, \sigma_1 \sigma_{3C} \tag{T.55}$$

$$K = 3I_1^2 - 27 \, \sigma_{3C}^2 \tag{T.56}$$

so that

$$\eta_2 = \frac{J + K\nu^p}{G + H\nu^p} \tag{T.57}$$

The assumption is that η_2 is linearly related to $\sqrt{\sigma_{3C}/P_a}$ and f_p'' by an equation of the form

$$\eta_2 = t + R \sqrt{\frac{\sigma_{3C}}{P_a}} + S \, f_p'' \tag{T.58}$$

The parameters t, R, and S can be found by multilinear regression.

284

TABLE T.1

VALUES OF z FOR LADE'S FAILURE CRITERION

	ø, DEG				
	50	45	40	35	30
	h				
w	0.01132	0.01808	0.02818	0.04362	0.06818
120	0.96989	0.87226	0.77128	0.66861	0.56569
115	0.94775	0.85720	0.76119	0.66199	0.56149
110	0.89779	0.82084	0.73557	0.64456	0.55012
105	0.84263	0.77766	0.70321	0.62138	0.53434
100	0.79238	0.73624	0.67057	0.59687	0.51694
95	0.74967	0.69987	0.64086	0.57374	0.49991
90	0.71456	0.66932	0.61530	0.55330	0.48442
85	0.68531	0.64356	0.59342	0.53551	0.47071
80	0.66106	0.62205	0.57501	0.52040	0.45893
75	0.64216	0.60520	0.56050	0.50840	0.44949
70	0.62872	0.59317	0.55007	0.49973	0.44263
65	0.62068	0.58596	0.54381	0.49450	0.43847
60	0.61801	0.58356	0.54173	0.49275	0.43708

285

APPENDIX U

ARA CONIC MODEL CROSS SECTIONS AND PARAMETER DETERMINATION

Triaxial cross sections of the conic model compressive and expansive yield surfaces appear as shown in Figure (U.1).

The conic model failure criterion (the expansive yield surface at its maximum extent) has the equation

$$f_p' = \left(\frac{\tau_{OCT}}{P_a}\right)\left(1 - E \cos 3\omega\right)\left(\frac{P_a}{\sigma_{OCT}} + m\right) = \eta_1 \tag{U.1}$$

or

$$\frac{\tau_{OCT}}{P_a} = \frac{\left(\dfrac{\eta_1}{1 - E \cos 3\omega}\right)\left(\dfrac{\sigma_{OCT}}{P_a}\right)}{1 + m\left(\dfrac{\sigma_{OCT}}{P_a}\right)} \tag{U.2}$$

When ω is fixed in Equation (U.2) the variation of τ_{OCT} with σ_{OCT} becomes hyperbolic, taking the form

$$\tau_{OCT} = \frac{\left(\dfrac{\eta_1}{1 - E \cos 3\omega}\right)\sigma_{OCT}}{1 + \left(\dfrac{m}{P_a}\right)\sigma_{OCT}} \tag{U.3}$$

The initial slope of the failure surface at zero octahedral normal stress is

$$\left(\frac{d\tau_{OCT}}{d\sigma_{OCT}}\right)_0 = \frac{\eta_1}{1 - E \cos 3\omega} \tag{U.4}$$

and the upper shear strength asymptotic limit is

286

$$\lim_{\sigma_{OCT} \to \infty} \left(\tau_{OCT} \right) = \left(1 - \frac{\eta_1}{E \cos 3\omega} \right) \left(\frac{p_a}{m} \right) \qquad (U.5)$$

When σ_{OCT} is fixed in Equation (U.2) the variation of τ_{OCT}/σ_{OCT} becomes a triple ellipse, taking the form

$$\frac{\tau_{OCT}}{\sigma_{OCT}} = \frac{\dfrac{\eta_1}{1 + m \left(\dfrac{\sigma_{OCT}}{p_a} \right)}}{1 - E \cos 3\omega} \qquad (U.6)$$

The parameters η_1, m, and E can be determined from a series of triaxial compression and extension tests. For triaxial compression ($\omega = 120°$), Equation (U.3) reduces to

$$\tau_{OCT} = \frac{\left(\dfrac{\eta_1}{1 - E} \right) \sigma_{OCT}}{1 + m \left(\dfrac{\sigma_{OCT}}{p_a} \right)}$$

or

$$\frac{\sigma_{OCT}}{\tau_{OCT}} = \frac{1 - E}{\eta_1} \left[1 + m \left(\frac{\sigma_{OCT}}{p_a} \right) \right] = k_{1c} + k_{2c} \left(\frac{\sigma_{OCT}}{p_a} \right) \qquad (U.7)$$

where

$$k_{1c} = \frac{1 - E}{\eta_1} \qquad (U.8)$$

$$k_{2c} = m \left(\frac{1 - E}{\eta_1} \right) \qquad (U.9)$$

For triaxial extension ($\omega = 60°$), Equation (U.3) reduces to

287

$$\tau_{OCT} = \frac{\left(\dfrac{\eta_1}{1 + E}\right) \sigma_{OCT}}{1 + m \left(\dfrac{\sigma_{OCT}}{p_a}\right)}$$

or

$$\frac{\sigma_{OCT}}{\tau_{OCT}} = \frac{1 + E}{\eta_1} \left[1 + m \left(\frac{\sigma_{OCT}}{p_a}\right)\right] = k_{1e} + k_{2e} \left(\frac{\sigma_{OCT}}{p_a}\right) \qquad (U.10)$$

where

$$k_{1e} = \frac{1 + E}{\eta_1} \qquad (U.11)$$

$$k_{2e} = m \left(\frac{1 + E}{\eta_1}\right) \qquad (U.12)$$

Plots of Equations (U.7) and (U.10) are shown in Figure (U.2). Having determined the parameters k_{1c}, k_{2c}, k_{1e}, and k_{2e}, the parameter m can be calculated from the expression

$$m = \frac{k_{2c}}{k_{1c}} = \frac{k_{2e}}{k_{1e}} \qquad (U.13)$$

which provides a consistency check. The parameters η_1 and E can be calculated from Equations (U.8) and (U.11), written in the form

$$k_{1c}\eta_1 + E = 1$$

$$k_{1e}\eta_1 - E = 1$$

so that

$$\eta_1 = \frac{2}{k_{1e} + k_{1c}} \qquad (U.14)$$

$$E = 1 - k_{1c}\eta_1 = 1 - \frac{2k_{1c}}{k_{1e} + k_{1c}} = \frac{k_{1e} - k_{1c}}{k_{1e} + k_{1c}} \qquad (U.15)$$

Having calculated the parameters η_1 and m (and E) from triaxial compression and extension tests, the accuracy of the assumed octahedral cross section form can be investigated by a series of true triaxial tests. If, in Equation (U.6) we set

$$\frac{\eta_1}{1 + m\left(\frac{\sigma_{OCT}}{p_a}\right)} = \Psi \qquad (U.16)$$

then Equation (U.6) can be written in the form

$$\frac{\tau_{OCT}}{\sigma_{OCT}} = \frac{\Psi}{1 - E \cos 3\omega} \qquad (U.17)$$

which is the equation of a triple ellipse in polar coordinates. Equation (U.17) can be written in a linear form to obtain the octahedral eccentricity, E, as a consistency check on the previously determined value from Equation (U.15).

$$\frac{\Psi\sigma_{OCT}}{\tau_{OCT}} = 1 - E \cos 3\omega \qquad (U.18)$$

A plot of Equation (U.18) is shown in Figure (U.3).

The method for computing the conic model octahedral cross section sets

$$\omega_2 = \omega \qquad (A.65b)$$

in Figure (C.2), so that

$$\tan \omega = \frac{\sqrt{3}}{\mu} \qquad (U.19)$$

where μ is Lode's parameter. And if we assume that $d = 0$ in Figure (C.2) and Equation (C.26), then

$$O'P' = \sqrt{3} \frac{\tau_{OCT}}{\sigma_{OCT}} = \sqrt{3} \ z \tag{U.20}$$

so that the horizontal projection of O'P' can be calculated in two ways:

$$\sqrt{3} \ z \sin \omega = \left(\sqrt{6} - \sqrt{3} \ z \cos \omega\right) \frac{\sin \phi}{\sqrt{3}} \tag{U.21}$$

Solving Equation (U.21) for z yields

$$z \left(\sqrt{3} \sin \omega + \cos \omega \sin \phi\right) = \sqrt{2} \sin \phi$$

or

$$z = \frac{\sqrt{2} \sin \phi}{\sqrt{3} \sin \omega + \cos \omega \sin \phi} \tag{U.22}$$

and solving Equation (U.21) for $\sin \phi$ yields

$$\sin \phi = \frac{\sqrt{3} \ z \sin \omega}{\sqrt{2} - z \cos \omega} \tag{U.23}$$

Note that when $m = 0$, Equations (U.7) and (U.10) yield

$$k_{1c} = \frac{1}{z_c} \tag{U.24}$$

$$k_{1e} = \frac{1}{z_e} \tag{U.25}$$

Octahedral cross section data for the case ($m = 0$; $\overline{\phi}_c = 32°$; $\overline{\phi}_e = 35°$) are tabulated in Table U.1 and plotted in Figure (U.4). The calculation sequence used to obtain the values shown in Table U.1 and Figure (U.4) is as follows:

$$\tan \omega = \frac{\sqrt{3}}{\mu} \qquad\qquad\qquad\qquad\qquad (U.19)$$

$$z_c = \frac{2 \sqrt{2} \sin \overline{\phi}_c}{3 - \sin \overline{\phi}_c} \qquad\qquad (\omega = 120°) \qquad (U.26)$$

$$z_e = \frac{2 \sqrt{2} \sin \overline{\phi}_e}{3 + \sin \overline{\phi}_e} \qquad\qquad (\omega = 60°) \qquad (U.27)$$

$$\eta_1 = \frac{2 z_c z_e}{z_c + z_e} \qquad\qquad\qquad\qquad (U.28)$$

$$E = \frac{z_c - z_e}{z_c + z_e} \qquad\qquad\qquad\qquad (U.29)$$

$$z = \frac{\eta_1}{1 - E \cos 3\omega} \qquad\qquad\qquad (U.30)$$

$$\sin \overline{\phi} = \frac{\sqrt{3} \; z \; \sin\omega}{2 - z \cos\omega} \qquad\qquad\qquad (U.31)$$

Determination of the unloading/reloading Young's modulus parameters, K_{ur} and n in Equation (4.6), for the conic model is accomplished in the same way as for the Lade model, as described in Appendix T. The same is true for the unloading/reloading Poisson's ratio, ν_{ur}.

At the present time the parameters A, M, λ, γ, and B in Equation (4.10) are determined by trial and error. When the unloading/reloading hysteresis option has been fully implemented, a method for determining the parameters will be developed.

The parameters C and p in the compressive hardening rule, Equation (3.8.3), can be determined in the same way as for the Lade model, as described in Appendix T, but there is an easier way which avoids the

291

numerical integration required to obtain W_c as a function of f_c'. It involves directly fitting the plastic hydrostat (the curve of σ_{OCT} against ε_v^c obtained from drained isotropic compression tests with unloading). Equation (T.25) can be written in the form

$$W_c = Cp_a \left[3 \left(\frac{\sigma_{OCT}}{p_a} \right)^2 \right] \tag{U.32}$$

so that the compressive plastic work increment generated by a compressive plastic volumetric strain increment is

$$dW_c = \sigma_{OCT} d\varepsilon_v^c = Cpp_a \left[3 \left(\frac{\sigma_{OCT}}{p_a} \right)^2 \right]^{p-1} \cdot 6 \frac{\sigma_{OCT}}{p_a} \cdot \frac{d\sigma_{OCT}}{p_a}$$

$$= \left\{ 6Cp \left[3 \left(\frac{\sigma_{OCT}}{p_a} \right)^2 \right]^{p-1} \frac{d\sigma_{OCT}}{p_a} \right\} \sigma_{OCT} \tag{U.33}$$

and therefore

$$d\varepsilon_v^c = 6Cp \left[3 \left(\frac{\sigma_{OCT}}{p_a} \right)^2 \right]^{p-1} \left(\frac{d\sigma_{OCT}}{p_a} \right) \tag{U.34}$$

Integration of Equation (U.34) yields

$$\varepsilon_v^c = \left(\frac{6Cp}{2p-1} \right) \left(3^{p-1} \right) \left(\frac{\sigma_{OCT}}{p_a} \right)^{2p-1} = L \left(\frac{\sigma_{OCT}}{p_a} \right)^Q \tag{U.35}$$

where

$$L = C \left(\frac{6p}{2p-1} \right) \left(3^{p-1} \right) \tag{U.36}$$

$$Q = 2p - 1 \tag{U.37}$$

Taking the logarithm of both sides of Equation (U.35) yields

$$\log_{10} \varepsilon_v^C = \log_{10} L + Q \log_{10} \left(\frac{\sigma_{OCT}}{p_a}\right) \tag{U.38}$$

so that the parameters L and Q can be obtained from a log log plot of ε_v^C against σ_{OCT}/p_a, which should appear as a straight line. The parameter p can then be determined by writing Equation (U.37) in the form

$$p = \frac{Q + 1}{2} \tag{U.39}$$

and the parameter C can then be determined by writing Equation (U.36) in the form

$$C = \left(\frac{2p - 1}{6p}\right)\left(3^{1-p}\right) L \tag{U.40}$$

The parameter r in Equation (4.3) is not determined uniquely, but rather adjusted by trial and error so the sum of the calculated elastic and compressive plastic volumetric strains in a triaxial compression test at constant cell pressure always exceeds the measured total volumetric strain, and the difference steadily increases. The difference is minus the expansive plastic volumetric strain, and if the above relationship is not maintained it means the expansive plastic potential surface is generating compressive plastic volumetric strain, which is impossible. The relationship to be maintained is

$$d\varepsilon_v^e + d\varepsilon_v^C > d\varepsilon_v \tag{U.41}$$

or

$$\left(\frac{1-2\nu_{ur}}{E_{ur}}\right) d\sigma_1 + \left\{\frac{6\sigma_{OCT}\left[r^2\sigma_1 + (1-r^2)\,\sigma_{OCT}\right]}{\left(\frac{p_a^3}{Cp}\right)\left(\frac{f_c'}{p_a^2}\right)^{2-p}}\right\} d\sigma_1 > d\varepsilon_v \tag{U.42}$$

293

Determination of the expansive yield surface parameters E, m, and η_1 in Equations (4.4) and (3.8.8) has already been discussed.

The parameters a, b, and q in the expansive hardening rule, Equation (3.8.9). can be determined in the same way as for the Lade model, as described in Appendix T, but there is another way which uses the entire curve of f_p' against W_p, rather than just the two values $W_{p,PEAK}$ and $W_{p,60}$. However, the method does involve a derivative.

Equation (3.8.9) gives

$$f_p' = ae^{-bW_p}\left(\frac{W_p}{p_a}\right)^{1/q} \tag{3.8.9}$$

so that

$$\ln f_p' = \ln a - (bp_a)\left(\frac{W_p}{p_a}\right) + \frac{1}{q}\ln\left(\frac{W_p}{p_a}\right) \tag{U.43}$$

Differentiation of Equation (U.43) with respect to W_p/p_a yields

$$\frac{1}{f_p'}\frac{df_p'}{d\left(\frac{W_p}{p_a}\right)} = -bp_a + \frac{1}{q}\left(\frac{p_a}{W_p}\right)$$

or

$$\frac{p_a}{W_p} = qbp_a + q\left[\frac{1}{f_p'}\frac{df_p'}{d\left(\frac{W_p}{p_a}\right)}\right] \tag{U.44}$$

The parameters q and b can be obtained from an arithmetic plot of p_a/W_p against

$$\frac{1}{f_p'}\frac{df_p'}{d\left(\frac{W_p}{p_a}\right)}$$

which should appear as a straight line.

294

The intercept is

$$qbp_a = \frac{p_a}{W_{P,PEAK}} \tag{U.45}$$

and the slope is q. Having b and q, the parameter a can be obtained from an arithmetic plot of f_p' against $e^{-bW_p}(W_p/p_a)^{1/q}$, which should appear as a straight line through the origin with slope a as predicted by Equation (3.8.9). The linear relation between σ_{3C}/p_a and q indicated by Equation (T.47), plus Equations (T.41) and (T.48) apply to the conic model as they do to the Lade model.

The parameter η_2 in Equation (4.5) can be obtained from the expansive plastic Poisson's ratio

$$\nu^p = -\frac{d\varepsilon_3^p}{d\varepsilon_1^p} \tag{T.49}$$

obtained from a drained triaxial compression test at constant cell pressure, as it is for the Lade model. The resulting expression is

$$\eta_2 = \frac{P(\nu^p - 0.5)}{H(1 + \nu^p)} \tag{T.50}$$

where

$$P = \frac{\sqrt{2}}{3p_a}(1 - E) \tag{T.51}$$

$$H = \frac{\frac{1}{3p_a}}{\left[1 + m\left(\frac{\sigma_{OCT}}{p_a}\right)\right]^2} \tag{T.52}$$

The linear relation between $\sqrt{\sigma_{3C}/p_a}$, f_p'', and η_2 indicated by Equation (T.58) applies to the conic model as it does to the Lade model.

295

TABLE U.1

ARA MODEL FAILURE SURFACE OCTAHEDRAL CROSS SECTION

FOR (m = 0; $\overline{\phi}_C$ = 32 DEGREES; $\overline{\phi}_E$ = 35 DEGREES)

μ	ω DEG	z	sin ϕ
-1.0	120.000	0.60679	0.530
-0.9	117.457	0.60589	0.550
-0.8	114.791	0.60304	0.569
-0.7	112.000	0.59810	0.586
-0.6	109.107	0.59105	0.602
-0.5	106.102	0.58198	0.614
-0.4	103.004	0.57118	0.625
-0.3	99.826	0.55901	0.632
-0.2	96.587	0.54597	0.636
-0.1	93.304	0.53259	0.637
0	90.000	0.51938	0.636
0.1	86.696	0.50681	0.633
0.2	83.413	0.49526	0.628
0.3	80.174	0.48500	0.622
0.4	76.996	0.47620	0.615
0.5	73.898	0.46894	0.608
0.6	70.893	0.46321	0.600
0.7	67.994	0.45897	0.593
0.8	65.209	0.45610	0.586
0.9	62.543	0.45449	0.580
1.0	60.000	0.45398	0.574
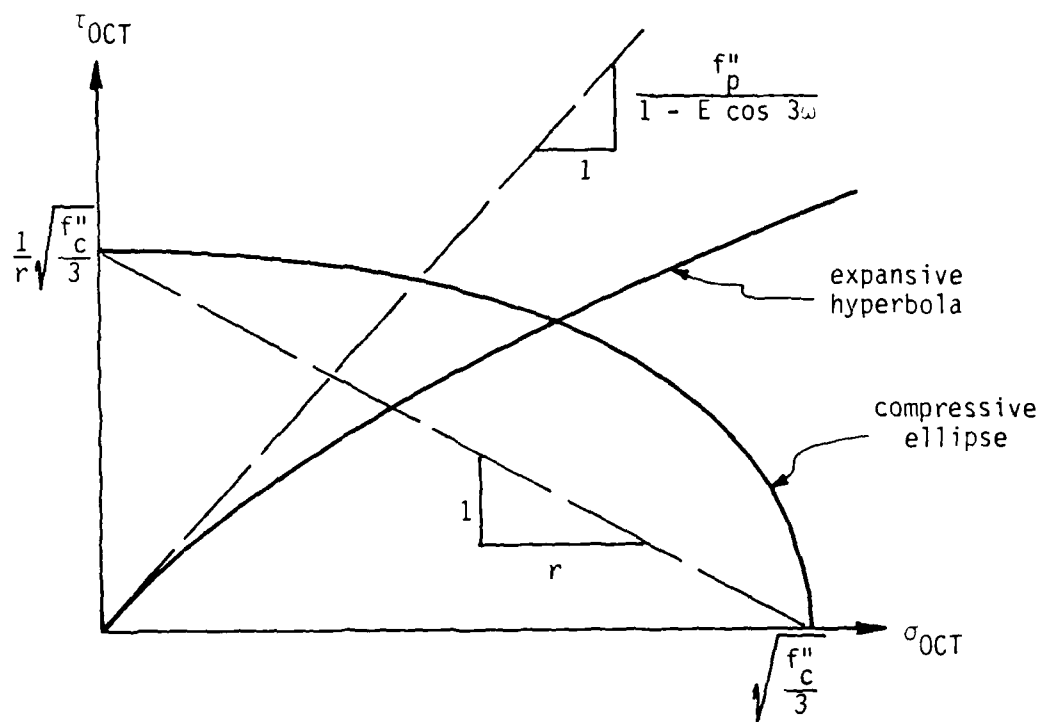
Figure U.1. Conic model yield surfaces.
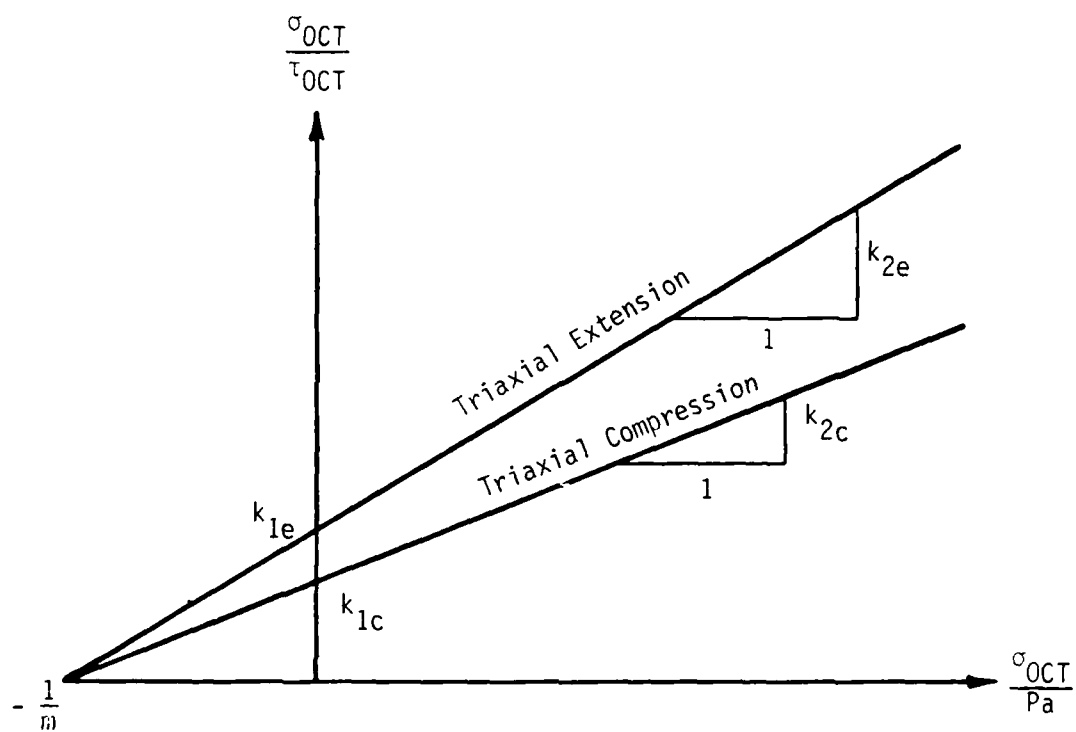
Figure U.2. Southwell plots to determine yield criterion parameters.
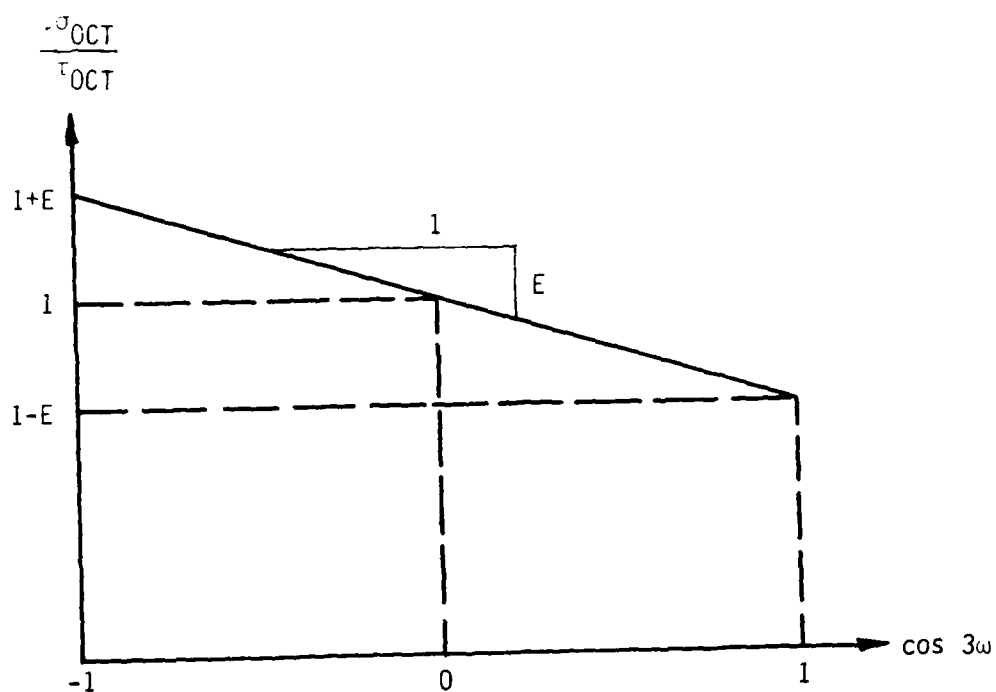
Figure U.3. Linear plot for checking the octahedral
eccentricity.
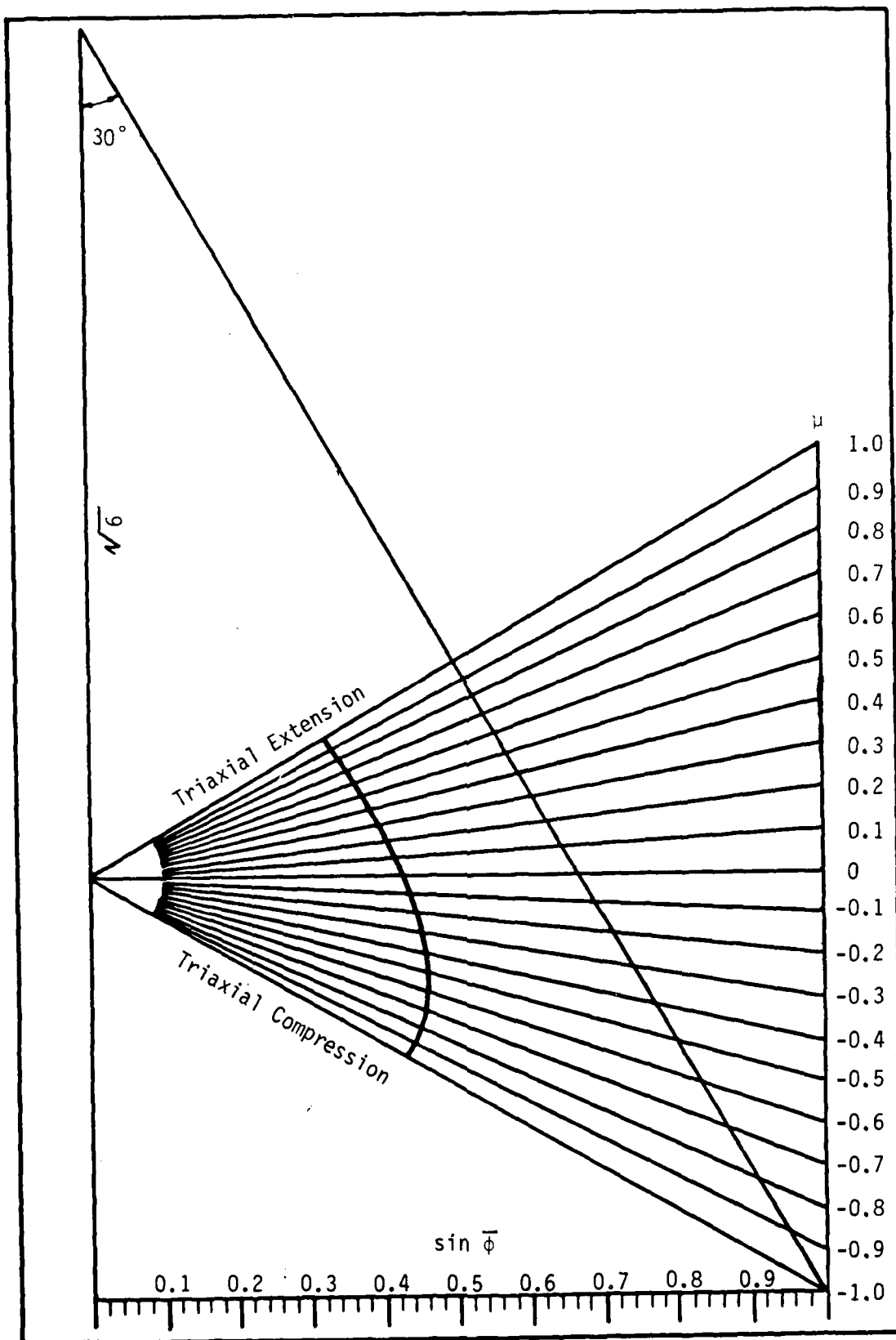
Figure U.4. Conic model failure surface octahedral cross-section for (m = 0, ϕ_c = 32 degrees; ϕ_e = 35 degrees).

APPENDIX V

EVALUATION OF EXISTING MODELS

V.1 Linear Elastic

V.1.1 Motivation

The principal advantages of a linear elastic constitutive model for transient soil dynamics problems are the availability of or possibility of obtaining closed form analytic solutions, and the existence of proven, stable numerical solution techniques for use when a closed form solution does not exist and is too difficult to obtain. The principal disadvantage is that real soil departs from linear elastic behavior even at strains of the order of 10^{-5}.

V.1.2 Assumptions

The classic theory of linear elasticity assumes a material to be homogeneous (having the same stress-strain characteristics at each point), and isotropic (having its stress-strain characteristics the same in all directions). The term elastic implies complete strain recovery upon unloading, no matter how large or small the applied stresses. The stresses at a point are assumed to depend only on the strains at that point, through a system of homogeneous linear equations [Timoshenko and Goodier (1970:1)]. Thus the linear elastic model is rate independent.

V.1.3 Basic Equations

The homogeneous linear equations relating strains to stresses in the theory of linear elasticity are of the form

$$
\begin{Bmatrix} \sigma_1 \\ \sigma_2 \\ \sigma_3 \\ \sigma_4 \\ \sigma_5 \\ \sigma_6 \end{Bmatrix} = M \begin{bmatrix} 1 & K_o & K_o & 0 & 0 & 0 \\ K_o & 1 & K_o & 0 & 0 & 0 \\ K_o & K_o & 1 & 0 & 0 & 0 \\ 0 & 0 & 0 & 1-K_o & 0 & 0 \\ 0 & 0 & 0 & 0 & 1-K_o & 0 \\ 0 & 0 & 0 & 0 & 0 & 1-K_o \end{bmatrix} \begin{Bmatrix} \varepsilon_1 \\ \varepsilon_2 \\ \varepsilon_3 \\ \varepsilon_4 \\ \varepsilon_5 \\ \varepsilon_6 \end{Bmatrix} \qquad (V.1.1)
$$

where the column vectors, $\{\sigma\}$ and $\{\varepsilon\}$, are defined by Equations (E.5) and (E.24), and the elastic constants, M (the constrained modulus) and K_o (the coefficient of lateral stress at rest), are defined by Equations (J.33) and (J.34).

V.1.4 Parameter Determination

There are a number of methods for measuring the elastic parameters, M and K_o. The constrained modulus, M, can be measured directly in the laboratory by a constrained compression (oedometer) test, in which all strains in Equation (V.1.1) are zero except ε_1. In a laboratory hydrostatic compression test

$$
\varepsilon_1 = \varepsilon_2 = \varepsilon_3 = \frac{\varepsilon_{VOL}}{3} \qquad (V.1.2)
$$

and

$$
\sigma_1 = \sigma_2 = \sigma_3 = \sigma_{OCT} \qquad (V.1.3)
$$

so that Equation (V.1.1) yields

$$
\sigma_{OCT} = M \left(\frac{1 + 2K_o}{3} \right) \varepsilon_{VOL} = B \varepsilon_{VOL} \qquad (V.1.4)
$$

302

where the elastic bulk modulus, B, is given by the expression

$$B = M \left(\frac{1 + 2K_0}{3} \right) \qquad (\text{V}.1.5)$$

and therefore

$$K_0 = \frac{1}{2} \left(\frac{3B}{M} - 1 \right) \qquad (\text{V}.1.6)$$

Laboratory test specimens often suffer from disturbance due to field sampling and specimen preparation, and may not be representative of an entire soil mass. A popular method for determining elastic parameters which are representative of an entire soil mass is by field measurements of the two elastic body wave velocities [Terzaghi (1943:463)]. They are:

$$C_1 = \sqrt{\frac{M}{\rho}} = \text{compressional wavespeed} \qquad (\text{V}.1.7)$$

and

$$C_2 = \sqrt{\frac{G}{\rho}} = \sqrt{\frac{M(1 - K_0)}{2\rho}} = \text{shear wavespeed} \qquad (\text{V}.1.8)$$

where
$$G = M \left(\frac{1 - K_0}{2} \right) = \text{elastic shear modulus} \qquad (\text{V}.1.9)$$

$$\rho = \text{mass density}$$

Then the elastic constants, M and K_0, are given by the expressions

$$M = \rho C_1^2 \qquad (\text{V}.1.10)$$

and

$$K_0 = 1 - 2 \left(\frac{C_2}{C_1} \right)^2 \qquad (\text{V}.1.11)$$

303

V.1.5 Computed Behavior

The parameters chosen to represent CARES-DRY Sand are listed in Table V.1.1. Since the linear elastic model cannot represent the behavior of a highly non-linear, non-elastic material such as this over any significant range of stress or strain, the choice of these parameters was completely arbitrary. Computed behavior for this model is very straightforward, as examination of Figures (V.1.1) through (V.1.41) shows.

304

TABLE V.1.1. ELASTIC MODEL PROPERTIES FOR CARES-DRY SAND

Parameter	Symbol	Variable	Value	Units
Bulk Modulus	B	BULK3	3.760×10^8	Pa
Shear Modulus	G	SHEAR3	1.440×10^8	Pa
Mass Density	ρ	RHOREF	1900	Kg/m^3
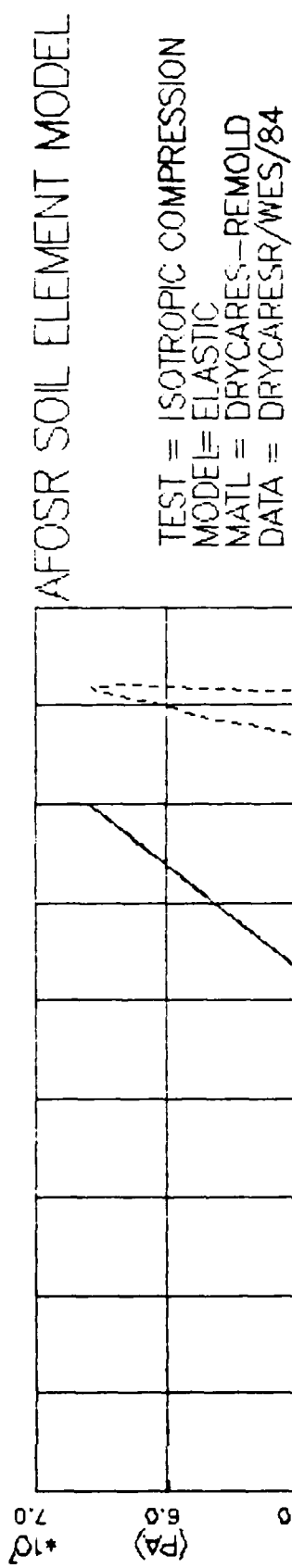
AFOSR SOIL ELEMENT MODEL

TEST = ISOTROPIC COMPRESSION
MODEL= ELASTIC
MATL = DRYCARES,--REMOLD
DATA = DRYCARESR/WES/84

LEGEND
CALCULATION
TEST DATA

FIGURE V.1.1 ELASTIC MODEL EXERCISE--ISOTROPIC COMP. - PRESSURE VS. VOLUMETRIC STRAIN .

TOTAL PRESSURE (PA) *10⁷

VOLUME STRAIN

AFOSR SOIL ELEMENT MODEL

TEST = STANDARD TRIAXIAL TEST
MODEL = ELASTIC
MATL = DRYCARES—REMOLD
DATA = DRYCARESR/WES/84

LEGEND

SIGMA.3C = 3.4E6
_____ TEST DATA
SIGMA.3C = 7.0E6
_____ TEST DATA
SIGMA.3C = 58.8E6
.... TEST DATA
SIGMA.3C = 100.0E6
_____ TEST DATA
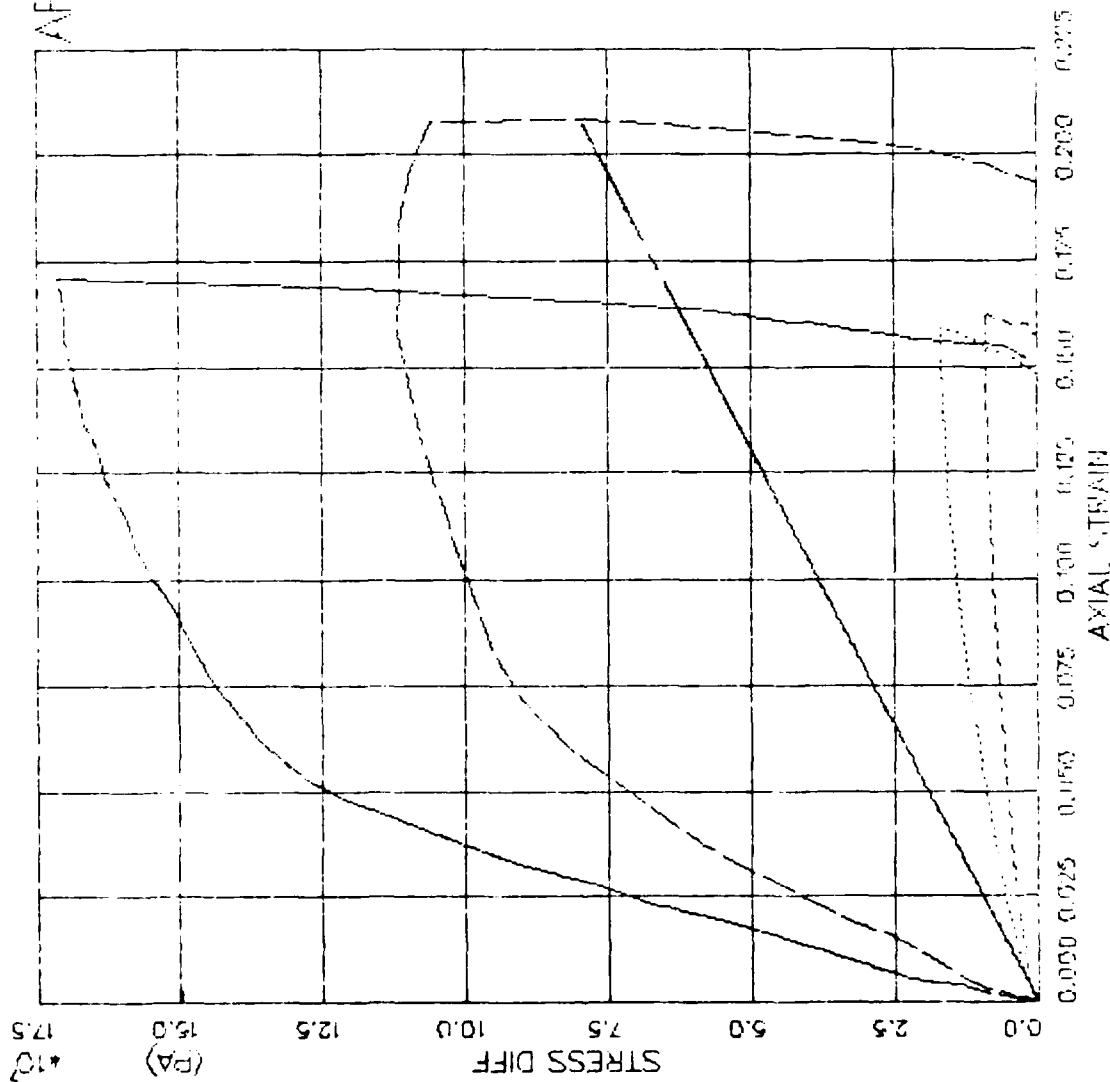
FIGURE V.1.2 ELASTIC MODEL EXERCISE—TRIAXIAL COMP(GTC) – STRESS DIFF VS. AXIAL STRAIN

AFOSR SOIL ELEMENT MODEL

TEST = STANDARD TRIAXIAL
MODEL = ELASTIC
MATL = DRYCAHFS-REMOLD
DATA = DRYCAHFSR/WES/84

LEGEND

SIGMA3C = 3.4E6
SIGMA3C = 7.0E6
SIGMA3C = 58.8E6
SIGMA3C = 101.0E6

FIGURE V.1.3 ELASTIC MODEL RESPONSE - TRIAXIAL COMP (CTC) - STRESS DIFF VS. STRAIN DIFF

AFOSR SOIL ELEMENT MODEL

TEST = STANDARD TRIAXIAL TEST
MODEL = ELASTIC
MATL = DRYCAPLES--REMOLD
DATA = DRYCAPESR/WES/84

LEGEND

SIGMA3C = 3.4E6
_____ TEST DATA
SIGMA3C = 7.0E6
_____ TEST DATA
SIGMA3C = 59.8E6
_____ TEST DATA
SIGMA3C =100.0E6
_____ TEST DATA

VOLUME STRAIN (VA)
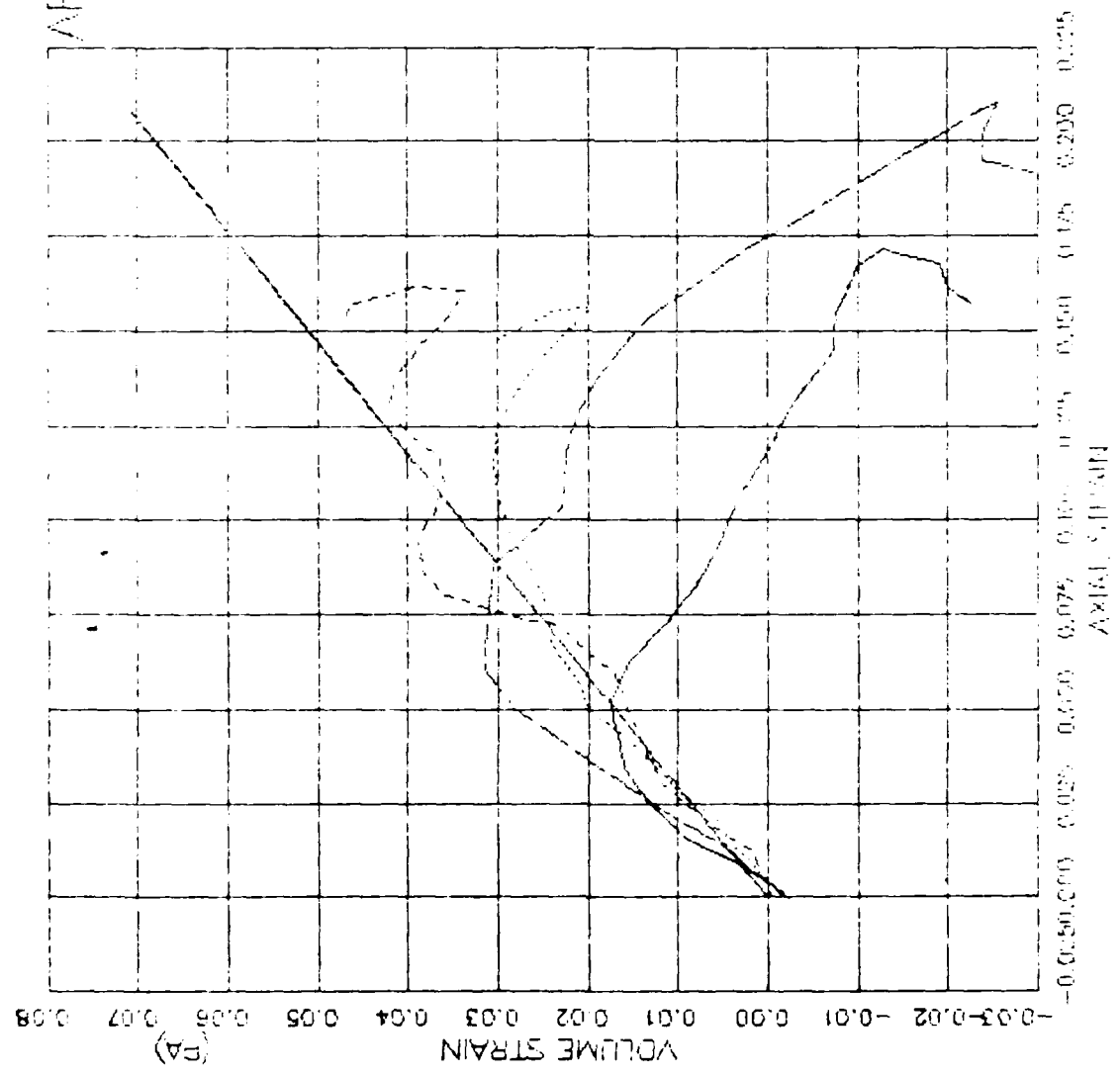
AXIAL STRAIN

FIGURE V.1.4 ELASTIC MODEL TRIPLE — TRIAXIAL COMP(CTC) — AXIAL STRAIN VS VOLUME STRAIN

309
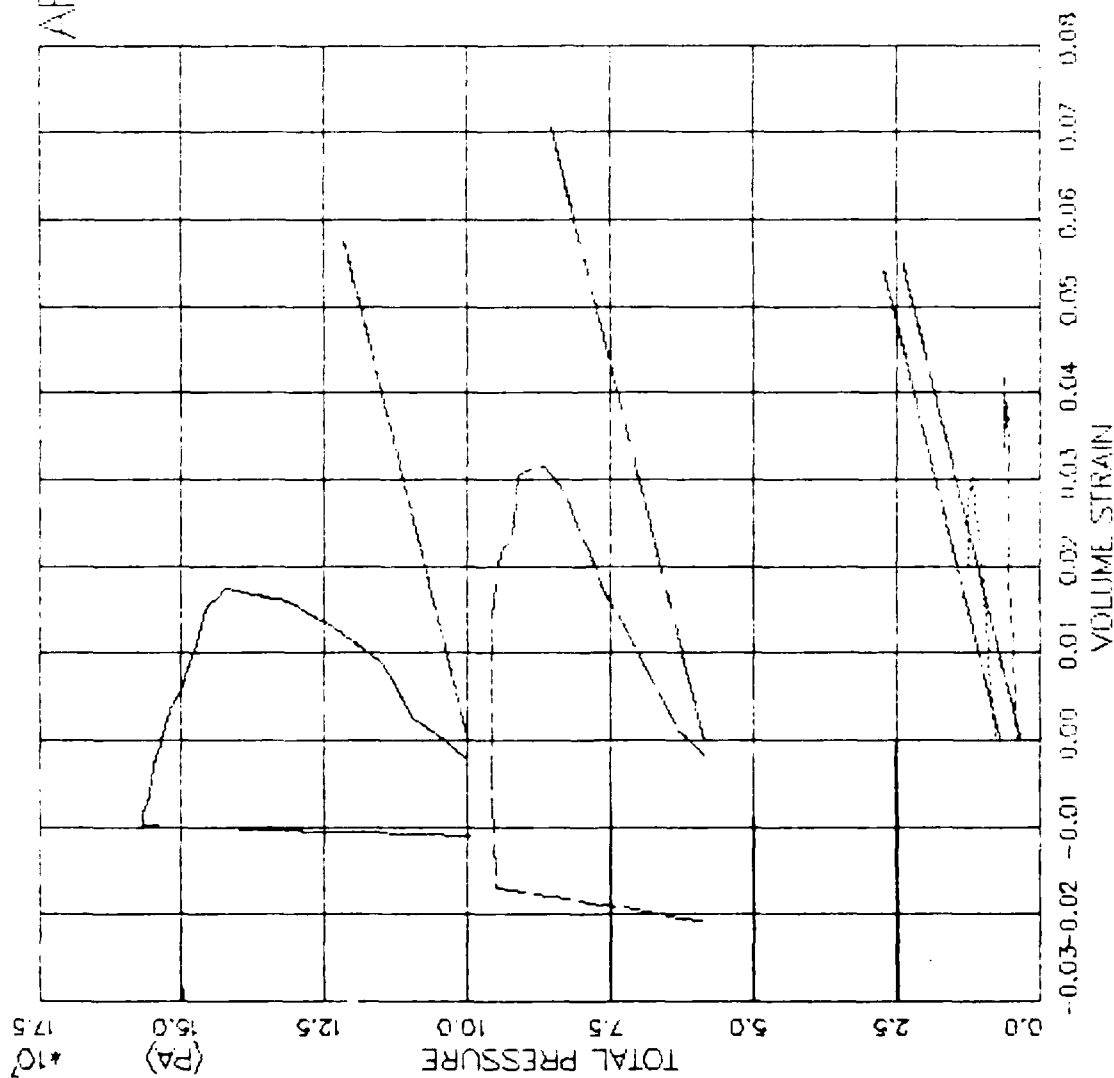
FIGURE V.1.5 ELASTIC MODEL EXERCISE – TRIAXIAL COMP(CTC) – PRESSURE VS. VOLUMETRIC STRAI

AFOSR SOIL ELEMENT MODEL

TEST = STANDARD TRIAXIAL TEST
MODEL= ELASTIC
MATL = DRYCARES—REMOLD
DATA = DRYCARESR/WES/84

LEGEND
S3C=1.8E6
TEST DATA
S3C=3.5E5
TEST DATA
S3C=7.1E6
TEST DATA
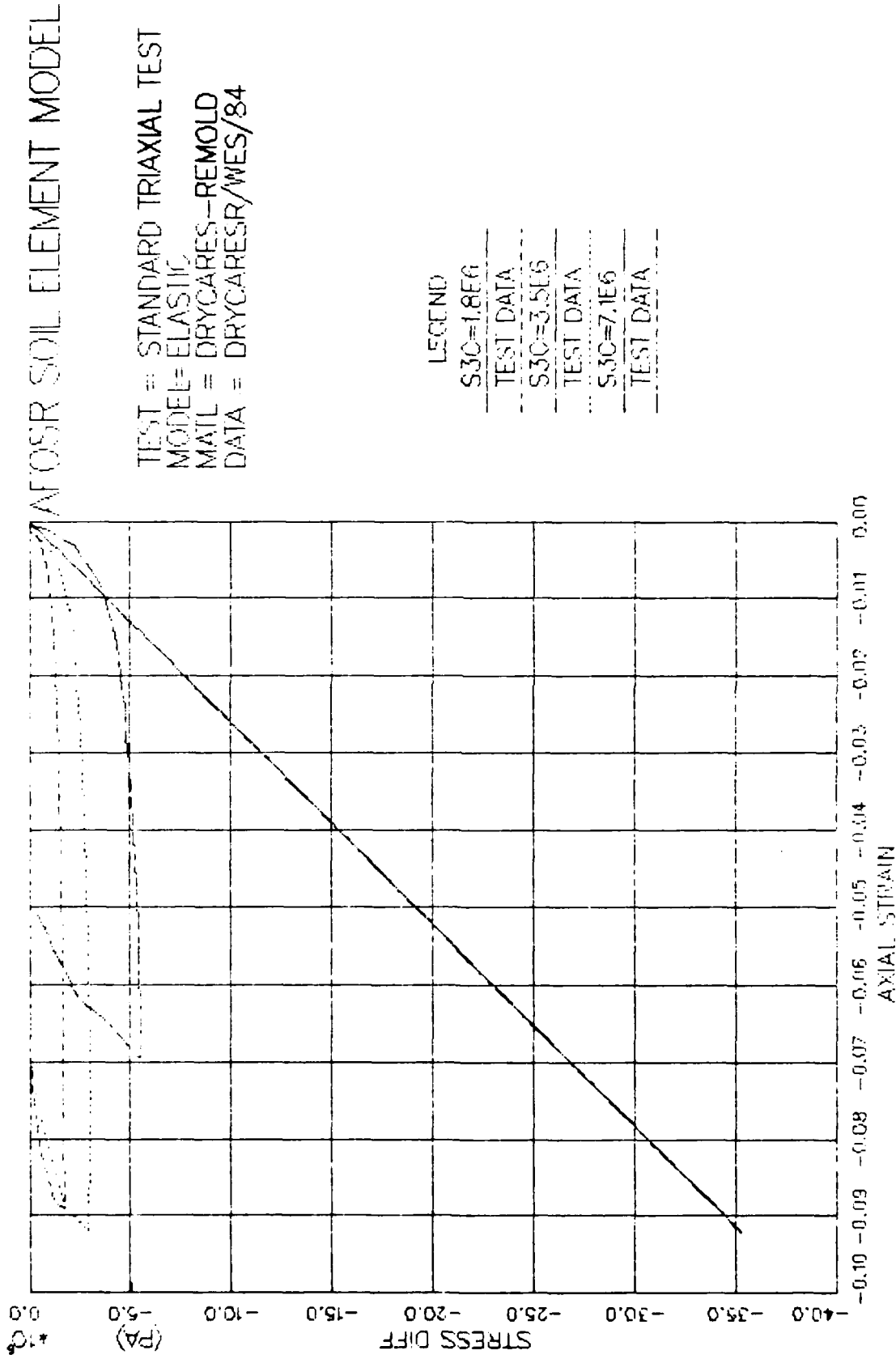
FIGURE V.1.6 ELASTIC MODEL FAILURE—TRIAX EXTENSION(CTE) — STRESS DIFF VS. AXIAL STRAIN

311

FIGURE V.1.7 ELASTIC MODEL EXERCISE—TRIAXIAL EXTEN(CTE) — STRESS DIFF VS. STRAIN DIFF

AFOSR SOIL ELEMENT MODEL

TEST = STANDARD TRIAXIAL
MODEL= ELASTIC
MATL = DRYCARES—REMOLD
DATA = DRYCARESR/WES/84

LEGEND
S3C=1.8E6
S3C=3.5E6
S3C=7.1E6

312
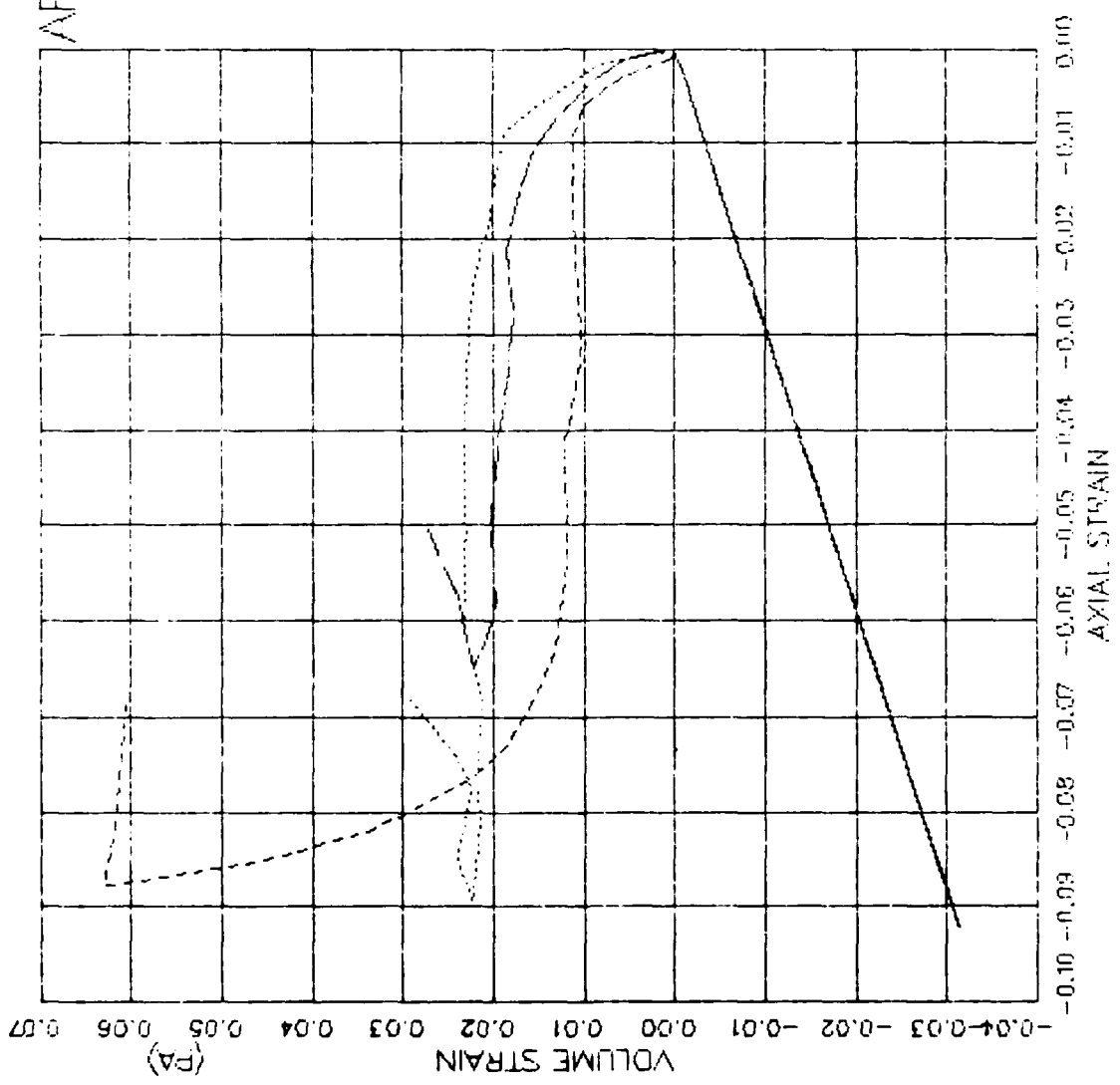
FIGURE V.1.8 ELASTIC MODEL EXERCISE— TRIAX EXTEN(CII) — AXIAL STRAIN VS VOLUME STRAIN

AFOSR SOIL ELEMENT MODEL

TEST = STANDARD TRIAXIAL TEST
MODEL= ELASTIC
MATL = DRYCARES—REMOLD
DATA = DRYCARESR/WES/84

LEGEND
S3C=1.8E6
        TEST DATA
S3C=3.5E6
        TEST DATA
S3C=7.1E6
        TEST DATA

313

AFOSR SOIL ELEMENT MODEL

TEST = STANDARD TRIAXIAL
MODEL = ELASTIC
MATL = DRYCARES-REMOLD
DATA = DRYCARESR/WES/84

LEGEND
S3C=1.8E6
S3C=3.5E6
S3C=7.1E6
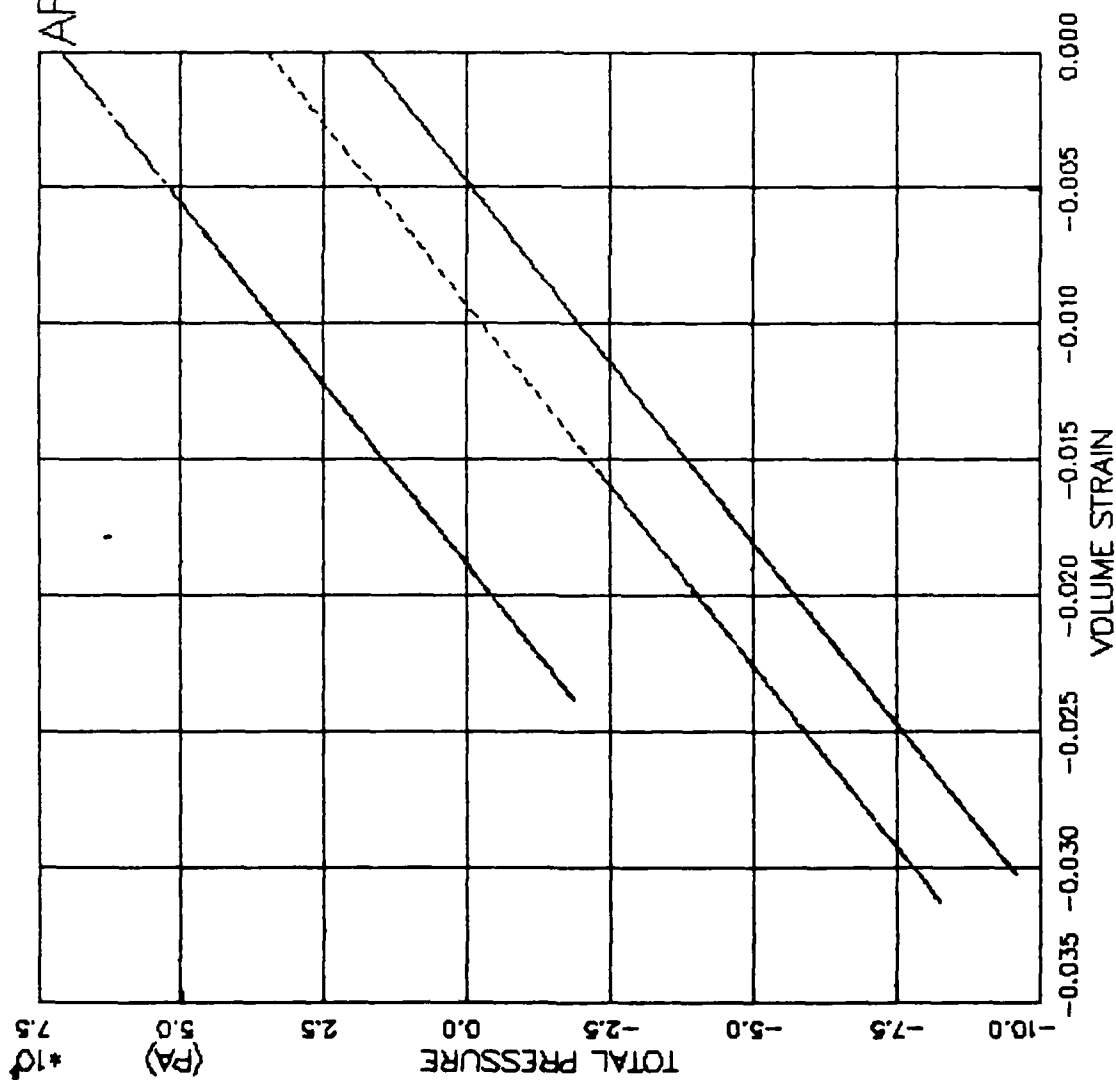
FIGURE V.1.9. ELASTIC MODEL EXERCISE–TRIAXIAL EXTEN(CTE) – PRESSURE VS. VOLUMETRIC STRAIN

314

AFOSR SOIL ELEMENT MODEL

TEST = STANDARD TRIAXIAL TEST
MODEL= ELASTIC
MATL = DRYCARES—REMOLD

LEGEND
RTC/S3C=1.8E6
RTC/S3C=1.8E6
RTC/S3C=3.5E6
RTC/S3C=3.5E6
RTC/S3C=7.1E6
RTC/S3C=7.1E6
RTE/S3C=1.8E6
RTE/S3C=1.8E6
RTE/S3C=3.5E6
RTE/S3C=3.5E6
RTE/S3C=7.1E6
RTE/S3C=7.1E6
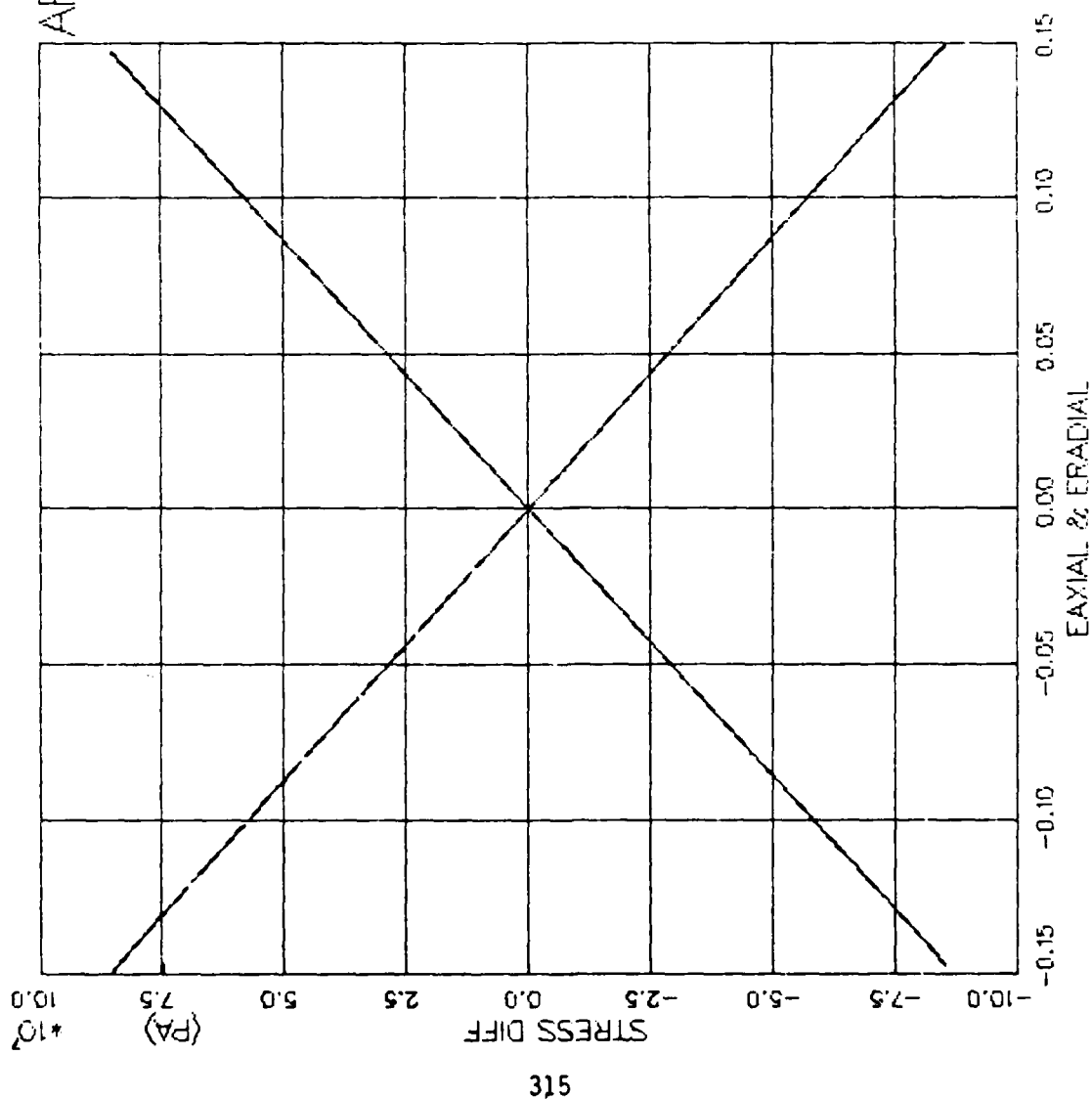
FIGURE V.1.10 ELASTIC MODEL EXER—REDUCED TX(RTC+RTE) — STRESS DIFF VS STRAIN

315

AFOSR SOIL ELEMENT MODEL

TEST = STANDARD TRIAXIAL TEST
MODEL= ELASTIC
MATL = DRYCARES—REMOLD

LEGEND
RTC/S3C=1.8E6
RTC/S3C=3.5E6
RTC/S3C=7.1E6
RTE/S3C=1.8E6
RTE/S3C=3.5E6
RTE/S3C=7.1E6
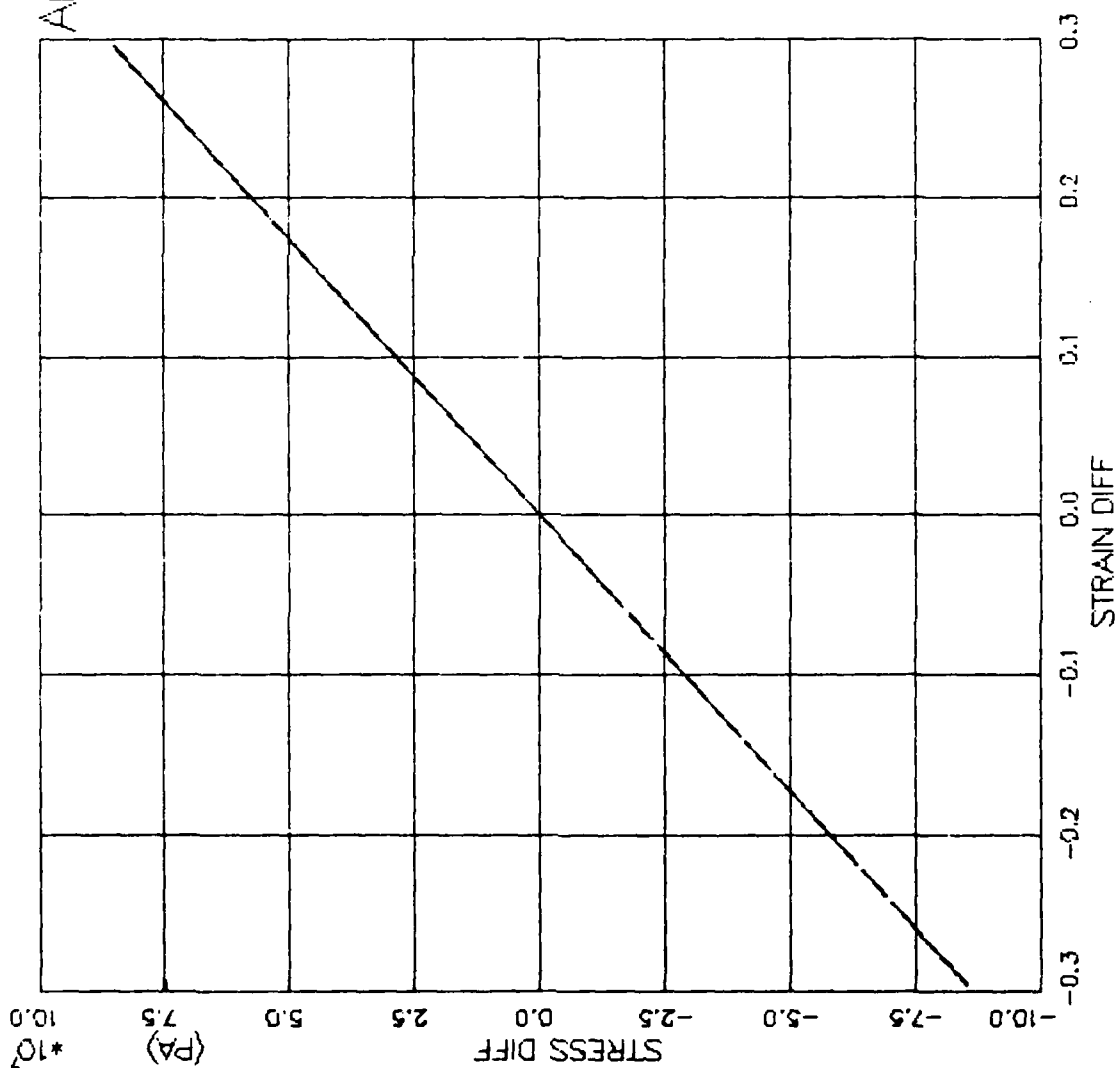
FIGURE V.1.11 ELASTIC MODEL EXER—REDUCED TX(RTC+RTE) — STRESS DIFF VS. STRAIN DIFF

AFOSR SOIL ELEMENT MODEL

TEST = STANDARD TRIAXIAL TEST
MODEL= ELASTIC
MATL = DRYCARES—REMOLD

LEGEND
RTC/S3C=1.8E6
RTC/S3C=3.5E6
RTC/S3C=7.1E6
RTE/S3C=1.8E6
RTE/S3C=3.5E6
RTE/S3C=7.1E6

AXIAL STRAIN
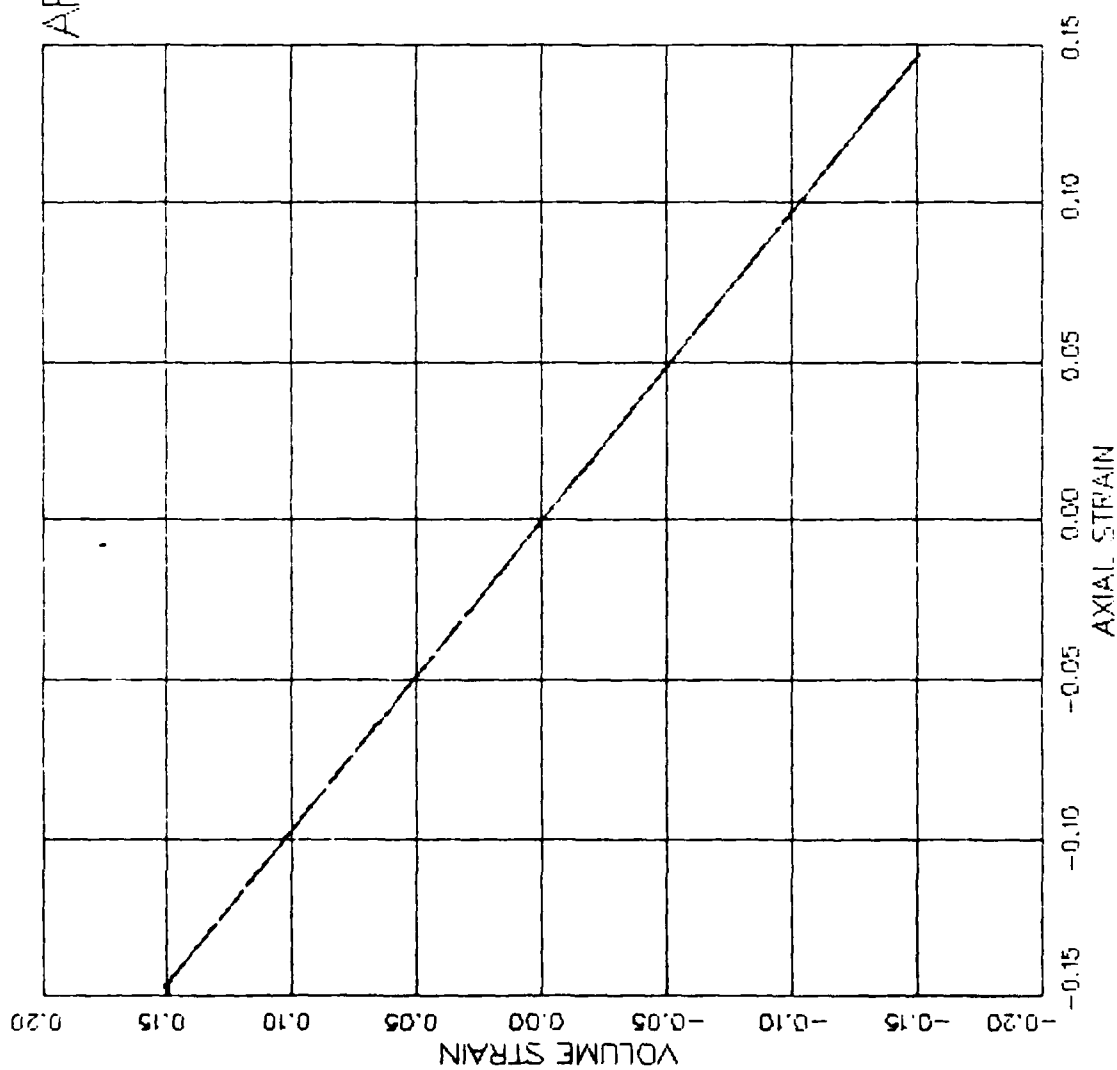
VOLUME STRAIN

FIGURE V.1.12 ELASTIC MODEL EXER—REDUCED TX(RTC+RTE) – AXIAL STRAIN VS VOLUME STRAIN
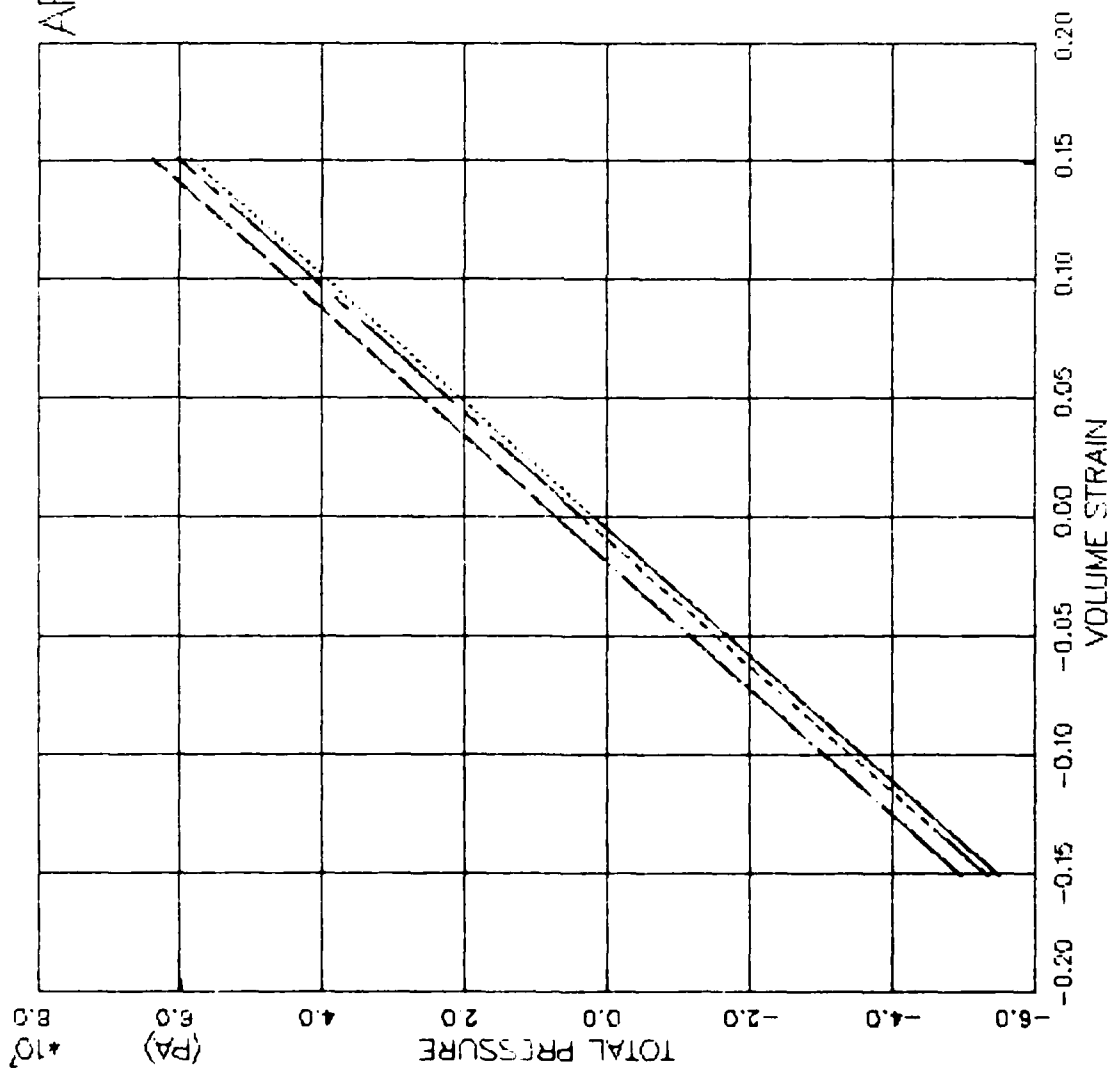
FIGURE V.1.13 ELASTIC MODEL EXER—REDUCED TX(RTC+RTE) — PRESSURE VS. VOLUMETRIC STRAIN

318
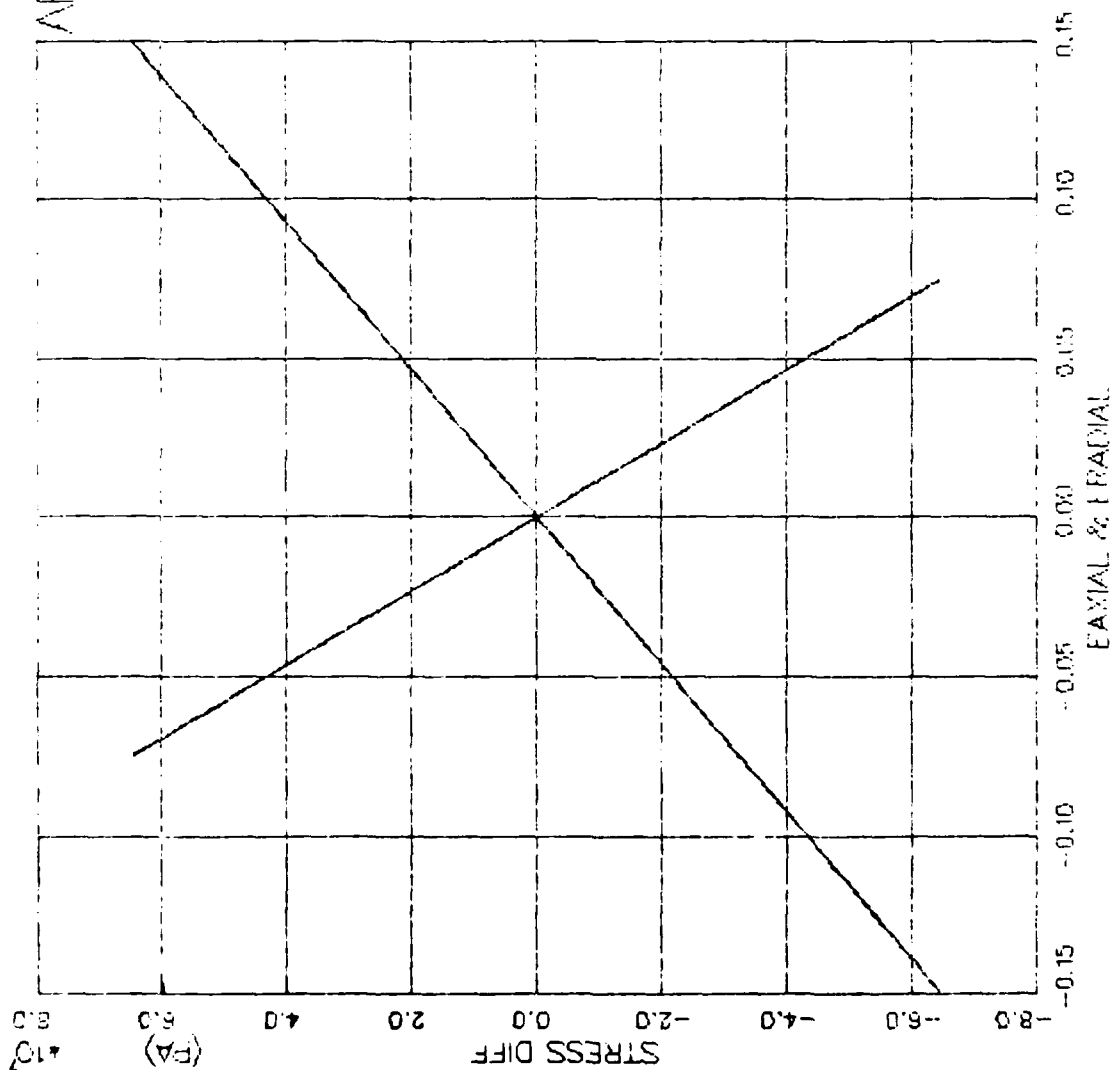
FIGURE V.1.14   ELASTIC MODEL EXERCISE—PURE SHEAR(PSC-PSE) — STRESS DIFF VS. STRAIN
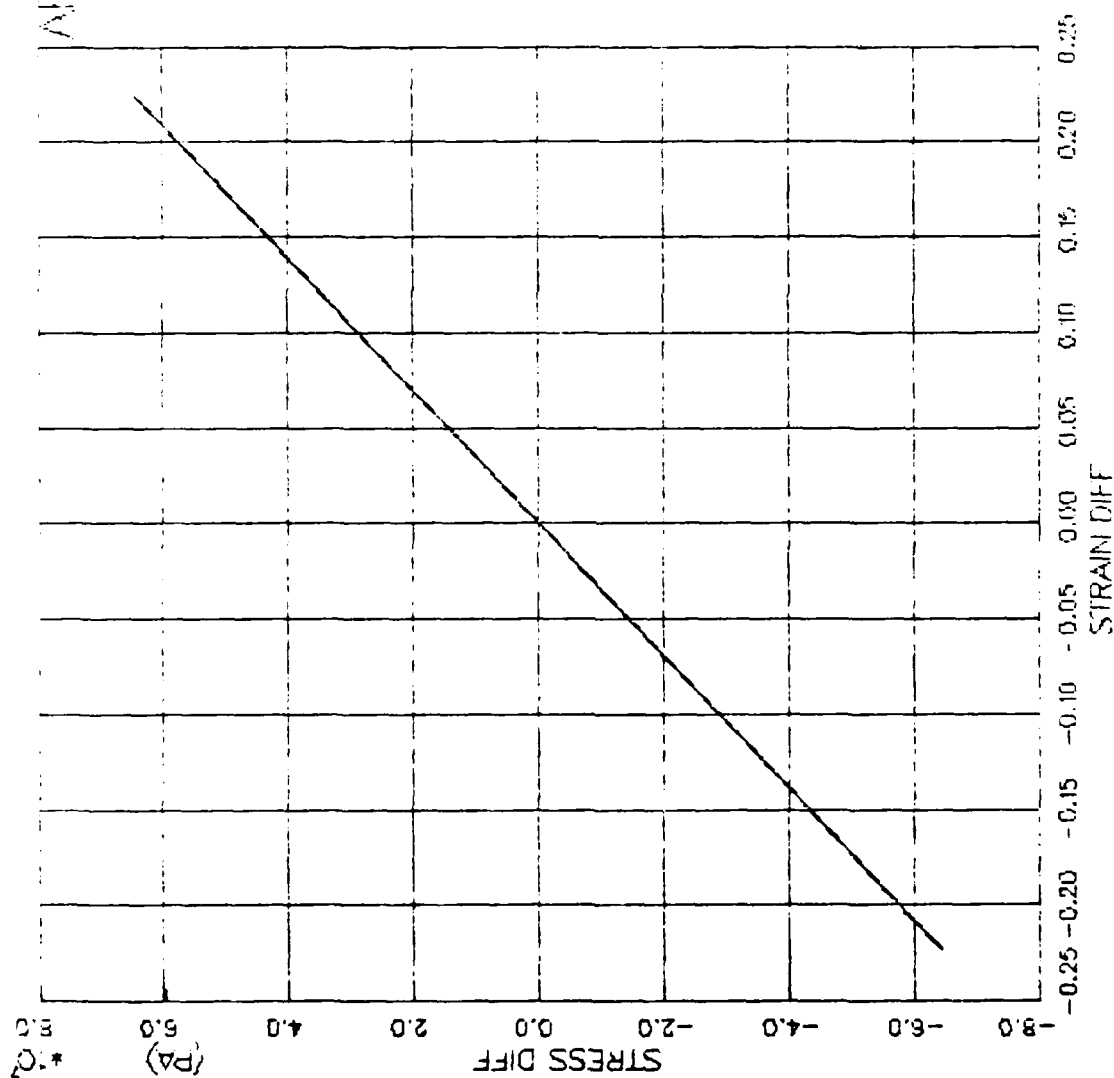
FIGURE V.1.15   ELASTIC MODEL EXERCISE—PURE SHEAR(PSC+PSE) – STRESS DIFF VS. STRAIN DIFF

AFOSR SOIL ELEMENT MODEL

TEST = STANDARD TRIAXIAL
MODEL = ELASTIC
MATL = DRYCARES-REMOLD

LEGEND
ISO EXTEN
RTC
PSC
CTC
ISO COMP
RTE
PSE
CTE

FIGURE V.1.16 ELASTIC MODEL BEHAVIOR SUMMARY (SIGC=7. MPA) — SDIFF/P/EV/EA   ANALYSIS

321
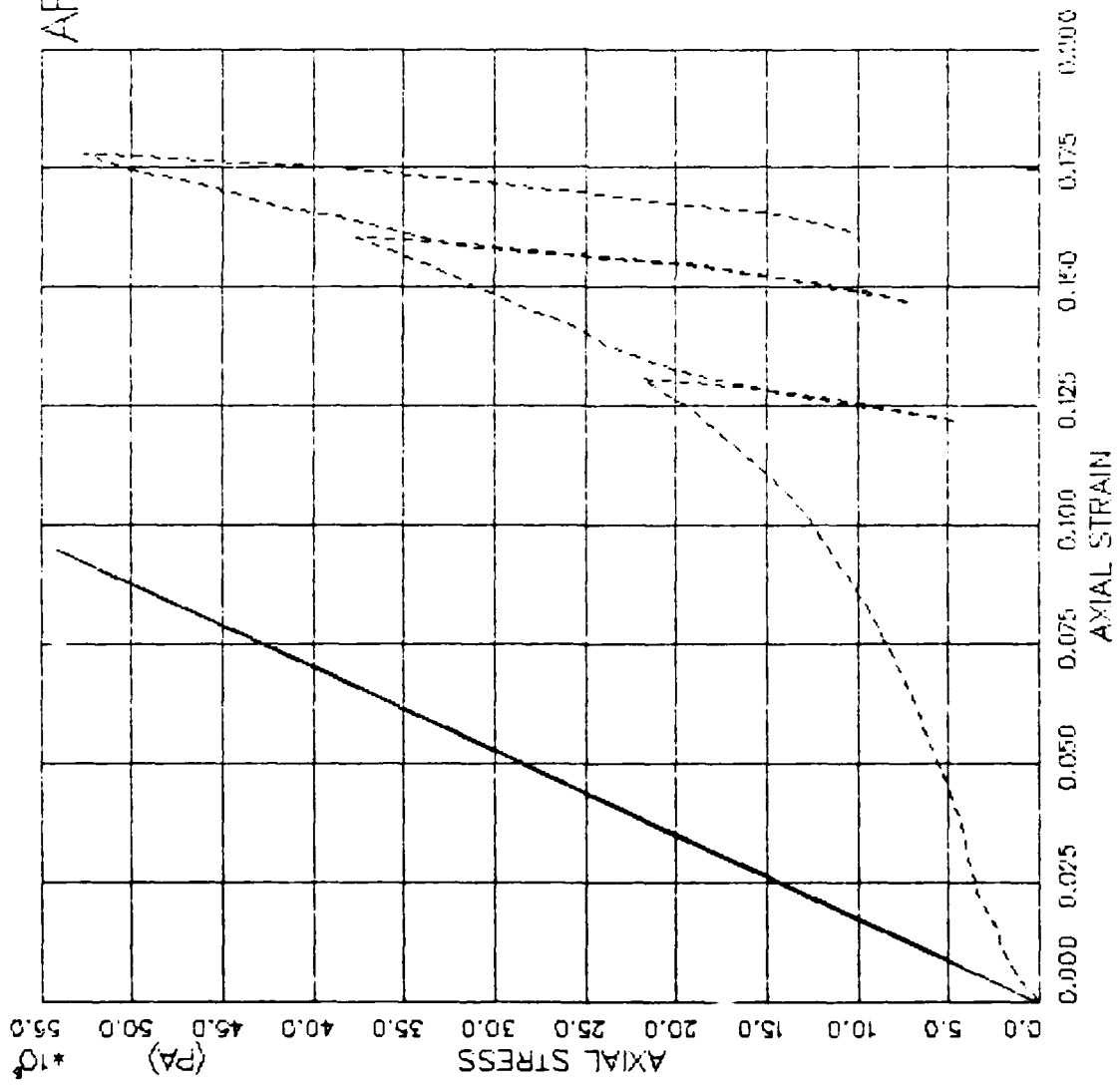
FIGURE V.1.17 ELASTIC MODEL EXERCISE— UNIAX STRAIN(UxC) – TOT AXL STRESS VS. AXL STRAIN .

AFOSR SOIL ELEMENT MODEL

TEST = UNIAXIAL STRAIN TEST
MODEL= ELASTIC
MATL = DRYCARES-REMOLD
DATA = DRYCARESR/WES/84

LEGEND
CALCULATION
TEST DATA
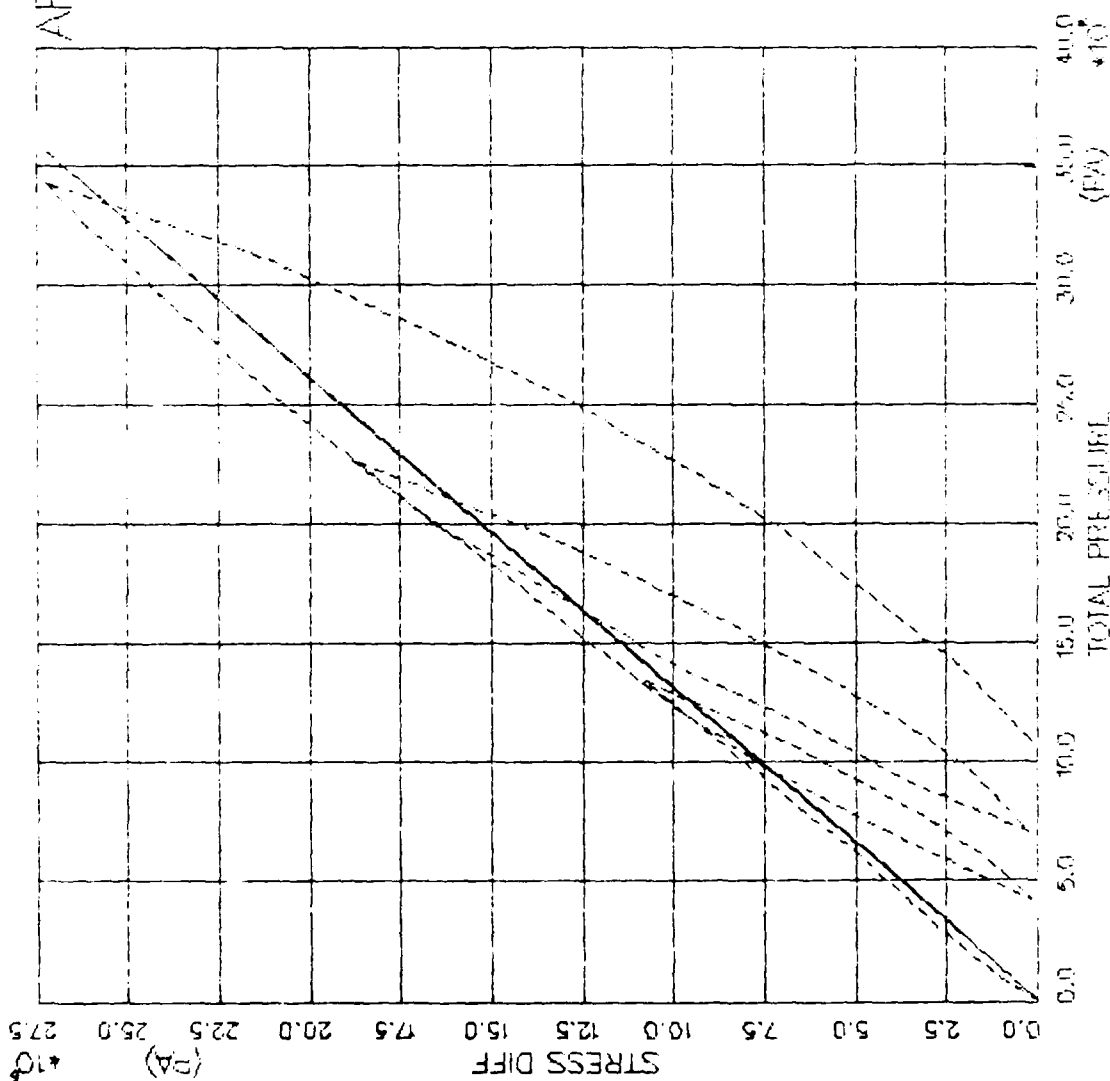
FIGURE V.1.18   ELASTIC MODEL EXERCISE – UNIAX STRAIN(UX) – STRESS DIFFERENCE VS. PRESSURE

323

AFOSR SOIL ELEMENT MODEL

TEST = UNIAXIAL STRAIN TEST
MODEL= ELASTIC
MATL = DRYCAFES-REMOLD
DATA = DRYCAFES.R/WES/84

LEGEND
CALCULATION
TEST DATA
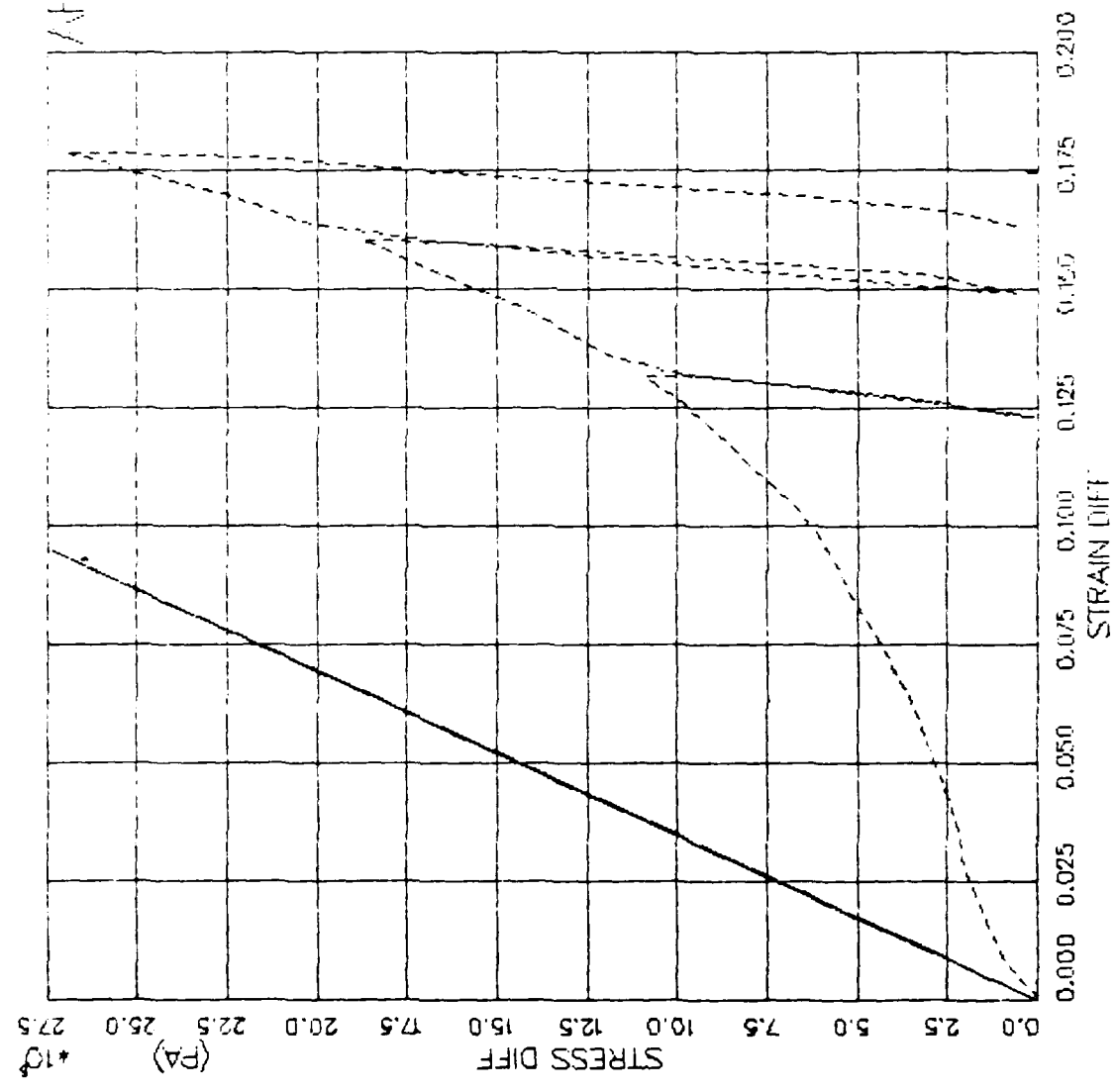
FIGURE V.1.19   ELASTIC MODEL EXERCISE— UNIAX STRAIN(UXC) — STRESS DIFF VS. STRAIN DIFF

324

AFOSR SOIL ELEMENT MODEL

TEST = UNIAXIAL STRAIN TEST
MODEL = ELASTIC
MATL = DRYCARES—REMOLD
DATA = DRYCARESR/WES/84

LEGEND
S3C=4.0E6
TEST DATA
S3C=20.E6
TEST DATA
S3C=32.E6
TEST DATA
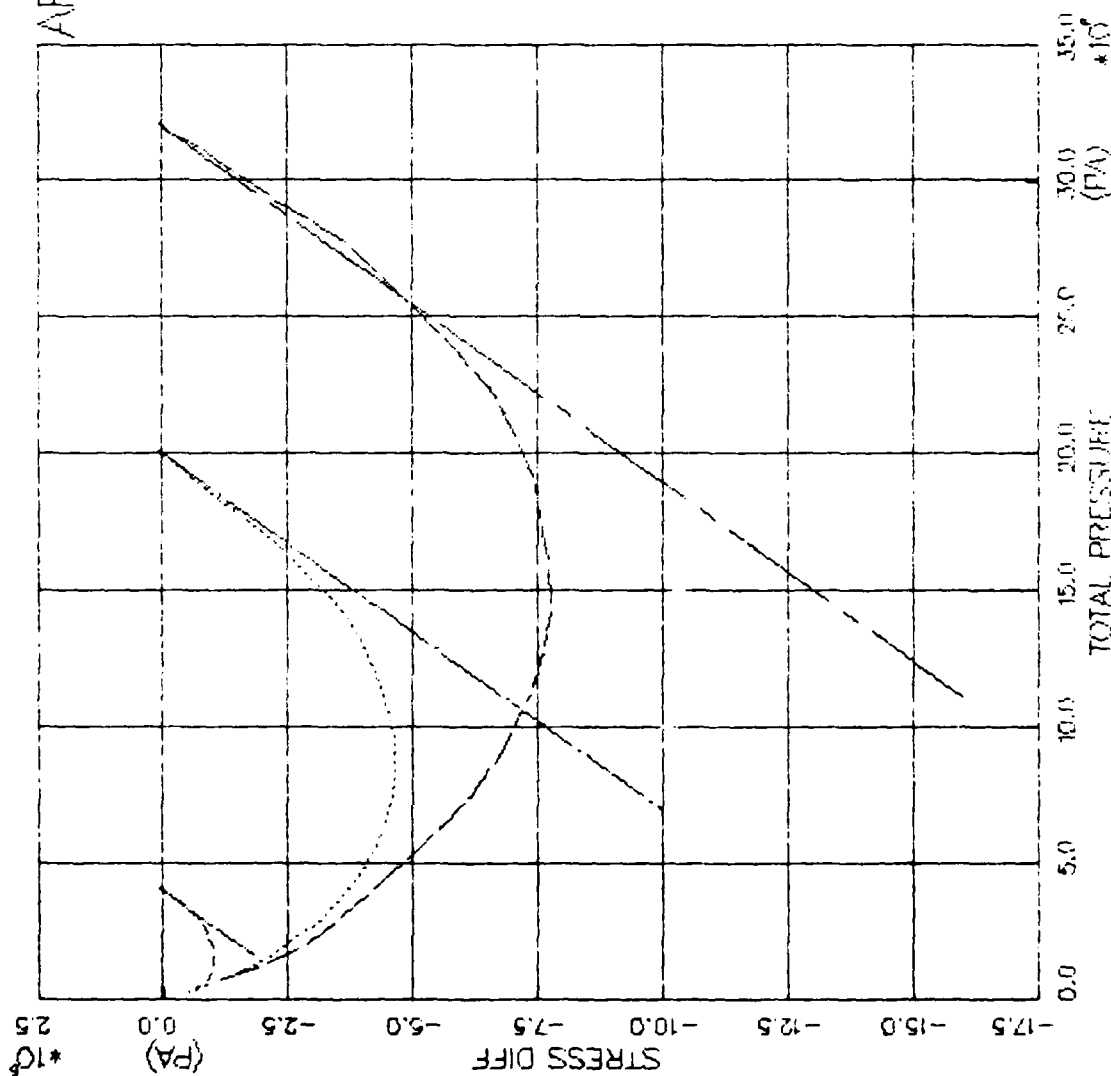
FIGURE V.1.20 ELASTIC MODEL EXERCISE—UNIAX EXTEN(ICK0) — STRESS DIFFERENCE VS. PRESSURE
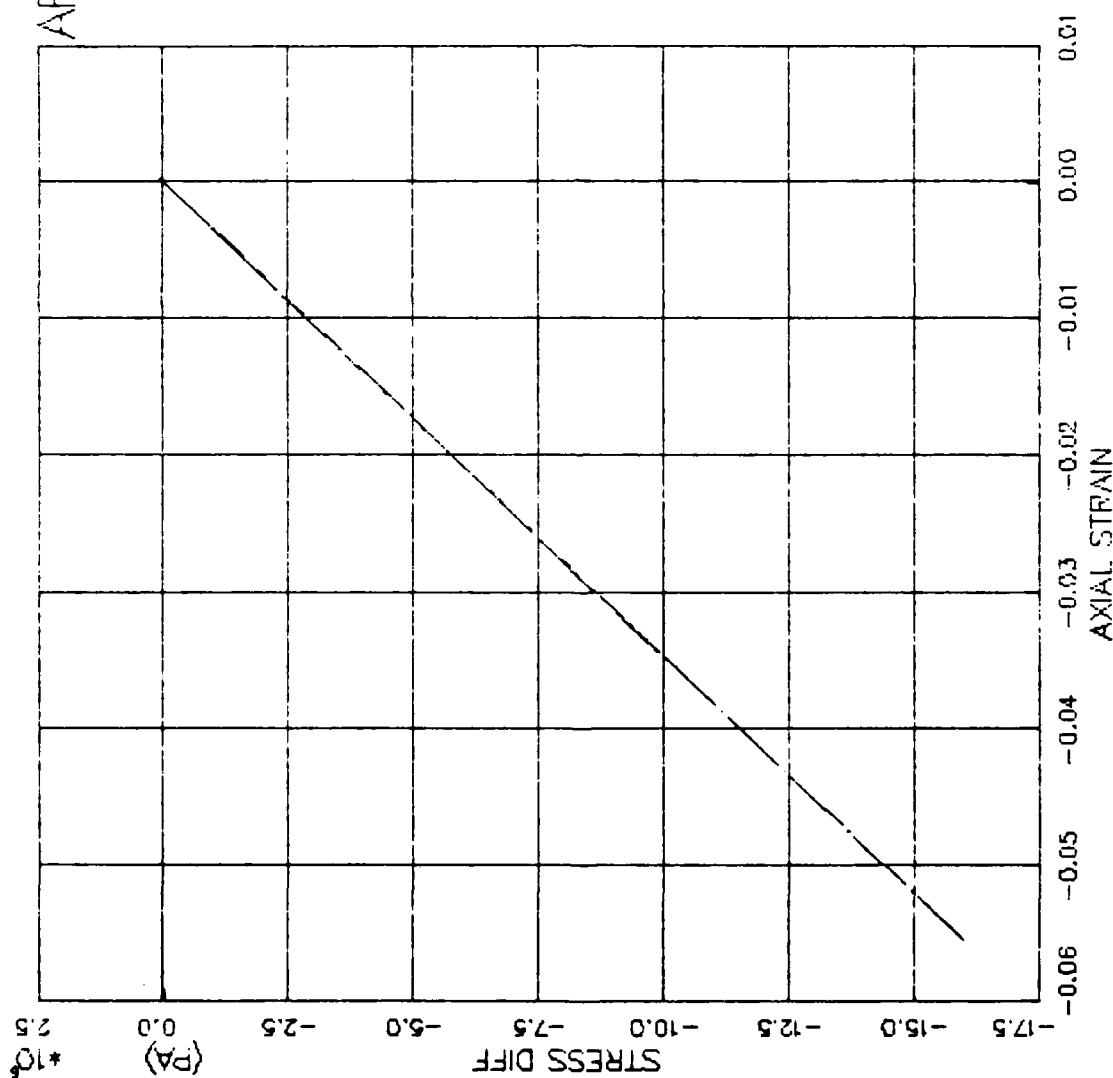
FIGURE V.1.21 ELASTIC MODEL EXERCISE—UNIAX EXTEN(ICK(I) — STRESS DIFF VS. AXIAL STRAIN

MOSER SOIL ELEMENT MODEL

TEST = STRAIN PATH
MODEL=ELASTIC
MATL = DRYCARES--REMOLD
DATA = DRYCARESR/WES/3A

LEGEND
WES PATH 3A
TEST DATA
WES PATH 3C
TEST DATA
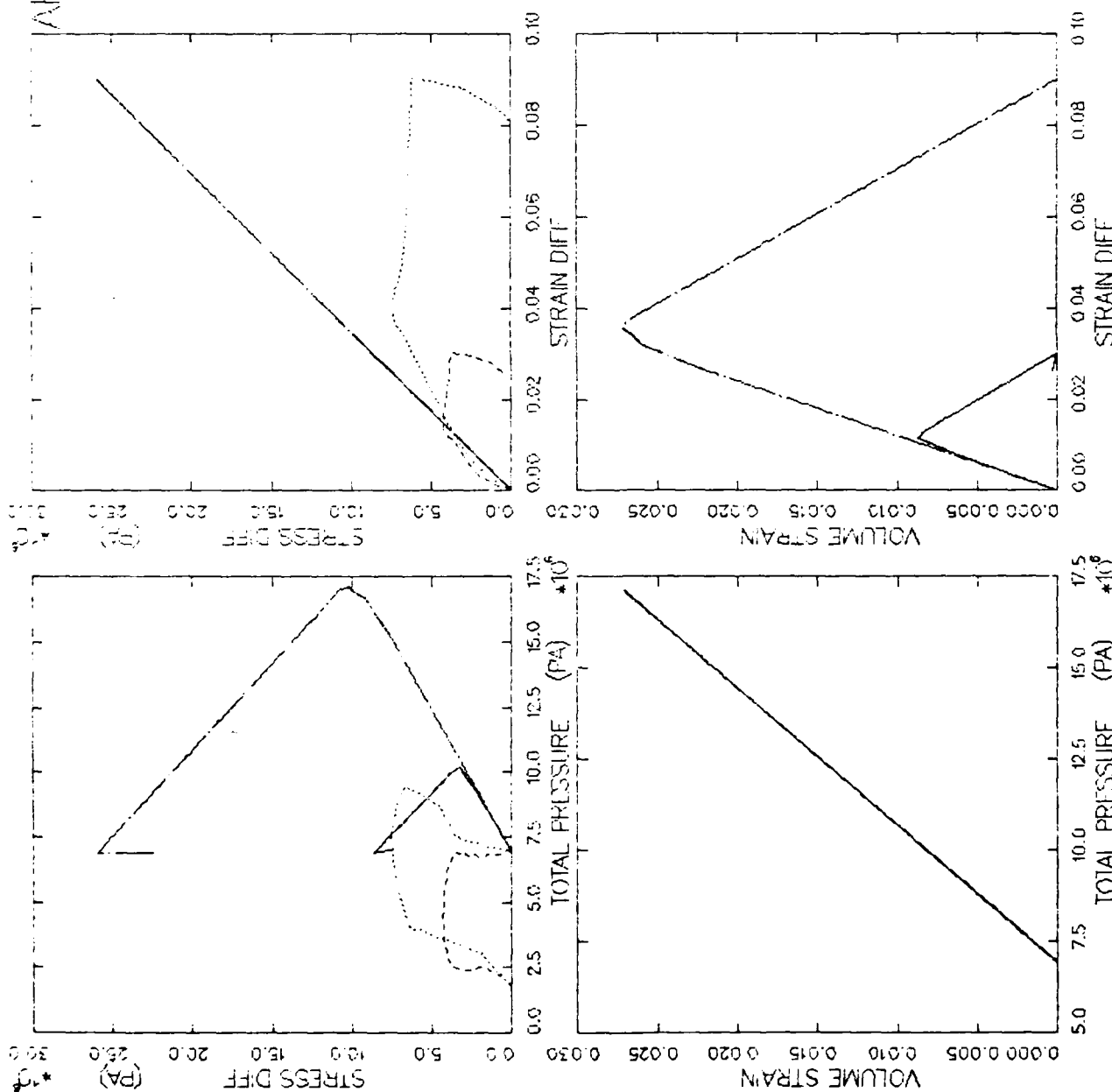
FIGURE V.1.22 ELASTIC MODEL EXLR-AXISYM LPATH3A+3C -- SDIFF/P/EV/EDIFF ANALYSIS
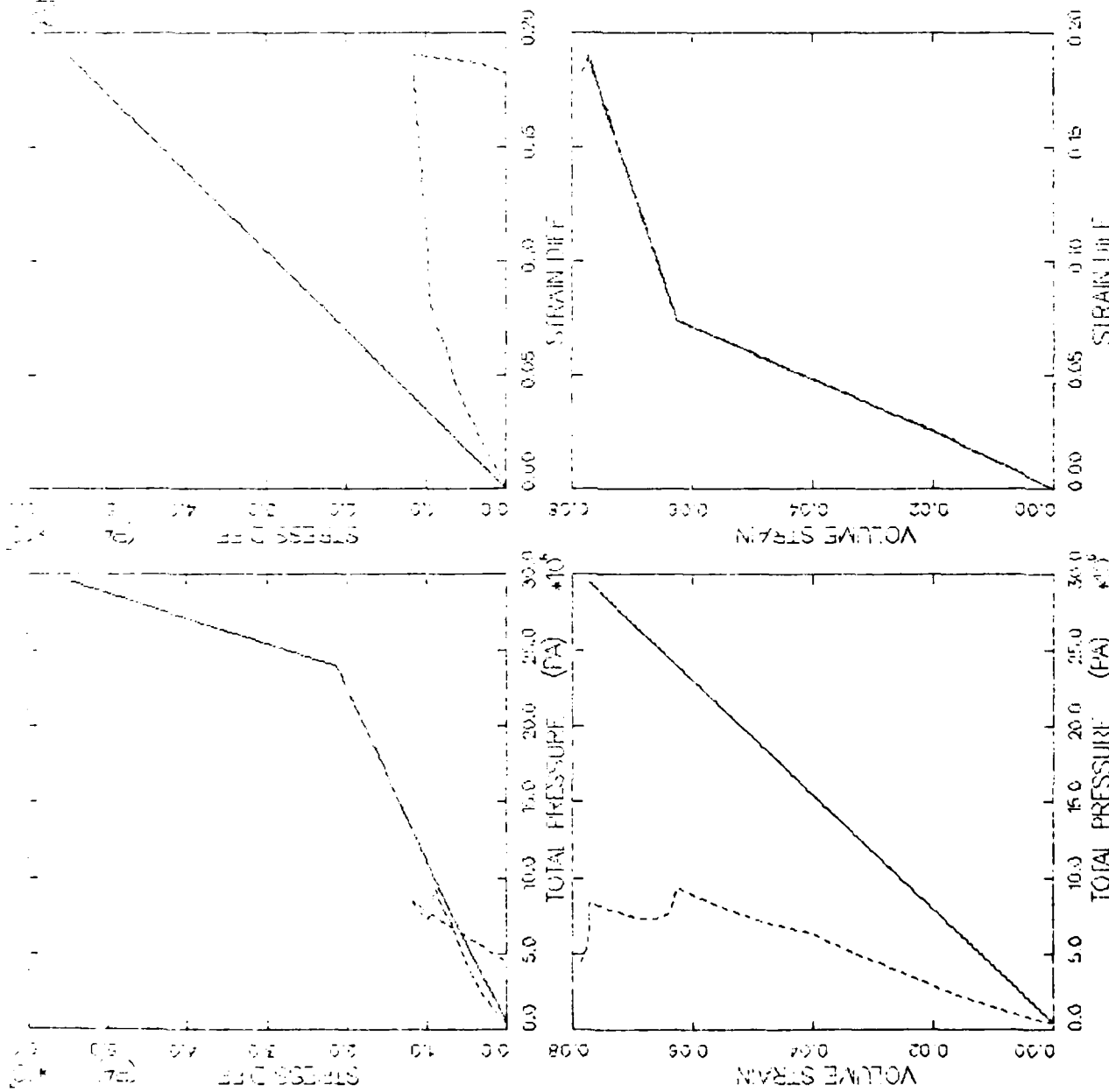
FIGURE V.1.23 ELASTIC MODEL EXE <-LADE FPATHI -- SUHI/P/LV/LDHT ANALYSIS
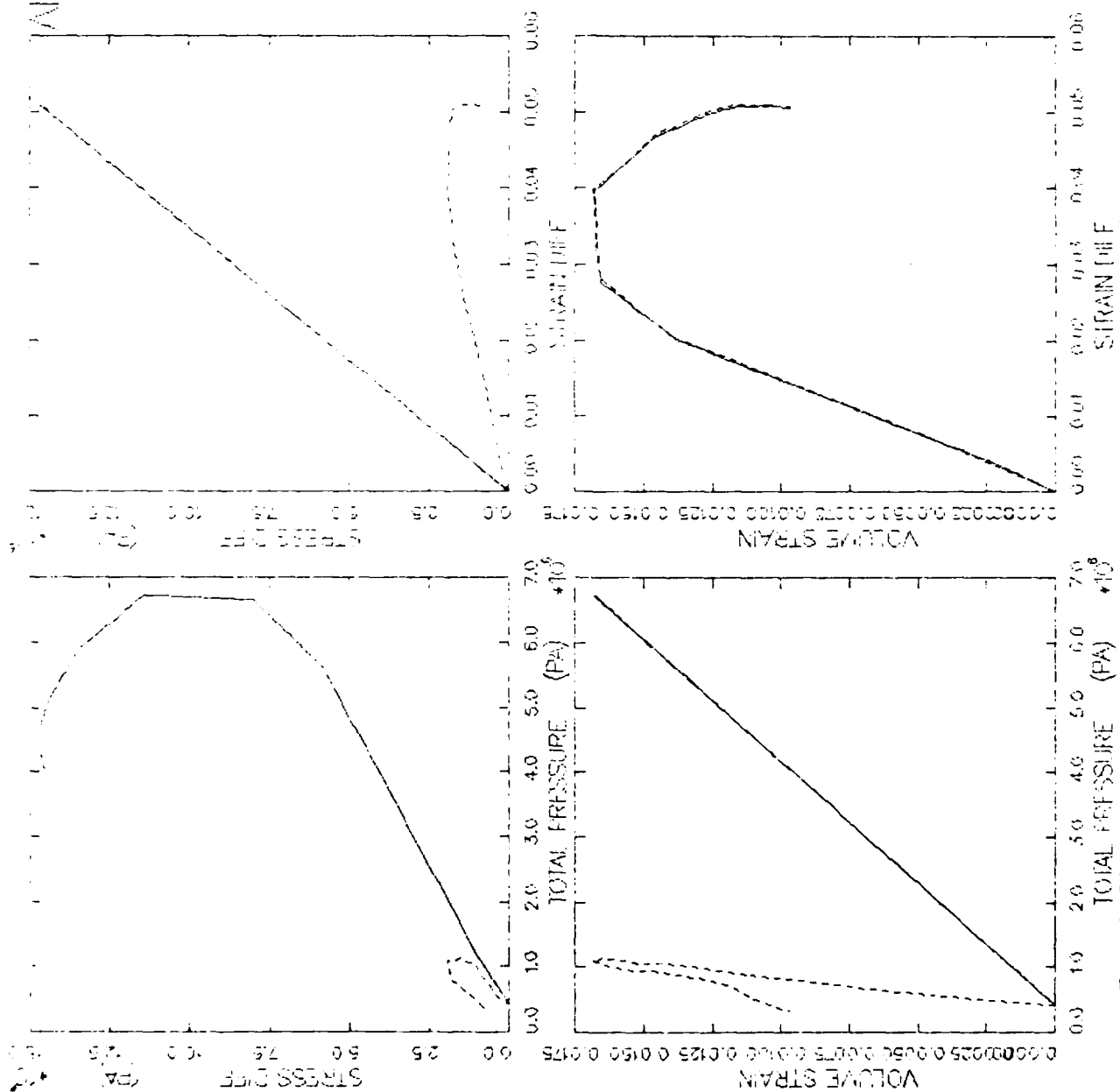
FIGURE V.1.24 ELASTIC MODEL EXERCISE LABORATORY — SOIL AMAVALIDITY ANALYSIS

AFOSR SOIL ELEMENT MODEL

TEST = STRAIN PATH
MODEL = ELASTIC
MATL = DRYCARES—REMOLD
DATA = NELLISB/KO/JAN83

LEGEND
CALCULATION
TEST DATA
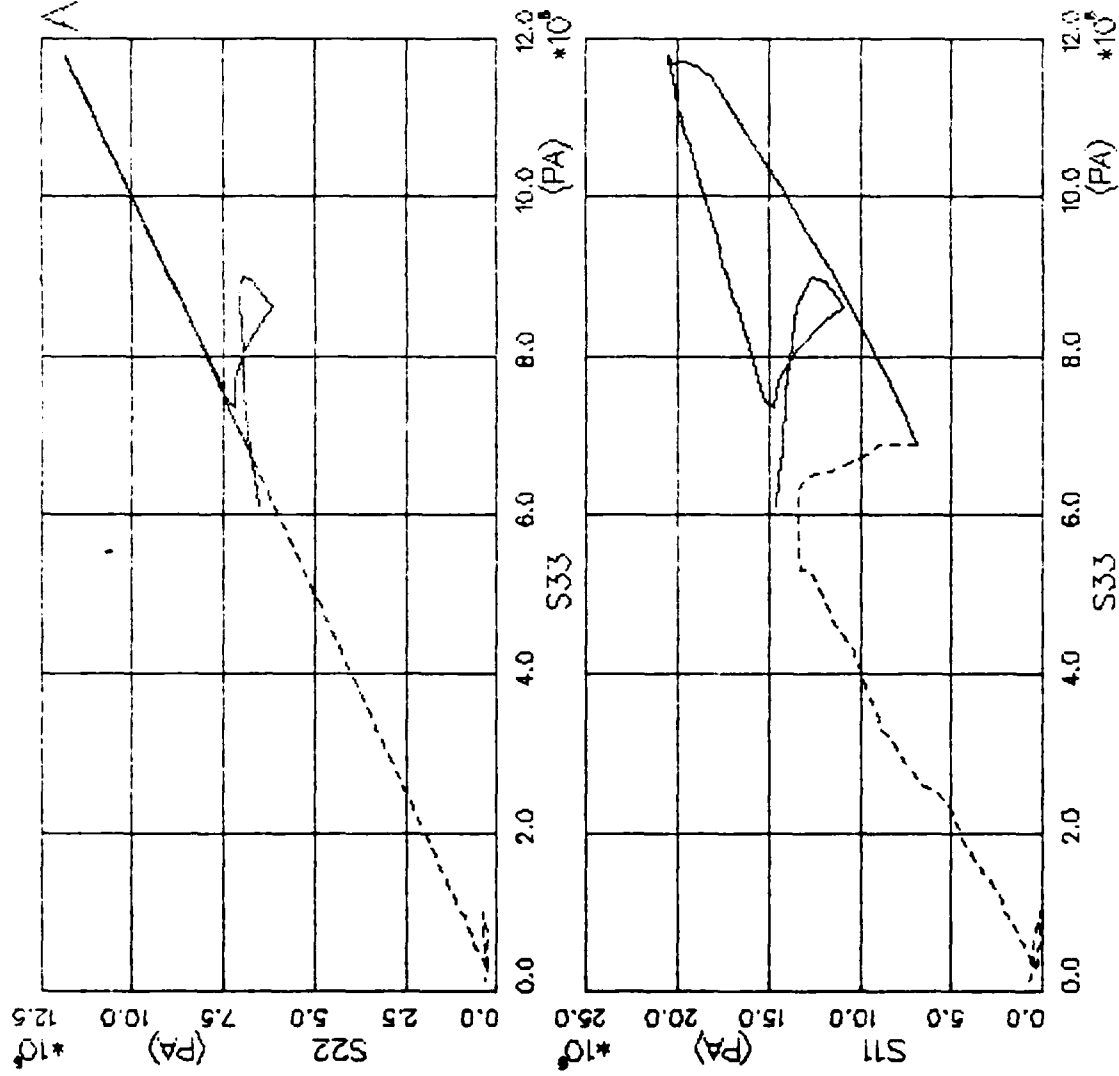
FIGURE V.1.25 ELASTIC MODEL EXERCISE—TRUE TRIAX — PRINCIPAL STRESS PATH
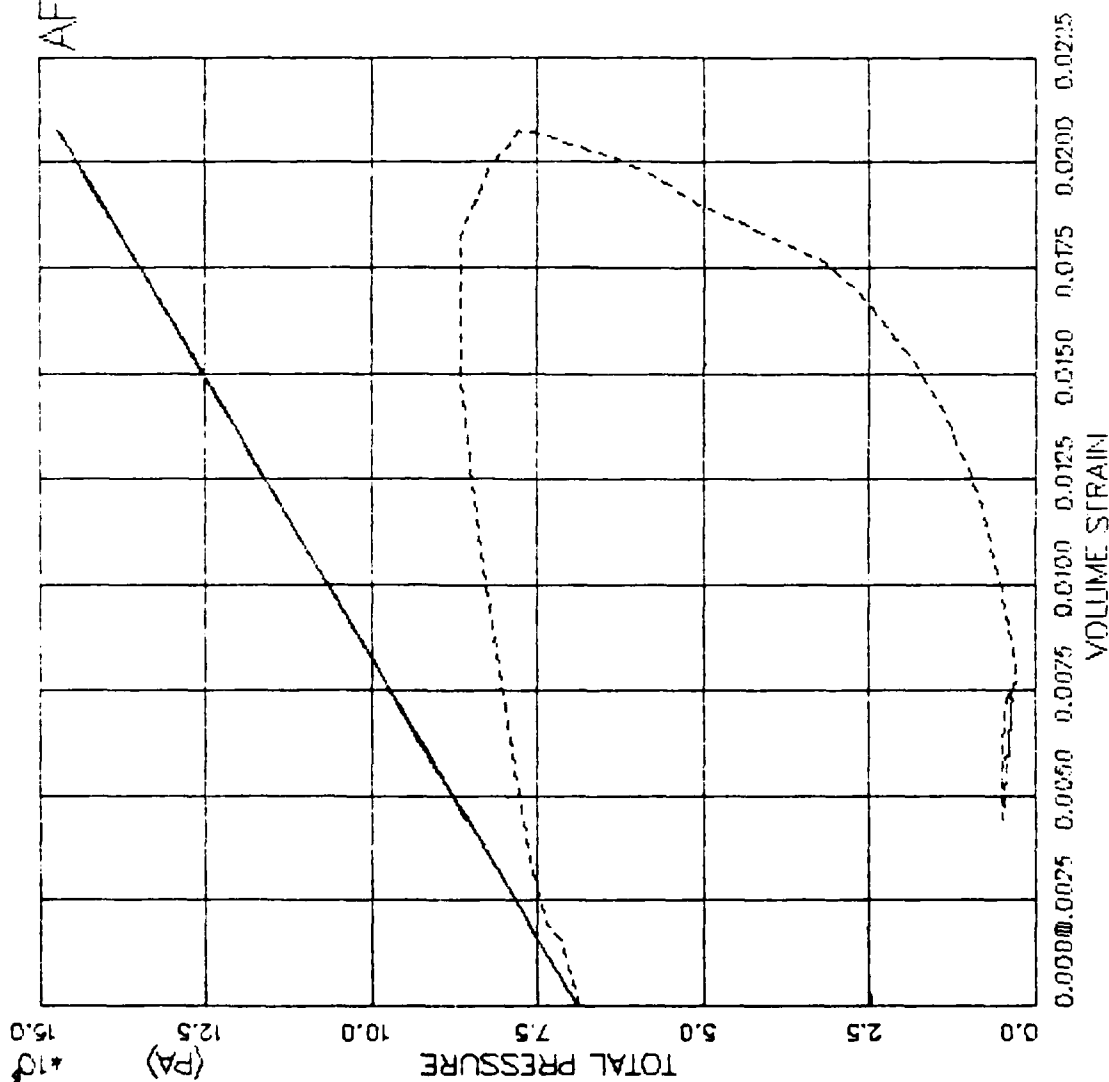
FIGURE V.1.26 ELASTIC MODEL EXERCISE—TRUE TRIAX -- PRESSURE VS. VOLUMETRIC STRAIN .

V.2 Linear Viscoelastic

V.2.1 Motivation

The principal advantages of a linear viscoelastic constitutive model for transient soil dynamics problems are the availability of or possibility of obtaining closed form solutions, the existence of proven, stable numerical solution techniques for use when a closed form solution does not exist and is too difficult to obtain, and the ability of the model to dissipate energy. The principal disadvantage is that the stress-strain behavior of real soil often departs significantly from linear viscoelasticity.

V.2.2 Assumptions

The classic theory of linear viscoelasticity assumes a material to be homogeneous and isotropic. The stresses and stress time derivatives at a point are assumed to depend only on the strains and strain time derivatives at that point, through a system of linear differential equations.

V.2.3 Basic Equations

The system of linear differential equations relating stress, strain and their time derivatives at a point yields a set of hereditary stress-strain relations of the same general form as Equation (V.1.1).

$$
\begin{Bmatrix} \sigma_1 \\ \sigma_2 \\ \sigma_3 \\ \sigma_4 \\ \sigma_5 \\ \sigma_6 \end{Bmatrix} = M \begin{bmatrix} 1 & K_0 & K_0 & 0 & 0 & 0 \\ K_0 & 1 & K_0 & 0 & 0 & 0 \\ K_0 & K_0 & 1 & 0 & 0 & 0 \\ 0 & 0 & 0 & 1-K_0 & 0 & 0 \\ 0 & 0 & 0 & 0 & 1-K_0 & 0 \\ 0 & 0 & 0 & 0 & 0 & 1-K_0 \end{bmatrix} * \begin{Bmatrix} d\varepsilon_1 \\ d\varepsilon_2 \\ d\varepsilon_3 \\ d\varepsilon_4 \\ d\varepsilon_5 \\ d\varepsilon_6 \end{Bmatrix} \qquad (V.2.1)
$$

except that the quantities M and K_0 are influence functions of time, rather than constants, and the notation x*dy indicates a superposition integral [Fung (1965:414)] of the form

$$x*dy = \int_0^t x(t-\tau) \frac{dy}{d\tau} d\tau \qquad (V.2.2)$$

V.2.4 Parameter Determination

There are a number of methods for measuring the parameters which define the viscoelastic influence functions $M(t)$ and $K_0(t)$ in Equation (V.2.1). The constrained modulus influence function, $M(t)$, can be measured directly in the laboratory by a constrained compression (oedometer) relaxation test, in which all strains in Equation (V.2.1) are zero except ϵ_1, and ϵ_1 is a step function. Similarly, the bulk modulus influence function,

$$B(t) = M(t) \left[\frac{1 + 2K_0(t)}{3} \right] \qquad (V.2.3)$$

can be measured directly in the laboratory by a hydrostatic compression relaxation test, in which the volumetric strain is a step function. It is often assumed that the bulk modulus influence function, $B(t)$, and the shear modulus influence function

$$G(t) = \frac{3[M(t) - B(t)]}{4} \qquad (V.2.4)$$

can be represented by simple viscoelastic models, such as the three element model discussed in Appendix L. The model parameters defining $B(t)$ and $G(t)$ can be determined from Figure (L.2) and Equations (L.30), (L.31) and (L.32). The influence function $M(t)K_0(t)$ can then be assembled using the expression

$$M(t)K_0(t) = \frac{3B(t) - M(t)}{2} \qquad (V.2.5)$$

333

Table (V.2.1) lists the parameters used for demonstrating the three-element viscoelastic model discussed in Appendix L. The parameters were chosen to show a range of behavior when the applied constant strain rate varied between 100/sec and 0.1/sec. Both static and dynamic uniaxial strain tests were actually performed on CARES-DRY sand and reported in Cargile (1984). The static tests were run at strain rates on the order of 0.001/sec. The dynamic tests were run at strain rates in the range of 20-85/sec. Some loading-rate effect (stiffening) was observed below 80 MPa [Cargile (1984:37)].

V.2.5 Computed Behavior

Only the uniaxial strain compression test will be shown for this model. Since the response would be linear and elastic but for the time-dependent and energy damping dashpot, this test will suffice to illustrate the effect of loading rate. Uniaxial strain load-unload cycles were applied at four constant strain rates: 100, 10, 1 and 0.1 per second. Figure (V.2.1) shows the axial stress-strain response for each strain rate. Note the stiffening effect with increasing rate of load application and the non-linear response, both a result of the dashpot elements. Response of the bulk element is shown in Figure (V.2.2) and the shear element response is shown in Figure (V.2.3). At very high strain rates, the element stiffnesses collapse to the stand-alone spring stiffnesses, K_1. At near-static strain rates, the net stiffness is that of two springs in series:

$$K_{long-term} = \frac{K_1 K_2}{K_1 + K_2} \qquad (V.2.6)$$

At intermediate strain rates, there is a gradual transition between the two cases.

The slope of the uniaxial stress path,

$$S = \frac{3(\Delta\sigma_1 - \Delta\sigma_3)}{\Delta\sigma_1 + 2\Delta\sigma_3} \tag{V.2.7}$$

can be expressed in terms of K_0 as follows:

$$S = \frac{3(1 - K_0)}{1 + 2K_0} \tag{V.2.8}$$

so that

$$K_0 = \frac{3 - S}{2S + 3} \tag{V.2.9}$$

The calculated uniaxial stress paths are shown in Figure (V.2.4). Here, K_0 is seen to vary between the value at high strain rates,

$$K_{0,1} = \frac{3K_1 - 2G_1}{3K_1 + 4G_1} \tag{V.2.10a}$$

$$K_{0,1} = \frac{3(480) - 2(360)}{3(480) + 4(360)} = 0.25 \qquad (S = 1.5) \tag{V.2.10b}$$

and the static value,

$$K_{0,2} = \frac{3\,\dfrac{K_1K_2}{K_1 + K_2} - 2\,\dfrac{G_1G_2}{G_1 + G_2}}{3\,\dfrac{K_1K_2}{K_1 + K_2} + 4\,\dfrac{G_1G_2}{G_1 + G_2}} \tag{V.2.11a}$$

$$K_{0,2} = \frac{3(185) - 2(86)}{3(185) + 4(86)} = 0.43 \qquad (S = .92) \tag{V.2.11b}$$

TABLE V.2.1.   VISCOELASTIC MODEL PARAMETERS FOR CARES-DRY SAND

Parameter	Symbol	Variable	Value	Units
Bulk Spring 1 Stiffness	K_1	BULK1	480×10^6	Pa
Bulk Spring 2 Stiffness	K_2	BULK2	300×10^6	Pa
Bulk Dashpot Constant	η_2	C2	10×10^6	Pa-s
Shear Spring 1 Stiffness	G_1	SHEAR1	360×10^6	Pa
Shear Spring 2 Stiffness	G_2	SHEAR2	114×10^6	Pa
Shear Dashpot Constant	η_{s2}	CS2	10×10^6	Pa-s
Mass Density	ρ	RHOREF	1900	kg/m^3

AFOSR SOIL ELEMENT MODEL

TEST = UNIAXIAL STRAIN
MODEL= VISCO
MATL = DRYCARES—REMOLD
DATA = DRYCARESR/WES/84

LEGEND
STRAIN—RATE=100
STRAIN—RATE=10
STRAIN—RATE=1.0
STRAIN—RATE=0.1
TEST DATA
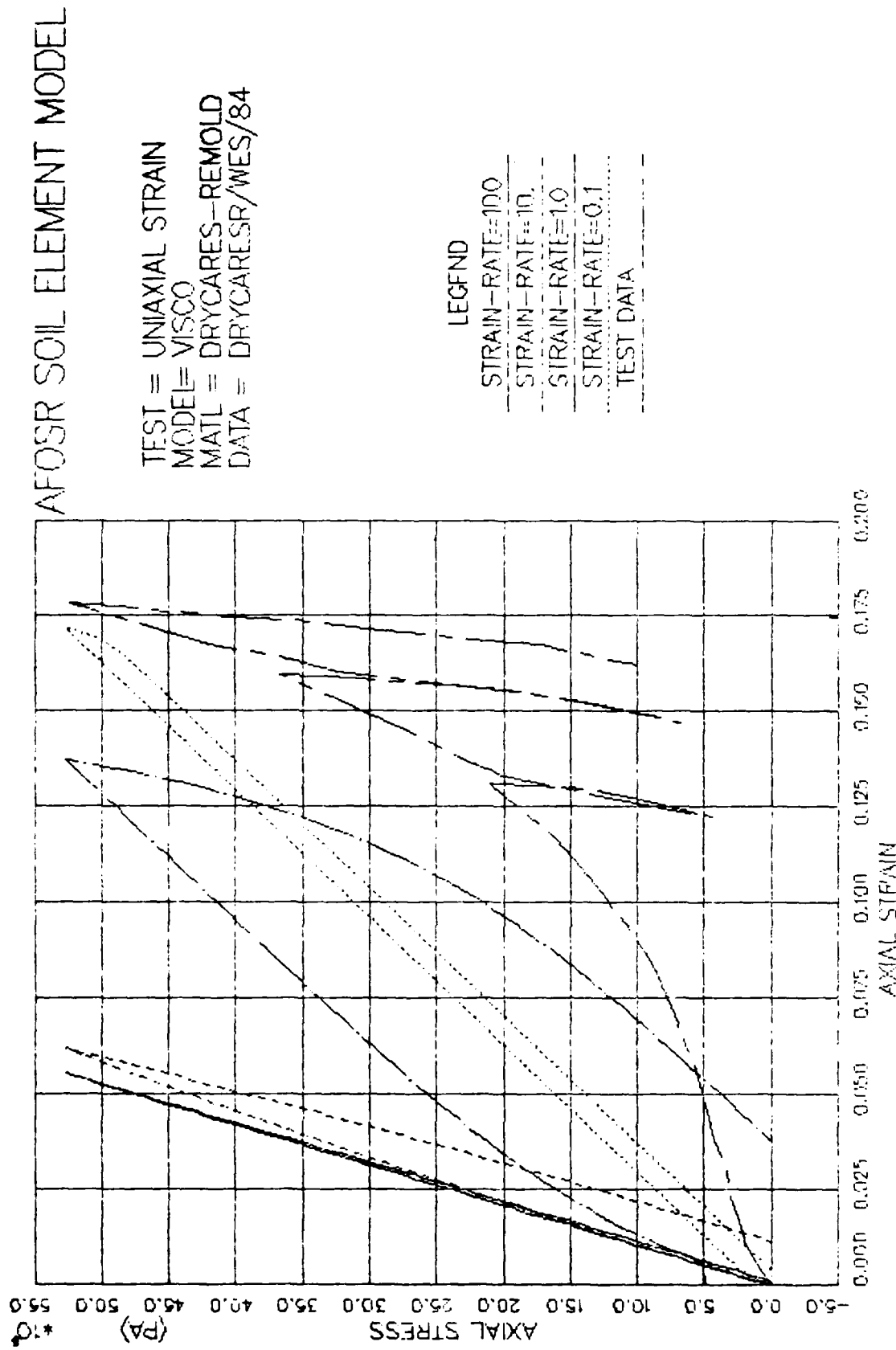
FIGURE V.2.1   VISCO MODEL EXERCISE- UNIAXIAL STRAIN -- TOT AXL STRESS VS. AXL STRAIN .

337
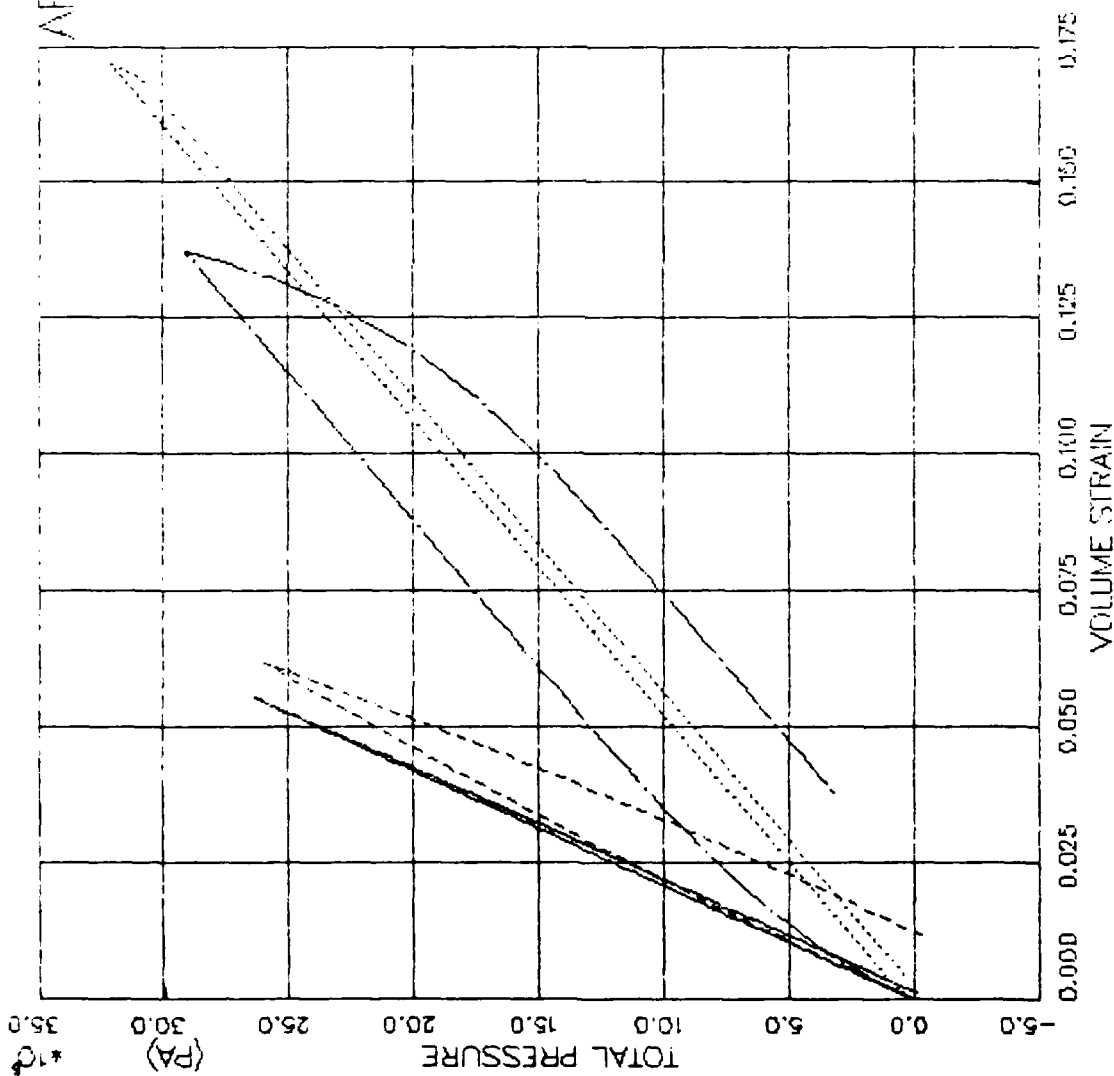
FIGURE V.2.2 VISCO MODEL EXERCISE—UNIAXIAL STRAIN -- PRESSURE VS. VOLUMETRIC STRAIN .
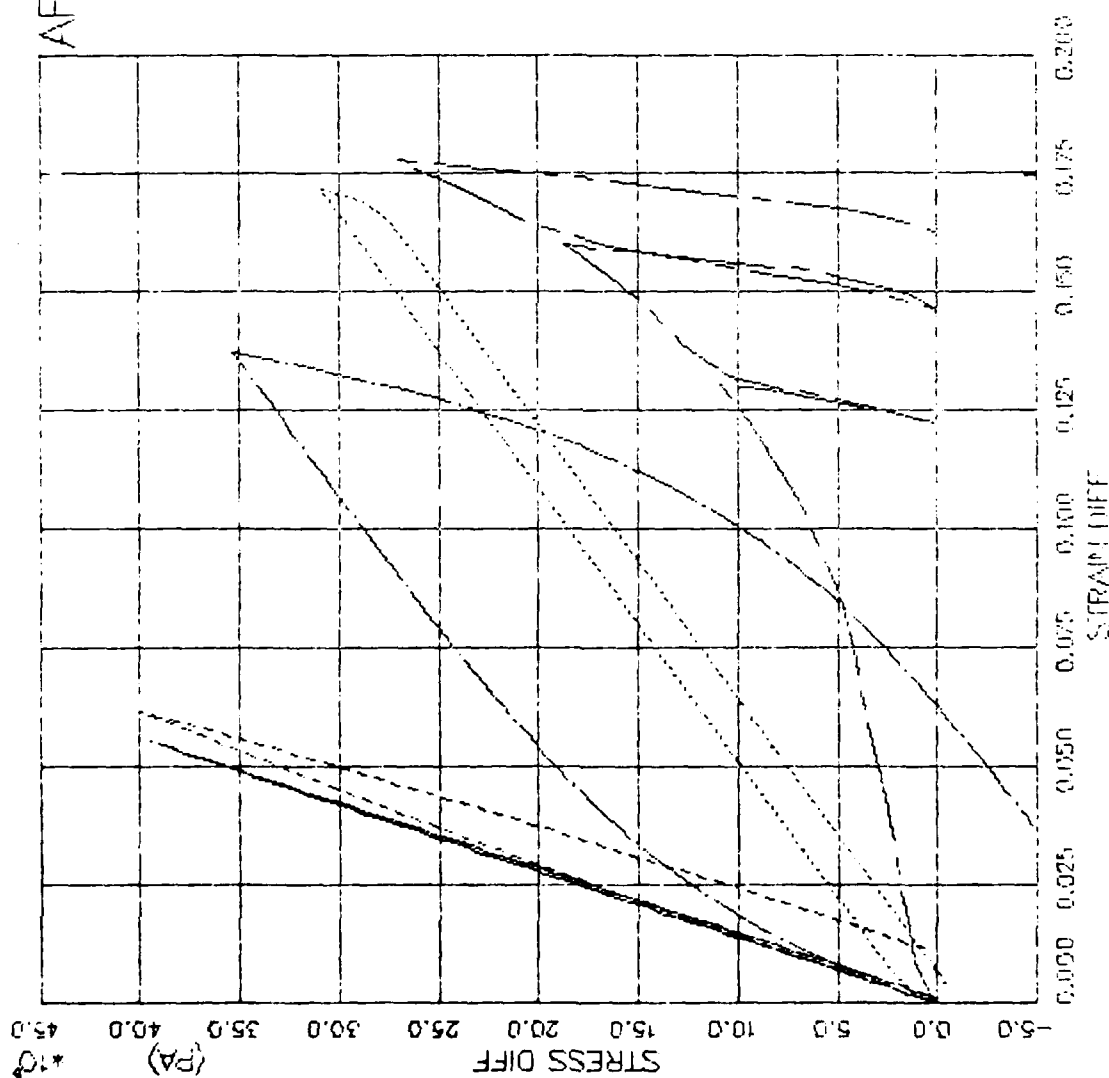
FIGURE V.2.3 VISCO MODEL EXERCISE—UNIAXIAL STRAIN — STRESS DIFF VS. STRAIN DIFF
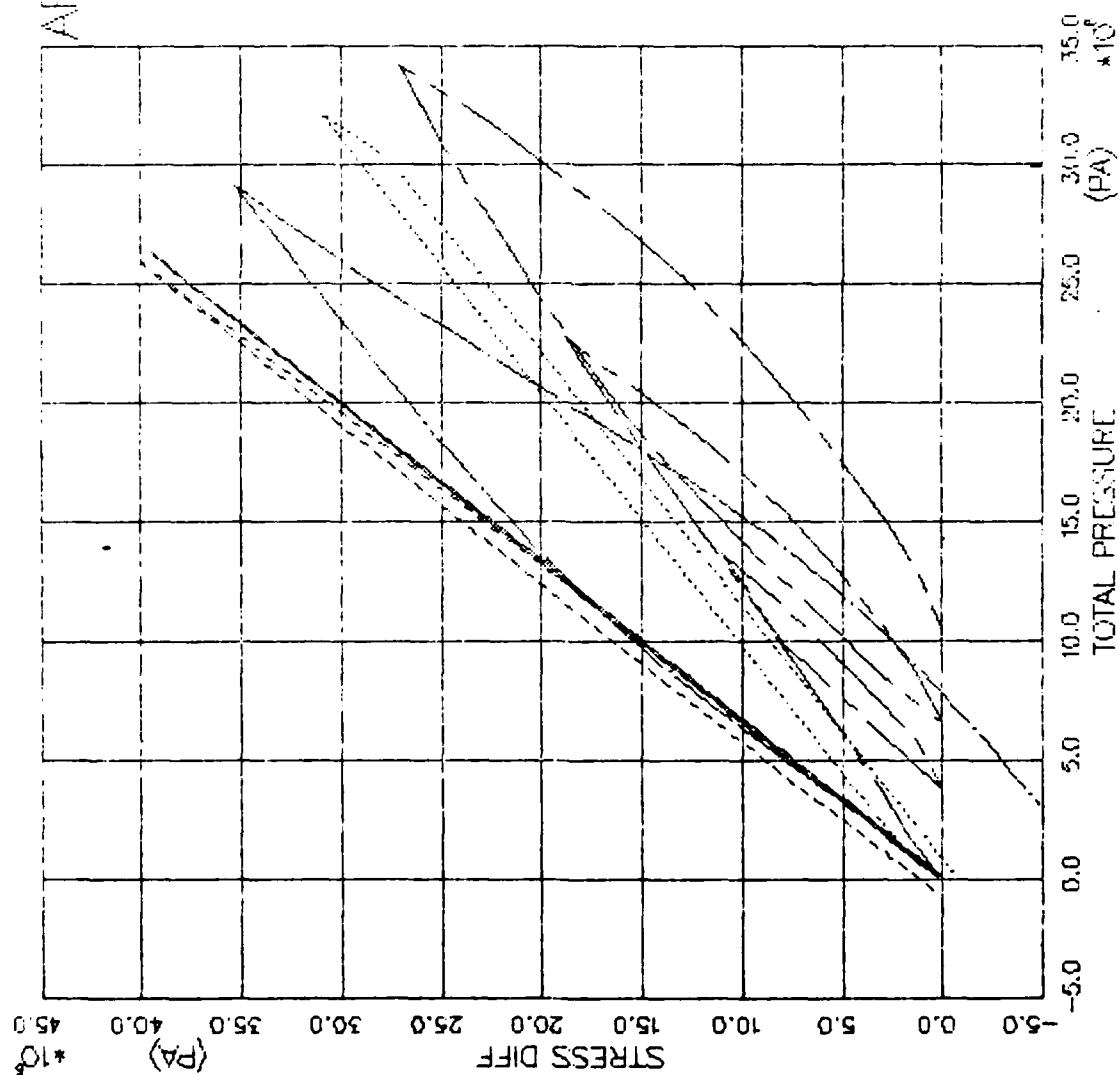
FIGURE V.2.4 VISCO MODEL EXERCISE—UNIAXIAL STRAIN — STRESS DIFFERENCE VS. PRESSURE .

340

V.3 Hyperbolic

V.3.1 Motivation

The hyperbolic model consists of formulas for computing the tangent
Young's modulus and Poisson's ratio, for use in an incremental elastic
analysis. It is a simple, practical procedure for representing the
nonlinear, stress-dependent, inelastic stress-strain behavior of soils
[Duncan and Chang (1970:1650)]. Values of required parameters can be
derived from the results of standard laboratory triaxial tests, or from
more sophisticated test results if available. The hyperbolic model's
principal drawbacks are that it does not fully account for stress path
effects on strength, stiffness, or dilatancy.

V.3.2 Assumptions

The material is assumed to be homogeneous and isotropic, and the
relation between the major and minor principal effective stresses and the
tangent Young's modulus measured in a triaxial compression test at
constant cell pressure is assumed to hold for any stress path. In their
original hyperbolic model Duncan and Chang assumed a constant Poisson's
ratio. An alternate version obtains a tangent Poisson's ratio by assuming
a hyperbolic relation between the major and minor principal strains,
together with the same hyperbolic relation between major principal strain
and principal stress difference used to obtain the tangent Young's
modulus. The tangent Poisson's ratio formulation is intended only for
stress levels well below failure.

V.3.3 Basic Equations

The equation for the tangent Young's modulus is

$$E_T = K p_a \left(\frac{\sigma_3}{p_a}\right)^n \left[1 - \frac{R_f(1 - \sin\phi)(\sigma_1 - \sigma_3)}{2(c \cos\phi + \sigma_3 \sin\phi)}\right]^2 \qquad (V.3.1)$$

where p_a = atmospheric pressure

K, n, R_f = dimensionless empirical constants

c, ϕ = Mohr-Coulomb strength parameters

σ_1, σ_3 = major and minor principal effective stresses

Equation (V.3.1) is derived in Appendix M, and is identical to Equation (M.21).

The equation for the tangent Poisson's ratio in the alternate version is

$$\nu_T = \frac{G - F \log_{10}\left(\frac{\sigma_3}{p_a}\right)}{(1 - A)^2} \qquad (V.3.2)$$

where

$$A = \frac{d(\sigma_1 - \sigma_3)}{K p_a \left(\frac{\sigma_3}{p_a}\right)^n \left[1 - \frac{R_f(1 - \sin\phi)(\sigma_1 - \sigma_3)}{2(c \cos\phi + \sigma_3 \sin\phi)}\right]} \qquad (V.3.3)$$

and, in addition to the quantities appearing in Equation (V.3.1),

d, G, F = dimensionless empirical constants

Equations (V.3.2) and (V.3.3) are derived in Appendix N, and are identical to Equations (N.7) and (N.8), respectively.

V.3.4   Parameter Determination

The determination of the parameters entering Equations (V.3.1), (V.3.2), and (V.3.3) is explained in Appendices M and N, where the equations are derived.

Parameters for a modified hyperbolic model were determined for CARES-DRY Sand. The principal differences between the model described in appendices M and N and the model actually used are:

(a) Maximum past axial strain was used as a state variable to define the *unloading condition*. Upon unloading, i.e.,

$$\epsilon_a < \epsilon_{a, \, max} \qquad (V.3.4)$$

the tangent Young's Modulus and Poisson's ratio are set to constant values,

$$E_T = E_{ur} = K_{ur} * p_a \qquad (V.3.5)$$

$$\nu_T = \nu_{ur} \qquad (V.3.6)$$

(b) Shear stresses were further constrained to lie within the failure envelope defined by the Mohr-Coulomb strength parameters, c and ϕ. Plastic strains were computed using a non-associated, Von Mises plastic potential.

(c) Pressure was not allowed to achieve negative values. If tensile failure occured, all stresses were set to zero.

Parameters for unloading-reloading behavior (K_{ur}, ν_{ur}) and strength parameters (c, ϕ) were determined by hand from examination of the data for remolded specimens as presented in [Cargile (1984)]. All other input parameters were automatically determined in the SEM. Figure (V.3.1) shows the triaxial stress-strain data used for this fitting

process. In Figure (V.3.2) the axial data has been replotted on a Kondner plot. Note that the data curves are very nearly hyperbolic, with most deviation occurring at low strains. Figure (V.3.3) shows a logarithmic plot of E_i vs. σ_{3c}, which is used for determining K and n. There is considerable scatter in this fit. Tangent values of Poisson's ratio are plotted in Figure (V.3.4) against radial strain. The data shows wide variation, and Poisson's ratio exceeds 0.5 when the specimens are dilating. A logarithmic fit for variation of initial Poisson's ratio with confining pressure is shown in Figure (V.3.5). In the actual model computation, the tangent Poisson's ratio is not allowed to exceed 0.5.

V.3.5 Calculated Behavior

Isotropic compression behavior for the hyperbolic model is compared with test data in Figure (V.3.6). Since triaxial data and not IC data were used to fit the loading modulus, and because the loading modulus is strictly dependent on initial confining pressure and axial strain, calculated and actual behavior are not expected to match for this test. CTC behavior is covered in Figures (V.3.7) through (V.3.10). Stress-strain data, used for parameter fitting, is matched well [Figure (V.3.7)]. The inclusion of special unloading-reloading modifications allows the model to undergo permanent compaction [Figures (V.3.7), (V.3.9), and (V.3.10)]. Since Poisson's ratio is artificially held to be less than 0.5, dilation is not predicted [Figure (V.3.9)]. Initial bulk stiffnesses are well matched, as seen in Figure (V.3.10), but once dilation commences, calculated and actual pressure-volume responses diverge.

Since the CTE test involves axial expansion, the model responds by unloading with a high modulus and the unload-reload value of Poisson's

ratio [Figures (V.3.11) and (V.3.12)]. Presence of the Mohr-Coulomb shear
failure envelope limits stress difference but does not predict the lower
observed values of shear strength in extension compared with those in
compression. Figure (V.3.13) shows that the predicted volume strains are
expansive while those measured were compressive. Pressure-volume behavior
is shown in Figure (V.3.14).

The RTC/E and PSC/E [Figures (V.3.15-V.3.18) and (V.3.19-V.3.20),
respectively] highlight features of this model, as it is currently
implemented:

(a) Loading and unloading behaviors, as determined by axial strain,
are substantially different [Figure (V.3.15) for RTC/E and
Figure (V.3.19) for PSC/E]. This is due to the modified nature
of the unloading part of the model.

(b) Without recognition of the Mohr-Coulomb failure surface in the
model itself, all loading stress paths would have an ultimate
shear strength equal to $(\sigma_1 - \sigma_{3c})_{ULT}$ as predicted by the
hyperbolic model for CTC behavior. This would severely
overestimate strength for certain stress paths such as CTE or
RTC. When the failure envelope is used, initial stress-strain
response is identical to CTC, but the material fails in shear
prior to $(\sigma_1 - \sigma_{3c})_{ULT}$. This can be seen in Figures
(V.3.15) and (V.3.16) for RTC and in Figures (V.3.19) and
(V.3.20) for PSC and PSE.

(c) No dilation behavior is predicted in this model [Figure
(V.3.17)], and the pressure-volume response is a function of
initial confining pressure and axial strain [Figure (V.3.18)].

345

The behavior of the modified Duncan and Chang hyperbolic model is summarized in Figures (V.3.21) and (V.3.22) for stress paths run in the triaxial cell from 7.1 MPa initial confining pressure.

Uniaxial compression response, starting at a low confining pressure and tested to a relatively high level of stress, cannot be well predicted by this model as is shown in Figures (V.3.23) through (V.3.25). Axial stress-strain response [Figure (V.3.23)] is much too stiff because of the large axial strains and modulus dependence on axial strain. Poisson's ratio also is affected and quickly reaches the 0.5 limit imposed. This limit affects the shear modulus, as can be seen in Figure (V.3.24). Unload-reload behavior and compaction are reasonably well modeled.

Predicted uniaxial extension behavior [Figures (V.3.26) through (V.3.28)] is essentially the same as that described for the elastic-plastic model in Section V.5. This is a result of the linear elastic unload-reload response with a Mohr-Coulomb failure surface.

The axisymmetric strain path exercises disclose some of the consequences when this type of model is used for more general conditions like those occurring in-situ. Predicted behavior for the WES strain paths is compared with the data in Figure (V.3.29). For this strain path, axial strain is increasing until the very last, while volume strain reverses. Therefore this model, which uses axial strain to signal unloading, never unloads and the result is the pressure-volume response shown. The bulk modulus does not change upon increased radial expansion, but continues to gradually decrease with increasing axial strain. Shear response is reasonable but does not respond to the strain path changes as does the data.

The Lade strain path 1 results [Figure (V.3.30)] show an initial break in the strain path and bulk modulus when the limit of 0.5 for Poisson's ratio is reached. This results in a large departure from observed behavior. Strain path 2 [Figure (V.3.31)] also causes the model to stiffen just prior to the reversal in volume strain. This causes a sharp drop in pressure (without unloading as defined by axial strain) and the stress path encounters the failure surface. Again, deficiency in the bulk response causes bad comparison with the data.

Results for the true triaxial strain path are shown in Figures (V.3.32) and (V.3.33). The axisymmetric portion of the response looks good, but when the strain path causes stress response out of the triaxial plane, the results are not good. Note that this model keys on axial and radial strains/stresses while ignoring the intermediate principal strain/stresses. Figure (V.3.33) shows that although provision is made for tensile failure, the material reloads before re-compacting.

TABLE V.3.1(a).   HYPERBOLIC MODEL PARAMETERS FOR CARES-DRY SAND

Parameter	Symbol	Variable	Value	Units
	K	HK	479.1	--
Constants	K_{ur}	HKUR	49320	--
	n	HN	0.6057	--
	R_f	HRF	0.8475	--
Mohr-Coulomb	c	HC	5.0×10^5	Pa
Strength	ϕ	HPHI	30.0	degrees
Poisson's Ratio	G	HG	0.4924	--
Constants	F	HF	-0.0935	--
	d	HD	2.004	--
Unload-Reload Poisson's Ratio	ν_{ur}	HNUR	0.200	--
Confining Pressure	σ_{3c}	HSIGMA3	See (b) below	Pa
Initial Young's Modulus	E_i	HEI	See (b) below	Pa
Stress Difference at CTC Failure	$(\sigma_1 - \sigma_{3c})_f$	HFSDIFF	See (b) below	Pa
Initial Poisson's Ratio	ν_i	HNUI	See (b) below	--
Mass Density	ρ	RHOREF	1900	kg/m^3

TABLE V.3.1(b) HYPERBOLIC MODEL CONFINING PRESSURE DEPENDENT PARAMETERS

σ_{3c} (MPa)	E_i (MPa)	HFSDIFF (MPa)	ν_i (--)
0.1	48.17	1.93	0.491
0.4	113.9	2.56	0.435
1.8	277.4	5.33	0.343
3.5	415.0	8.73	0.350
7.0	631.5	15.73	0.321
20.0	1193	41.73	0.278
32.0	1585	65.73	0.259
59.0	2292	119.3	0.234
100.0	3161	201.7	0.213
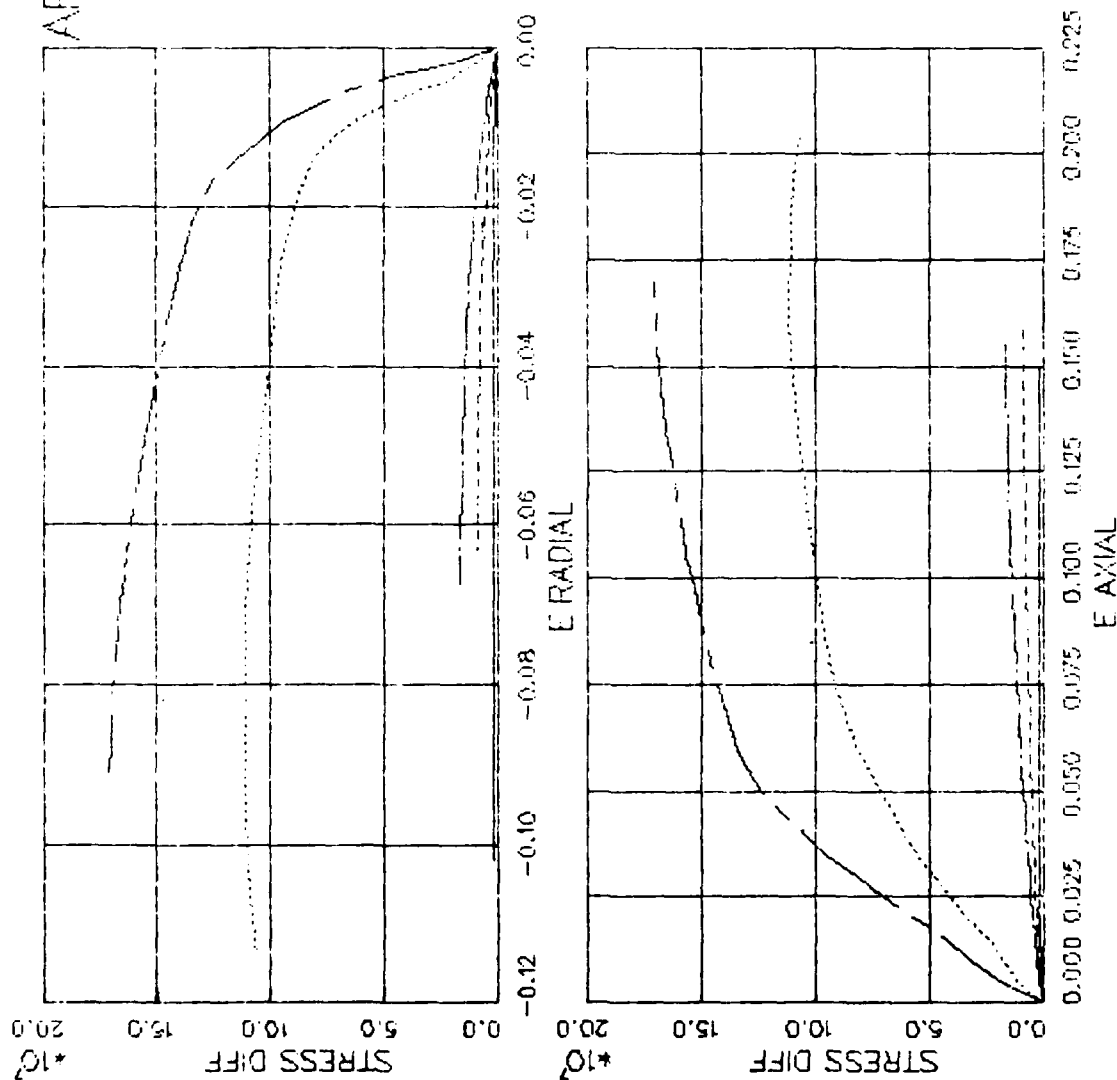
FIGURE V.3.1 HYPERBOLIC MODEL FIT — TRIAXIAL TEST DATA

AFOSR SOIL ELEMENT MODEL

TEST = PARAMETER FIT
MODEL= HYPER
MATL = DRYCARES-REMOLD
DATA = DRYCARESR/WES/84

S_{3c} (MPa)

EI = 3.980*10^6
QULT= 2.385*10^5   0.7
EI = 1.903*10^6
QULT= 1.318*10^7   3.4
EI = 2.778*10^8
QULT= 2.842*10^7   7.0
EI = 2.918*10^8
QULT= 1.441*10^6   58.8
EI = 4.751*10^9
QULT= 2.252*10^8   100.0
HEI= 1.707*10^0
HRF= 8.475*10^-1

FIGURE V.3.2 HYPERBOLIC MODEL FIT — TRANSFORMED STRESS—STRAIN CURVES.

350
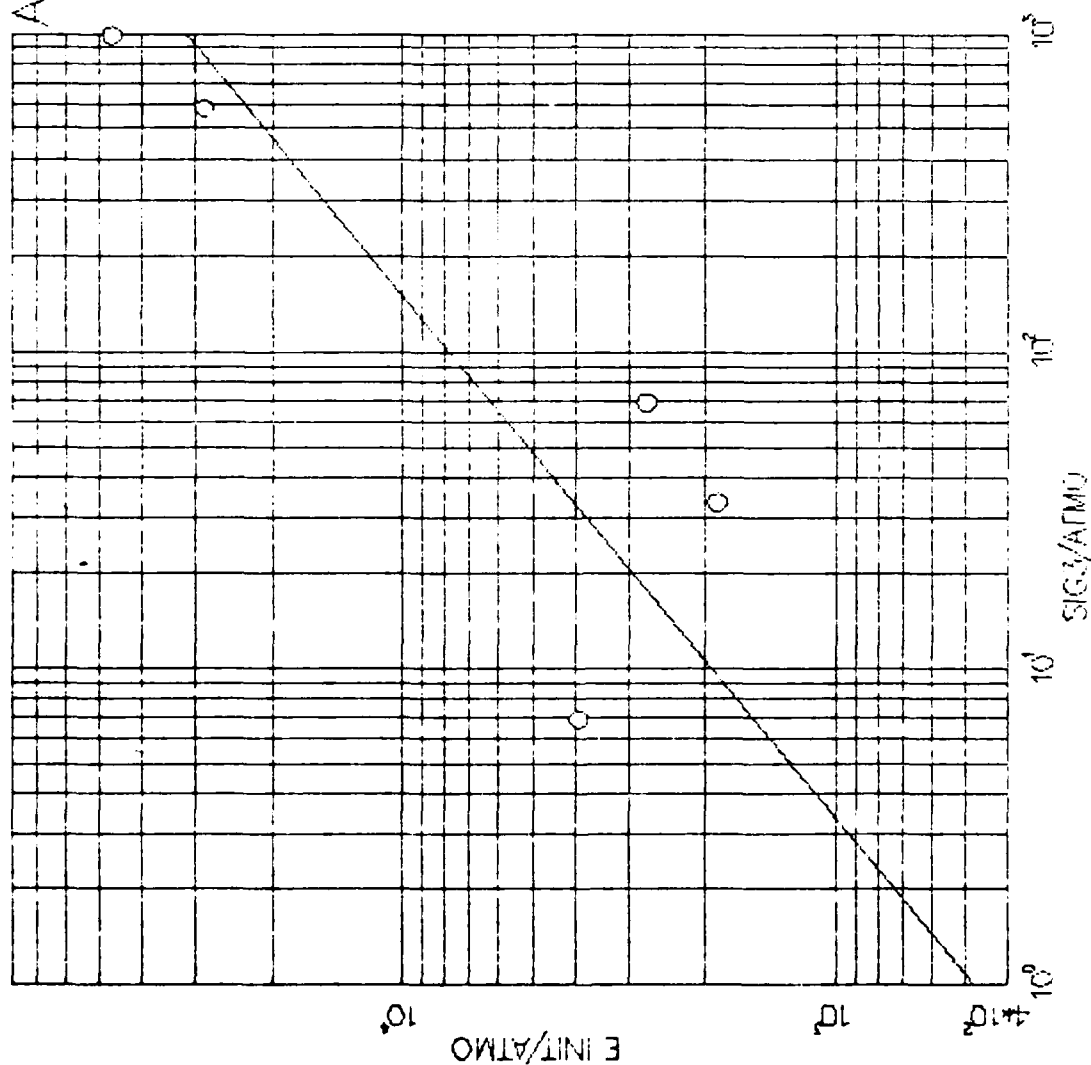
FIGURE V.3.3 HYPERBOLIC MODEL FIT — INITIAL YOUNG'S MODULUS FIT

351

AFOSR SOIL ELEMENT MODEL

TEST = PARAMETER FIT
MODEL= HYPER
MATL = DRYCARES-REMOLD
DATA = DRYCARESR/WES/84

	S_{3c} (MPa)
POIS= $4.290*10^{-1}$ HD = $2.660*10^{0}$	0.7
POIS= $3.392*10^{-1}$ HD = $1.291*10^{-1}$	3.4
POIS= $3.292*10^{-1}$ HD = $1.073*10^{0}$	7.0
POIS= $2.434*10^{-1}$ HD = $2.851*10^{0}$	58.8
POIS= $2.839*10^{-1}$ HD = $3.307*10^{0}$	100.0
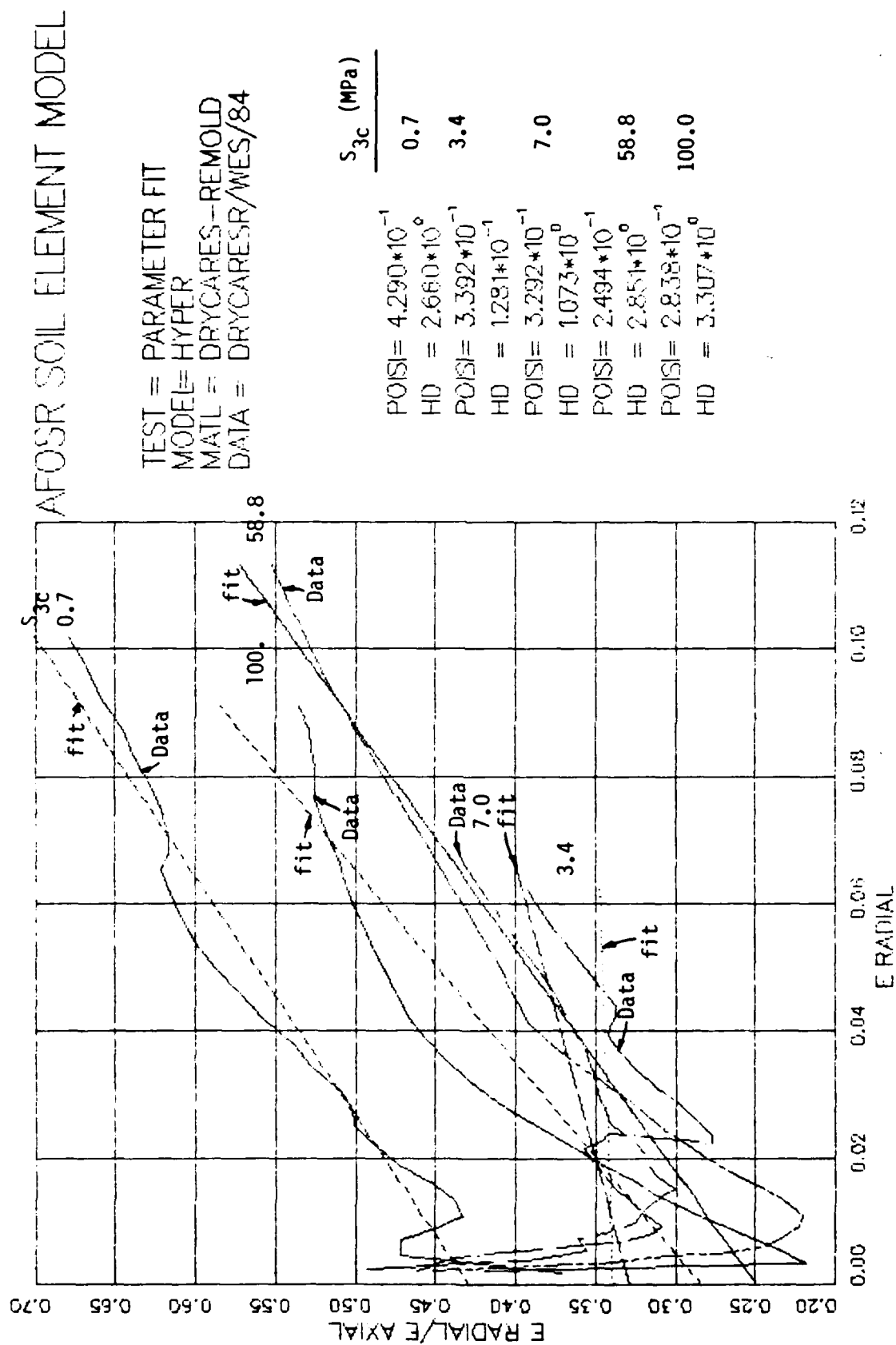
FIGURE V.3.4 HYPERBOLIC MODEL FIT — INCREMENTAL POISSONS RATIO

352
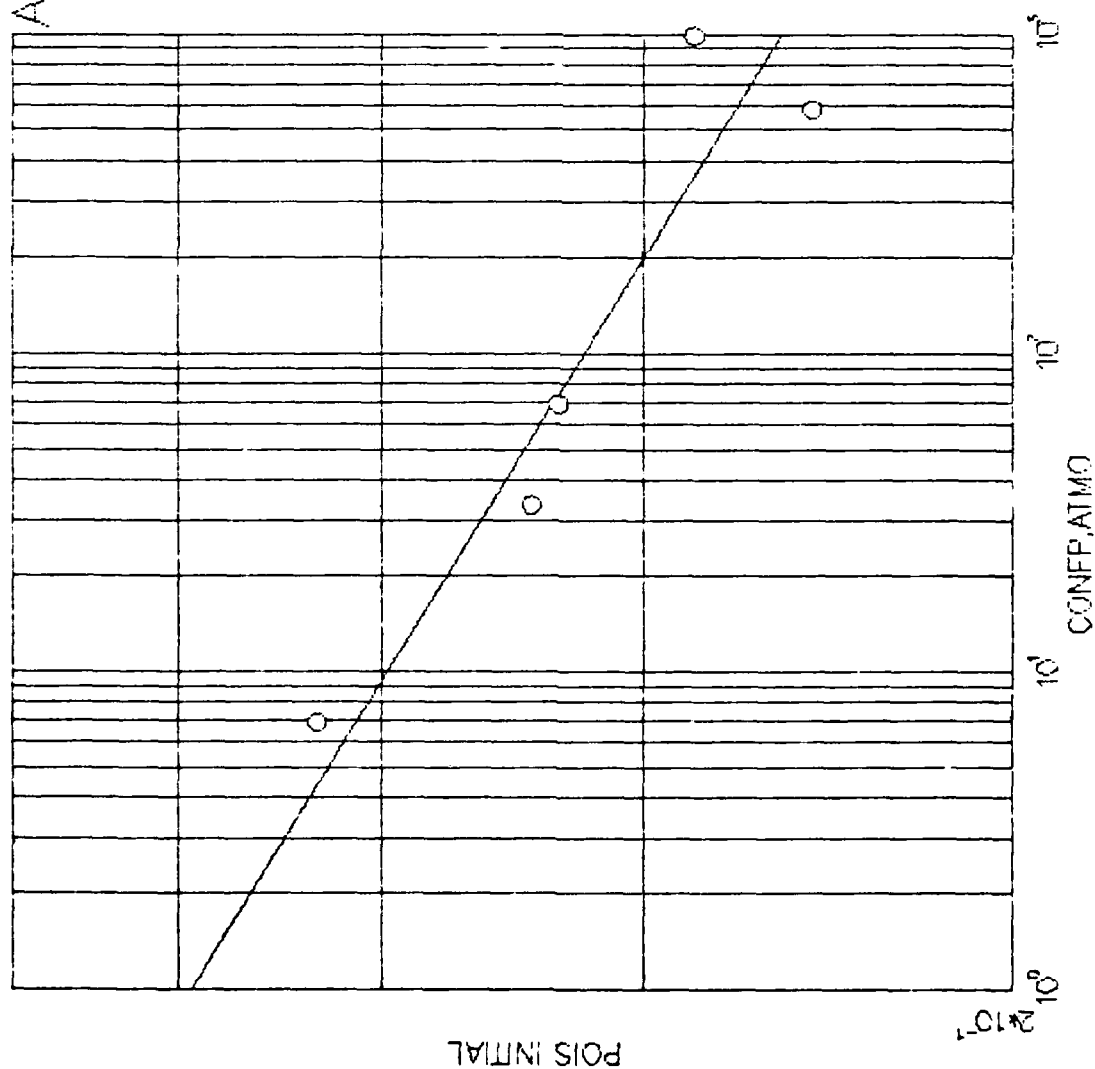
FIGURE V.3.5 HYPERBOLIC MODEL FIT — POISSONS RATIO FIT

353
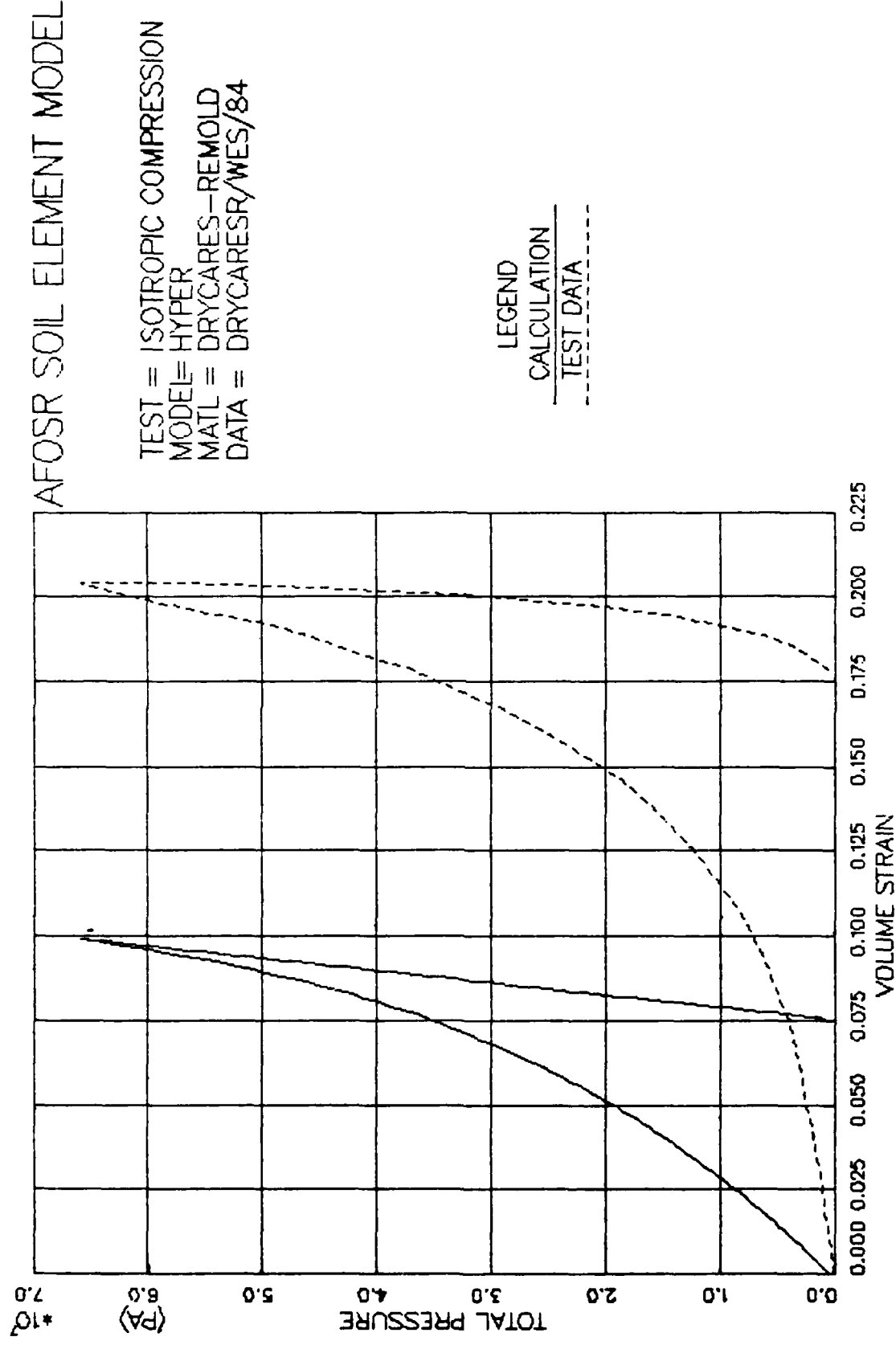
FIGURE V.3.6 HYPER MODEL EXERCISE- ISOTROPIC COMP. - PRESSURE VS. VOLUMETRIC STRAIN .

AFOSR SOIL ELEMENT MODEL

TEST = STANDARD TRIAXIAL
MODEL= HYPER
MATL = DRYCARES—REMOLD
DATA = DRYCARESR/WES/84

LEGEND
SIGMA3C= 3.4E6
TEST DATA
SIGMA3C= 7.0E6
TEST DATA
SIGMA3C= 58.8E6
TEST DATA
SIGMA3C=100.0E6
TEST DATA
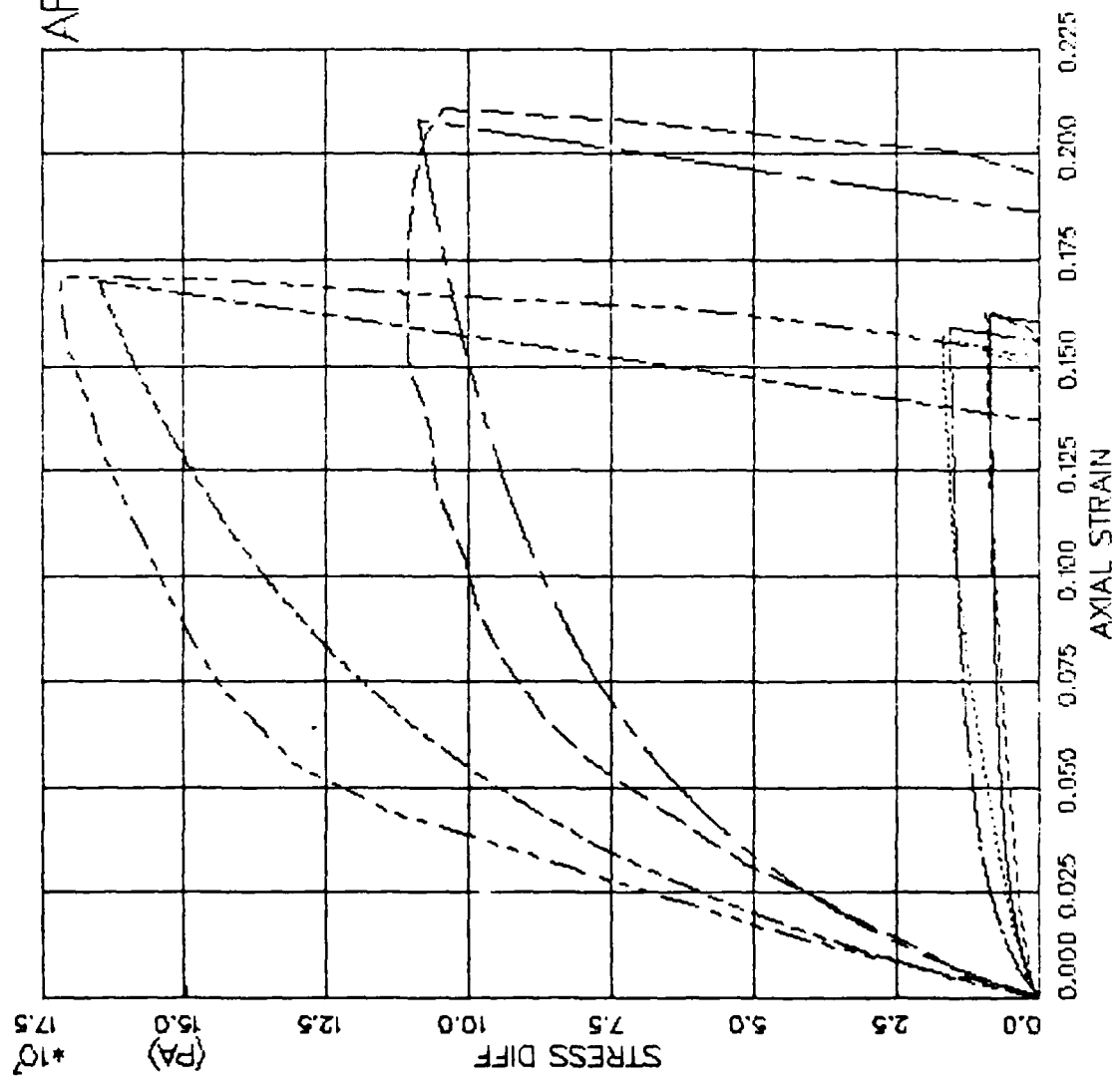
FIGURE V.3.7 HYPER MODEL EXERCISE—TRIAXIAL COMP(CTC) — STRESS DIFF VS. AXIAL STRAIN

355

AN OCR'D SOIL ELEMENT MODEL

TEST = STANDARD TRIAXIAL
MODEL = HYILR
MAT'L = DRY CAREFS – REMOLD
DATA = DRY CAREFS/WES/84

LEGEND

SIGMA3C = 3.4F 6
SIGMA3L = 7.0F 6
SIGMA3C = 53.PF6
SIGMA3L = 100.0F 6

FIGURE V.3.8 IHE UPMODE LABORA – TRIAXIAL COMP (TC) – STRESS DIFF VS STRAIN DIFF

356

FIGURE V.3.9 HYPER MODEL EXERCISE—TRIAXIAL COMP(CTC) — AXIAL STRAIN VS VOLUME STRAIN
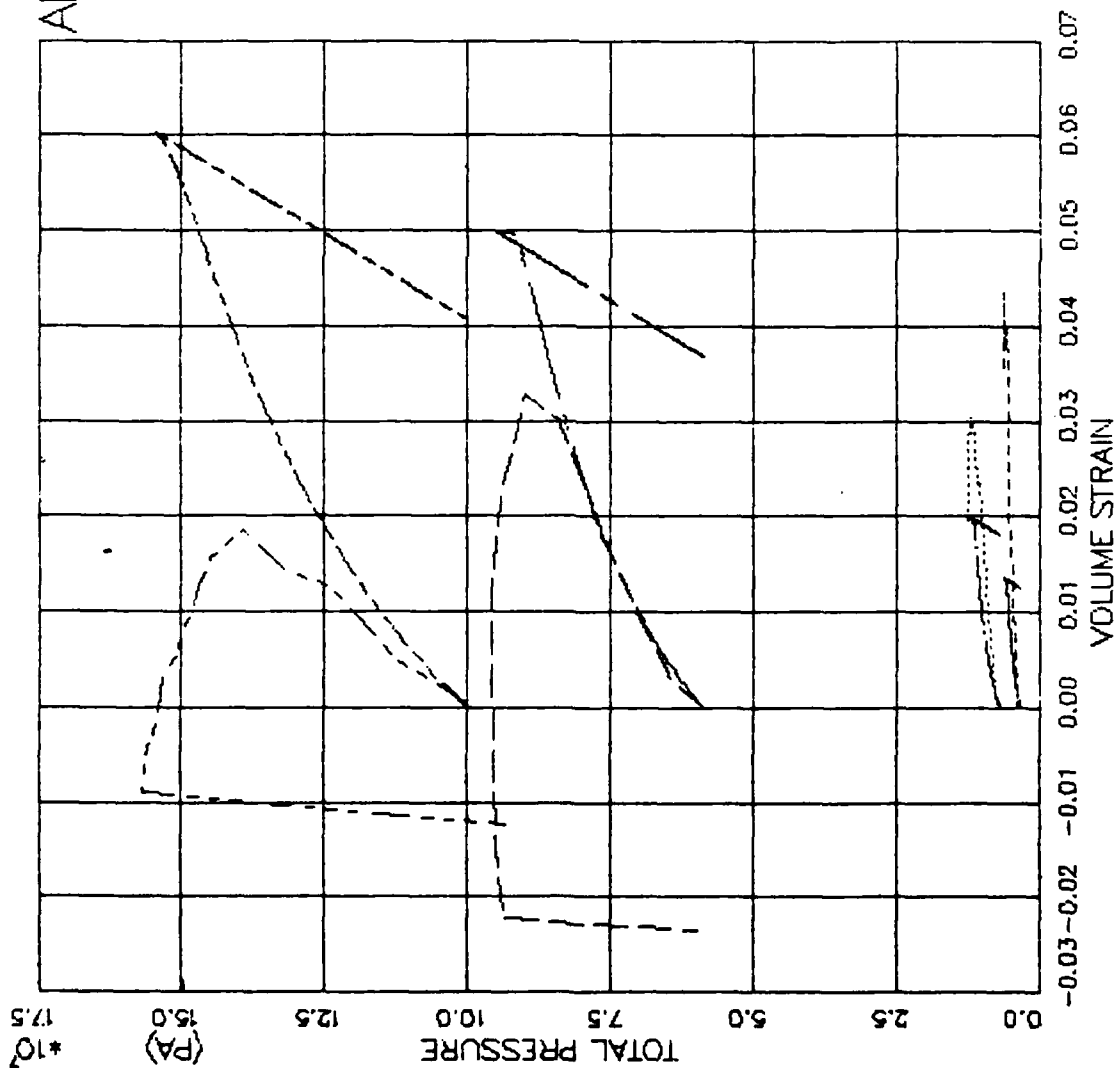
FIGURE V.3.10 HYPER MODEL EXERCISE—TRIAXIAL COMP(CTC) — PRESSURE VS. VOLUMETRIC STRAIN

358

AFOSR SOIL ELEMENT MODEL

TEST = STANDARD TRIAXIAL
MODEL= HYPER
MATL = DRYCARES–REMOLD
DATA = DRYCARESR/WES/84

LEGEND
S3C=1.8E6
TEST DATA
S3C=3.5E6
TEST DATA
S3C=7.1E6
TEST DATA
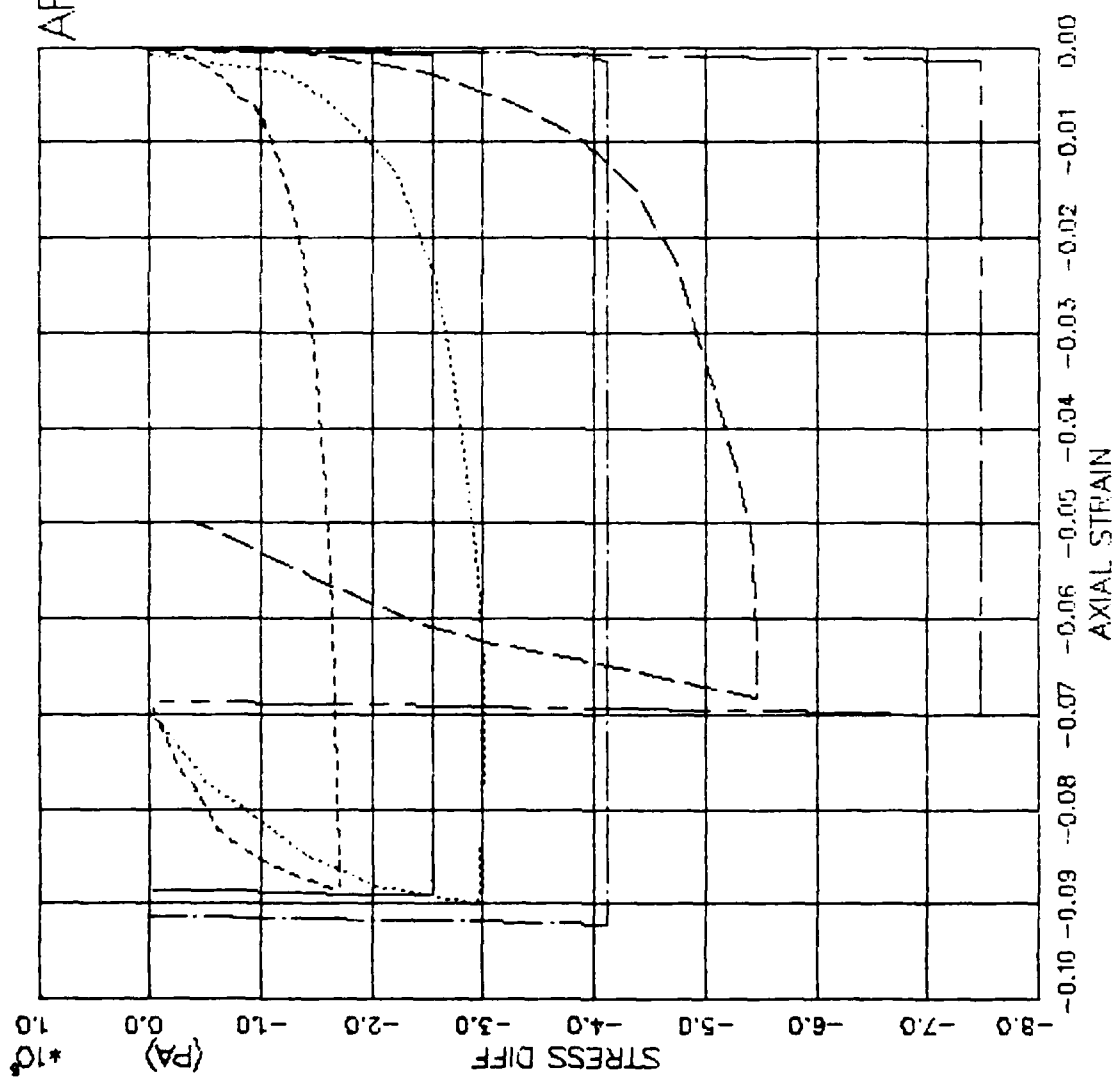
FIGURE V.3.11 HYPER MODEL EXERCISE–TRIAXIAL EXTEN(CTE) – STRESS DIFF VS. AXIAL STRAIN

359

FIGURE V.3.12 HYPER MODEL EXERCISE—TRIAXIAL EXTEN(CTE) – STRESS DIFF VS. STRAIN DIFF

360

AFOSR SOIL ELEMENT MODEL

TEST = STANDARD TRIAXIAL
MODEL= HYPER
MATL = DRYCARES−REMOLD
DATA = DRYCARESR/WES/84

LEGEND
S3C=1.8E6
TEST DATA
S3C=3.5E6
TEST DATA
S3C=7.1E6
TEST DATA
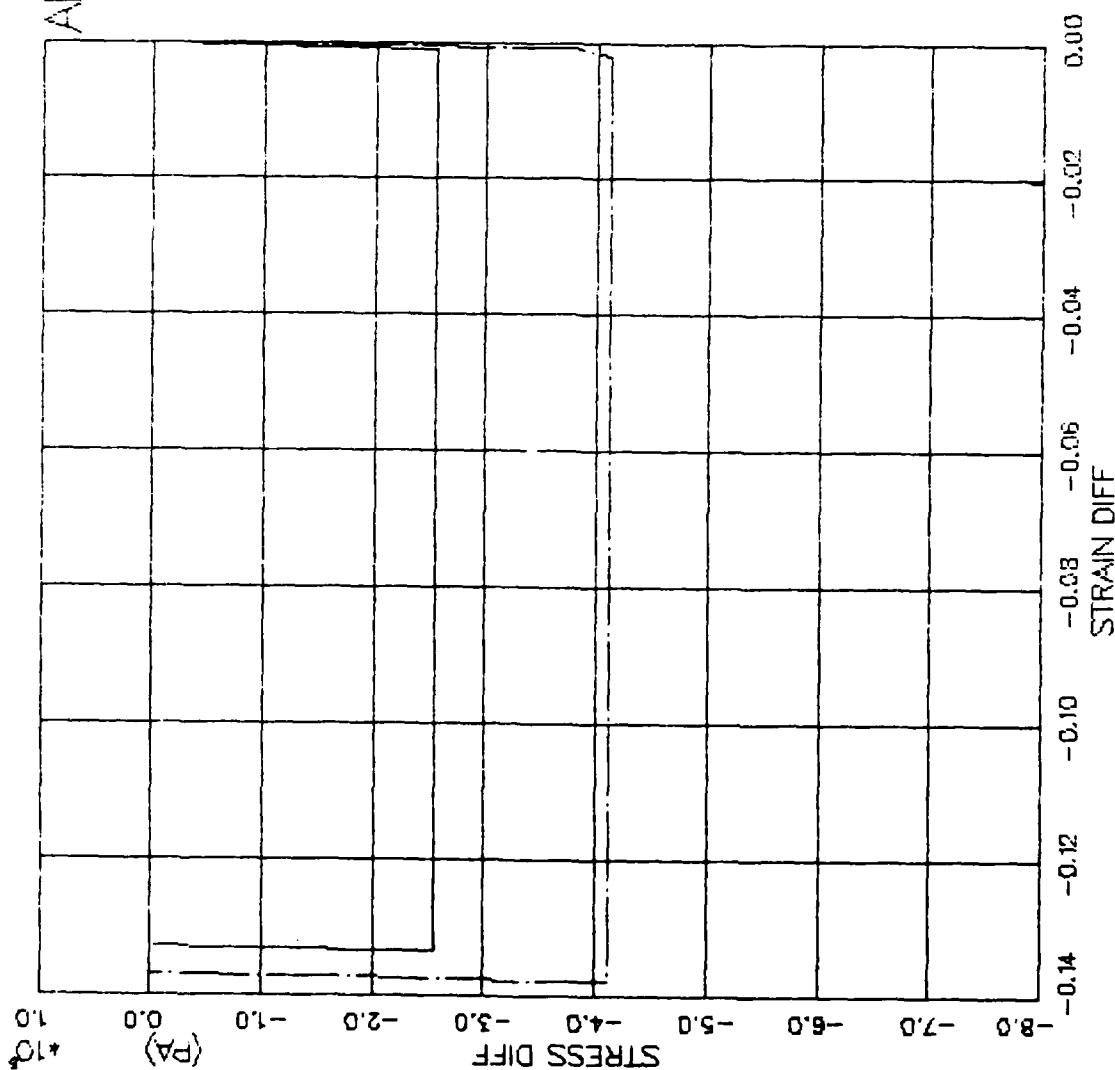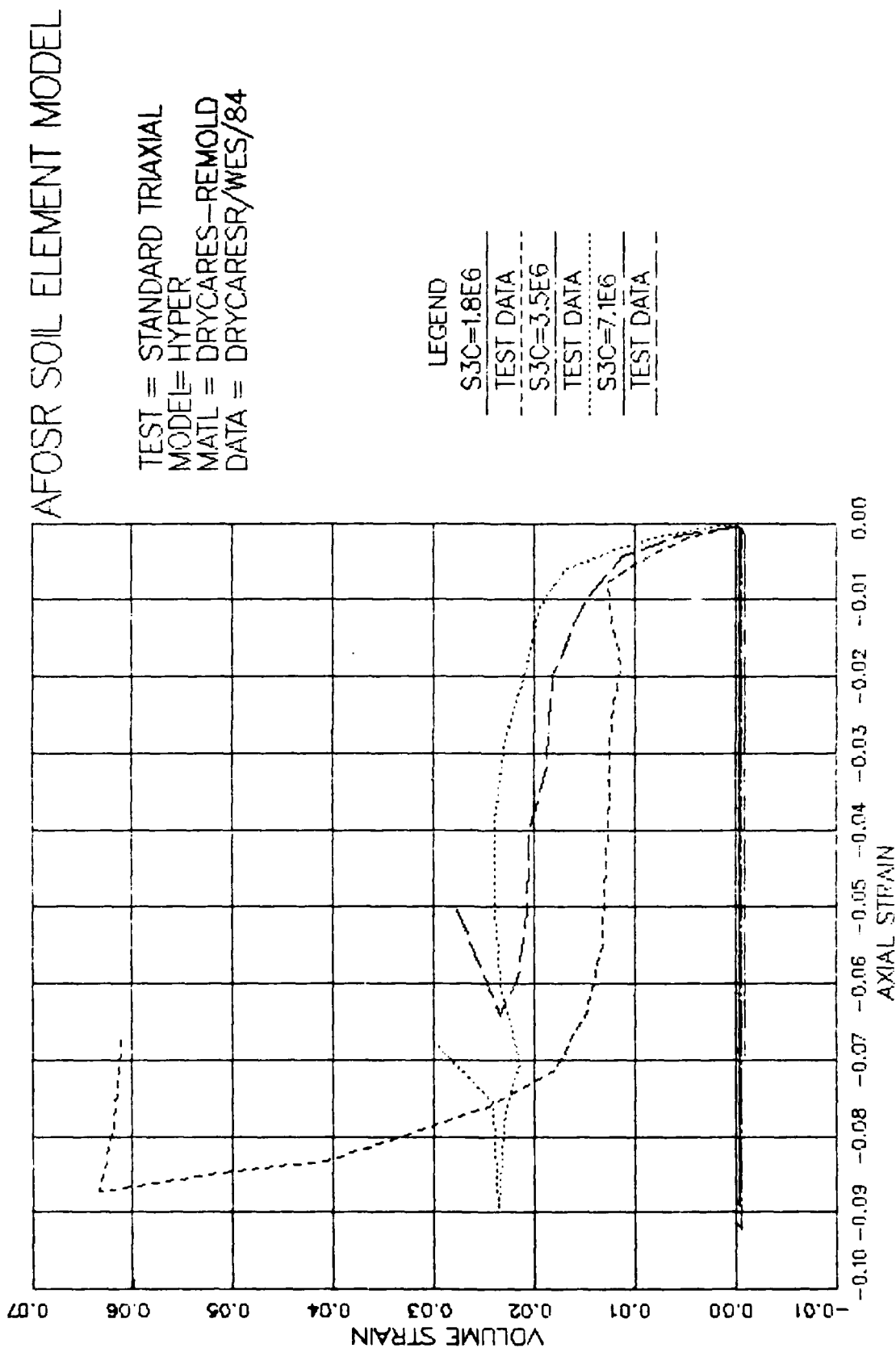
FIGURE V.3.13 HYPER MODEL EXERCISE−TRIAXIAL EXTEN(CTE) − AXIAL STRAIN VS VOLUME STRAIN
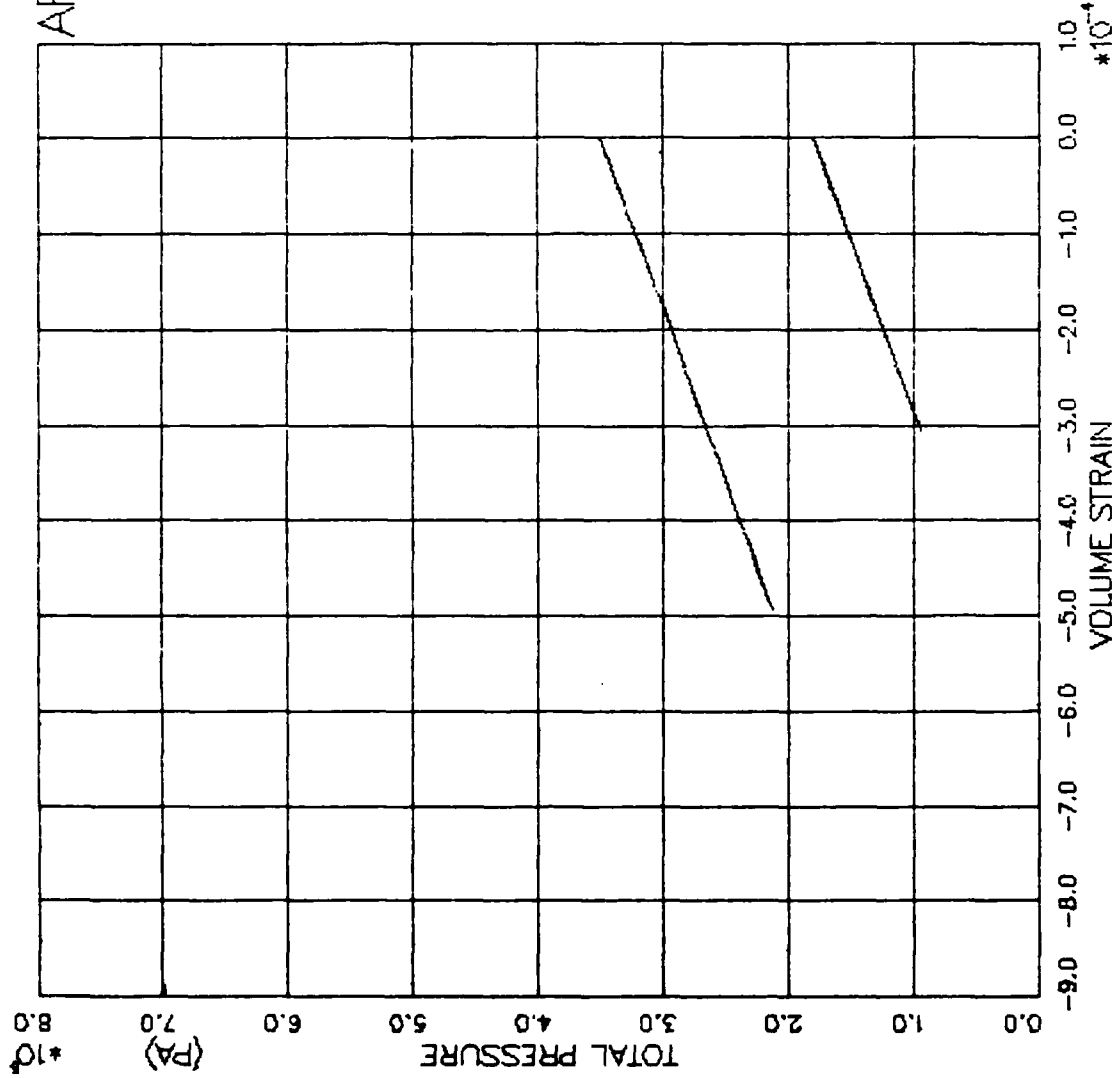
FIGURE V.3.14 HYPER MODEL EXERCISE–TRIAXIAL EXTEN(CTE) – PRESSURE VS. VOLUMETRIC STRAIN

AFOSR SOIL ELEMENT MODEL

TEST = STANDARD TRIAXIAL
MODEL = HYPER
MATL = DRYCARES—REMOLD

LEGEND
RTC/S3C=1.8E6
RTC/S3C=1.8E6
RTC/S3C=3.5E6
RTC/S3C=3.5E6
RTC/S3C=7.1E6
RTC/S3C=7.1E6
RTE/S3C=1.8E6
RTE/S3C=1.8E6
RTE/S3C=3.5E6
RTE/S3C=3.5E6
RTE/S3C=7.1E6
RTE/S3C=7.1E6

FIGURE V.3.15 HYPER MODEL (REP—REDUCED TRIAX(RTC→RTE) — STRESS DIFF VS. STRAIN

363
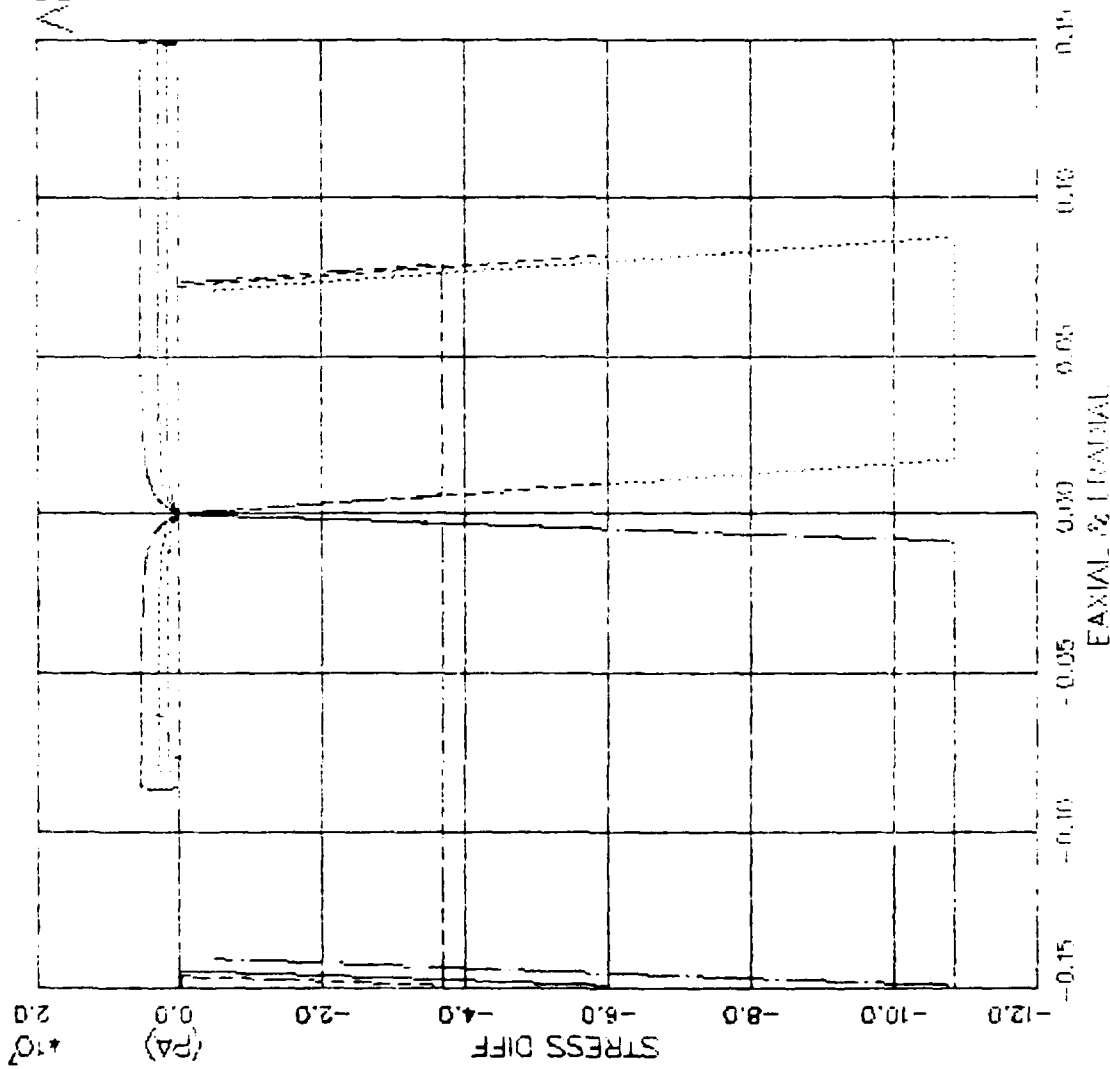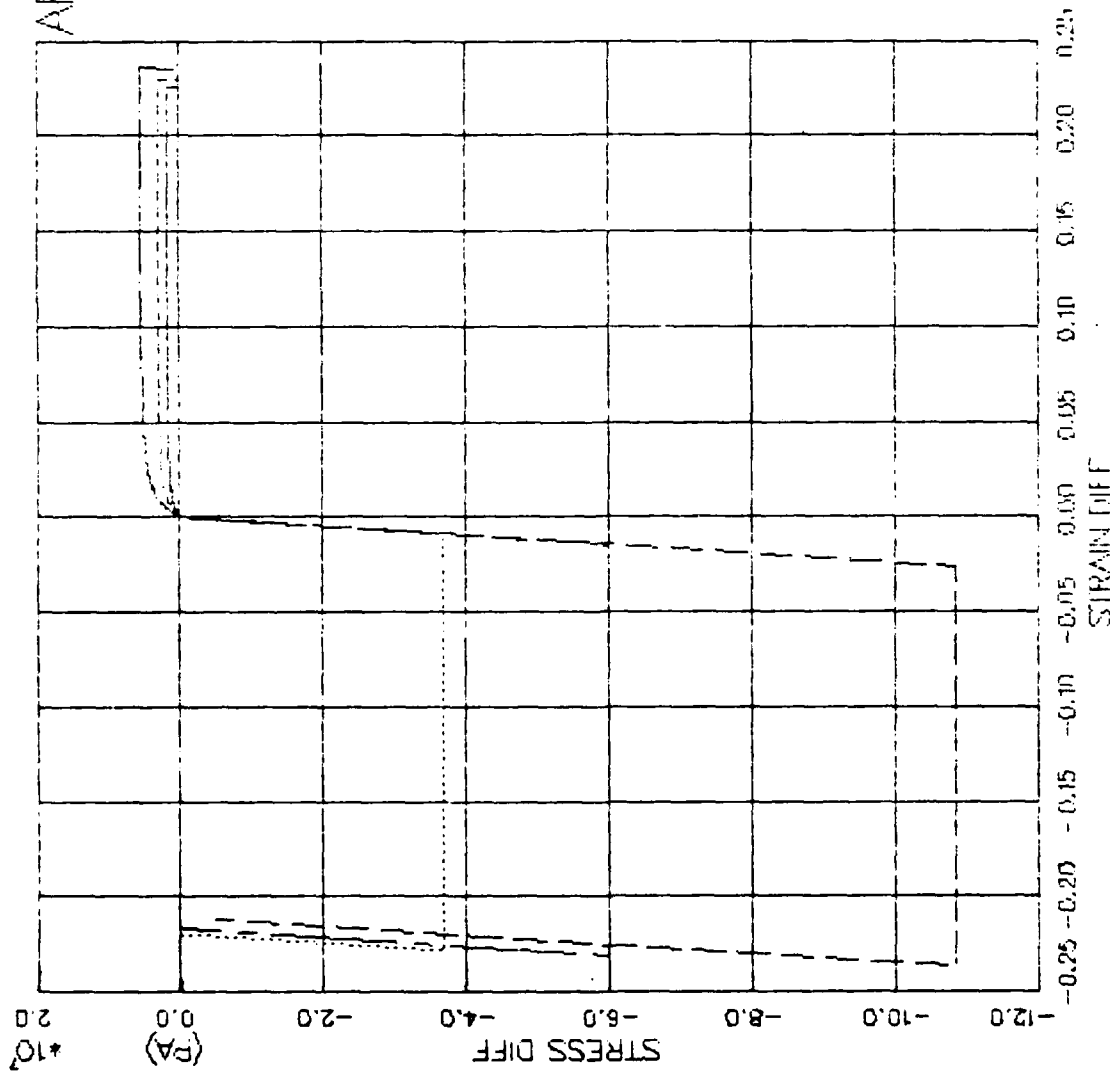
FIGURE V.3.16 HYPER MODEL EXT R- REDUCED TRIAX(RTC+RTE) — STRESS DIFF VS. STRAIN DIFF

364
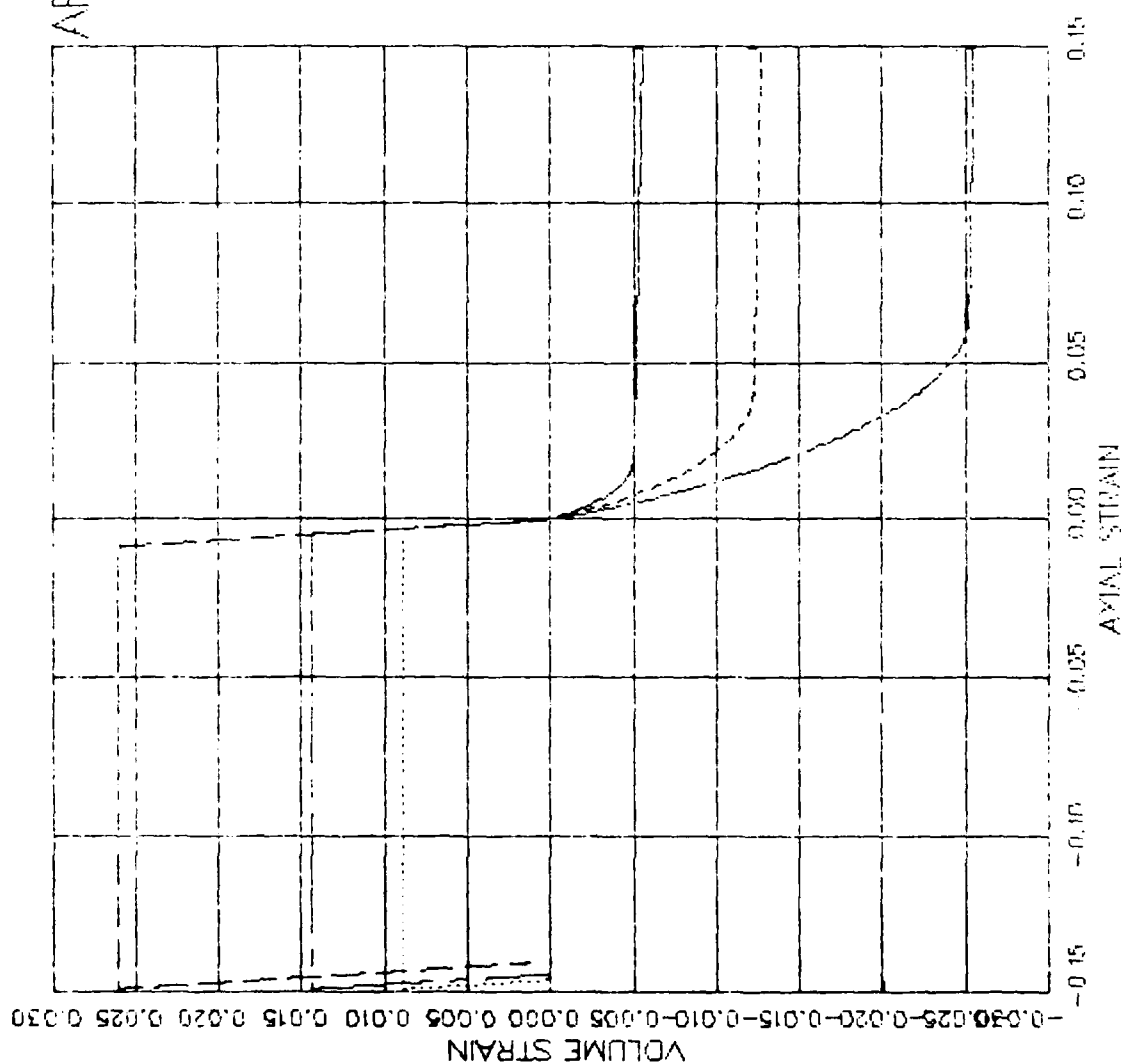
FIGURE V.3.17 HYPER MODEL FIXED—REDUCED TRIAX(FIC+RTC) – AXIAL STRAIN VS VOLUME STRAIN
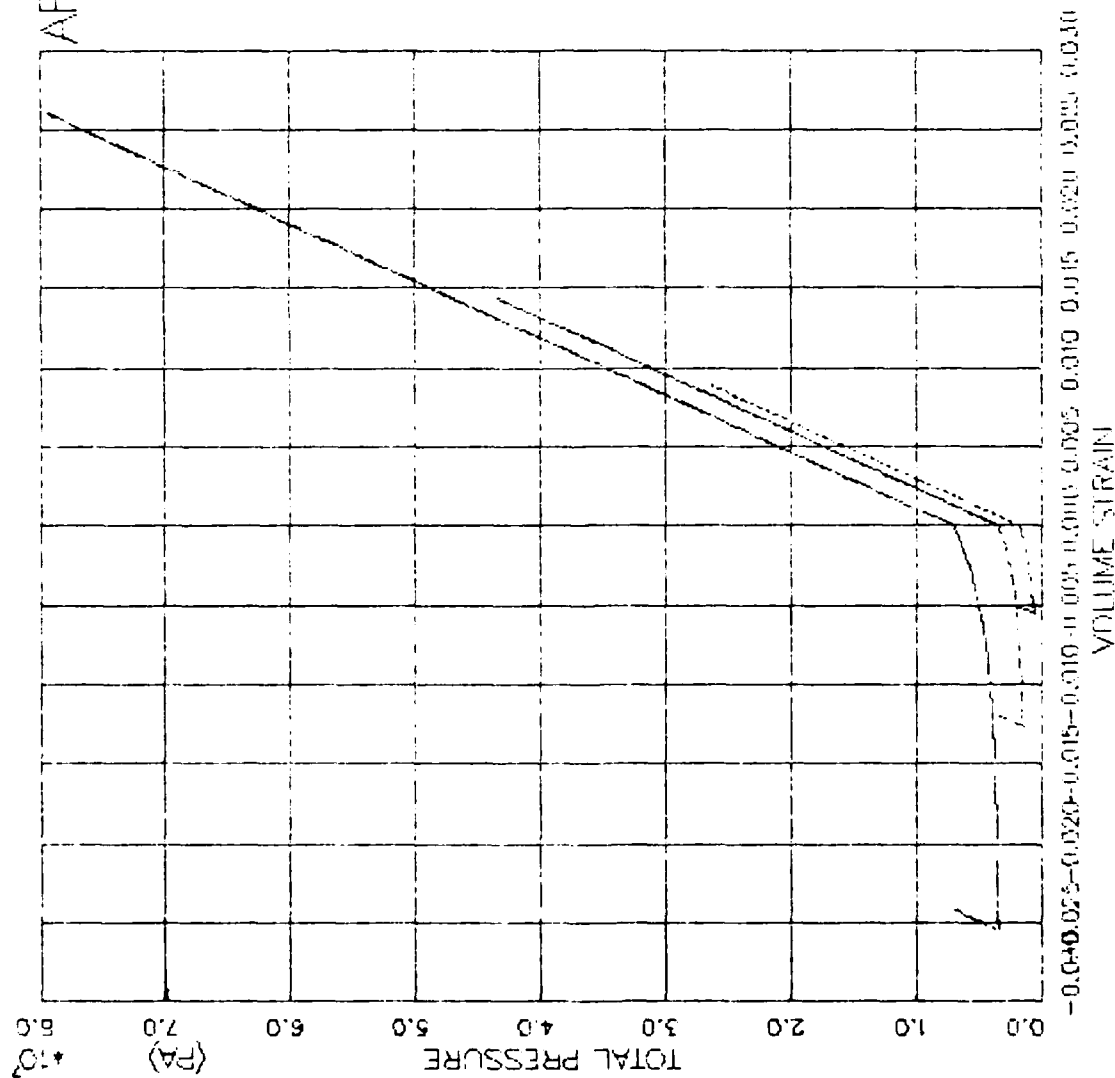
FIGURE V.3.18 HYPER MODEL EXER—REDUCED TRIAX(RTC-RTE) — PRESSURE VS. VOLUMETRIC STRA'
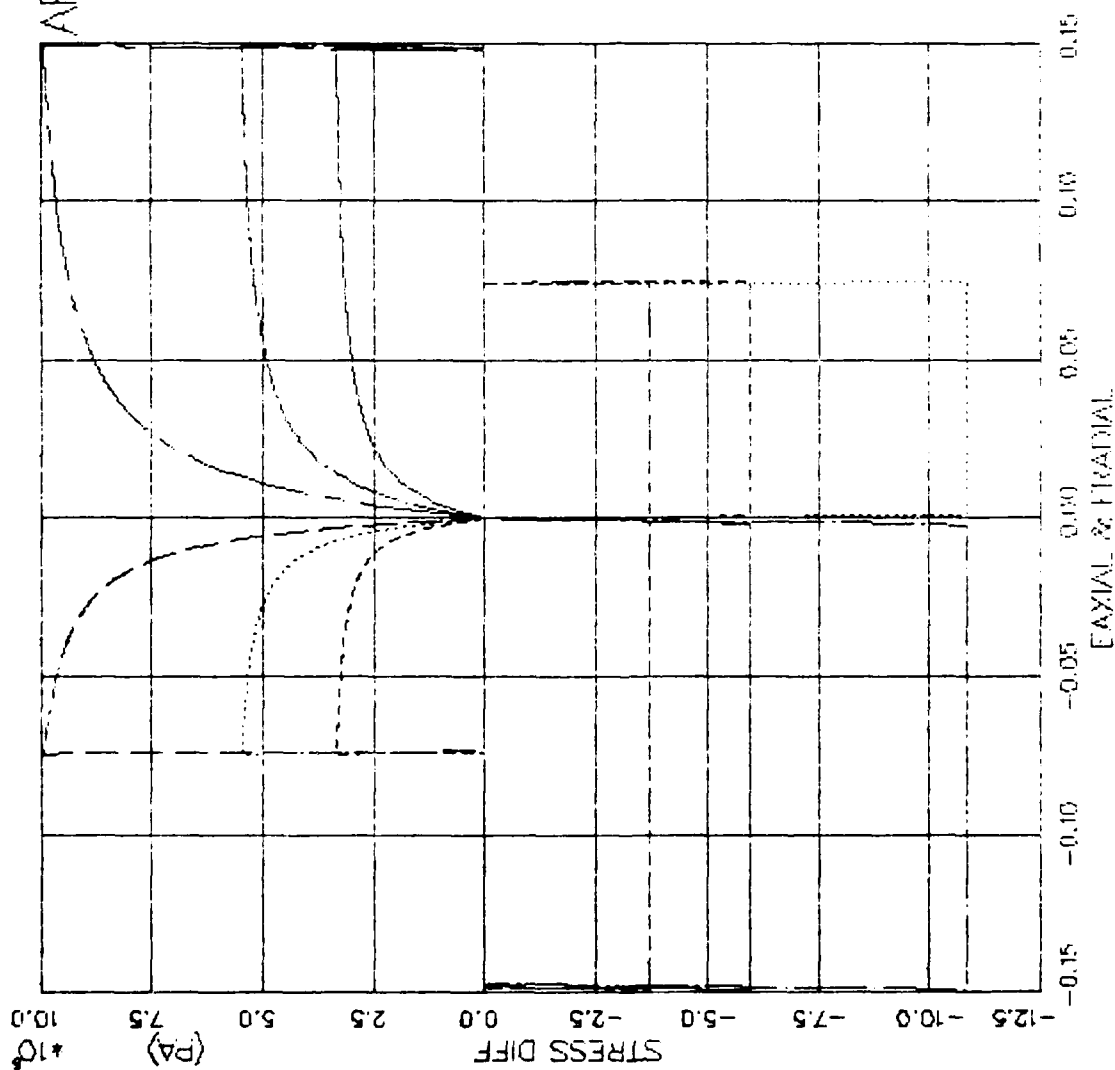
AFOSR SOIL ELEMENT MODEL

TEST = STANDARD TRIAXIAL
MODEL = HYPER
MATL = DRYCARES—REMOLD

LEGEND
PSC/S3C=1.8E6
PSC/S3C=1.8E6
PSC/S3C=3.5E6
PSC/S3C=3.5E6
PSC/S3C=7.1E6
PSC/S3C=7.1E6
PSE/S3C=1.8E6
PSE/S3C=1.8E6
PSE/S3C=3.5E6
PSE/S3C=3.5E6
PSE/S3C=7.1E6
PSE/S3C=7.1E6

FIGURE V.3.19 HYPER MODEL EXERCISE — PURE SHEAR AP(PSC+PSE) — STRESS DIFF VS. STRAIN

367
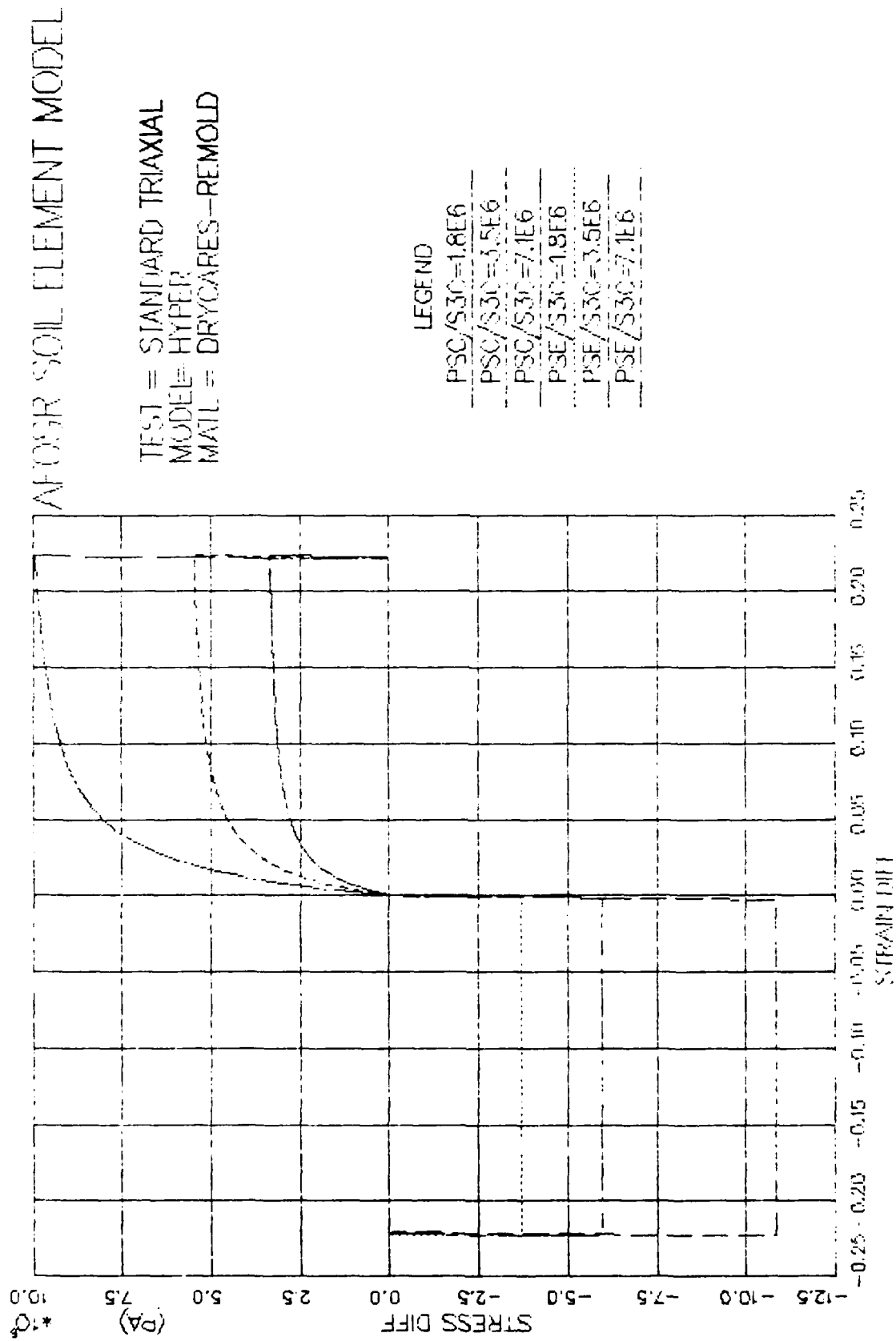
FIGURE V.3.20 HYPER MODEL EMBODIES --PURE SHEAR(PSC+PSE) -- STRESS DIFF VS. STRAIN DIFF

368
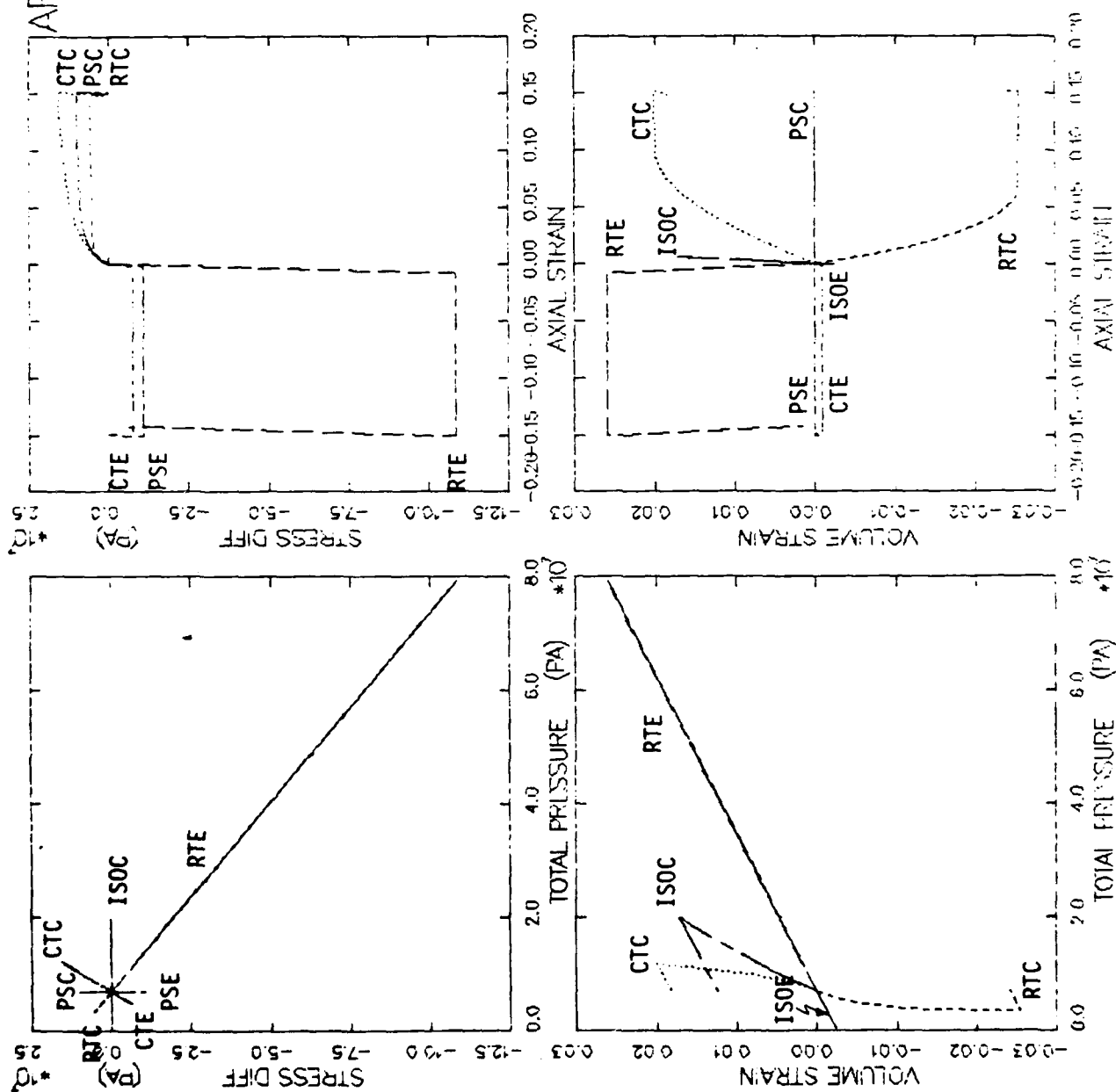
FIGURE V.3.21. HYPERBOLIC MODEL BEHAVIOR SUMMARY (7.1MPa) - SOIL/TP/AVTA ANALYSIS
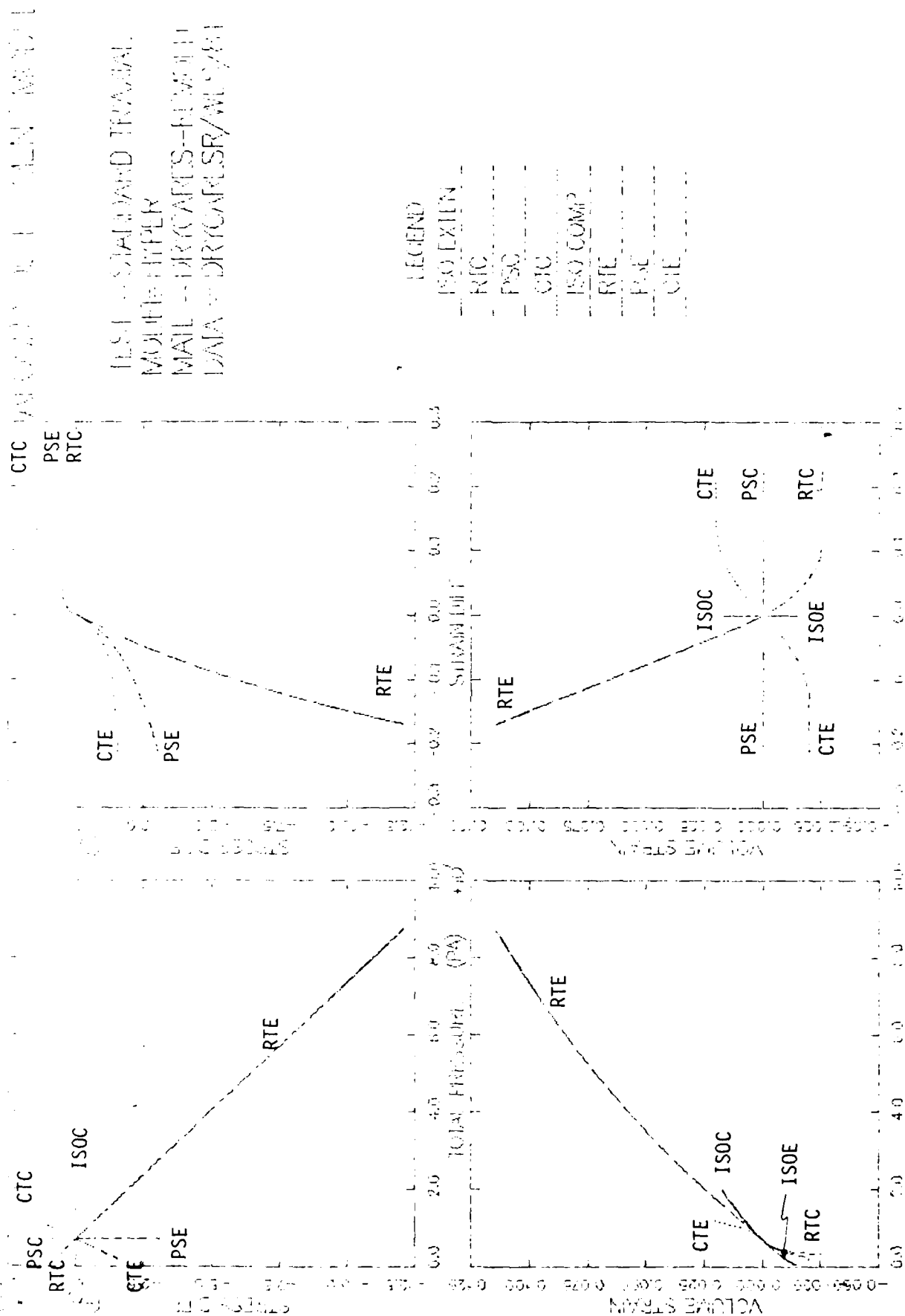
FIGURE V.3.22 THE MODAL MODEL (V.3.4.2) RESPONSE FOR ...

AFOSR SOIL ELEMENT MODEL

TEST = UNIAXIAL STRAIN
MODEL = HYPER
MATL = DRYCARES—REMOLD
DATA = DRYCARES.R/WES/84

LEGEND
CALCULATION
TEST DATA
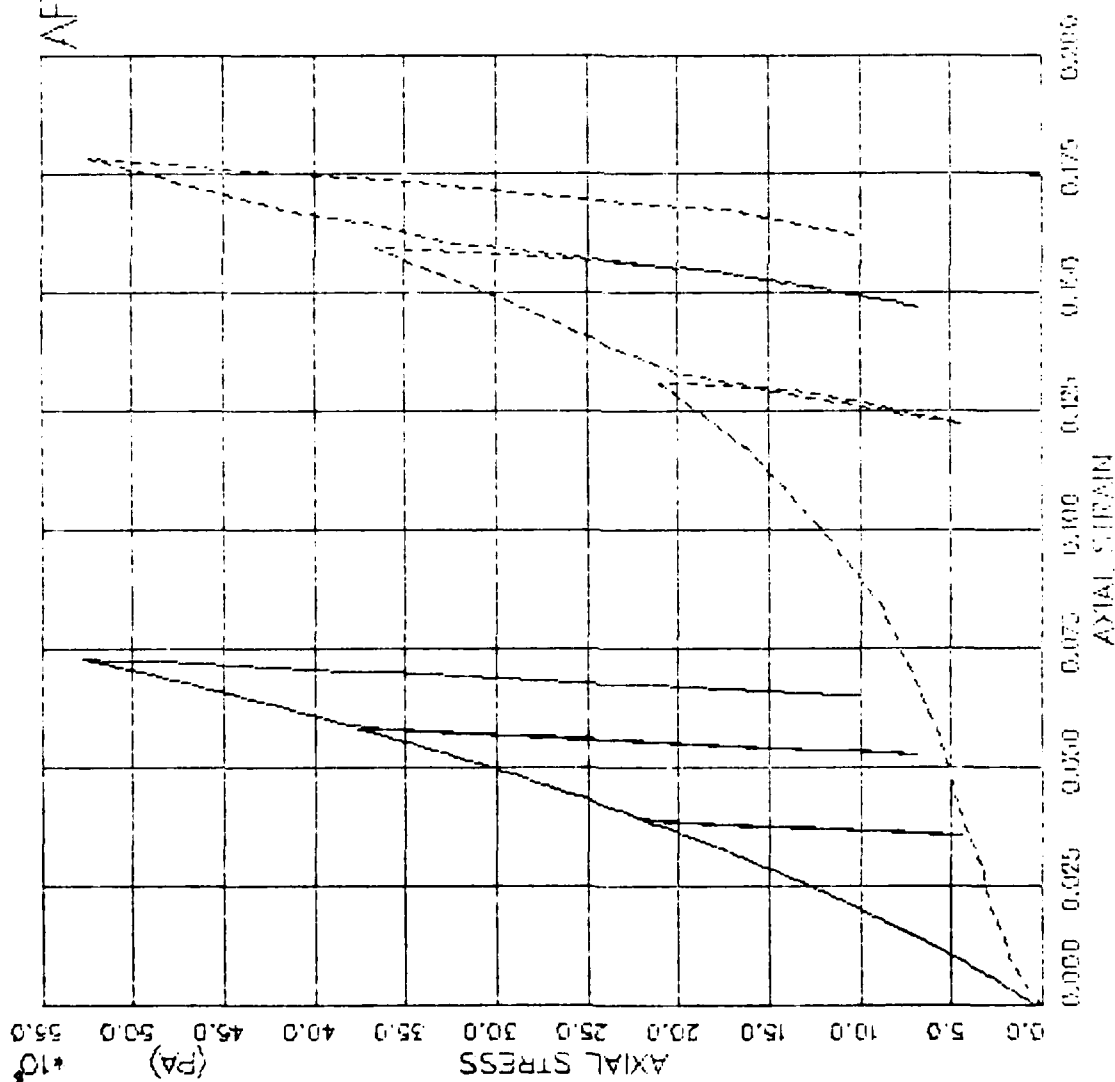
FIGURE V.3.23 HYPERBOLIC MODEL - UNIAXIAL STRAIN(MC) - TOTAL AXIAL STRESS VS. AXL STRAIN.
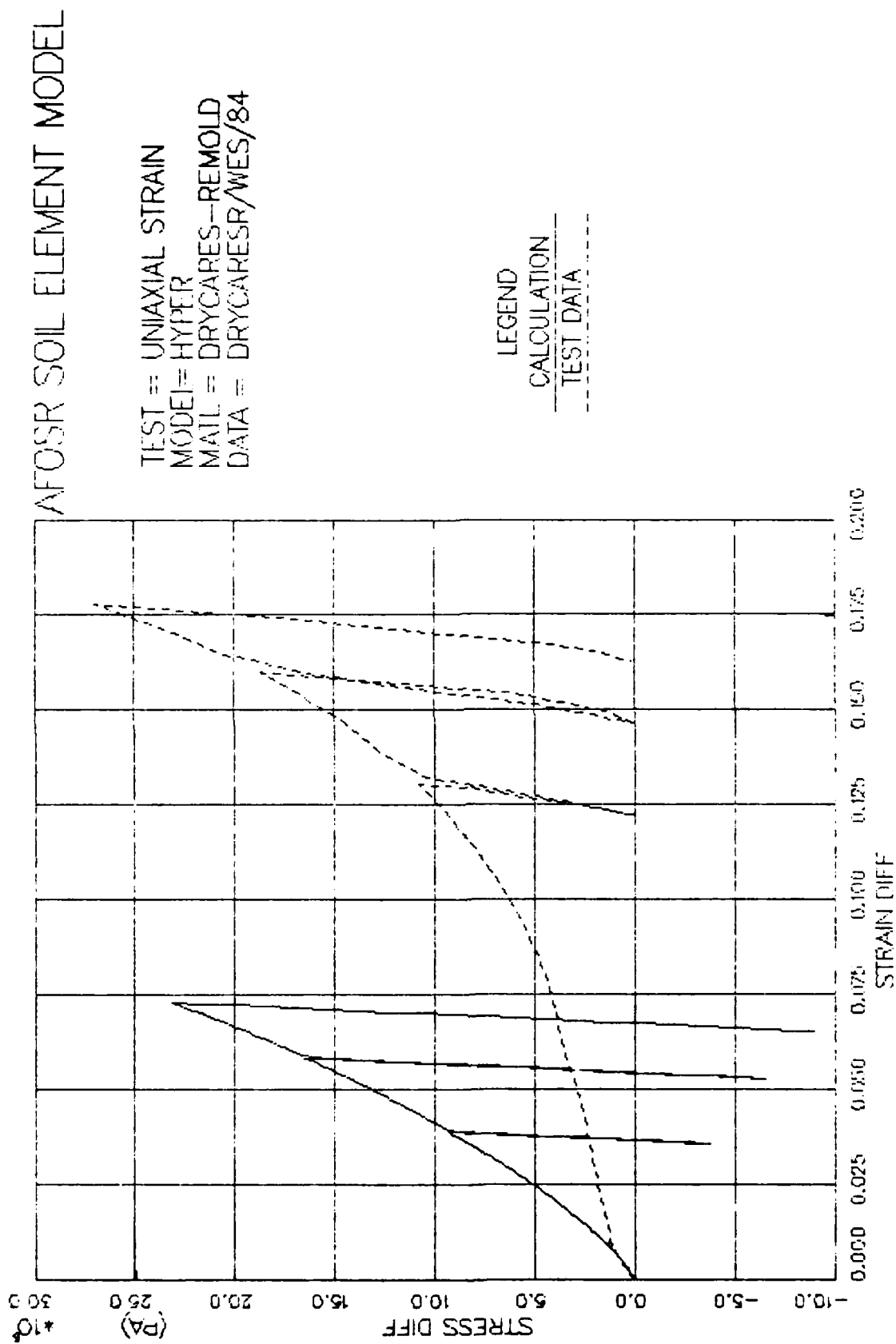
FIGURE V.3.24 HYPERBOLIC MODEL—UNIAXIAL STRAIN(UMC) — STRESS DIFF VS. STRAIN DIFF
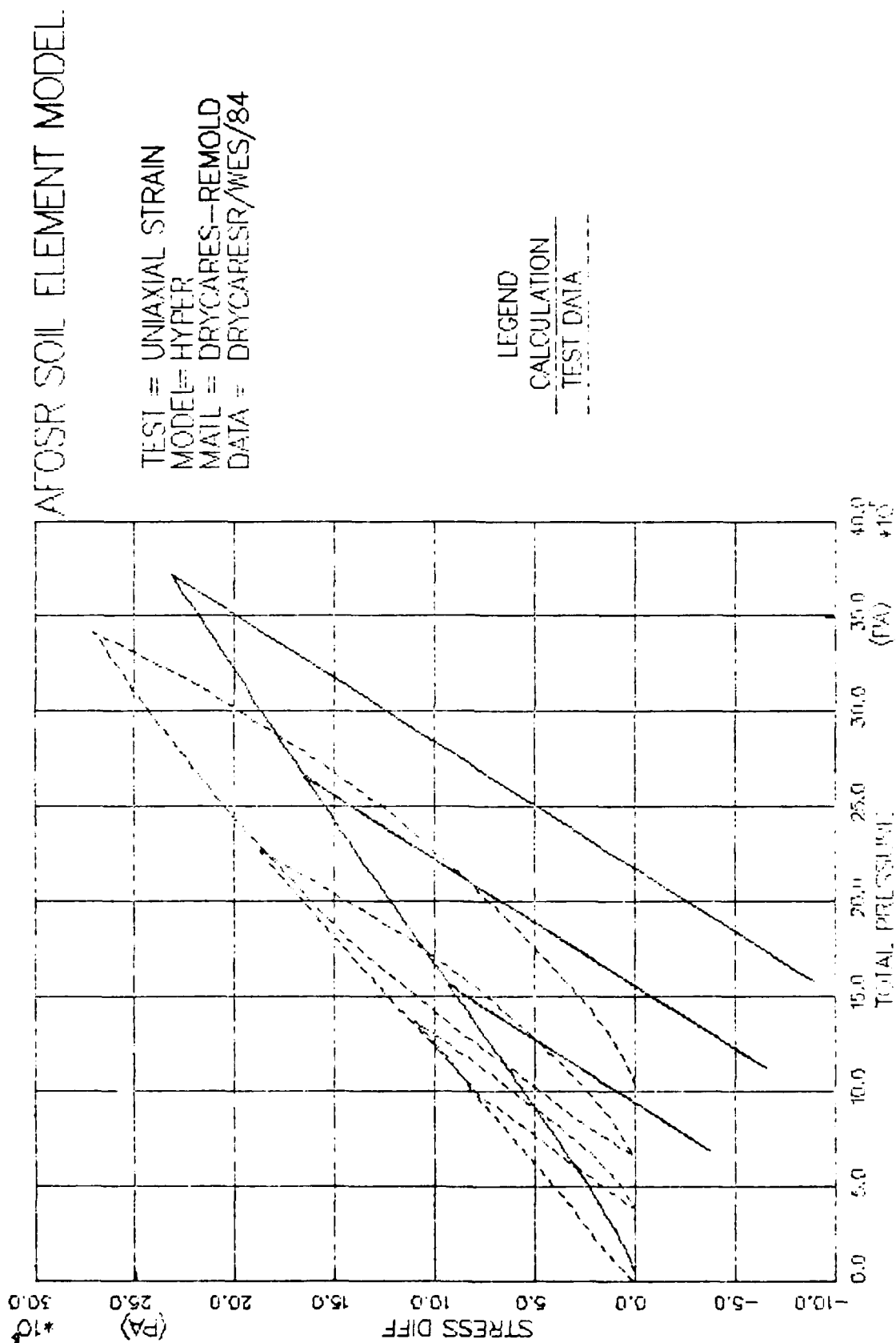
FIGURE V.3.25 HYPERBOLIC MODEL – UNIAXIAL STRAIN(UEC) – STRESS DIFFERENCE VS. PRESSURE

373
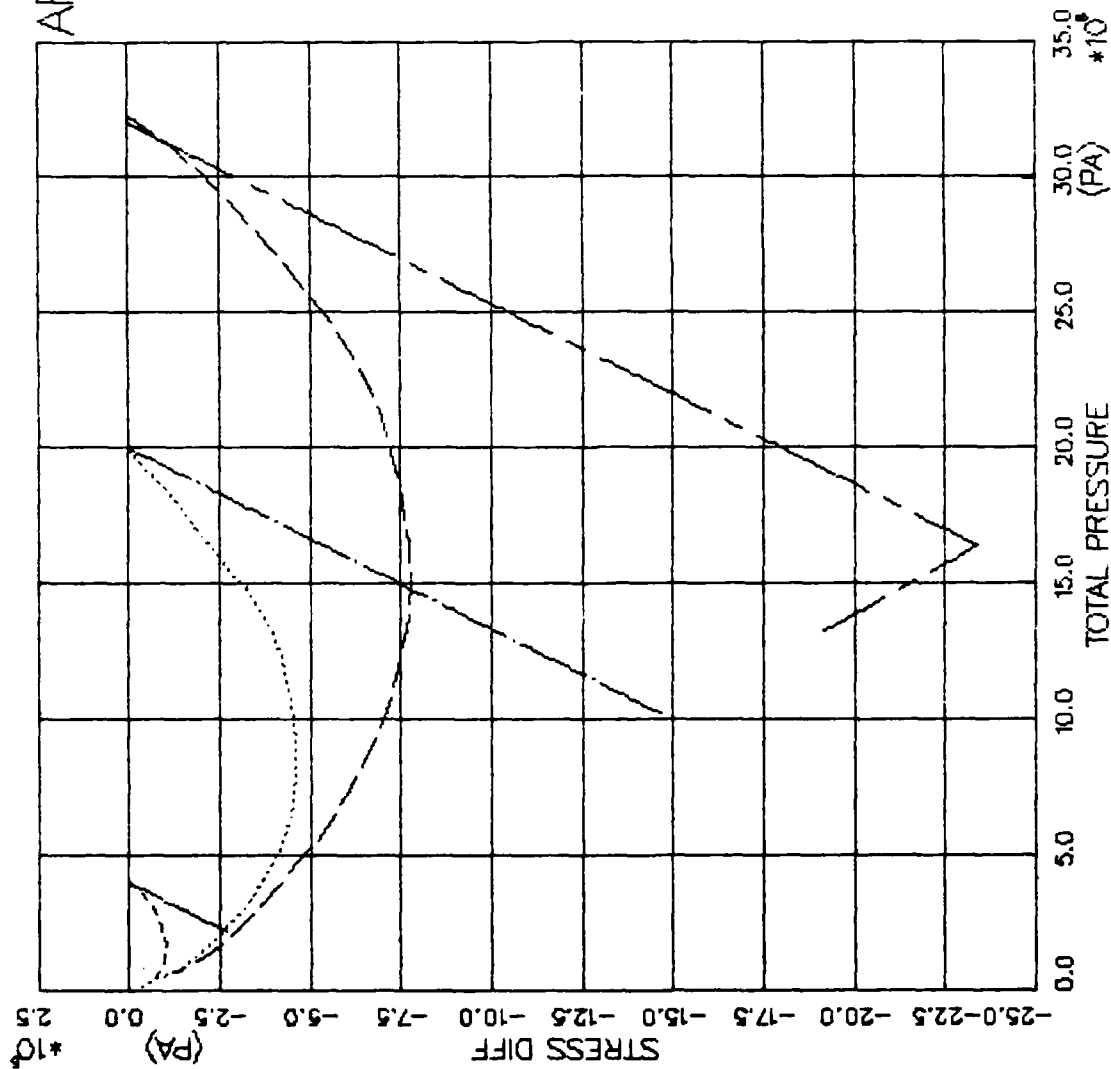
FIGURE V.3.26 HYPER MODEL EXERCISE—UNIAX STRAIN EXTEN (ICKO) — STRESS DIFFERENCE VS. PRE

AFOSR SOIL ELEMENT MODEL

TEST = UNIAXIAL STRAIN
MODEL= HYPER
MATL = DRYCARES—REMOLD
DATA = DRYCARESR/WES/84

LEGEND
S3C=4.0E6
TEST DATA
S3C=20.E6
TEST DATA
S3C=32.E6
TEST DATA
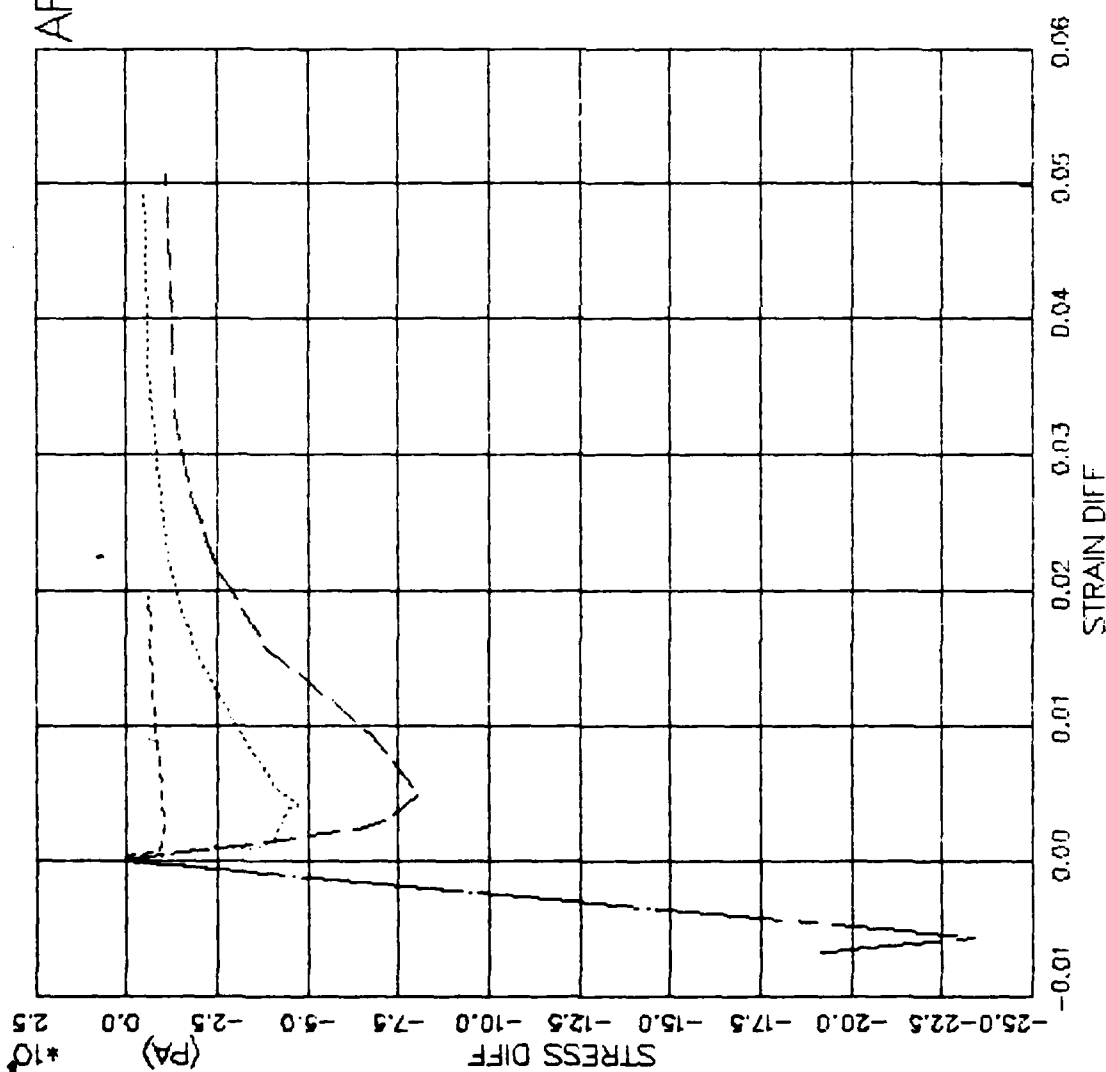
FIGURE V.3.27 HYPER MODEL EXERCISE—UNIAX STRAIN EXTEN (ICKO) -- STRESS DIFF VS. STRAIN DIFF
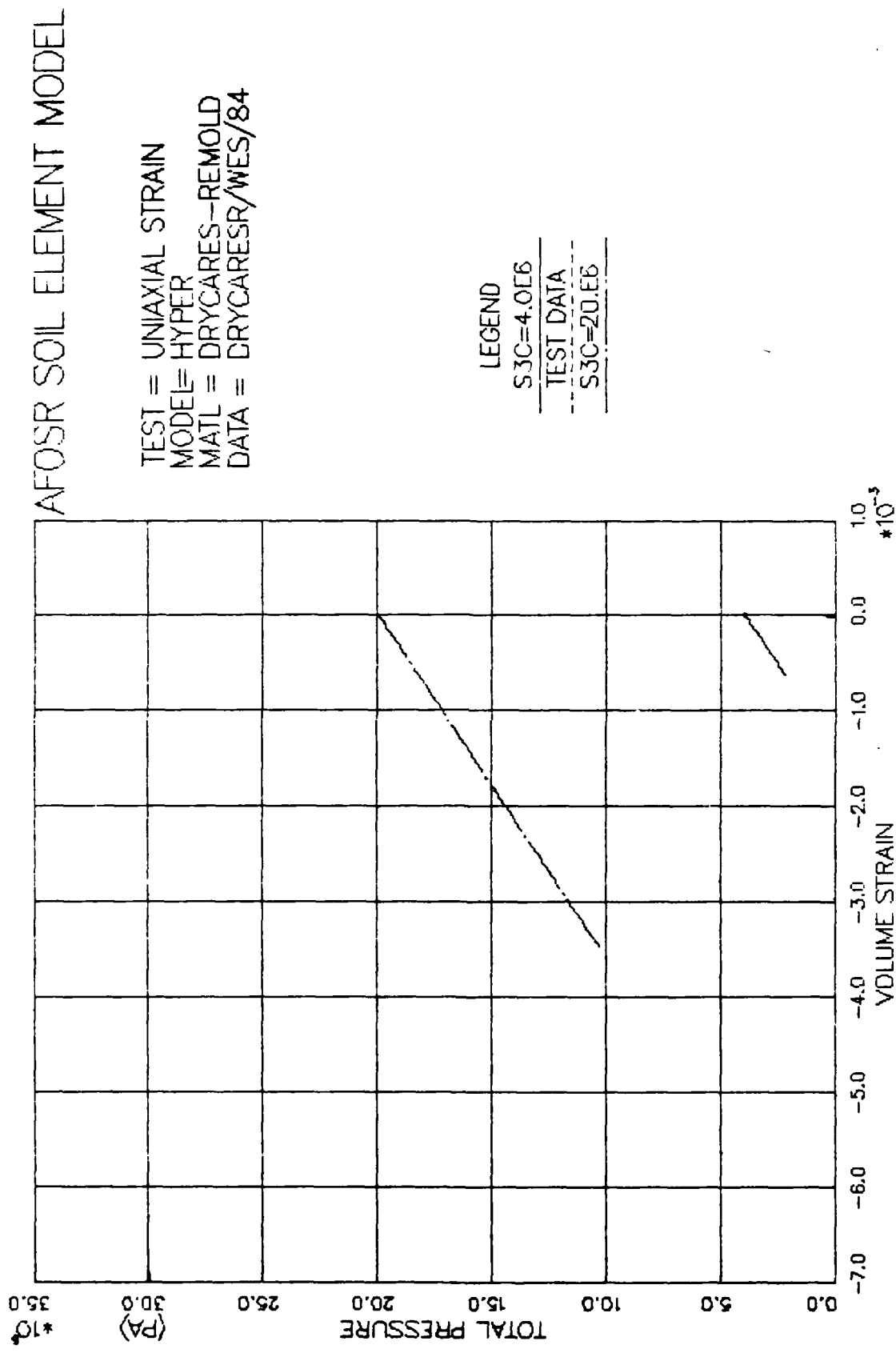
FIGURE V.3.28 HYPER MODEL EXERCISE—UNIAX STRAIN EXTEN (ICKO) — PRESSURE VS. VOLUMETRIC
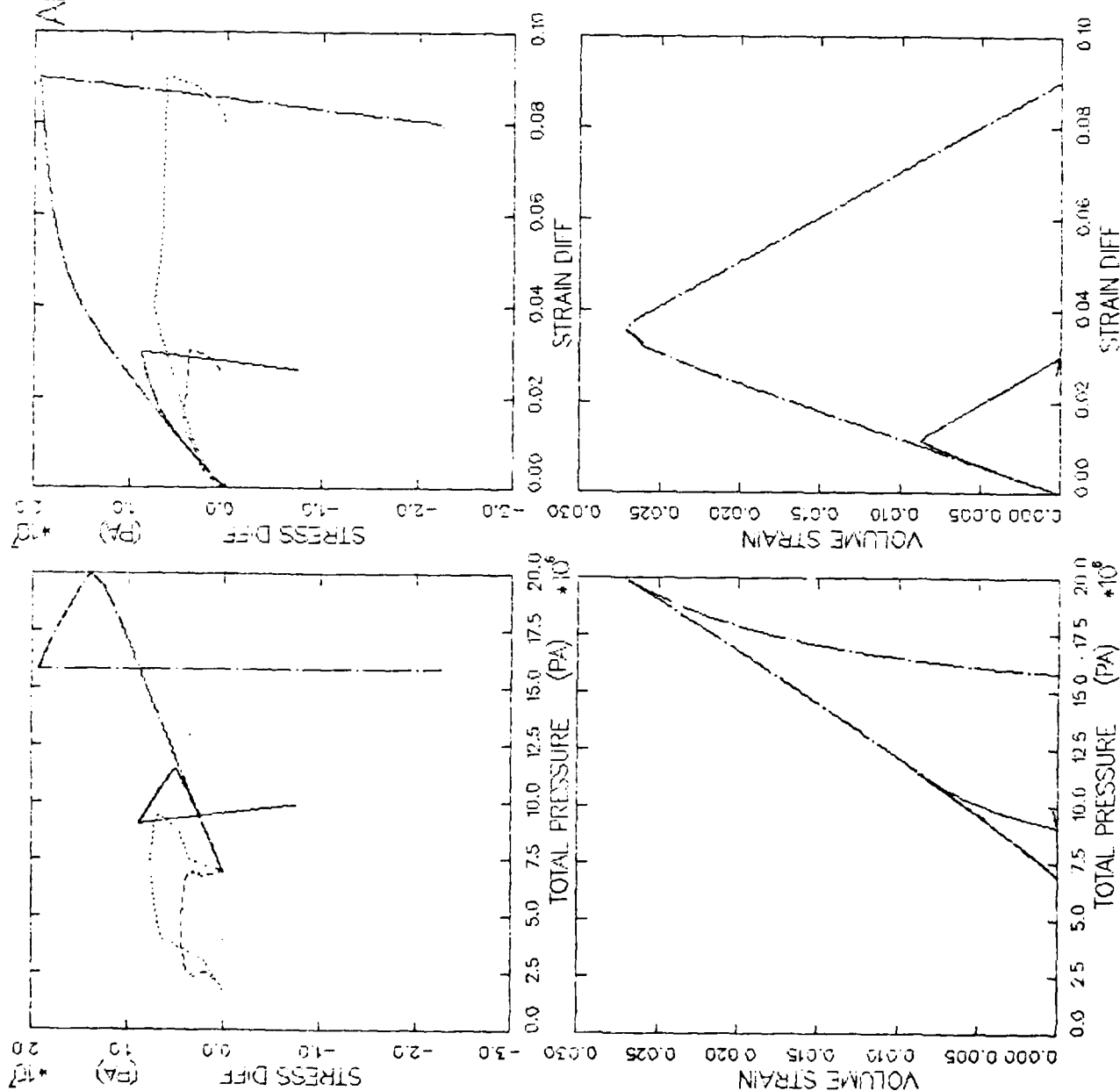
FIGURE V.3.29 HYPERBOLIC MODEL—WES AXISYM EPATH 3A+3C — SDIFF/P/EV/EDIFF ANALYSIS
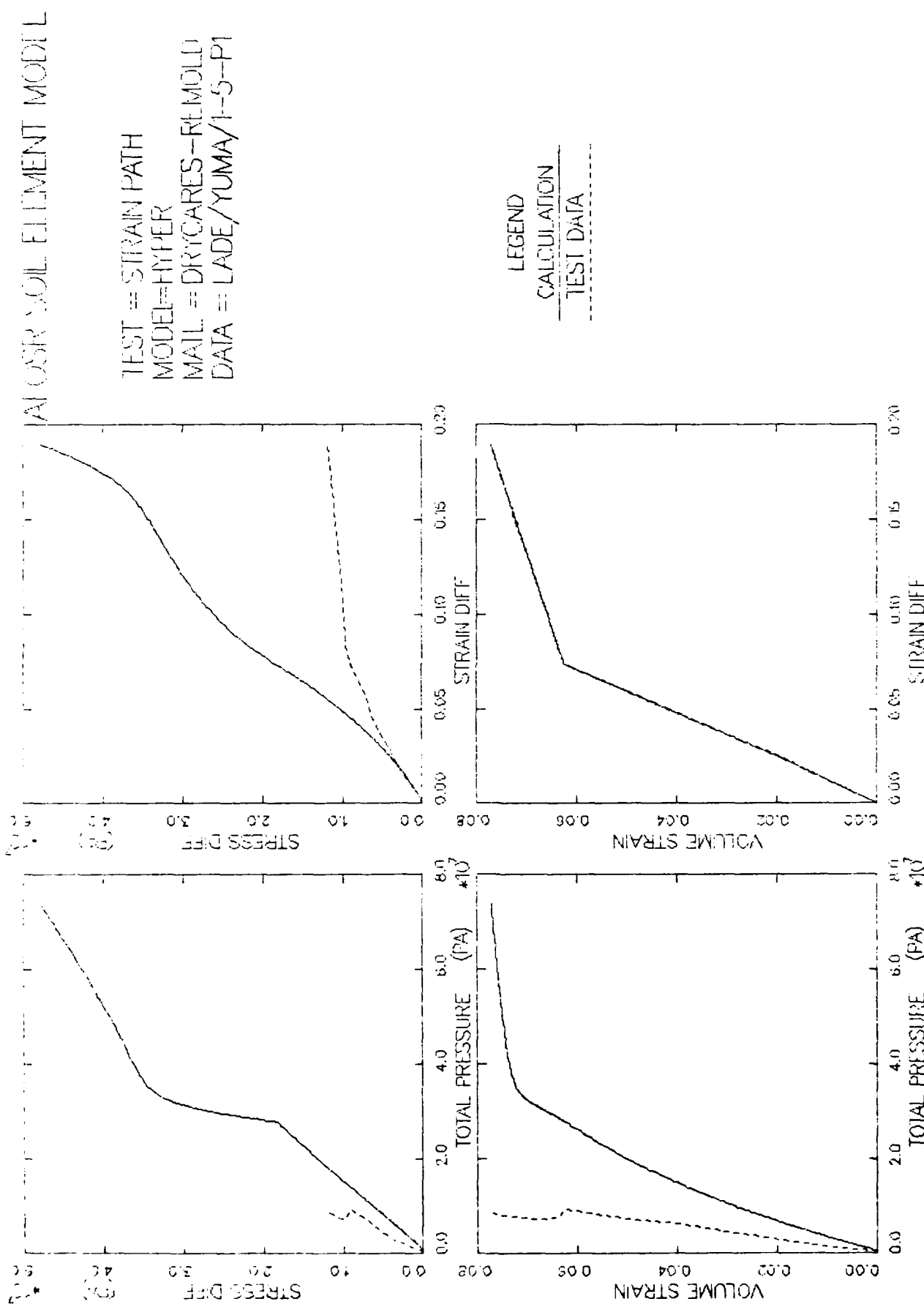
FIGURE V.3.30 HYPERBOLIC MODEL—LADE AXISYM DEPTH — SDIFF/A/V/V/DIFF ANALYSIS

AFOSR SOIL ELEMENT MODEL

TEST = STRAIN PATH
MODEL=HYPER
MATL = DRYCARES-REMOLD
DATA = LADE/YUMA/1-3-P2

LEGEND
CALCULATION
TEST DATA
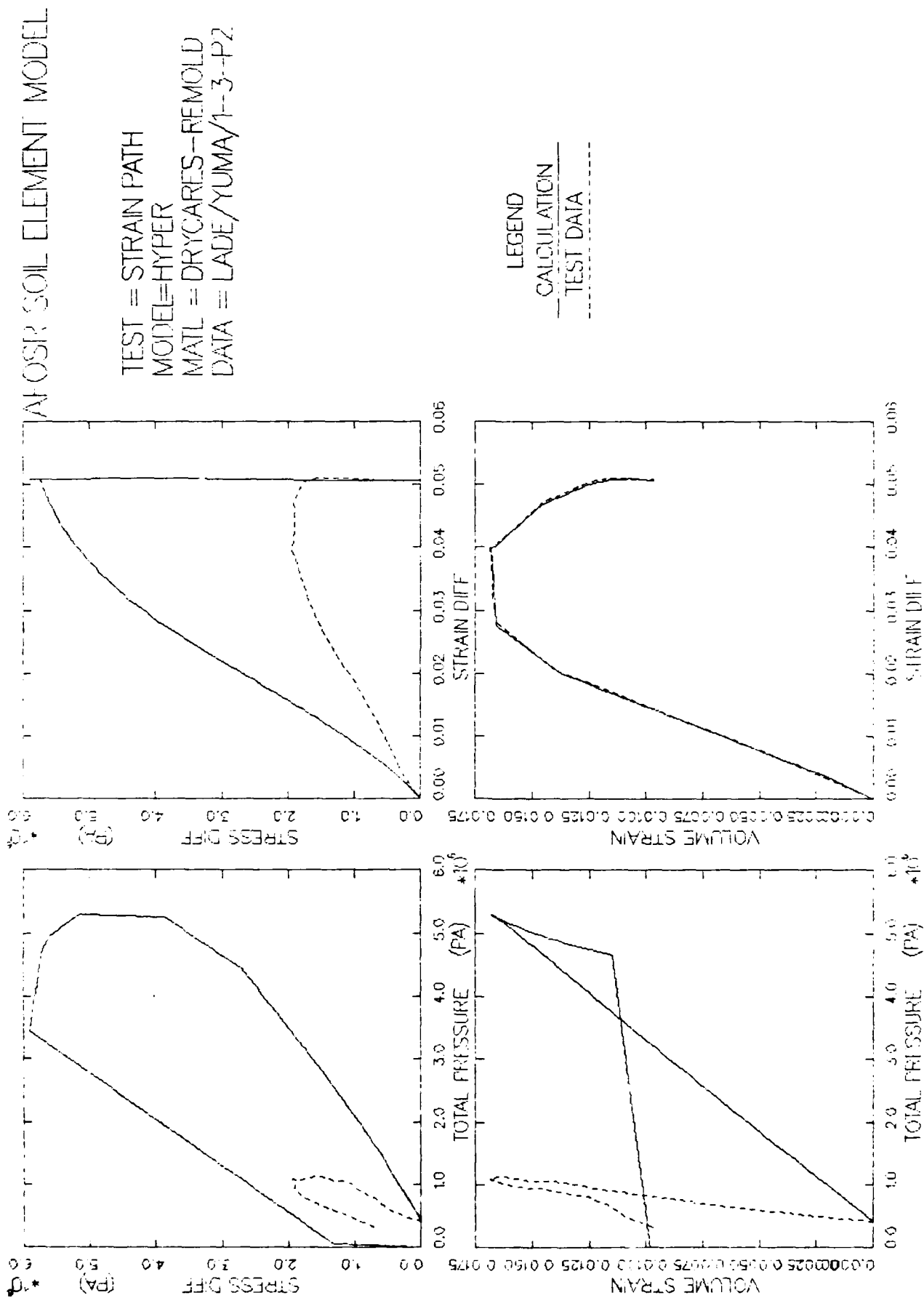
FIGURE V.3.31 HYPERBOLIC MODEL - LADE AXISYM-EFFALE - SOME/PAV/DIFF ANALYSIS
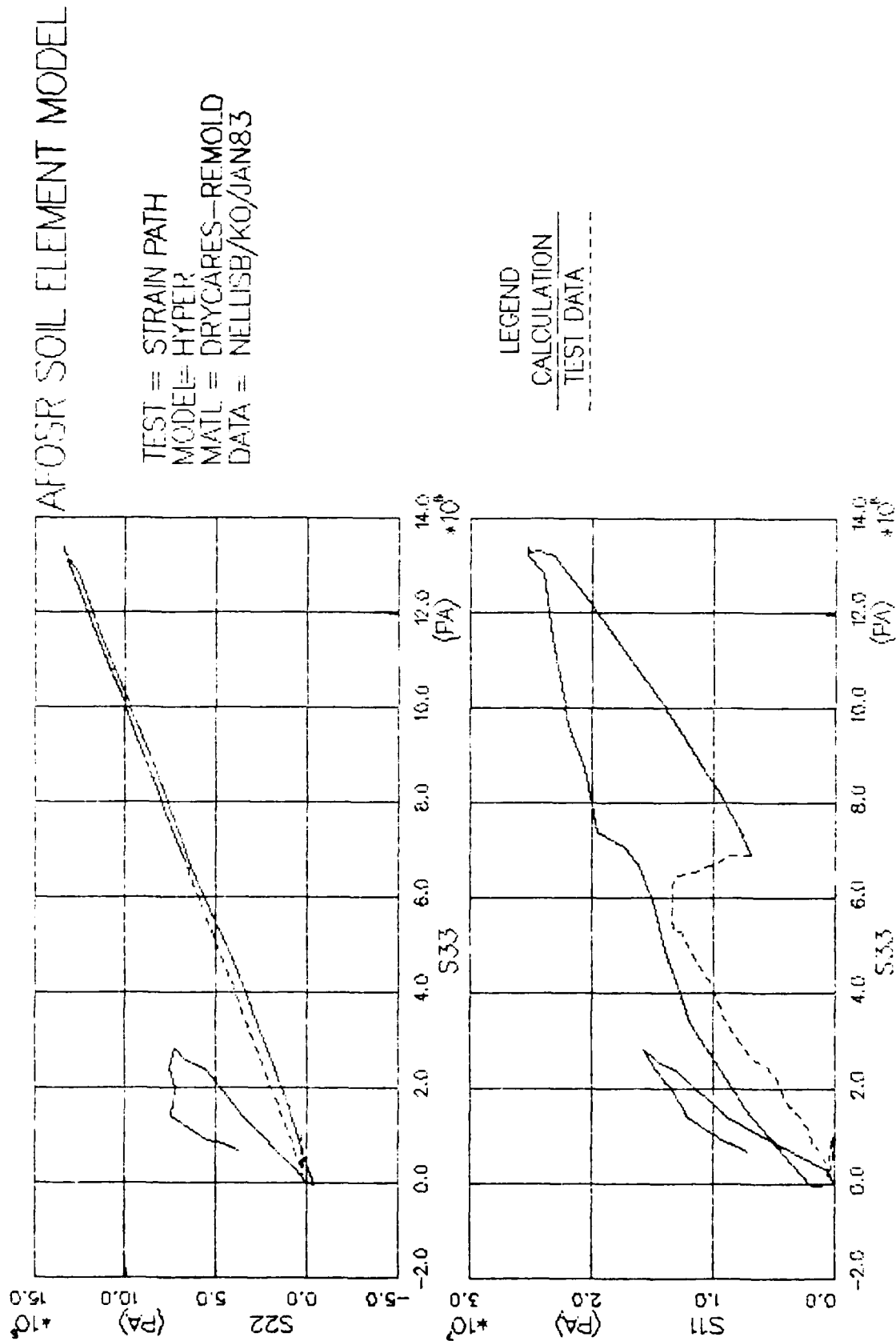
FIGURE V.3.32 HYPERBOLIC MODEL—TRUE TRIAX (PATH — PRINCIPAL STRESS PATH
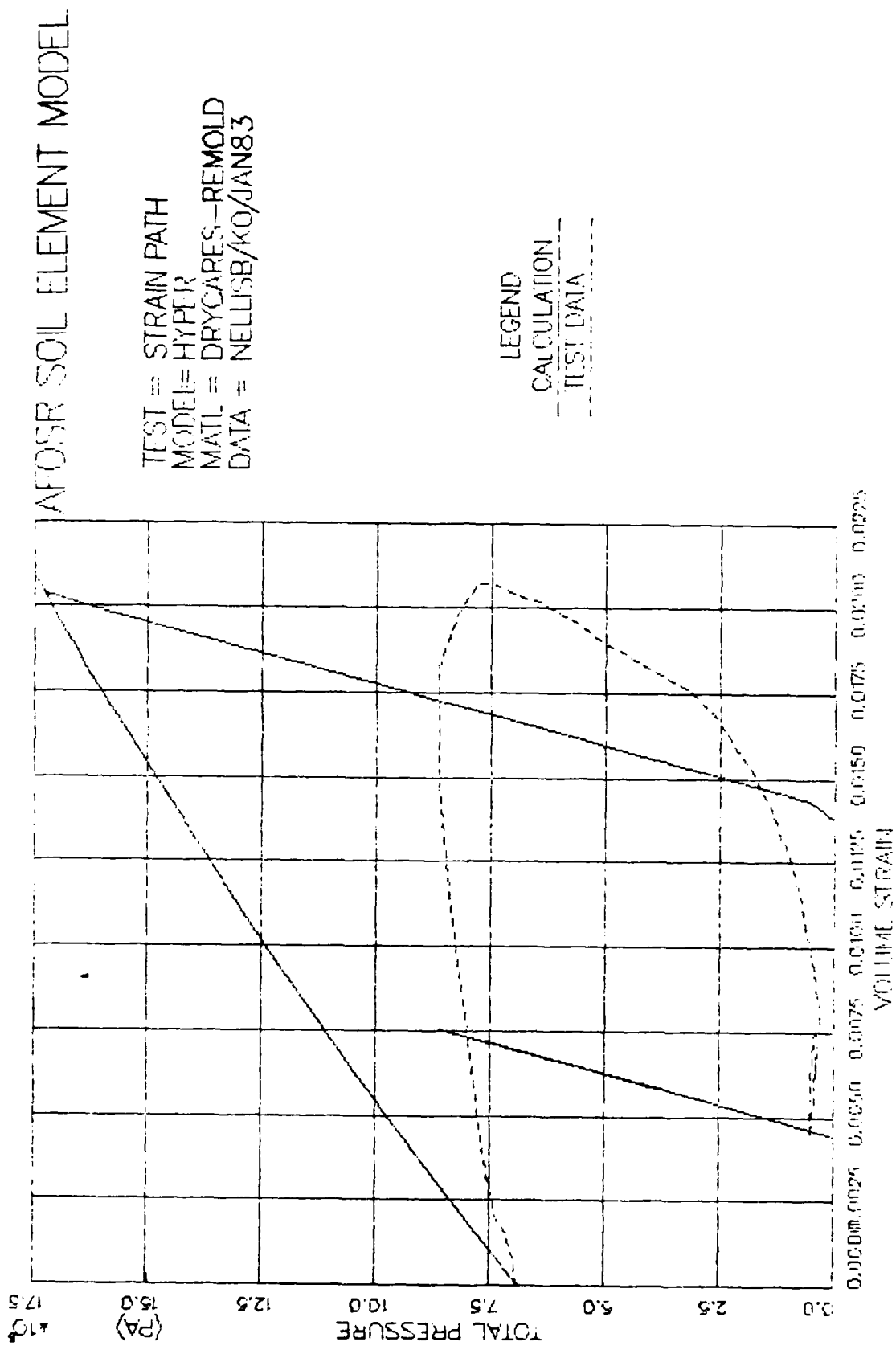
FIGURE V.3.33 HYPERBOLIC MODEL - TRUE TRIAX EPATH - PRESSURE VS. VOLUMETRIC STRAIN

V.4 Pyke Cyclic Simple Shear

V.4.1 Motivation

[Pyke (1979)] proposed a hyperbolic model for irregular cyclic simple shear, which, unlike Masing-type models, limits the peak shear stress under arbitrary loading. This is the model's principal advantage. Its principal disadvantage is its restriction to one-dimensional simple shear. In its present form, Pyke's model is not capable of handling general multiaxial stress-strain paths, because:

a) The asymptotic strength is prescribed as a single magnitude.

b) The tangent shear modulus is computed for simple shear about one axis only.

c) There is no provision for a second tangent elastic constant.

V.4.2 Assumptions

The basic assumption of the Pyke cyclic simple shear model is that the simple shear stress-strain curve between any two consecutive points of shear strain reversal is a hyperbola, with fixed initial slope immediately after shear strain reversal, and fixed upper and lower shear stress asymptotic limits of equal magnitude.

V.4.3 Basic Equations

The general relation between shear stress and shear strain for irregular cyclic simple shear is

$$\tau - \tau_c = \frac{G_{MAX}(\gamma - \gamma_c)}{1 + \left(\dfrac{G_{MAX}}{\tau_y^* - \tau_c}\right)(\gamma - \gamma_c)} \tag{V.4.1}$$

where γ, τ = simple shear strain and stress

γ_c, τ_c = simple shear strain and stress at last point of strain reversal

G_{MAX} = slope of the simple shear stress-strain curve immediately after strain reversal

τ_y = magnitude of the upper and lower shear stress asymptotic limits

and

$$\tau_y^* = \tau_y \text{ sgn } (d\gamma) \qquad (V.4.2)$$

Equations (V.4.1) and (V.4.2) are derived in Appendix O, and are identical to Equations (O.4) and (O.5). Differentiation of Equation (V.4.1) yields the tangent shear modulus,

$$\frac{d(\tau - \tau_c)}{d(\gamma - \gamma_c)} = G_T = \frac{G_{MAX}}{\left[1 + \left(\frac{G_{MAX}}{\tau_y^* - \tau_c}\right)(\gamma - \gamma_c)\right]^2} \qquad (V.4.3)$$

Equation (V.4.3) is identical to Equation (O.6).

V.4.4 Parameter Determination

The parameters G_{MAX} and τ_y are determined from the virgin simple shear stress-strain curve for monotonic loading, using a plot of τ/γ versus τ based on the linear form of Equation (V.4.1) when

$$\gamma_c = \tau_c = 0,$$

which is

$$\frac{\tau}{\gamma} = G_{MAX}\left(1 - \frac{\tau}{\tau_y}\right) \qquad (V.4.4)$$

Equation (V.4.4) is identical to Equation (O.8), and the corresponding plot is shown in Figure (O.2).

383

Table (V.4.1) shows the parameters which were used for illustrating the behavior of Pyke's 1-D shear model. The parameters were chosen somewhat arbitrarily, as no simple shear test data is available for CARES-DRY Sand.

V.4.5 Computed Behavior

Figure (V.4.1) is the behavior predicted for simple shear by Pyke's model. The test shown consisted of three fully-reversed cycles of shear strain at each of three maximum strain levels: 0.5 percent, 2 percent, and 4 percent. The important features of the model's response are:

(a) ratcheting of stress-strain loops upon cycling at a given strain limit

(b) softening of response at progressively higher strain magnitudes

(c) stiffened response upon reversal of strain direction

The model, as it is currently implemented in the SEM, is not general enough to handle the suite of exercises performed for the other models in this report.

TABLE V.4.1. PYKE MODEL PARAMETERS FOR CARES-DRY SAND

Parameter	Symbol	Variable	Value	Units
Yield Shear Stress	y	TAUY	1.0×10^6	Pa
Maximum Shear Modulus	G_{max}	GMAX	1.0×10^8	Pa
Mass Density	ρ	PHOREF	1900	kg/m^3

FIGURE V.4.1 PYKE MODEL EXERCISE — CYCLIC SHEAR — SHEAR STRESS vs. SHEAR STRAIN

ABAQUS SOIL ELEMENT MODEL

TEST = PURE SHEAR TEST
MODEL = PYKE
MATL = DRYCARES-REMOLD

386

V.5 Elastic-Perfectly Plastic

V.5.1 Motivation

The principal advantages of an elastic-perfectly plastic model are that it incorporates stress state limits observed in laboratory strength tests, and produces inelastic strains when a limiting stress state is reached. The principal disadvantages are that nonlinear, inelastic behavior does not occur until the failure surface is reached, and, with an associated flow rule, predicted plastic volume increases at failure are frequently too large.

V.5.2 Assumptions

An elastic-perfectly plastic, rate independent model assumes the material remains linearly elastic until a limiting state of stress is reached, defined by a failure criterion based on strength test data. Neither stress nor strain rate affects the stress-strain relation. Inelastic strains occur only at failure. The flow rule can be associative or non-associative.

V.5.3 Basic Equations

The particular elastic-perfectly plastic model studied here has a modified, associative Drucker-Prager failure criterion [DiMaggio and Sandler (1971:942)], of the form

$$f\left(I_1, \sqrt{J_2}\right) = \sqrt{J_2} - \left(A - Ce^{-BI_1}\right) = 0 \qquad (V.5.1)$$

When the stress point lies below the failure surface, so that

$$f\left(I_1, \sqrt{J_2}\right) < 0 \qquad (V.5.2)$$

the material behaves elastically, in accordance with the equations of Appendices V and J. When a stress increment calculated assuming elastic

behavior moves the stress point through the failure surface, so that

$$f\left[(I_1)_E, (\sqrt{J_2})_E\right] = \delta > 0 \qquad (V.5.3)$$

a correction procedure is invoked to return the stress point to the
failure surface. The correction procedure is developed in Appendix P. It
starts by computing

$$d\lambda = \frac{\delta}{9Kf_I^2 + Gf_{II}^2} \qquad (V.5.4)$$

where K, G = elastic bulk and shear moduli

$$f_I = \left(\frac{\partial f}{\partial I_1}\right)_E = -BCe^{-B(I_1)_E} \qquad (V.5.5)$$

$$f_{II} = \left(\frac{\partial f}{\partial \sqrt{J_2}}\right)_E = 1 \qquad (V.5.6)$$

Adjustments to the elastically computed invariant stress point coordinates
are then computed using the equations

$$(I_1)_{ADJ} = (I_1)_E - 9Kf_I d\lambda \qquad (V.5.7)$$

$$\left(\sqrt{J_2}\right)_{ADJ} = \left(\sqrt{J_2}\right)_E - Gf_{II}d\lambda \qquad (V.5.8)$$

$$\{s\}_{ADJ} = \sqrt{\frac{(J_2)_{ADJ}}{(J_2)_E}} \{s\}_E \qquad (V.5.9)$$

Unless

$$f\left[(I_1)_{ADJ}, (\sqrt{J_2})_{ADJ}\right] \le 0 \qquad (V.5.10)$$

the correction procedure is repeated.

V.5.4 Parameter Determination

The elastic bulk and shear moduli, K and G, are determined by the
methods described in Appendices V and J. The failure criterion

388

parameters, A, B, and C, are determined by nonlinear regression or simply by eye, using shear strength data and the relations

$$\lim_{I_1 \to 0} \sqrt{J_2} = A - C \qquad (V.5.11)$$

$$\lim_{I_1 \to \infty} \sqrt{J_2} = A \qquad (V.5.12)$$

$$\lim_{I_1 \to 0} \frac{\partial \sqrt{J_2}}{\partial I_1} = -BC \qquad (V.5.13)$$

Parameters for the elastic-perfectly plastic model exercises are shown in Table V.5.1. The bulk and shear moduli and density are equal to those chosen for the elastic model. The only difference between the models is the introduction of a shear failure surface.

V.5.5 Computed Behavior

The behavior of the elastic and elastic-plastic models is identical for isotropic compression [Figure (V.5.1)] and uniaxial strain compression [Figures (V.5.17-V.5.19)]. Note that the uniaxial strain compression stress path lies entirely under the failure surface [Figure (V.5.18)] for these parameters. CTC and CTE stress-strain behavior [Figures (V.5.2-V.5.9)] is much improved over the elastic model by the failure surface, but only for lower confining pressures ($\sigma_{3c} < 10$ MPa). A non-associated flow rule was used here, so the tendency for this material to dilate with shearing is not predicted [Figures (V.5.2-V.5.5) for CTC, and Figures (V.5.6-V.5.9) for CTE].

The RTC/E [Figures (V.5.10-V.5.13)] and PSC/E [Figures (V.5.14-V.5.15)] calculated behavior again shows elastic behavior until

the stress path reaches the failure surface. Behavior in the triaxial cell as predicted by the elastic-perfectly plastic model is summarized in Figure (V.5.16).

Predicted UXE behavior [Figures (V.5.20) and (3.5.21)] is more like the data than the elastic model because of the addition of the failure surface, but still does not match the overall shape of the observed stress path.

The results of the axisymmetric strain path calculations are shown in Figures (V.5.22) (WES paths) and (V.5.23-V.5.24) (Lade paths). In both cases the bulk modulus is too high in comparison with the data, and so is the shear modulus for the Lade paths. The true-triaxial strain path has a similar problem as seen in Figures (V.5.25) and (V.5.26).

TABLE V.5.1. ELASTIC-PERFECTLY PLASTIC MODEL
PARAMETERS FOR CARES-DRY SAND

Parameter	Symbol	Variable	Value	Units
Bulk Modulus	K	BULK	3.76×10^8	Pa
Shear Modulus	G	SHEAR	1.44×10^8	Pa
	A	CA	2.88×10^5	Pa
Failure Surface	B	CB	0.00	1/Pa
Constants	C	CC	0.00	Pa
	M	CAM	0.215	--
Tension Cutoff	T	TCUT1	6.0×10^4	Pa
Flow Rule Switch*	-	RULE	1.0	--
Mass Density	ρ	PHOREF	1900	kg/m^3

*0.0 = Associated
 1.0 = Non-Associated (von Mises plastic potential)
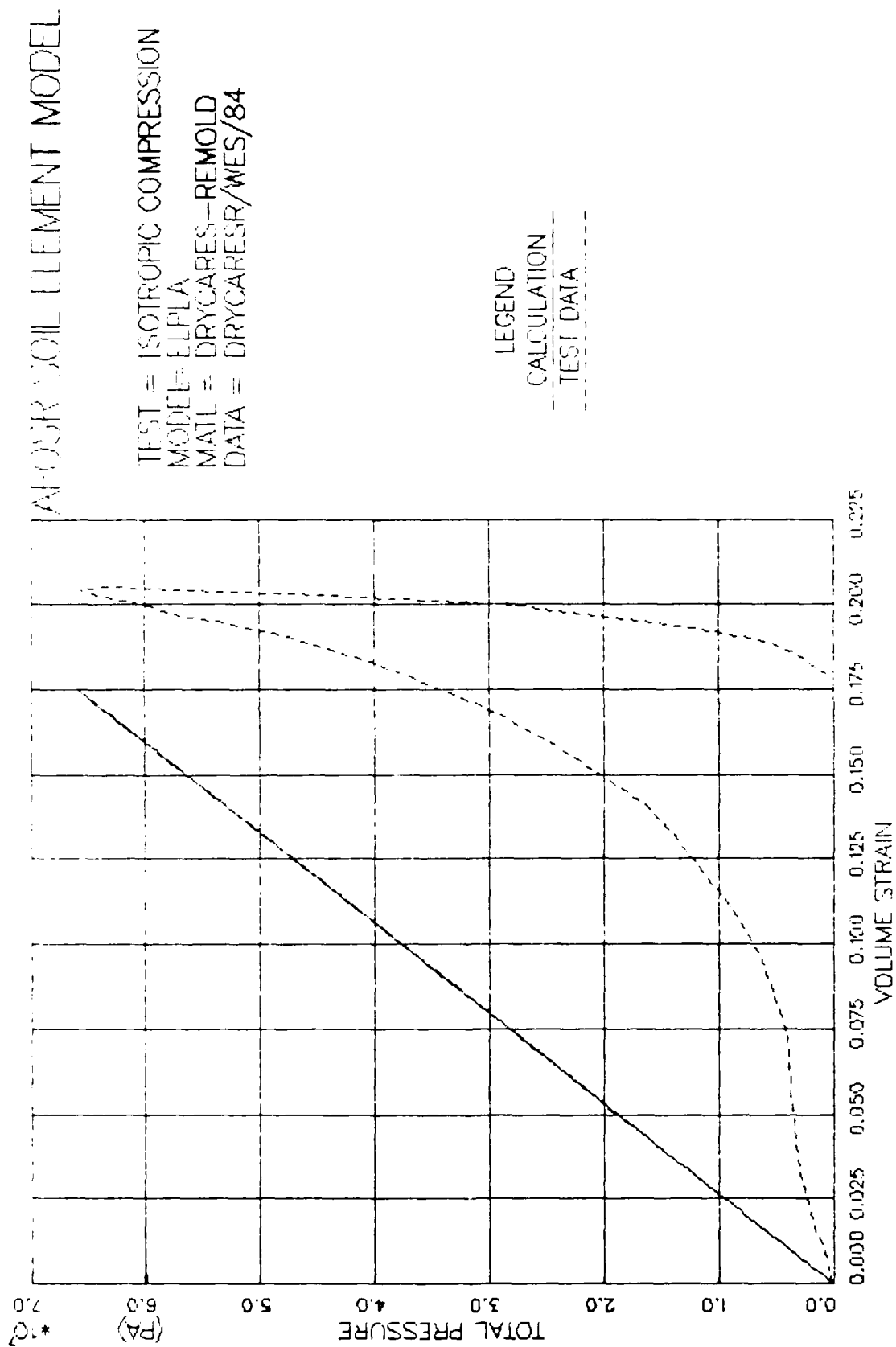
FIGURE V.5.1 ELPLA MODEL EXERCISE — ISOTROPIC COMP. — PRESSURE VS. VOLUMETRIC STRAIN .

FIGURE V.5.2 ELPLA MODEL PREDICTIONS — TRIAXIAL COMPRESSION STRESS DIFFERENCE vs. AXIAL STRAIN

393
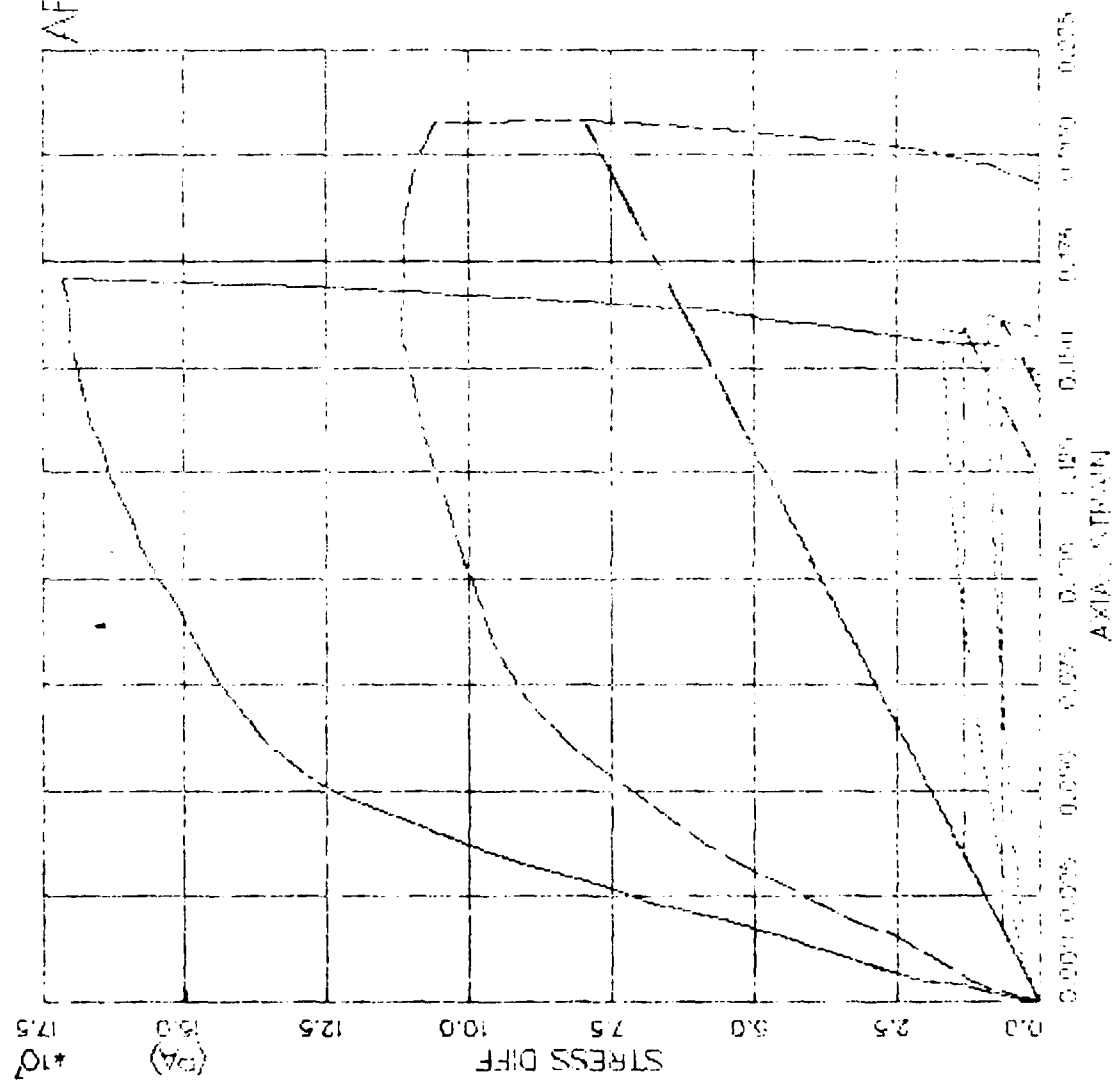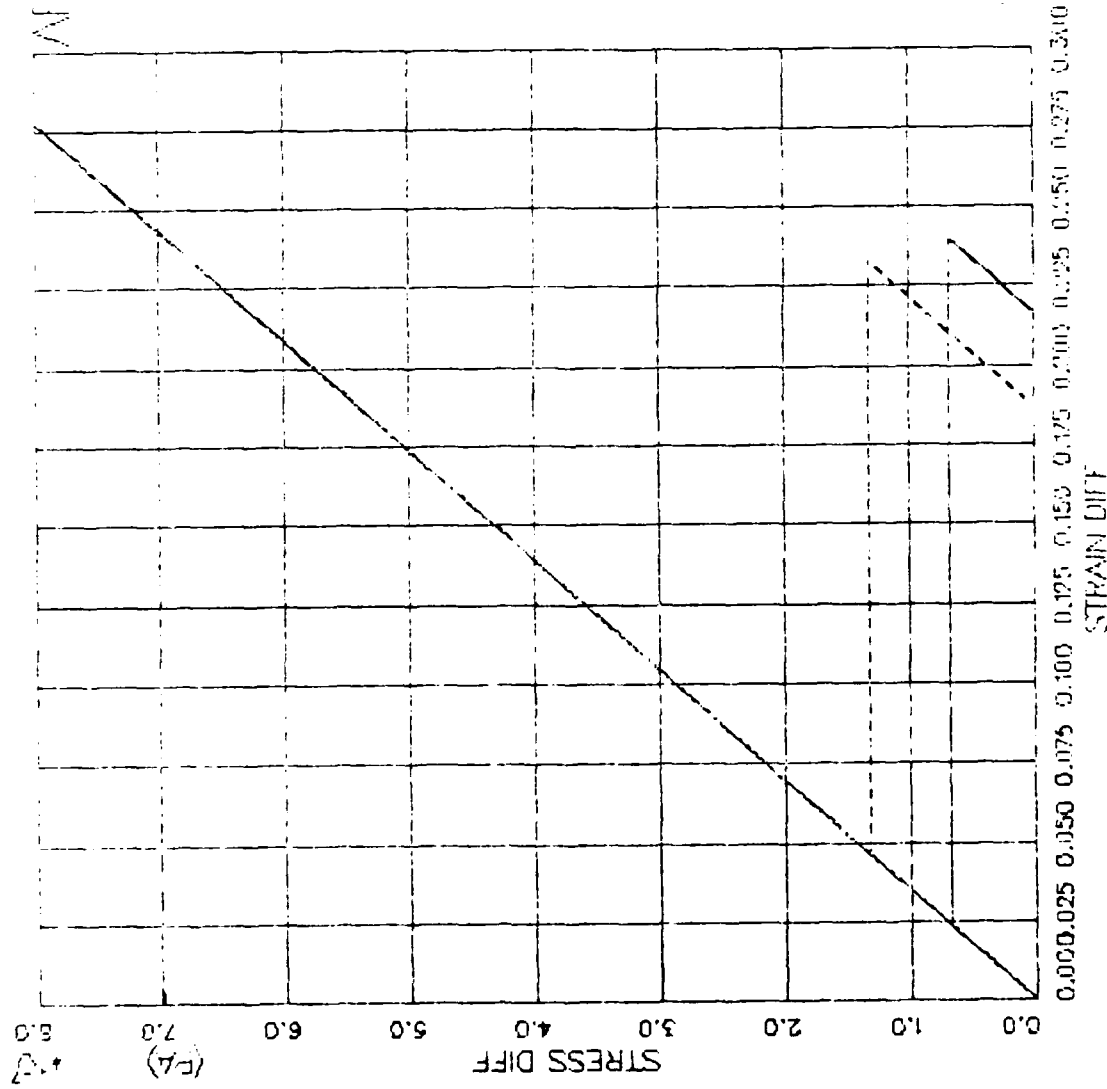
FIGURE V.5.3 ELPLA MODEL EXERCISE—TRIAXIAL COMP(CTC) — STRESS DIFF VS. STRAIN DIFF

394

AFOSR SOIL ELEMENT MODEL

TEST = STANDARD TRIAXIAL TEST
MODEL = ELPLA
MATL = DRYCARES—REMOLD
DATA = DRYCARESR/WES/84

LEGEND

SIGMA3C = 3.4E6
TEST DATA
SIGMA3C = 7.0E6
TEST DATA
SIGMA3C = 58.8E6
TEST DATA
SIGMA3C = 100.0E6
TEST DATA
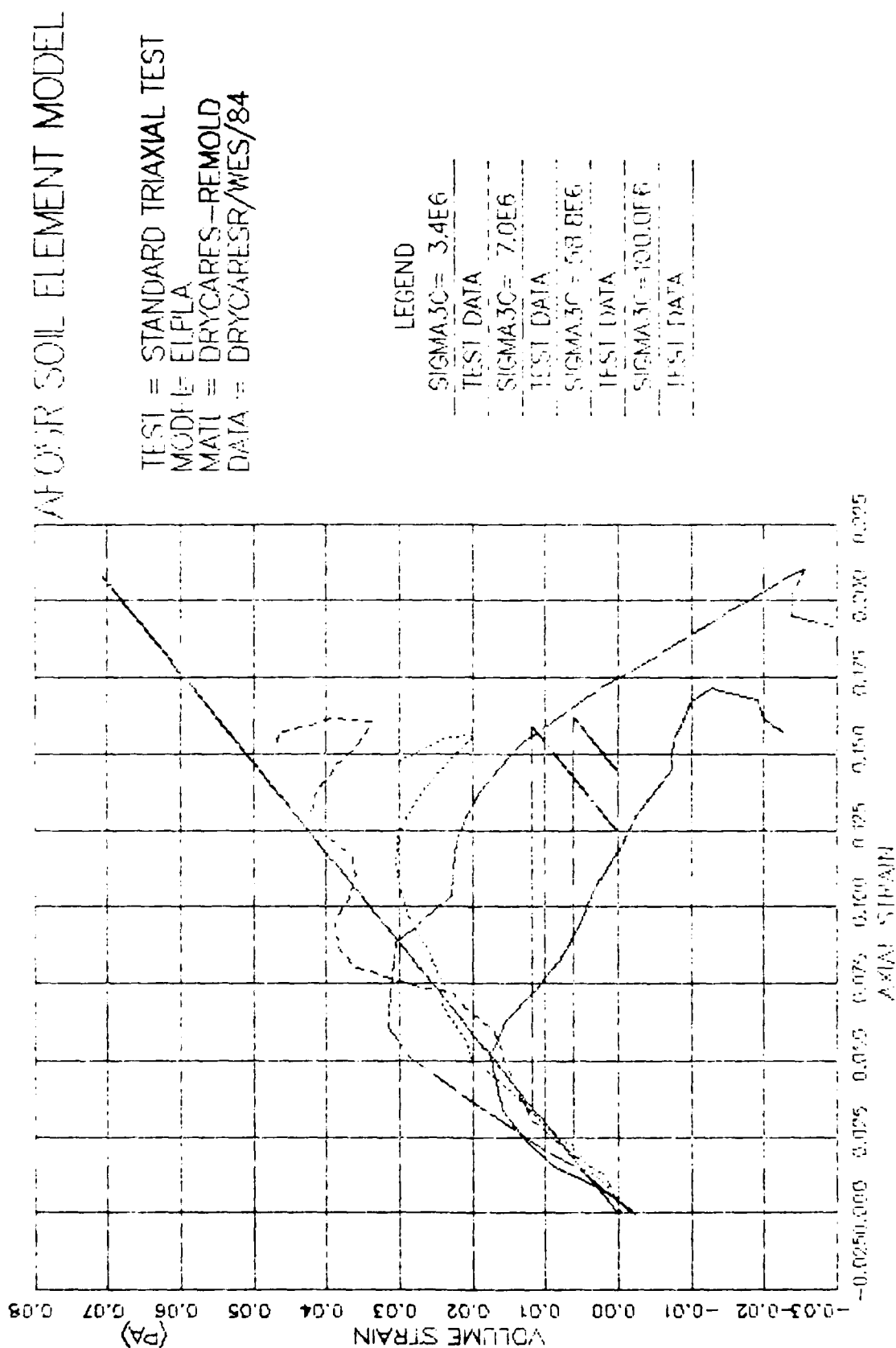
FIGURE V.5.4 ELPLA MODEL EXERCISE — TRIAXIAL COMP(UTC) — AXIAL STRAIN VS VOLUME STRAIN

395
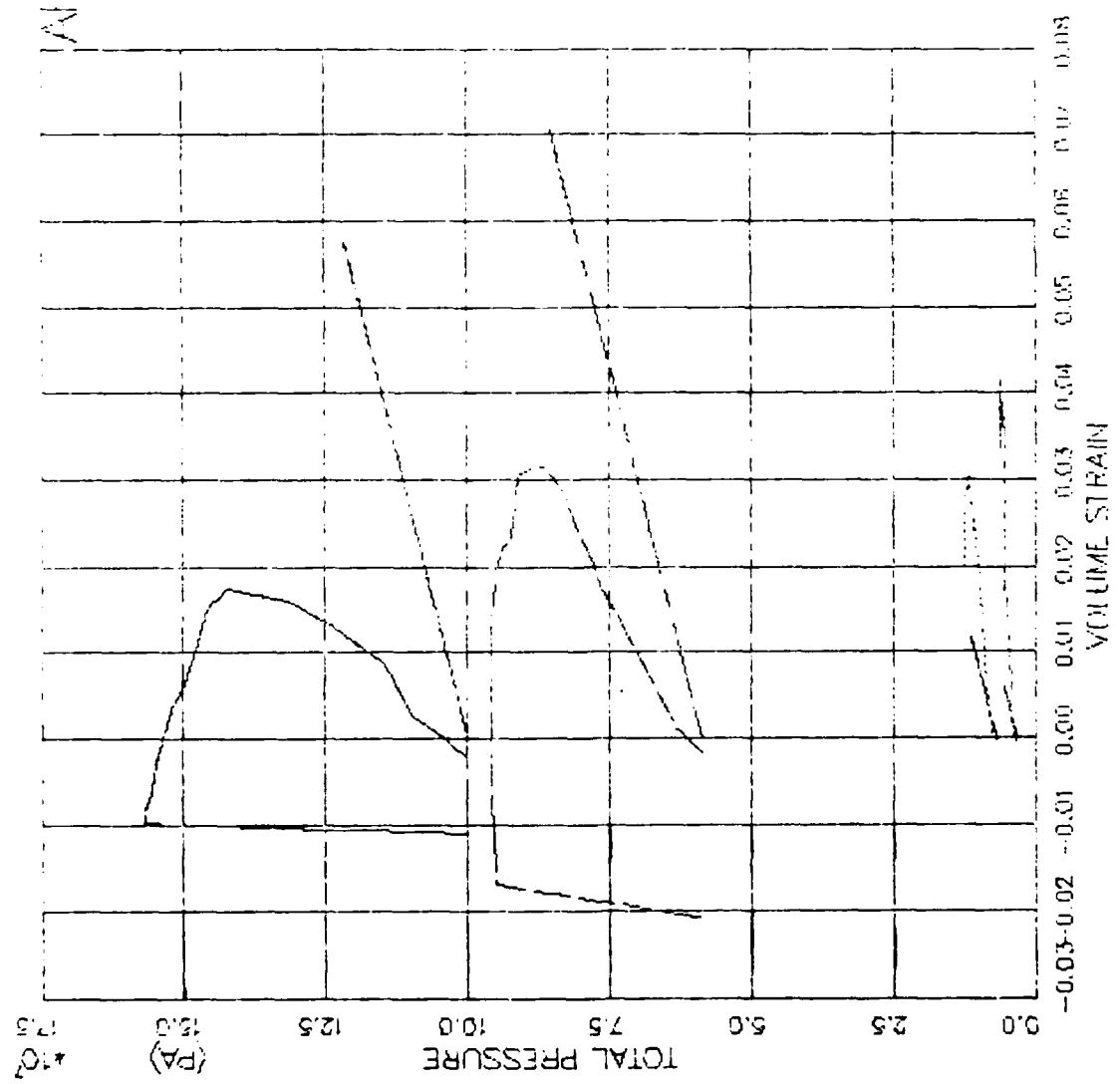
FIGURE V.5.5 ELPLA MODEL EXERCISE—TRIAXIAL COMP(UTC) — PRESSURE VS. VOLUMETRIC STRAIN

AFOSR SOIL ELEMENT MODEL

TEST = STANDARD TRIAXIAL TEST
MODEL= ELPLA
MATL = DRYCARES-REMOLD
DATA = DRYCARESR/WES/84

LEGEND
S3C=1.8E6
TEST DATA
S3C=3.5E6
TEST DATA
S3C=7.1E5
TEST DATA
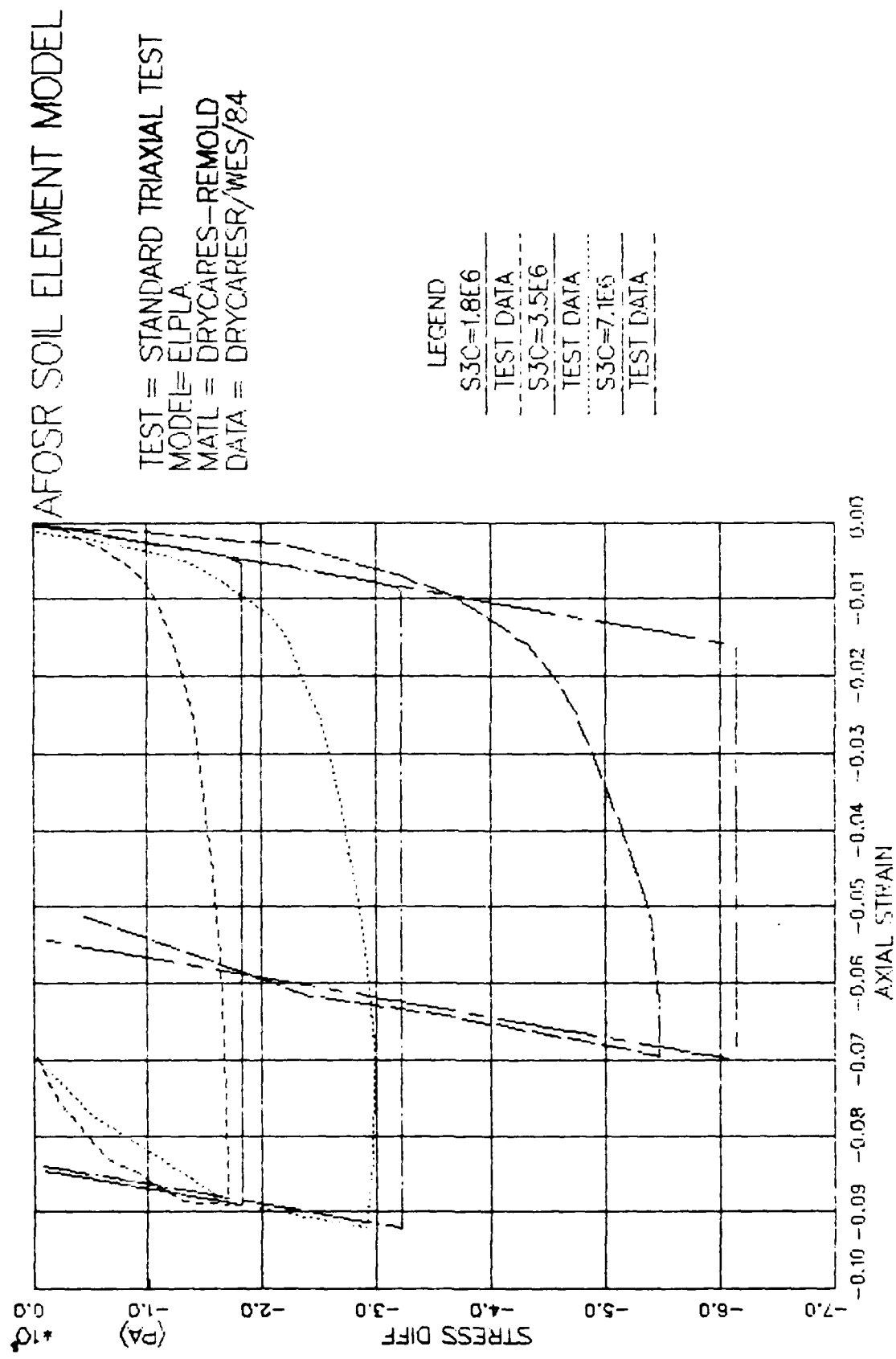
FIGURE V.5.6 ELPLA MODEL EXERCISE— TRIAXIAL EXTEN(CTE) - STRESS DIFF VS. AXIAL STRAIN

397
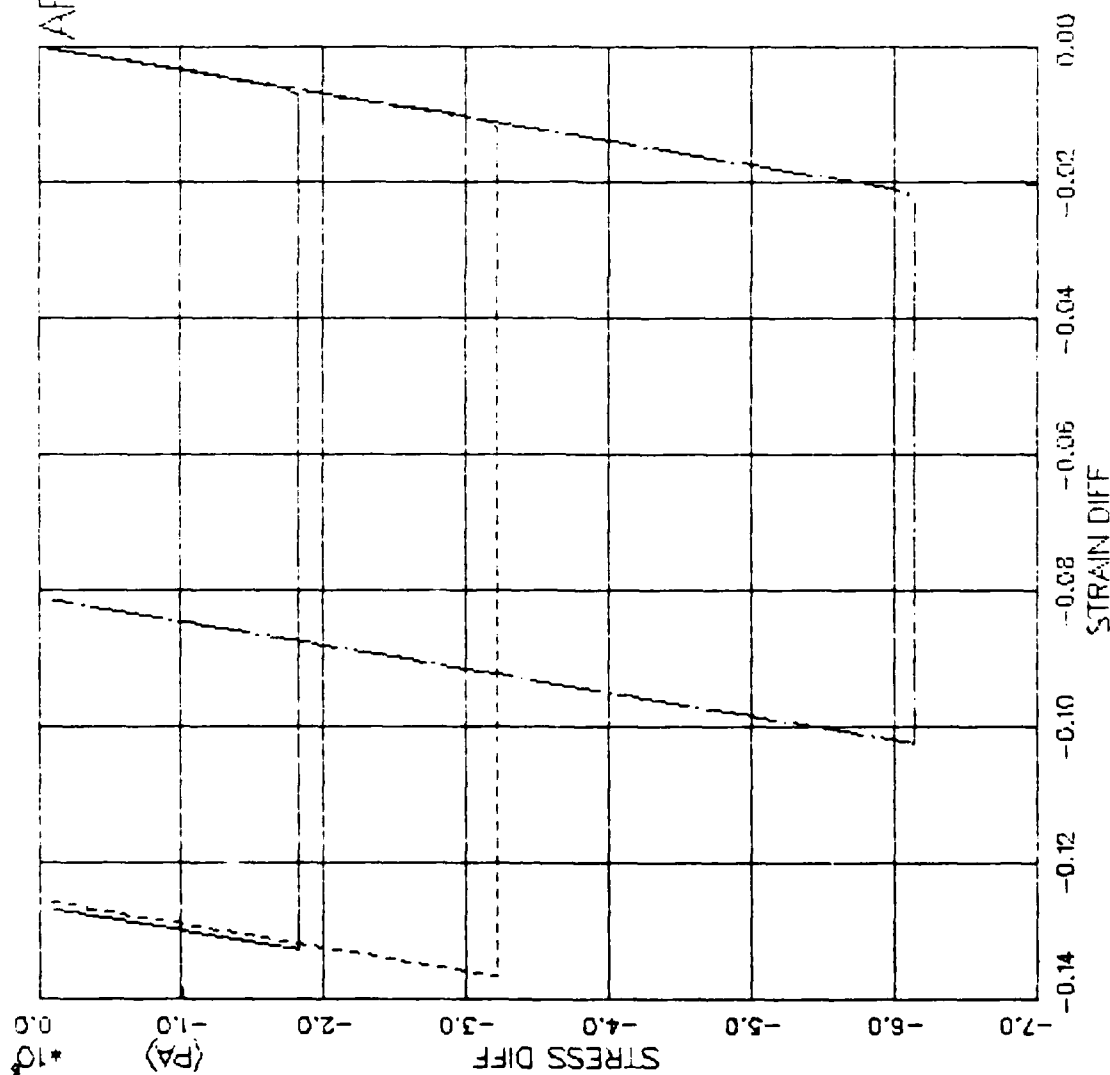
FIGURE V.5.7 ELPLA MODEL EXERCISE—TRIAXIAL EXTEN(.IE) — STRESS DIFF VS. STRAIN DIFF
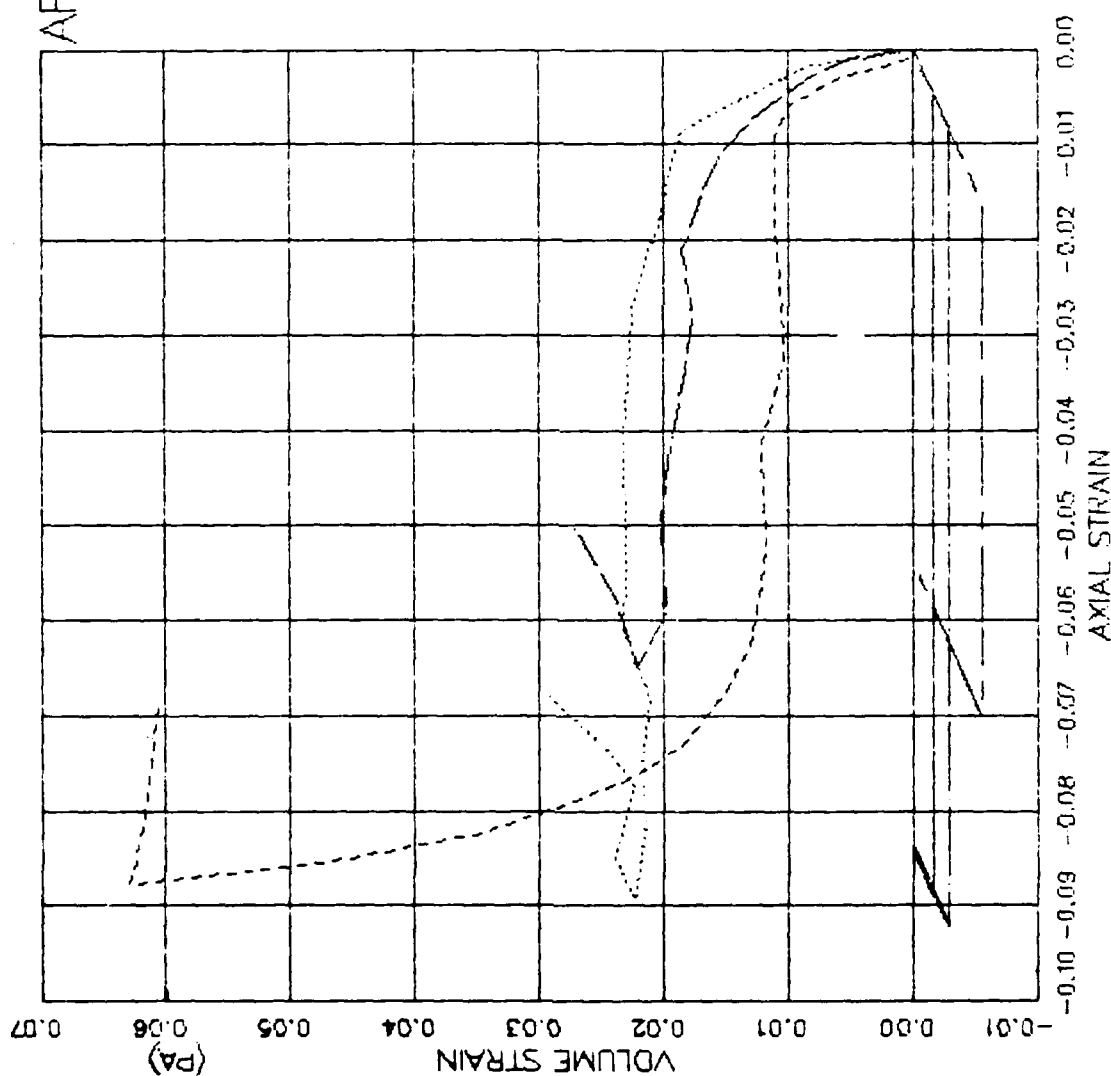
FIGURE V.5.8 ELPLA MODEL EXERCISE— TRIAXIAL EXTEN(CTE) — AXIAL STRAIN VS VOLUME STRAIN

AFOSR SOIL ELEMENT MODEL

TEST = STANDARD TRIAXIAL TEST
MODEL= ELPLA
MATL = DRYCARES-REMOLD
DATA = DRYCARESR/WES/84

LEGEND
S3C=1.8E6
S3C=3.5E6
S3C=7.1E6
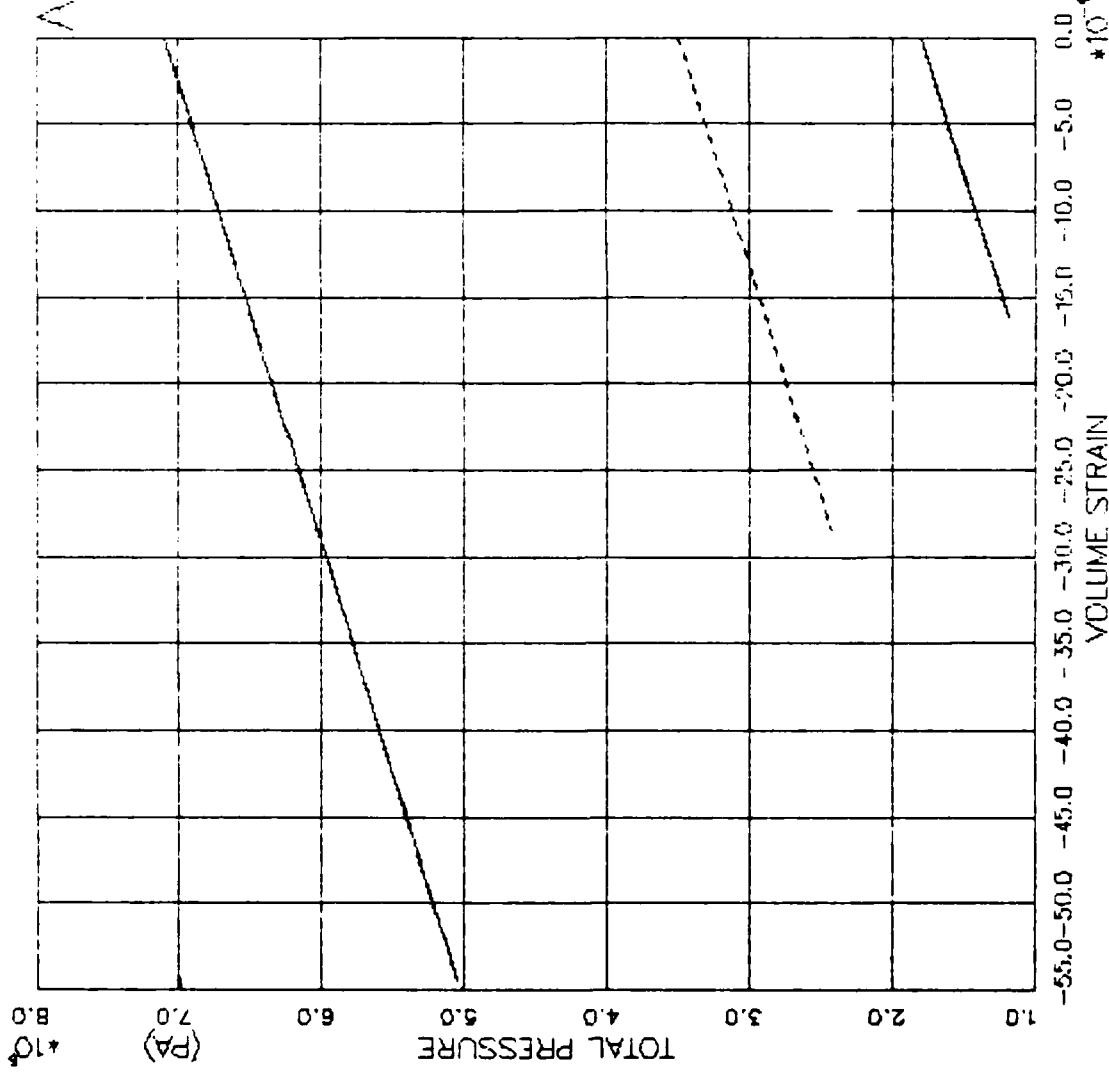
FIGURE V.5.9 ELPLA MODEL EXERCISE—TRIAXIAL EXTEN(CTE) – PRESSURE VS. VOLUMETRIC STRAIN

VOLUME STRAIN

TOTAL PRESSURE (PA)
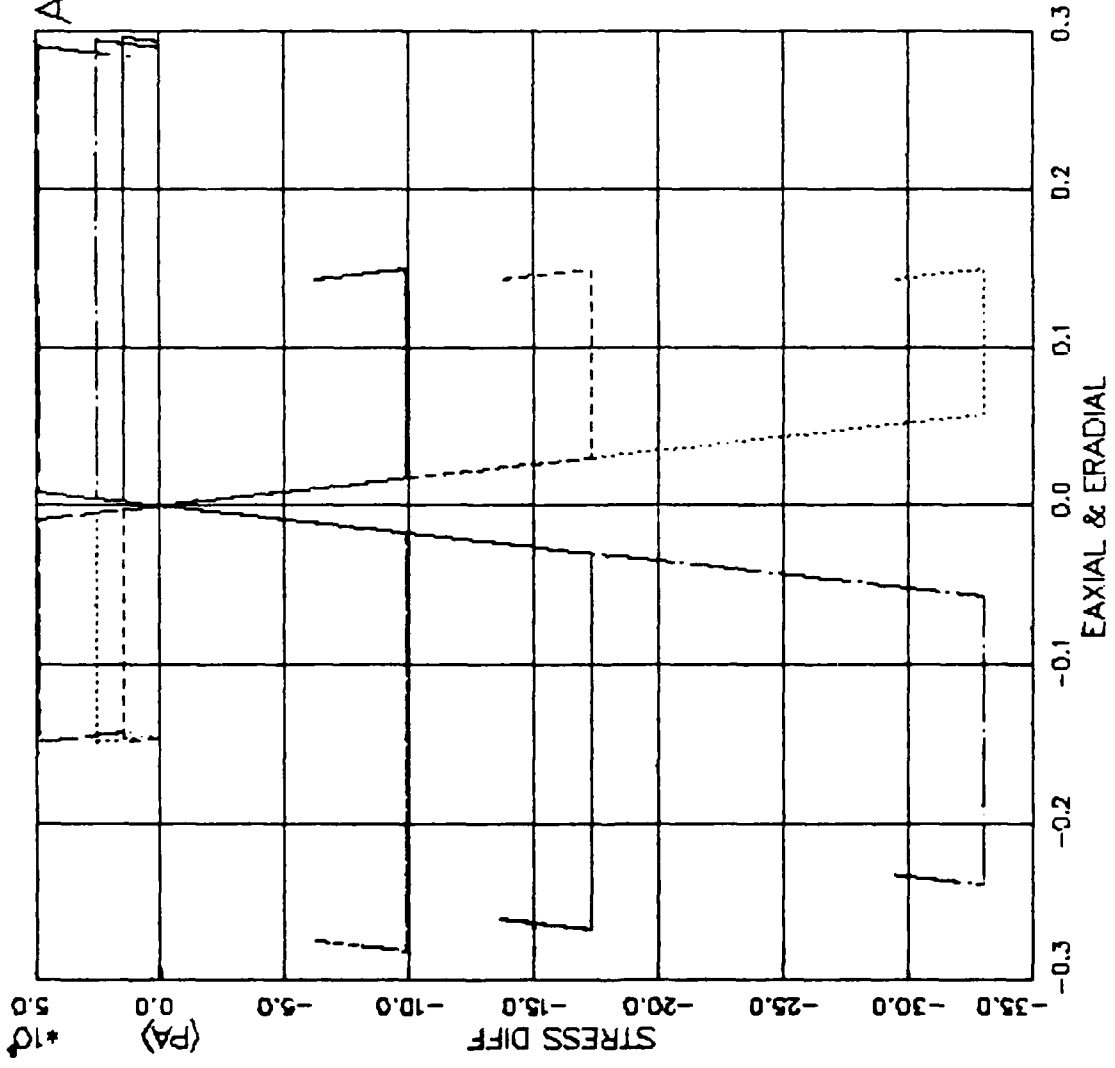
FIGURE V.5.10 ELPLA MODEL EXER—REDUCED TRIAX(RTC+RTE) — STRESS DIFF VS. STRAIN

AFOSR SOIL ELEMENT MODEL

TEST = STANDARD TRIAXIAL TEST
MODEL= ELPLA
MATL = DRYCARES—REMOLD

LEGEND
RTC/S3C=1.8E6
RTC/S3C=3.5E6
RTC/S3C=7.1E6
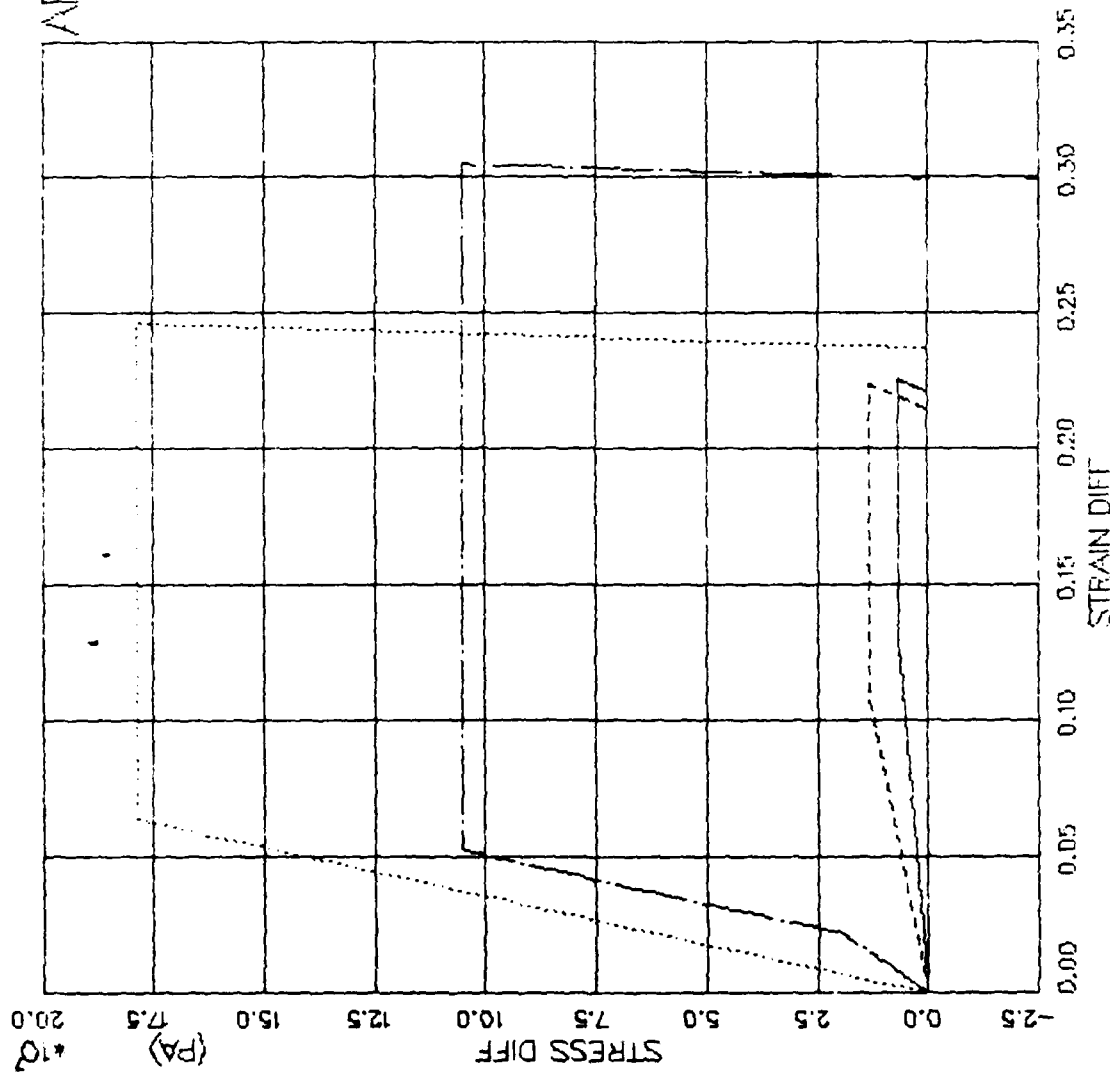RTE/S3C=1.8E6
RTE/S3C=3.5E6
RTE/S3C=7.1E6
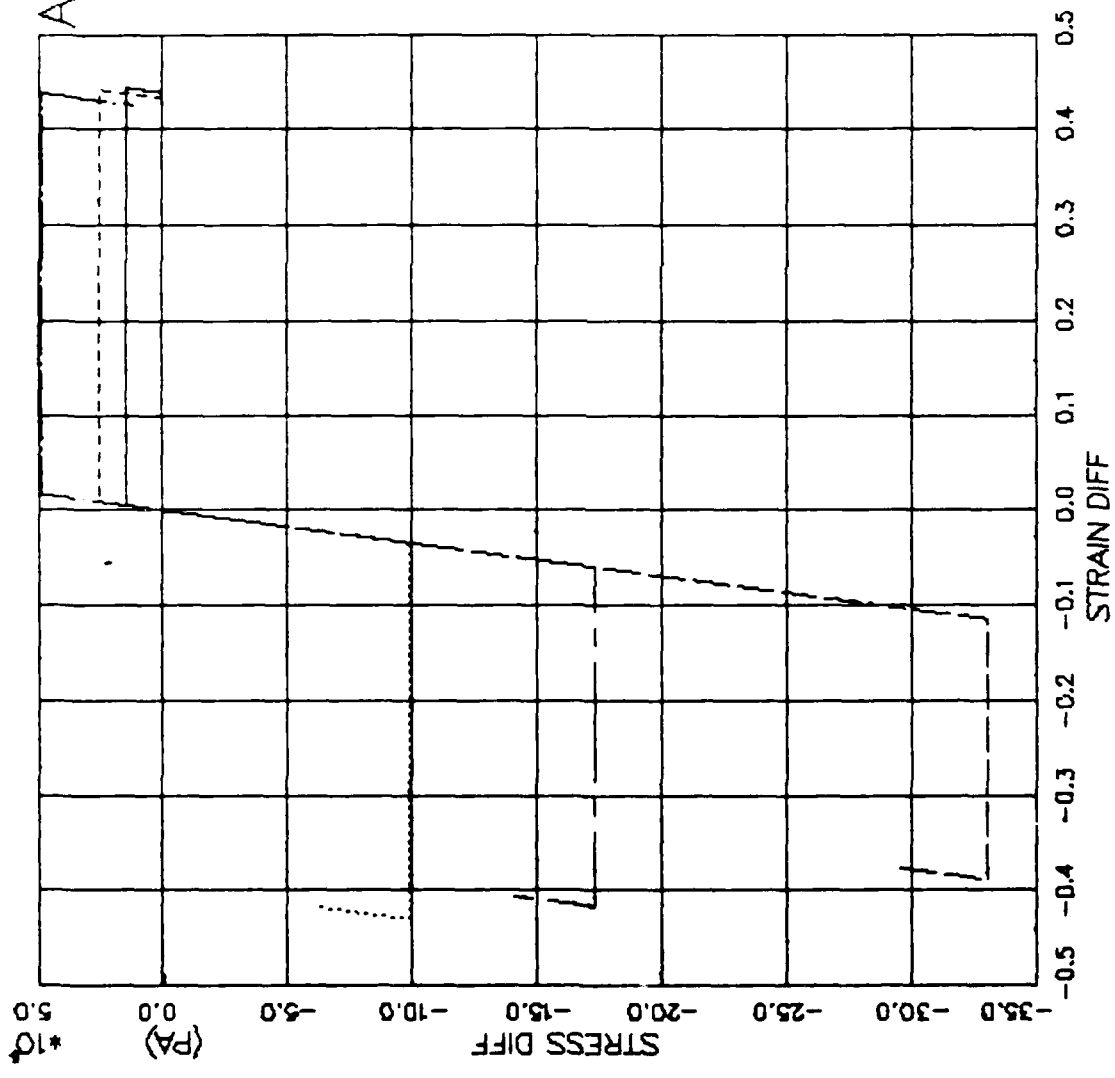
FIGURE V.5.11 ELPLA MODEL EXER—REDUCED TRIAX(RTC+RTE) — STRESS DIFF VS. STRAIN DIFF

AFOSR SOIL ELEMENT MODEL

TEST = STANDARD TRIAXIAL TEST
MODEL= ELPLA
MATL = DRYCARES—REMOLD

LEGEND
RTC/S3C=1.8E6
RTC/S3C=3.5E6
RTC/S3C=7.1E6
RTE/S3C=1.8E6
RTE/S3C=3.5E6
RTE/S3C=7.1E6
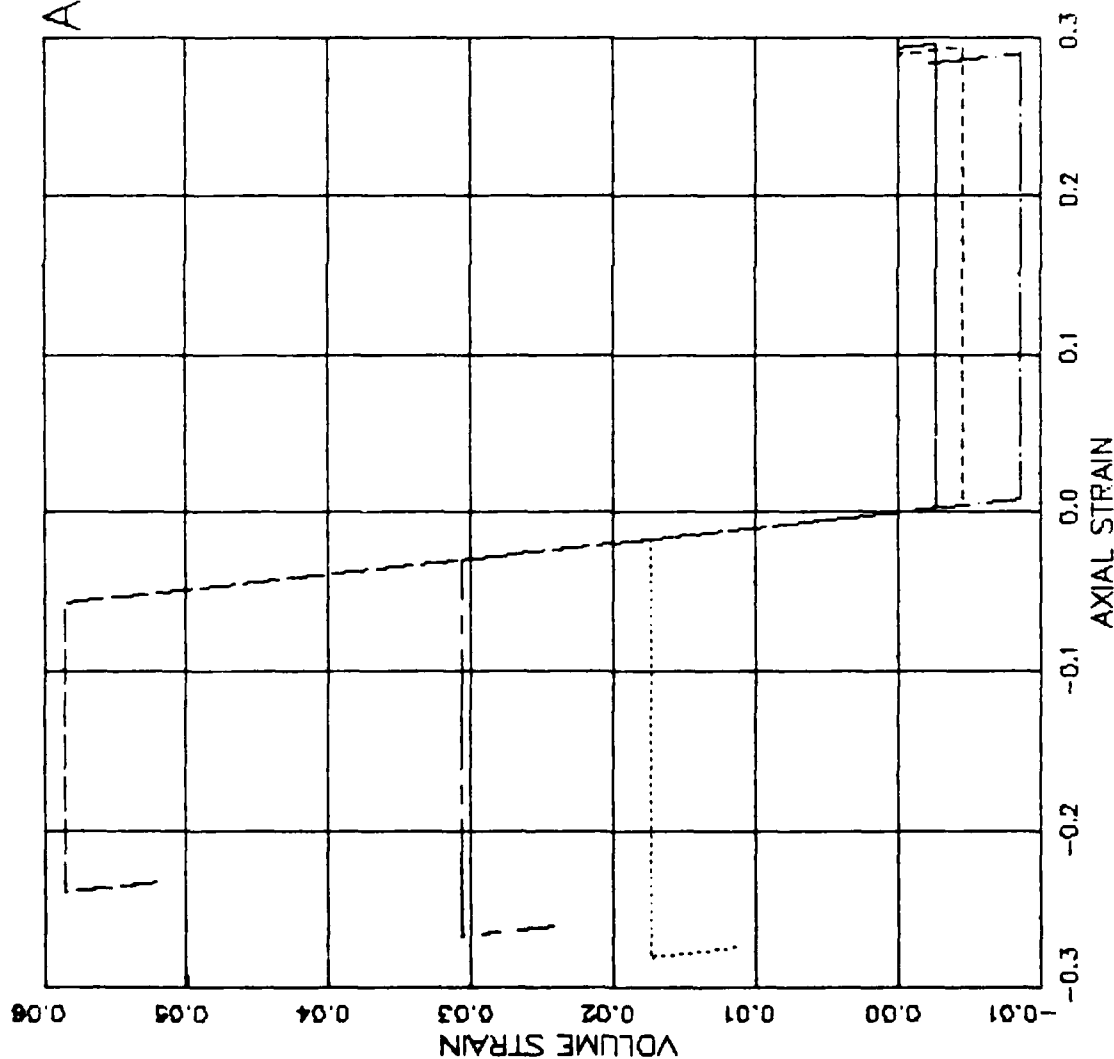
FIGURE V.5.12 ELPLA MODEL EXER—REDUCED TRIAX(RTC+RTE) — AXIAL STRAIN VS VOLUME STRAIN

403

AFOSR SOIL ELEMENT MODEL

TEST = STANDARD TRIAXIAL TEST
MODEL= ELPLA
MATL = DRYCARES—REMOLD

LEGEND
RTC/S3C=1.8E6
RTC/S3C=3.5E6
RTC/S3C=7.1E6
RTE/S3C=1.8E6
RTE/S3C=3.5E6
RTE/S3C=7.1E6
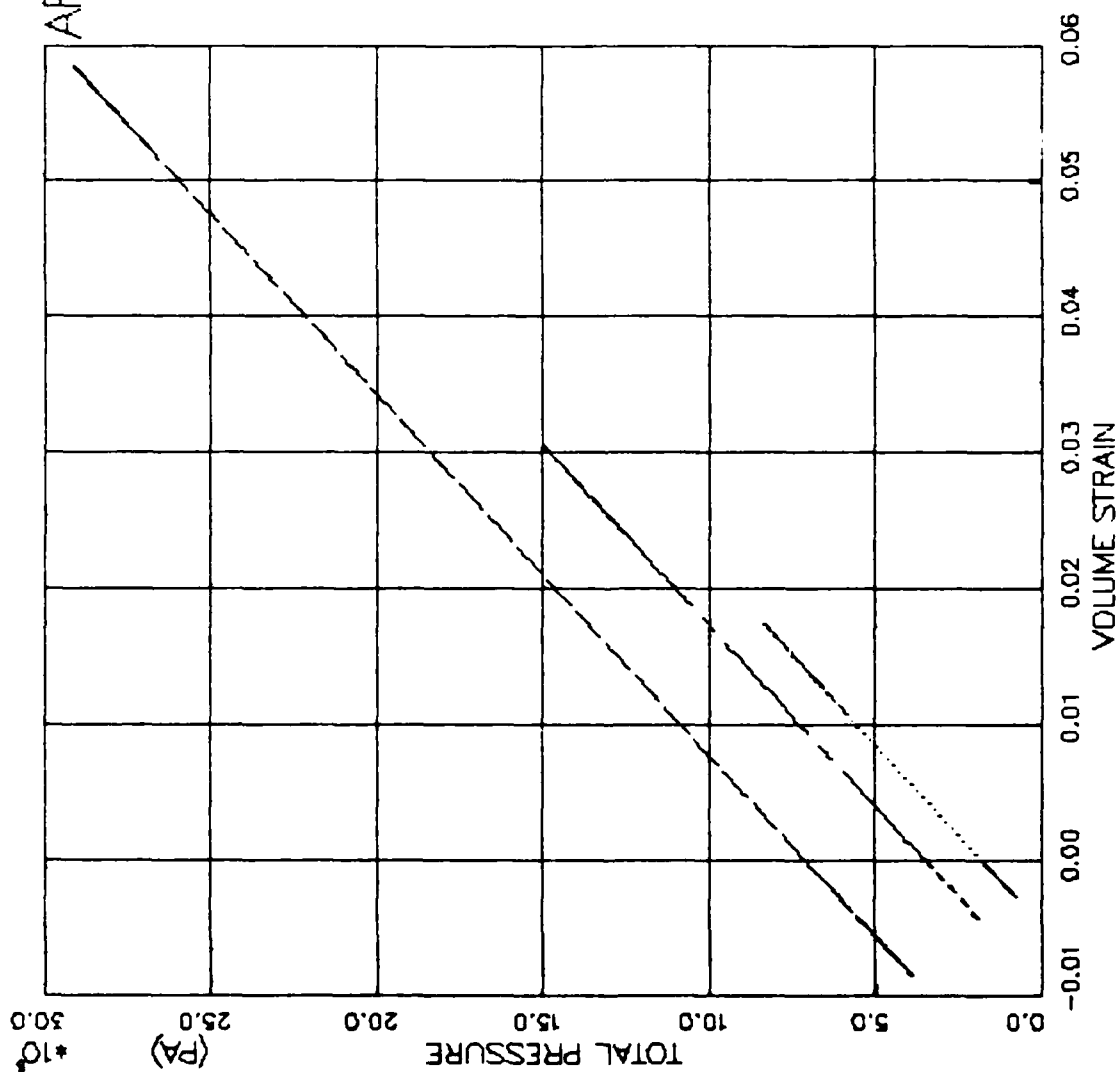
FIGURE V.5.13 ELPLA MODEL EXER—REDUCED TRIAX(RTC+RTE) — PRESSURE VS. VOLUMETRIC STRAIN

AFOSR SOIL ELEMENT MODEL

TEST = STANDARD TRIAXIAL TEST
MODEL= ELPLA
MATL = DRYCARES—REMOLD

LEGEND

PSC/S3C=1.8E6
PSC/S3C=1.8E6
PSC/S3C=3.5E6
PSC/S3C=3.5E6
PSC/S3C=7.1E6
PSC/S3C=7.1E6
PSE/S3C=1.8E6
PSE/S3C=1.8E6
PSE/S3C=3.5E6
PSE/S3C=3.5E6
PSE/S3C=7.1E6
PSE/S3C=7.1E6
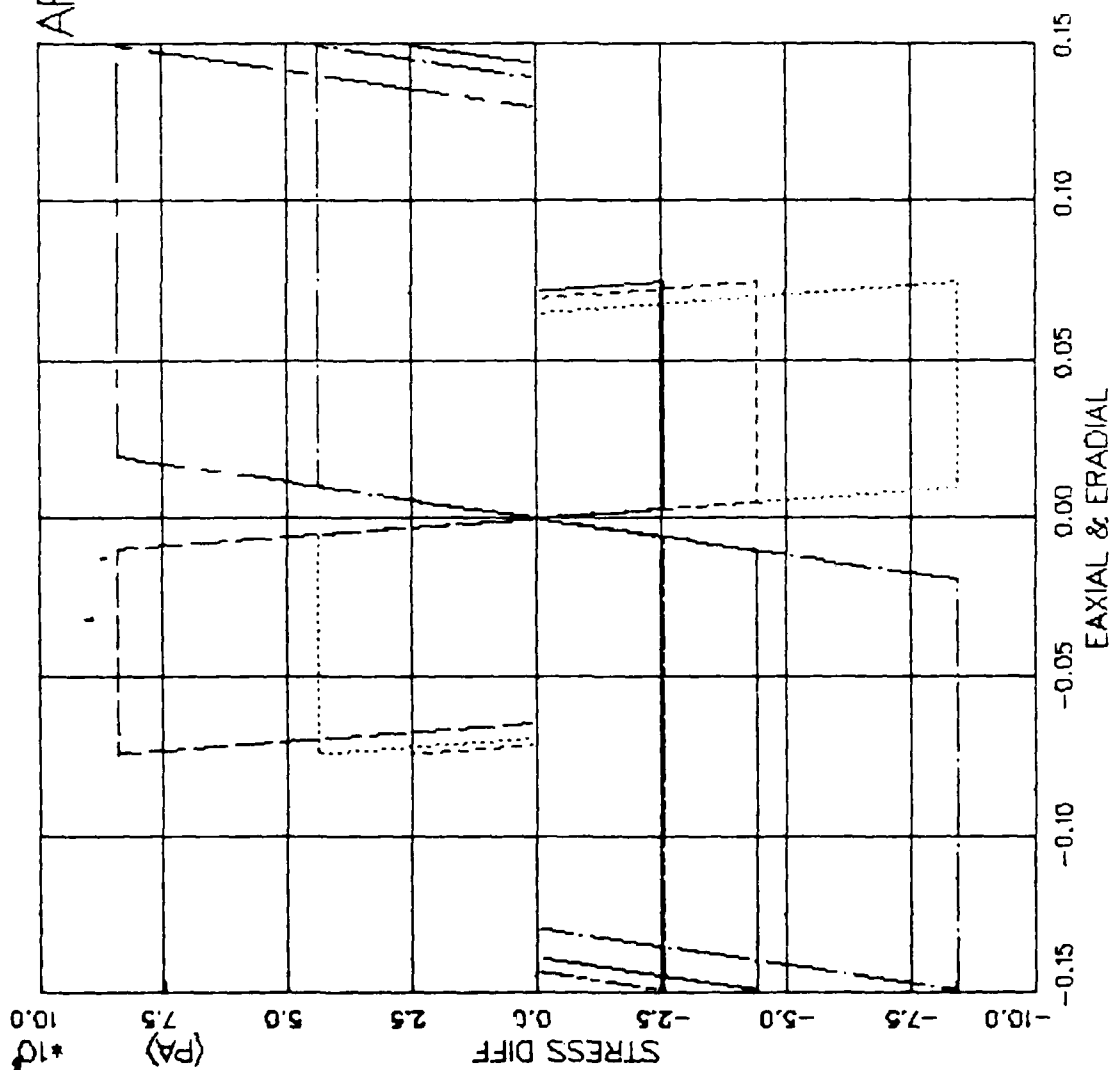
FIGURE V.5.14 ELPLA MODEL EXERCISE—PURE SHEAR(PSC+PSE) — STRESS DIFF VS. STRAIN

EAXIAL & ERADIAL
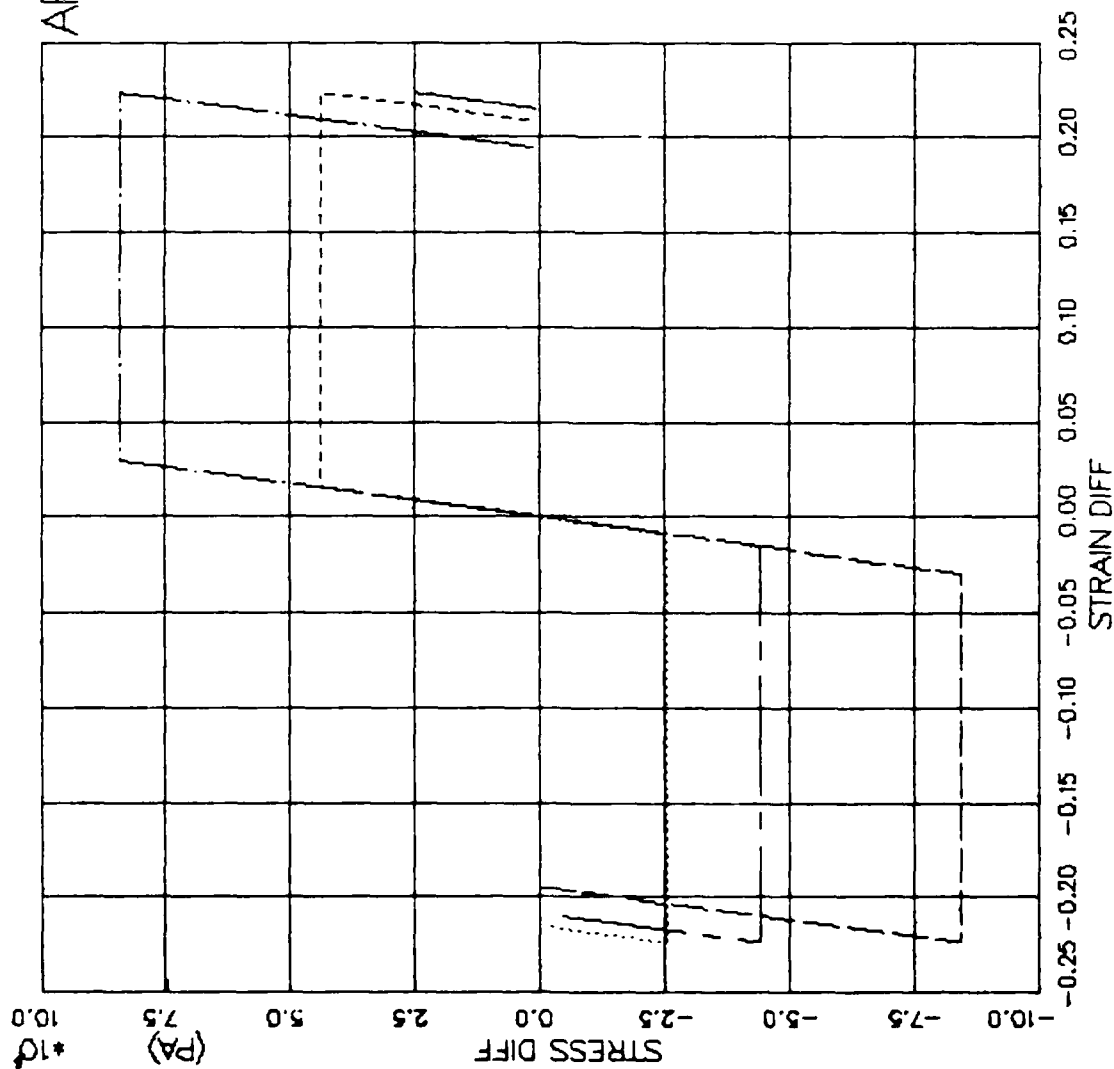
STRESS DIFF (PA) *10^6

FIGURE V.5.15 ELPLA MODEL EXERCISE—PURE SHEAR(PSC+PSE) – STRESS DIFF VS. STRAIN DIFF
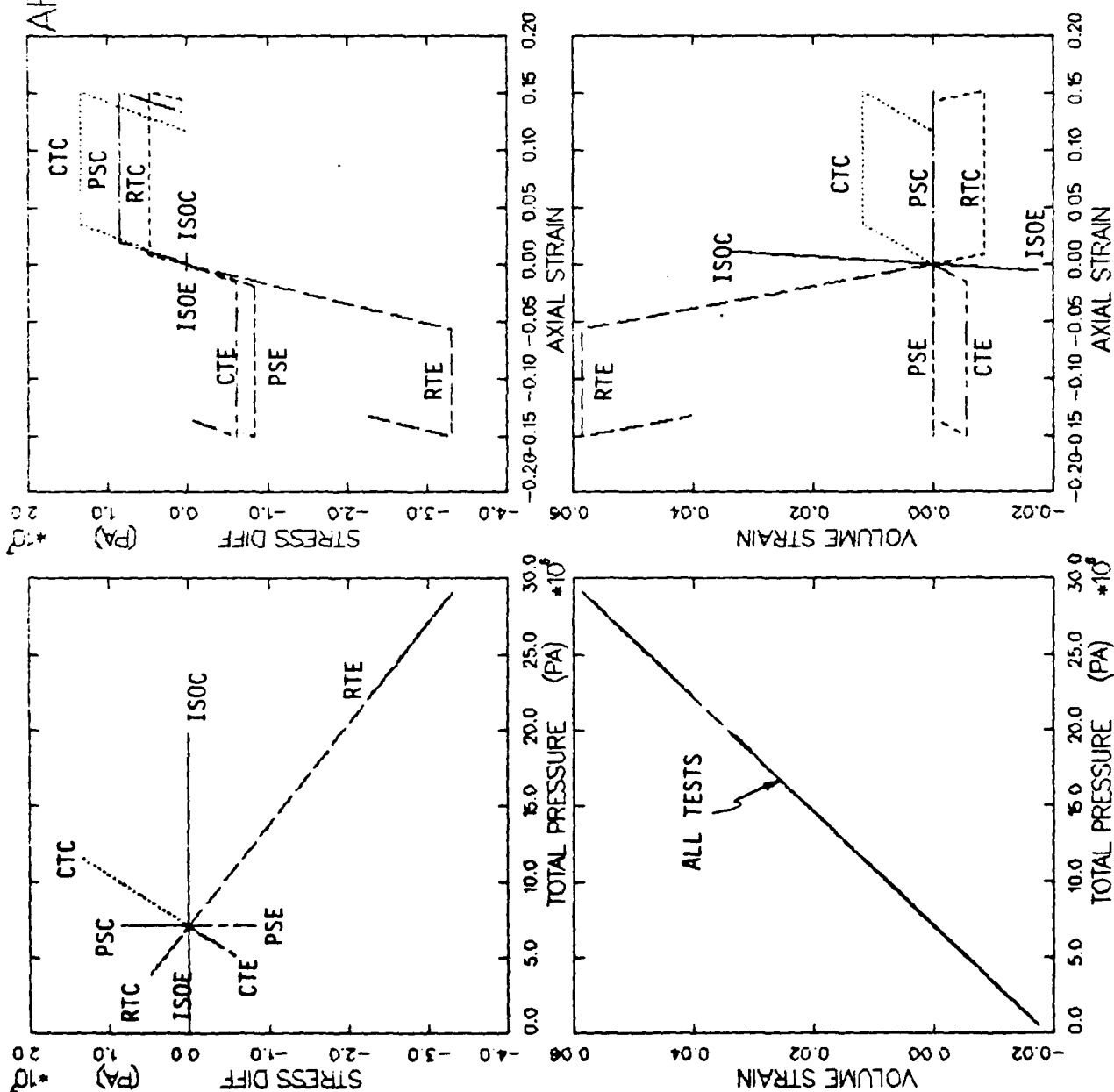
FIGURE V.5.16. ELASTIC–PLASTIC MODEL BEHAVIOR SUMMARY(S3C=7.1MPDRYCARES–REMOLD – SDIFF/P/EV/EA

AFOSR SOIL ELEMENT MODEL

TEST = UNIAXIAL STRAIN TEST
MODEL= ELPLA
MATL = DRYCARES—REMOLD
DATA = DRYCARESR/WES/84

LEGEND
CALCULATION
TEST DATA
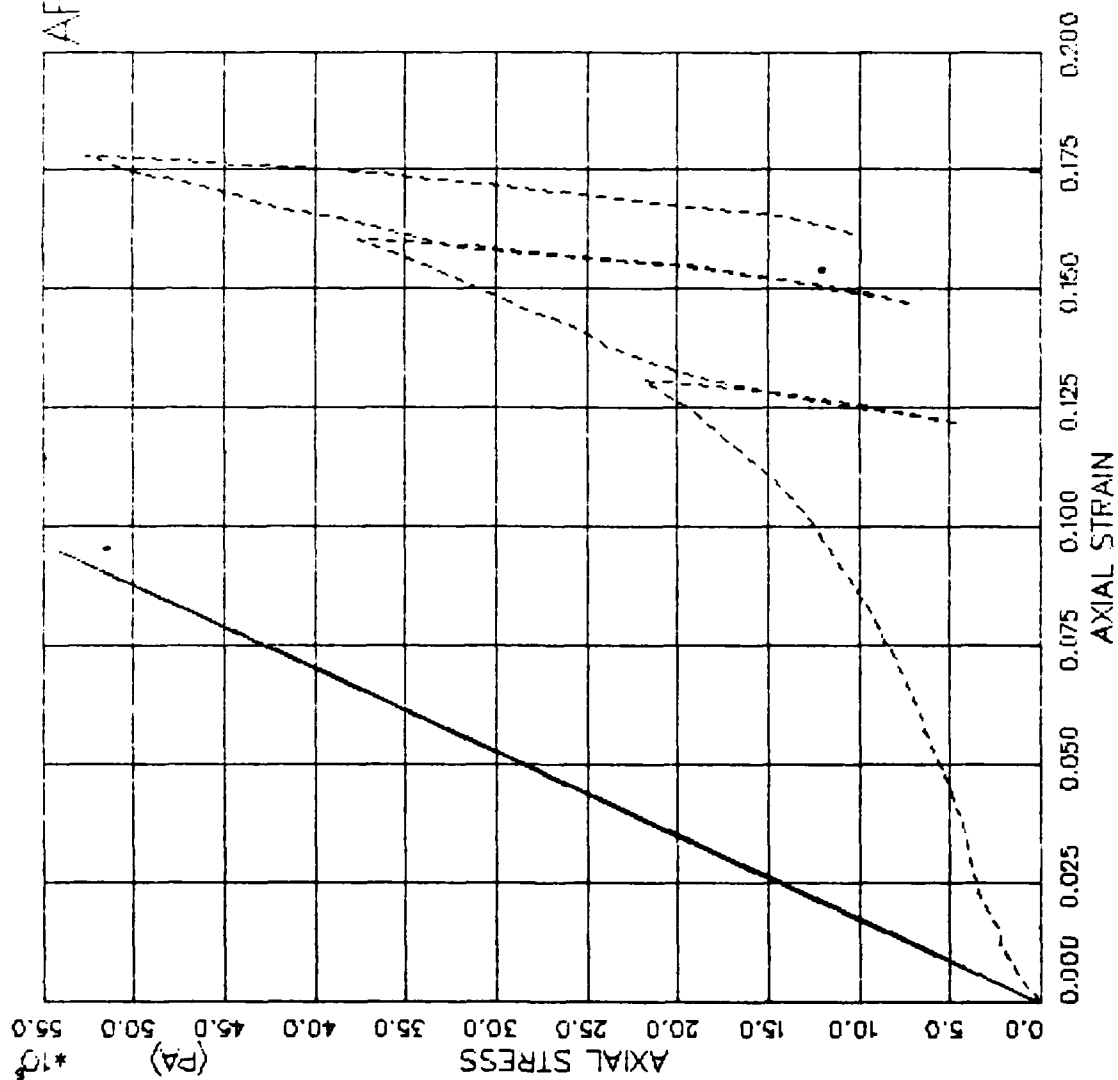
FIGURE V.5.17 ELPLA MODEL EXERCISE— UNIAXIAL STRAIN (UXC) -- TOT AXL STRESS VS. AXL STRAIN

408
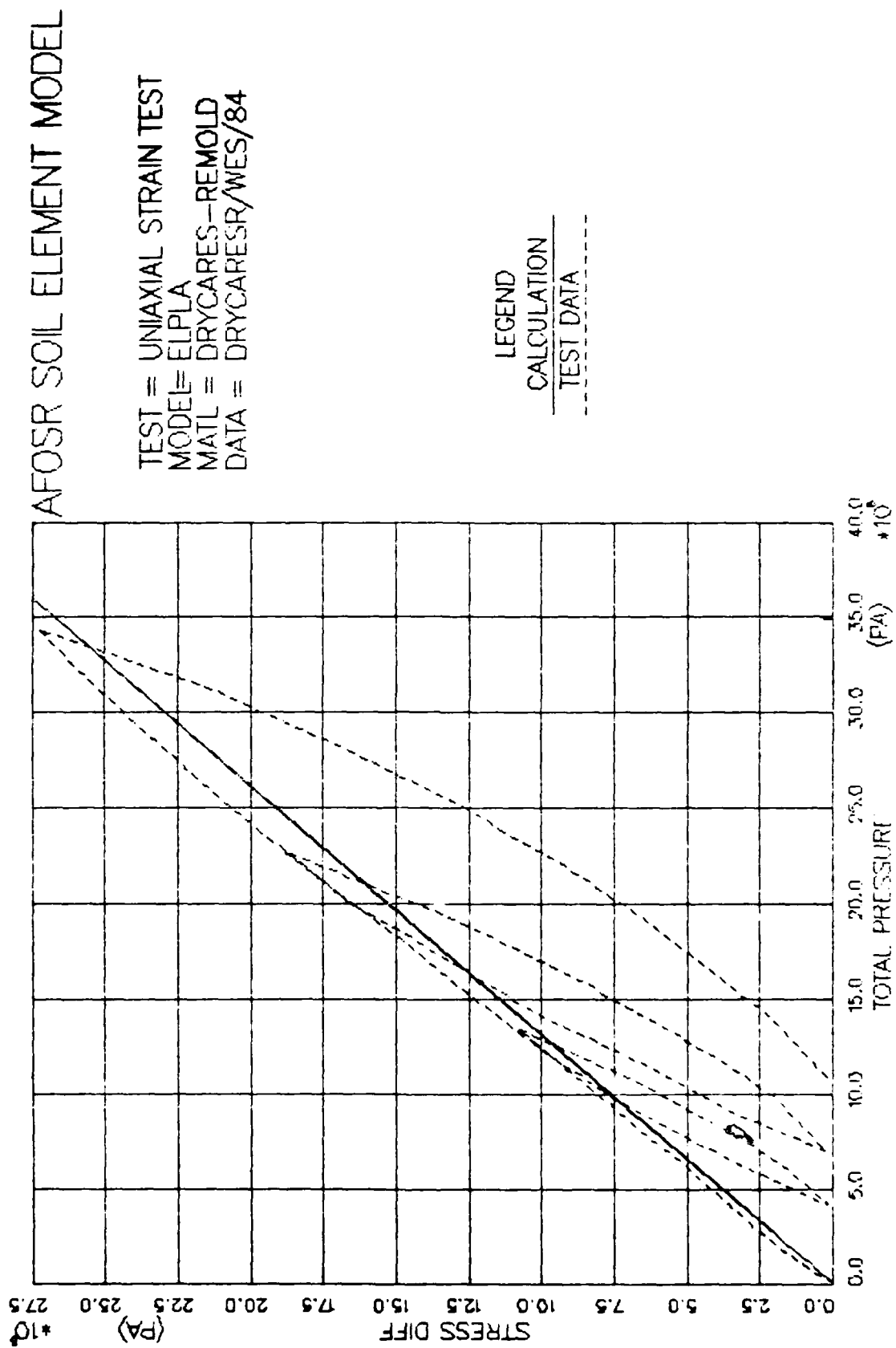
FIGURE V.5.18 ELPLA MODEL EXERCISE — UNIAXIAL STRAIN ($UX()$) — STRESS DIFFERENCE VS. PRESSURE

AFOSR SOIL ELEMENT MODEL

TEST = UNIAXIAL STRAIN TEST
MODEL= ELPLA
MATL = DRYCARES-REMOLD
DATA = DRYCARESR/WES/84

LEGEND
CALCULATION
TEST DATA
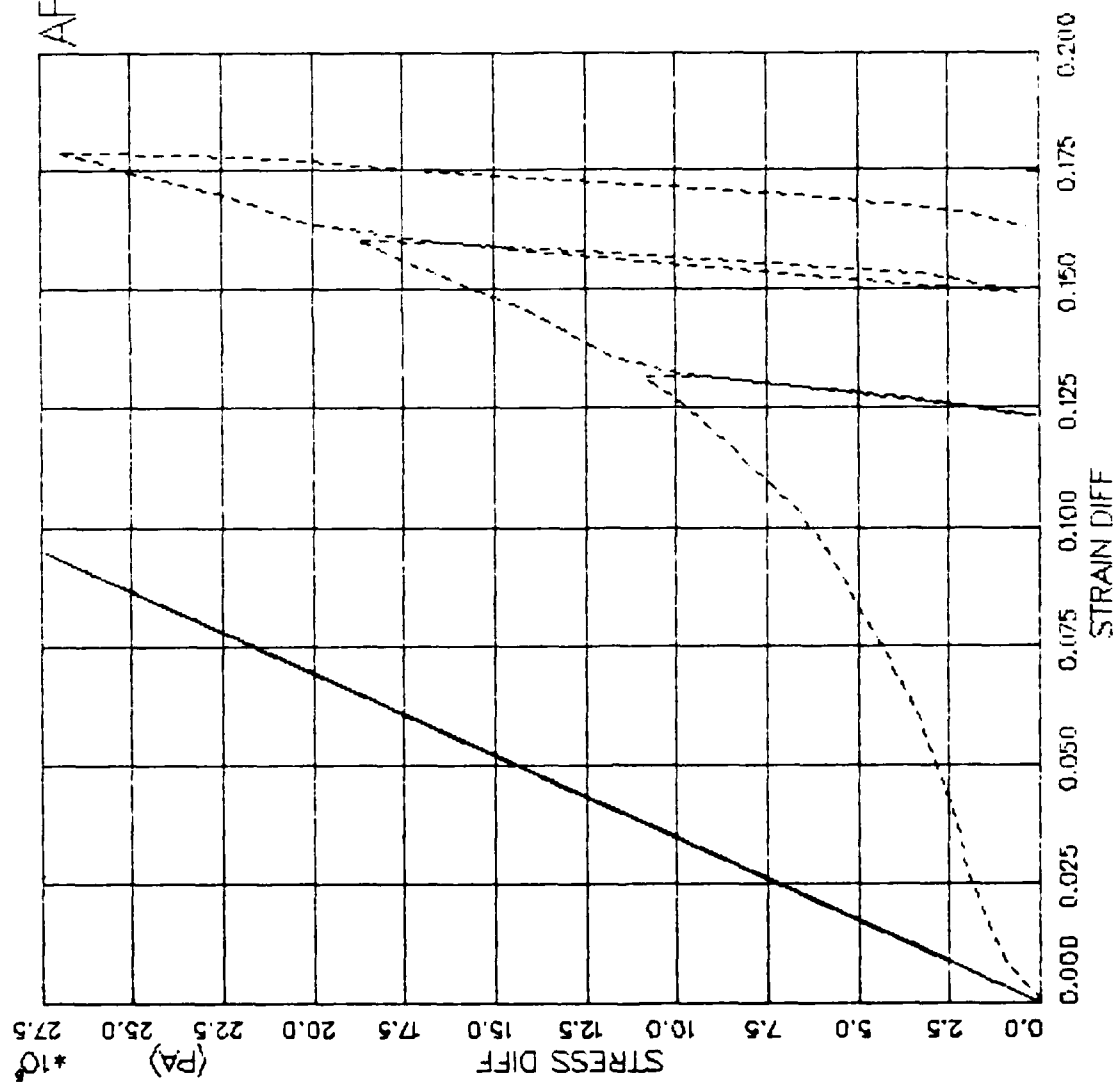
FIGURE V.5.19 ELPLA MODEL EXERCISE— UNIAXIAL STRAIN (UXC) – STRESS DIFF VS. STRAIN DIFF

AFOSR SOIL ELEMENT MODEL

TEST = UNIAXIAL STRAIN TEST
MODEL= ELPLA
MATL = DRYCARES—REMOLD
DATA = DRYCARESR/WES/84

LEGEND
S3C=4.0E6
TEST DATA
S3C=20.E6
TEST DATA
S3C=32.E6
TEST DATA
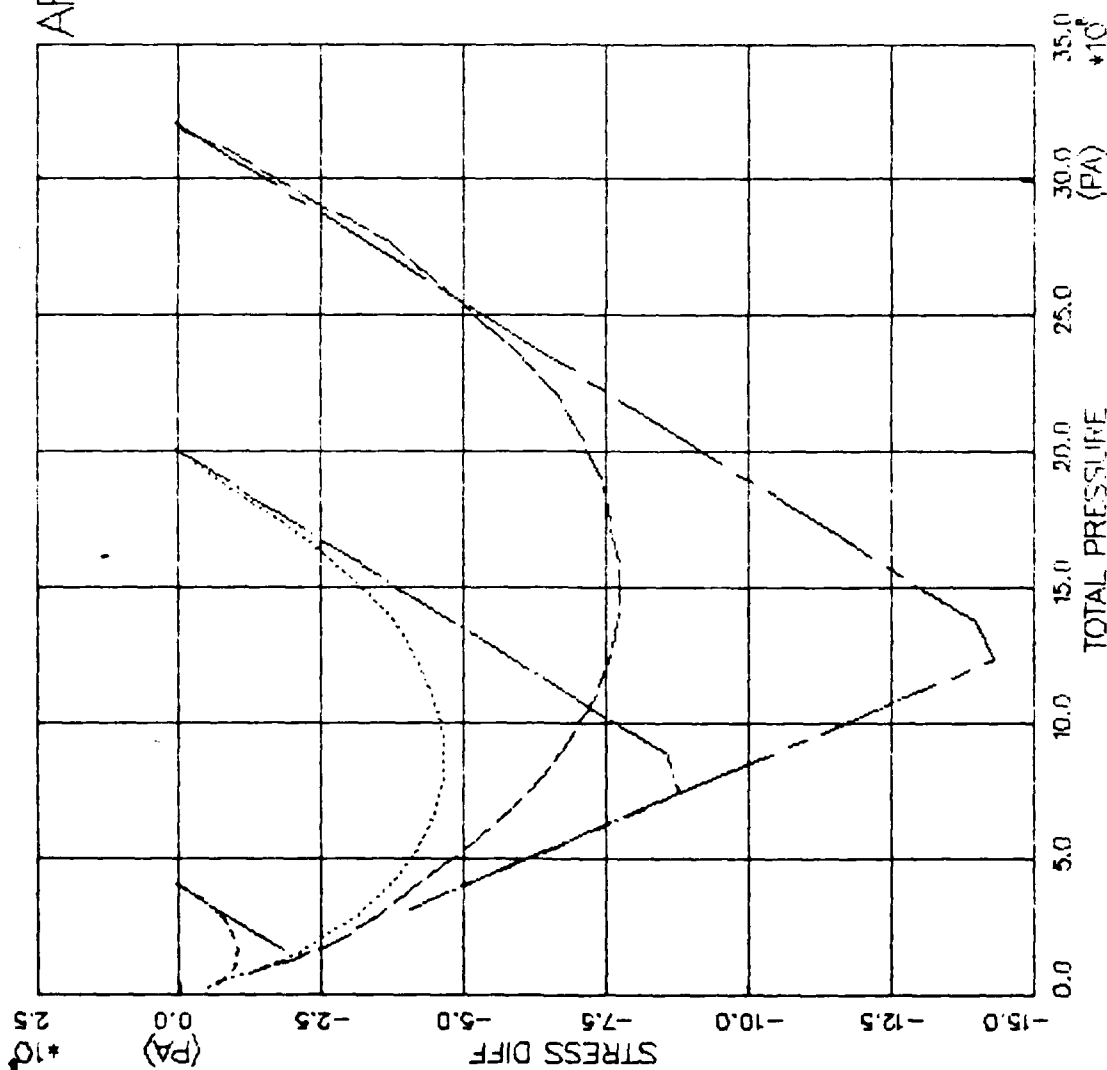
FIGURE V.5.20 ELPLA MODEL EXERCISE—UNIAX EXTEN(1CK0) — STRESS DIFFERENCE VS. PRESSURE

AFOSR SOIL ELEMENT MODEL

TEST = UNIAXIAL STRAIN TEST
MODEL= ELPLA
MATL = DRYCARFS--REMOLD
DATA = DRYCARESR/WES/84

LEGEND
S3C=4.0E6
S3C=20.E6
S3C=32.E6
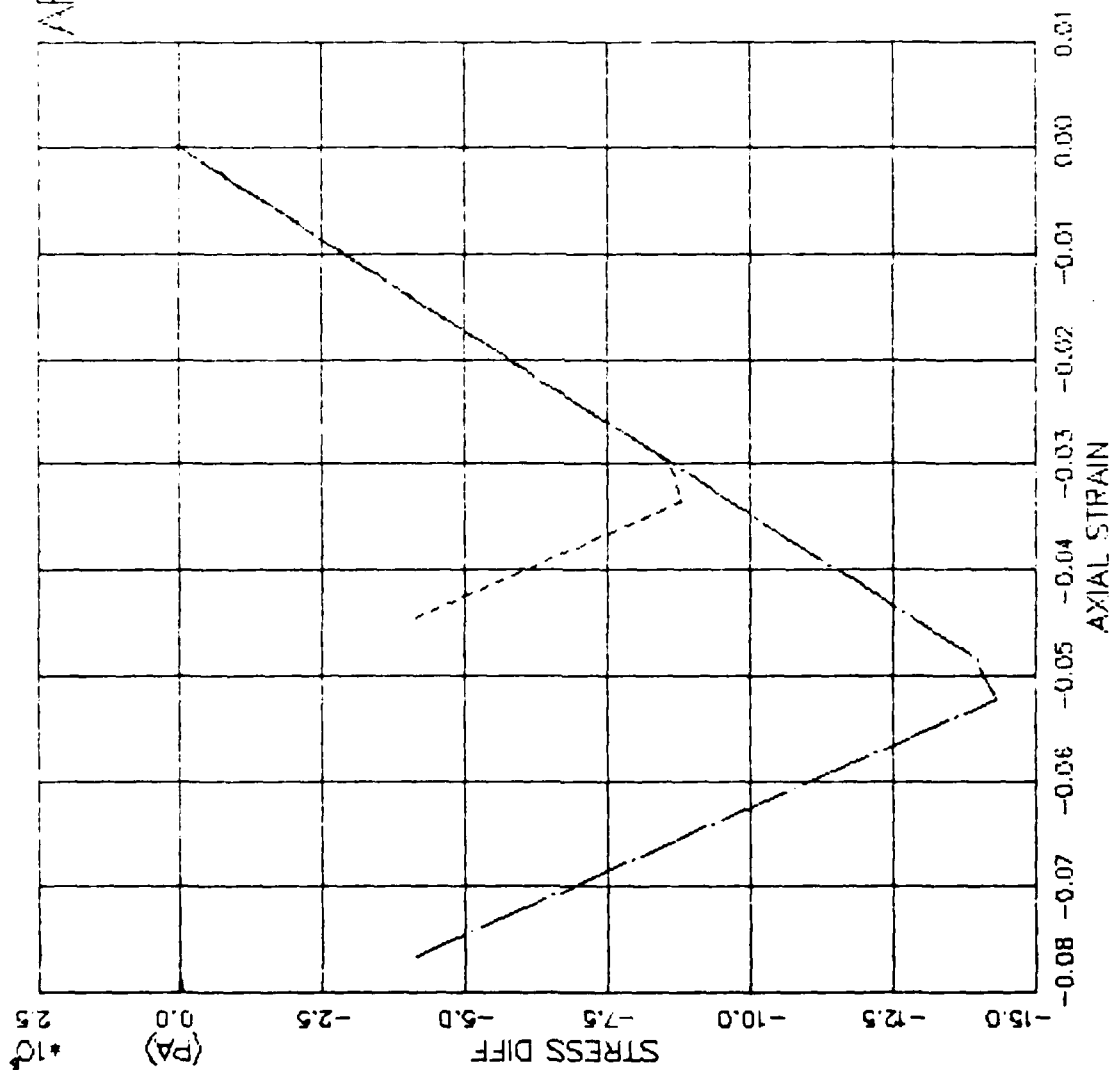
FIGURE V.5.21 ELPLA MODEL EXERCISE—UNIAX EXTEN(ICK0) – STRESS DIFF VS. AXIAL STRAIN

AFOSR SOIL ELEMENT MODEL

TEST = STRAIN PATH
MODEL=ELPLA
MATL = DRYCARLES-REMOLD
DATA = DRYCARLSR/WES/3A

LEGEND
WES. PATH 3A
TEST DATA
WES. PATH 3C
TEST DATA
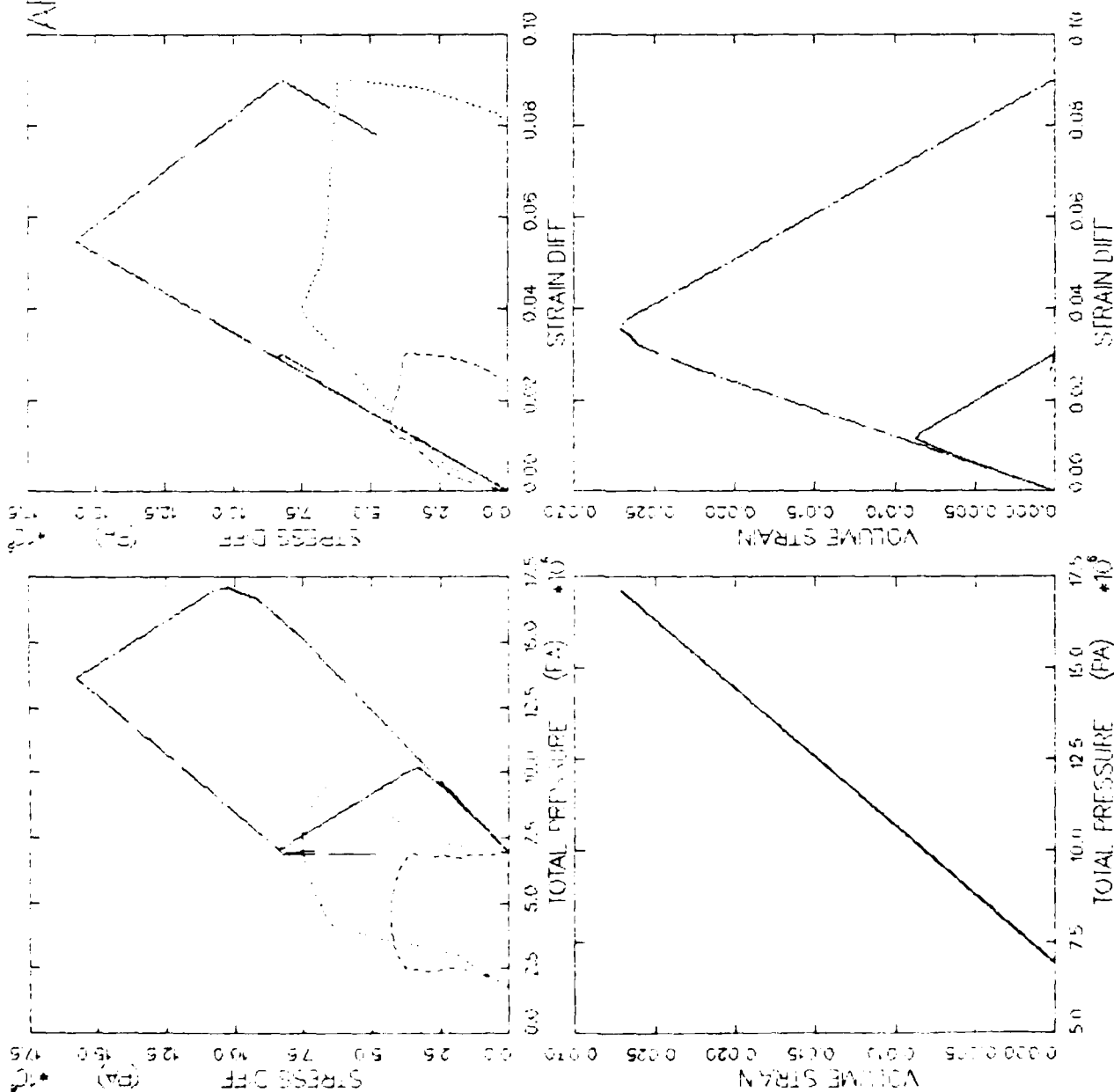
FIGURE V.5.22 ELPLA MODEL EXFR-AXISYM EPATH3A+3C — SDIFF/P/LV/EDIFF ANALYSIS
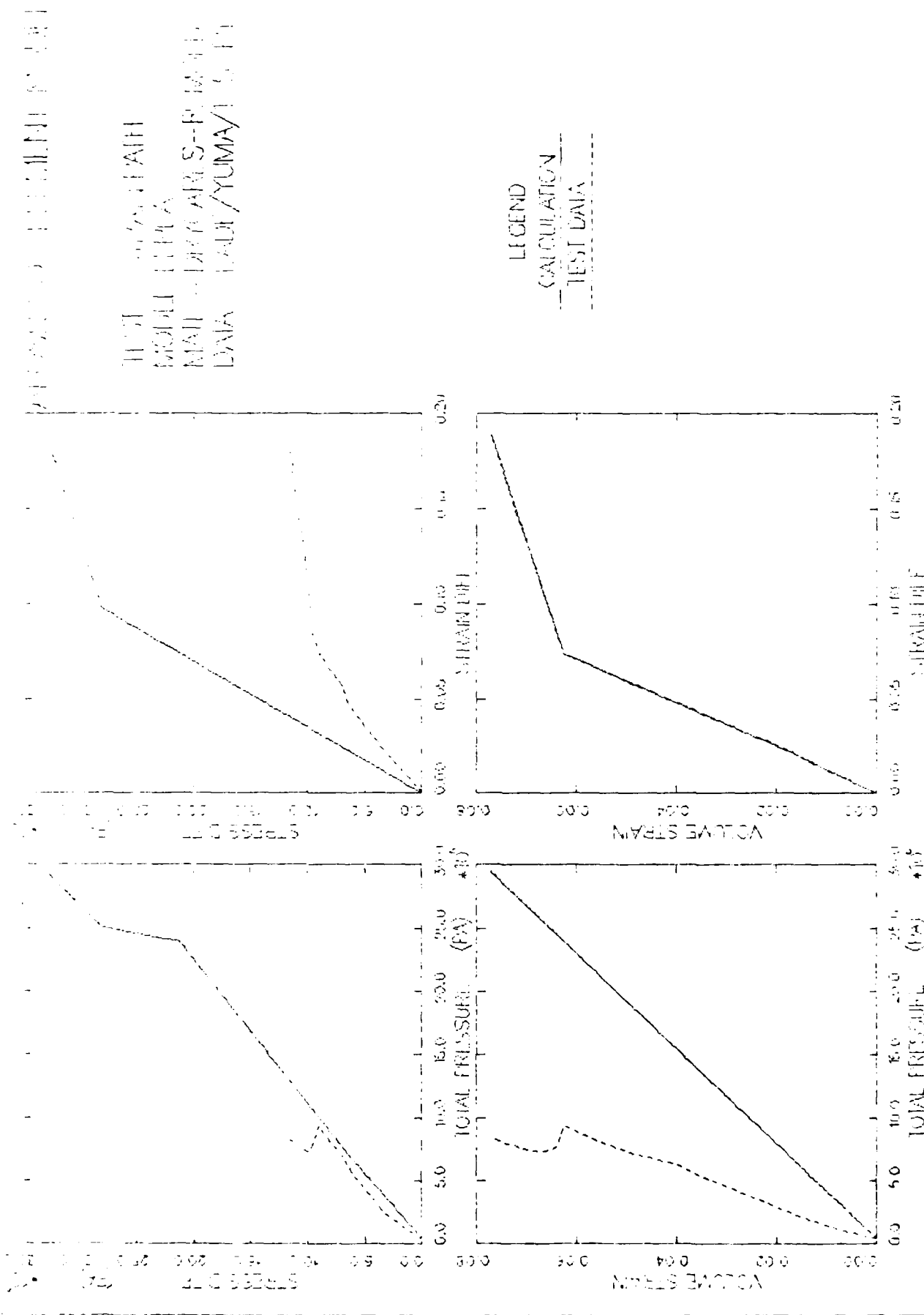
FIGURE V.5.23 ELEPHANT BALL — LAR AXISYMMETRIC II — SEMI-ANALYTIC ANALYSIS
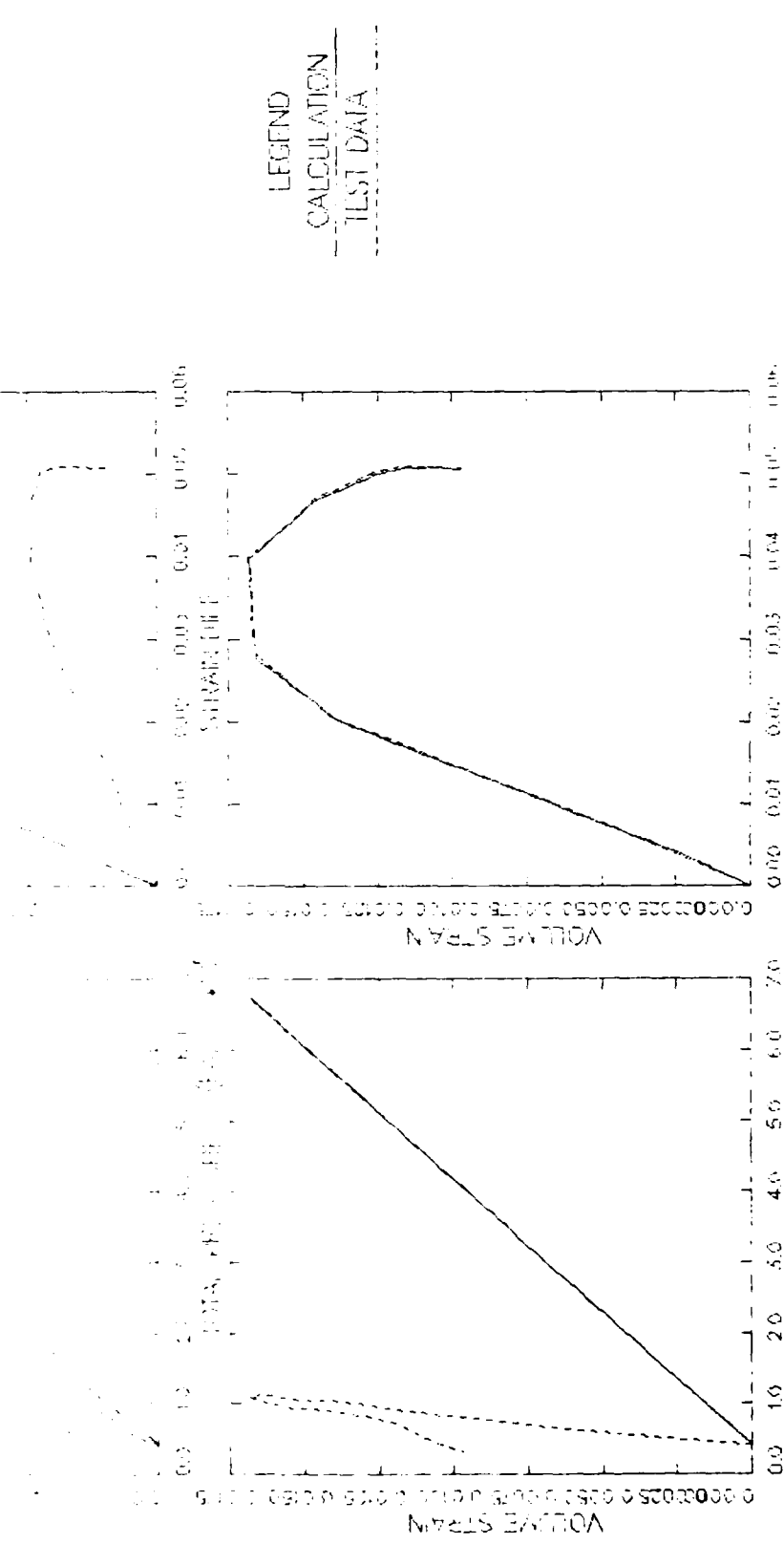
FIGURE V.5.24   ELPLA MODEL – LADE AXISYMETRIC – SOIL ELEMENT VOLUME ANALYSIS
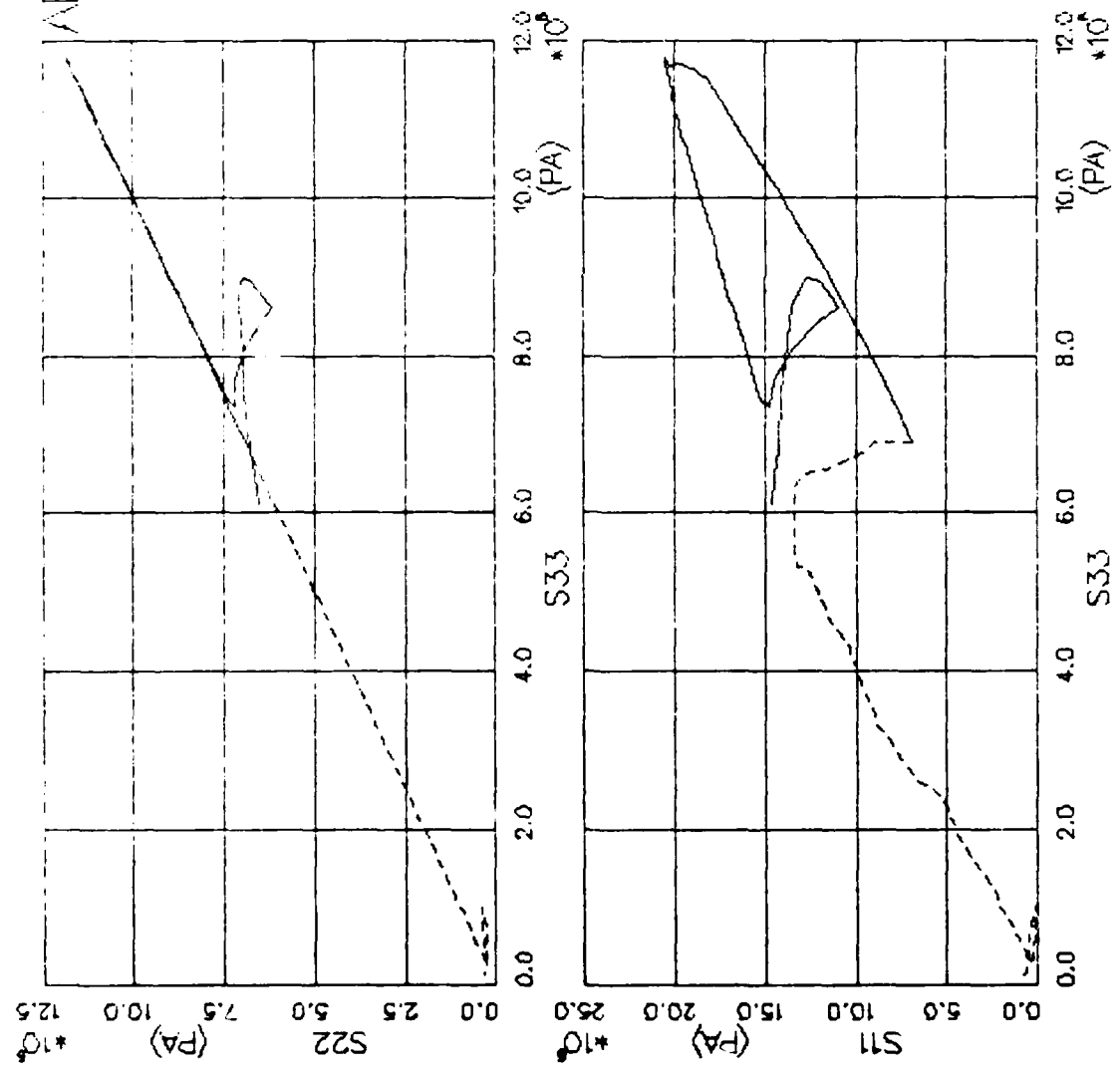
FIGURE V.5.25 ELPLA MODEL EXERCISE--TRUE TRIAX -- PRINCIPAL STRESS PATH

AFOSR SOIL ELEMENT MODEL

TEST = STRAIN PATH
MODEL= ELPLA
MATL = DRYCARES—REMOLD
DATA = NELLISB/KO/JAN83

LEGEND
CALCULATION
TEST DATA
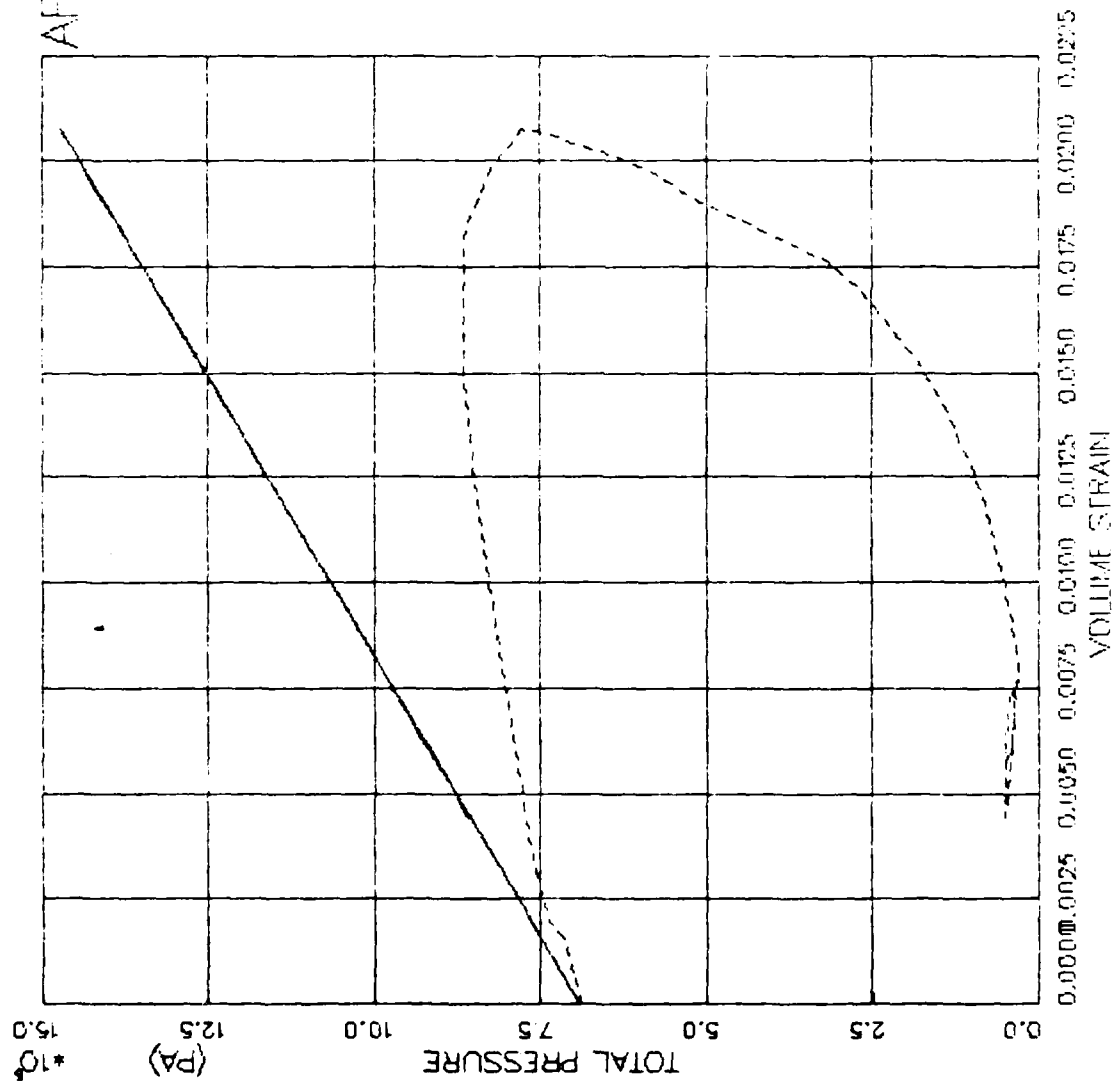
FIGURE V.5.26   ELPLA MODEL EXERCISE—TEUJI TRIAX - PRESSURE VS. VOLUMETRIC STRAIN

V.6 Modified AFWL Engineering

V.6.1 Motivation

The AFWL engineering model is hypoelastic-perfectly plastic in shear,
and hypoelastic in compression. A hypoelastic material is one for which
the stress increments are homogenous linear functions of the strain
increments. The coefficients in the linear functions may depend on stress
[Fung (1965:445); Nelson, Baron, and Sandler (1971:314)]. The principal
advantages of the AFWL engineering model are ease of fitting to laboratory
and in-situ test data, simplicity of the shear plasticity formulation, and
the fact that the model exhibits compressive hysteresis, which most soils
do but many elastic-perfectly plastic models do not. Its principal
disadvantages are lack of hysteresis in pure shear at constant volume
below the failure surface, and lack of dilatancy because the plastic
potential function for yielding in shear is the von Mises function (a
right circular cylinder centered on the hydrostatic axis), which causes
plastic incompressibility in shear.

V.6.2 Assumptions

Figure (0.1) shows the shear failure surface, plastic potential
surface, and hysteretic hydrostat which partially define a modified
version of the AFWL engineering model in use at Applied Research
Associates. The initial loading hydrostat governs only when the
Printout cancelled by operator

segment slopes must be specified so as to avoid compressive energy creation, and Poisson's ratio must be specified on each hydrostat segment so as to avoid distortional energy creation, as well as match constrained compression stress paths for both initial loading and unloading/ reloading. When the compressive volumetric strain falls below the value at which the unloading hydrostat yields a value of I_1 less than T, the tension cutoff, both I_1 and the bulk modulus, K, are set equal to zero. As the material recompresses after tensile failure, both I_1 and K remain zero until the compressive volumetric strain exceeds the value at which the unloading/reloading hydrostat crosses the volumetric strain axis. As long as K is zero the shear modulus, G, is also zero, so that no hypoelastic deviator stress increments are generated. This means that all stresses are zero, because the only point in Figure (Q.1a) at which the tension limit can be reached without previously violating the shear failure surface is the point where the shear failure surface meets the I_1 axis, and there the deviator stresses are already zero. Therefore when tensile failure occurs the stress point automatically moves from the tension cutoff point to the origin in Figure (Q.1a), and stays there until the hydrostatic stress starts to build up from zero. When that happens the shear modulus again becomes nonzero, and hypoelastic deviator stress increments once again start to accumulate. The AFWL engineering model is rate independent, and the shear plastic flow rule is nonassociative with respect to the Drucker- Prager portions of the shear failure surface and associative with respect to the von Mises portion.

V.6.3 Basic Equations

The hydrostat defines the incremental elastic (hypoelastic) bulk modulus as a function of current and maximum past compressive volumetric strain, and compressive volumetric strain increment.

$$K = K(\varepsilon_V, \varepsilon_{VM}, d\varepsilon_V) \qquad (V.6.1)$$

where

$$\varepsilon_{VM} = \text{maximum past compressive volumetric strain}$$

Poisson's ratio is also defined for each hydrostat segment, so that

$$\nu = \nu(\varepsilon_V, \varepsilon_{VM}, d\varepsilon_V) \qquad (V.6.2)$$

Hypoelastic constrained compression and shear moduli are then computed from the expressions

$$M = \frac{3K(1 - \nu)}{1 + \nu} \qquad (V.6.3)$$

$$G = \frac{3K(1 - 2\nu)}{2(1 + \nu)} \qquad (V.6.4)$$

The shear failure surface is a series of conical segments, each having an equation of the form

$$f\left(I_1, \sqrt{J_2}\right) = \sqrt{J_2} - (a + bI_1) = 0 \qquad (V.6.5)$$

When the stress point lies below the failure surface, so that

$$f\left(I_1, \sqrt{J_2}\right) < 0 \qquad (V.6.6)$$

the material behaves incrementally elastically, in accordance with the equations of Appendix J. When a stress increment calculated assuming incrementally elastic behavior moves the stress point through the shear failure surface, so that

$$f\left[(I_1)_E, \left(\sqrt{J_2}\right)_E\right] = \delta > 0 \qquad (V.6.7)$$

a correction procedure is invoked to return the stress point to the shear failure surface. The correction procedure is a special case of that

developed in Appendix P. Since the von Mises plastic potential function has the form

$$g = \sqrt{J_2} \tag{V.6.8}$$

it follows from Equations (V.6.5) and (V.6.8) that

$$f_I = -b \tag{V.6.9}$$

$$f_{II} = 1 \tag{V.6.10}$$

$$g_I = 0 \tag{V.6.11}$$

$$g_{II} = 1 \tag{V.6.12}$$

so that Equations (P.17), (P.22), (P.25), (P.26), (P.28), (P.29), and (P.32) yield

$$d\lambda = \frac{f_3}{G} \tag{V.6.13}$$

$$\{de^p\} = \frac{f_3}{2G\sqrt{J_2}} \{s\} \tag{V.6.14}$$

$$(dI_1)_p = 0 \tag{V.6.15}$$

$$\left(d\sqrt{J_2}\right)_p = -f_3 \tag{V.6.16}$$

$$\left(\sqrt{J_2}\right)_4 = a + b(I_1)_3 \tag{V.6.17}$$

$$\{s\}_4 = \sqrt{\frac{(J_2)_4}{(J_2)_3}} \{s\}_3 \tag{V.6.18}$$

$$\underline{C}^{ep} = \underline{C}^e + \frac{3Kb}{\sqrt{J_2}} \{s\}\{m\}^T - \frac{G}{J_2} \{s\}\{s\}^T \tag{V.6.19}$$

From Equation (V.6.19), the incremental constrained modulus for a point on the shear failure surface is

$$M_v = M + \frac{3Kb}{\sqrt{J_2}} s_1 - \frac{G}{J_2} s_1^2 \tag{V.6.20}$$

421

and the incremental constrained horizontal modulus for a point on the shear failure surface is

$$M_H = K_o M + \frac{3Kb}{\sqrt{J_2}} s_2 - \frac{G}{J_2} s_1 s_2 \qquad (V.6.21)$$

Equations (V.6.20) and (V.6.21) provide the information required to compute the constrained compression stress-strain curve and stress path, since

$$\left(\frac{d\sigma_1}{d\epsilon_1}\right)_{K_o} = M_V \qquad (V.6.22)$$

$$\left(\frac{d\sigma_1}{d\sigma_3}\right)_{K_o} = \frac{M_V}{M_H} \qquad (V.6.23)$$

It is shown in Appendix Q that the incremental stiffness matrix defined by Equation (V.6.19) does produce a stress increment that lies in the shear failure surface.

V.6.4 Parameter Determination

The parameters of the AFWL engineering model are determined by fitting a series of straight lines to shear strength, hydrostatic compression, and constrained (uniaxial) compression or K_o test data.

For triaxial compression, Equations (K.3) and (K.9) yield

$$I_1 = \sigma_a + 2\sigma_r \qquad (V.6.24)$$

and

$$\sqrt{J_2} = \frac{|\sigma_a - \sigma_r|}{\sqrt{3}} \qquad (V.6.25)$$

Then assuming shear strength data are obtained from drained triaxial compression tests at constant cell pressure, straight lines are fit to consecutive portions of the data, plotted as σ_{af} (the dependent variable) versus σ_r (the independent variable) either by eye or by linear regression. Successive linear relations between $\sqrt{J_2}$ and I_1 are

422

then obtained by a simple linear transformation, and these relations constitute the shear failure criterion.

Since axial strain equals volumetric strain in a constrained compression test, Poisson's ratio can be calculated if both hydrostatic and constrained compression test data are available, and if the fitted straight line segments to both curves have common volumetric strain break points. Equation (V.6.3) yields

$$\nu = \frac{3K - M}{3K + M} = \frac{3 - \frac{M}{K}}{3 + \frac{M}{K}} \tag{V.6.26}$$

Otherwise, Poisson's ratio is assumed, and either M is calculated from Equation (V.6.3) when only hydrostatic test data are available, or K is calculated from the equation

$$K = \frac{M(1 + \nu)}{3(1 - \nu)} \tag{V.6.27}$$

when only constrained compression test data are available.

In case K_o test data are available (from constrained compression tests conducted in a triaxial cell, in which the confining stress is measured), Poisson's ratio can be computed from the hyperbolic relations

$$K_o = \frac{M_H}{M_V} = \frac{\nu}{1 - \nu} \tag{V.6.28}$$

$$\nu = \frac{K_o}{1 + K_o} \tag{V.6.29}$$

This last method is the most desirable for airblast loading applications, but K_o tests are more difficult and expensive than either simple constrained compression (oedometer) or hydrostatic compression tests.

Modified AFWL engineering model parameters were determined for remolded CARES-DRY sand by fitting uniaxial strain data (stress-strain and stress path) and triaxial compression shear failure data. These parameters are listed in Table (V.6.1).

423

V.6.5 Computed Behavior

By examining Figures (V.6.17-V.6.19) one can see that an excellent fit is achieved for uniaxial compression (UXC), since this data was used for fitting. Isotropic compression behavior (which is a prediction) is also well matched, as shown in Figure (V.6.1). CTC behavior [Figures (V.6.2-V.6.5)] is well fit with respect to ultimate shear strength [Figure (V.6.2)], but the match of stress-strain response prior to failure deteriorates with increasing confining pressures and the model does not predict any dilatancy [Figures (V.6.4) and (V.6.5)]. Because the AFWL engineering model considers any stress excursion causing volume expansion to be unloading, and subsequently invokes a very high stiffness, CTE stress-strain behavior is rather poorly predicted [Figures (V.6.6) through (V.6.9)]. Note also that a failure surface which is symmetrical about the P-axis does not match triaxial extension data well. The sharp discontinuities in stress-strain behavior caused by the load-unload bifurcation are again demonstrated in the RTC/E calculated results [Figures (V.6.10-V.6.13)]. Calculated pure shear behavior, which by AFWL engineering standards is neither loading nor unloading, shows very stiff behavior [Figures (V.6.14) and (V.6.15)] because of the μ_{max} convention for deciding which bulk modulus to use. Figure (V.6.16) summarizes the behavior calculated by the AFWL engineering model for stress paths run in the triaxial device starting at 7.1 MPa confining pressure. An important aspect of behavior to notice is the single $P-\varepsilon_v$ response enforced for all stress paths.

Stress paths generated by uniaxial strain extension are not characteristic of the data [Figure (V.6.20)] because of the symmetrical

failure surface and elastic response prior to encountering the failure surface. Shear response for the UXE test is shown in Figure (V.6.21).

Comparisons of calculated strain path results for this model with actual data are only fair. Stress path shapes for both the WES strain paths [Figure (V.6.22)] and the Lade strain paths [Figures (V.6.23-V.6.24)] are similar to the data, but off in both pressure and stress difference magnitudes. A large part of the deviation occurs when the specified strain path dictates expansive volumetric strain. At this point, as shown in Figure (V.6.22), the shear modulus jumps due to the abrupt bulk modulus change at unloading. Eventually the failure surface is reached and followed back down to its apex. The calculated response for the true-triaxial strain path is compared with the data from Nellis Baseline Sand in Figures (V.6.25) and (V.6.26). With the exception of the initial direction of the stress path, these results are good.

TABLE V.6.1. MODIFIED AFWL ENGINEERING MODEL
PAREMETERS FOR CARES-DRY SAND

Parameter	Symbol	Variable	Value	Units
No. Load Slopes	n_l	RNLS	8	--
No. Unload Slopes	n_u	RNUS	5	--
		BKL(1)	9.302×10^7	Pa
		BKL(2)	6.261×10^7	Pa
		BKL(3)	1.491×10^8	Pa
Loading	K_l	BKL(4)	3.530×10^8	Pa
Bulk Moduli		BKL(5)	1.088×10^9	Pa
		BKL(6)	3.419×10^9	Pa
		BKL(7)	9.042×10^9	Pa
		BKL(8)	2.792×10^{10}	Pa
		EBL(1)	0.01181	--
		EBL(2)	0.08191	--
		EBL(3)	0.1292	--
Loading Strain	ϵ_{bl}	EBL(4)	0.1642	--
Break Points		EBL(5)	0.2014	--
		EBL(6)	0.2294	--
		EBL(7)	0.2516	--
		EBL(8)	1.0000	--
Loading		POL(1)-		
Poisson's Ratio	ν_l	POL(8)	0.32	--
		BKU(1)	9.000×10^{11}	Pa
		BKU(2)	4.500×10^{10}	Pa
Unloading		BKU(3)	1.390×10^{10}	Pa
Bulk Moduli	K_u	BKU(4)	4.725×10^9	Pa
		BKU(5)	1.000×10^9	Pa
Unloading		PBU(1)	1.045×10^{10}	Pa
Hydrostatic	P_{bu}	PBU(2)	2.800×10^8	Pa
Pressure		PBU(3)	3.000×10^7	Pa
Break Points		PBU(4)	2.000×10^7	Pa
		PBU(5)	-2.880×10^5	Pa
Unloading		POU(1)-		
Poisson's Ratio	ν_u	POU(5)	0.20	--
Tension Cutoff	T	ST1	-2.880×10^5	Pa
F.S. Intercept	Y	Y1	2.880×10^5	Pa
F.S. Slope	S	S1	0.215	--
Von Mises Cutoff	VM	VM1	1.750×10^8	Pa
Mass Density	ρ	RHOREF	1900	kg/m^3
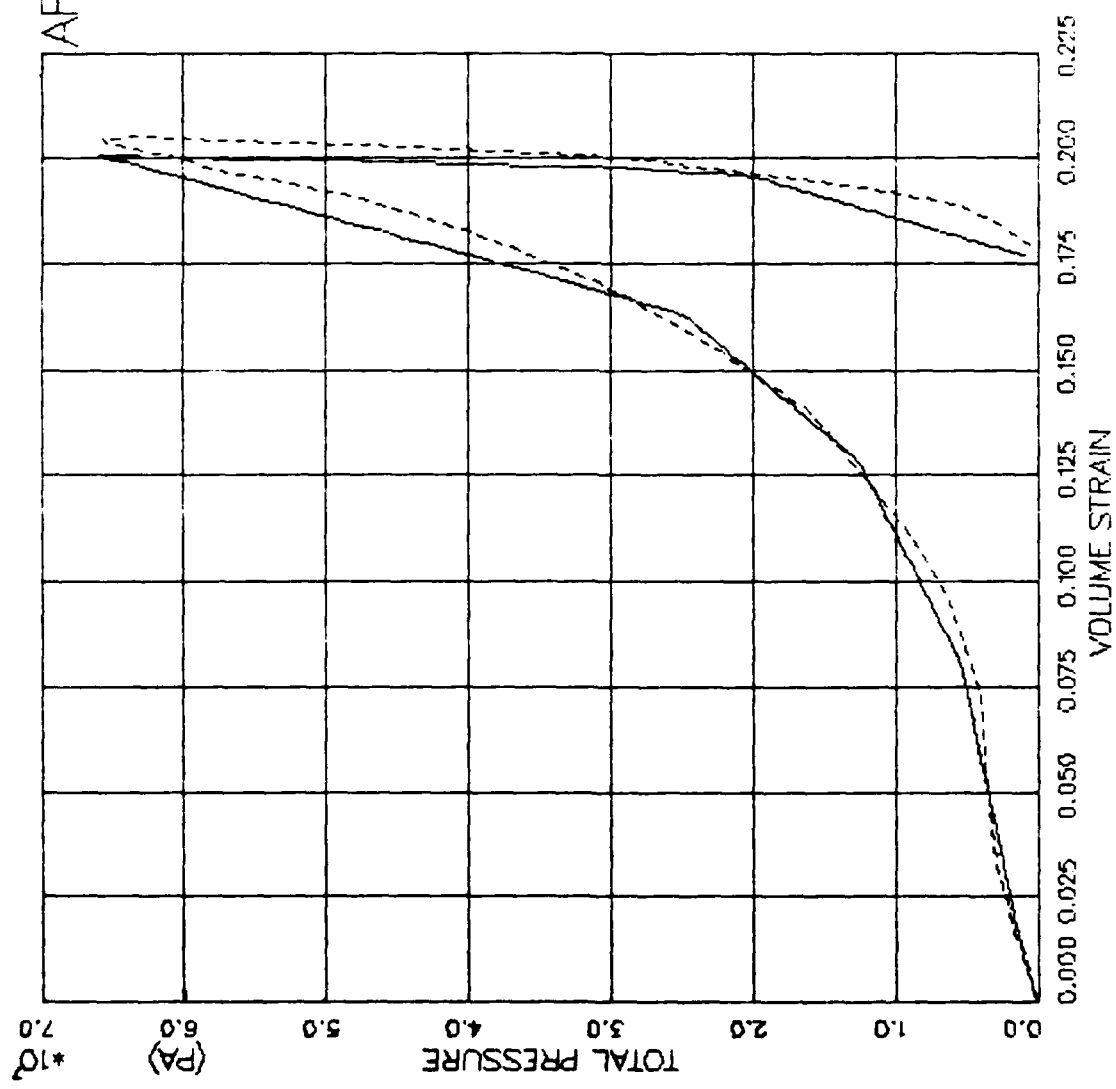
FIGURE V.6.1 AFWL MODEL EXERCISE – ISOTROPIC COMP. – PRESSURE VS. VOLUMETRIC STRAIN .
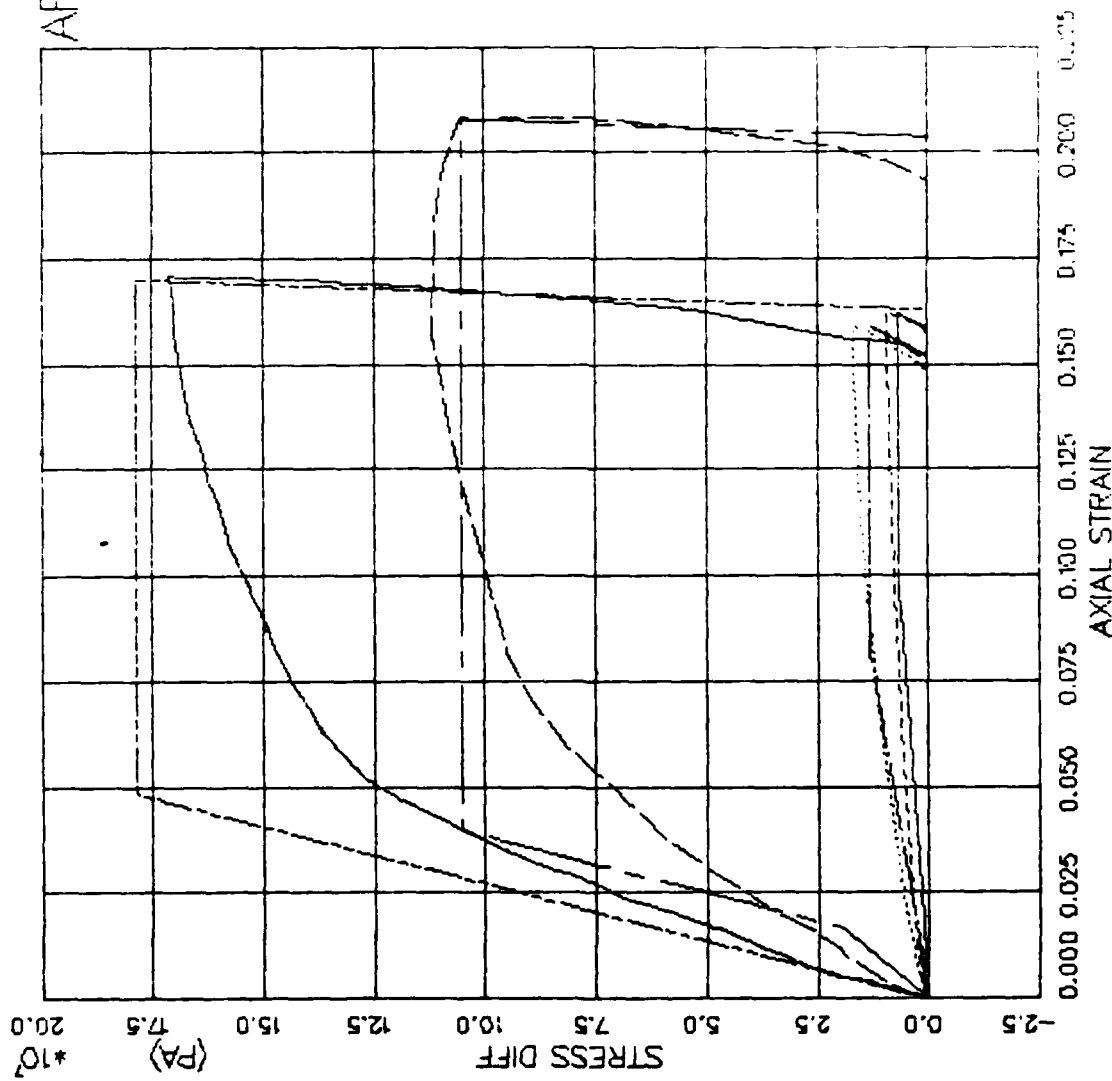
FIGURE V.6.2   AFWL MODEL EXERCISE—TRIAXIAL COMP(CTC)

428

AFOSR SOIL ELEMENT MODEL

TEST = STANDARD TRIAXIAL TEST
MODEL = AFWL
MATL = DRYCARES-REMOLD
DATA = DRYCARESR/WES/84

LEGEND
SIGMA3C= 3.4E6
SIGMA3C= 7.0E5
SIGMA3C= 58.8E6
SIGMA3C=100.0E6

FIGURE V.6.3   AFWL MODEL EXERCISE—TRIAXIAL COMP(CTC) — STRESS DIFF VS. STRAIN DIFF

429

AFOSR SOIL ELEMENT MODEL

TEST = STANDARD TRIAXIAL TEST
MODEL= AFWL
MATL = DRYCARES—REMOLD
DATA = DRYCARESR/WES/84

LEGEND
SIGMA3C= 3.4E6
TEST DATA
SIGMA3C= 7.0E6
TEST DATA
SIGMA3C= 58.8E6
TEST DATA
SIGMA3C=100.0E6
TEST DATA

AXIAL STRAIN
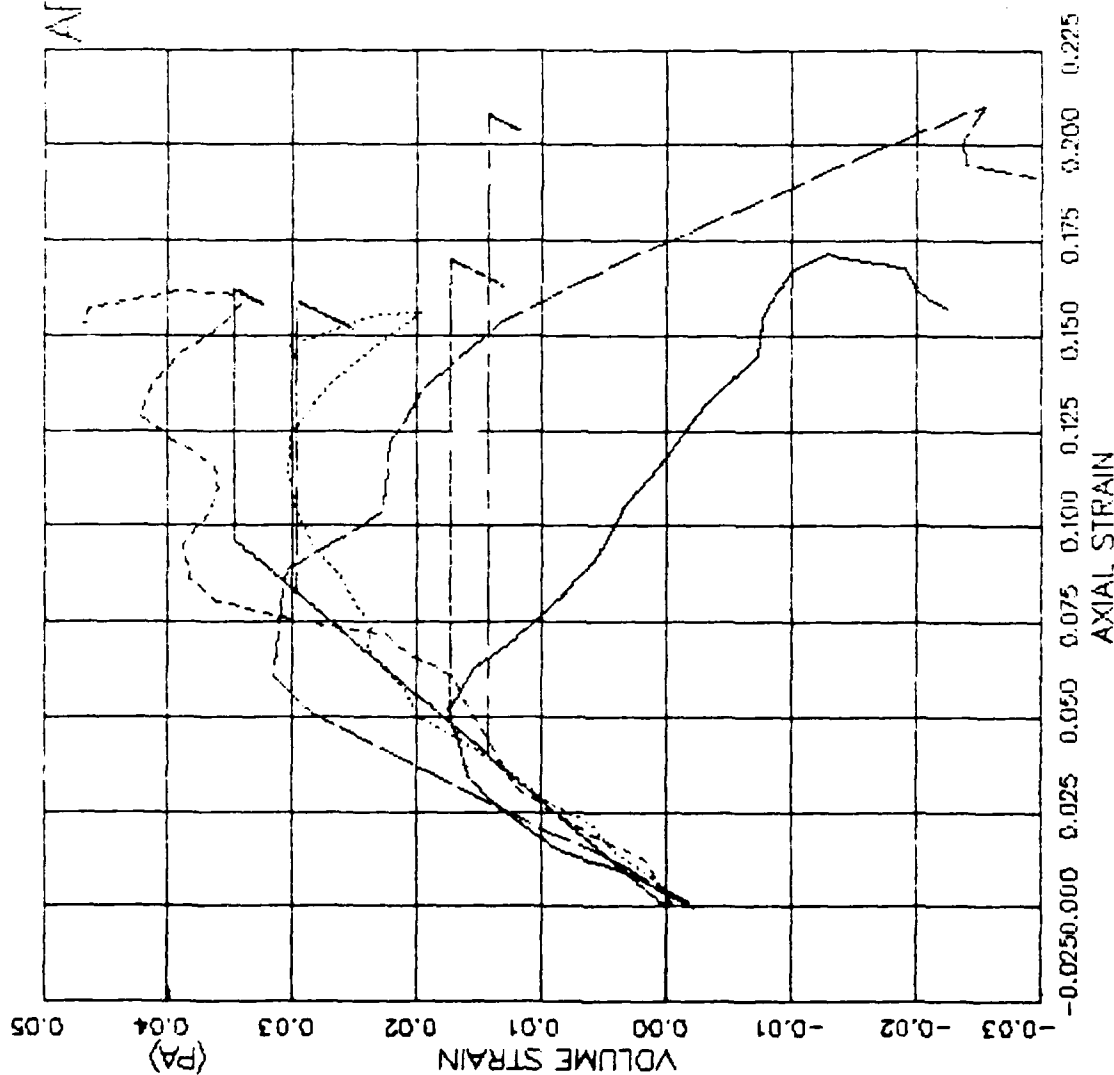
VOLUME STRAIN (PA)

FIGURE V.6.4 AFWL MODEL EXERCISE--TRIAXIAL COMP(CTC) - AXIAL STRAIN VS VOLUME STRAIN

AFOSR SOIL ELEMENT MODEL

TEST = STANDARD TRIAXIAL TEST
MODEL= AFWL
MATL = DRYCARES—REMOLD
DATA = DRYCARESR/WES/84

LEGEND
SIGMA3C= 3.4E6
TEST DATA
SIGMA3C= 7.0E6
TEST DATA
SIGMA3C= 53.8E6
TEST DATA
SIGMA3C=100.0E6
TEST DATA

FIGURE V.6.5 AFWL MODEL EXERCISE—TRIAXIAL COMP(CTC) — PRESSURE vs. VOLUMETRIC STRAIN .
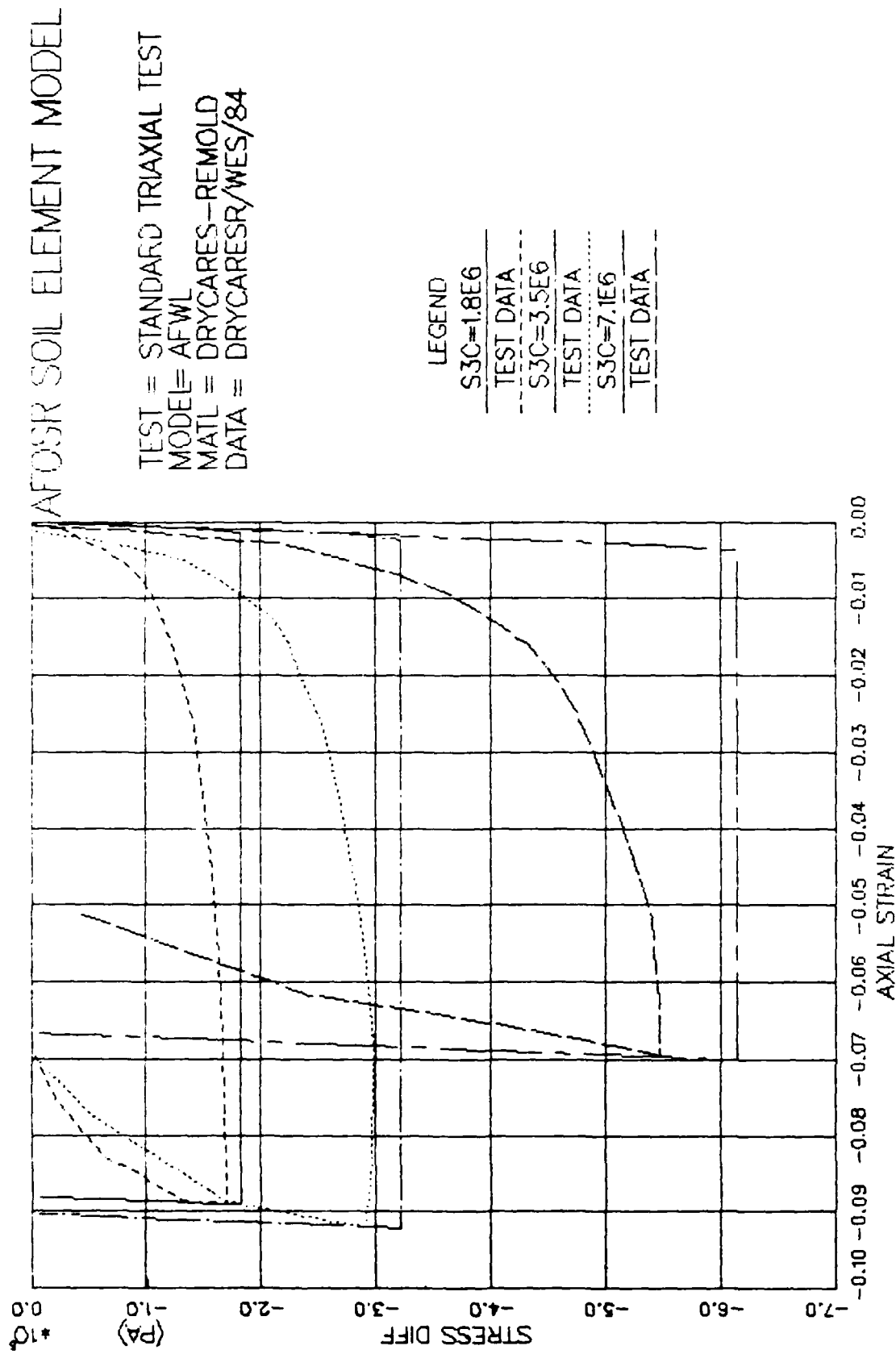
FIGURE V.6.6   AFWL MODEL EXERCISE—TRIAXIAL EXTEN(CTE) — STRESS DIFF VS. AXIAL STRAIN

AFOSR SOIL ELEMENT MODEL

TEST = STANDARD TRIAXIAL TEST
MODEL= AFWL
MATL = DRYCARES-REMOLD
DATA = DRYCARESR/WES/84

LEGEND
S3C=1.8E6
S3C=3.5E6
S3C=7.1E6
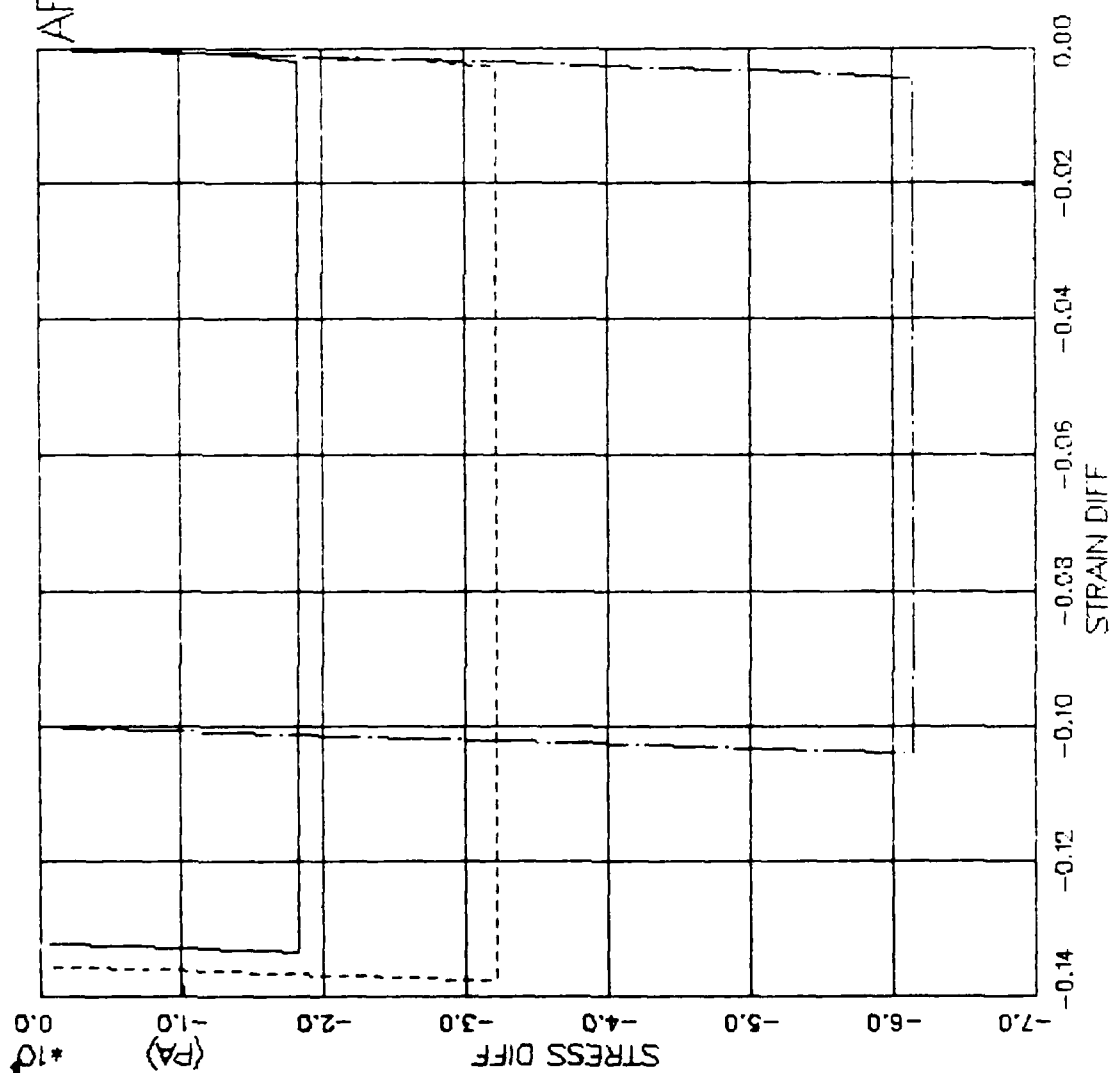
FIGURE V.6.7   AFWL MODEL EXERCISE—TRIAXIAL EXTEN(CTE) — STRESS DIFF VS. STRAIN DIFF

433
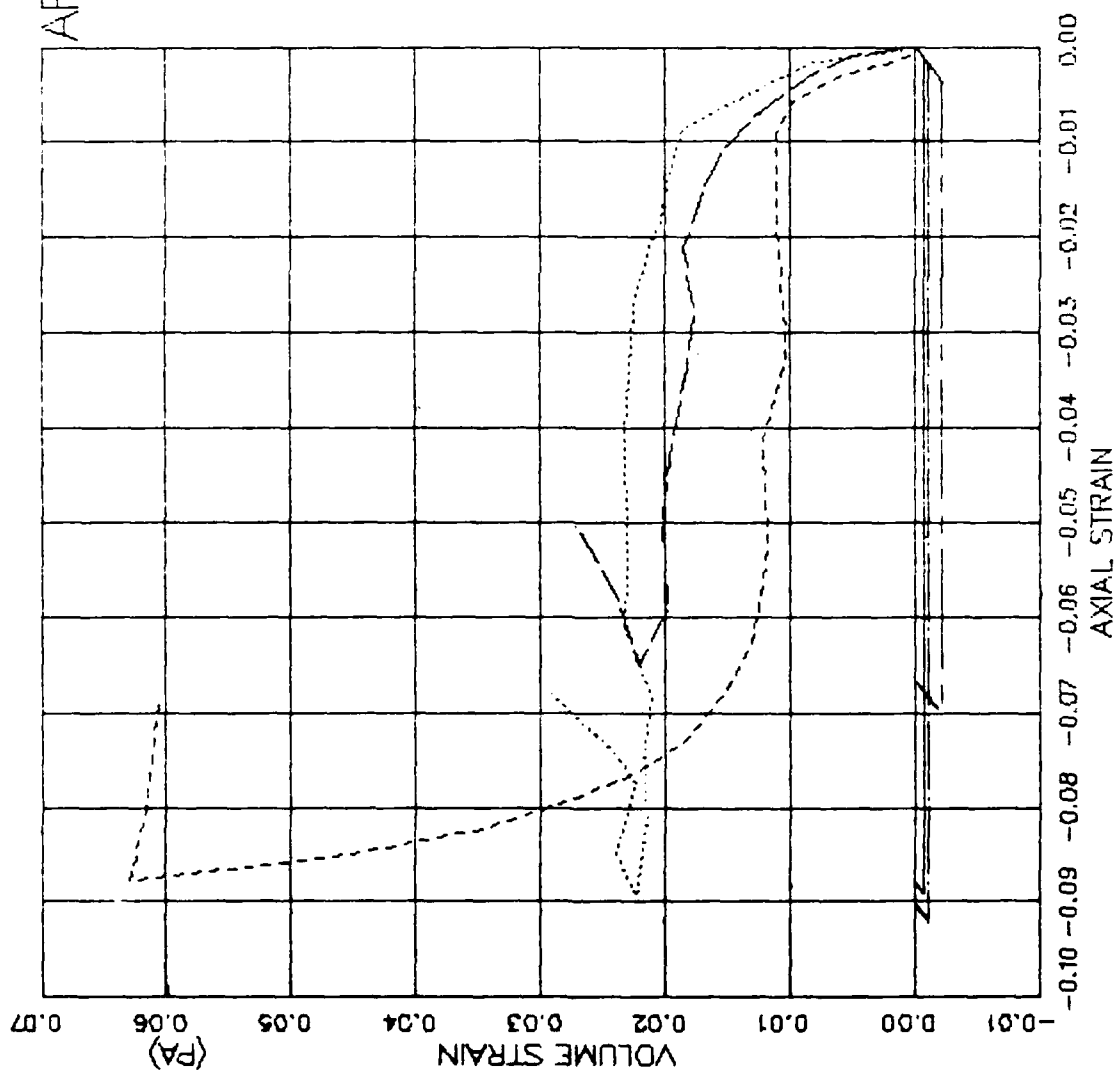
FIGURE V.6.8   AFWL MODEL EXERCISE—TRIAXIAL EXTEN(CTE) — AXIAL STRAIN VS VOLUME STRAIN

AFOSR SOIL ELEMENT MODEL

TEST = STANDARD TRIAXIAL TEST
MODEL= AFWL
MATL = DRYCARES—REMOLD
DATA = DRYCARESR/WES/84

LEGEND
S3C=1.8E6
S3C=3.5E6
S3C=7.1E6
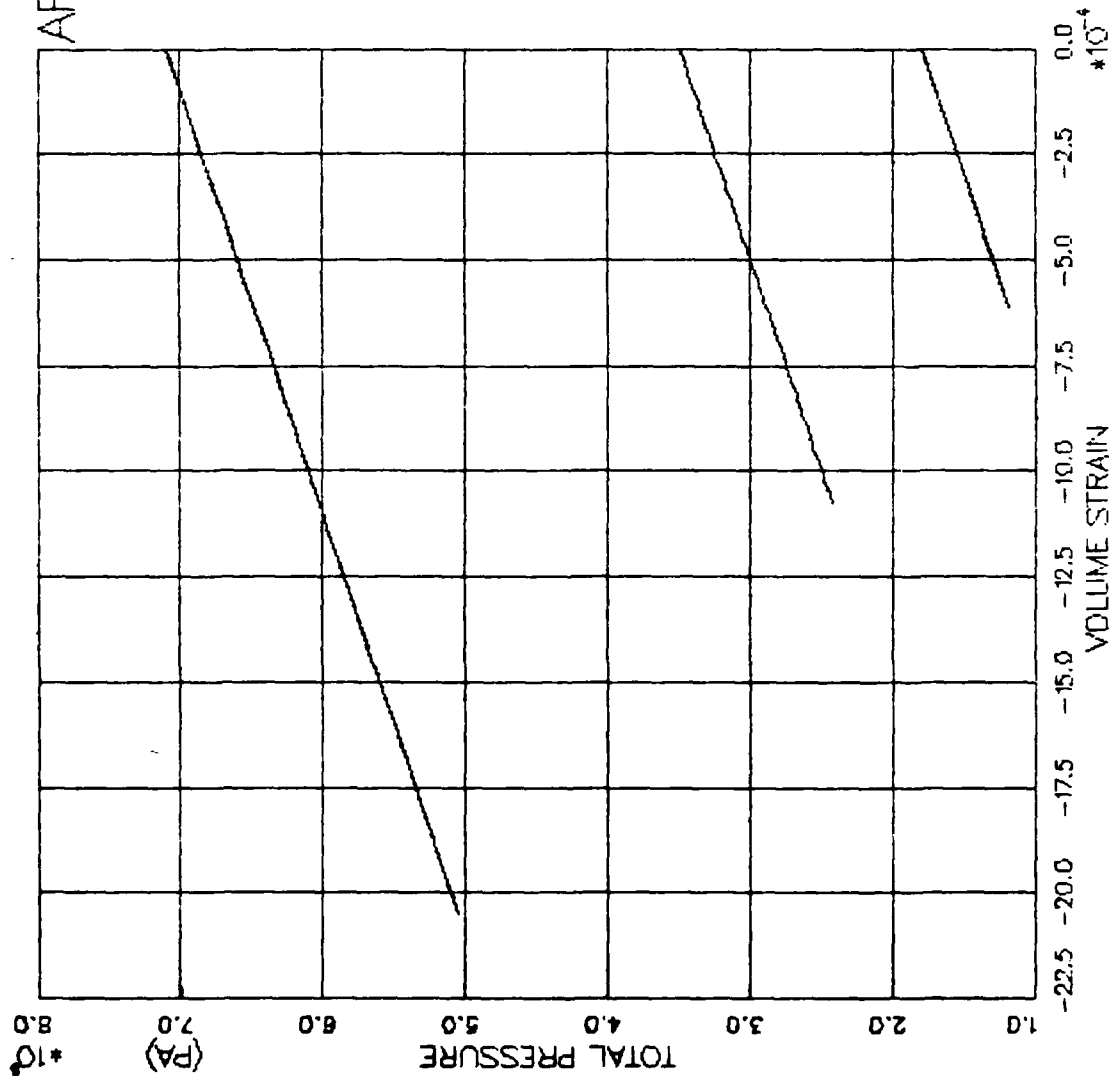
FIGURE V.6.9   AFWL MODEL EXERCISE–TRIAXIAL EXTEN(CTE) – PRESSURE VS. VOLUMETRIC STRAIN

435

AFOSR SOIL ELEMENT MODEL

TEST = STANDARD TRIAXIAL TEST
MODEL= AFWL
MATL = DRYCARES-REMOLD

LEGEND
RTC/S3C=1.8E6
RTC/S3C=1.8E6
RTC/S3C=3.5E6
RTC/S3C=3.5E6
RTC/S3C=7.1E6
RTC/S3C=7.1E6
RTE/S3C=1.8E6
RTE/S3C=1.8E6
RTE/S3C=3.5E6
RTE/S3C=3.5E6
RTE/S3C=7.1E6
RTE/S3C=7.1E6
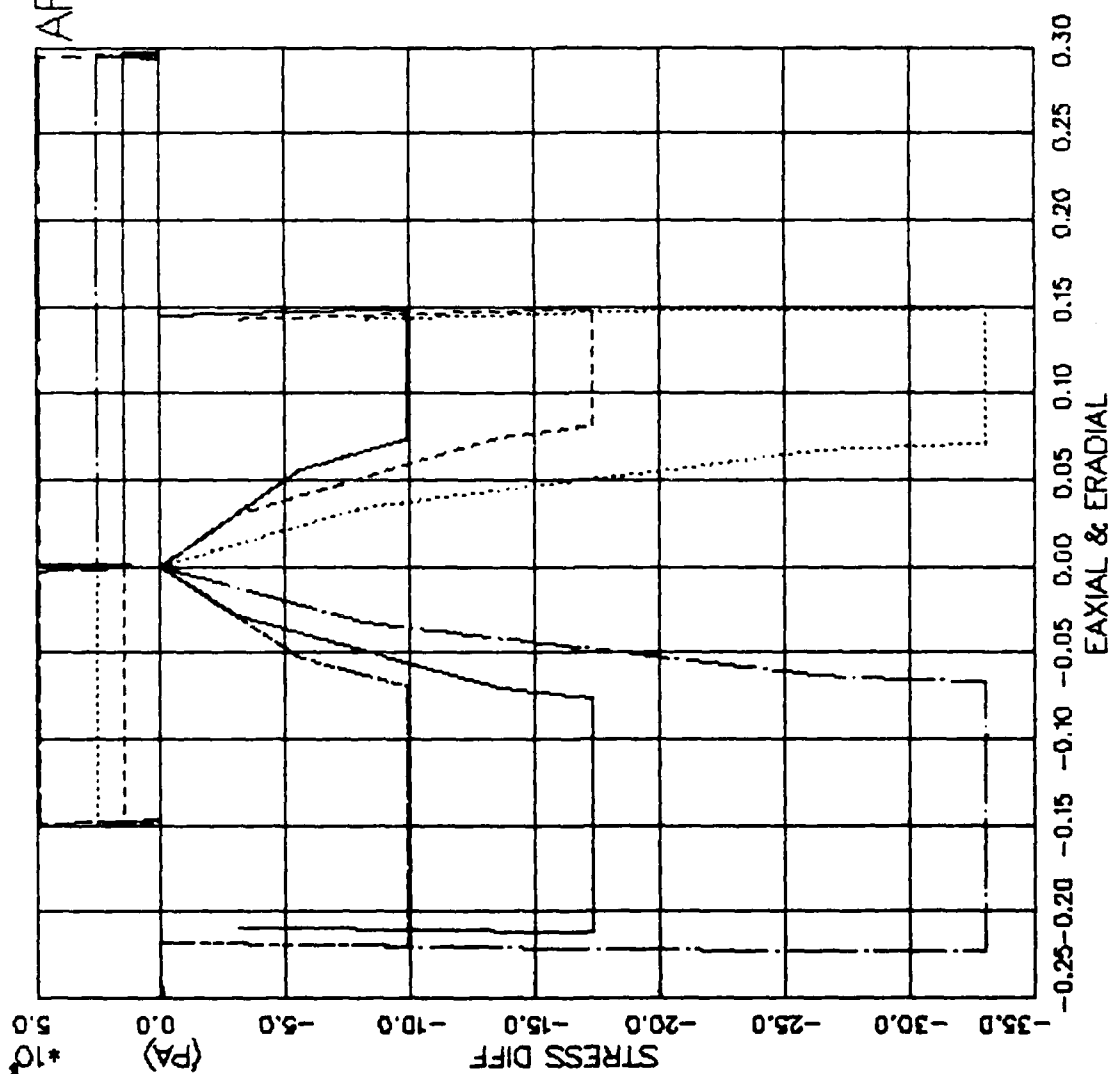
FIGURE V.6.10 AFWL MODEL EXER-REDUCED TRIAX(RTC+RTE) - STRESS DIFF VS. STRAIN

436
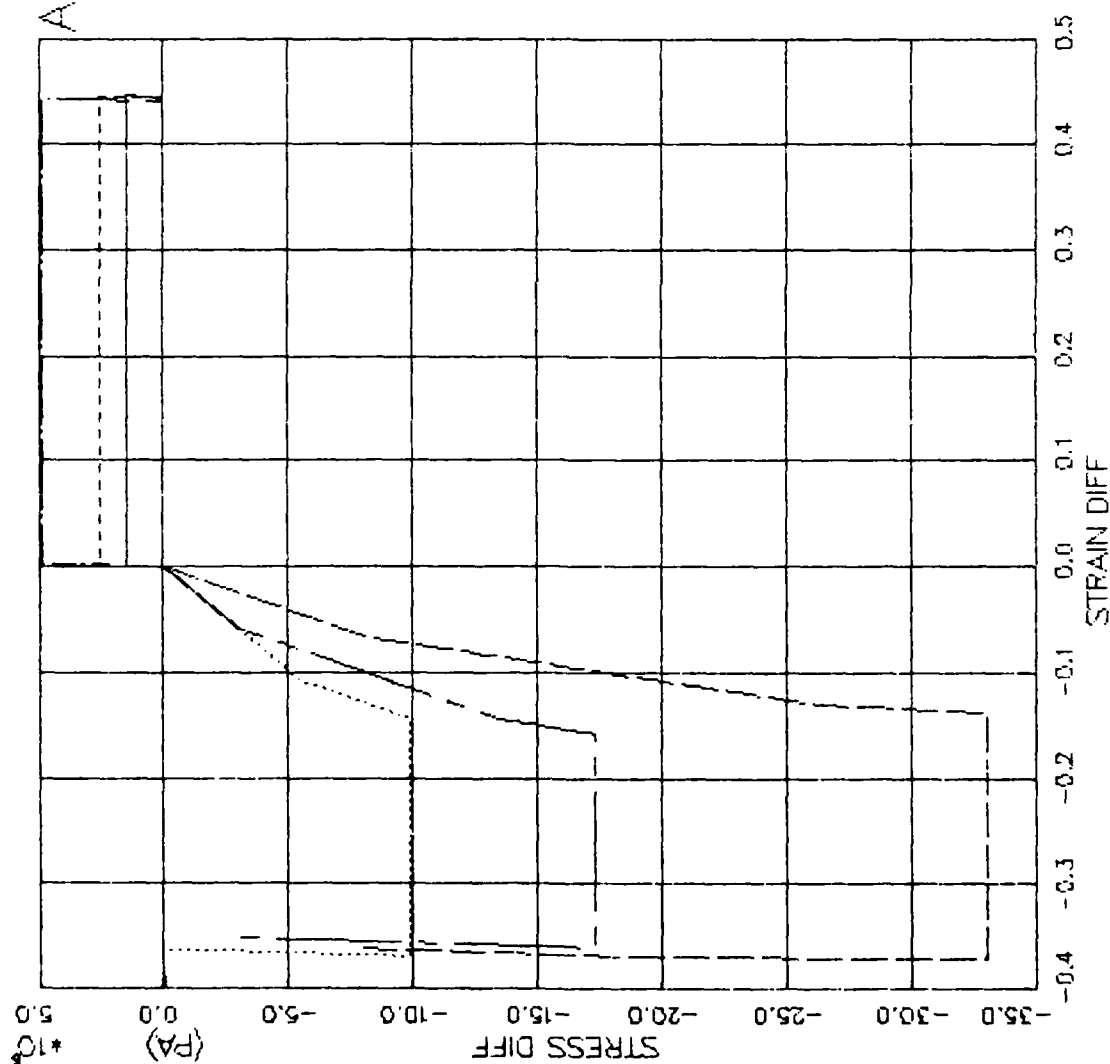
FIGURE V.6.11 AFWL MODEL EXER—REDUCED TRIAX(PTC+RTE) — STRESS DIFF VS. STRAIN DIFF

AFOSR SOIL ELEMENT MODEL

TEST = STANDARD TRIAXIAL TEST
MODEL= AFWL
MATL = DRYCARES—REMOLD

LEGEND
PTC/S3C=1.8E6
RTC/S3C=3.5E6
RTC/S3C=7.1E6
RTE/S3C=1.8E6
RTE/S3C=3.5E6
RTE/S3C=7.1E6
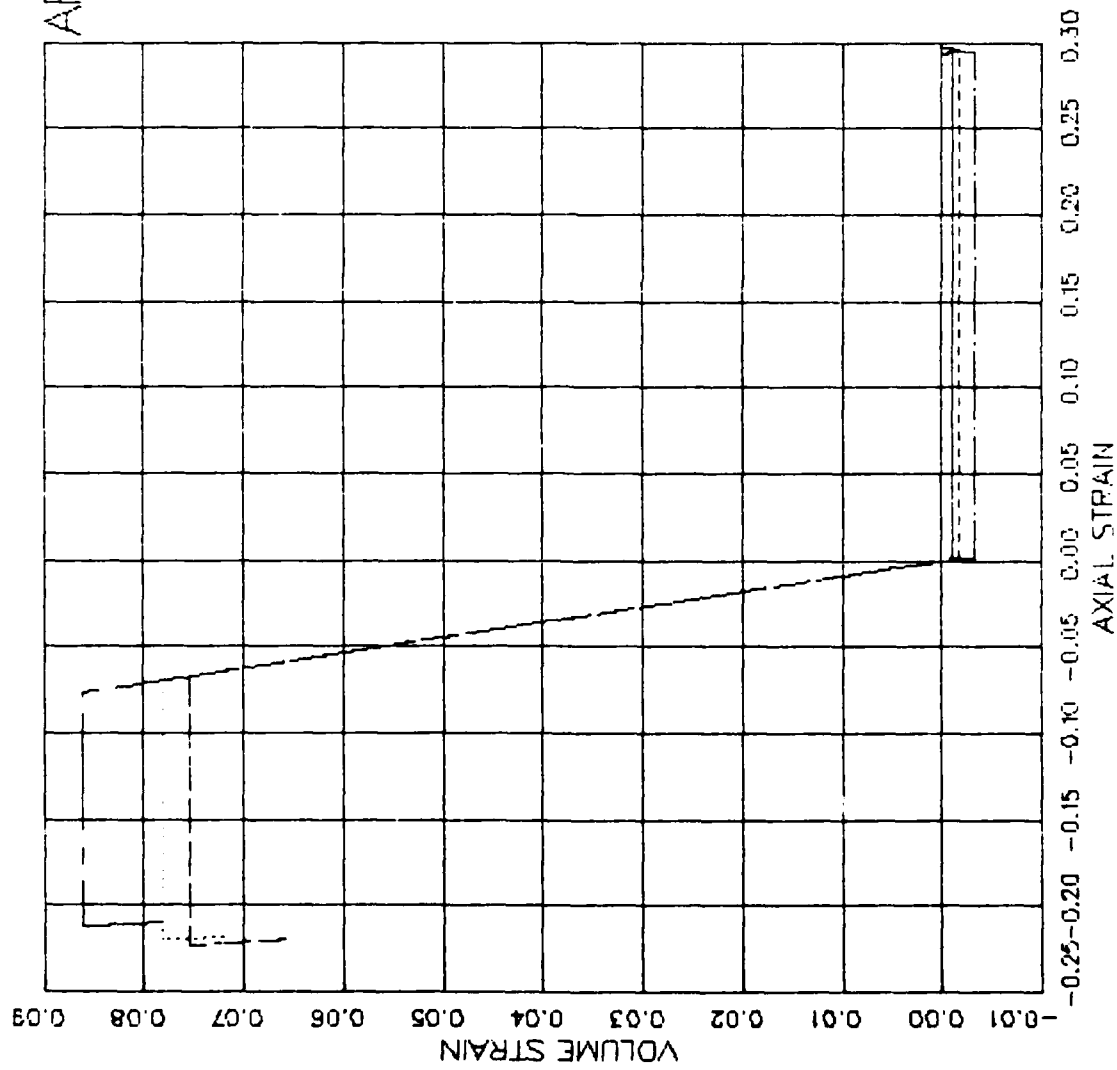
FIGURE V.6.12 AFWL MODEL EXER-REDUCED TRIAX(RTC+RTE) - AXIAL STRAIN VS VOLUME STRAIN

AFOSR SOIL ELEMENT MODEL

TEST = STANDARD TRIAXIAL TEST
MODEL= AFWL
MATL = DRYCARES–REMOLD

LEGEND
RTC/S3C=1.8E6
RTC/S3C=3.5E6
RTC/S3C=7.1E6
RTE/S3C=1.8E6
RTE/S3C=3.5E6
RTE/S3C=7.1E6
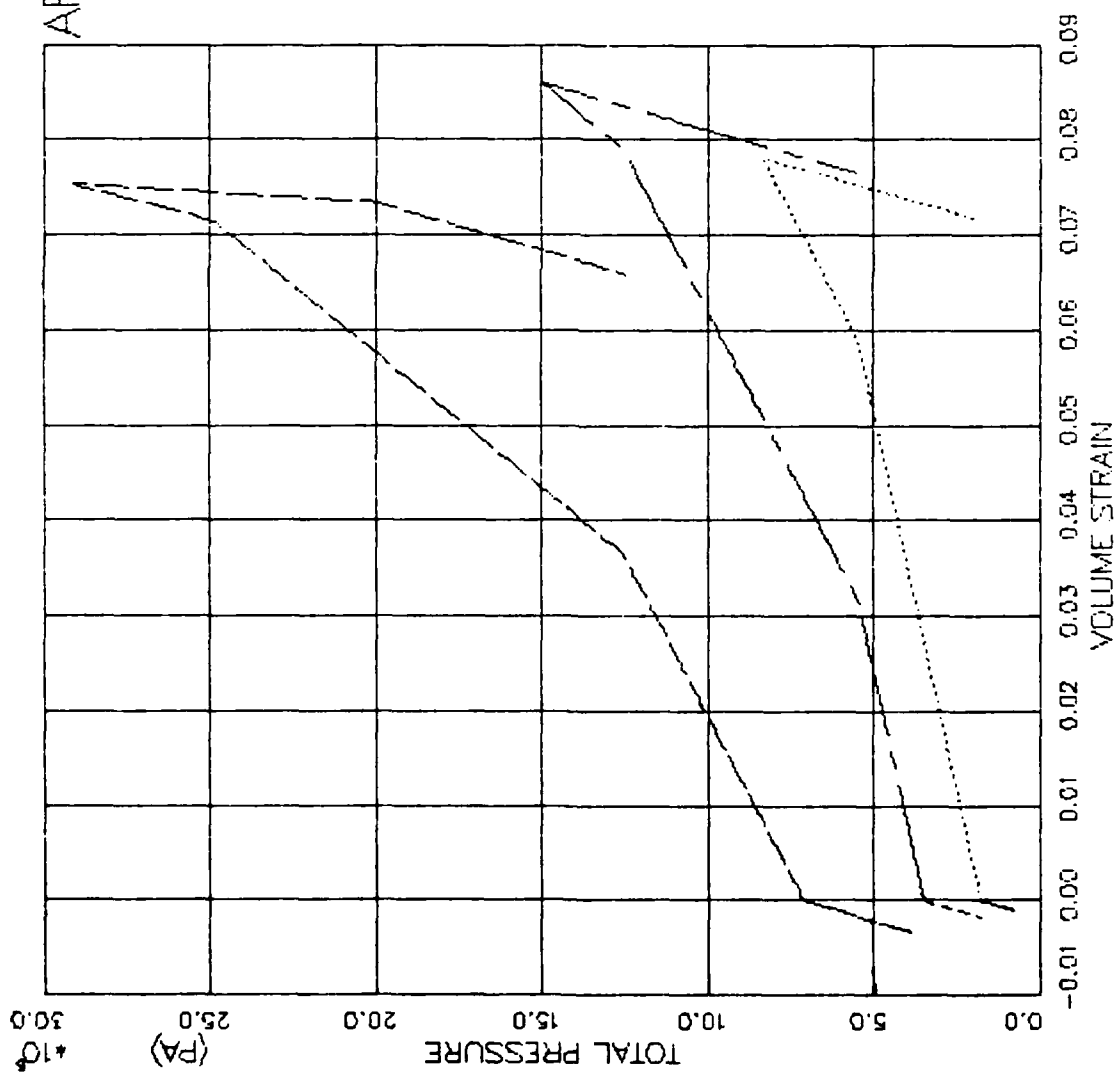
FIGURE V.6.13 AFWL MODEL EXER–REDUCED TRIAX(RTC+RTE) – PRESSURE VS VOLUMETRIC STRAIN

439

AFOSR SOIL ELEMENT MODEL

TEST = STANDARD TRIAXIAL TEST
MODEL= AFWL
MATL = DRYCARES—REMOLD

LEGEND
PSC/S3C=1.8E6
PSC/S3C=1.8E6
PSC/S3C=3.5E6
PSC/S3C=3.5E6
PSC/S3C=7.1E6
PSC/S3C=7.1E6
PSE/S3C=1.8E6
PSE/S3C=1.8E6
PSE/S3C=3.5E6
PSE/S3C=3.5E6
PSE/S3C=7.1E6
PSE/S3C=7.1E6
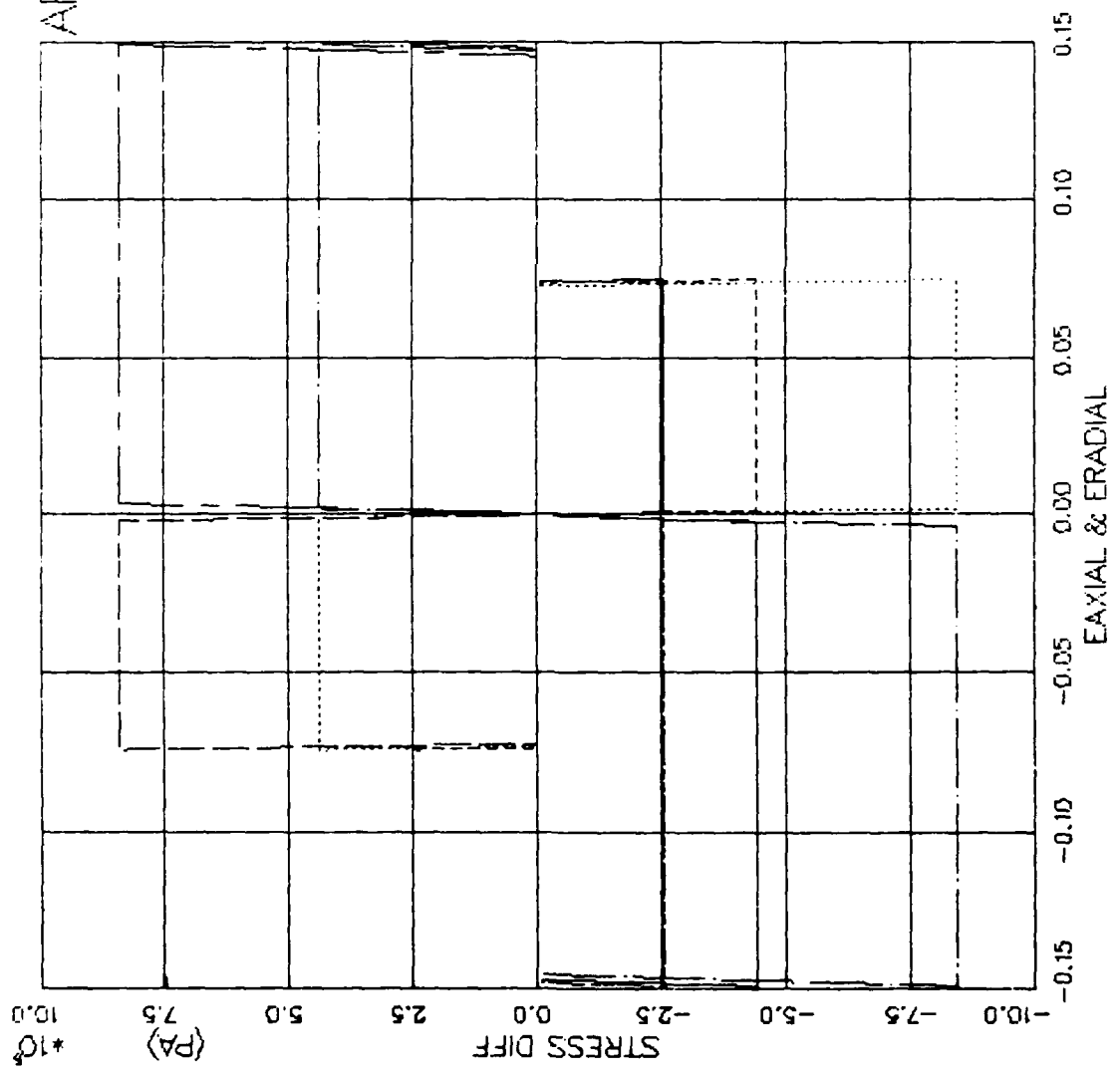
FIGURE V.6.14 AFWL MODEL EXERCISE—PURE SHEAR(PSC+PSE) — STRESS DIFF VS. STRAIN

440

AFOSR SOIL ELEMENT MODEL

TEST = STANDARD TRIAXIAL TEST
MODEL= AFWL
MATL = DRY ARES—REMOLD

LEGEND

PSC/S3C=1.8E6
PSC/S3C=3.5E6
PSC/S3C=7.1E6
PSE/S3C=1.8E6
PSE/S3C=3.5E6
PSE/S3C=7.1E6
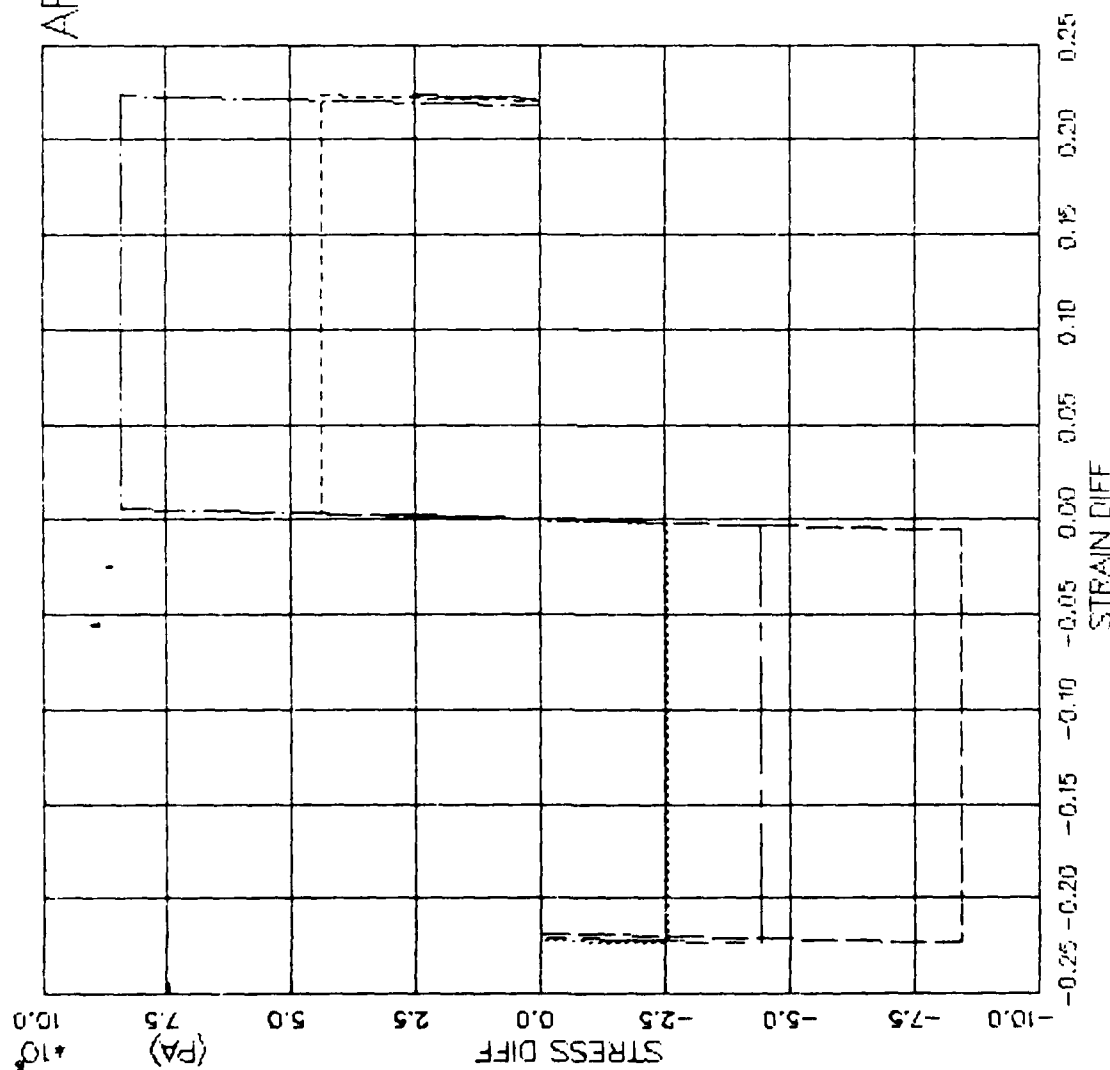
FIGURE V.6.15 AFWL MODEL EXERCISE—PURE SHEAR(PSC+PSE) — STRESS DIFF VS. STRAIN DIFF

FIGURE V.6.16. AFWL ENG MODEL BEHAVIOR SUMMARY (S3C=7.1MPA) — SDIFF/P/EV/EA ANALYSIS

442
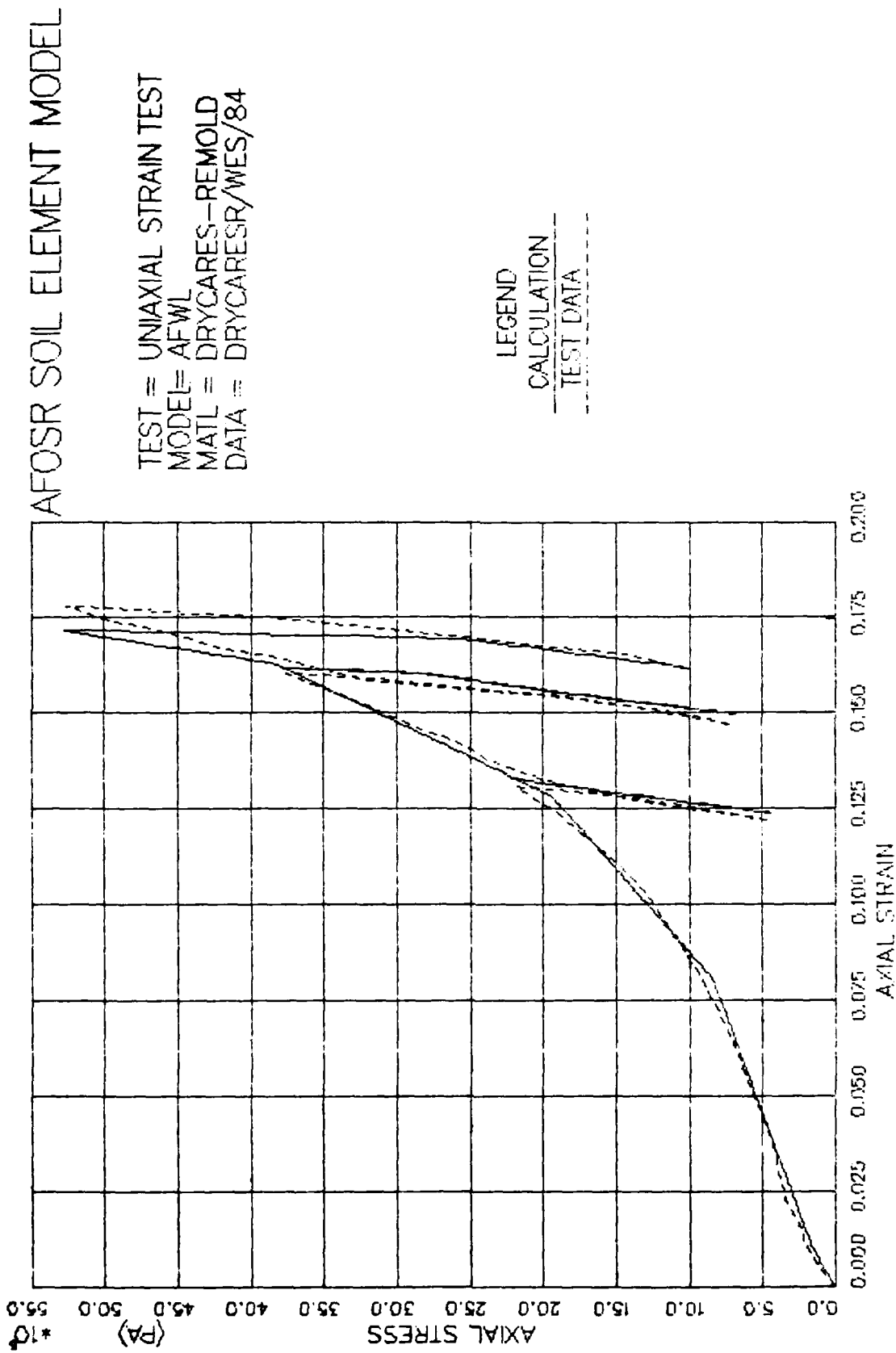
FIGURE V.6.17 AFWL MODEL EXERCISE — UNIAX STRAIN — TOT AXL STRESS VS. AXL STRAIN .
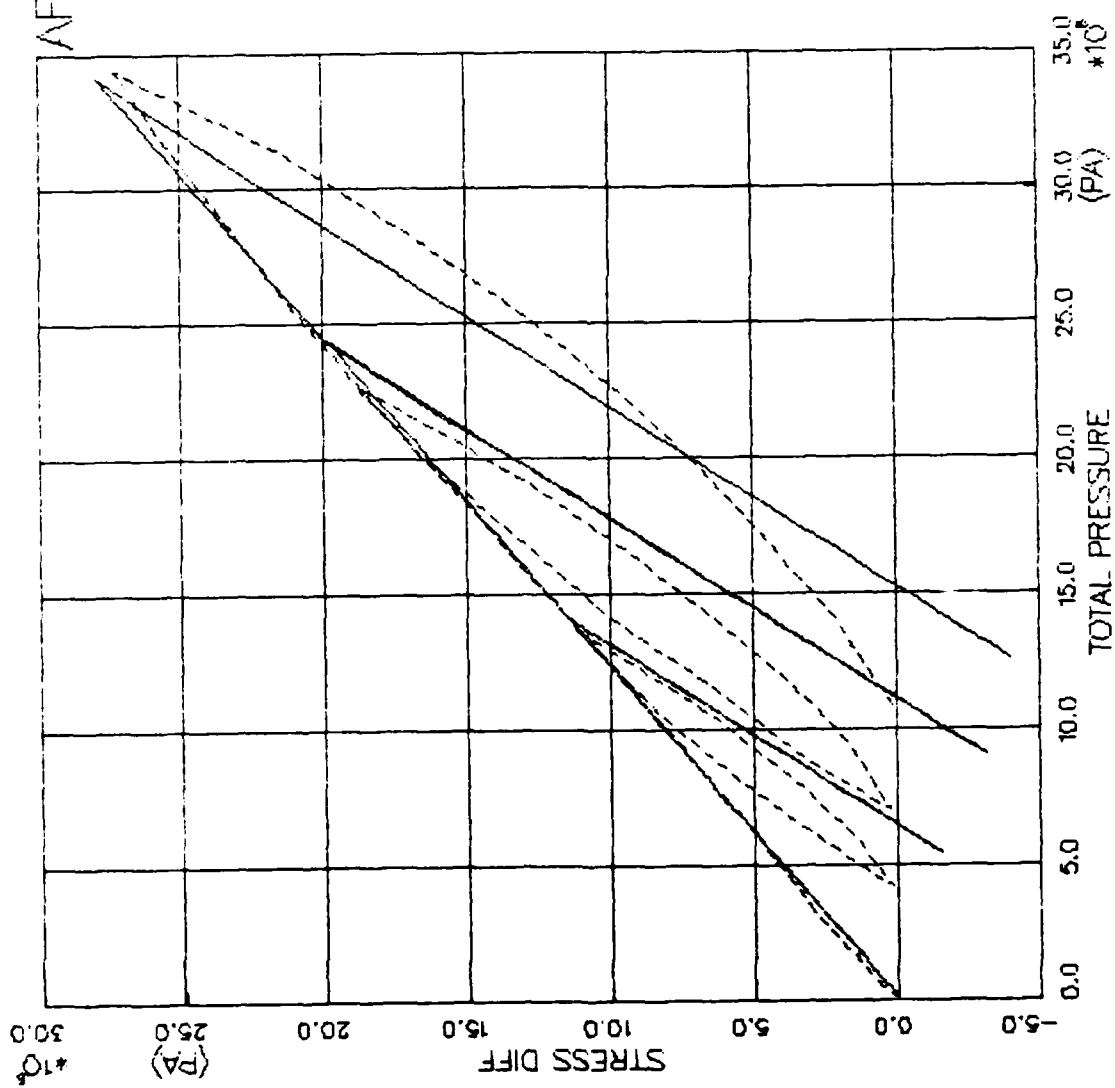
FIGURE V.6.18 AFWL MODEL EXERCISE— UNIAX STRAIN(UXC) — STRESS DIFFERENCE VS. PRESSURE
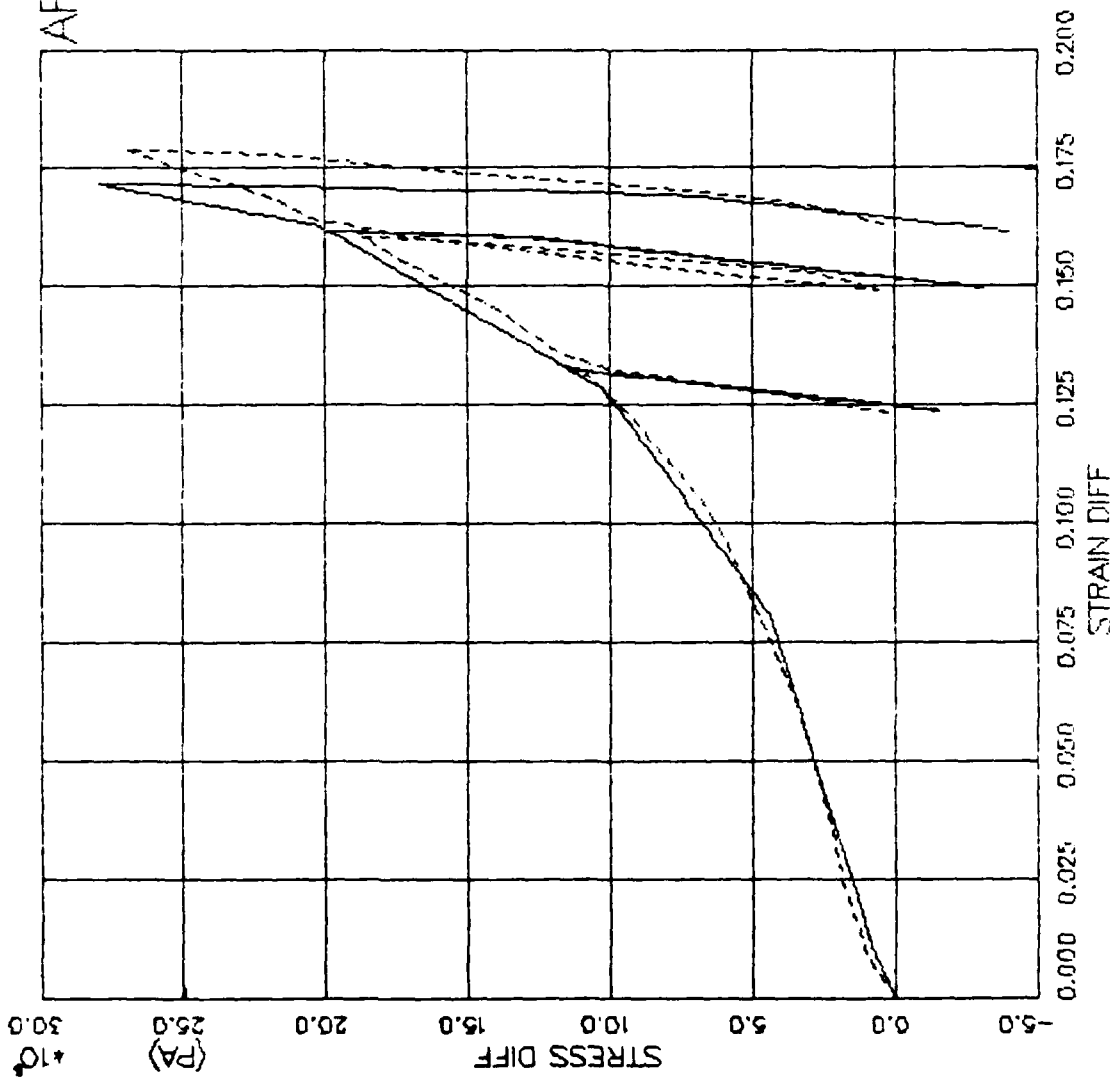
FIGURE V.6.19 AFWL MODEL EXERCISE— UNIAX STRAIN(UXO) -- STRESS DIFF VS. STRAIN DIFF

445
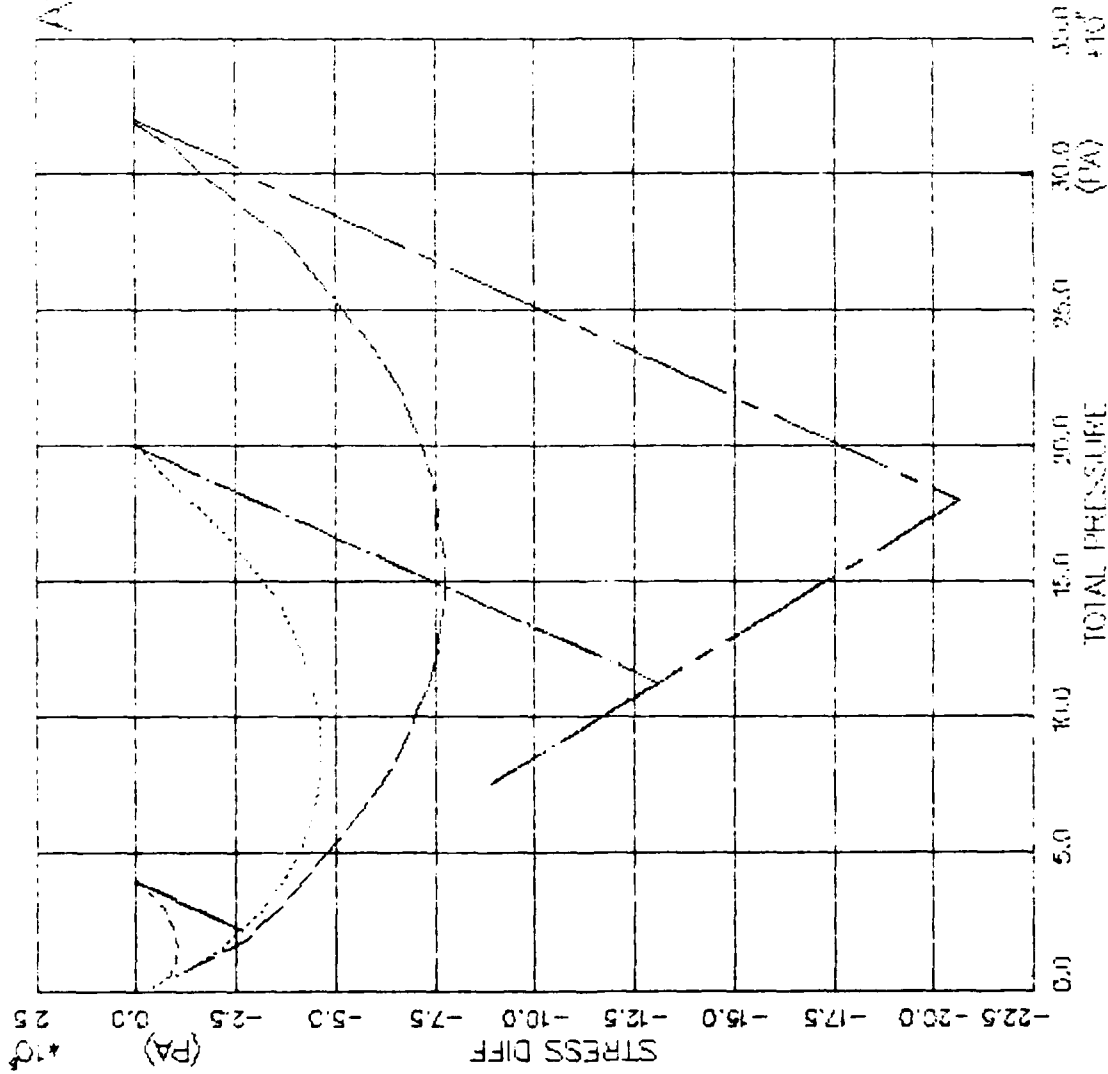
FIGURE V.6.20 AFWL MODEL EXERCISE – UNIAX STRAIN EXTEN (USX) – STRESS DIFFERENCE VS. PRE
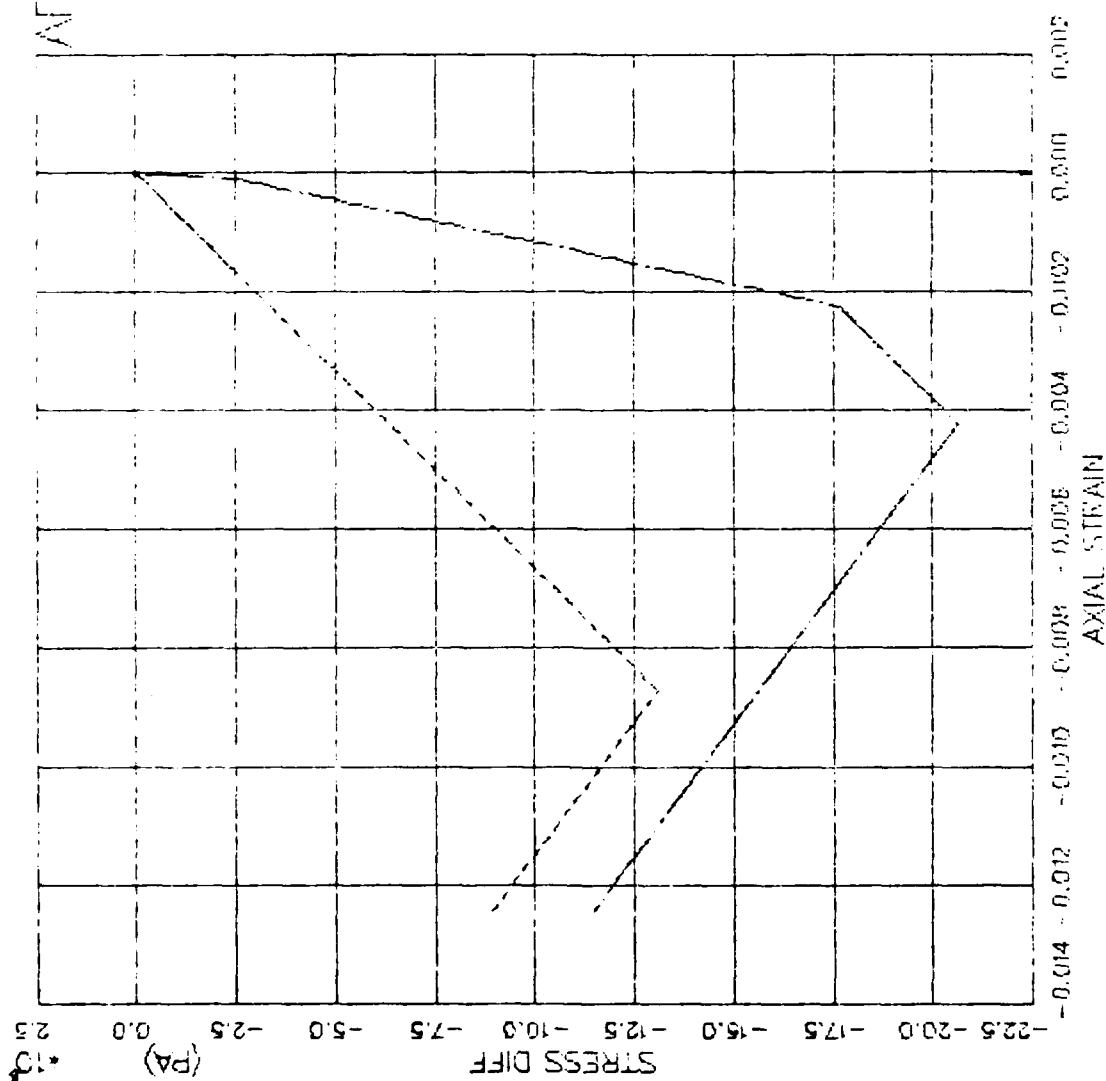
FIGURE V.6.21 AFWL MODEL EXERCISE—UNIAX. STRAIN EXTEN (LOK2) — STRESS, DIFF VS. AXIAL STRAIN

FIGURE V.6.22 AFWL MODEL EXER-AXISYM EFAII=I3A+3C - SDIFF/P/EV/EDIFF ANALYSIS
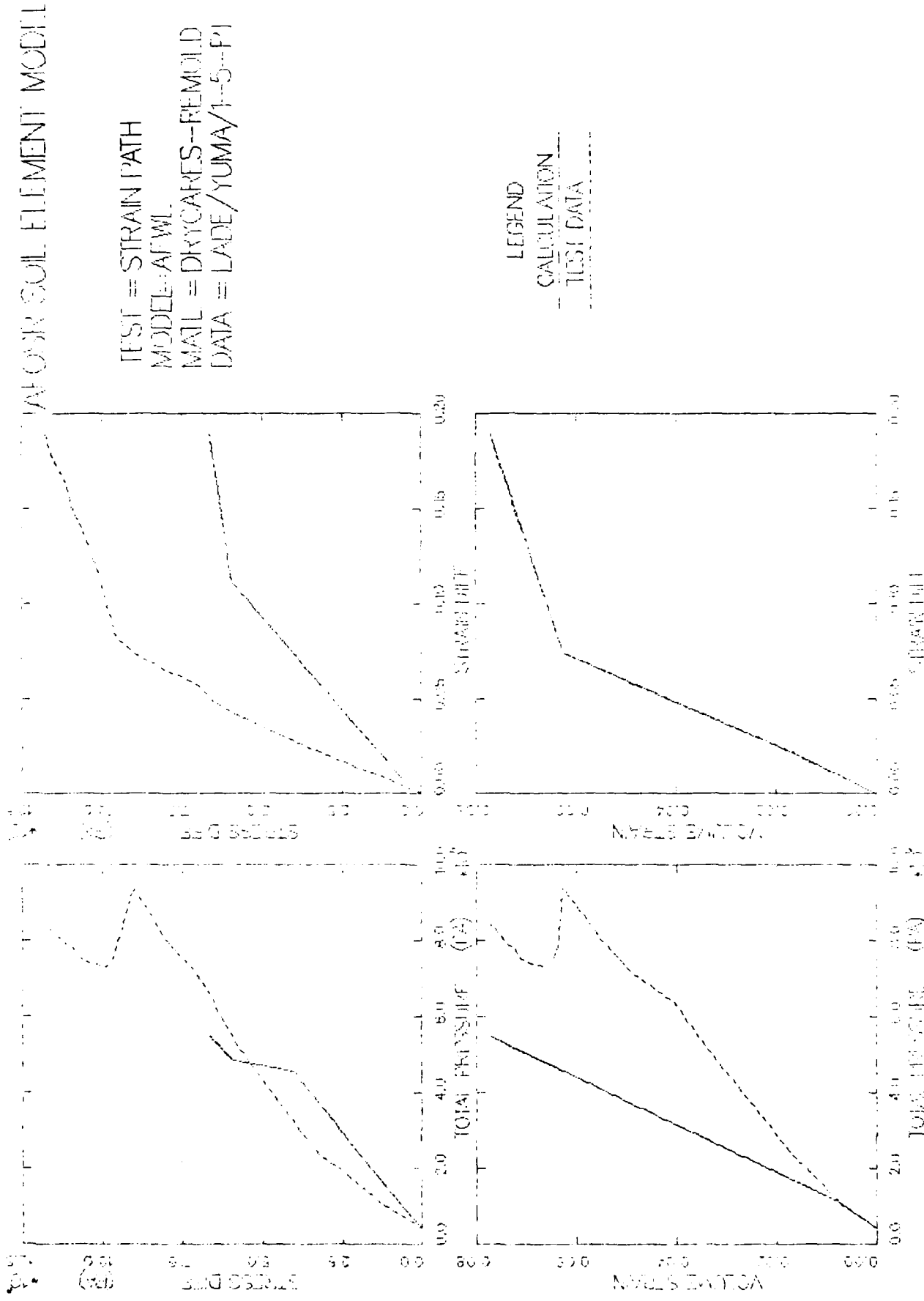
FIGURE V.6.23

449
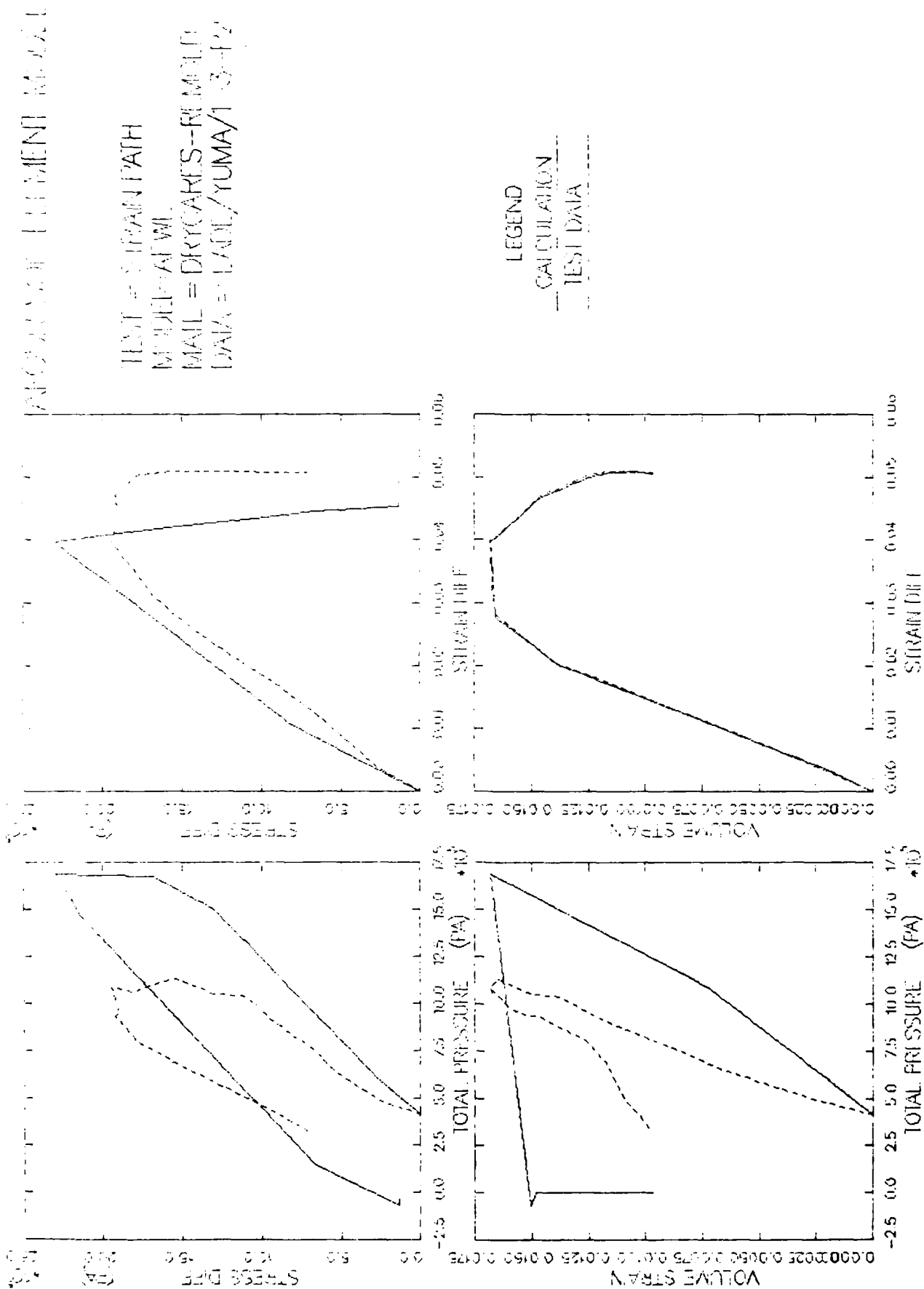
FIGURE V.6.24 AFWL MODEL — LADE AXISYM. PATH2 — SEMI-ANALYTICAL ANALYSES

AFOSR SOIL ELEMENT MODEL

TEST = STRAIN PATH
MODEL= AFWL
MATL = DRYCARES—REMOLD
DATA = NELLISB/KO/JAN83

LEGEND
CALCULATION
TEST DATA
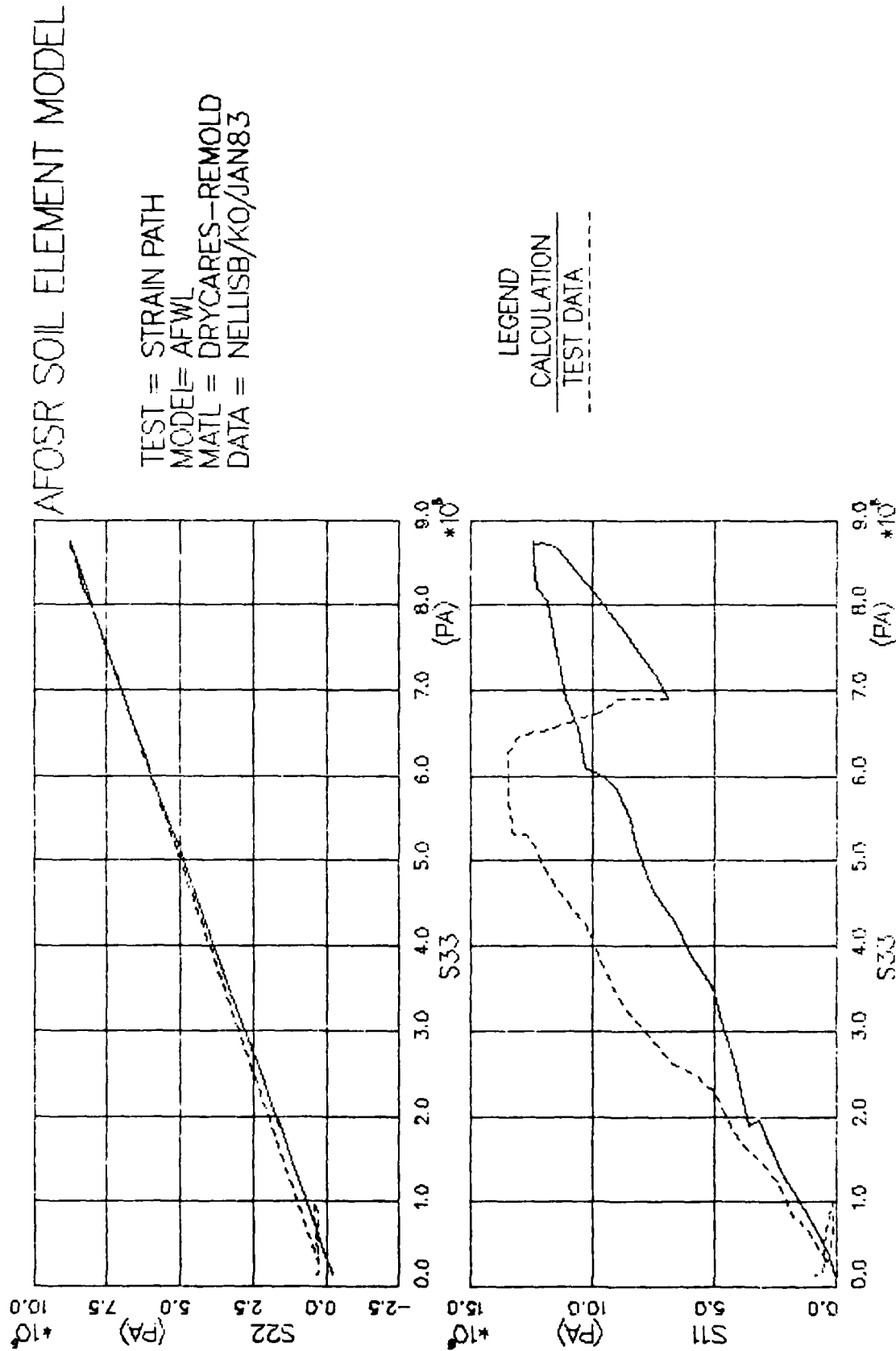
FIGURE V.6.25   AFWL MODEL EXERCISE—TRUE TRIAX — PRINCIPAL STRESS PATH

451
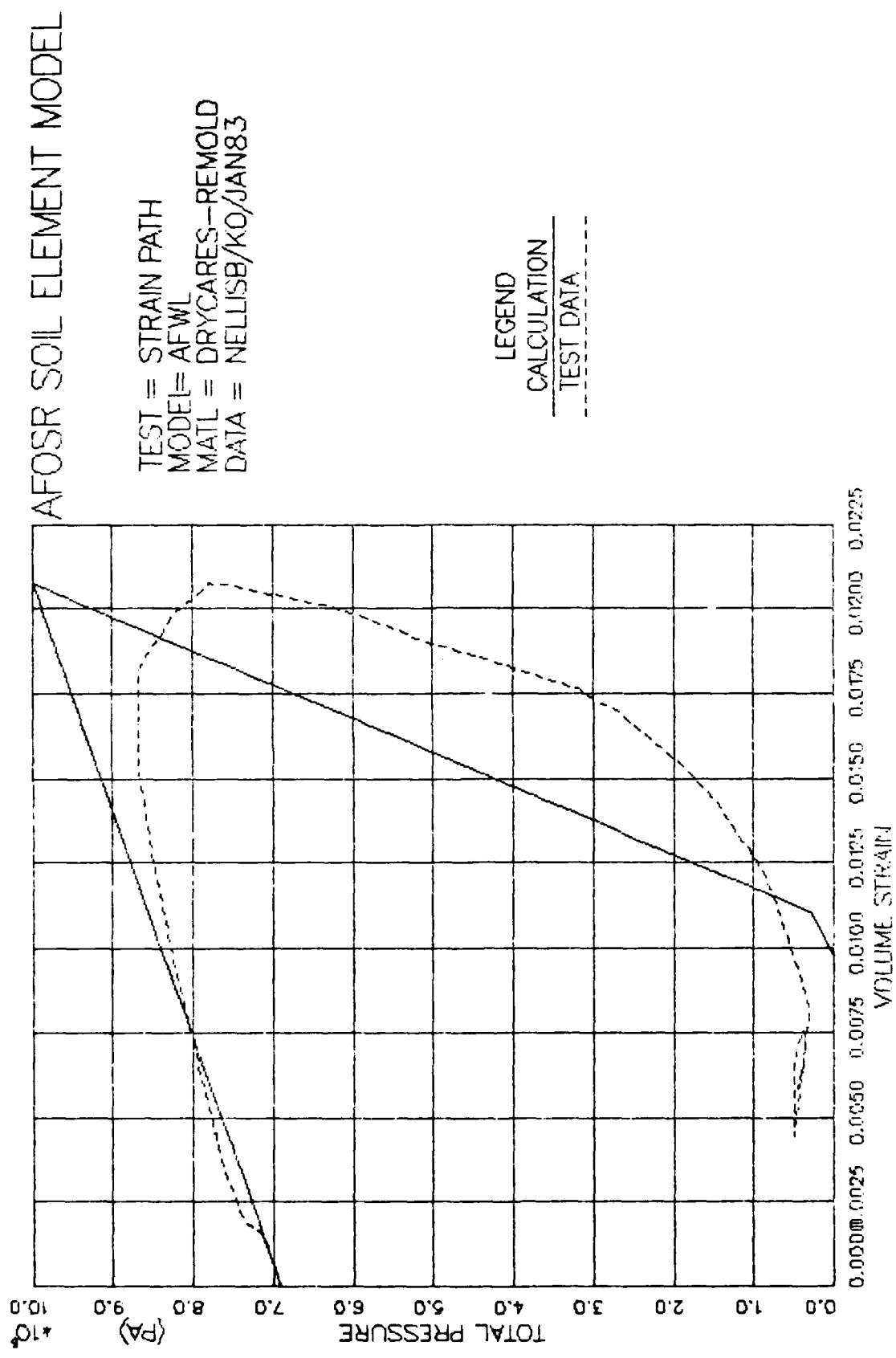
FIGURE V.6.26 AFWL MODEL EXERCISE—TRUE TRIAX — PRESSURE VS. VOLUMETRIC STRAIN .

452

V.7 Effective Stress Cap

V.7.1 Motivation

The cap model, in its various forms, sacrifices some analytical and computational simplicity for a more accurate representation of soil behavior than provided by simpler models. The perfectly plastic, associative shear failure surface of the cap model discussed here transitions exponentially from a Drucker-Prager asymptote at low confining pressure to a von Mises asymptote at high confining pressure. Volumetric hysteresis, and control over excessive dilatancy are provided by a strain hardening, associative, ellipsoidal cap yield surface which intersects both the shear failure surface and the hydrostatic axis. Inside the failure and yield surfaces the material is hypoelastic without hysteresis, with volumetric and deviatoric behavior uncoupled. The cap model satisfies Drucker's stability postulate and the continuity condition, and thus produces stable, unique solutions. The basic model is a drained (effective stress) model, but an undrained (total stress) hydrostat is also used to calculate pore pressure during undrained loading. The principal advantage of the cap model is accuracy in representing most aspects of soil stress-strain behavior. The principal disadvantages are the large number of material parameters required, the amount of trial and error based on experience needed to determine the parameters, inability to predict dilatancy prior to shear failure, computational complexity, an oversimplified approach to undrained response analysis, and lack of a closed form relation between total volumetric strain and effective octahedral normal stress.

V.7.2 Assumptions

The cap model assumes shear failure to be governed by a perfectly plastic, associative failure surface, and plastic deformation beneath the shear failure surface to be governed by a strain hardening/softening, associative cap yield surface which intersects both the shear failure surface and the hydrostatic axis. The cap strain hardening parameter is plastic volumetric strain, which increases during compression causing cap expansion, and decreases due to dilatancy on the shear failure surface causing cap contraction. Uncoupled volumetric and deviatoric hypoelastic relations inside the failure and yield surfaces assume the bulk modulus to be a function of the octahedral normal stress, and the shear modulus to be a function of the octahedral shear stress. Dilatancy is recognized in the drained (effective stress) model at failure, but not in the undrained (total stress) model, which is represented by an undrained hydrostat. The assumption is that total octahedral normal stress is *uniquely* related to total volumetric strain, regardless of shear deformation. Pore pressure is calculated as the difference between total and effective octahedral normal stress.

V.7.3 Basic Equations

The shear failure surface has the equation

$$\sqrt{J_2} = f(I_1) = (C_s + \alpha I_1') + C\left(1 - e^{-BI_1'}\right) \qquad (I_1' \geq T) \qquad (V.7.1)$$

$$= 0 \qquad\qquad\qquad\qquad (I_1' < T) \qquad (V.7.2)$$

where T is the tension cutoff, but the shear failure surface exists only for $I_1' < k$, where k is the value of I_1' at which the shear failure surface and the cap yield surface intersect. (See Figure (R.1).)

In the cap model discussed here k is prevented from becoming negative, so that $k = L$, where L is the value of I_1' at the center of the ellipsoidal cap yield surface. Thus the ellipsoidal cap has a horizontal tangent where it meets the shear failure surface, and there is no von Mises transition. The cap yield surface equation is

$$\sqrt{J_2} = F(I_1',k) = \frac{1}{R} \sqrt{(X - L)^2 - (I_1' - L)^2} \quad (L \leq I_1' \leq X) \quad (V.7.3)$$

where

$$R = \frac{X - L}{f(k)} \quad (V.7.4)$$

and X, L, and R are all related to plastic volumetric strain, as shown in Figure (R.4). In particular, X, the value of I_1' at which the ellipsoidal cap yield surface intersects the hydrostatic axis, is related to plastic volumetric strain by the equations

$$X = 3G_r' + \frac{1}{D} \ln \left(\frac{1}{1 - \frac{z}{W}} \right) \quad (V.7.5)$$

where G_r' is the hydrostatic component of geostatic effective stress, D and W are material constants, and

$$z = \int dz \quad (V.7.6)$$

where

$$dz = 0 \qquad\qquad (k = 0 \text{ and } d\varepsilon_{KK}^p < 0)$$

$$ = d\varepsilon_{KK}^p \qquad\qquad (\text{otherwise}) \quad (V.7.7)$$

Below the yield surfaces the material is hypoelastic without hysteresis, with volumetric and deviatoric behavior uncoupled. Thus

$$dI_1' = 3K_s d\varepsilon_{KK} \quad (V.7.8)$$

$$ds_{ij} = 2G de_{ij} \quad (V.7.9)$$

455

where

$$K_s = \frac{K_{is}}{1 - K_{1s}} \left[1 - K_{1s}e^{-K_{2s}(I_1' - 3G_r')} \right]$$ (V.7.10)

$$G = \frac{G_i}{1 - G_1} \left[1 - G_1 e^{-G_2\sqrt{J_2}} \right]$$ (V.7.11)

and K_{is}, K_{1s}, K_{2s}, G_i, G_1, and G_2 are material constants.

Equations (V.7.1) through (V.7.11) apply to the drained (effective stress) cap model. In addition, an undrained (total stress) bulk modulus for isotropic compressive loading is defined by an equation identical in form to Equations (V.7.10) and (V.7.11).

$$K_m = \frac{K_{im}}{1 - K_{1m}} \left[1 - K_{1m}e^{-K_{2m}(I_1 - 3G_r)} \right]$$ (V.7.12)

In an undrained calculation pore pressure is calculated by the equation

$$u = \frac{I_1 - I_1'}{3}$$ (V.7.13)

A more detailed mathematical description of the cap model is given in Appendices R and S.

V.7.4 Parametric Determination

All the cap model parameters can in principle be determined from standard laboratory isotropic compression and triaxial compression tests at constant cell pressure, as explained in Appendicies R and S. However, the parameters thus determined are usually refined by trial and error to match uniaxial and triaxial compression test data, and sometimes even dynamic field test data. The trial and error process is based on experience, and has not been explained in step by step fashion in the literature.

456

Table (V.7.1) lists the cap model parameters used for modeling remolded CARES-DRY Sand. The functions for the elastic bulk and shear moduli have been reduced to constant linear relationships (K_i, G_i). This is because when $K = K(I_1)$ and $G = G\left(\sqrt{J_2'}\right)$ it is difficult to maintain a reasonable uniaxial strain unload-reload stress path shape. The failure surface parameters (C_s, α) were fit to standard triaxial test results on dry material. The cap shape (R) was chosen based on previous experience with dry alluvium, and its hardening parameters (W, D) were iteratively fit to uniaxial compression stress-strain data.

V.7.5 Computed Behavior

V.7.5.1 Drained (or Dry) Model

As noted above, uniaxial compression stress-strain data was used for fitting the cap model. Figure (V.7.18) shows this data, compared with computed behavior. The model cannot match the changes in curvature of the stress-strain data because of the single exponential formulation of the cap hardening function [Equation (R.21)]. Rather, it is fit to produce an acceptable response over the stress range of interest ($\sigma_a = 0 - 50$ MPa, in this case). Stress path data from the K_o test [Figure (V.7.19)] is matched reasonably well, but this model does not produce any unload-reload loops due to the purely elastic behavior under both the failure surface and cap. The variation of shear stiffness in the uniaxial test is shown in Figure (V.7.20). A comparison of the calculated isotropic compression response with test data [Figure (V.7.1)] is similar to the calculated vs. observed UXC comparison. Overall, the fit is good, but sharp changes in stiffness with increasing pressure cannot be matched.

457

Calculated CTC stress-strain response is better at lower confining pressures than at the higher ones [see Figures (V.7.2) and (V.7.3)]. The tests at 59 MPa and 100 MPa confining pressure show much too stiff a response but with a reasonable stress difference at failure. This is because at higher initial confining pressures, the capacity for irrecoverable volumetric compaction has nearly been exhausted, causing very stiff volumetric response [see Figure (V.7.5)]. Figure (V.7.4) shows that no dilation is predicted by the cap model for CTC because the stress point is always located on the cap or at the intersection of the cap and failure surface. Here, the plastic strain rate vector is forced to be perpendicular to the P-axis.

CTE response [Figures (V.7.6-V.7.9)] at low strains is very stiff, because initially the cap does not need to expand in order for the stress point to move away from the P-axis. Thus, this initial behavior is elastic [Figures (V.7.6) and (V.7.7)]. However, further outward movement of the stress point requires the cap to move out to maintain its shape (R = 2.5). This cap hardening is accompanied by compressive volumetric strain [Figure (V.7.9)] and a much softer stress-strain response. Eventually, the shear failure surface is reached, whereupon volumetric straining stops [see Figure (V.7.8)]. Thus there is no predicted dilation here either, and in fact, the data tends to support this [Figure (V.7.8)].

The RTC and RTE exercises yield very different behavior from each other, as shown in Figures (V.7.10) through (V.7.13). During the RTC test, the stress point moves off the P-axis into the elastic region and thus yields very stiff initial stress-strain behavior. The failure surface is soon encountered, however, and the material fails in shear and

458

begins to dilate [Figure (V.7.12)] at constant pressure [Figure (V.7.13)]. The cap subsequently retracts to meet the current stress point and dilation is then stopped. RTE behavior, conversely, is initially soft because the cap is being forced outward constantly [Figure (V.7.10)]. RTE volume response is purely compressive. In fact, at 15 percent radial strain in this test, the shear failure surface has still not been reached at any of the confining pressures.

The PSC and PSE stress paths [Figures (V.7.14-V.7.16)] both force the stress point directly outward from the P-axis, causing cap expansion and therefore volumetric compression [Figure (V.7.16)]. When the failure surface is reached, the plastic strain rate vector swings perpendicular to the P-axis and volumetric strain ceases.

Figure (V.7.17) summarizes the behavior of the cap model for the tests performed in the triaxial cell starting at 7.1 MPa confining pressure. Cap model uniaxial extension (UXE) behavior is elastic until shear failure, producing a stress path substantially different from that actually observed [Figure (V.7.21)]. Figure (V.7.22) shows that dilation occurs when the stress point is on the failure surface, meaning that the cap retraction in this case is not fast enough to overtake the stress point and limit subsequent dilation.

Cap model predictions of axisymmetric strain path experiments are shown in Figures (V.7.23) through (V.7.25). The initial behavior in these tests is dominated by an adjustment from isotropic stress to uniaxial strain conditions. Apparently, the stress point moves up the cap until a point on the cap is reached which has an outward-normal plastic strain-rate vector which produces a compressive increase in radial stress under

uniaxial strain boundary conditions. Until this point is reached, radial stress increments are tensile and the mean normal stress drops. When this point is reached, the stress path assumes a slope more typical of uniaxial total strain. From there, the stress path breaks over toward the failure surface when the strain path dictates volume expansion, and subsequently follows the failure surface. With the exception of this initial behavior the cap model matches both the WES data [Figure (V.7.23)] and the Lade data [Figures (V.7.24) and (V.7.25)] reasonably well.

Figures (V.7.26) and (V.7.27) compare the truly-triaxial strain path prediction for remolded CARES-DRY Sand with data from Ko's tests on Nellis Baseline Sand [Ko and Meier (1983)]. The major departures from typical alluvium data occur again at initial departure from the P-axis and during reloading from the spalled condition.

V.7.5.2 Undrained Model

Since no data exists for undrained tests on saturated remolded CARES-DRY Sand, only calculated results for CTC/CTE will be shown. This will serve to illustrate how the undrained portion of the effective stress cap model works.

Figure (V.7.28) shows the total and effective stress paths for the CTC and CTE tests at three confining pressures (7, 59, and 100 MPa). The difference between the two paths is the predicted pore pressure, which is plotted against axial strain in Figure (V.7.29). Stress-strain response for the axial and radial directions is shown in Figure (V.7.30) and the volume strain prediction is plotted against axial strain in Figure (V.7.31). Note that the volume strain in Figure (V.7.31), while not zero for undrained loading, is almost two orders of magnitude less than that in Figure (V.7.1).

TABLE V.7.1. EFFECTIVE STRESS CAP MODEL PARAMETERS
FOR REMOLDED CARES-DRY SAND

Parameter	Symbol	Variable	Value	Units
Drained Elastic	K_i	AKI	4.0×10^9	Pa
Bulk Modulus	K_1	AK1	-0-	
	K_2	AK2	-0-	
Undrained	K_{im}	AKIM	8.0×10^9	Pa
Bulk Modulus	K_{1m}	AK1M	-0-	
	K_{2m}	AK2M	-0-	
	G_i	AGI	3.0×10^9	Pa
Shear Modulus	G_1	AG1	-0-	
	G_2	AG2	-0-	
	C_s	AC	2.88×10^5	Pa
Failure Surface	α	AM	0.215	--
	B	BB	-0-	
	C	CCC	-0-	
	R_i	ARI	2.50	--
Cap Shape	R_1	AR1	-0-	
	R_2	AR2	-0-	
Cap Hardening	W	AW	0.200	--
	D	AD	1.800×10^{-8}	1/Pa
Mass Density	ρ	RHOREF	1900	kg/m^3
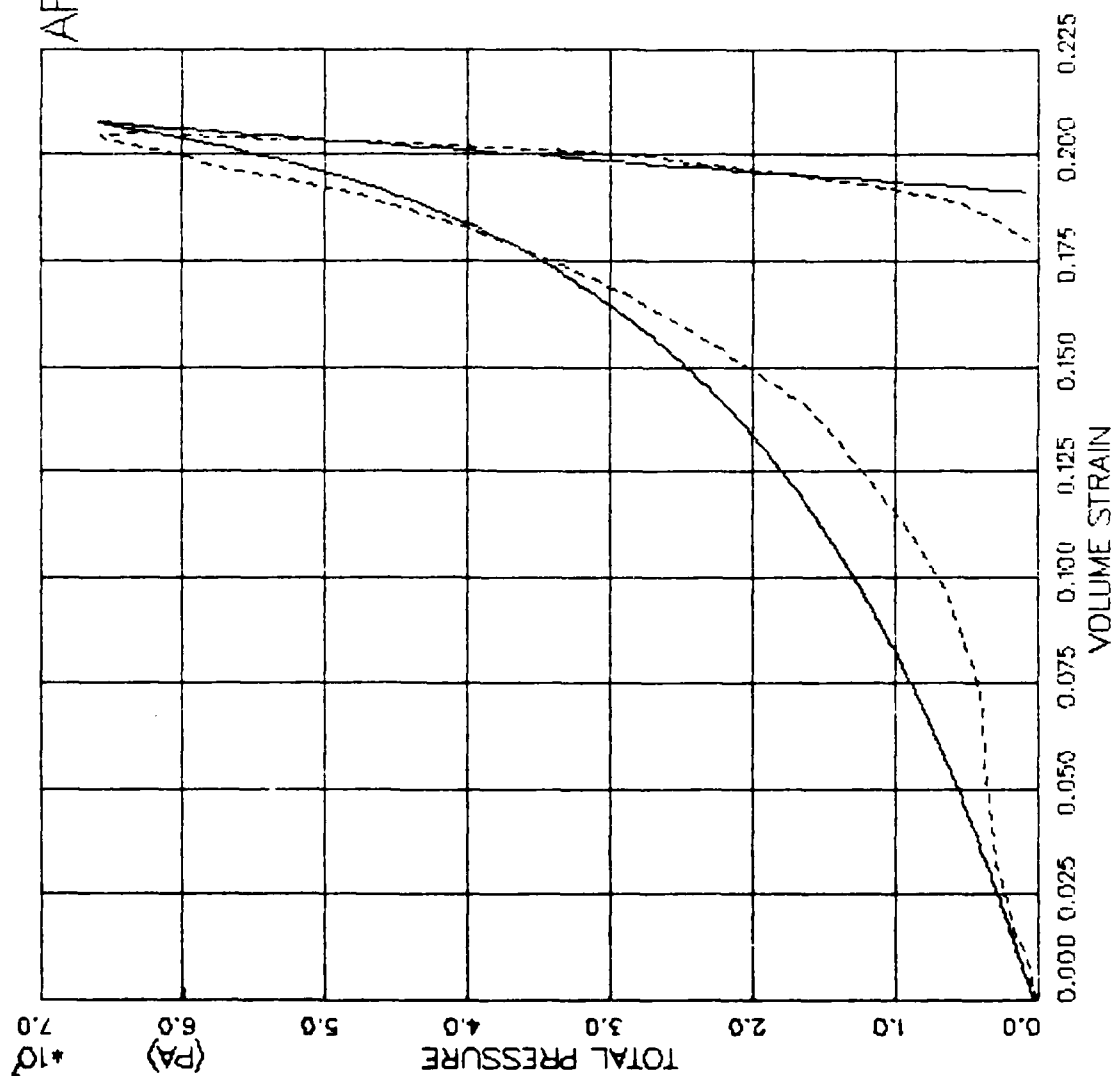
FIGURE V.7.1 CAP MODEL EXERCISE— ISOTROPIC COMP. — PRESSURE VS. VOLUMETRIC STRAIN .
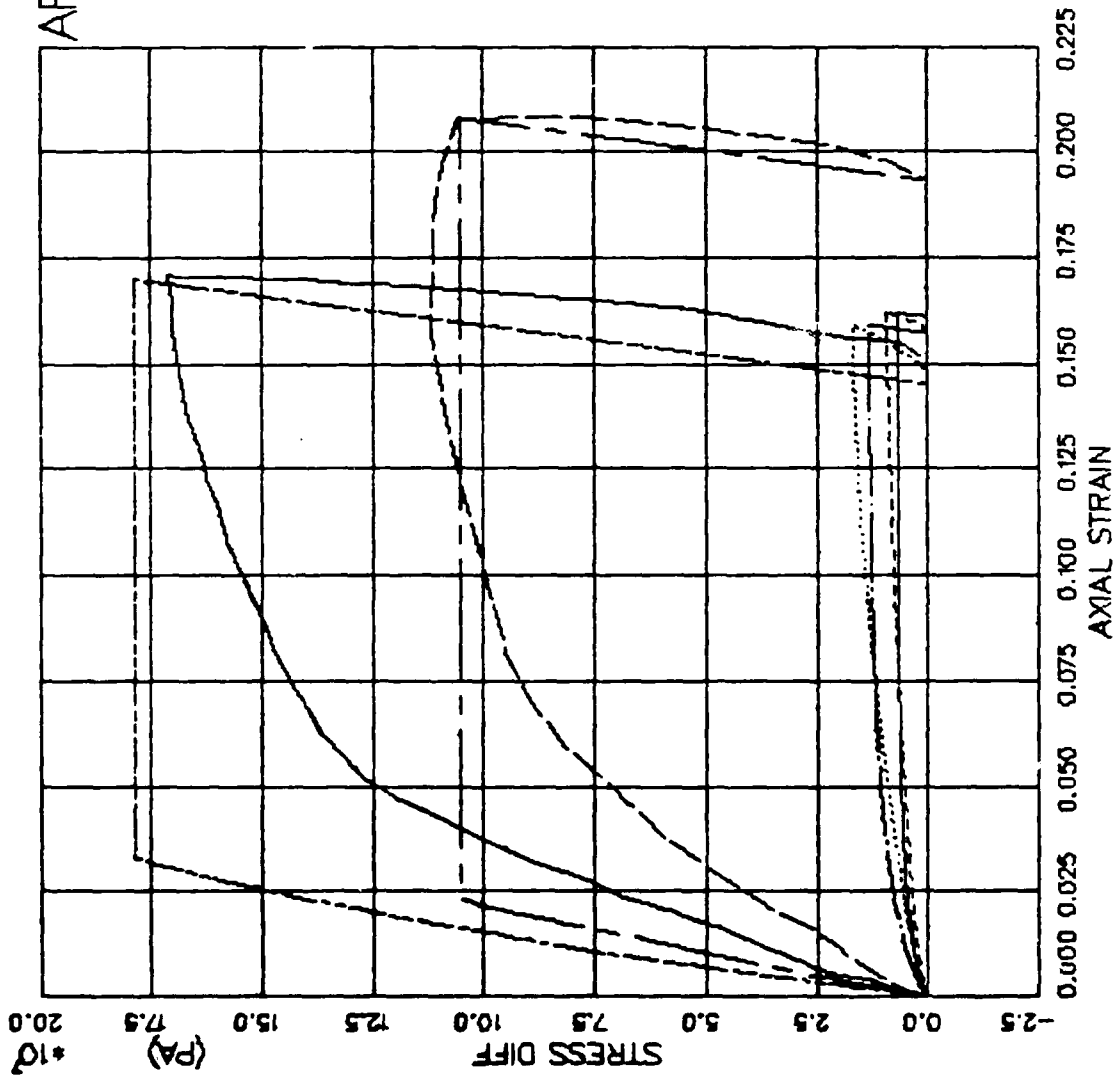
FIGURE V.7.2   CAP MODEL EXERCISE—TRIAXIAL COMP(CTC) — STRESS DIFF VS. AXIAL STRAIN

FIGURE V.7.3 CAP MODEL EXERCISE—TRIAXIAL COMP(CTC) — STRESS DIFF VS. STRAIN DIFF

AFOSR SOIL ELEMENT MODEL

TEST = STANDARD TRIAXIAL TEST
MODEL= CAP
MATL = DRYCARES—REMOLD
DATA = DRYCARESR/WES/84

LEGEND
SIGMA3C= 3.4E6
SIGMA3C= 7.0E6
SIGMA3C= 58.8E6
SIGMA3C=100.0E6

AFOSR SOIL ELEMENT MODEL

TEST = STANDARD TRIAXIAL TEST
MODEL= CAP
MATL = DRYCARES—REMOLD
DATA = DRYCARESR/WES/84

LEGEND
SIGMA3C= 3.4E6
TEST DATA
SIGMA3C= 7.0E6
TEST DATA
SIGMA3C= 58.8E6
TEST DATA
SIGMA3C=100.0E6
TEST DATA

AXIAL STRAIN
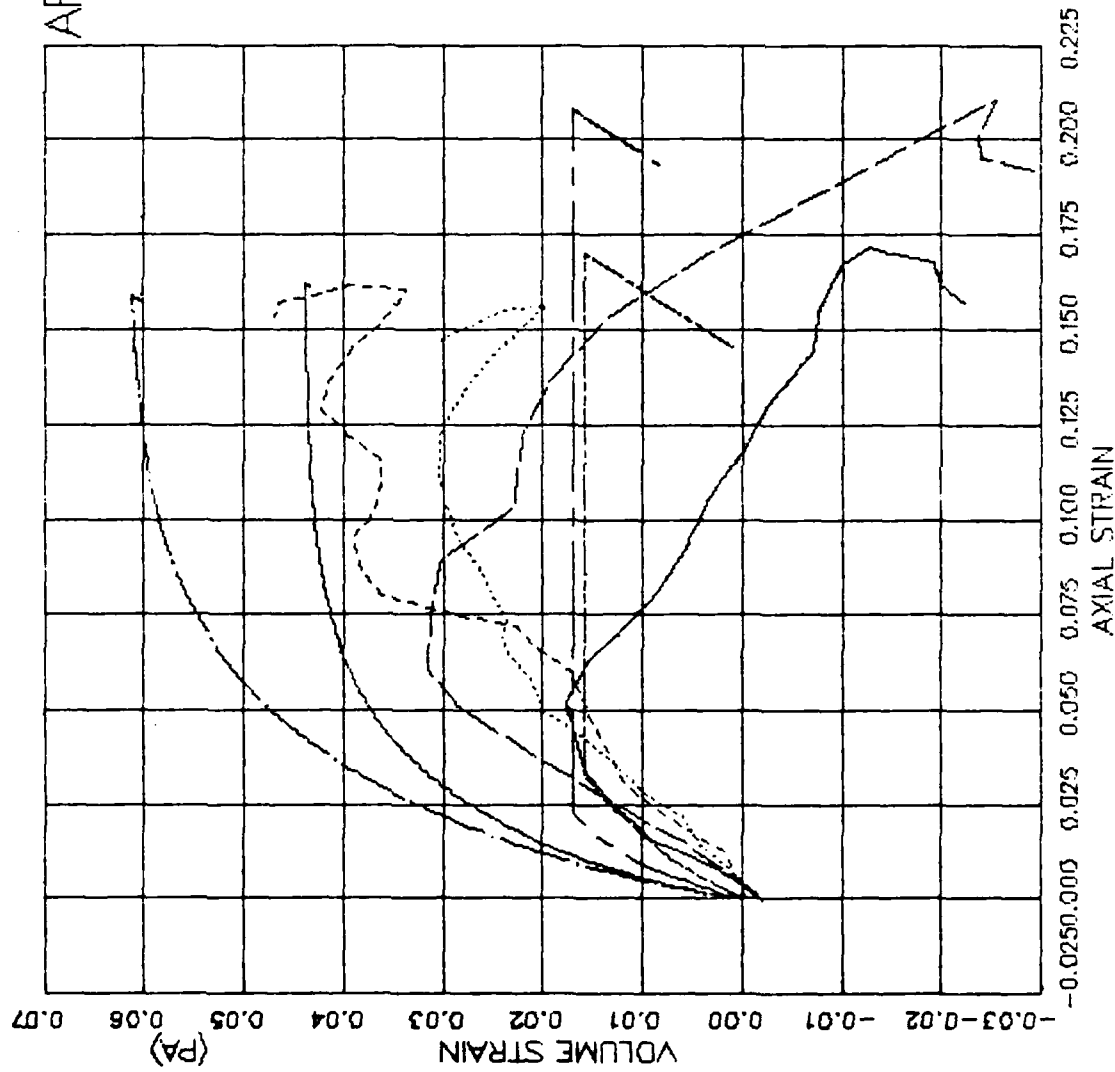
VOLUME STRAIN (PA)

FIGURE V.7.4 CAP MODEL EXERCISE—TRIAXIAL COMP(CTC) — AXIAL STRAIN VS VOLUME STRAIN .

465

AFOSR SOIL ELEMENT MODEL

TEST = STANDARD TRIAXIAL TEST
MODEL= CAP
MATL = DRYCARES—REMOLD
DATA = DRYCARESR/WES/84

LEGEND
SIGMA3C= 3.4E6
_____
TEST DATA
SIGMA3C= 7.0E6
_____
TEST DATA
SIGMA3C= 58.8E6
_____
TEST DATA
SIGMA3C=100.0E6
_____
TEST DATA
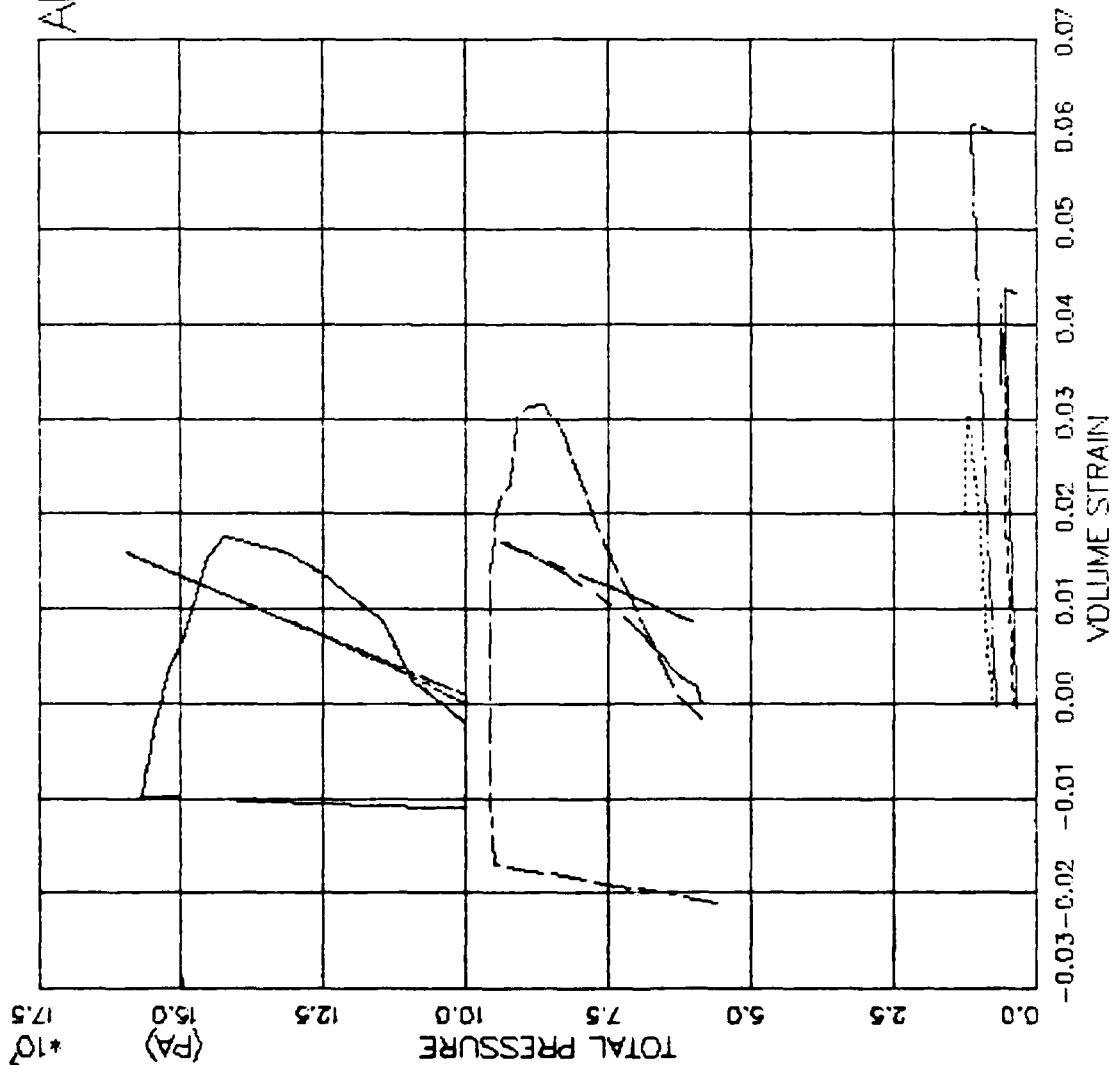
FIGURE V.7.5   CAP MODEL EXERCISE—TRIAXIAL COMP(CTC) — PRESSURE VS. VOLUMETRIC STRAIN

466

AFOSR SOIL ELEMENT MODEL

TEST = STANDARD TRIAXIAL TEST
MODEL= CAP
MATL = DRYCARES–REMOLD
DATA = DRYCARESR/WES/84

LEGEND
S3C=1.8E6
_____TEST DATA_____
S3C=3.5E6
_____TEST DATA_____
S3C=7.1E6
_____TEST DATA_____
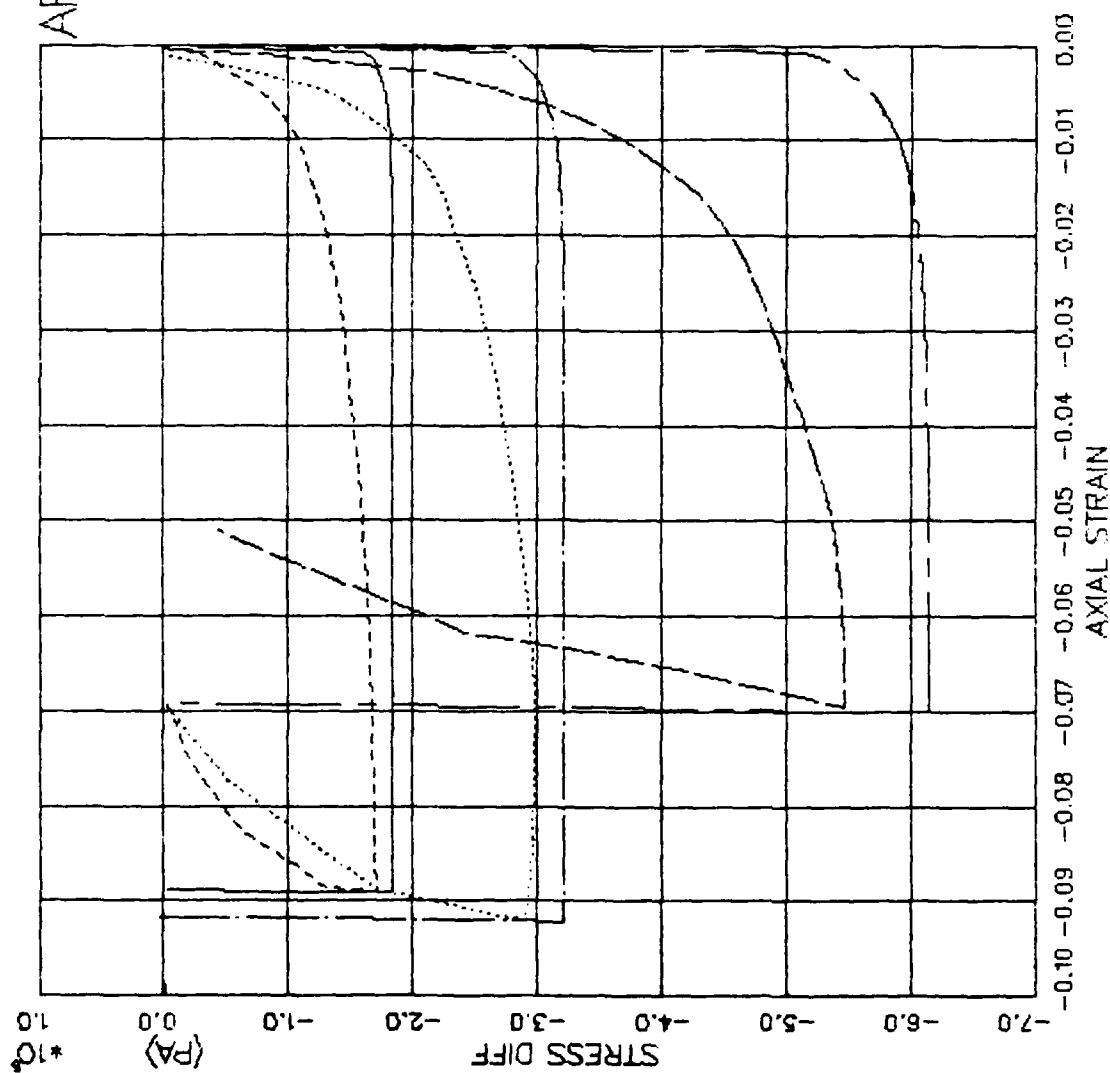
FIGURE V.7.6   CAP MODEL EXERCISE–TRIAXIAL EXTEN(CTE) – STRESS DIFF VS. AXIAL STRAIN

467
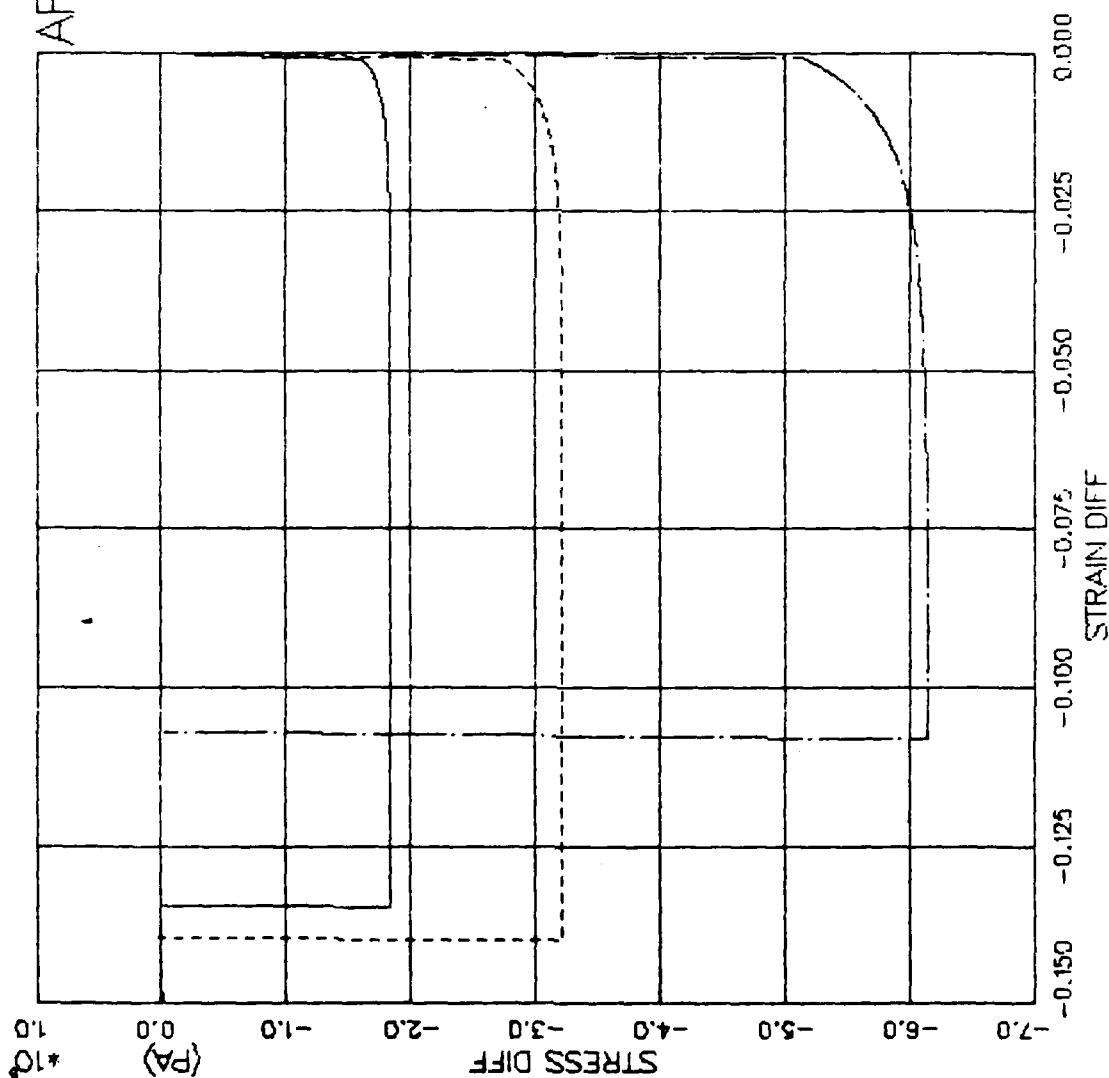
FIGURE V.7.7 CAP MODEL EXERCISE—TRIAXIAL EXTEN(CTE) — STRESS DIFF VS. STRAIN DIFF

468

AFOSR SOIL ELEMENT MODEL

TEST = STANDARD TRIAXIAL TEST
MODEL= CAP
MATL = DRYCARES-REMOLD
DATA = DRYCARESR/WES/84

LEGEND
S3C=1.8E6
TEST DATA
S3C=3.5E6
TEST DATA
S3C=7.1E6
TEST DATA
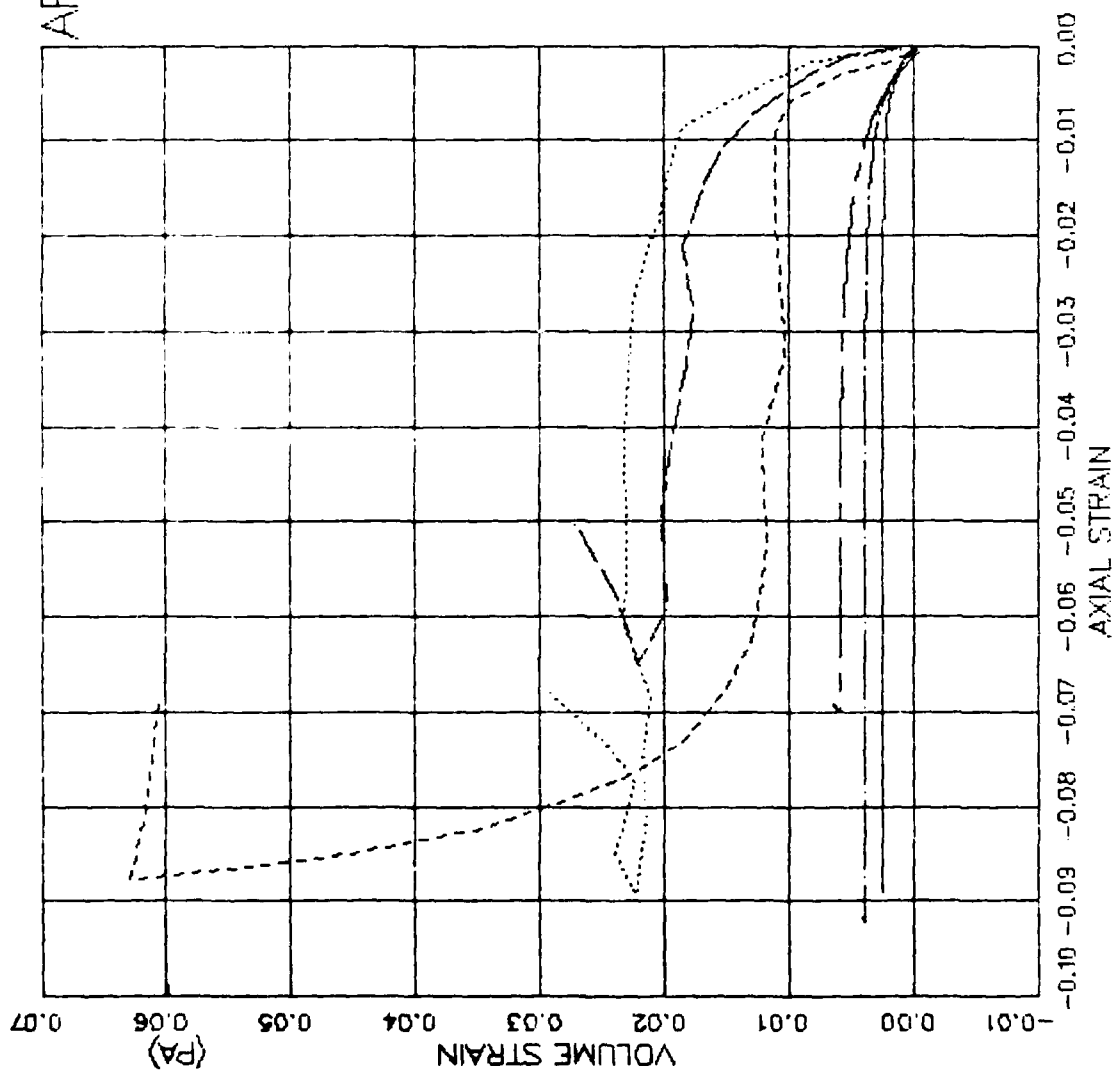
FIGURE V.7.8   CAP MODEL EXERCISE—TRIAXIAL EXTEN(CTE.) — AXIAL STRAIN VS VOLUME STRAIN

469
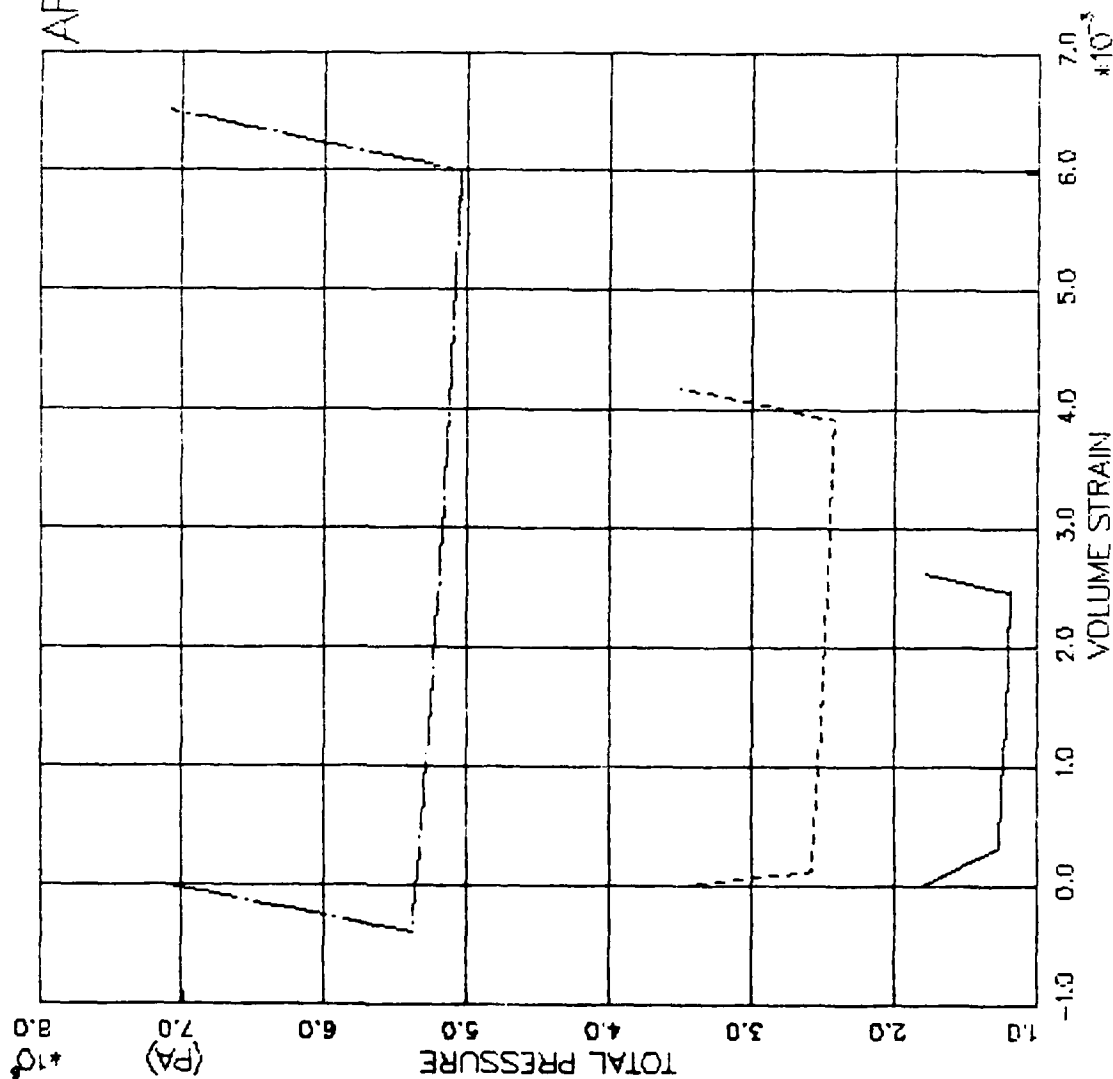
FIGURE V.7.9 CAP MODEL EXERCISE--TRIAXIAL EXTEN(CTE) -- PRESSURE VS. VOLUMETRIC STRAIN .
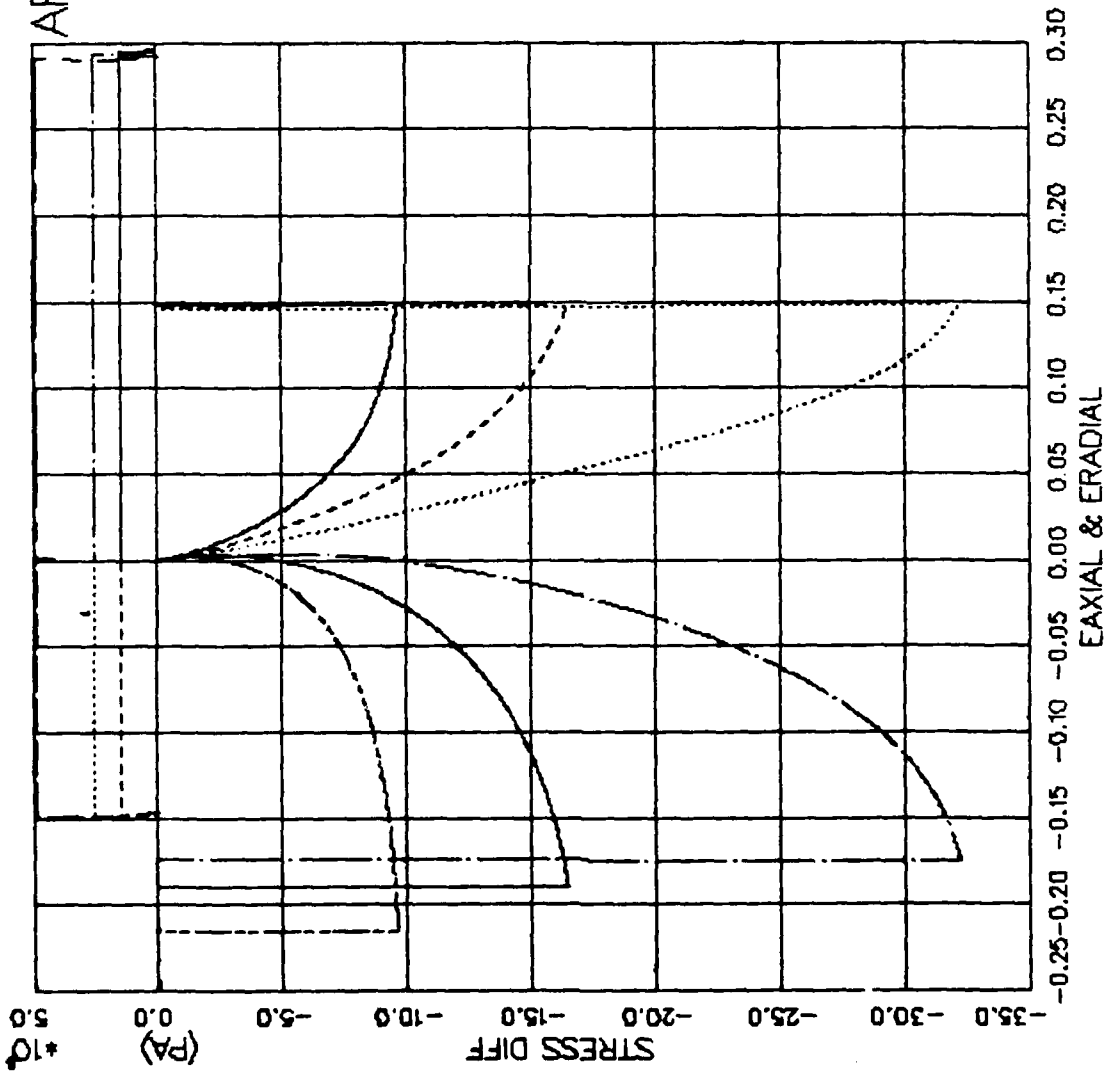
AFOSR SOIL ELEMENT MODEL

TEST = STANDARD TRIAXIAL TEST
MODEL= CAP
MATL = DRYCARES—REMOLD

LEGEND
RTC/S3C=1.8E6
RTC/S3C=1.8E6
RTC/S3C=3.5E6
RTC/S3C=3.5E6
RTC/S3C=7.1E6
RTC/S3C=7.1E6
RTE/S3C=1.8E6
RTE/S3C=1.8E6
RTE/S3C=3.5E6
RTE/S3C=3.5E6
RTE/S3C=7.1E6
RTE/S3C=7.1E6

FIGURE V.7.10 CAP MODEL EXER—REDUCED TRIAX(RTC+RTE) — STRESS DIFF VS. STRAIN

471

AFOSR SOIL ELEMENT MODEL

TEST = STANDARD TRIAXIAL TEST
MODEL= CAP
MATL = DRYCARES—REMOLD

LEGEND
RTC/S3C=1.8E6
RTC/S3C=3.5E6
RTC/S3C=7.1E6
RTE/S3C=1.8E6
RTE/S3C=3.5E6
RTE/S3C=7.1E6
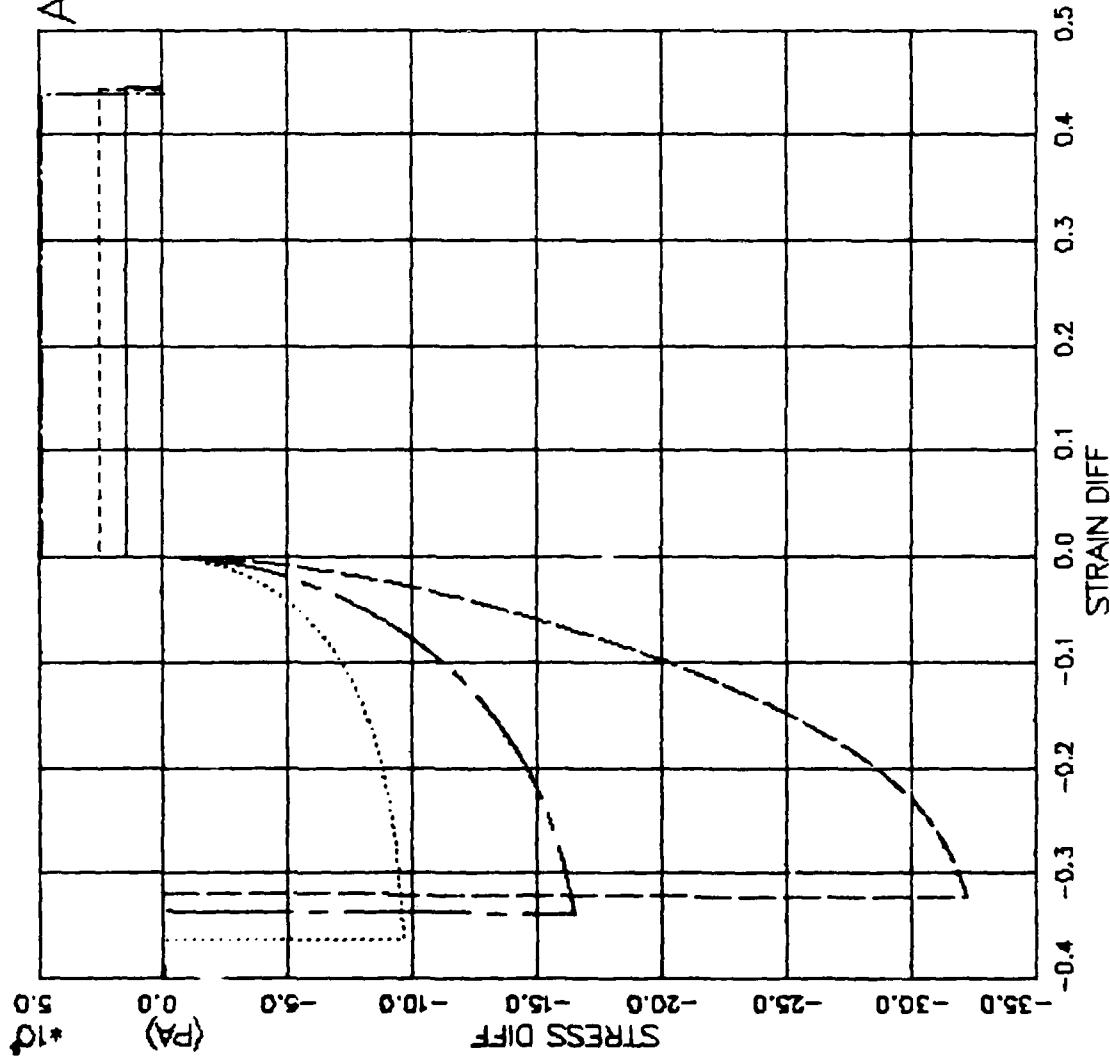
FIGURE V.7.11 CAP MODEL EXER—REDUCED TRIAX(RTC+RTE) — STRESS DIFF VS. STRAIN DIFF

472

AFOSR SOIL ELEMENT MODEL

TEST = STANDARD TRIAXIAL TEST
MODEL= CAP
MATL = DRYCARES—REMOLD

LEGEND
RTC/S3C=1.8E6
RTC/S3C=3.5E6
RTC/S3C=7.1E6
RTE/S3C=1.8E6
RTE/S3C=3.5E6
RTE/S3C=7.1E6
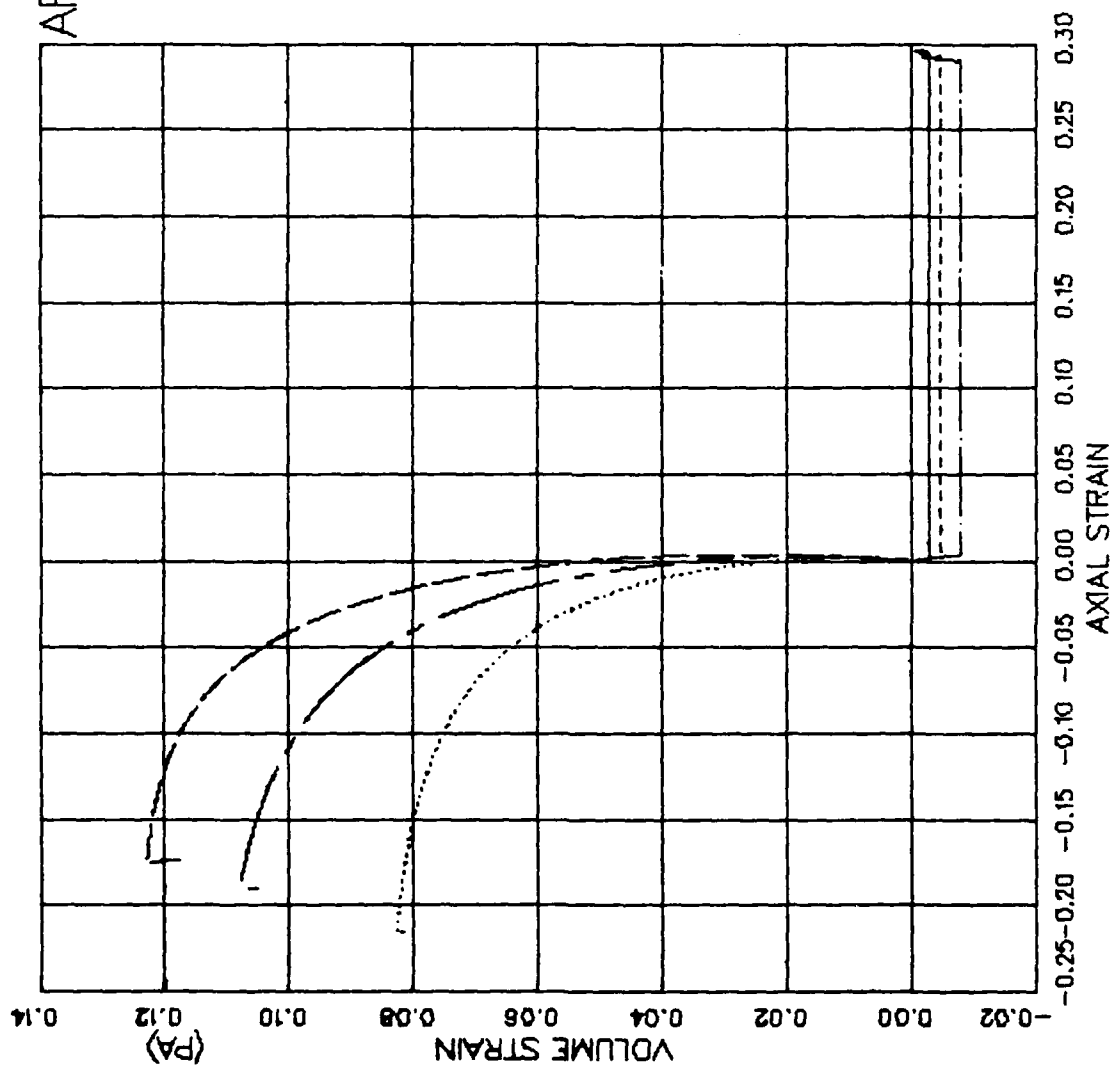
FIGURE V.7.12 CAP MODEL EXER—REDUCED TRIAX(RTC+RTE) — AXIAL STRAIN VS VOLUME STRAIN
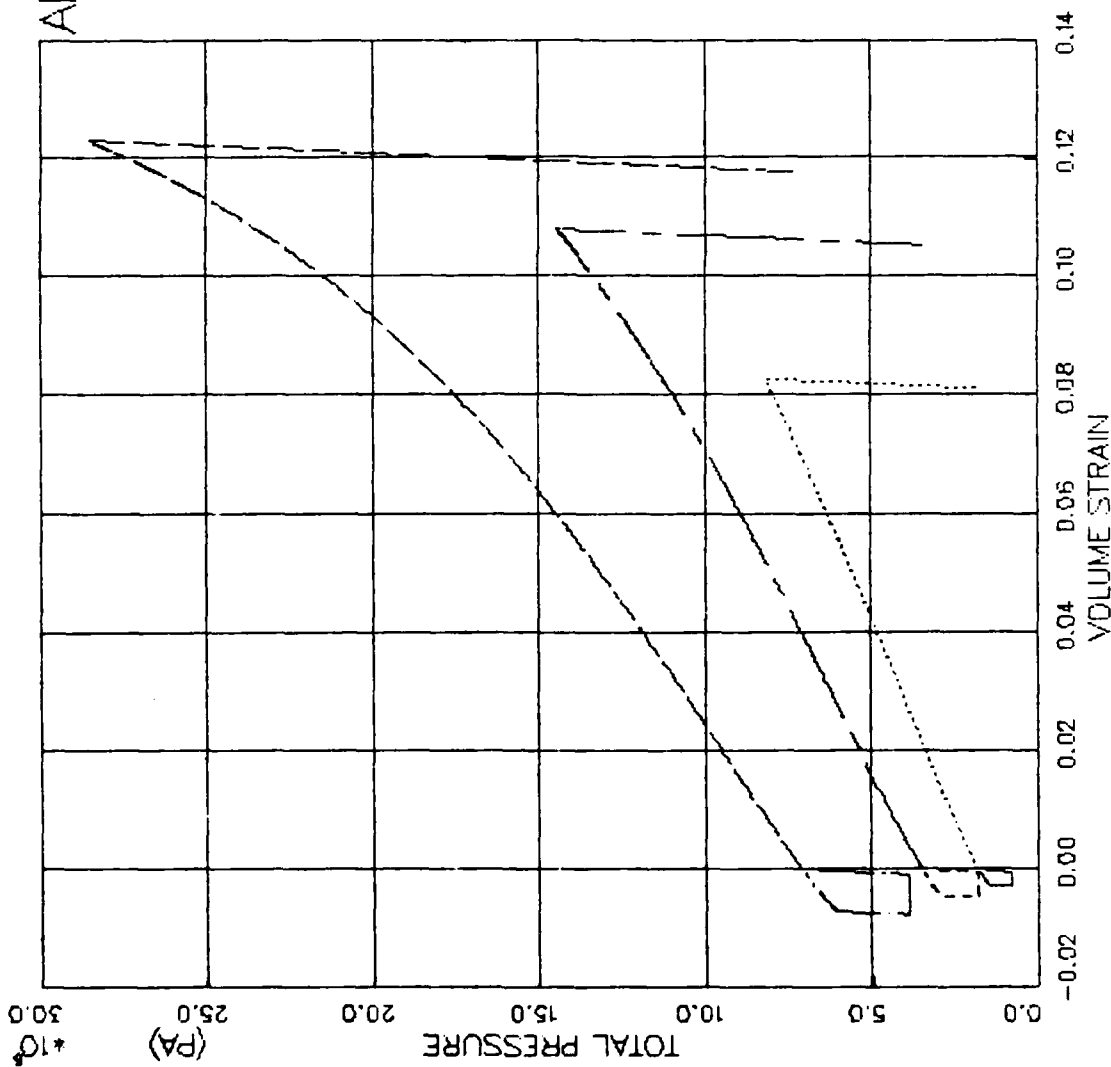
473

AFOSR SOIL ELEMENT MODEL

TEST = STANDARD TRIAXIAL TEST
MODEL= CAP
MATL = DRYCARES—REMOLD

LEGEND
RTC/S3C=1.8E6
RTC/S3C=3.5E6
RTC/S3C=7.1E6
RTE/S3C=1.8E6
RTE/S3C=3.5E6
RTE/S3C=7.1E6

FIGURE V.7.13 CAP MODEL EXER—REDUCED TRIAX(RTC+RTE) — PRESSURE VS. VOLUMETRIC STRAIN

AFOSR SOIL ELEMENT MODEL

TEST = STANDARD TRIAXIAL TEST
MODEL= CAP
MATL = DRYCARES—REMOLD

LEGEND
PSC/S3C=1.8E6
PSC/S3C=1.8E6
PSC/S3C=3.5E6
PSC/S3C=3.5E6
PSC/S3C=7.1E6
PSC/S3C=7.1E6
PSE/S3C=1.8E6
PSE/S3C=1.8E6
PSE/S3C=3.5E6
PSE/S3C=3.5E6
PSE/S3C=7.1E6
PSE/S3C=7.1E6

EAXIAL & ERADIAL

STRESS DIFF (PA) *10⁴
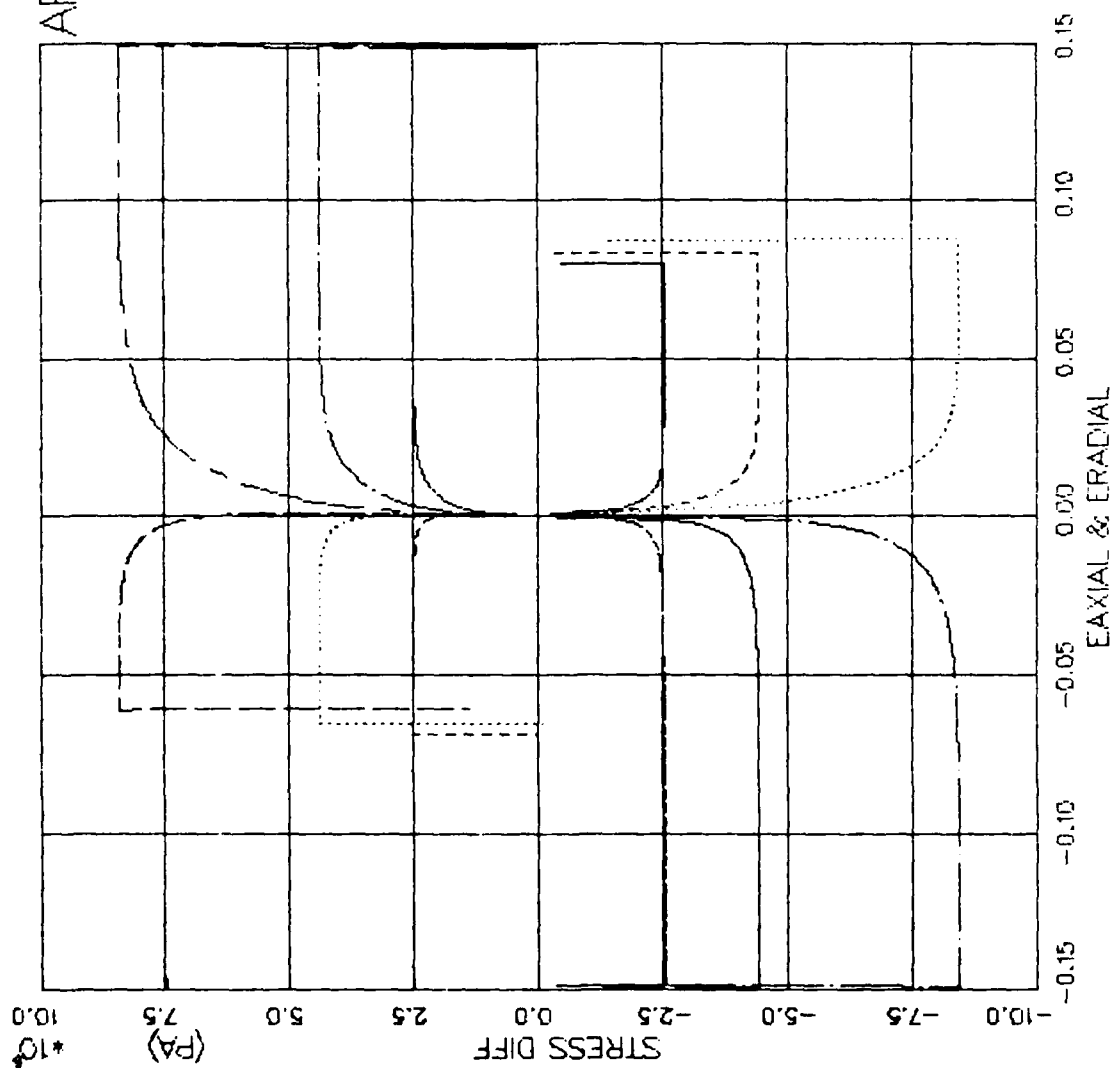
FIGURE V.7.14 CAP MODEL EXERCISE—PURE SHEAR(PSC+PSE) – STRESS DIFF VS. STRAIN

AFOSR SOIL ELEMENT MODEL

TEST = STANDARD TRIAXIAL TEST
MODEL= CAP
MATL = DRYCARES–REMOLD

LEGEND
PSC/S3C=1.8E6
PSC/S3C=3.5E6
PSC/S3C=7.1E6
PSE/S3C=1.8E6
PSE/S3C=3.5E6
PSE/S3C=7.1E6
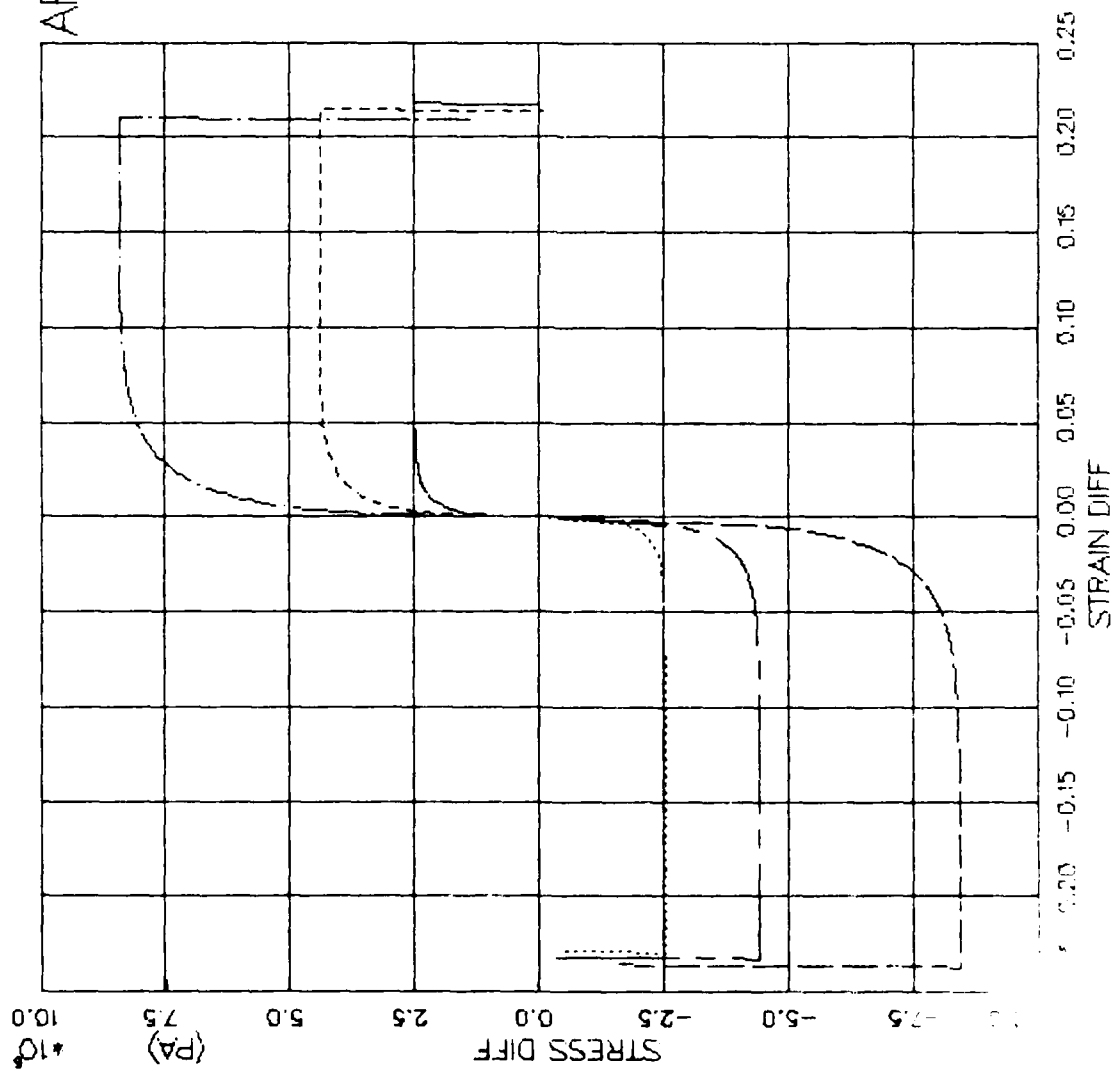
7.15 CAP MODEL EXERCISE–PURE SHEAR(PSC+PSE) – STRESS DIFF VS. STRAIN DIFF

AFOSR SOIL ELEMENT MODEL

TEST = STANDARD TRIAXIAL TEST
MODEL = CAP
MATL = DRYCARES—REMOLD

LEGEND
PSC/S3C=1.8E6
PSC/S3C=3.5E6
PSC/S3C=7.1E6
PSE/S3C=1.8E6
PSE/S3C=3.5E6
PSE/S3C=7.1E6
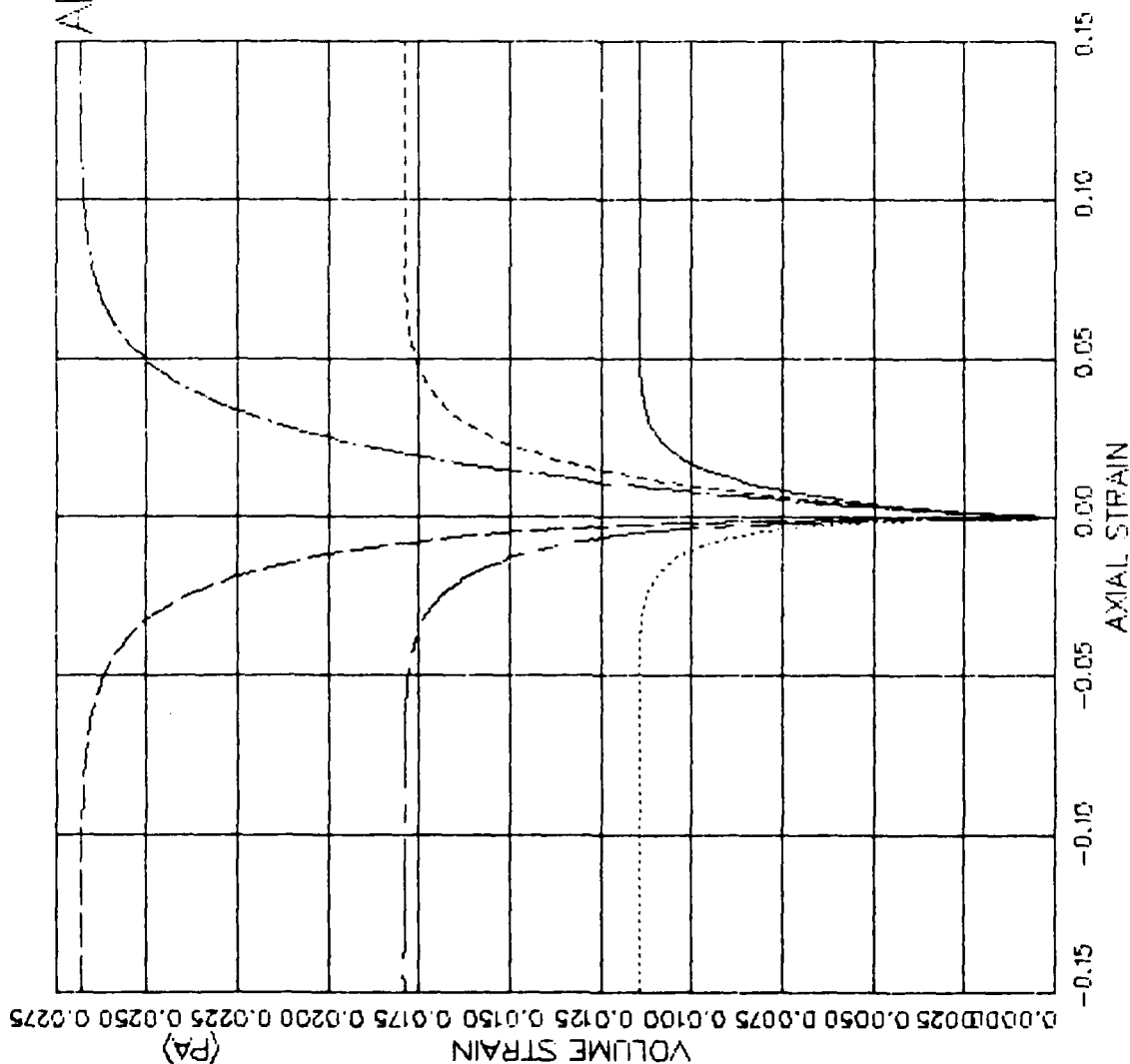
FIGURE V.7.16 CAP MODEL EXERCISE—PURE SHEAR(PSC+PSE) — AXIAL STRAIN VS VOLUME STRAIN

AFOSR SOIL ELEMENT MODEL

TEST = STANDARD TRIAXIAL
MODEL=CAP
MATL = DRYCARES-REMOLD

LEGEND
ISO EXTEN
RTC
PSC
CTC
ISO COMP
RTE
CTE
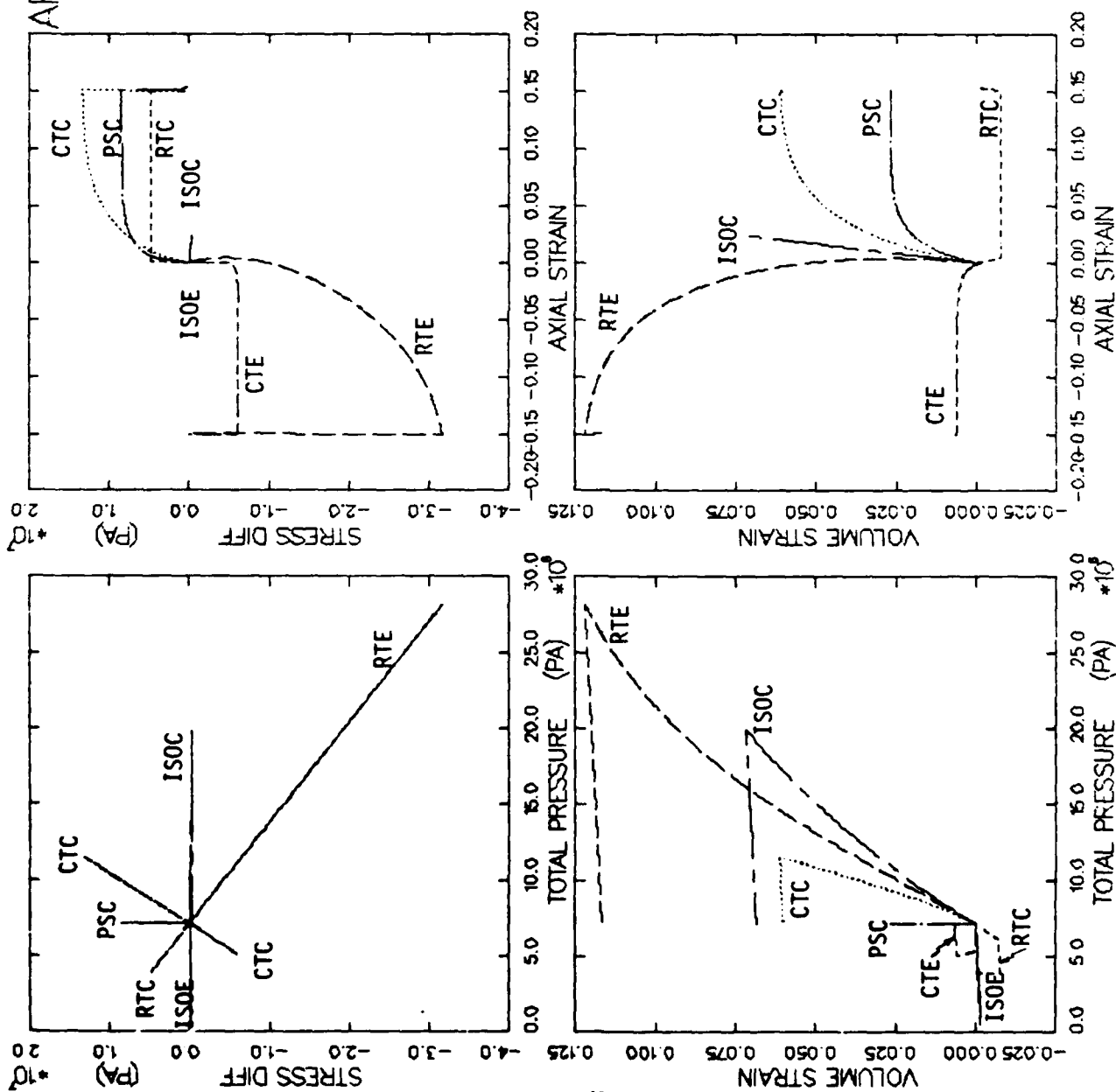
FIGURE V.7.17. CAP MODEL BEHAVIOR SUMMARY (S3C=7.1MPA) — SDIFF/P/EV/EA ANALYSIS

478

FIGURE V.7.18 CAP MODEL EXERCISE— UNIAX STRAIN(UXC) — TOT AXL STRESS VS. AXL STRAIN .
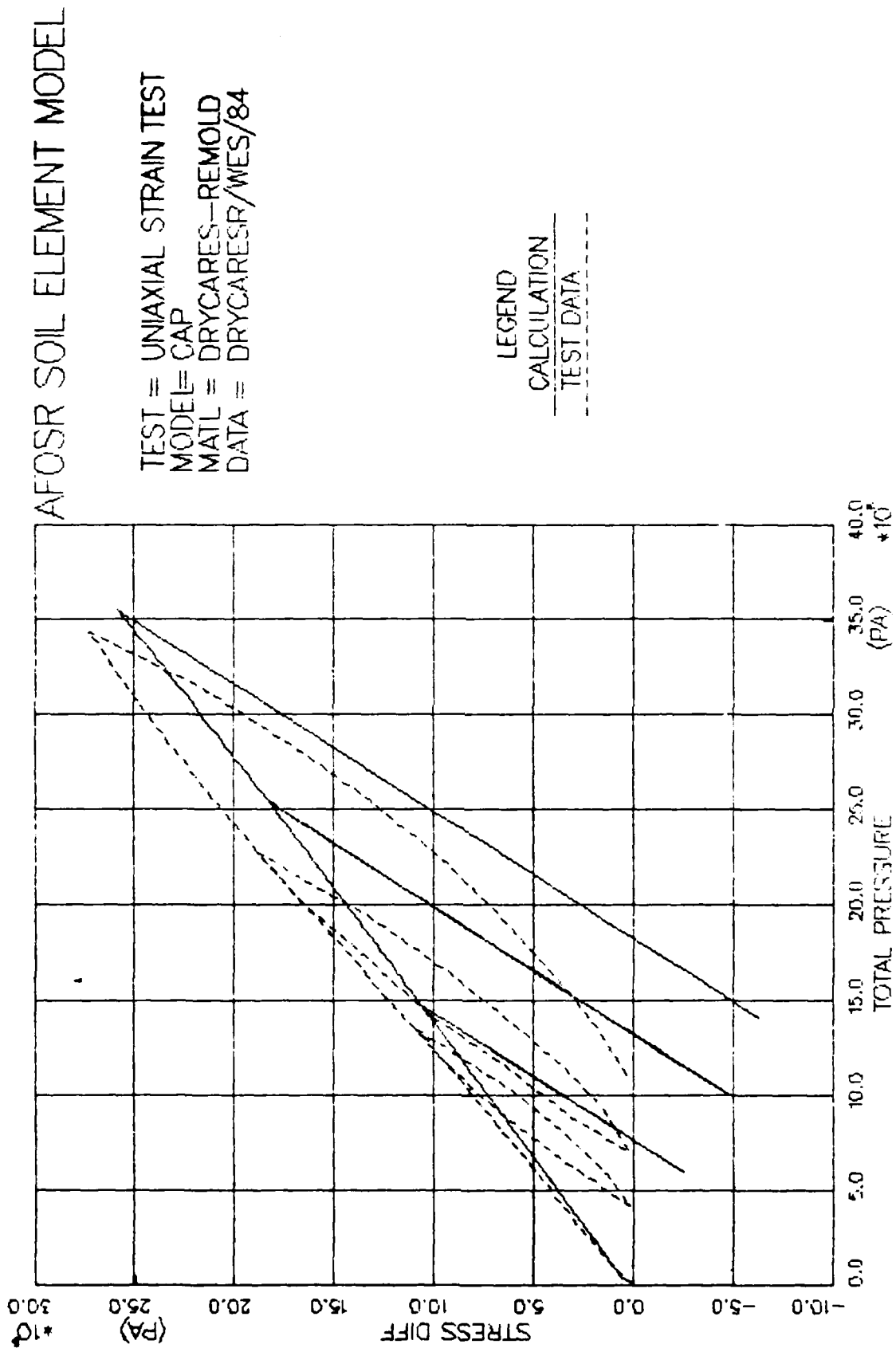
FIGURE V.7.19 CAP MODEL EXERCISE -- UNIAX STRAIN(UXC) -- STRESS DIFFERENCE VS. PRESSURE .

480

AFOSR SOIL ELEMENT MODEL

TEST = UNIAXIAL STRAIN TEST
MODEL= CAP
MATL = DRYCARES—REMOLD
DATA = DRYCARESR/WES/84

LEGEND
CALCULATION
TEST DATA
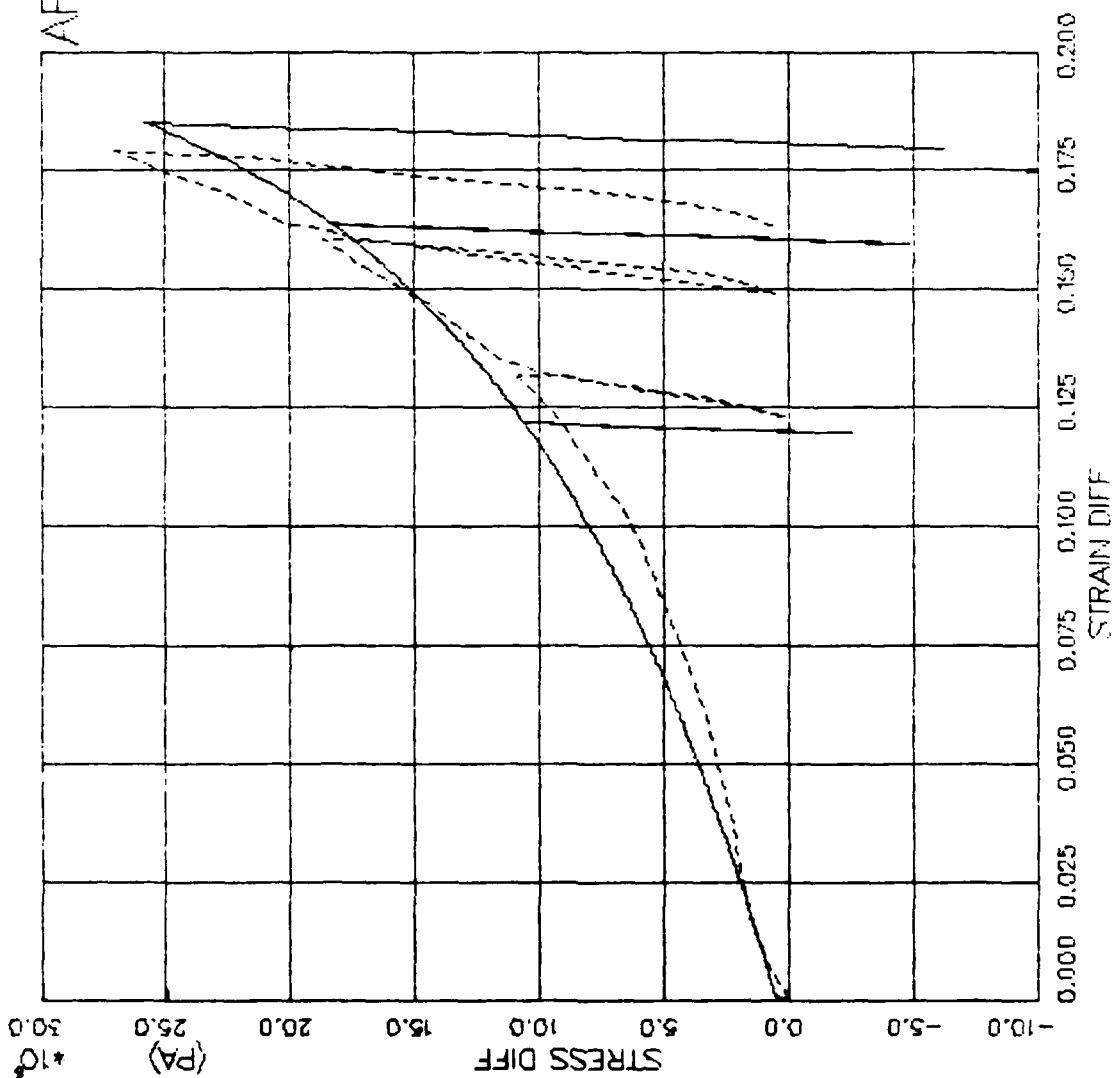
FIGURE V.7.20 CAP MODEL EXERCISE— UNIAX STRAIN(UXC) — STRESS DIFF VS. STRAIN DIFF
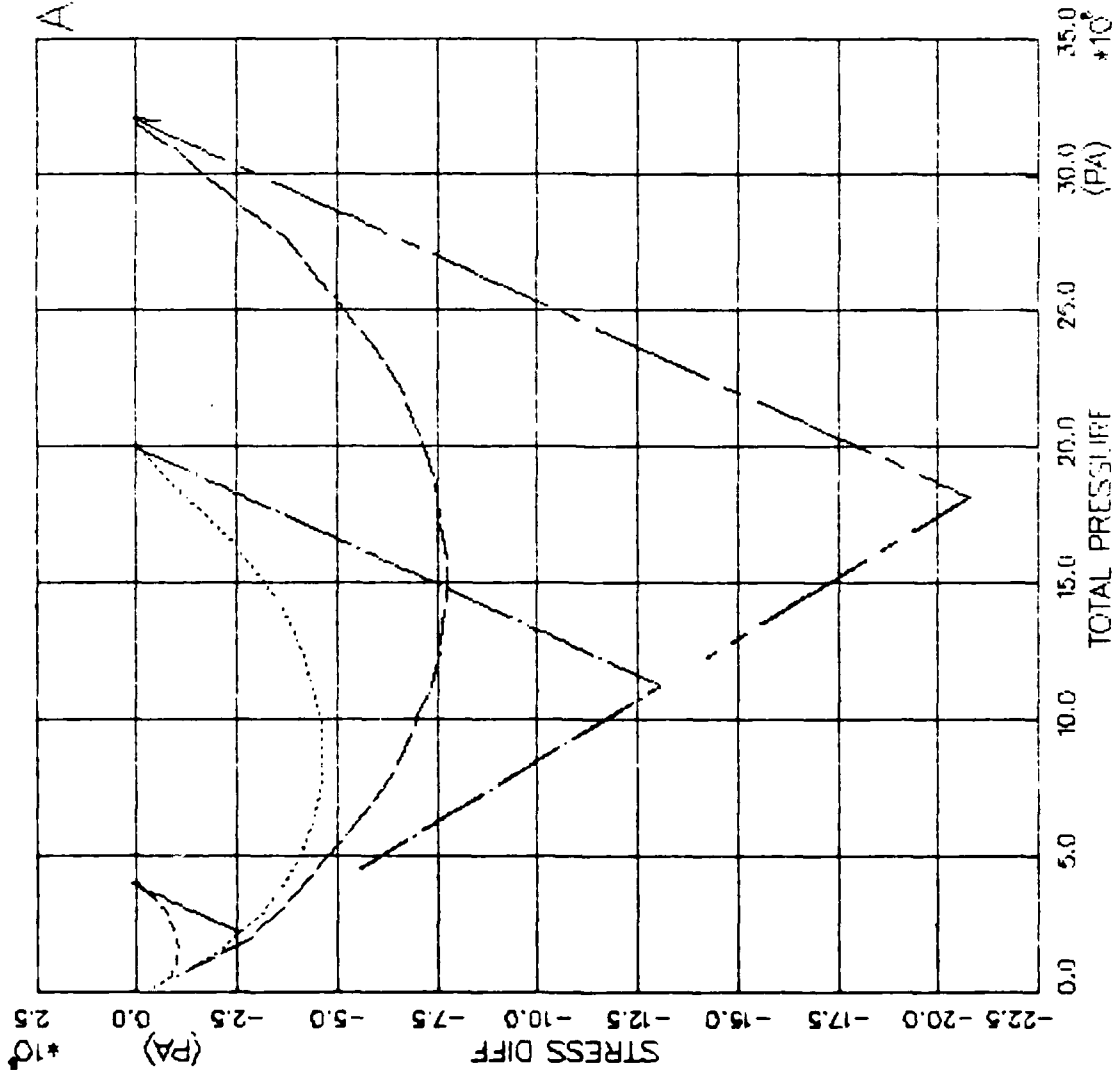
FIGURE V.7.21 CAP MODEL EXERCISE — UNIAX STRAIN EXTEN (f(kk0)) -- STRESS DIFFERENCE VS. PRESS
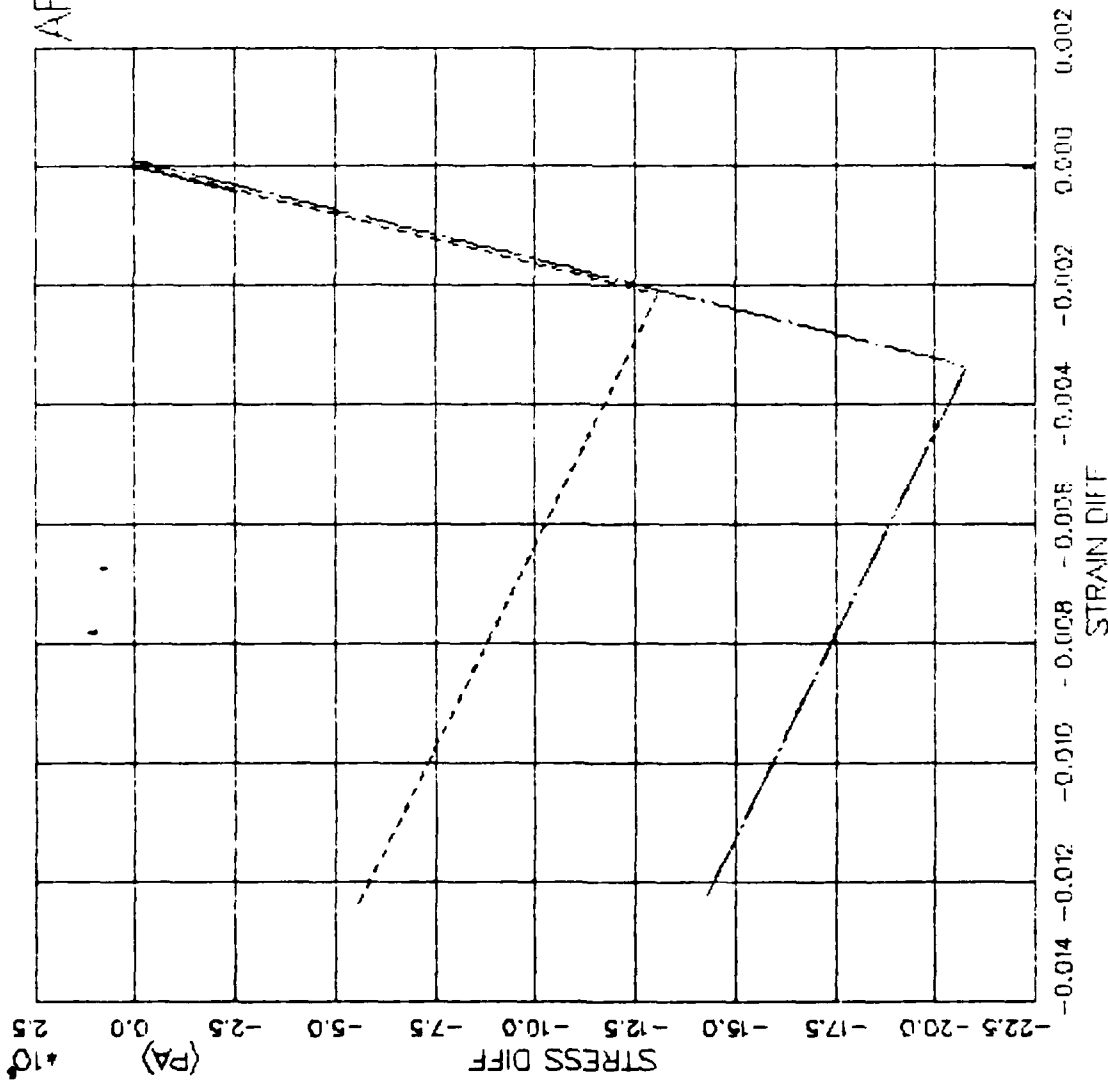
FIGURE V.7.22 CAP MODEL EXERCISE—UNIAX STRAIN EXTEN (ICKO) – STRESS DIFF VS. STRAIN DIFF

FIGURE V.7.23 CAP MODEL EXER-AXISYM FPATH3A+3C -- 3DIFF/P/EV/ELDIFF ANALYSIS
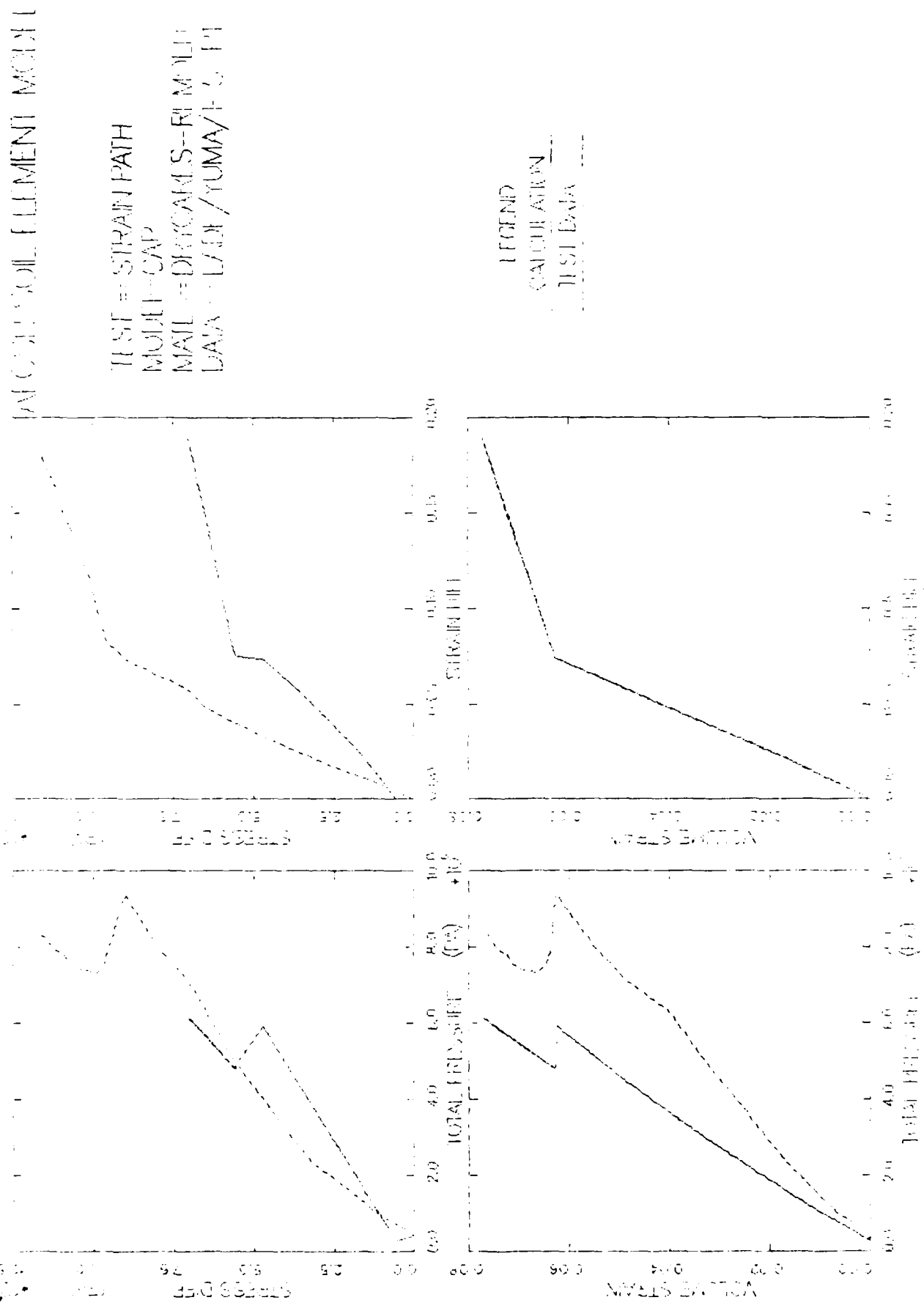
AFOSR SOIL ELEMENT MODEL

TEST = STRAIN PATH
MODEL=CAP
MATL = DRYCARES-REMOLD
DATA = DRYCARESR/WES/3A

LEGEND
WES PATH 3A
TEST DATA
WES PATH 3C
TEST DATA

484
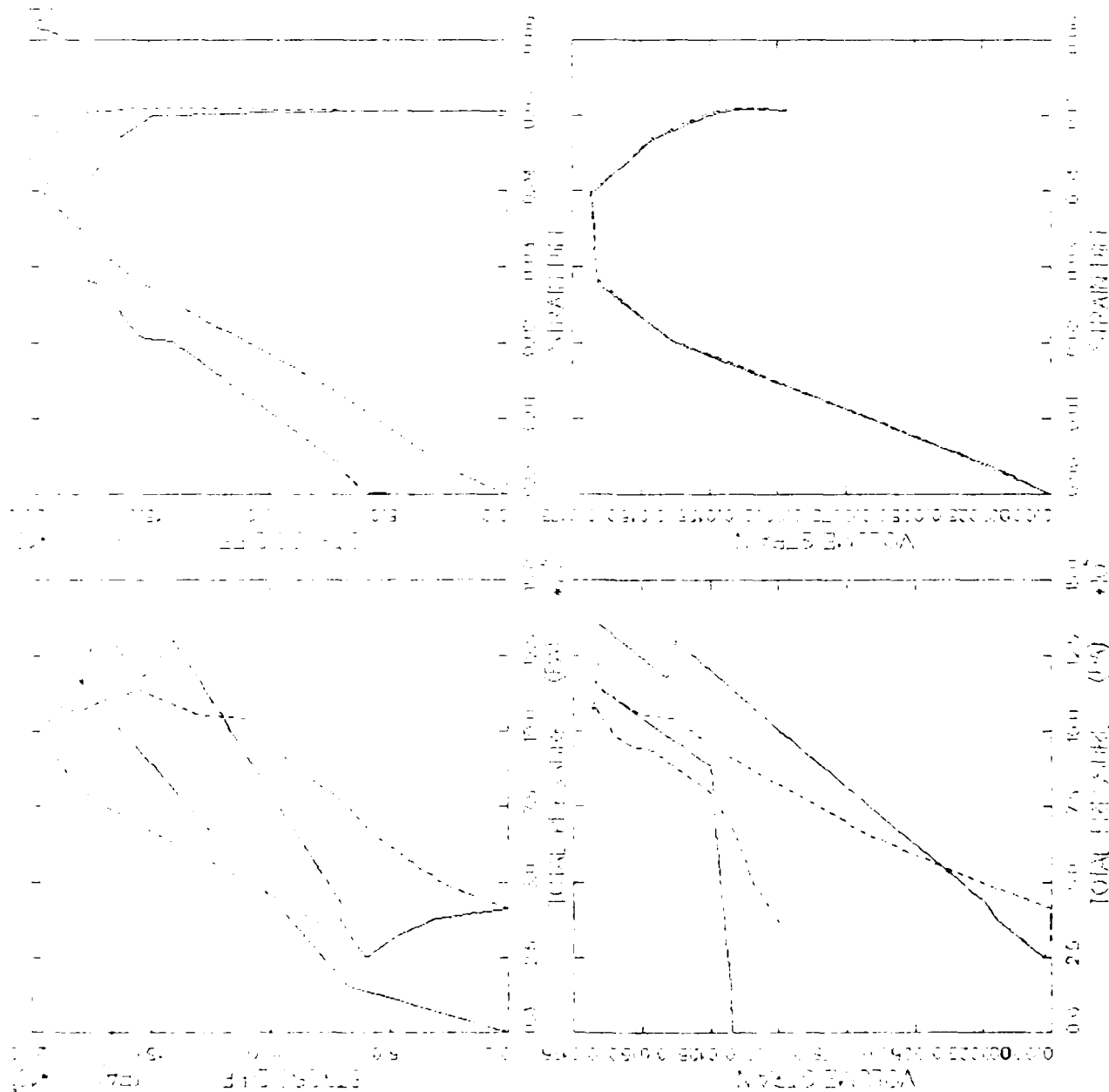
FIGURE V.7.24
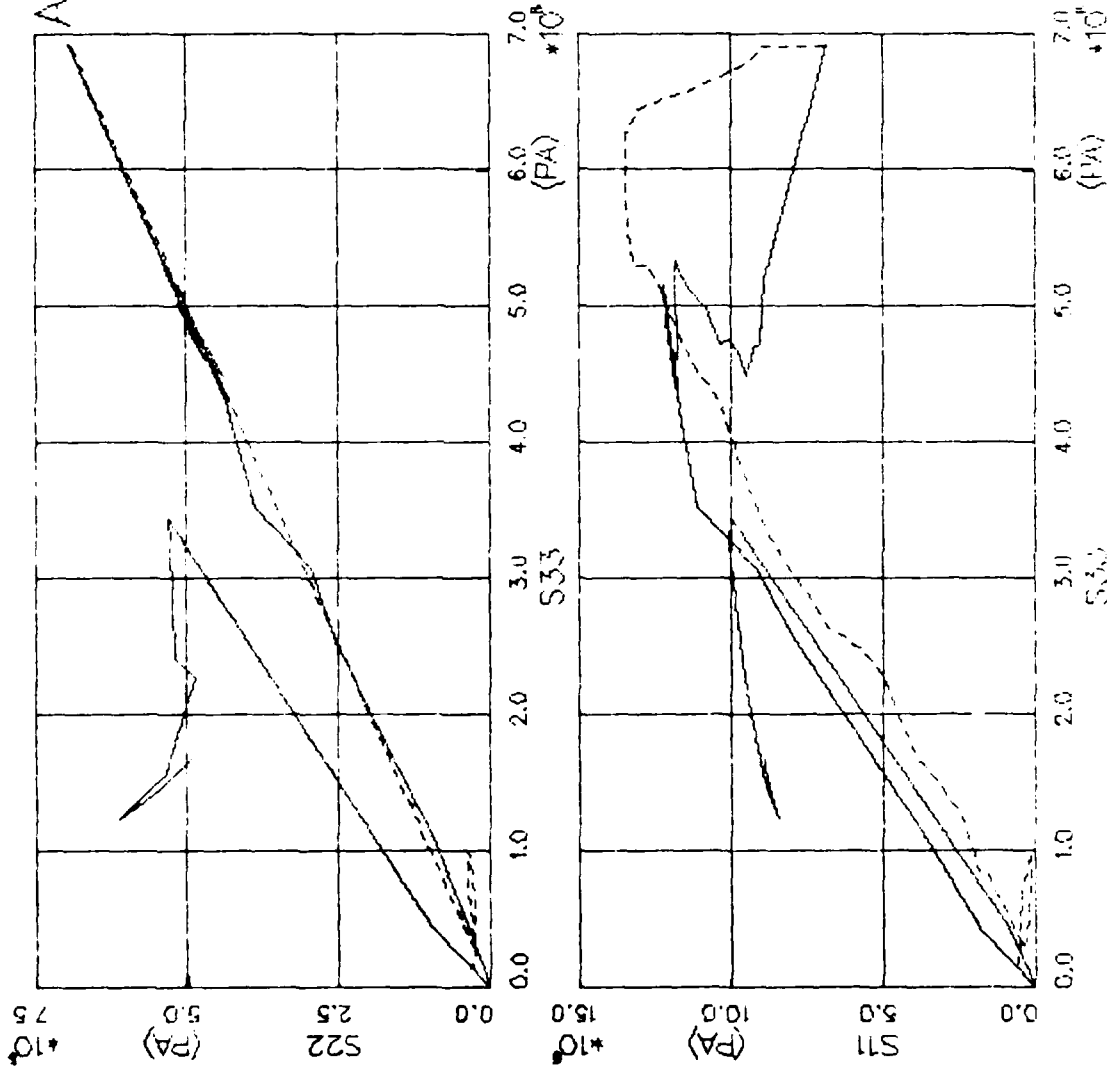
FIGURE V.7.25

FIGURE V.7.26 CAP MODEL EXERCISE — TRUE TRIAX — PRINCIPAL STRESS PATH

487

ADOIR SOIL ELEMENT MODEL

TEST = STRAIN PATH
MODEL = CAP
MAIL = DRYCARES—REMOLD
DATA = NELLISB/KO/JAN83

LEGEND
CALCULATION
TEST DATA
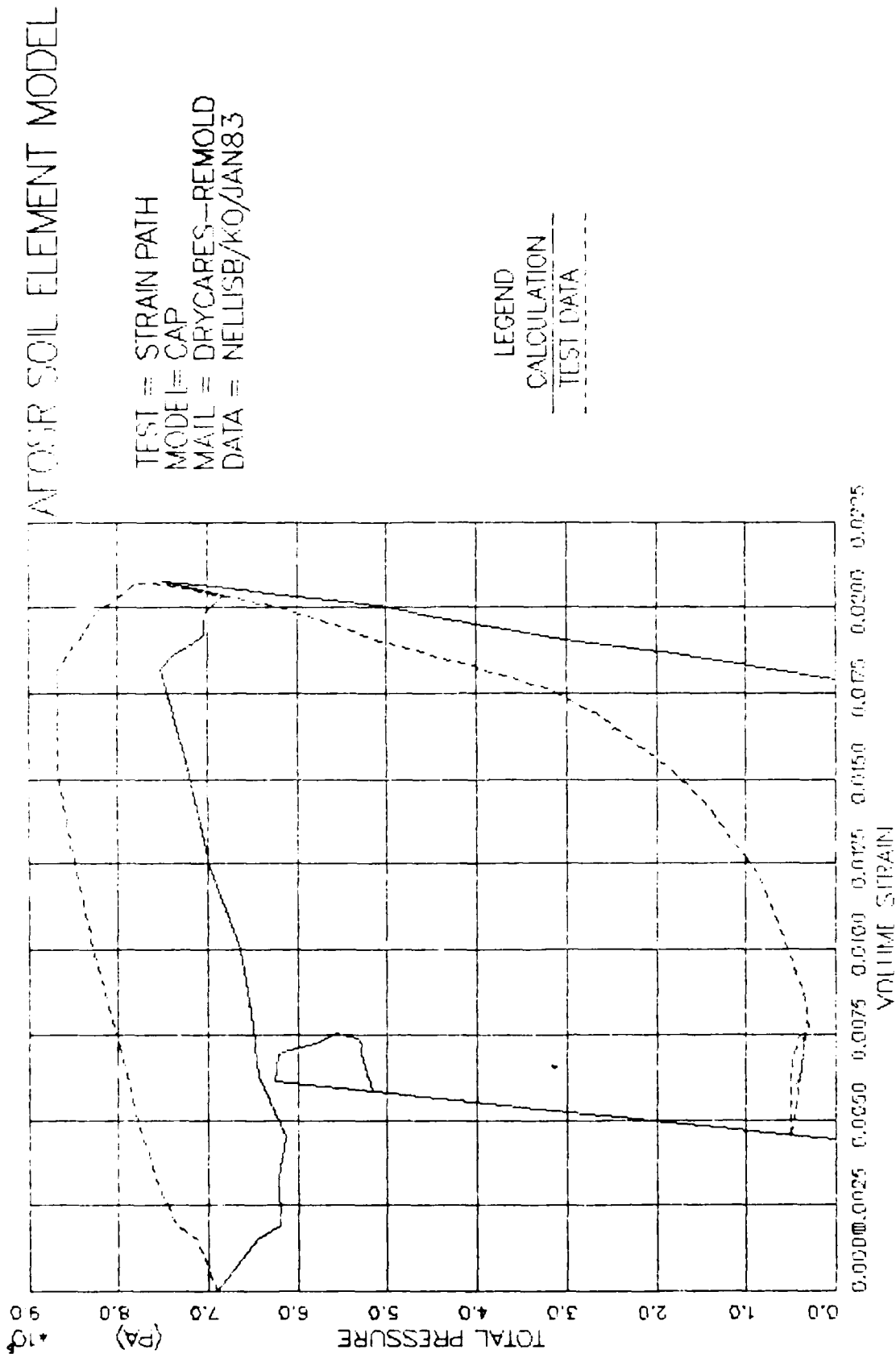
FIGURE V.7.27 CAP MODEL EXERCISE TRUE TRIAX — PRESSURE VS. VOLUMETRIC STRAIN .

488

AFOSR SOIL ELEMENT MODEL

TEST = STANDARD TRIAXIAL
MODEL= CAP
MATL = DRYCARES—REMOLD

LEGEND
CTC/S3C=7.1MPA
CTC/S3C=7.1MPA
CTC/SC3=58.8MPA
CTC/SC3=58.8MPA
CTC/SC3=100.MPA
CTC/SC3=100.MPA
CTE/SC3=7.1MPA
CTE/SC3=7.1MPA
CTE/SC3=58.8MPA
CTE/SC3=58.8MPA
CTE/SC3=100.MPA
CTE/SC3=100.MPA
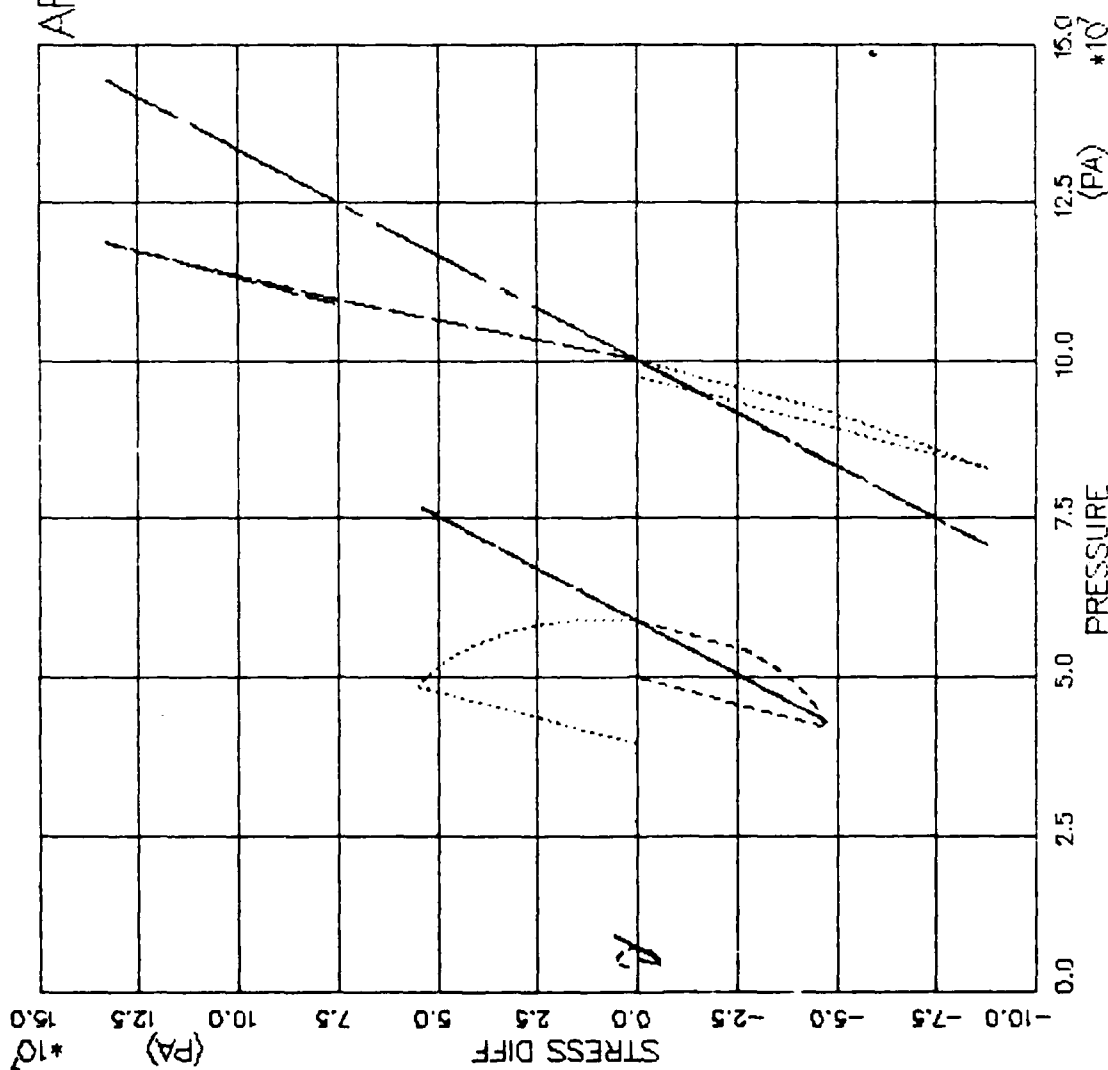
FIGURE V.7.28 ECAP EXERCISE - CONST S3C TRIAXIAL CTC+CTE — TOTAL AND EFF STRESS PATHS

489

AFOSR SOIL ELEMENT MODEL

TEST = STANDARD TRIAXIAL
MODEL= CAP
MATL = DRYCARES–REMOLD

LEGEND
CTC/S3C=7.1MPA
CTC/SC3=58.8MPA
CTC/SC3=100.MPA
CTE/SC3=7.1MPA
CTE/SC3=58.8MPA
CTE/SC3=100.MPA
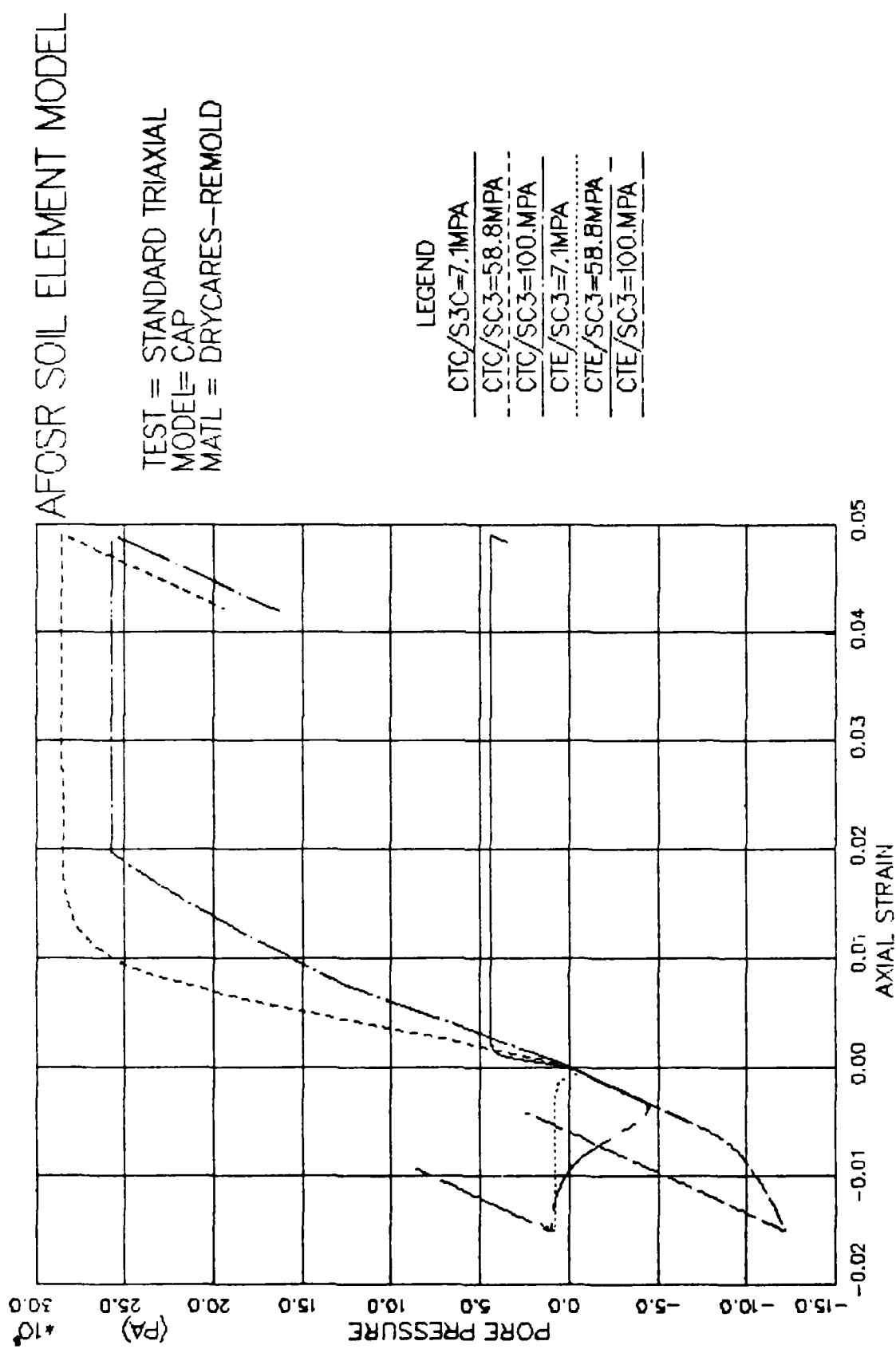
FIGURE V.7.29   ECAP EXERCISE–CONST S3C TRIAXIAL CTC+CTE – PORE PRESSURE VS. AXIAL STRAI

AFOSR SOIL ELEMENT MODEL

TEST = STANDARD TRIAXIAL
MODEL= CAP
MATL = DRYCARES—REMOLD

LEGEND
CTC/S3C=7.1MPA
CTC/S3C=7.1MPA
CTC/SC3=58.8MPA
CTC/SC3=58.8MPA
CTC/SC3=100.MPA
CTC/SC3=100.MPA
CTE/SC3=7.1MPA
CTE/SC3=7.1MPA
CTE/SC3=58.8MPA
CTE/SC3=58.8MPA
CTE/SC3=100.MPA
CTE/SC3=100.MPA
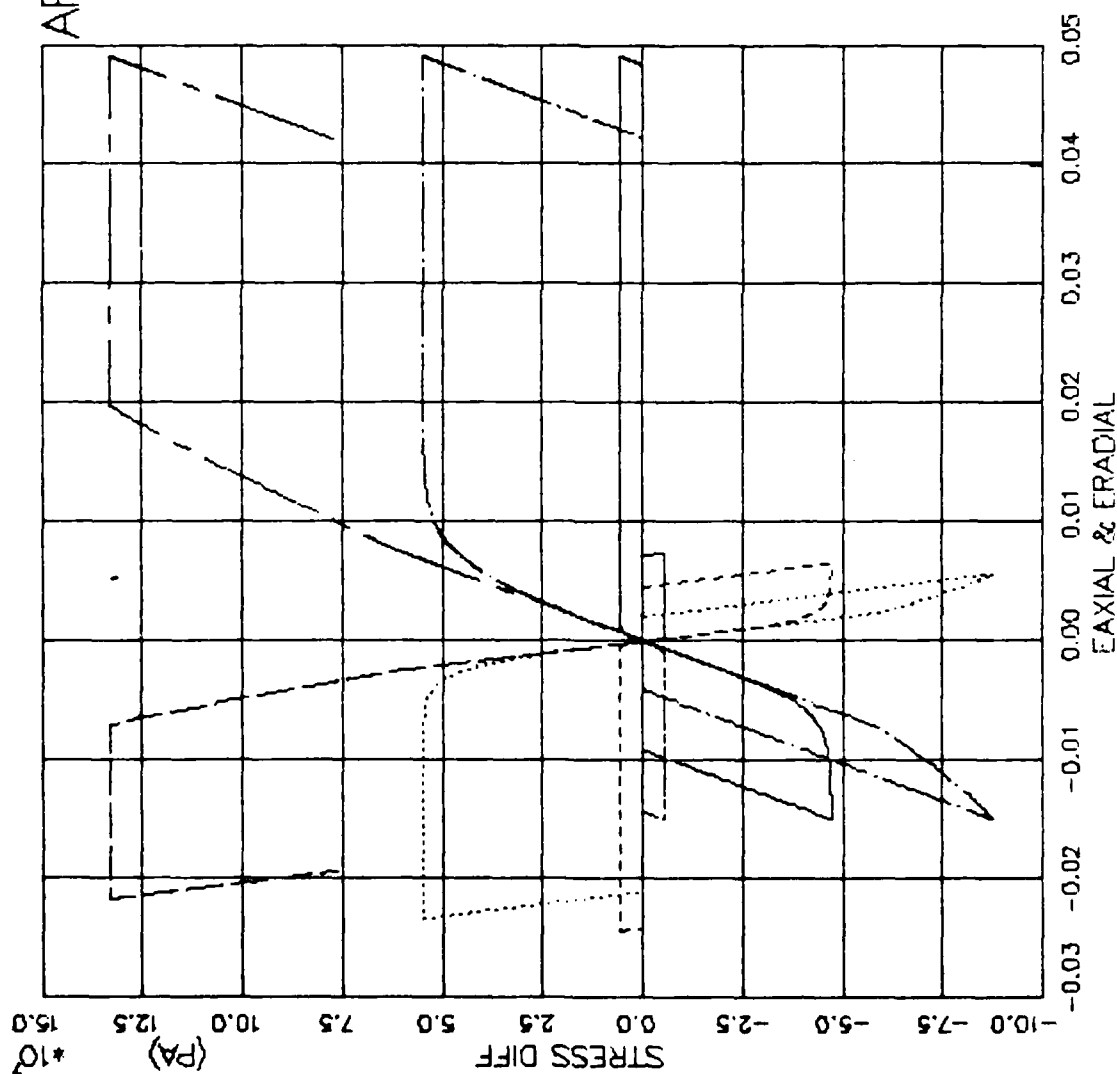
FIGURE V.7.30 ECAP EXERCISE—CONST S3C TRIAXIAL CTC+CTE — STRESS DIFF VS. STRAIN

AFOSR SOIL ELEMENT MODEL

TEST = STANDARD TRIAXIAL
MODEL = CAP
MATL = DRYCARES—REMOLD

LEGEND
CTC/S3C=7.1MPA
CTC/SC3=58.8MPA
CTC/SC3=100.MPA
CTE/SC3=7.1MPA
CTE/SC3=58.8MPA
CTE/SC3=100.MPA
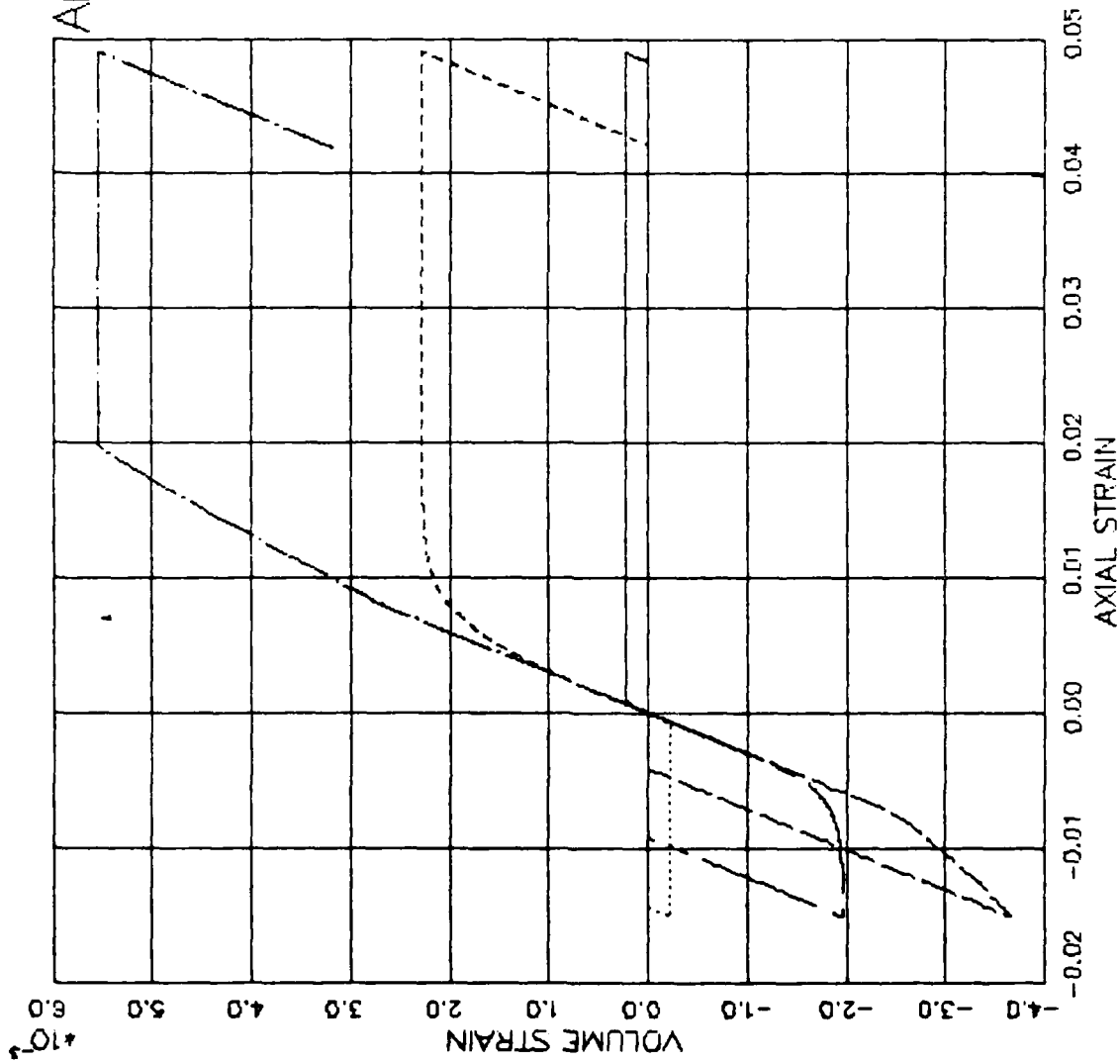
FIGURE V.7.31 ECAP EXERCISE—CONST S3C TRIAXIAL CTC+CTE — AXIAL STRAIN VS VOLUME STRAIN

492

V.8 Lade

V.8.1 Motivation

The Lade model discussed here is an elastoplastic model with two yield surfaces. One, called the expansive yield surface, is bullet shaped with its nose at the origin in stress space. The other, called the collapse yield surface, is spherical with its center at the origin. Both yield surfaces harden in response to the corresponding plastic work, and the expansive yield surface also softens when the corresponding plastic work exceeds a certain value. The collapse yield surface is associative and the expansive yield surface non-associative. The principal advantage of the Lade model is accuracy in representing most aspects of soil stress-strain behavior. The model exhibits nonlinear, inelastic behavior in both shear and compression even at small strains, and the expansive yield surface has a non-circular octahedral cross-section and therefore indicates an influence of the intermediate principal effective stress (or Lode's parameter) on shear strength. The principal disadvantages of the Lade model are possible underprediction of compressibility under the influence of shear at small strains, lack of flexibility in matching true triaxial shear strength data in the octahedral plane, lack of a device to prevent negative plastic work, and possible instability and lack of uniqueness due to strain softening of the expansive yield surface.

V.8.2 Assumptions

The assumptions underlying the Lade model are basically those discussed in Appendix D, except the dissipation condition is not enforced. Instead of a yield function defining the stress levels at which plastic strain increments can occur, it defines the stress levels at which plastic strain increments will occur [Lade and Nelson (1981:504,507)].

The strain hardening parameter for each yield surface is the corresponding plastic work, rather than plastic volumetric strain as with the cap model. The use of two separate yield surfaces, each with its own potential surface and hardening rule, assumes that a material really has two separate yield surfaces.

V.8.3 Basic Equations

The collapse yield criterion has the equation

$$f_c = f_c' - f_c'' = 0 \qquad\qquad (V.8.1)$$

in which

$$f_c' = I_1^2 + 2I_2 = 3(\sigma_{OCT}^2 + \tau_{OCT}^2) \qquad\qquad (V.8.2)$$

$$f_c'' = p_a^2 \left(\frac{W_c}{Cp_a}\right)^{1/p} \qquad\qquad (V.8.3)$$

where

$$p_a = \text{atmospheric pressure}$$

$$C, p = \text{material parameters}$$

and

$$W_c = \int \{\sigma\}^T \{d\epsilon^c\} \qquad\qquad (V.8.4)$$

The collapse plastic potential, to which the collapse plastic strain increment vector, $\{d\epsilon^c\}$, is normal, is

$$g_c = f_c' = I_1^2 + 2I_2 \qquad\qquad (V.8.5)$$

The expansive yield criterion has the equation

$$f_p = f_p' - f_p'' = 0 \qquad\qquad (V.8.6)$$

494

in which

$$f_p' = \left(\frac{I_1^3}{I_3} - 27\right)\left(\frac{I_1}{p_a}\right)^m \qquad (V.8.7)$$

$$f_p' = f_{p,MAX}' = \eta_1 \text{ at failure} \qquad (V.8.8)$$

$$f_p'' = ae^{-bW_p}\left(\frac{W_p}{p_a}\right)^{1/q} \qquad (V.8.9)$$

where

   m, η_1, a, b, q = material parameters

and

$$W_p = \int\{\sigma\}^T\{d\epsilon^p\} \qquad (V.8.10)$$

The expansive plastic potential, to which the expansive plastic strain increment vector, $\{d\epsilon^p\}$, is normal, is

$$g_p = I_1^3 - \left[27 + \eta_2\left(\frac{p_a}{I_1}\right)^m\right]I_3 \qquad (V.8.11)$$

where η_2 is also a material parameter.

   The unloading/reloading elastic modulus is assumed to be given by the expression

$$E_{ur} = K_{ur}p_a\left(\frac{\sigma_3}{p_a}\right)^n \qquad (V.8.12)$$

where

   K_{ur}, n = material parameters

Poisson's ratio is usually assumed constant.

   A method for calculating the octahedral cross-section of Lade's failure surface (the expansive yield surface at its maximum extent) is given in Appendix T.

The computational features of Lade's model are covered in Appendices F, G, H, I, J, K, and T. Using the value of Young's modulus from Equation (V.8.12) and an assumed Poisson's ratio, the elastic incremental stiffness matrix is given by Equation (J.31). The general equations of elastoplasticity given in Appendix D apply, except that the dissipation condition, Equation (D.8) is not enforced. The elastoplastic incremental stiffness matrices are calculated as described in Appendix G, but the polar mode check described in Appendix I is not used. Instead, if the stress point lies on a yield surface, that surface is assumed to be active. However, only positive plastic work increments are accumulated in calculating total plastic work.

V.8.4 Parameter Determination

Determination of the material parameters in Equations (V.8.1) through (V.8.12) by a series of linear laboratory test data plots is explained in Appendix T. Parameters for CARES-DRY sand were determined by using an automatic fitting routine in the Soil Element Model which is based on Appendix T. Step-by-step results from this fitting process are shown in Figures (V.8.1) through (V.8.18).

Elastic stiffness data (Young's Modulus) as determined from the *unload-reload portions of isotropic compression, uniaxial strain, and triaxial compression tests presented by* [Cargile (1984)] are plotted versus radial confining pressure in Figure (V.8.1). This plot yields values for the modulus number, K_{ur}, and exponent, n.

Figure (V.8.2) shows the loading hydrostatic data used for obtaining collapse yield surface parameters. In Figure (V.8.3) the hydrostat has been integrated to show collapse plastic work versus radial confining pressure squared. Elastic properties are varied according to the

previously determined relationship with σ_3 during integration. A single straight line is passed through the data (open circles) to determine the collapse constant, C, and the exponent, p.

Figure (V.8.4) shows triaxial stress-strain data at five confining pressures. When the data does not approach a "peak" response, it needs to be artificially extended by some method. Extension to peak is necessary for this type of hardening model to produce reasonably shaped stress-strain curves having the correct value of expansive plastic work at peak stress difference. The method arbitrarily chosen here was to assume a hyperbolic shape for the last twenty-five percent of both the axial and radial stress difference-strain curves. A Kondner plot of strain divided by stress difference vs. strain is then used to extend the data to ninety-five percent of peak stress difference as predicted by the straight line fit. Two such plots are shown in Figures (V.8.5) and (V.8.6) for the CARES-DRY data at 3.4 MPa and 7.0 MPa, respectively.

Peak response data from the extended stress-strain curves are plotted in Figure (V.8.7) as $f'_{p,max}$ vs. p_a/I_1. The parameters from this fit, n_1 and m, define the shape and most expanded position of the expansive yield surface, f'_p.

Given the previously determined elastic and collapse plastic work relationships, collapse and expansive plastic strains resulting from the triaxial test are calculated and plotted in Figures (V.8.8) and (V.8.9), respectively. Figures (V.8.10) through (V.8.14) show the components of volume strain which are relevant to the Lade model: total, elastic, collapse plastic, and expansive plastic (which is the difference between total and elastic + collapse). The basic theory of the model requires

that the strain associated with the expansive yield surface always be expansive. But in Figures (V.8.11), (V.8.12), and (V.8.13), this does not always happen. The reason for this is that at these confining pressures, collapse behavior as determined by the isotropic test is stiffer than would be indicated by the triaxial test. One remedy for this inconsistency is to use an envelope of pressure-volume response which encompasses both tests.

The triaxial data and calculated expansive plastic strains are used to determine the variation of the expansive yield surface, f_p', with expansive plastic work, W_p. This is shown in Figure (V.8.15). Note that the data does not conform to the idealized shapes for these curves as postulated by the model. Values of plastic work at peak stress difference lay roughly on a straight line in log space [Figure (V.8.16)], but the shape parameter, α, in arithmetic space does not [Figure (V.8.17)].

The expansive plastic potential parameters are derived from Figure (V.8.18), which shows the variation of n_2 with both f_p'' and σ_{3C}. The straight lines lie in a plane which passes through the entire set of data. The rough appearance of the data is primarily a result of three factors:

(a) The data was digitized by hand from small plots, and radial strain was calculated by graphically subtracting strain difference from axial strain.

(b) Unload-reload loops were eliminated from the data, but did in fact have a significant effect on volumetric response.

(c) The fitting process up to this point may introduce some inconsistency between test data and predicted model response.

If raw data had been available in digital form, and only loading had been performed in these specific tests, a much smoother plot would be expected.

498

Table (V.8.1) summarizes the Lade model parameters for remolded CARES-DRY sand.

V.8.5 Computed Behavior

With a two-parameter exponential fit to the hydrostat, the Lade model can produce a curve of single inflection only, either convex or concave. Figure (V.8.19) shows this, compared with the test data. The fit is reasonable at higher stresses, but cannot match the low stress variations in bulk modulus trend.

CTC stress-strain data, used to fit the model, is well matched [Figures (V.8.20) and (V.8.21)]. Volumetric response is qualitatively good [Figure (V.8.22)], but overestimates the tendency for dilation in the looser (lower σ_{3c}) sands. Pressure-volume response comparisons [Figure (V.8.23)] are very good, again with the exception of over-dilation at low stresses. CTE shear failure levels [Figure (V.8.24)] could be matched better with a slightly lower asymmetry in the expansive yield surface. Initial shear stiffness is too high [Figure (V.8.25)]. The test specimens tended to compact only, while the model predicts a small amount of initial elastic expansion, subsequent plastic compaction as the collapse yield surface is pushed out, and finally dilation as the expansive yield surface is pushed toward its ultimate position [Figures (V.8.26) and (V.8.27)].

The constant axial stress (RTC/RTE) and constant mean normal stress (PSC/PSE) triaxial test exercises serve to illustrate the principal aspects of the Lade model: work hardening/softening, asymmetric yield surface, and shear-volume coupling (dilatancy). Due to the work-hardening expansive yield surface, stress-strain behavior is smooth for both the RTC/E tests [Figures (V.8.28-V.8.31)] and PSC/E tests [Figures (V.8.32-V.8.34)]. Different levels of stress difference near shear failure for

PSC and PSE [Figure (V.8.32)] are a result of the asymmetry of the failure surface. Work softening is most evident in the RTE test [Figure (V.8.28)]. Note that this causes a negative net shear stiffness, as seen in Figure (V.8.29). Dilation is evident for both the RTC/RTE tests [Figures (V.8.30) and (V.8.31)] and the PSC/PSE tests [Figure (V.8.34)]. This is especially important in the constant pressure tests.

Behavior predicted by the Lade model for tests run in the triaxial device from 7.1 MPa confining pressure is summarized in Figure (V.8.35). Note the variability in pressure volume response due to varying dilation.

Predicted uniaxial strain compression (UXC) behavior compares poorly with the data [Figures (V.8.36) through (V.8.38)]. The calculated uniax is very soft at low axial stress, due to the low initial confining pressure (0.1 MPa) and subsequent low elastic stiffness (E_{ur} is a function of radial stress). The model also suddenly softens at about $\sigma_a = 38$ MPa [Figures (V.8.36) and (V.8.37)] because the peak expansive plastic work is attained. Clearly, this type of softening behavior is not appropriate for this material under these test conditions. Qualitatively, the UXE stress paths compare quite well with the data [Figure (V.8.39)], but again it appears that somewhat more shear capacity in extension is required. Figure (V.8.40) shows calculated UXE stress-strain response.

Calculated results for the WES strain paths, shown in Figure (V.8.41) are reasonable but show a slightly high shear stiffness, as can be seen in the plot of $(\sigma_1-\sigma_3)$ vs. $(\varepsilon_1-\varepsilon_3)$. Neither calculated stress path shows the rather flat stress difference response upon increased radial expansion as is observed in the data. The second set of strain paths (denoted "Lade") originates at a low confining pressure ($\sigma_{3c} = 0.4$ MPa).

500

This causes the Lade model to have a very low initial volumetric stiffness and causes underestimated pressures [Figures (V.8.42) and (V.8.43)]. The overall shape of the calculated stress paths is very good. Figures (V.8.44) and (V.8.45) show predicted response for the true triaxial strain path. Data for Nellis Baseline Sand is included on the plots for comparison. Both the stress path and volume response comparisons look quite reasonable.

TABLE V.8.1(a). LADE MODEL PARAMETERS FOR
REMOLDED CARES-DRY SAND

Parameter	Symbol	Variable	Value	Units
Modulus Number	K_{ur}	EKUP	363.5	--
Modulus Exponent	n	EN	0.8412	--
Poisson's Ratio	ν	POIS	0.20	--
Collapse Constant	C	C	2.700×10^{-3}	--
Collapse Exponent	p	PC	0.6482	--
Yield Constant	η_1	ETA1	84.52	--
Yield Exponent	m	CURVM	0.2261	--
	r	R	0.1806	--
Plastic Potential	s	SS	0.7309	--
Constants	t	T	-14.52	--
	α	ALPHA	1.972	--
Work-Hardening	β	BETA	2.140×10^{-4}	--
Constants	P	PW	0.6379	--
	l	ELW	0.8077	--
	q	Q		--
Peak Plastic	$W_{p,pk}$	WPPK		Pa
Exp. Work	a	A	varies, see	--
	b	B	Table V.8.1(b)	--
Initial Confining Pressure	σ_{3c}	SIGMA3		MPa
Initial Plastic Comp. Work	$W_{c,o}$	WC		Pa
Mass Density	ρ	RHOREF	1900	kg/m^3

TABLE V.8.1(b). LADE MODEL PARAMETERS WHICH VARY WITH CONFINING PRESSURE

σ_{3c} (MPa)	Q	W_{ppk} (Pa)	A	B	$W_{c,o}$ (Pa)
0.1	1.972	6.40×10^4	177.3	7.928×10^{-6}	5.48×10^2
0.4	1.973	2.02×10^5	99.06	2.516×10^{-6}	3.46×10^3
1.8	1.976	6.60×10^5	54.31	7.664×10^{-7}	2.32×10^4
3.5	1.979	1.13×10^6	41.44	4.471×10^{-7}	5.50×10^4
7.0	1.987	1.98×10^6	31.34	2.545×10^{-7}	1.35×10^5
20.0	2.014	4.62×10^6	20.85	1.075×10^{-7}	5.27×10^5
32.0	2.040	6.75×10^6	17.62	7.264×10^{-8}	9.70×10^5
59.0	2.096	1.10×10^7	14.54	4.324×10^{-8}	2.13×10^6
100.0	2.183	1.69×10^7	12.81	2.704×10^{-8}	4.25×10^6

AFOSR SOIL ELEMENT MODEL

TEST = PARAMETER FIT
MODEL= LADE
MATL = DRYCARES-REMOLD
DATA = DRYCARESR/WES/84
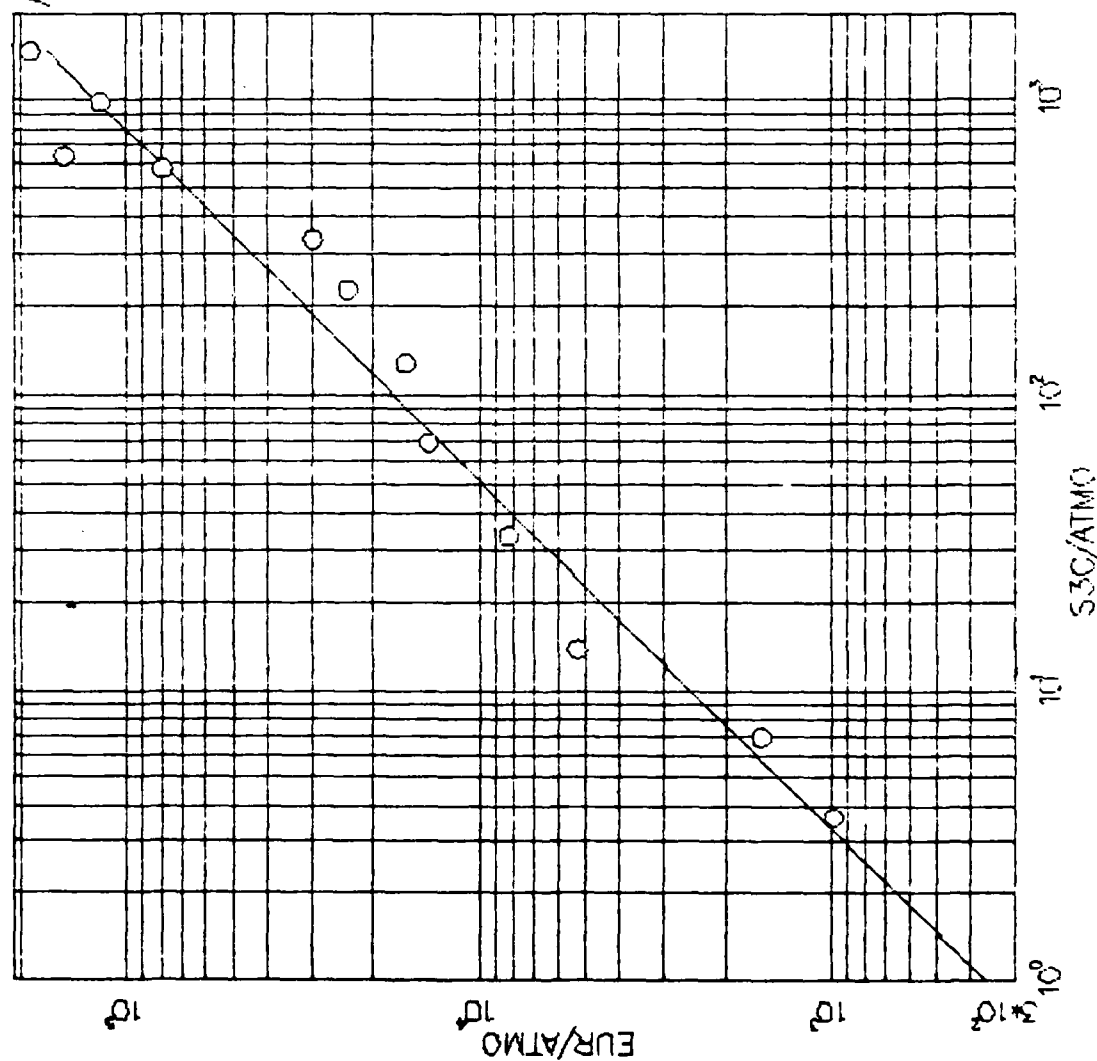
FIGURE V.8.1   LADE MODEL FIT/DATA=DRYCARESR/WES/84 — ELASTIC MODULUS DATA

504
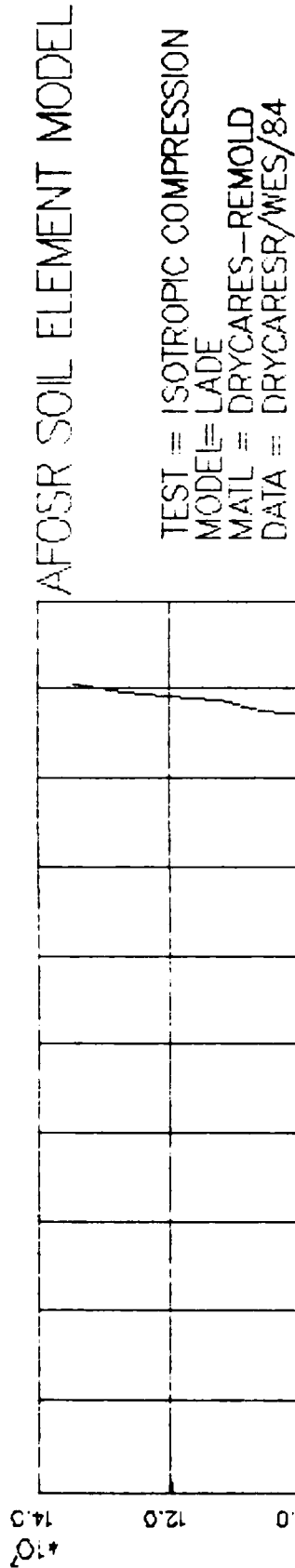
FIGURE V.8.2   LADE MODEL FIT/DATA=DRYCARESR/WES/84 — HYDROSTATIC COMPRESSION DATA

AFOSR SOIL ELEMENT MODEL

TEST = PARAMETER FIT
MODEL= LADE
MATL = DRYCARES-REMOLD
DATA = DRYCARESR/WES/84

$C = 2.700*10^{-3}$
$PC = 6.482*10^{-1}$

FIGURE V.8.3   LADE MODEL FIT/DATA: DRYCARESR/WES/84 — COMPRESSIVE PLASTIC WORK FIT

506
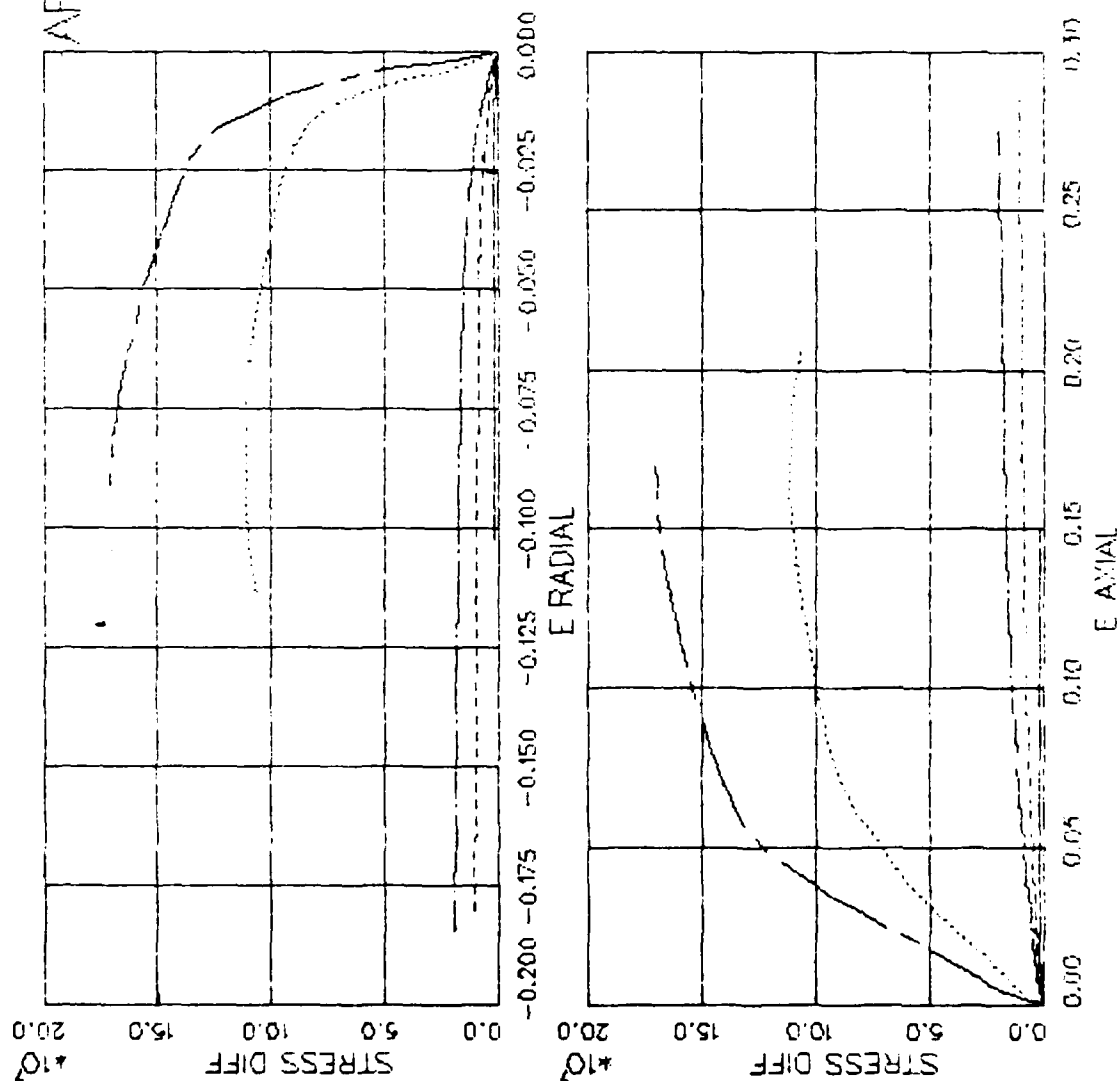
FIGURE V.8.4 LADE MODEL FIT/DATA: DRYCARESR/WES/84 — TRIAXIAL TEST DATA

507

AFOSR SOIL ELEMENT MODEL

TEST = STANDARD TRIAXIAL TEST
MODEL= LADE
MATL = DRYCARES—REMOLD
DATA = DRYCARESR/WES/84

LEGEND
○ AXIAL
LSQFIT
□ RADIAL
LSQFIT

$E(A) = 1.833*10^{8}$
$SDMEA = 1.363*10^{7}$
$EADMAX = 1.600*10^{-1}$
$E(R) = 8.205*10^{8}$
$SDMER = 1.135*10^{7}$
$ERDMAX = -6.310*10^{-2}$
$S3C = 3.400*10^{6}$
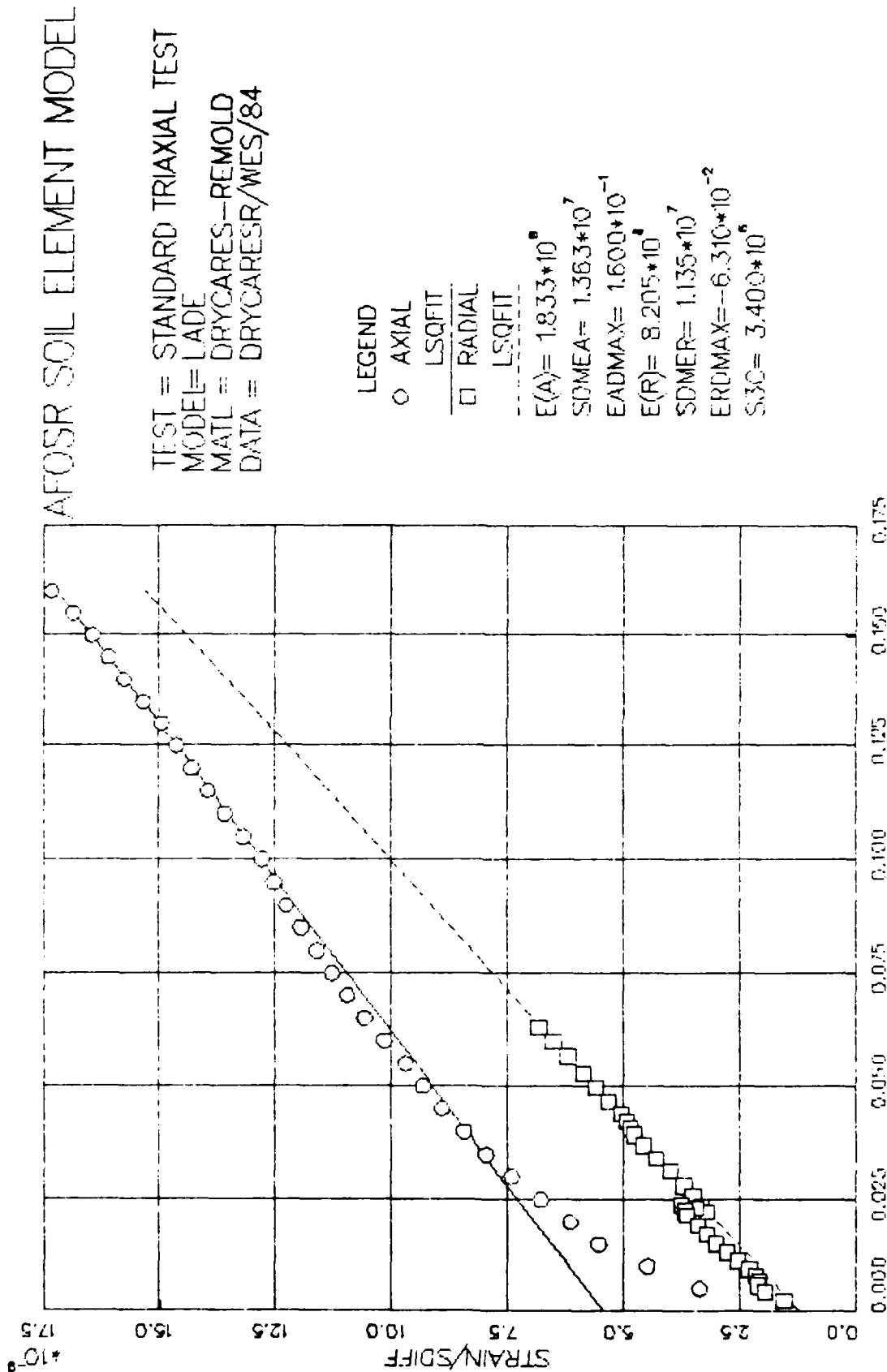
FIGURE V.8.5 LADE MODEL FIT/DATA-DRYCARESR/WES/84 — DATA EXTENSION - HYPERBOLIC FIT

508

AFOSR SOIL ELEMENT MODEL

TEST = STANDARD TRIAXIAL TEST
MODEL= LADE
MATL = DRYCARES-REMOLD
DATA = DRYCARESR/WES/84

LEGEND
O AXIAL
___ LSQFIT
□ RADIAL
- - - LSQFIT

$E(A) = 3.469*10^8$
$SDMEA = 2.479*10^7$
$EADMAX = 1.550*10^{-1}$
$E(R) = 1.388*10^9$
$SDMER = 2.071*10^7$
$ERDMAX = -6.740*10^{-2}$
$SIG = 7.000*10^6$

FIGURE V.8.6 LADE MODEL FIT/DATA= DRYCARESR/WES/84 -- DATA EXTENSION -HYPERBOLIC FIT
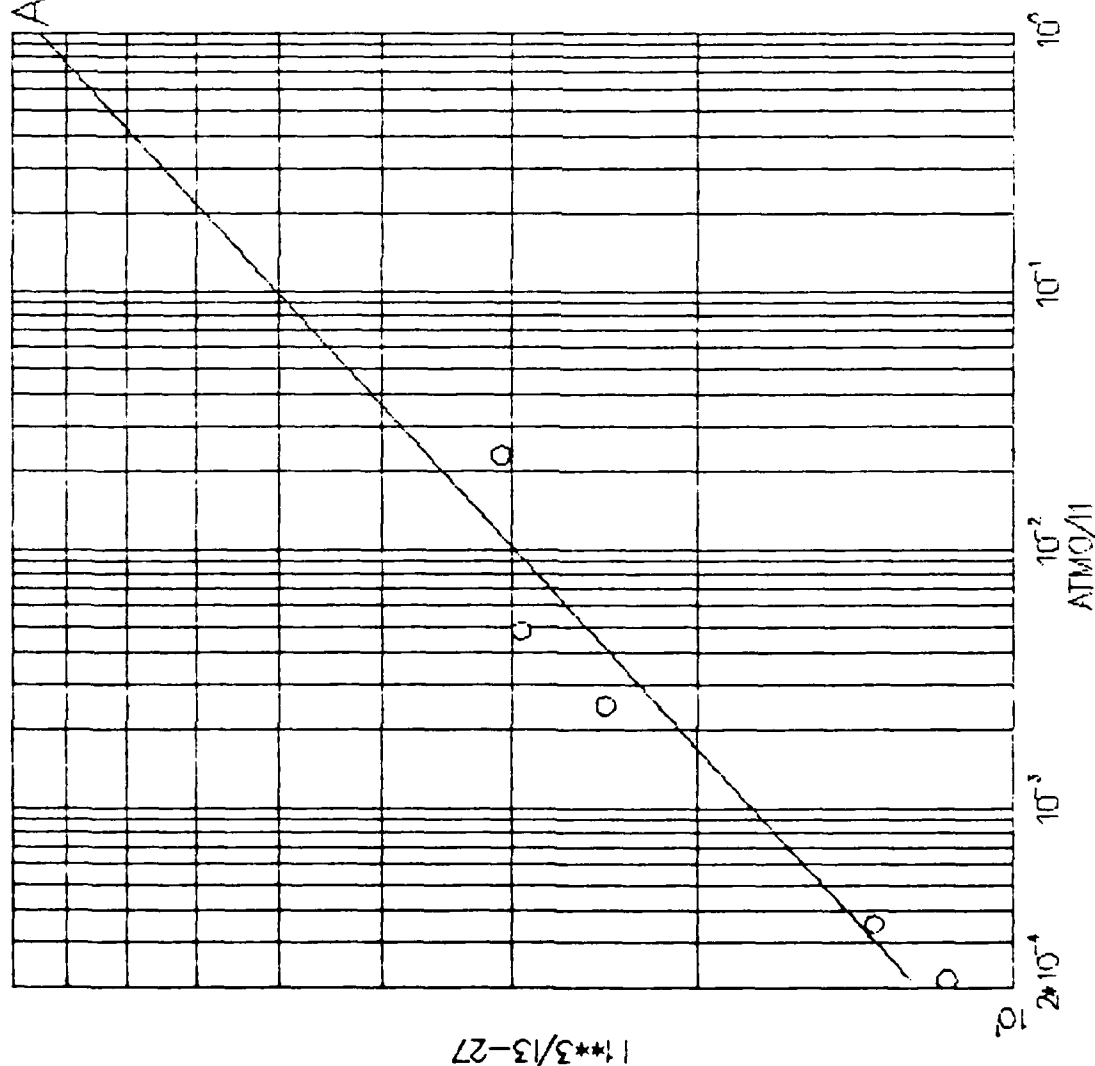
FIGURE V.8.7   LADE MODEL FIT/DATA=DRYCARESR/WES/84 -- FFMAX VS I1MAX

510
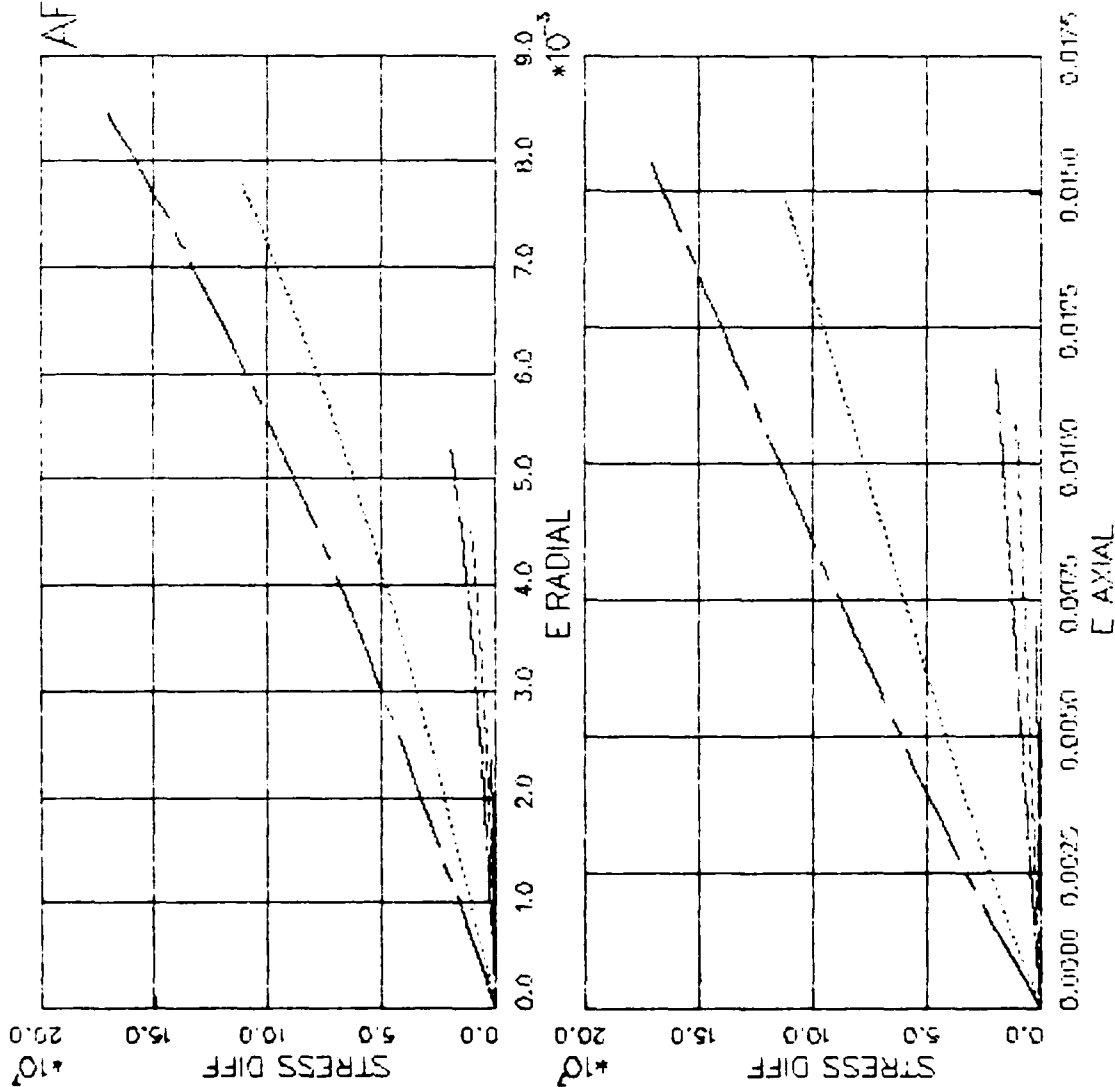
FIGURE V.8.8 LADE MODEL FIT/DATA=DRYCARESR/WES/84 — COMPRESS. PLASTIC STRAINS
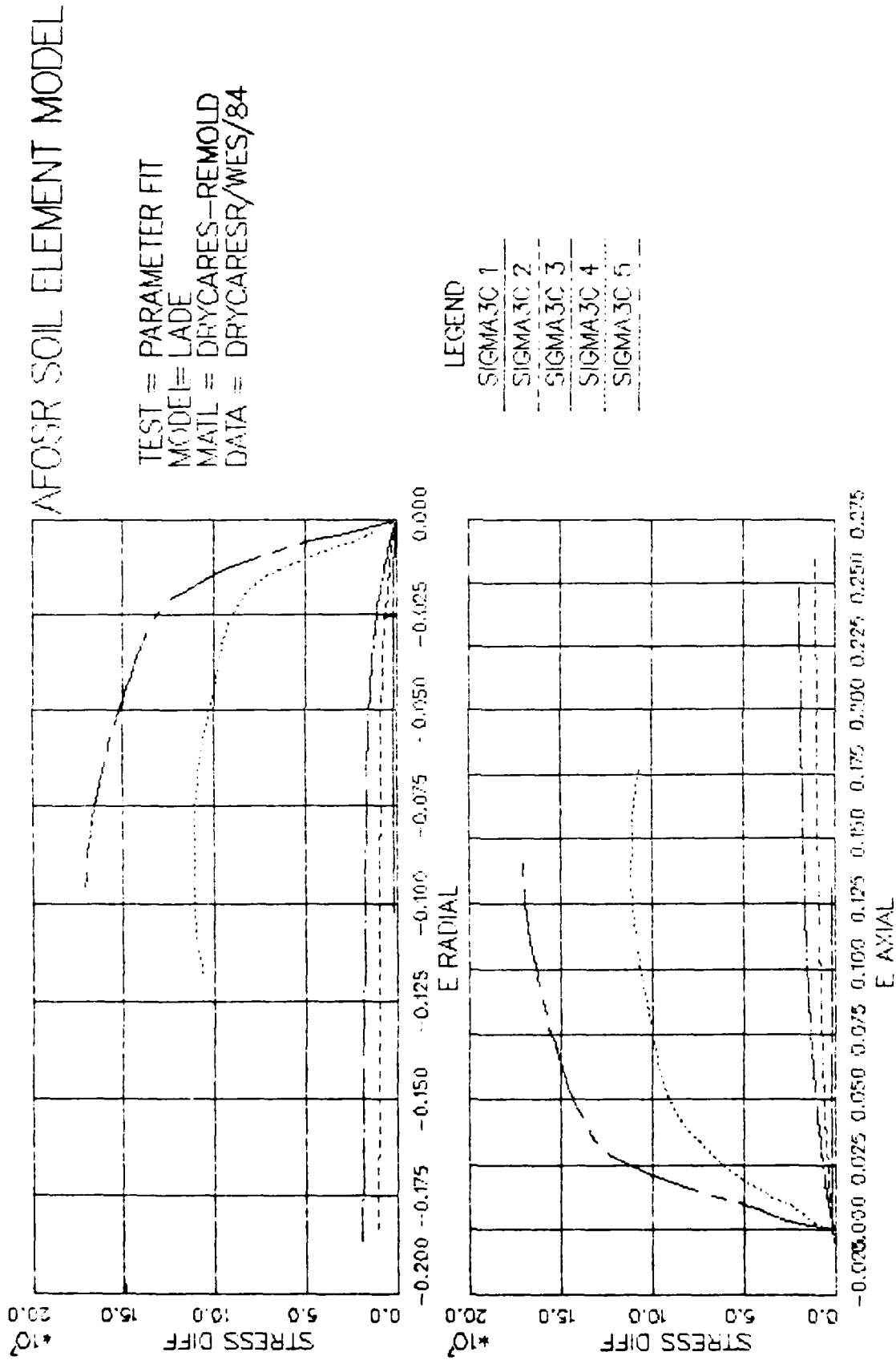
FIGURE V.8.9 LADE MODEL FIT/DATA-DRYCARESR/WES/84 - EXPANSIVE PLASTIC STRAINS

AFOSR SOIL ELEMENT MODEL

TEST = PARAMETER FIT
MODEL= LADE
MATL = DRYCARES-REMOLD
DATA = DRYCARESR/WES/84

LEGEND
TOTAL
ELASTIC
ELAS+COMP
$S30 = 7.000 \times 10^{6}$

VOLUME STRAIN COMPONENTS
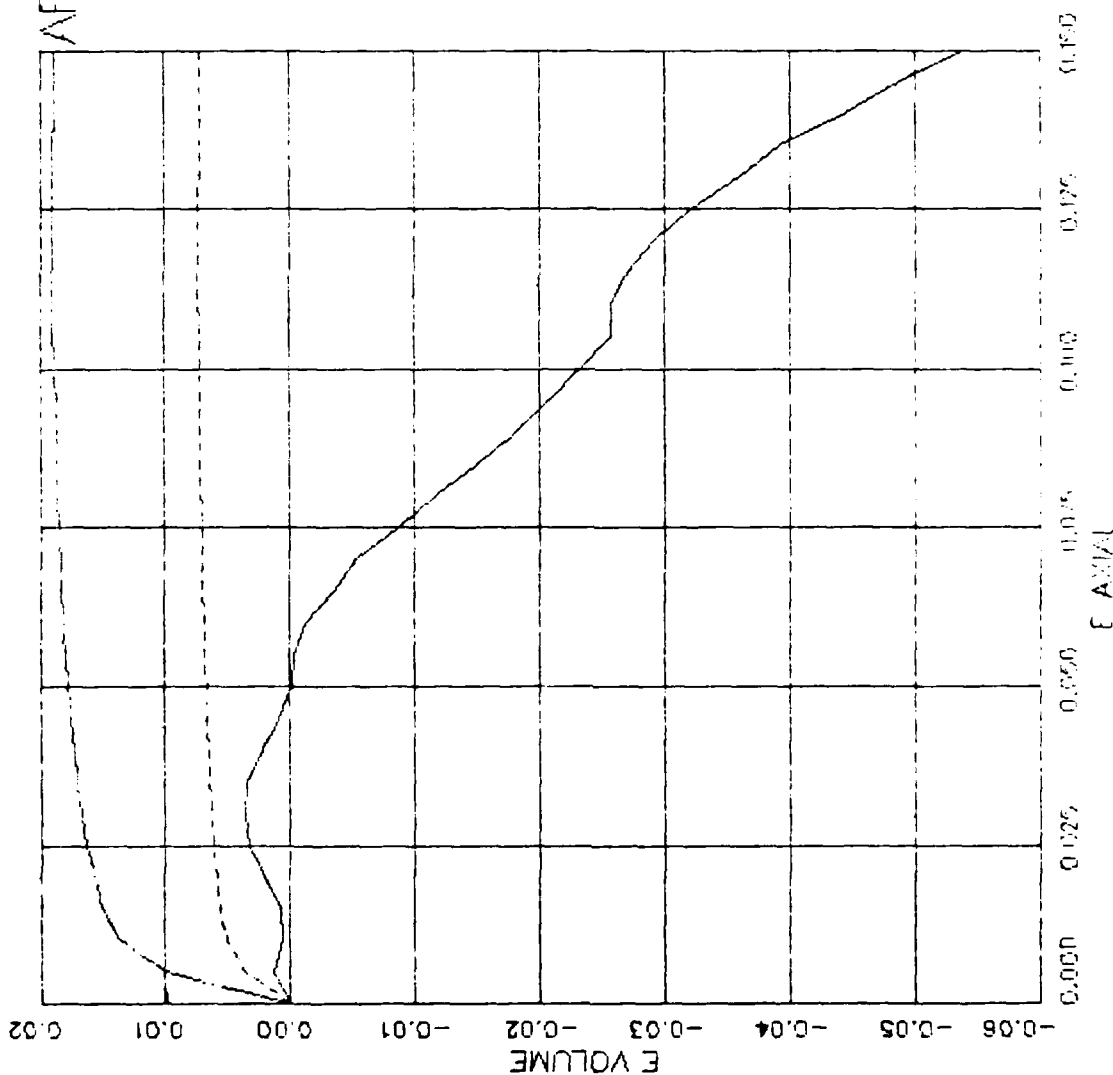
FIGURE V.8.10 LADE MODEL FIT/DATA DRYCARESR/WES/84

513

FIGURE V.8.11 LADE MODEL FIT/DATA=DRYCARESR/WES/84 - VOLUME STRAIN COMPONENTS
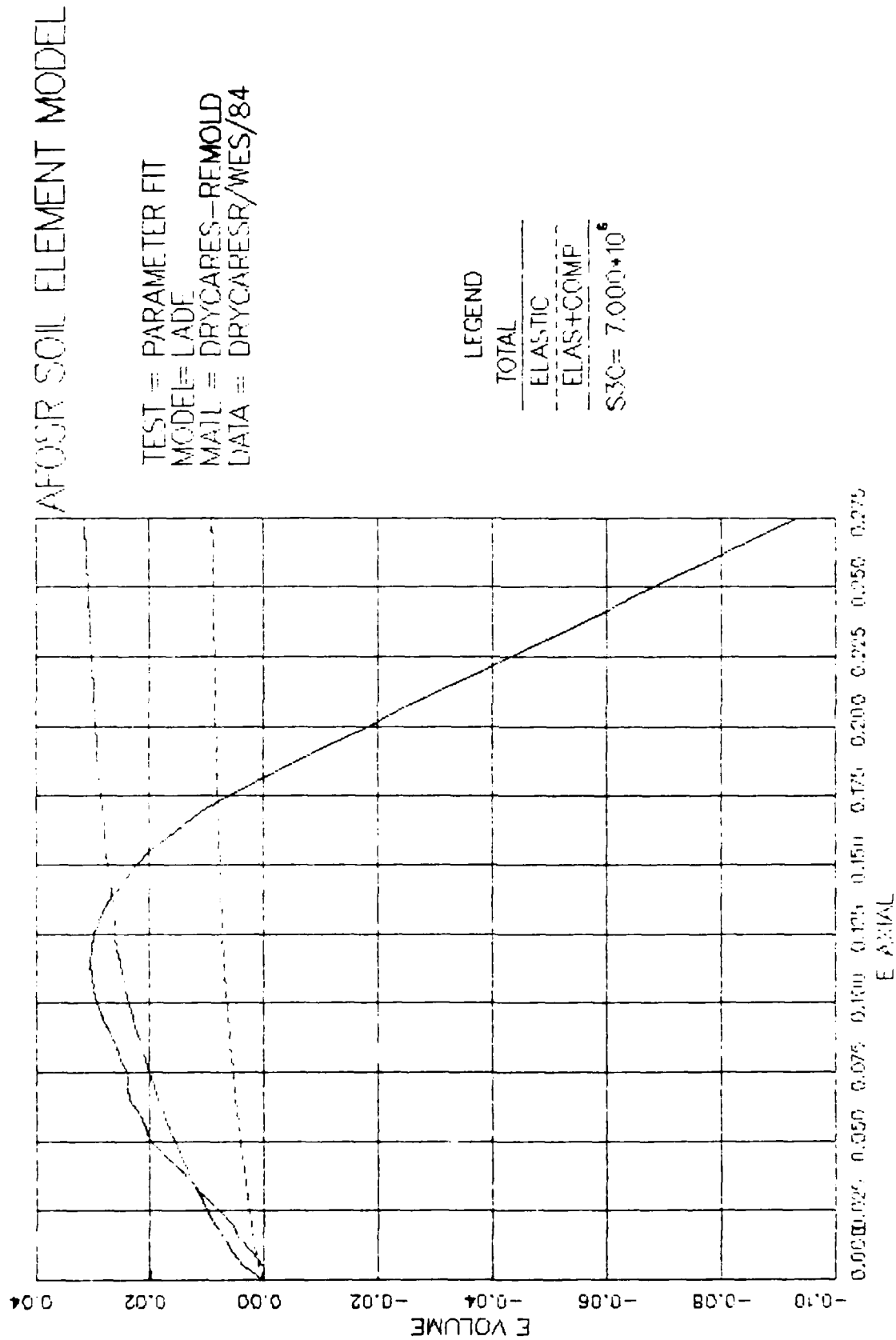
FIGURE V.8.12 LADE MODEL FIT/DATA: DRYCARESR/WES/84 - VOLUME STRAIN COMPONENTS

515
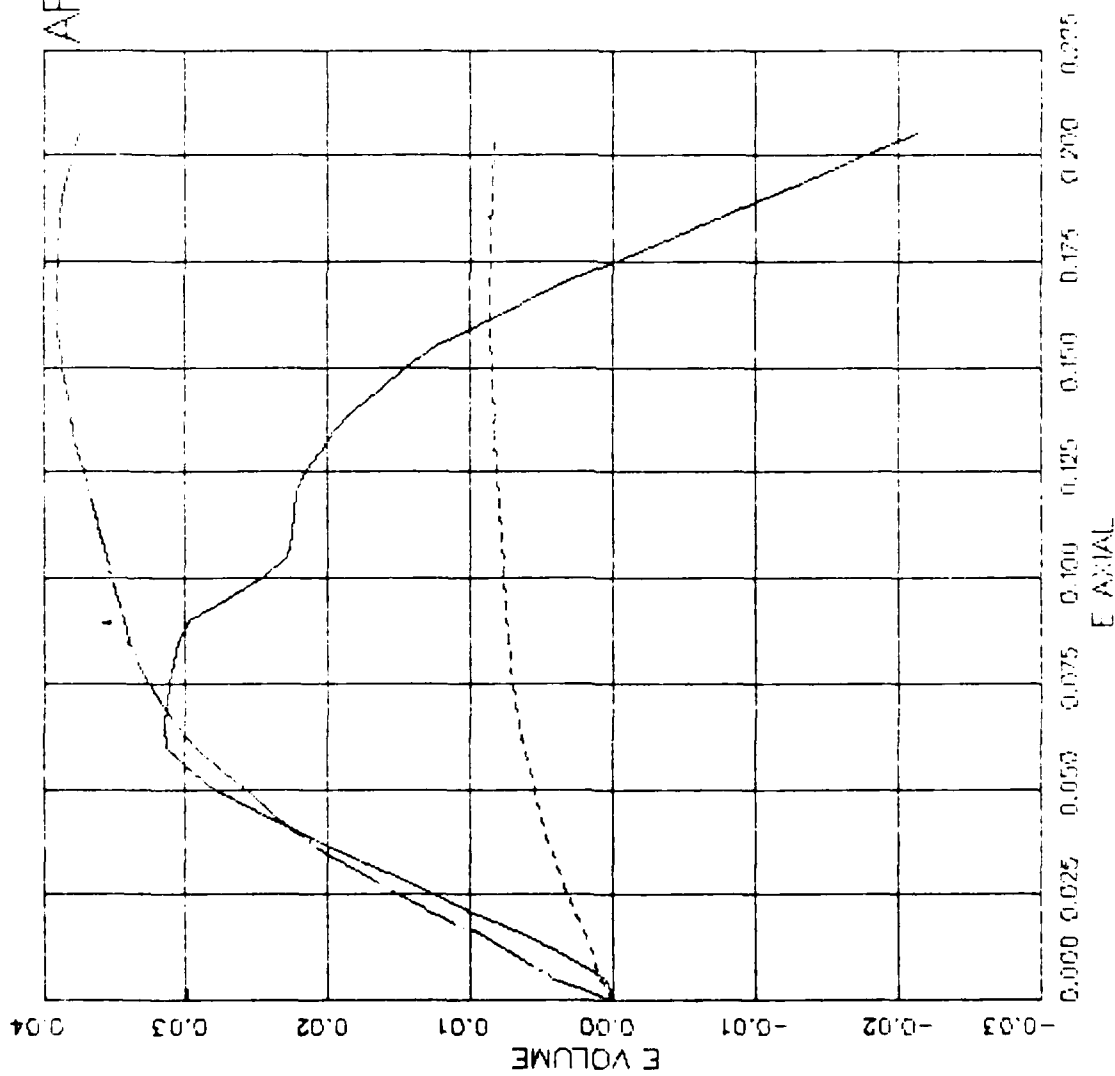
FIGURE V.8.13 LADE MODEL FIT/DATA-DRYCARESR/WES/84 - VOLUME STRAIN COMPONENTS
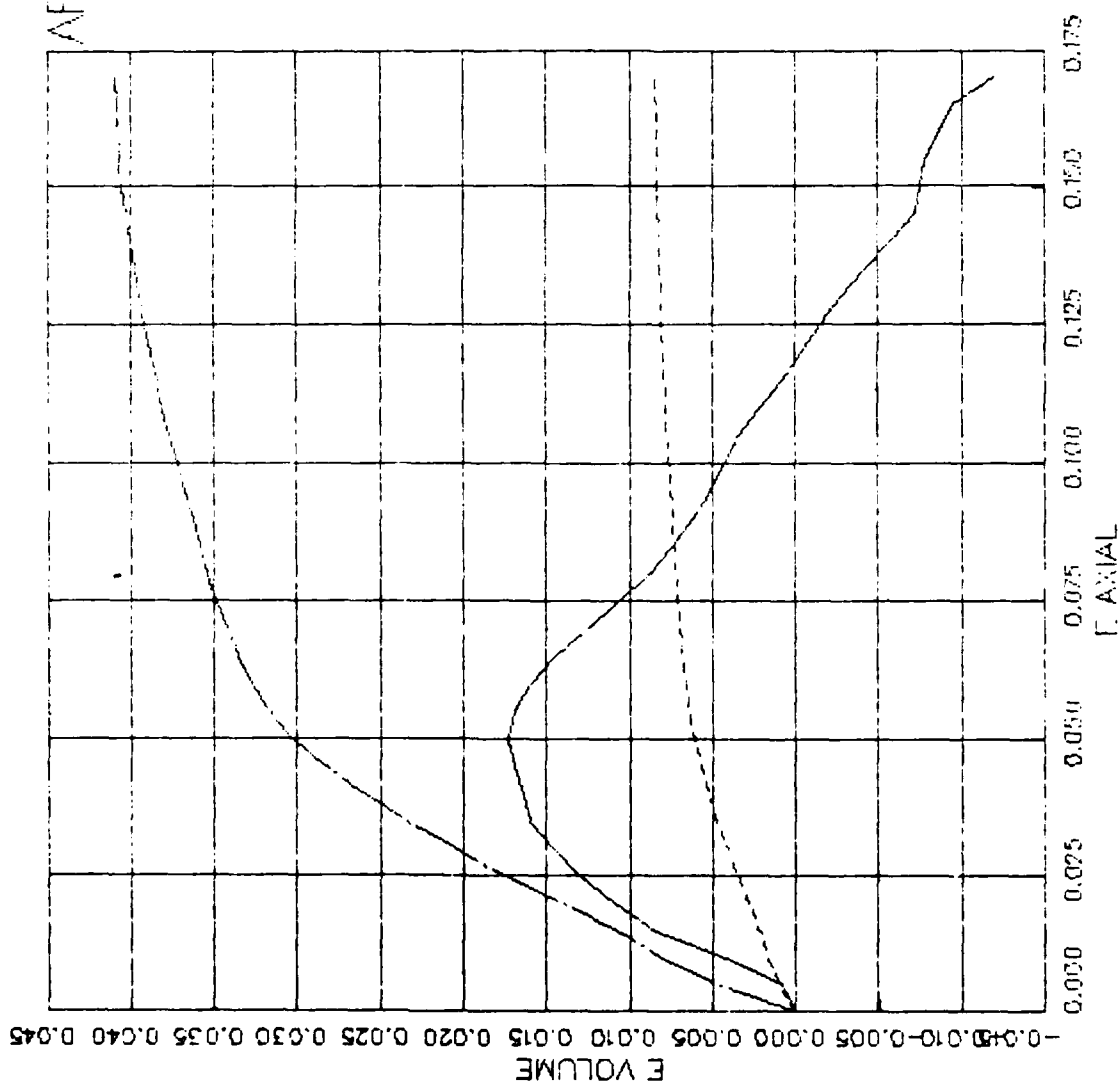
FIGURE V.8.14 LADE MODEL FIT/DATA-DRYCAFESR/WES/84 --- VOLUME STRAIN COMPONENTS
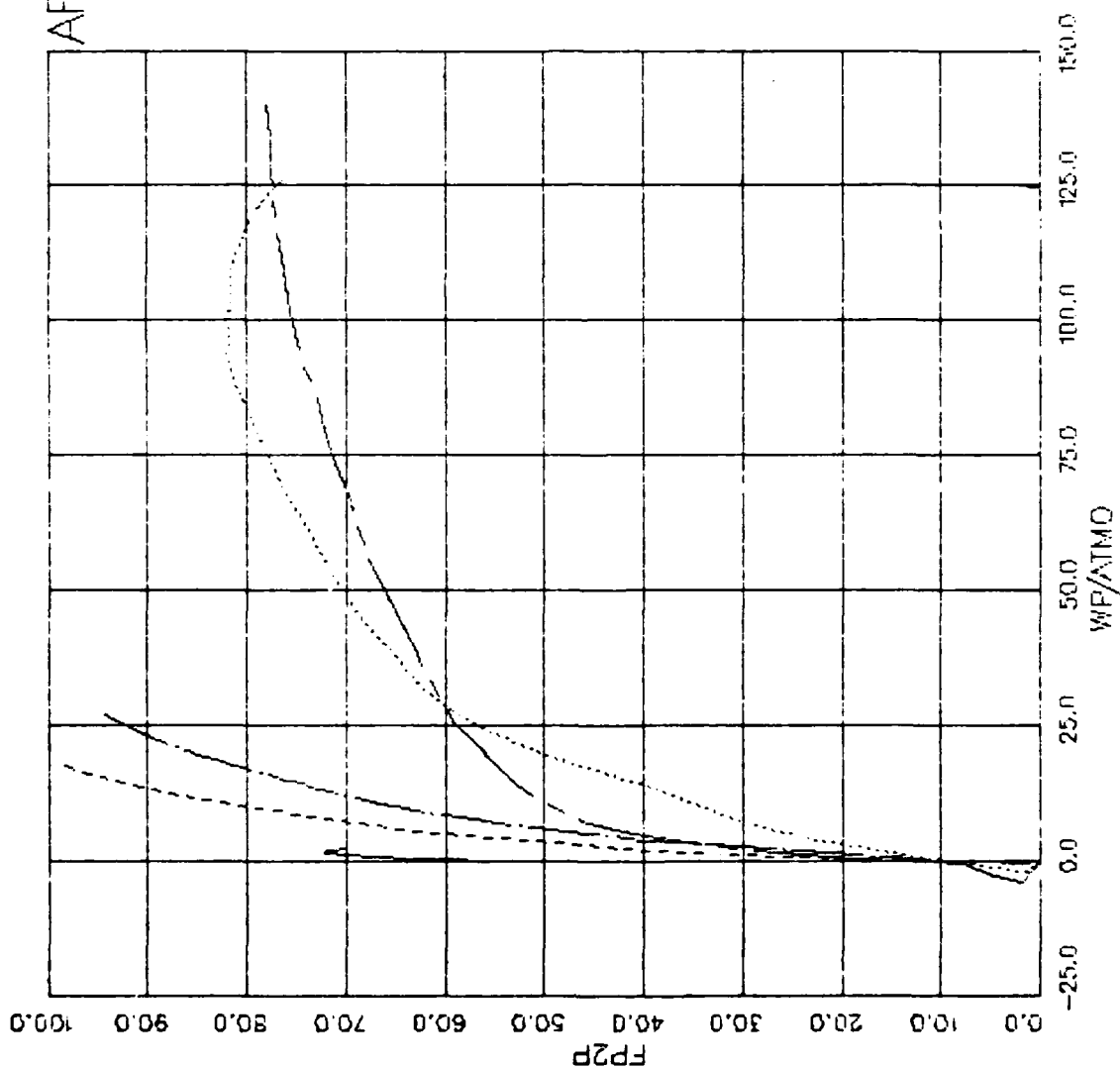
FIGURE V.8.15 LADE MODEL FIT/DATA- DRYCARESR/WES/84 - EXPANSIVE PLASTIC WORK

518

AFOSR SOIL ELEMENT MODEL

TEST = PARAMETER FIT
MODEL= LADE
MATL = DRYCARES-REMOLD
DATA = DRYCARESR/WES/84

PW= 6.379*10^{-1}
ELW= 8.077*10^{-1}

FIGURE V.8.16   LADE MODEL FIT/DATA=DRYCARESR/WES/84 — WP—PEAK FIT

FIGURE V.8.17 LADE MODEL FIT/DATA- DRYCARESR/WES/84 - Q FIT

AFOSR SOIL ELEMENT MODEL

TEST = PARAMETER FIT
MODEL = LADE
MAIL = DRYCARES—REMOLD
DATA = DRYCARESR/WES/84

ALPHA= 1.972*10^0
BETA= 2.14D*10^{-4}
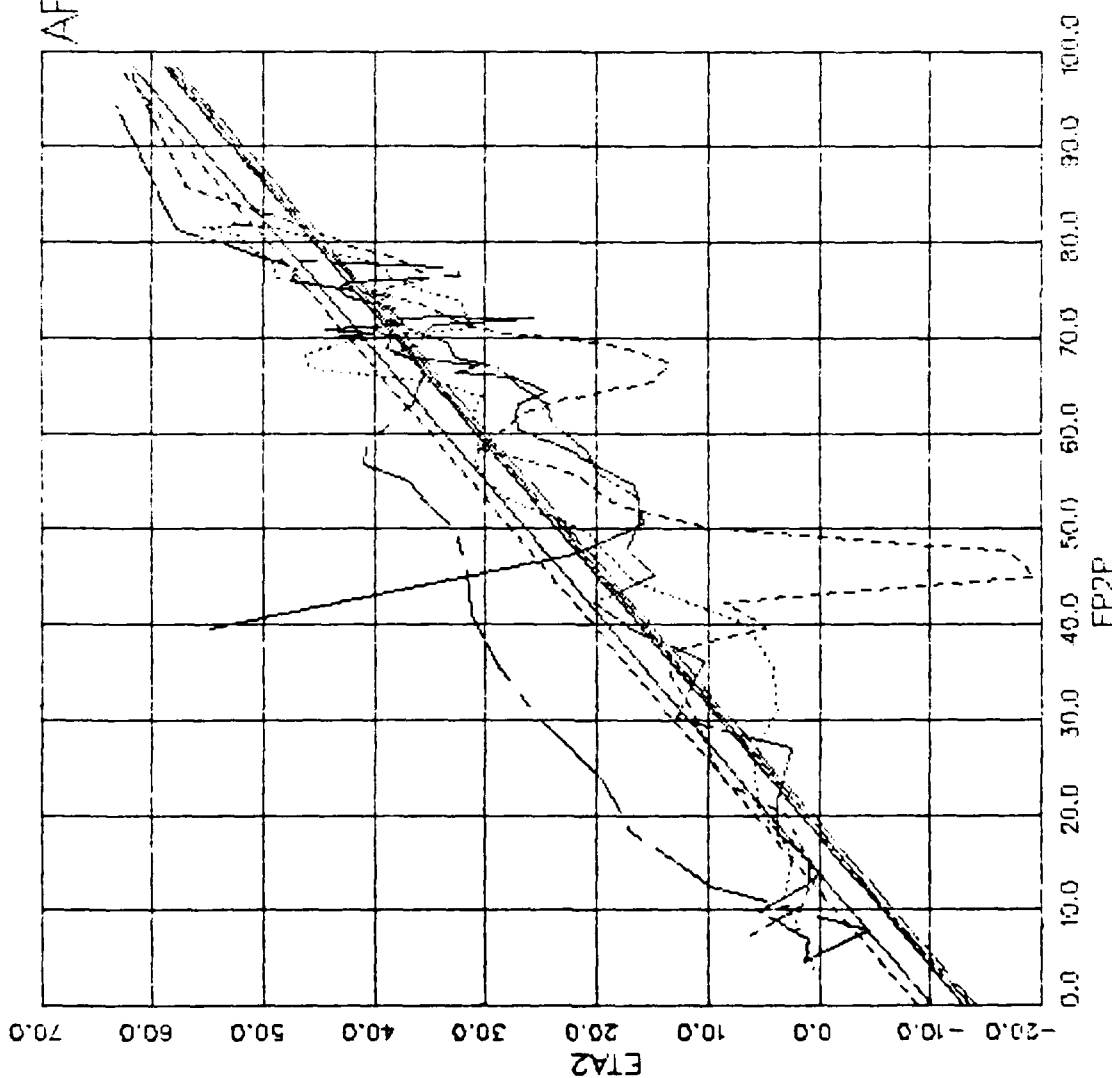
FIGURE V.8.18 LADE MODEL FIT/DATA-DRYCARESR/WES/84 — ETA2 VS. FP2P

FIGURE V.8.19 LADE MODEL EXERCISE — ISOTROPIC COMP. — PRESSURE VS. VOLUMETRIC STRAIN .
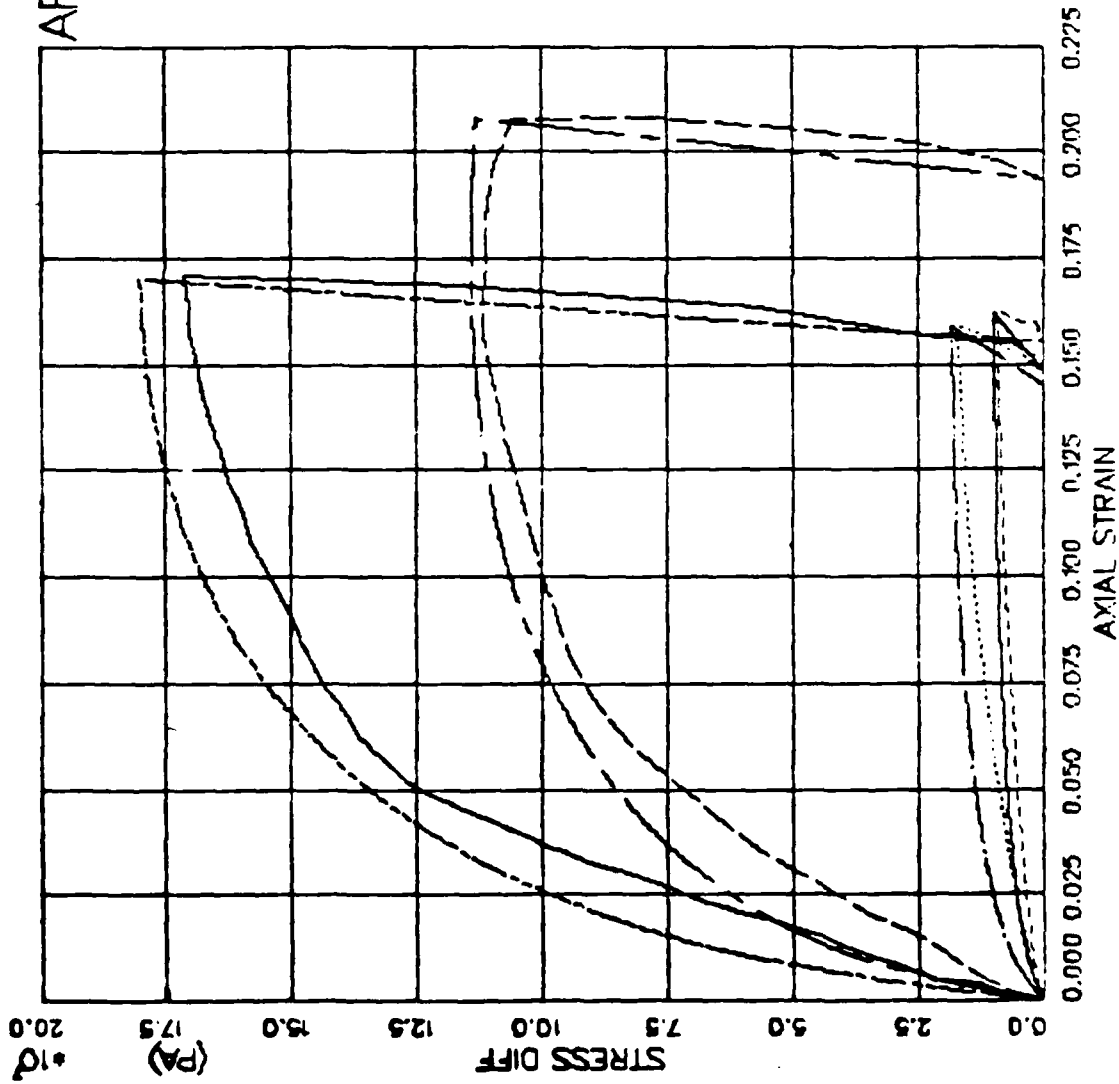
FIGURE V.8.20 LADE MODEL EXERCISE – TRIAXIAL COMP(CTC) – STRESS DIFF VS. AXIAL STRAIN

523
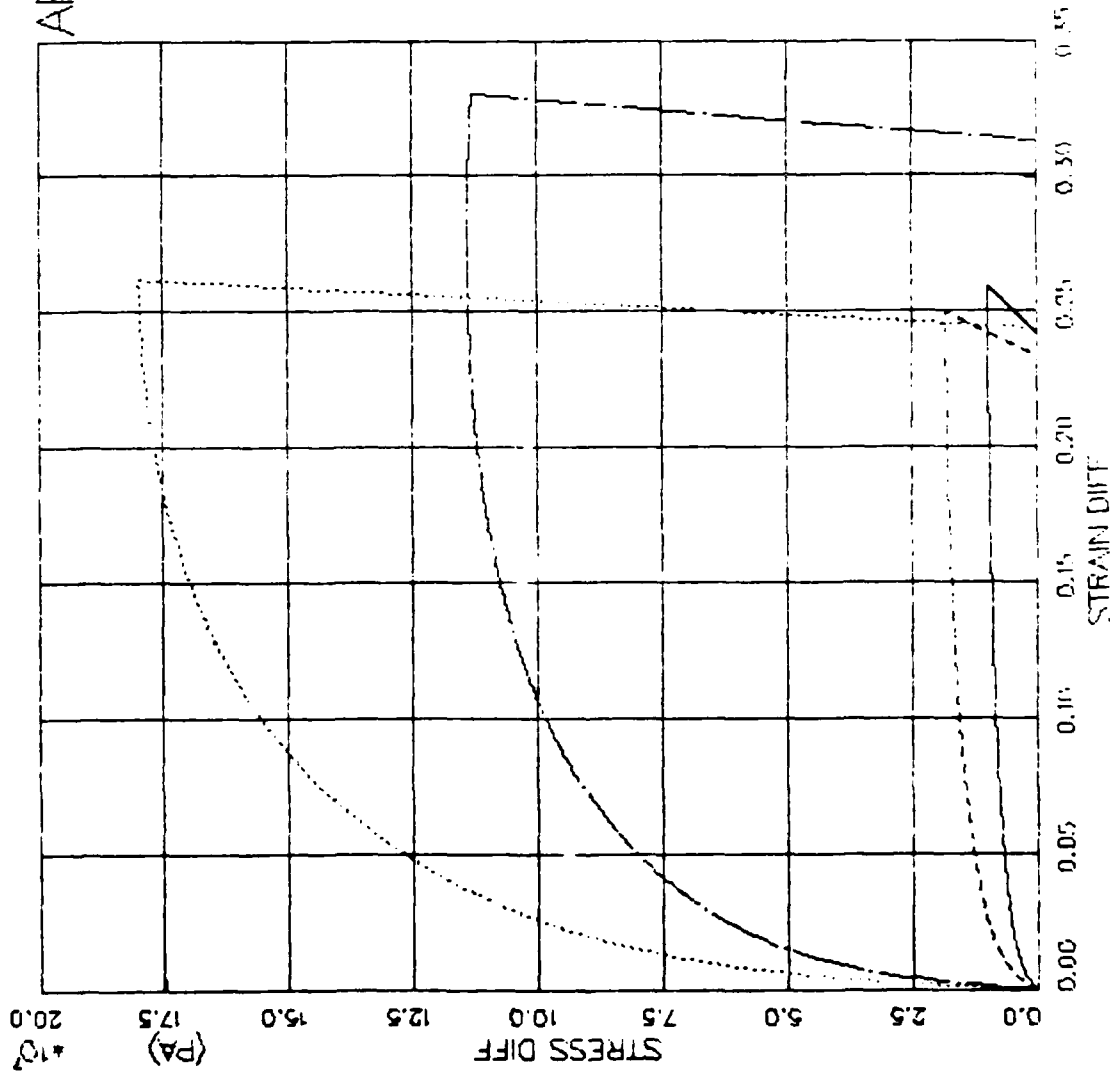
FIGURE V.8.21 LADE MODEL EXERCISE — TRIAXIAL COMP(CTC) — STRESS DIFF VS. STRAIN DIFF

524

AFOSR SOIL ELEMENT MODEL

TEST = STANDARD TRIAXIAL TEST
MODEL = LADE
MATL = DRYCARES,-REMOLD
DATA = DRYCARES,R/WES/84

LEGEND
SIGMA3C = 3.4E6
TEST DATA
SIGMA3C = 7.0E6
TEST DATA
SIGMA3C = 58.8E6
TEST DATA
SIGMA3C = 100.0E6
TEST DATA

VOLUME STRAIN (PA)

AXIAL STRAIN

FIGURE V.8.22 LADE MODEL ELEMENT -TRIAXIAL COMP-(CTC) - AXIAL STRAIN VS VOLUME STRAIN

525
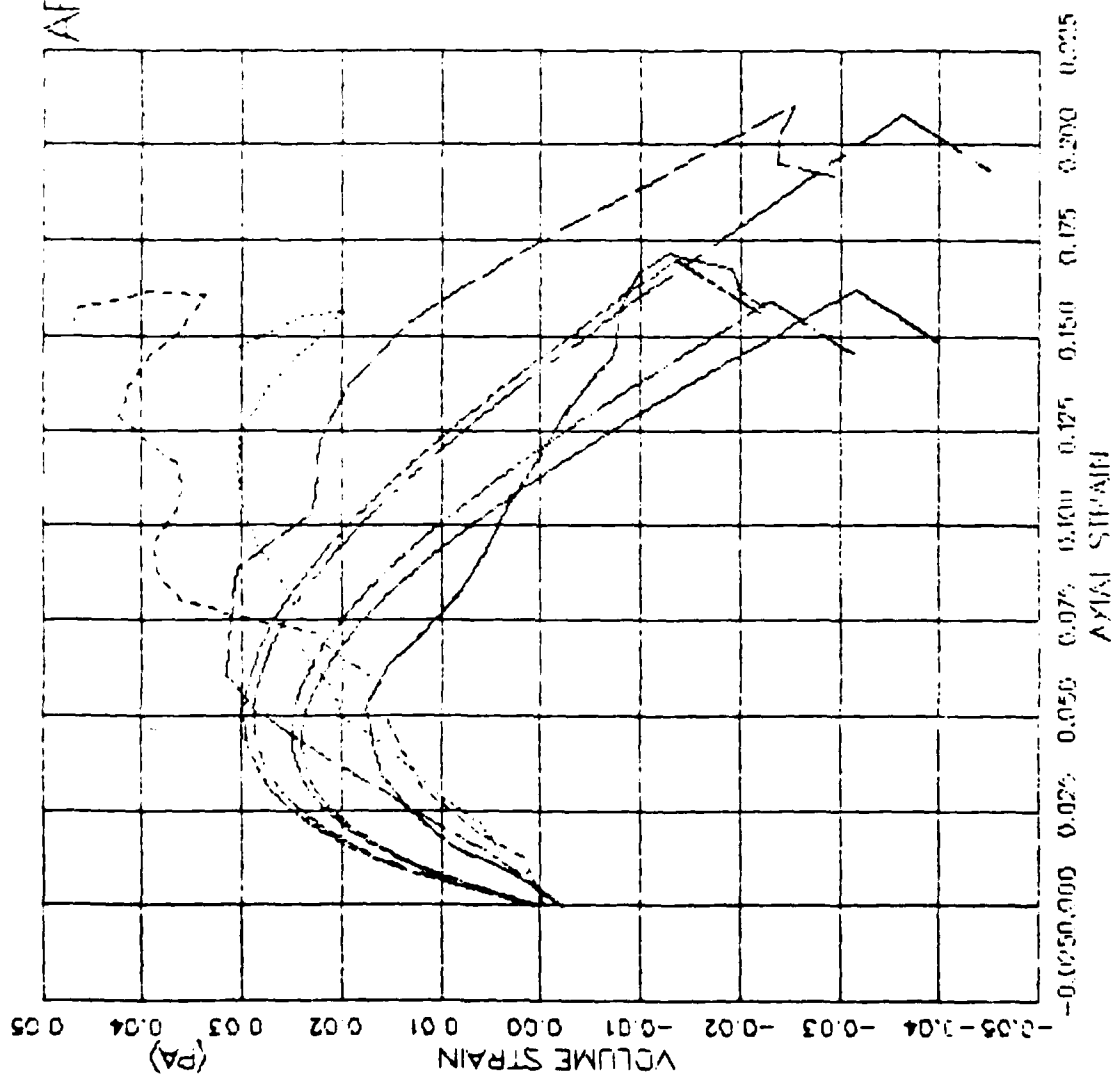
FIGURE V.8.23 LADE MODEL EXERCISE-TRIAXIAL COMP(CTC) - PRESSURE VS. VOLUMETRIC STRAIN .

526

AFOSR SOIL ELEMENT MODEL

TEST = STANDARD TRIAXIAL TEST
MODEL = LADE
MATL = DRYCARES—REMOLD
DATA = DRYCARESR/WES/84

LEGEND
S3C=1.8E6
TEST DATA
S3C=3.5E6
TEST DATA
S3C=7.1E6
TEST DATA
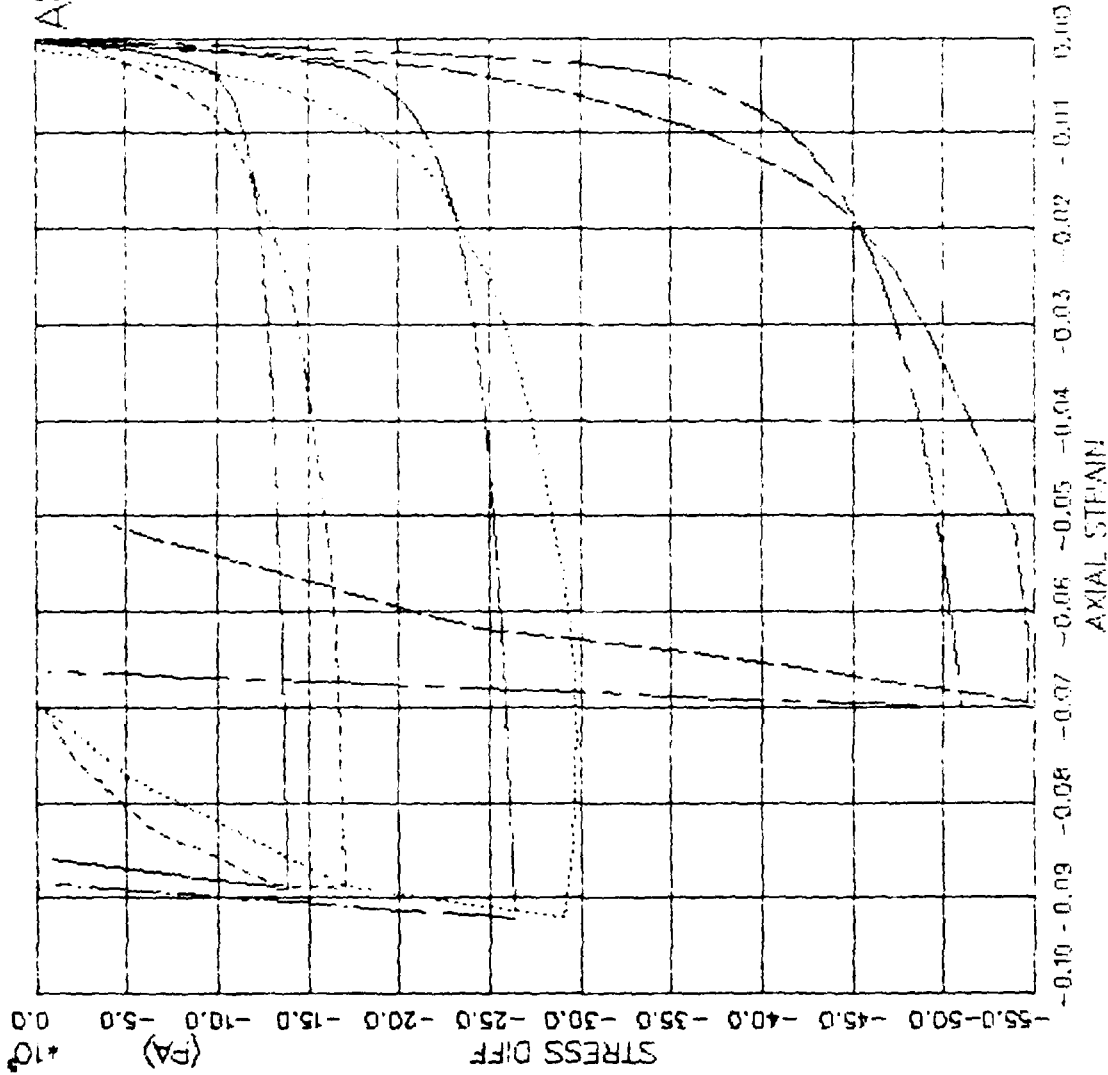
FIGURE V.8.24 LADE MODEL EXERCISE—TRIAXIAL EXTENSION) — STRESS DIFF VS. AXIAL STRAIN

527

FIGURE V.8.25 LADE MODEL EXERCISE—TRIAXIAL EXTENSION(TIL) — STRESS DIFF VS STRAIN DIFF

528

AFOSR SOIL ELEMENT MODEL

TEST = STANDARD TRIAXIAL TEST
MODEL= LADE
MATL = DRYCARES,—REMOLD
DATA = DRYCARESR/WES/84

LEGEND
S3C-18F6
TEST DATA
S3C-3.5F6
TEST DATA
S3C=7.1E6
TEST DATA
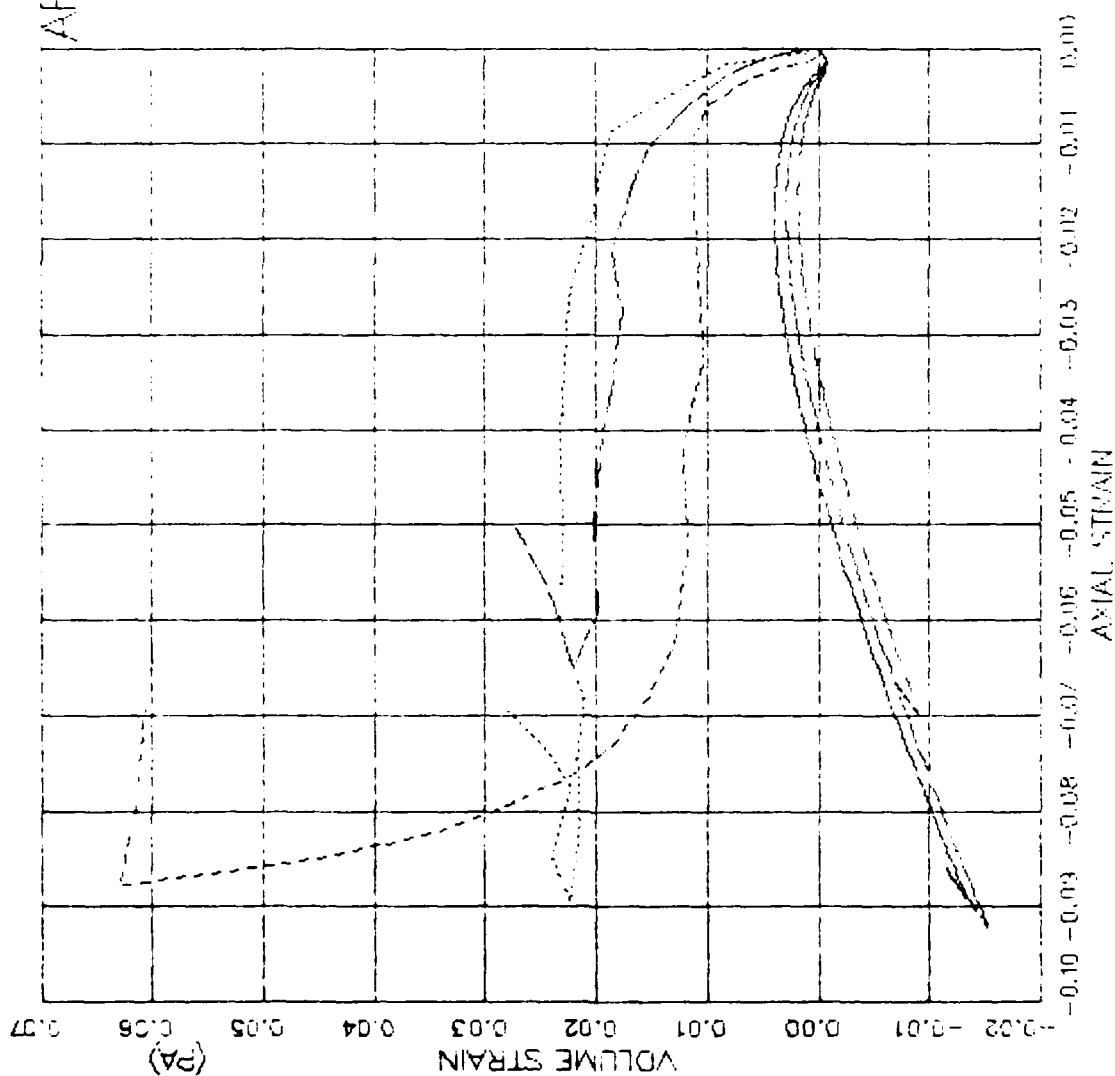
FIGURE V.8.26 LADE MODEL EXTRUDE - TRIAXIAL EXTENSION)   AXIAL STRAIN VS VOLUME STRAIN

529

AFOSR SOIL ELEMENT MODEL

TEST = STANDARD TRIAXIAL TEST
MODEL = LADE
MATL = DRYCARES--REMOLD
DATA = DRYCARESR/WES/84

LEGEND
S3C=1.8E6
S3C=3.5E6
S3C=7.1E6
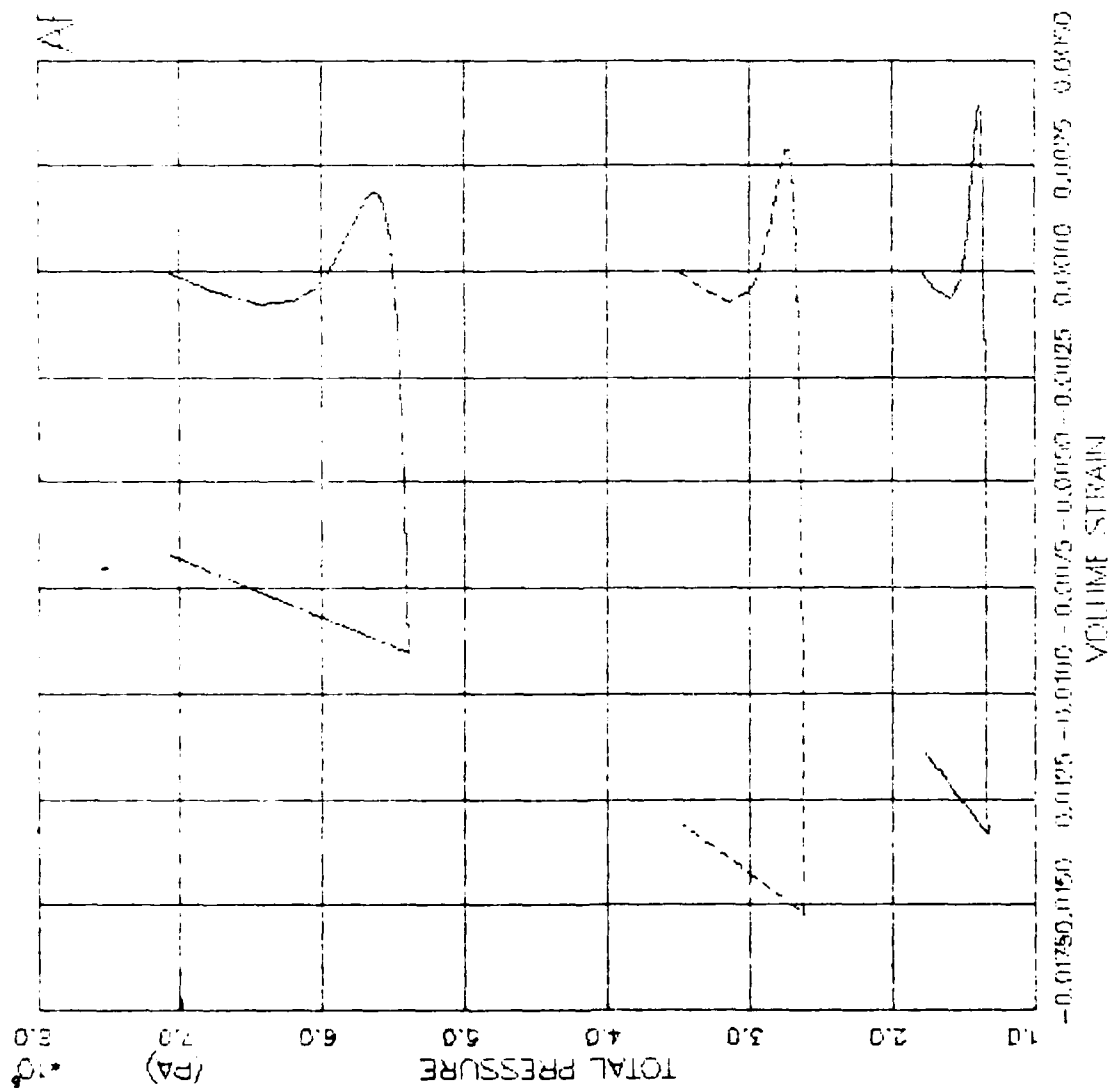
FIGURE V.8.27 LADE MODEL EXPLODED - TRIAXIAL EXTENSION - PRESSURE VS. VOLUMETRIC STRAIN

AFOSR SOIL ELEMENT MODEL

TEST = STANDARD TRIAXIAL TEST
MODEL= LADE
MATL = DRYCARES-REMOLD
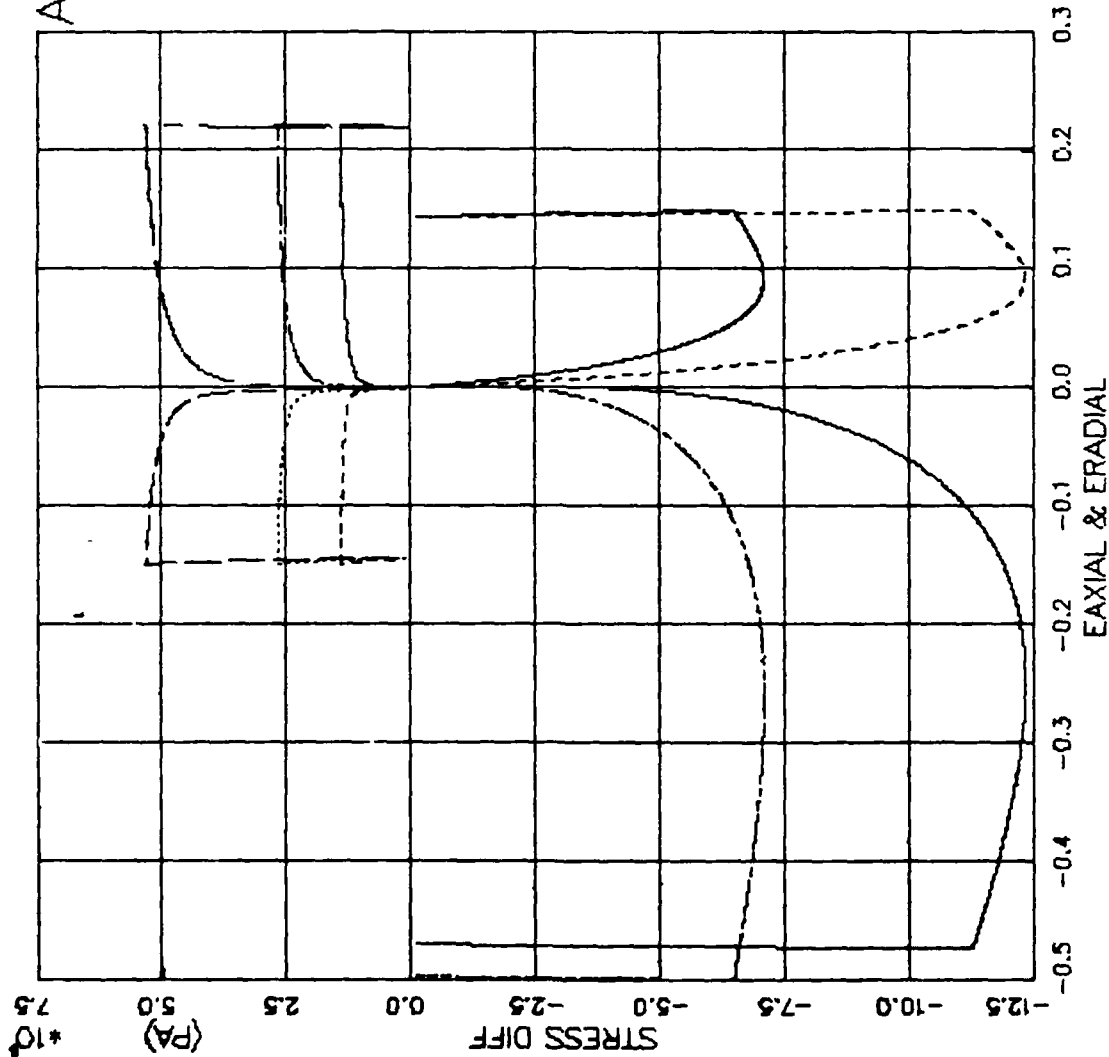
LEGEND

RTC/S3C=1.8E6
RTC/S3C=1.8E6
RTC/S3C=3.5E6
RTC/S3C=3.5E6
RTC/S3C=7.1E6
RTC/S3C=7.1E6
RTE/S3C=1.8E6
RTE/S3C=1.8E6
RTE/S3C=3.5E6
RTE/S3C=3.5E6

FIGURE V.8.28 LADE MODEL EXER-REDUCED TRIAX(RTC+RTE) - STRESS DIFF VS. STRAIN

AFOSR SOIL ELEMENT MODEL

TEST = STANDARD TRIAXIAL TEST
MODEL= LADE
MATL = DRYCARES—REMOLD

LEGEND
RTC/S3C=1.8E6
RTC/S3C=3.5E6
RTC/S3C=7.1E6
RTE/S3C=1.8E6
RTE/S3C=3.5E6
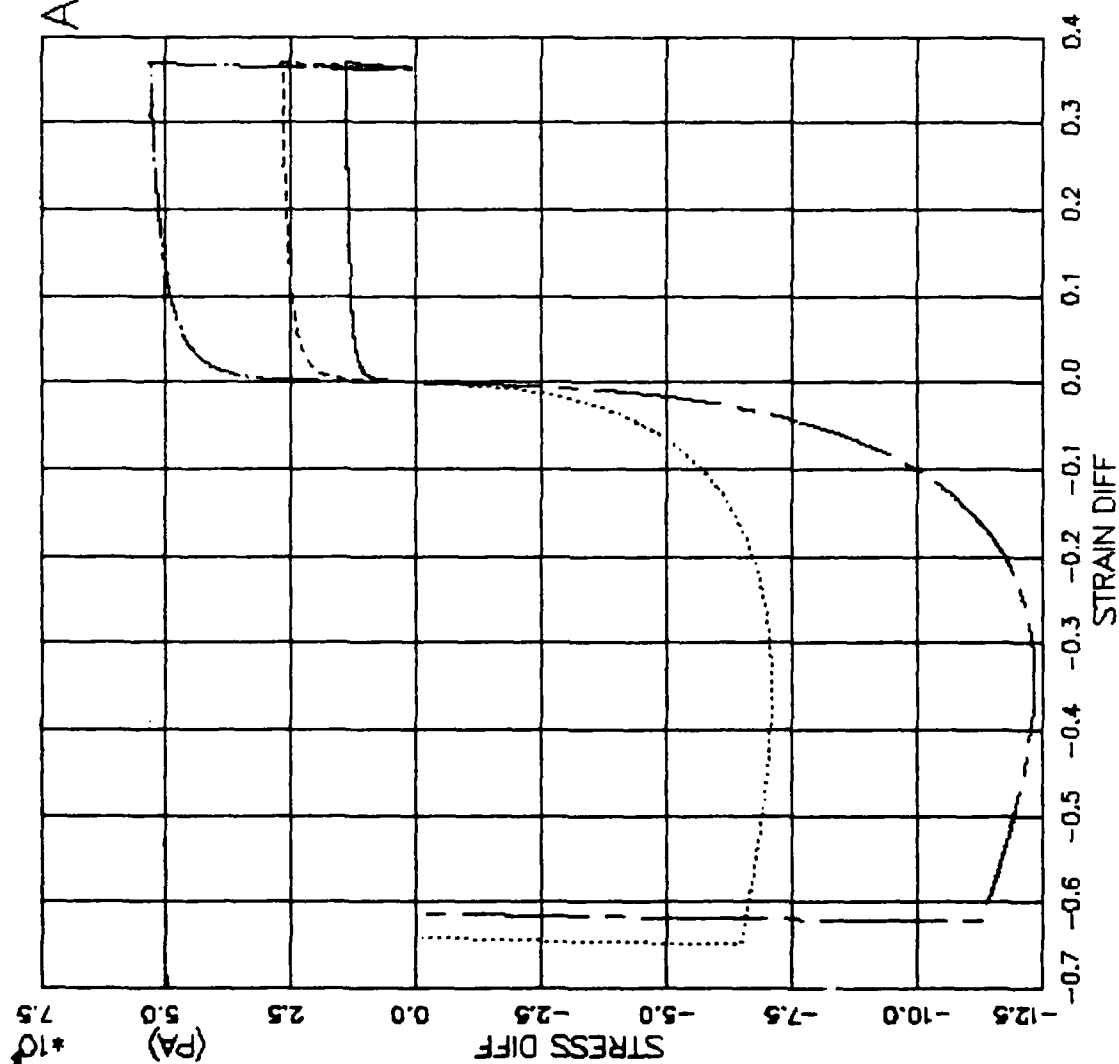
FIGURE V.8.29 LADE MODEL EXER—REDUCED TRIAX(RTC+RTE) — STRESS DIFF VS. STRAIN DIFF

AFOSR SOIL ELEMENT MODEL

TEST = STANDARD TRIAXIAL TEST
MODEL= LADE
MATL = DRYCARES–REMOLD

LEGEND
RTC/S3C=1.8E6
RTC/S3C=3.5E6
RTC/S3C=7.1E6
RTE/S3C=1.8E6
RTE/S3C=3.5E6

AXIAL STRAIN
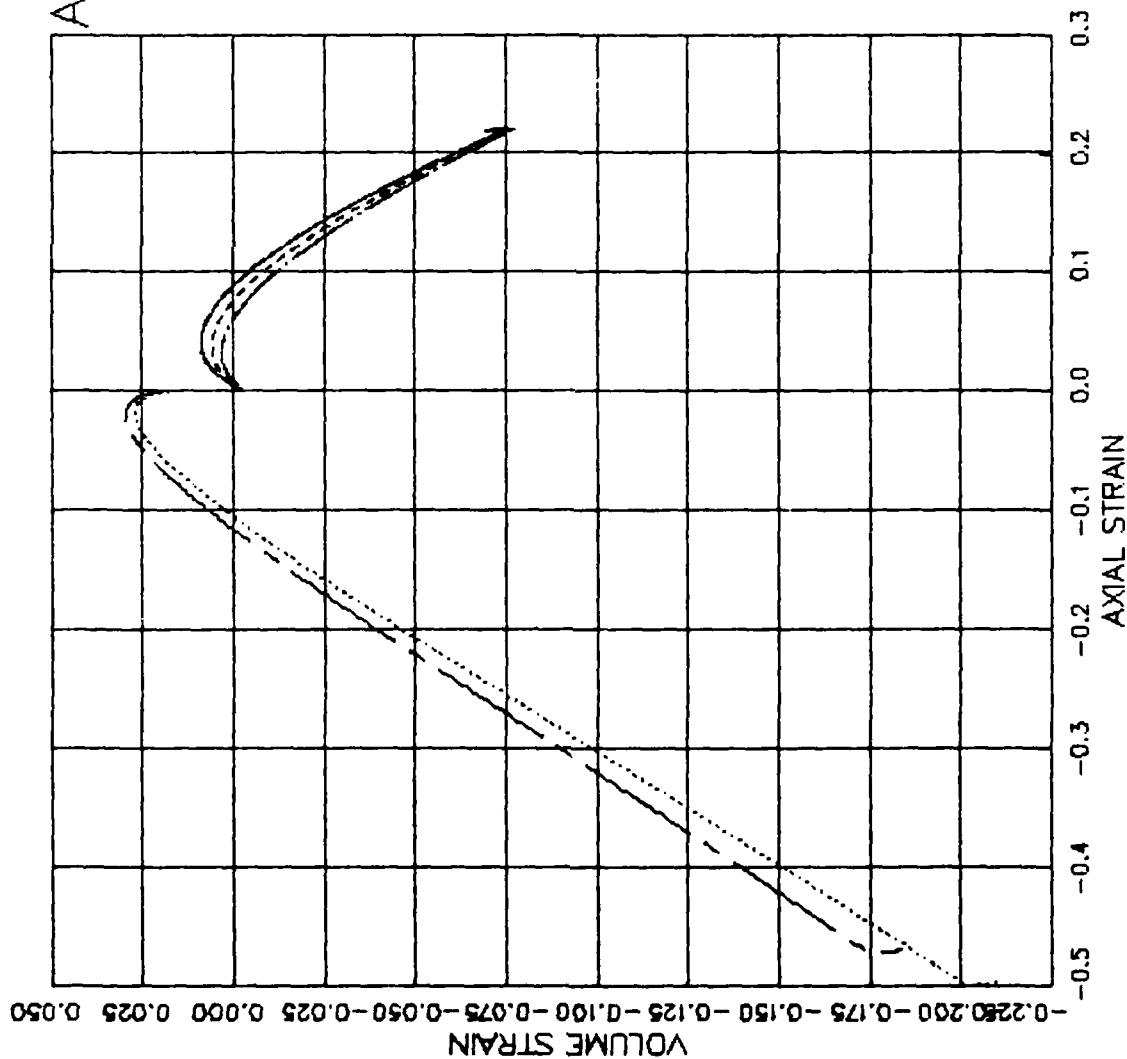
VOLUME STRAIN

FIGURE V.8.30 LADE MODEL EXER–REDUCED TRIAX(RTC+RTE) – AXIAL STRAIN VS VOLUME STRAIN
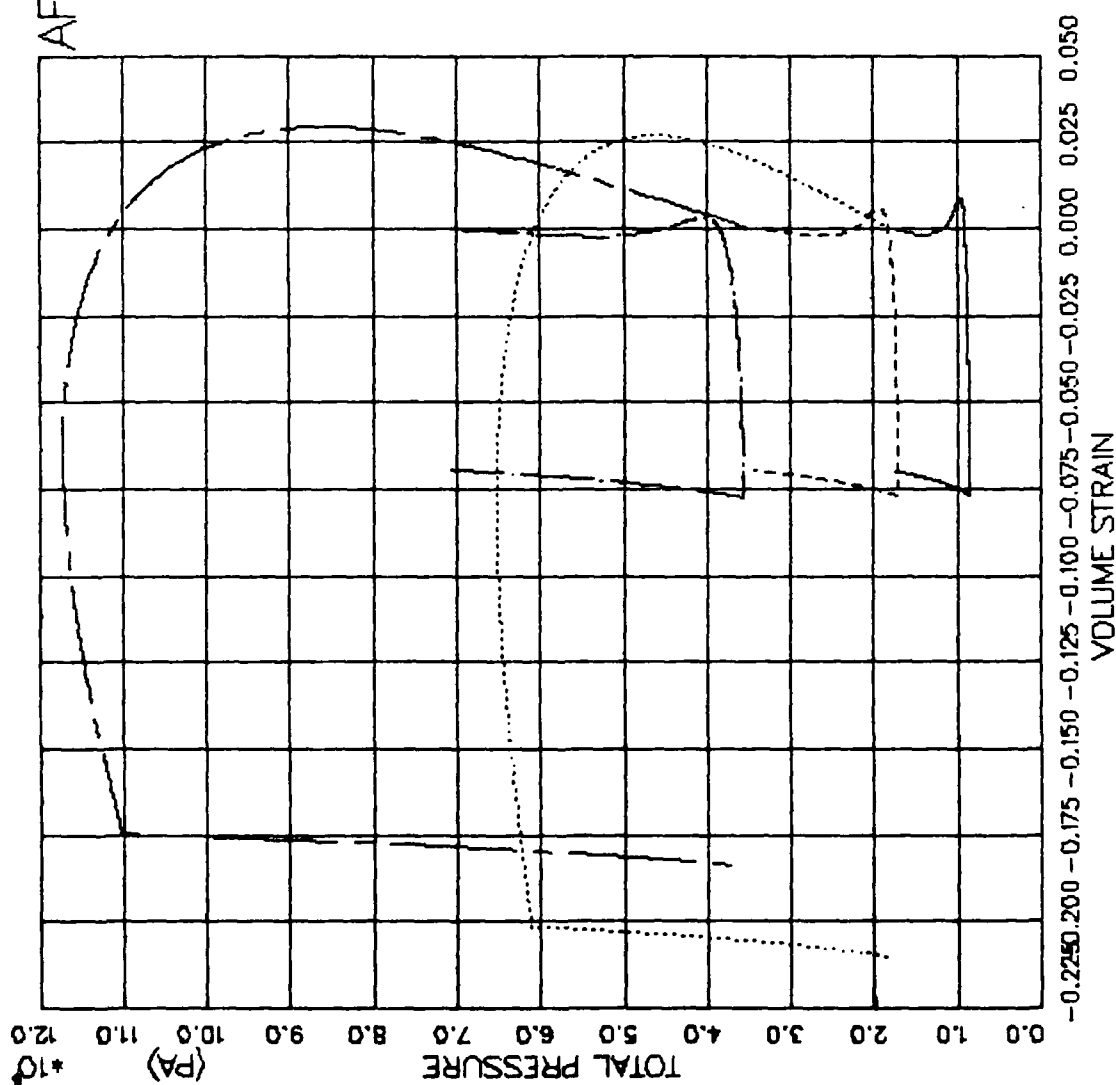
FIGURE V.8.31 LADE MODEL EXER—REDUCED TRIAX(RTC+RTE) — PRESSURE VS. VOLUMETRIC STRAIN

AFOSR SOIL ELEMENT MODEL

TEST = STANDARD TRIAXIAL TEST
MODEL= LADE
MATL = DRYCARES—REMOLD

LEGEND
RTC/S3C=1.8E6
RTC/S3C=3.5E6
RTC/S3C=7.1E6
RTE/S3C=1.8E6
RTE/S3C=3.5E6

534

AFOSR SOIL ELEMENT MODEL

TEST = STANDARD TRIAXIAL TEST
MODEL= LADE
MATL = DRYCARES-REMOLD

LEGEND
PSC/S3C=1.8E6
PSC/S3C=1.8E6
PSC/S3C=3.5E6
PSC/S3C=3.5E6
PSC/S3C=7.1E6
PSC/S3C=7.1E6
PSE/S3C=1.8E6
PSE/S3C=1.8E6
PSE/S3C=3.5E6
PSE/S3C=3.5E6
PSE/S3C=7.1E6
PSE/S3C=7.1E6

EAXIAL & ERADIAL

STRESS DIFF (PA) $*10^7$
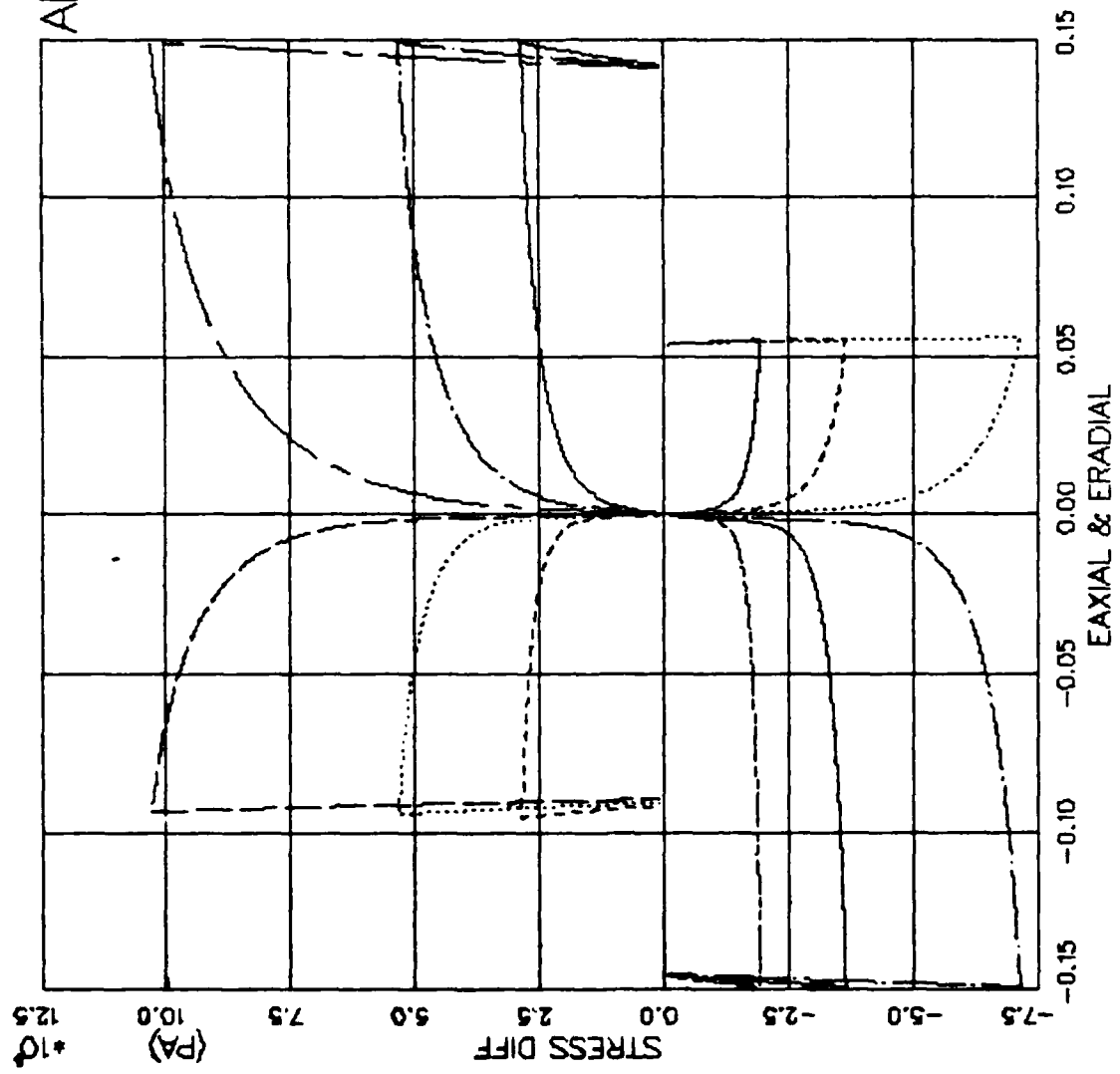
FIGURE V.8.32 LADE MODEL EXERCISE-PURE SHEAR(PSC+PSE) - STRESS DIFF VS. STRAIN

535
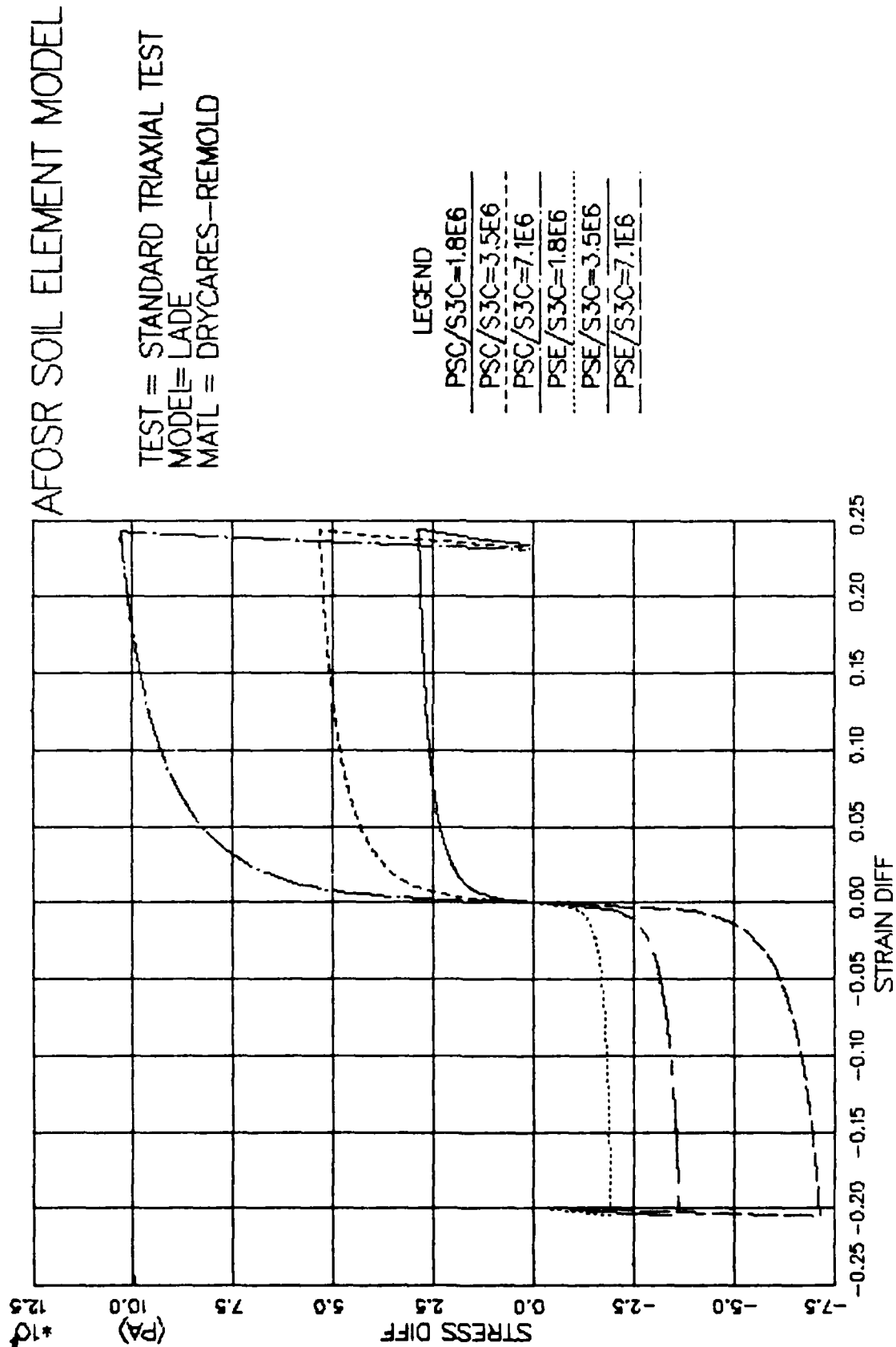
FIGURE V.8.33 LADE MODEL EXERCISE–PURE SHEAR(PSC+PSE) – STRESS DIFF VS. STRAIN DIFF

AFOSR SOIL ELEMENT MODEL

TEST = STANDARD TRIAXIAL TEST
MODEL= LADE
MATL = DRYCARES—REMOLD

LEGEND
PSC/S3C=1.8E6
PSC/S3C=3.5E6
PSC/S3C=7.1E6
PSE/S3C=1.8E6
PSE/S3C=3.5E6
PSE/S3C=7.1E6

AXIAL STRAIN
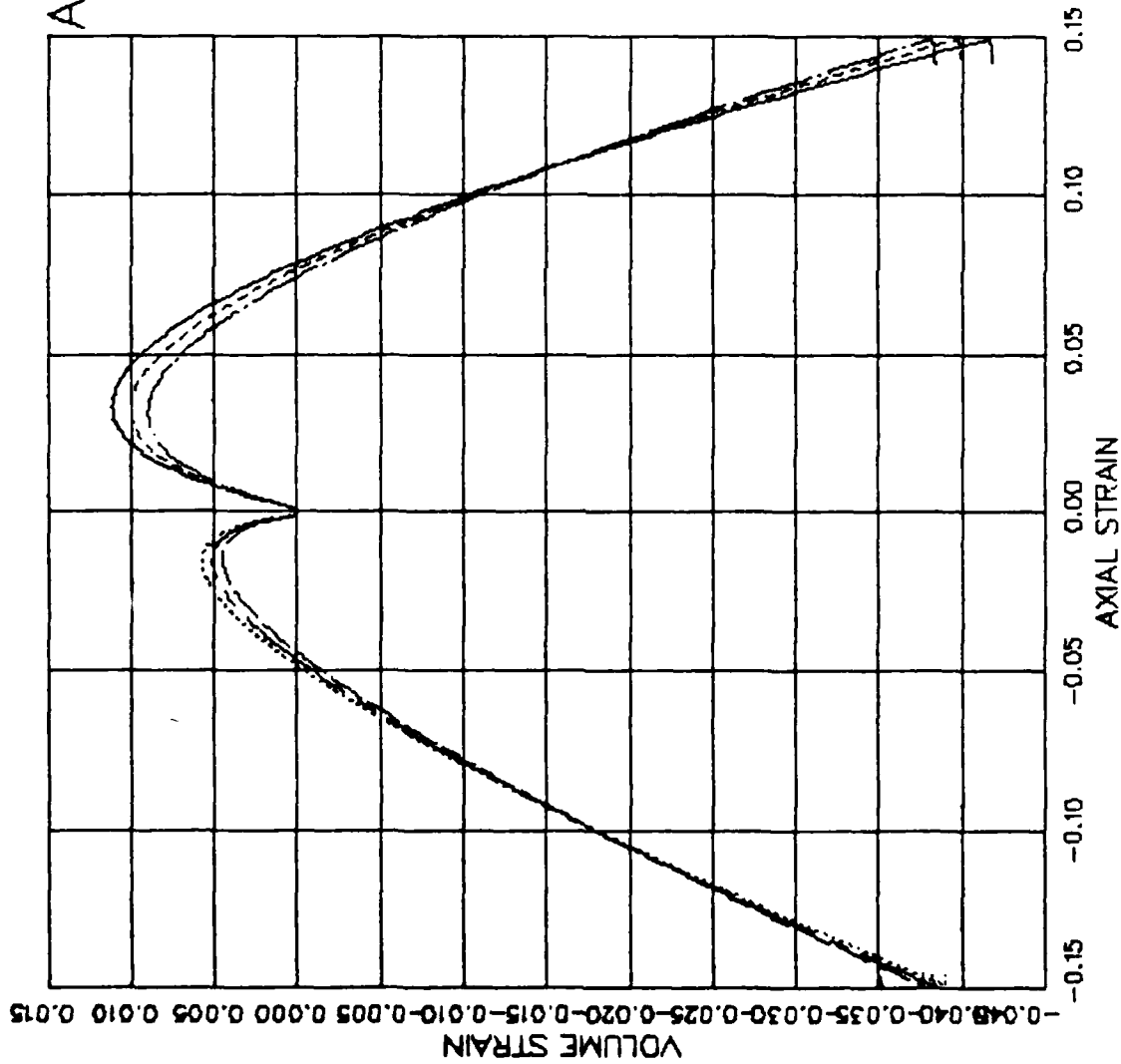
VOLUME STRAIN

FIGURE V.8.34 LADE MODEL EXERCISE—PURE SHEAR(PSC+PSE) — AXIAL STRAIN VS VOLUME STRAIN

FIGURE V.8.35 LADE MODEL BEHAVIOR SUMMARY (SIGC =7.1MPA) — SDIFF/P/EV/EA ANALYSIS

AFOSR SOIL ELEMENT MODEL

TEST = STANDARD TRIAXIAL
MODEL=LADE
MATL = DRYCARES-REMOLD
DATA = DRYCARESR/WES/84

LEGEND
ISO EXTEN
RTC
PSC
CTC
ISO COMP
RTE
PSE
CTE

538

FIGURE V.8.36 LADE MODEL EXERCISE -- UNIAX STRAIN(UXC) -- TOT AXL STRESS VS. AXL STRAIN .

AFOSR SOIL ELEMENT MODEL

TEST = UNIAXIAL STRAIN TEST
MODEL= LADE
MATL = DRYCARES-REMOLD
DATA = DRYCARESR/WES/84

LEGEND
CALCULATION
TEST DATA

FIGURE V.8.37 LADE MODEL EXERCISE — UNIAX STRAIN(UXC) — STRESS DIFFERENCE VS. PRESSURE

540
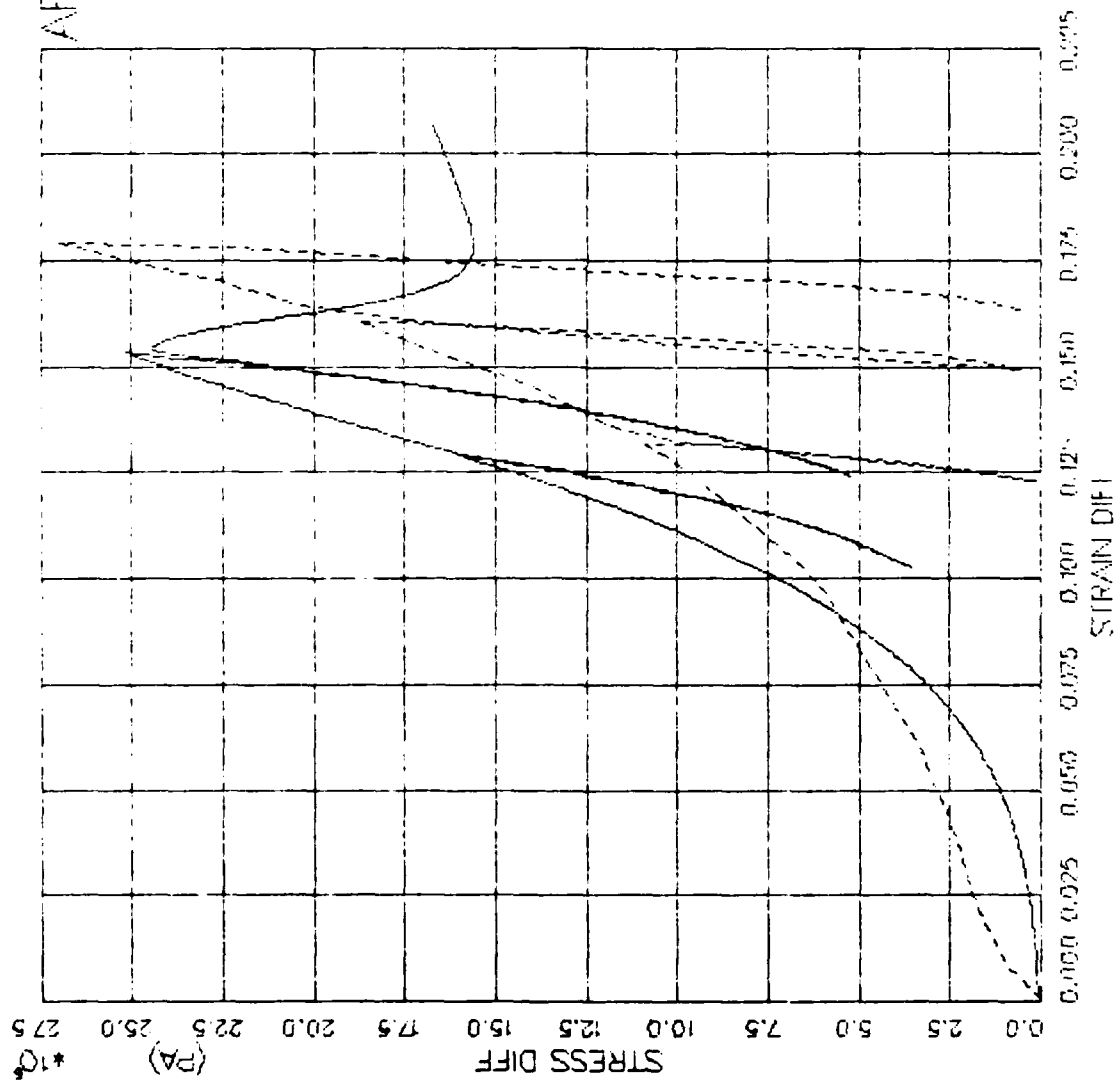
FIGURE V.8.38 LADE MODEL EXERCISE - UNIAX STRAIN(1:KC) - STRESS DIFF VS STRAIN DIFF
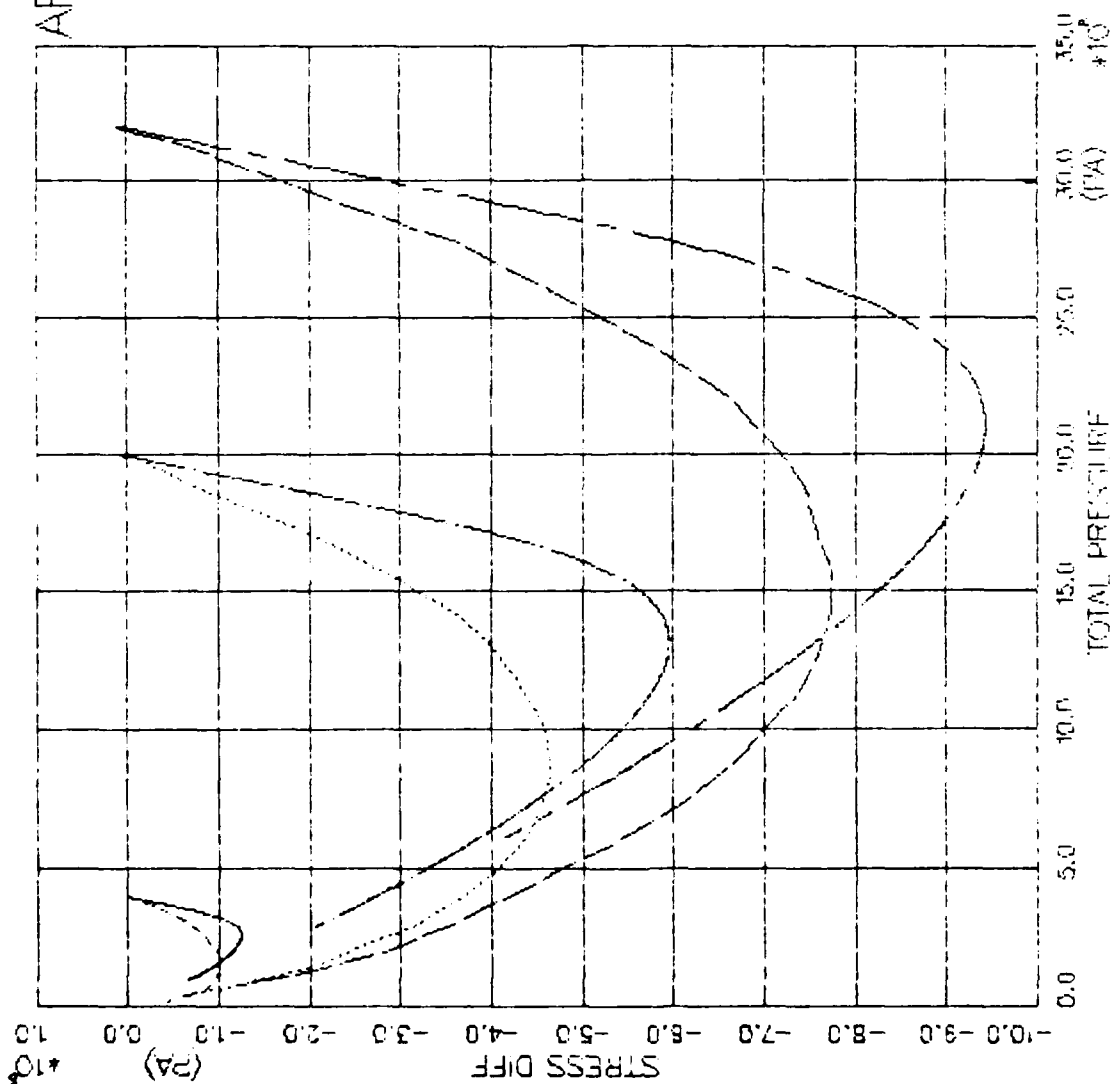
FIGURE V.8.39 LADE MODEL DIFFERENCE—UNIAX STRAIN EXTEN (ICKO) - STRESS DIFFERENCE VS. PRE

542

AFOSR SOIL ELEMENT MODEL

TEST = UNIAXIAL STRAIN TEST
MODEL= LADE
MAT'L = DRYCARES--REMOLD
DATA = DRYCARESR/WES/84

LEGEND
S3C=4.0E6
S3C=20.E6
S3C=32.E6

FIGURE V.8.40 LADE MODEL RESPONSE--UNIAX STRAIN EXTEN (ICK0) -- STRESS DIFF vs. AXIAL STRAIN

AFOSR SOIL ELEMENT MODEL

TEST = STRAIN PATH
MODEL=LADE
MATL = DRYCARES-REMOLD
DATA = DRYCARESR/WES/3A

LEGEND
WES PATH 3A
TEST DATA
WES PATH 3C
TEST DATA
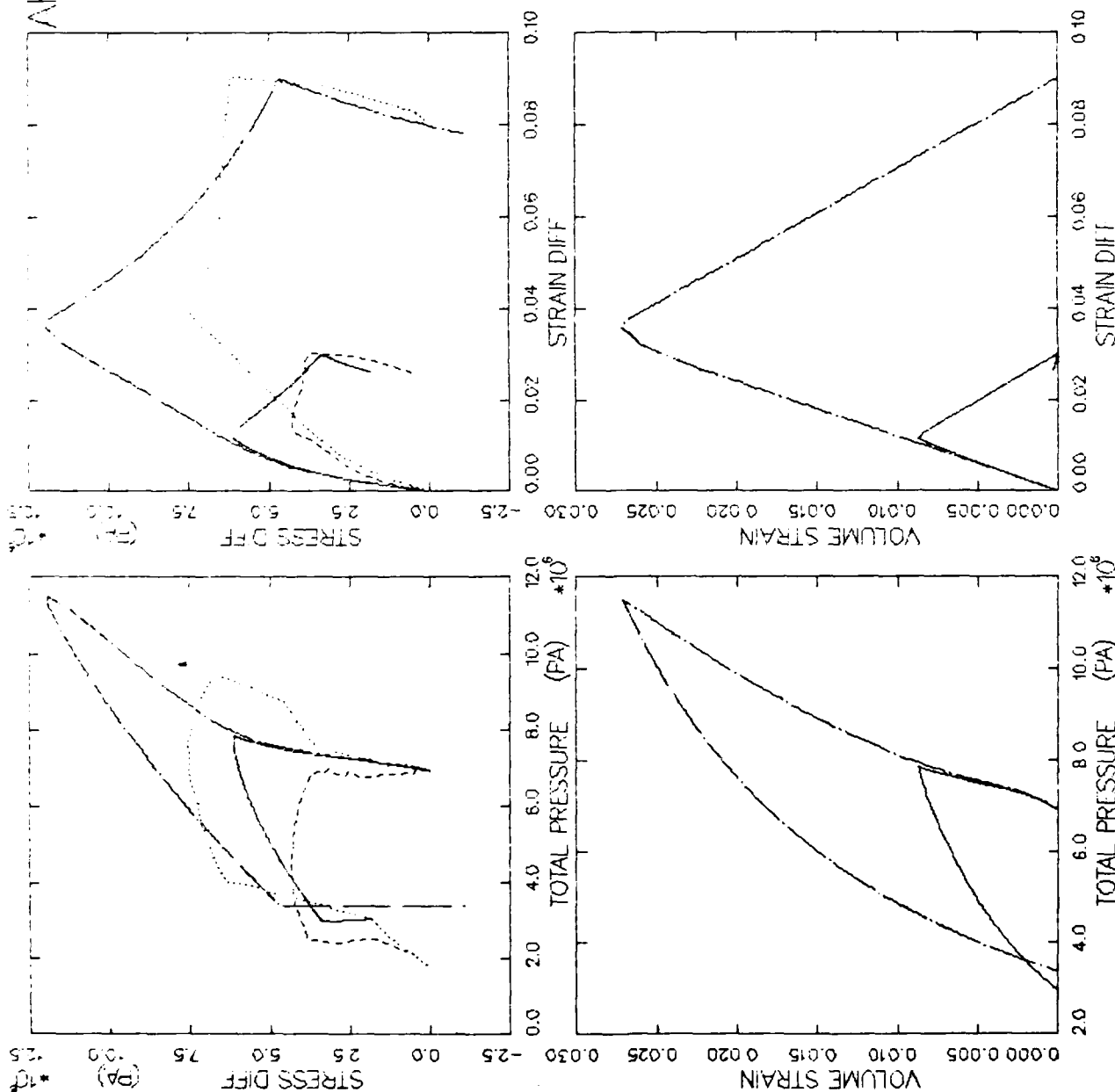
FIGURE V.8.41 LADE MODEL EXER-AXISYM EPATH3A+3C — SDIFF/P/EV/EDIFF ANALYSIS

544
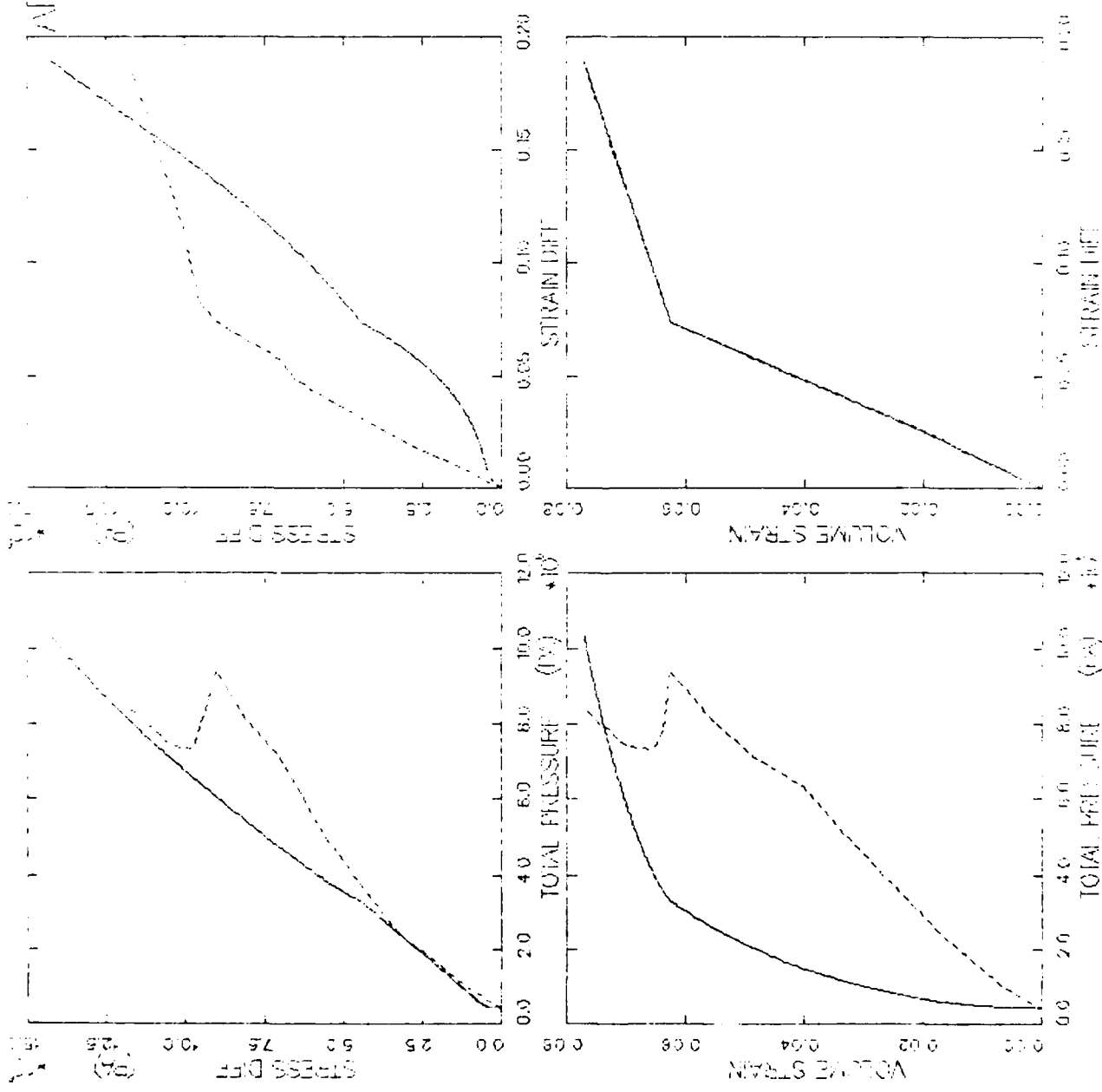
FIGURE V.8.42 LADE MODEL - LADE A/LYMP.PATH - ...BRA A/LYMP.PATH. ...BRE
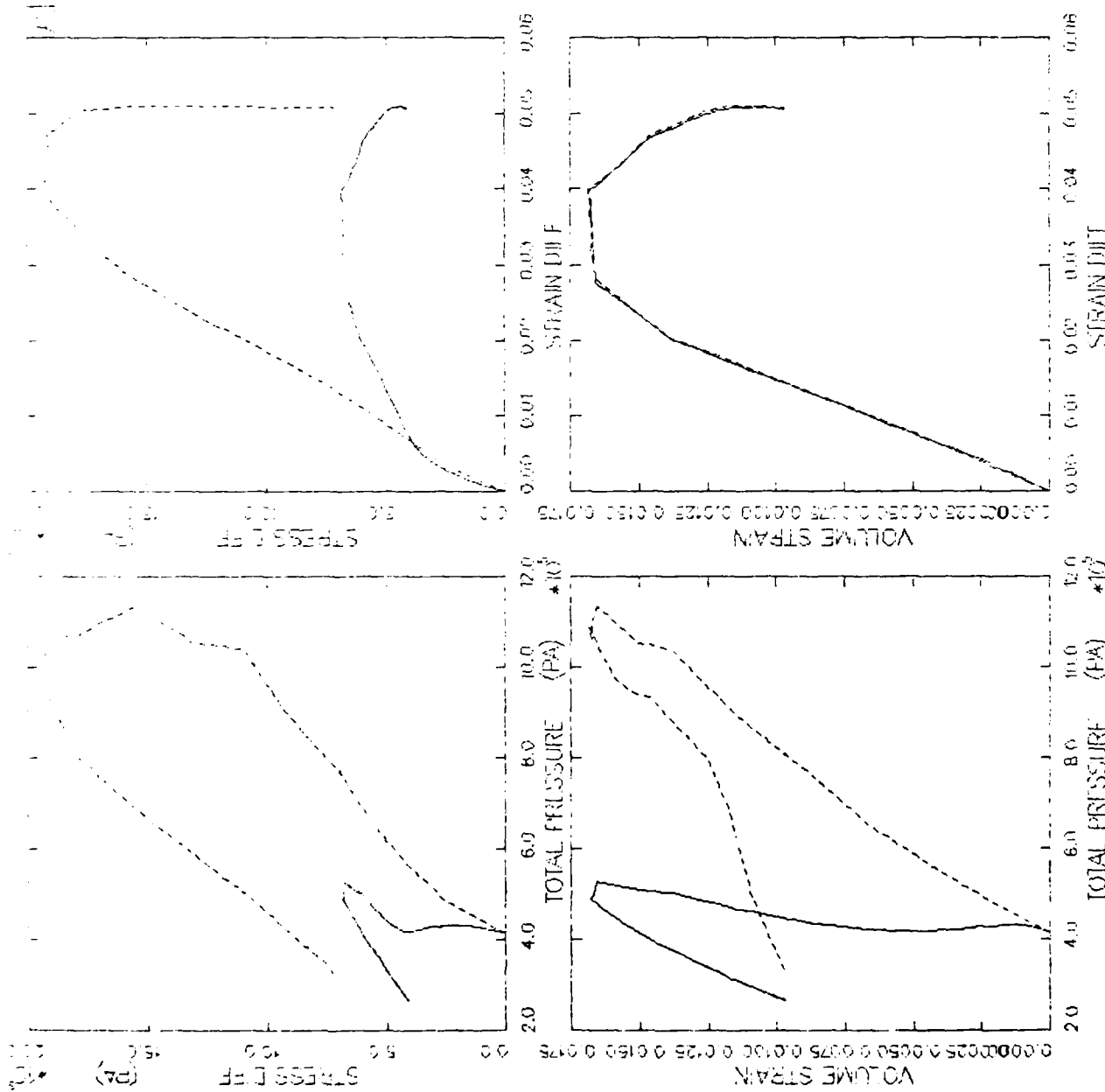
FIGURE V.8.43 LADE MODEL - LADE ASYM EXALIR -- SDE1/AVL/VCDIF ANALYSIS

AFOSR SOIL ELEMENT MODEL

TEST = STRAIN PATH
MODEL= LADE
MATL = DRYCARES—REMOLD
DATA = NELLISB/KO/JAN83
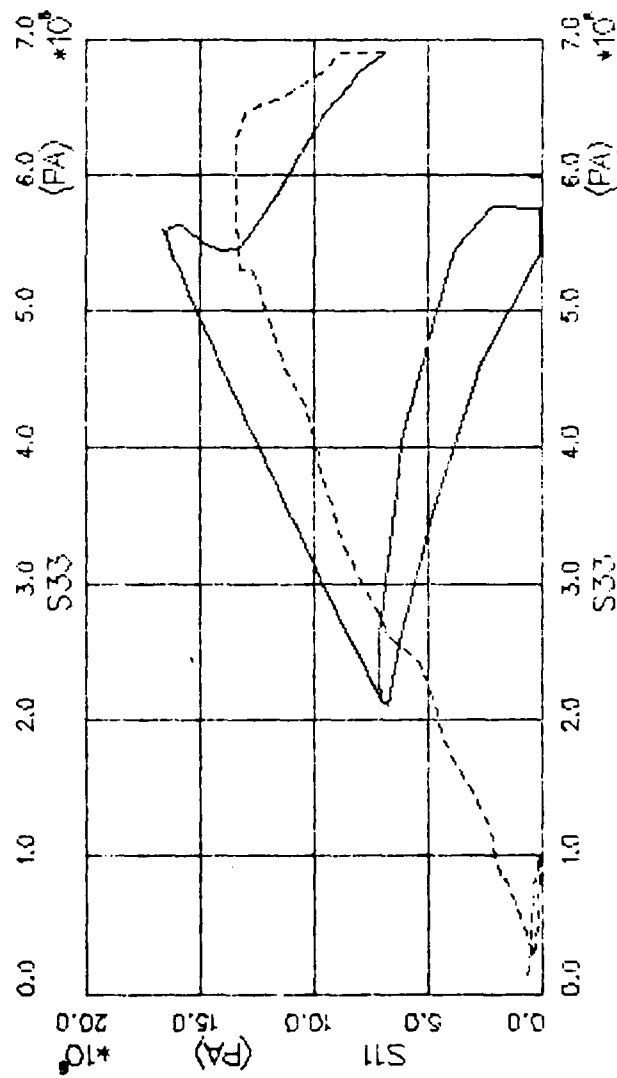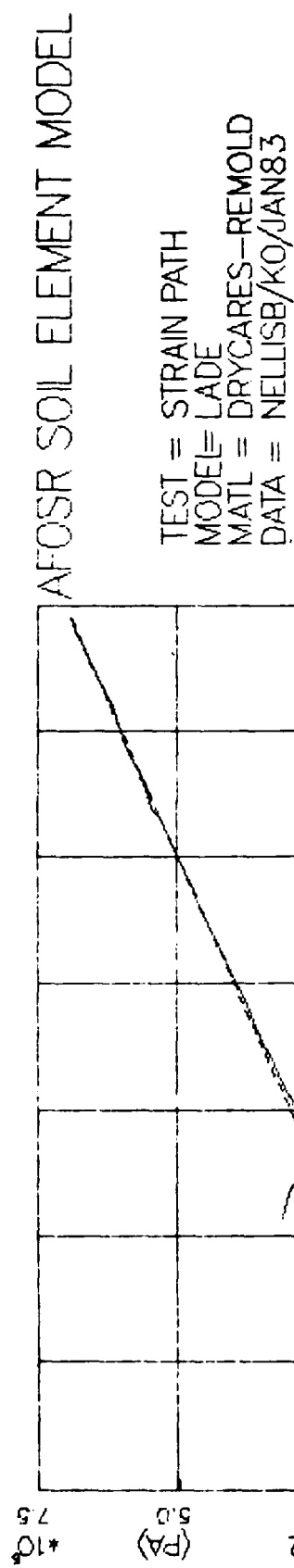
LEGEND
CALCULATION
TEST DATA

FIGURE V.8.44 LADE MODEL EXERCISE—TRUE TRIAX — PRINCIPAL STRESS PATH

547

AFOSR SOIL ELEMENT MODEL

TEST = STRAIN PATH
MODEL= LADE
MATL = DRYCARES—REMOLD
DATA = NELLISB/KO/JAN83

LEGEND
CALCULATION
TEST DATA
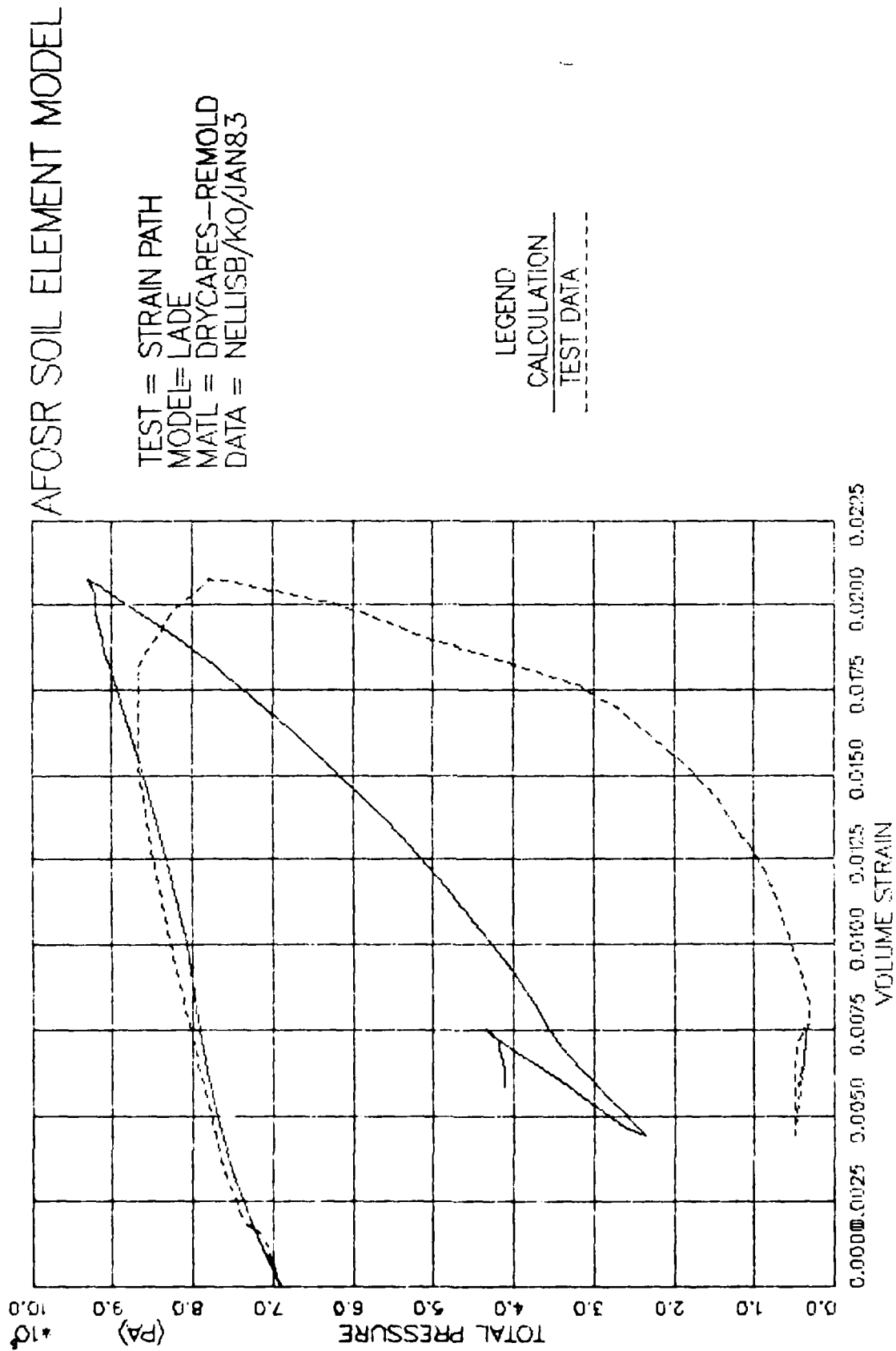
FIGURE V.8.45   LADE MODEL EXERCISE—TRUE TRIAX — PRESSURE VS. VOLUMETRIC STRAIN .

548

APPENDIX W

DEVELOPMENT OF THE ARA CONIC MODEL

W.1 Motivation

Of the eight soil constitutive models examined in Section 3 and Appendix V, the Lade model is most appealing from three important standpoints:

a) favorable rating with respect to seven of the ten evaluation criteria in Table 3.1;

b) accuracy and flexibility in representing soil stress-strain behavior; and

c) ease of developing intuition for parameter physical significance and accuracy.

Consequently ARA elected to modify the Lade model rather than create a completely new one, to develop a soil constitutive model suitable for analyzing the response of soil masses to complex dynamic loadings.

The modifications were designed to achieve the following additional desirable features:

a) better volumetric strain response under non-isotropic loading;

b) greater flexibility in matching shear strength data, in both the triaxial and octahedral planes;

c) correct plastic mode selection based on the thermodynamically related dissipation condition that a positive plastic work increment accompany yielding;

d) finite, reasonable friction angle at low confining pressure;

e) essentially constant shear strength at high confining pressure; and

f) direct (noniterative) shear strength calculation in both the

549

triaxial and octahedral planes.

Several Lade model features have been retained:

a) the basic model construction, i.e., two yield surfaces, one compressive and one expansive, both strain hardening, the compressive yield surface associative and the expansive yield surface non-associative;

b) both the compressive and expansive work hardening formulations; and

c) the unloading/reloading elastic modulus formulation.

New features include:

a) an ellipsoidal compressive yield surface to increase compressibility in the presence of shear deformation;

b) a hyperbolic expansive yield surface with a triple ellipsoidal octahedral cross section, possessing a finite, adjustable slope (friction angle) at low confining pressure, essentially constant shear strength at high confining pressure, flexibility in matching both compression and extension shear strength data, a completely smooth octahedral cross section, and directly computable shear strength;

c) enforcement of the dissipation condition;

d) development of a polar mode check based on the dissipation condition, to determine uniquely and without trial and error which yield surfaces are active under a given state of stress and prescribed total strain increment; and

e) determination of compressive yield surface parameters by fitting the plastic hydrostat directly (using a linear transformation) rather than having to compute compressive plastic work.

In addition, the work softening feature of the expansive hardening function may be modified or deleted in future versions of the conic model to insure uniqueness and stability, and to achieve a finite, constant shear strength at large shear strain (a non-zero critical state). The model is called a conic model because all three controlling surfaces in principal stress space have both triaxial and octahedral cross sections which are conic sections. It is also called a three invariant model because the expansive yield surface involves three independent stress invariants: the first total stress invariant and the second and third deviator stress invariants. The ARA conic model rates favorably with respect to all ten evaluation criteria in Table 3.1.

At present the conic model uses the incremental stiffness formulation developed in Appendix G, rather than a trial and error yield surface violation correction procedure such as that discussed in Appendix S for the cap model. However, the initial strain increments needed for numerical stability of the conic model are very small (of the order of 10^{-6}), and a trial and error correction procedure may be an economic necessity when using it to solve dynamic or static boundary value problems.

W.2 Assumptions

With one important exception, the assumptions underlying the conic model are the same as those underlying the Lade model, discussed in Section V.8.2. The one exception is the conic model enforces the dissipation condition, whereas the Lade model does not. Using two separate yield surfaces, each with its own potential surface and hardening rule, assumes a material really has two separate yield surfaces. The strain hardening parameter for each yield surface is the corresponding

551

plastic work. Of course all these elements of an elastoplastic model really amount to physically motivated curve fitting, the acid tests of which are predictive accuracy and ease of use.

W.: Basic Equations

The conic model compressive yield criterion has the same general form as does the Lade model.

$$f_c = f_c' - f_c'' = 0 \qquad (V.8.1)$$

but the stress related function, f_c', has a slightly different form.

$$f_c' = 3\sigma_{OCT}^2 + 3r^2 \tau_{OCT}^2 \qquad (W.1)$$

where

$\quad r$ = compressive yield surface ellipse axis ratio (see Figure (U.1)).

The compressive hardening function, f_c'', has the same form as does the Lade model.

$$f_c'' = p_a^2 \left(\frac{W_c}{Cp_a}\right)^{1/p} \qquad (V.8.3)$$

where

$\quad P_a$ = atmospheric pressure

$\quad C, p$ = material parameters

and the compressive plastic work, W_c is defined by the equation

$$W_c = \int \{\sigma\}^T \{d\epsilon^c\} \qquad (W.2)$$

The compressive plastic potential, to which the compressive plastic strain increment vector, $\{d\epsilon^c\}$, is normal, is

$$g_c = f_c' = 3\sigma_{OCT}^2 + 3r^2 \tau_{OCT}^2 \qquad (W.3)$$

The conic model expansive yield criterion has the same general form as does the Lade model.

$$f_p = f_p' - f_p'' = 0 \qquad (V.8.6)$$

but the stress related function, f_p', has a different form.

$$f_p' = \left(\frac{\tau_{OCT}}{P_a}\right)(1 - E\cos 3\omega)\left(\frac{P_a}{\sigma_{OCT}} + m\right) \tag{W.4}$$

in which

$$f_p' = f_{p,max}' = \eta_1 \qquad \text{at failure} \tag{V.8.8}$$

The expansive hardening function, f_p'', has the same form as does the Lade model.

$$f_p'' = ae^{-bW_p}\left(\frac{W_p}{P_a}\right)^{1/q} \tag{V.8.9}$$

In Equations (W.4), (V.8.8) and (V.8.9)

E, m, η_1, a, b, q = material parameters

and the expansive plastic work, W_p, is defined by the equation

$$W_p = \int \{\sigma\}^T \{d\epsilon^p\} \tag{V.8.10}$$

The expansive plastic potential, to which the expansive plastic strain increment vector, $\{d\epsilon^p\}$, is normal, is

$$g_p = \left(\frac{\tau_{OCT}}{P_a}\right)(1 - E\cos 3\omega) - \frac{\eta_2\left(\frac{\sigma_{OCT}}{P_a}\right)}{1 + m\left(\frac{\sigma_{OCT}}{P_a}\right)} \tag{W.5}$$

where η_2 is also a material parameter.

The unloading/reloading elastic modulus is assumed to be given by the expression

$$E_{ur} = K_{ur}P_a\left(\frac{\sigma_{OCT}}{P_a}\right)^n \tag{W.6}$$

where

K_{ur}, n = material parameters

and the unloading/reloading Poisson's ratio, ν_{ur}, is computed as

553

described in Appendix T, or assumed. When neither yield surface is active the material response is incrementally elastic.

An unloading/reloading hysteresis option for cyclic loading has been formulated but not yet fully implemented. The deviatoric strain increments are considered completely elastic, so that the deviator stress increments are given by the equation

$$ds_{ij} = \frac{E_{ur}}{1 + \nu_{ur}} de_{ij} \qquad (W.7)$$

However, a portion of the volumetric strain increment is attributed to unloading/reloading shear hysteresis rather than to a change in octahedral normal stress. In other words, a volumetric strain increment, $d\theta$, would accompany an octahedral shear strain increment, dz, even under constant octahedral normal stress. If the octahedral shear strain is

$$z = \sqrt{\frac{1}{3} e_{ij} e_{ij}} \qquad (W.8)$$

then the octahedral shear strain increment, dz, is given by the expressions

$$dz = \frac{e_{ij} de_{ij}}{3z} \qquad (z > 0)$$

$$= \sqrt{\frac{1}{3} de_{ij} de_{ij}} \qquad (z = 0) \qquad (W.9)$$

The octahedral shear strain, z, is nonnegative, but the octahedral shear strain increment, dz, can be positive, zero, or negative. The volumetric strain increment due to shear, $d\theta$, is assumed to be related to the octahedral shear strain increment, dz, by the equation

$$d\theta = \frac{dz}{A - z^M e^{-\lambda N}(\gamma + \beta \operatorname{sgn} dz)} \qquad (W.10)$$

554

where

A, M, λ, γ, β = material parameters

N = number of octahedral shear strain reversals

The parameters are chosen so the denominator in Equation (W.10) will always be positive. Equation (W.10) can accommodate irregular cyclic loading, and produces hysteresis loops which narrow progressively as the number of octahedral shear strain reversals, N, increases. The octahedral normal stress increment is calculated by the equation

$$d\sigma_{OCT} = K(d\varepsilon_{kk} - d\theta) \qquad (W.11)$$

The method for calculating the octahedral cross section of the conic failure surface (the expansive yield surface at its maximum extent) is given in Appendix U.

The computational features of the conic model are covered in the appendices. Using the value of Young's modulus from Equation (W.6) and an assumed Poisson's ratio, the elastic incremental stiffness matrix is given by Equation (J.32). The general equations of elastoplasticity given in Appendix D apply. The elastoplastic incremental stiffness matrices are calculated as described in Appendix G, and the polar mode check described in Appendix I is used when the stress point is at the intersection of the two yield surfaces.

W.4 Parameter Determination

Determination of the material parameters in Equations (V.8.1) through (W.10) is discussed in Appendix U. Figures (W.1) through (W.20) illustrate the fitting process for the ARA model using remolded CARES-DRY Sand data. All the fitting was performed automatically by the Soil Element Model. Figure (W.1) shows the variation of Young's modulus with

555

maximum past pressure for this material. This plot represents the best straight line fit to observed unload-reload stiffness from isotropic compression, uniaxial strain, and triaxial compression tests reported by [Cargile (1984)]. The corresponding pressures are the test pressures at which unloading commenced.

Figure (W.2) is the hydrostatic data (loading only) used to obtain the compressive plastic work parameters. In Figure (W.3), this curve has been integrated to show compressive plastic work versus pressure. The integration process assumes the variation of elastic properties with confining pressure as previously determined. The data, shown as open circles, does not fall along a single straight line, even in log-log space. Therefore, several straight line segments have been fit, as shown, with breakpoints between them defined on the basis of compressive plastic work. The ARA conic model is presently formulated so that up to four segments can be used.

Figure (W.4) shows triaxial compression stress-strain data, which, at some confining pressures, has been artificially extended to near peak response. This has been done by assuming a hyperbolic shape for the last twenty-five percent of both the axial and radial stress difference-strain curves. A Kondner plot of strain/stress difference vs. strain is then used to extend the data to ninety-five percent of peak stress difference as predicted by the straight line fit. Two such plots are shown in Figures (W.5) and (W.6), for confining pressures of 3.4 MPa and 7.0 MPa, respectively. Some type of data extension to "failure" is necessary for this type of model to yield reasonable values of peak expansive work.

Figure (W.7) defines the shape and maximum extension of the expansive yield surface, f_p'. Peak values have been plotted for triaxial tests run at five different confining pressures.

Given the previously determined elastic and compressive plastic work behaviors, Figures (W.8) and (W.9) show the predicted compressive and expansive plastic strains during the triaxial test. Figures (W.10) through (W.14) break down the total volumetric strain response at each confining pressure into components. Shown are the total, elastic, and elastic plus compressive plastic strains. Expansive plastic strain is the difference between the total and elastic plus compressive plastic curves. According to the model theory, this should always be a negative quantity, i.e., the expansive yield surface should always produce expansive volume strain components. At some confining pressures, however, this does not hold true. [See Figures (W.11), (W.13) and (W.14)]. This implies that the volumetric response determined from the isotropic compression test cannot be totally representative of the triaxial test volumetric response. Note that this can be remedied by using an envelope of pressure-volume behavior which encompasses both tests. Further adjustment of the r factor may also help.

The observed shape of the expansive surface hardening function is shown in Figure (W.15) for each confining pressure. Peak values from these curves are plotted in Figure (W.16), and shape-related values are plotted in Figure (W.17).

Parameters for the expansive plastic potential surface are derived from a plot of η_2 vs. f_p'' for several confining pressures, as shown in Figure (W.18). The data are derived from triaxial volume response and

model predictions, and a plane is passed through the entire set. The very rough appearance of the data is due to three factors:

(a) rough hand digitization of test data which had been plotted on a small area;

(b) elimination of unload-reload loops from the data, which did in fact have a significant effect on volumetric response (the large dips, most noticeable at $\sigma_{3c,5}$, coincide with the eliminated loops);

(c) previous fitting processes which may introduce some inconsistencies between test data and predicted model response.

Figures (W.19) and (W.20) summarize the shape of the fitted expansive and compressive surfaces in the triaxial and octahedral planes, respectively. Table (W.1) summarizes the ARA parameters for remolded CARES-DRY Sand.

W.5 Calculated Behavior

The multi-linear fit to compressive plastic work produces an excellent fit to loading isotropic compression stress-strain data, as shown in Figure (W.21). Note that both concave and convex behavior can be matched for a large range of pressure. The model currently predicts only linear elastic behavior on unloading-reloading, so the observed "tail" on the unload curve is not well modeled.

CTC stress-strain behavior is matched fairly accurately, as shown in Figures (W.22) through (W.25). The model cannot follow the uneven volume strain response shown in Figure (W.24), but does match the overall trends of compaction and subsequent dilation at each confining pressure. Figure (W.25) shows very good prediction of pressure-volume behavior for this test.

Peak values of stress difference for the CTE test were used for defining the asymmetry of the expansive yield surface, so they are well matched, as shown in Figure (W.26). The shape of the stress-strain behavior is also predicted quite well [Figures (W.26) and (W.27)]. Observed volume behavior for this test is essentially all compaction, and this is true for the calculated behavior as well [Figures (W.28) and (W.29)]. Note, however, that the model predicts dilation past 4-5 percent axial strain, while the samples apparently did not dilate at all.

Calculated RTC/RTE behavior [Figures (W.30) through (W.33)] illustrates several important features of the ARA model. Stress-strain curves [Figures (W.30), (W.31) and (W.33)] are smooth for both tests. Substantial softening of the expansive yield surface occurs during the RTE tests. As shown in Figure (W.31), this results in a negative shear stiffness past 20-25 percent strain difference. Dilation is predicted for both tests [Figures (W.32) and (W.33)].

PSC/PSE calculations show non-symmetric stress strain behavior [Figures (W.34) and (W.35)], as would be expected due to the non-symmetric yield surface. Note that no work softening is predicted, because $W_{p,pk}$ has not been achieved for any of the confining pressures. Volume strains are predicted to be initially compressive due to outward movement of the elliptical cap, and then expansive due to shear dilation [Figure (W.36)]. Figure (W.37) summarizes calculated behavior of the ARA model for several different tests run in the triaxial device. All tests start at 7 MPa initial confining pressure.

Uniaxial strain (UXC) data vs. calculation comparisons are shown in Figures (W.38) through (W.40). Stress-strain behavior is only marginally

559

good, because of the model's tendency to stiffen (due to dilation) under non-isotropic stress paths. The stress path is predicted quite well, with the exception of the non-linear unload-reload excursions.

The observed shape of the UXE stress path is predicted very well by the ARA model as shown in Figure (W.41). Apparently, the ultimate expansive yield surface position is somewhat more expanded than predicted by the model. Figure (W.42) shows calculated UXE stress-strain response.

Axisymmetric strain path results for the ARA model [Figures (W.43) through (W.45)] indicate that the determined parameters produce behavior which is too stiff at the WES level of confining pressure (7 MPa). This point can be confirmed by re-comparing UXC calculation and test data at an axial stress of about 12 MPa (corresponding to a pressure of about 7 MPa) in Figure (W.38). The stresses from the WES strain paths [Figure (W.43)] are substantially overpredicted as a result. Stress difference also drops too quickly, as radial expansion is intensified. The model does somewhat better with the Lade strain paths [Figures (W.44) and (W.45)], perhaps because the initial confining pressure is lower. In fact, for these paths, both shear and volume stiffness are somewhat underpredicted.

Figure (W.46) shows the predicted stress path for the true triaxial test strain path, and Figure (W.47) shows the predicted pressure-volume response.

TABLE W.1(a)   ARA MODEL PARAMETERS FOR REMOLDED CARES-DRY SAND

Parameter	Symbol	Variable	Value	Units
Modulus Constant	K_{ur}	AKUR	36.35	--
Modulus Exponent	n	AN	0.8412	--
Poisson's Ratio	ν_e	APOI	0.200	--
No. f_c' Segments	n_{crv}	ACRV	3	--
Hardening Constant	C_1	AACC(1)	4.645×10^{-5}	--
Hardening Exponent Seg. 1	P_1	AAPC(1)	1.401	--
Hardening Breakpoint	hk_1	ABRK(1)	2.195	--
	C_2	AACC(2)	6.086×10^{-2}	--
Seg. 2	P_2	AAPC(2)	0.4667	--
	bk_2	ABRK(2)	22.84	--
	C_3	AACC(3)	7.516×10^{-1}	--
Seg. 3	P_3	AAPC(3)	0.2688	--
CAP Axes Ratio	r	AR	0.250	--
Yield Constant	E	AEY	0.111	--
Yield Exponent	m	AMY	2.875×10^{-4}	--
Failure Constant	η_1	AETA1	0.6454	--
	P	APBAR	0.5057	--
Work Hardening Constants	l	AL	0.8691	--
	α	AALPH	5.000	--
	β	ABETA	-2.631×10^{-3}	--
	t	ATG	-0.9646	--
Plastic Potential Constants	R	ARG	2.182×10^{-3}	--
	S	ASG	1.860	--
Plastic Expansive Work	$\sigma_{OCT,max}$	ASOCT		Pa
at $f_{p,max}'$	$W_{p,pk}$	AWPPK		Pa
Work Hardening Constants	q	AO	varies, see	--
	a	AA	Table W.1(b)	--
	b	AB		--
Plastic Potential Constant	$\eta_{2,0}$	AETA20		--
Initial Plastic Comp. Work	$W_{c,0}$	AWC		Pa
Mass Density	ρ	RHOREF	1900	kg/m^3

TABLE W.1(b)   CONFINING PRESSURE DEPENDENT
ARA MODEL PARAMETERS

σ_{3c} (MPa)	$W_{p,pk}$ (Pa)	q	a	b	$\eta_{2,0}$	$W_{c,0}$ (Pa)
0.1	5.07×10^4	4.997	0.9058	3.950×10^{-8}	-0.9624	3.03×10^0
0.4	1.74×10^5	4.989	0.7076	1.151×10^{-6}	-0.9602	1.62×10^2
1.8	6.25×10^5	4.953	0.5471	3.232×10^{-7}	-0.9554	9.97×10^3
3.5	1.11×10^6	4.909	0.4856	1.830×10^{-7}	-0.9518	6.42×10^4
7.0	2.03×10^6	4.818	0.4263	1.021×10^{-7}	-0.9465	6.87×10^5
20.0	5.06×10^6	4.481	0.3370	4.407×10^{-8}	-0.9340	1.21×10^6
32.0	7.62×10^6	4.170	0.2911	3.148×10^{-8}	-0.9258	1.56×10^6
59.0	1.29×10^7	3.474	0.2132	2.227×10^{-8}	-0.9121	2.16×10^6
100.0	2.05×10^7	2.405	0.1075	2.027×10^{-8}	-0.8961	2.87×10^6

AFOSR SOIL ELEMENT MODEL

TEST = PARAMETER FIT
MODEL= ARA1
MATL = DRYCARES-REMOLD
DATA = DRYCARESR/WES/84

AKUR= $3.635*10^2$
AN = $8.412*10^{-1}$

S3C/ATMO

EUR/ATMO
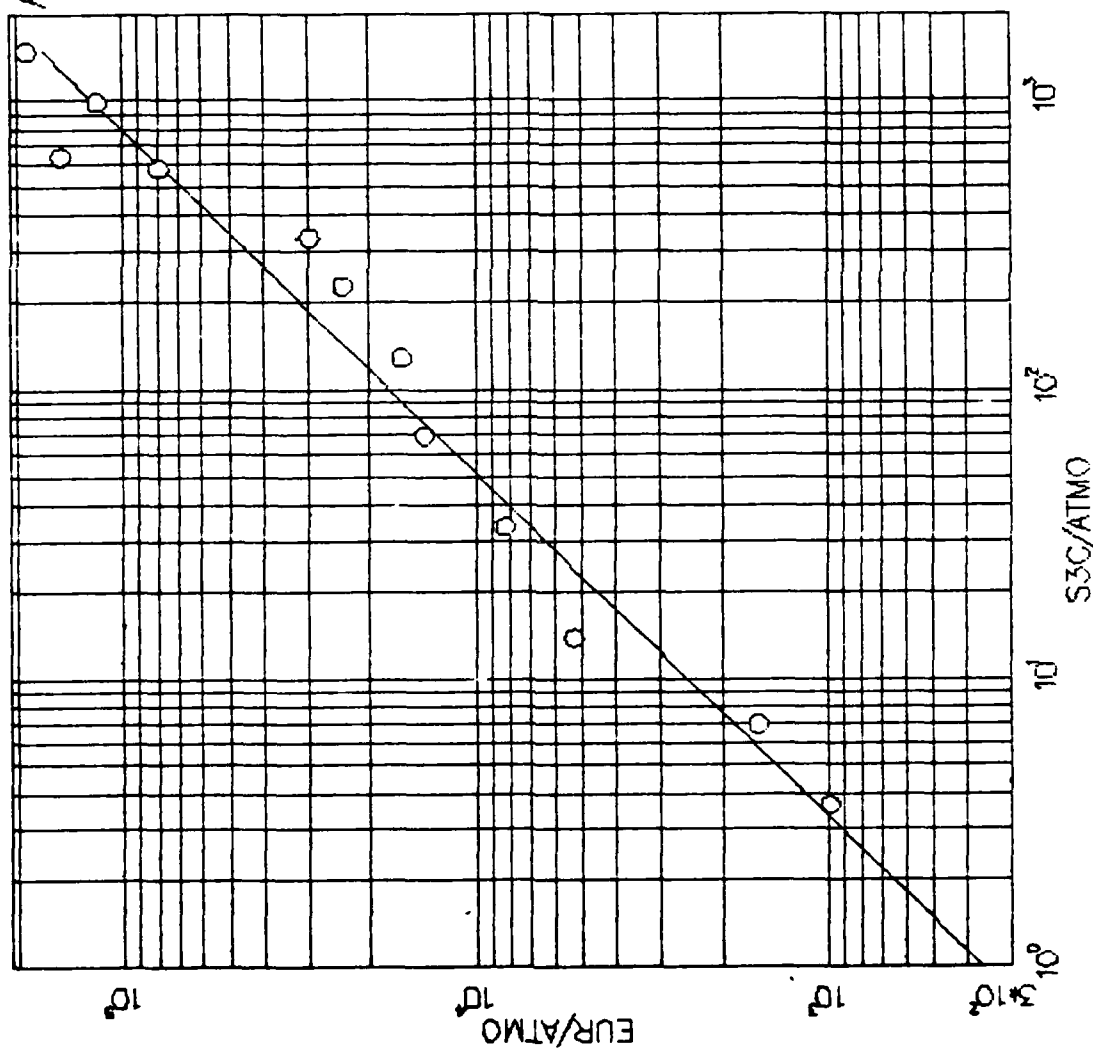
FIGURE M.1   ARA MODEL PARAMETER FIT — ELASTIC MODULUS DATA

563

AFOSR SOIL ELEMENT MODEL

TEST = ISOTROPIC COMPRESSION
MODEL= ARA1
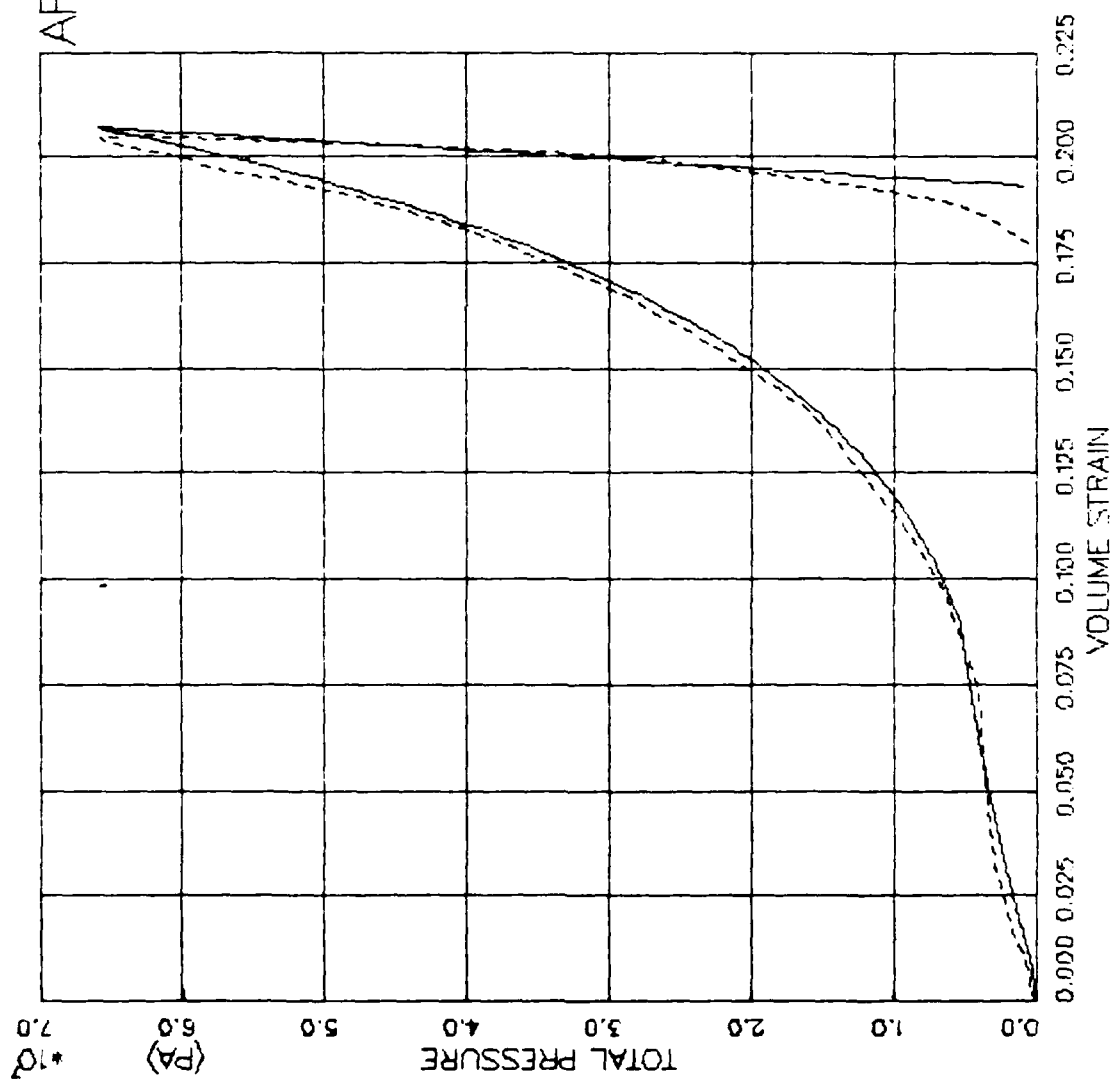MATL = DRYCARES-REMOLD
DATA = DRYCARESR/WES/84
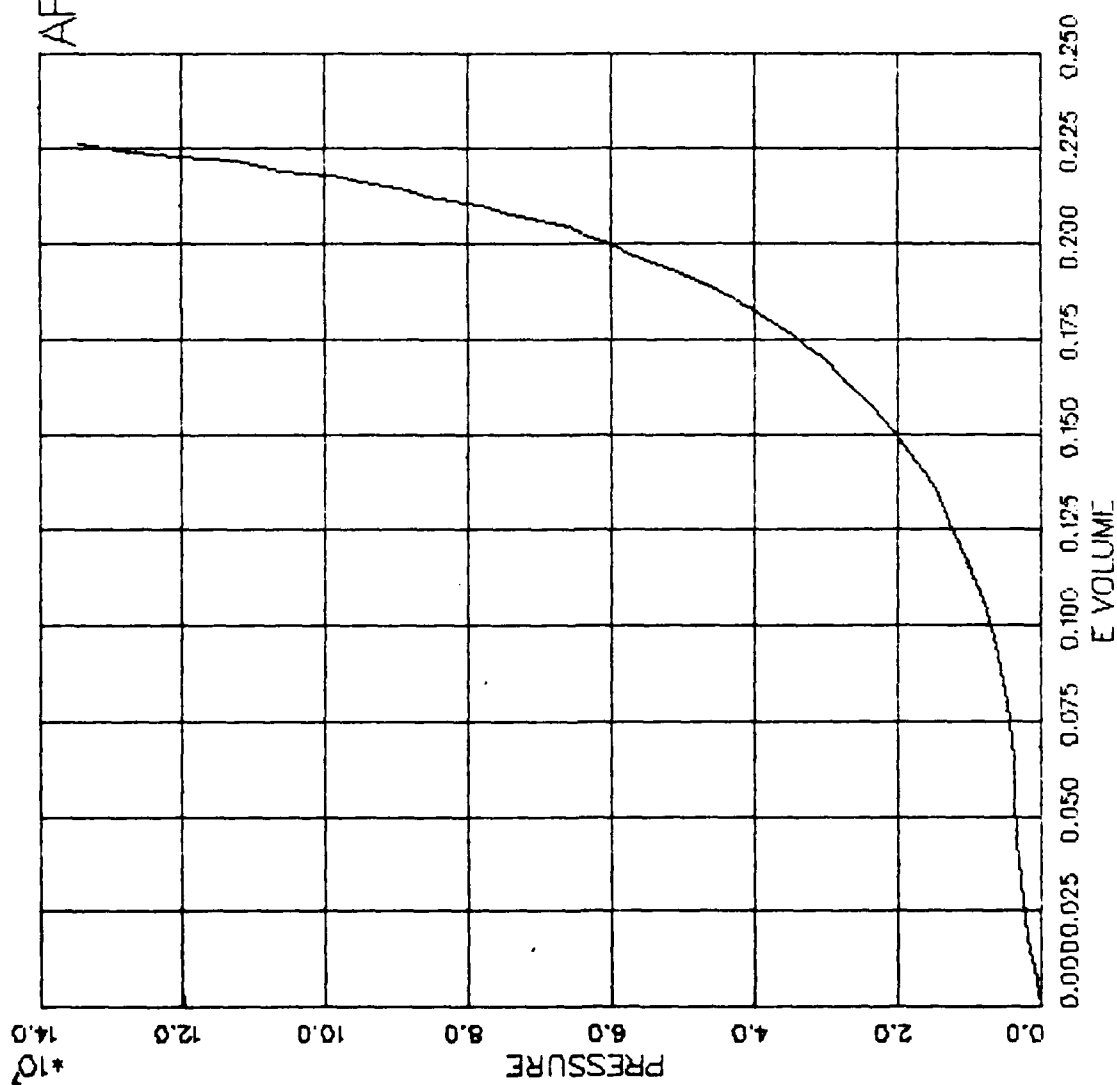
FIGURE W.2   ARA MODEL PARAMETER FIT — HYDROSTATIC COMPRESSION DATA

564

AFOSR SOIL ELEMENT MODEL

TEST = PARAMETER FIT
MODEL= ARA1
MATL = DRYCARES-REMOLD
DATA = DRYCARESR/WES/84

AR= $2.500*10^{-1}$
APC= $1.402*10^{0}$
INT= $6.650*10^{-8}$
ACC= $4.642*10^{-8}$
ABRK= $2.192*10^{0}$
APC= $4.667*10^{-1}$
INT= $3.187*10^{-2}$
ACC= $6.086*10^{-2}$
ABRK= $2.282*10^{1}$
APC= $2.688*10^{-1}$
INT= $5.178*10^{-1}$
ACC= $7.516*10^{-1}$

WC/ATMO

$3*(S3C/PA)**2$
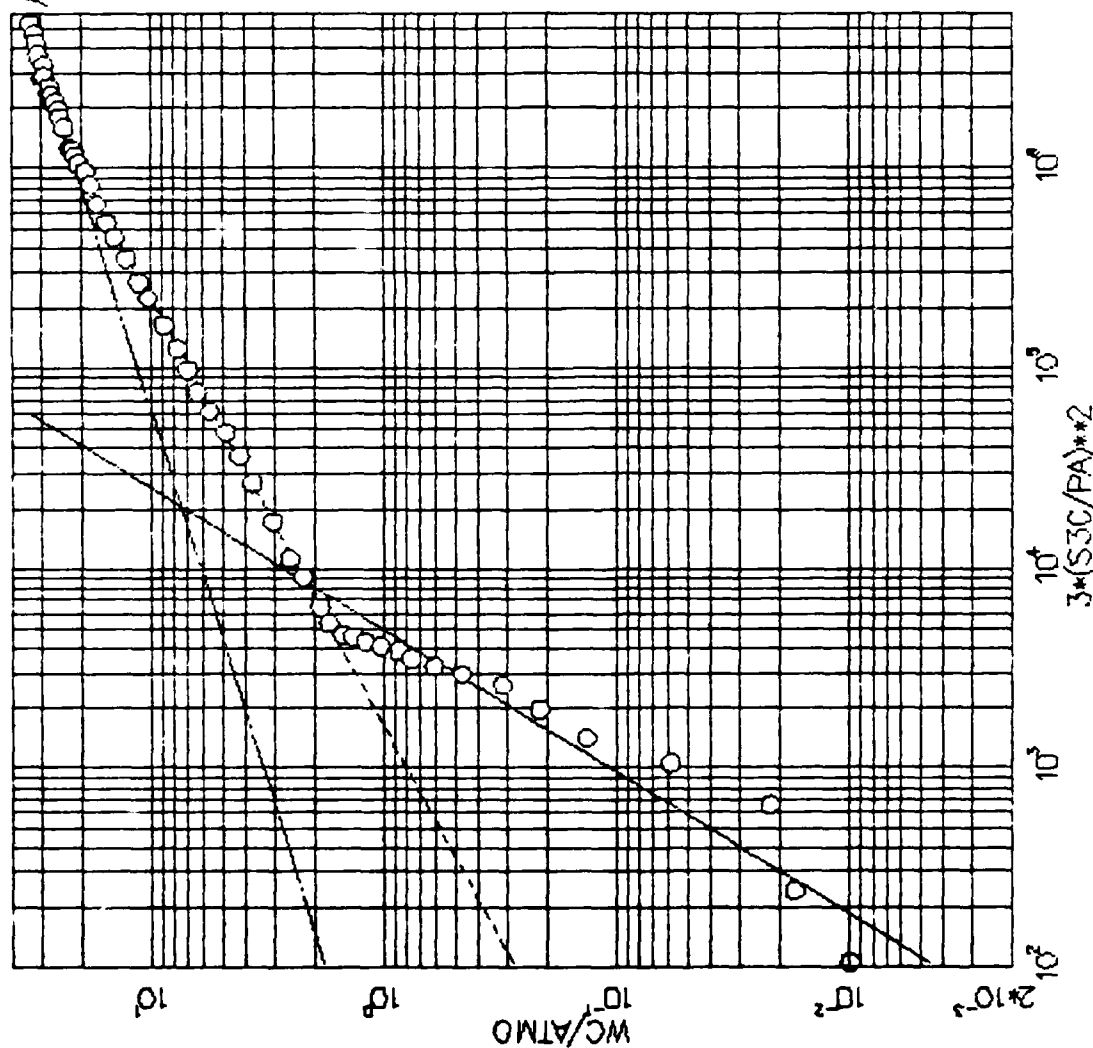
FIGURE W.3   ARA MODEL PARAMETER FIT — COMPRESSIVE PLASTIC WORK FIT

565

AFOSR SOIL ELEMENT MODEL

TEST = STANDARD TRIAXIAL TEST
MODEL= ARA1
MATL = DRYCARES—REMOLD
DATA = DRYCARESR/WES/84
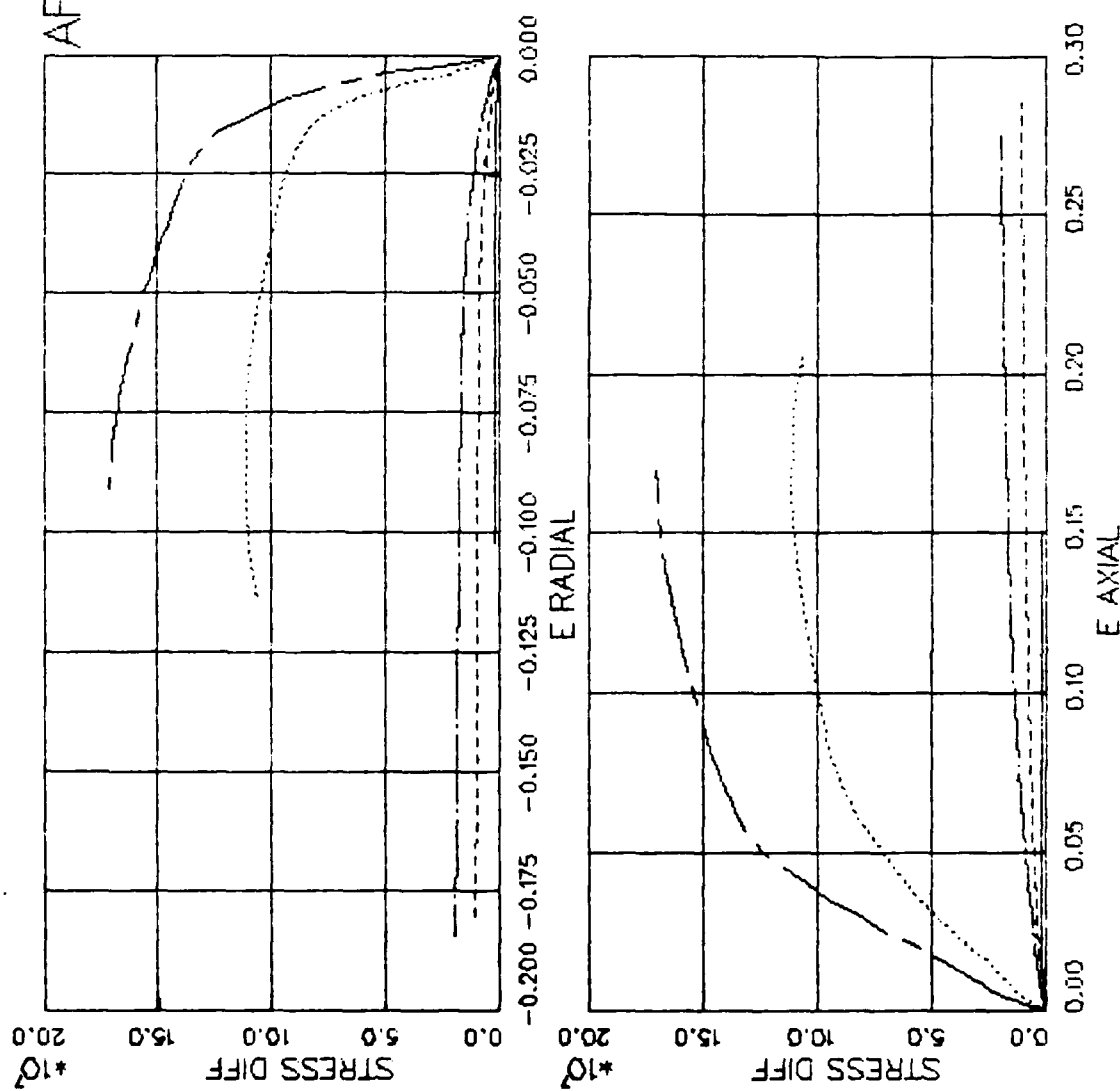
S3C= $7.000*10^{5}$
S3C= $3.400*10^{6}$
S3C= $7.000*10^{6}$
S3C= $5.880*10^{7}$
S3C= $1.000*10^{8}$
EDELTA= $5.000*10^{-3}$

FIGURE W.4   ARA MODEL PARAMETER FIT -- TRIAXIAL TEST DATA

AFOSR SOIL ELEMENT MODEL

TEST = STANDARD TRIAXIAL TEST
MODEL= ARA1
MATL = DRYCARES–REMOLD
DATA = DRYCARESR/WES/84

LEGEND
○ AXIAL
 LSQFIT
□ RADIAL
 LSQFIT

$E(A)= 1.833*10^{8}$
$SDMEA= 1.363*10^{7}$
$EADMAX= 1.600*10^{-1}$
$E(R)= 8.205*10^{6}$
$SDMER= 1.135*10^{7}$
$ERDMAX=-6.310*10^{-2}$
$S3C= 3.400*10^{6}$
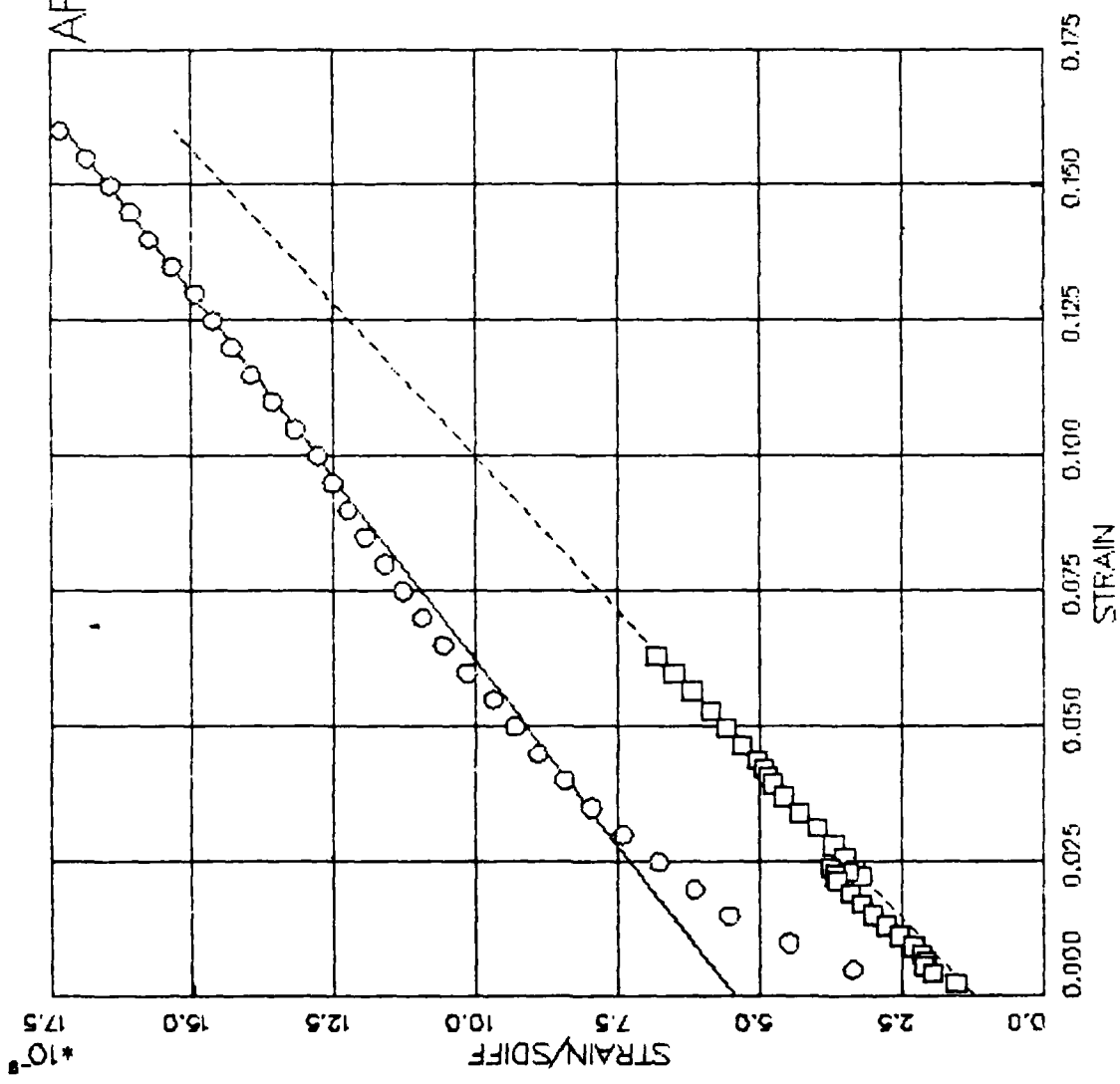
FIGURE W.5   ARA MODEL PARAMETER FIT — DATA EXTENSION —HYPERBOLIC FIT .

FIGURE W.6 ARA MODEL PARAMETER FIT — DATA EXTENSION — HYPERBOLIC FIT .

AFOSR SOIL ELEMENT MODEL

TEST = STANDARD TRIAXIAL TEST
MODEL= ARA1
MATL = DRYCARES–REMOLD
DATA = DRYCARESR/WES/84

LEGEND
○ AXIAL
___ LSQFIT
□ RADIAL
___ LSQFIT

E(A)= $3.469*10^8$
SDMEA= $2.479*10^7$
EADMAX= $1.550*10^{-1}$
E(R)= $1.388*10^9$
SDMER= $2.071*10^7$
ERDMAX=$-6.740*10^{-2}$
S3C= $7.000*10^6$

568

AFOSR SOIL ELEMENT MODEL

TEST = PARAMETER FIT
MODEl= ARA1
MATL = DRYCARES—REMOLD
DATA = DRYCARESR/WES/84

$AK1C = 1.377*10^0$
$AK2C = 3.960*10^{-4}$
$AEY = 1.111*10^{-1}$
$AMY = 2.875*10^{-4}$
$AETA1 = 6.454*10^{-1}$
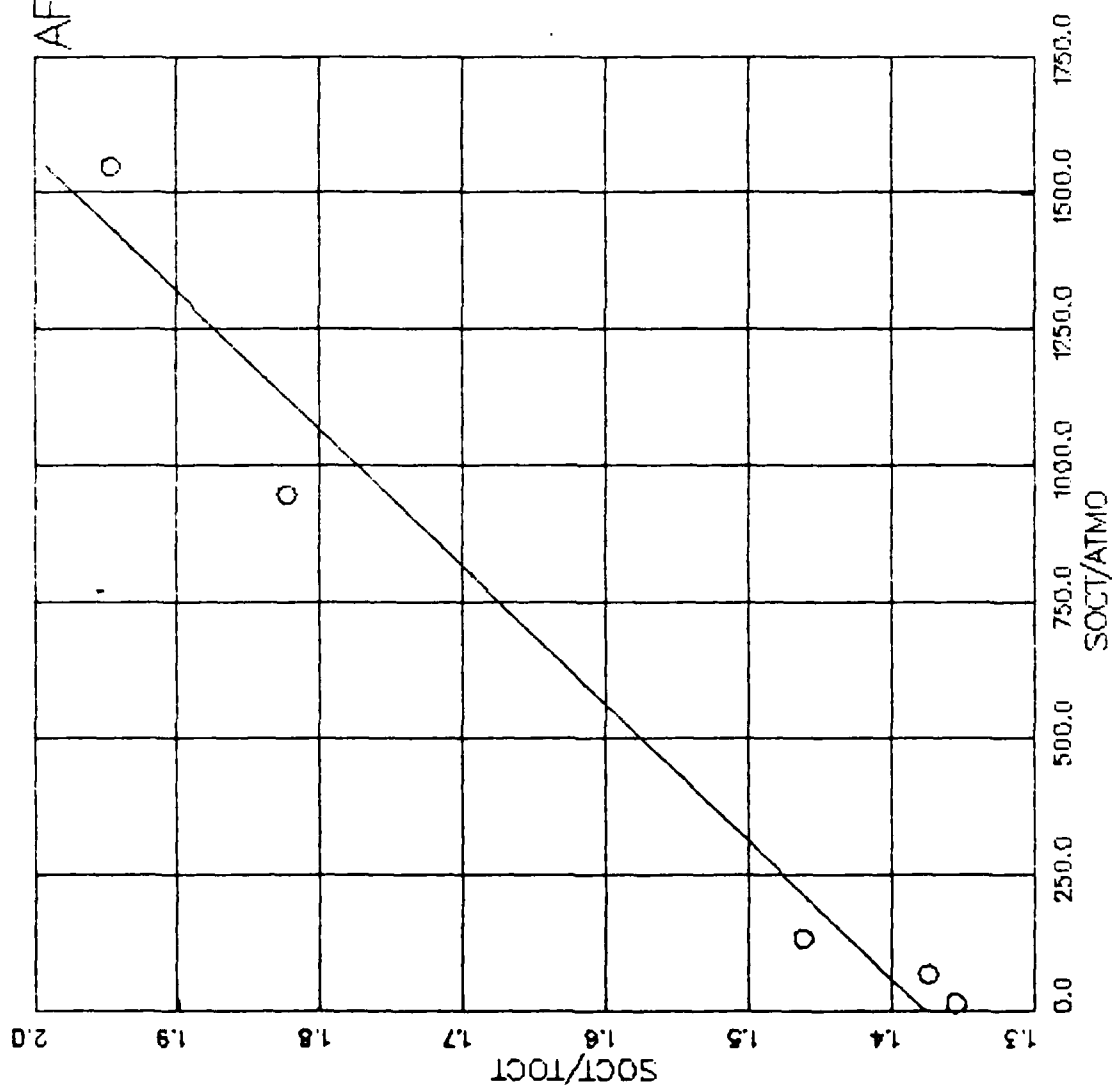
FIGURE W.7   ARA MODEL PARAMETER FIT — SHEAR FAILURE DATA

569
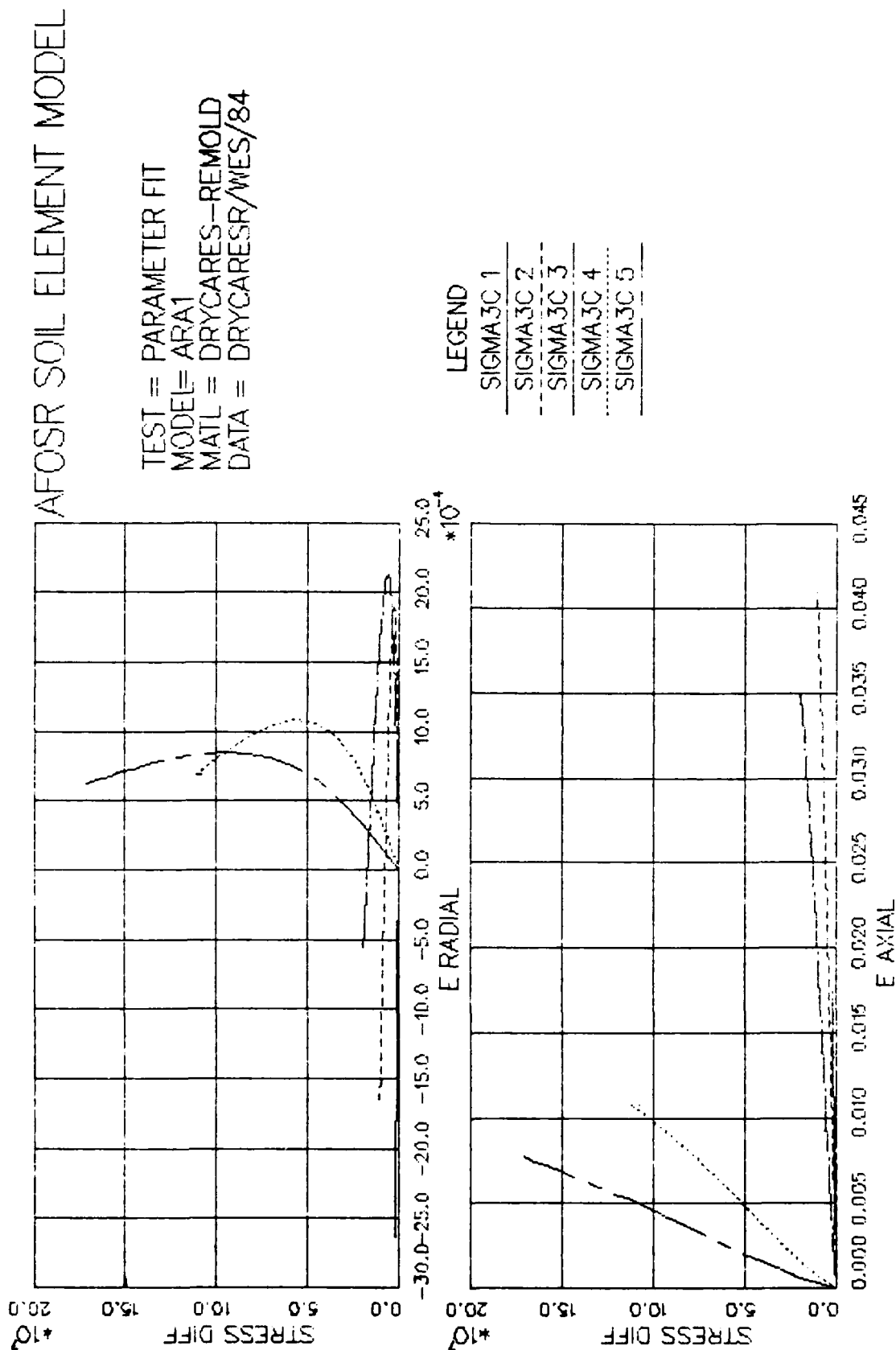
FIGURE W.8 ARA MODEL PARAMETER FIT — COMPRESS. PLASTIC STRAINS
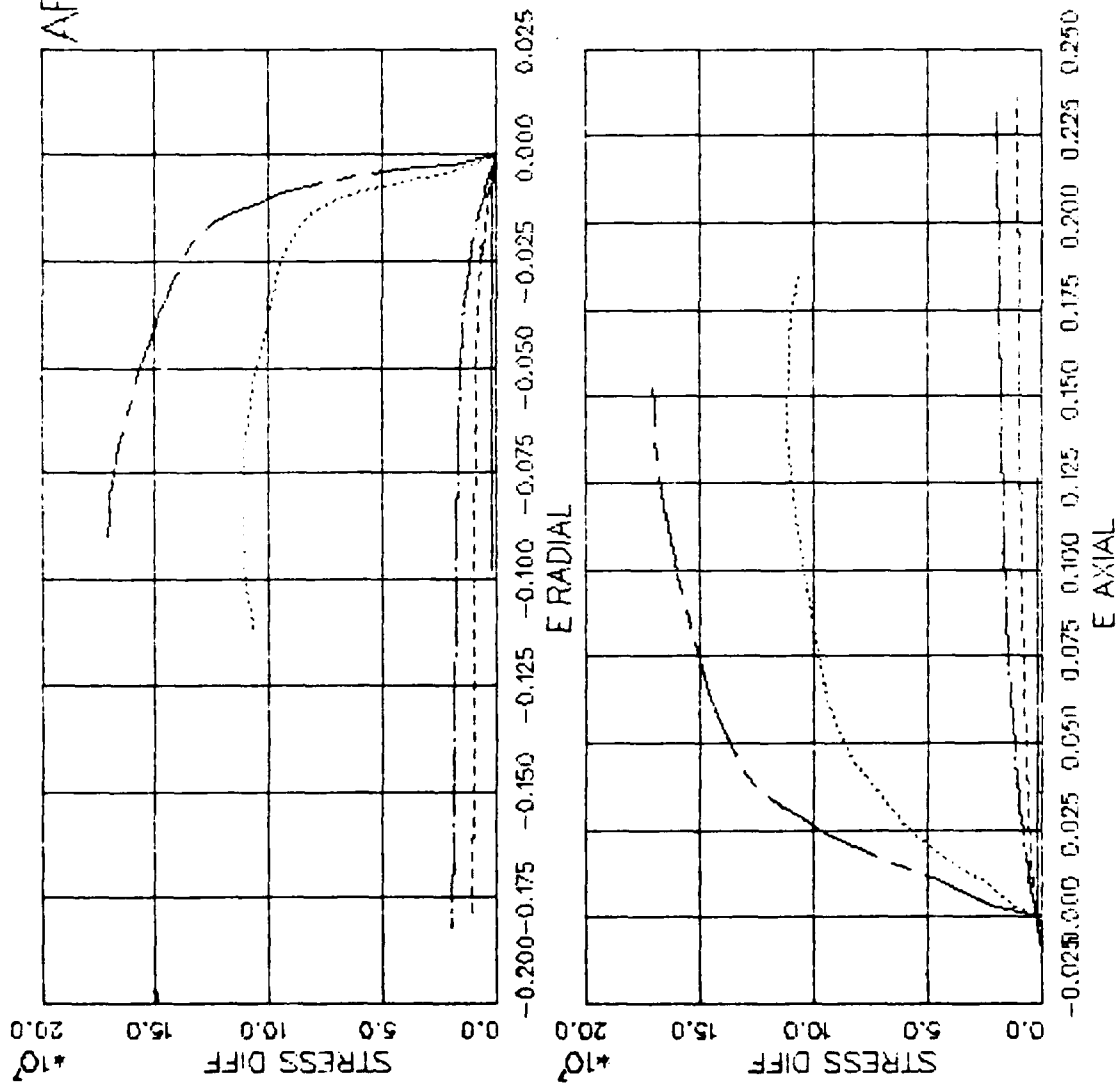
FIGURE K.9 ARA MODEL PARAMETER FIT — EXPANSIVE PLASTIC STRAINS

AFOSR SOIL ELEMENT MODEL

TEST = PARAMETER FIT
MODEL = ARA1
MATL = DRYCARES—REMOLD
DATA = DRYCARESR/WES/84

LEGEND

TOTAL
ELASTIC
ELAS+COMP

S3C= 7.000*10^5
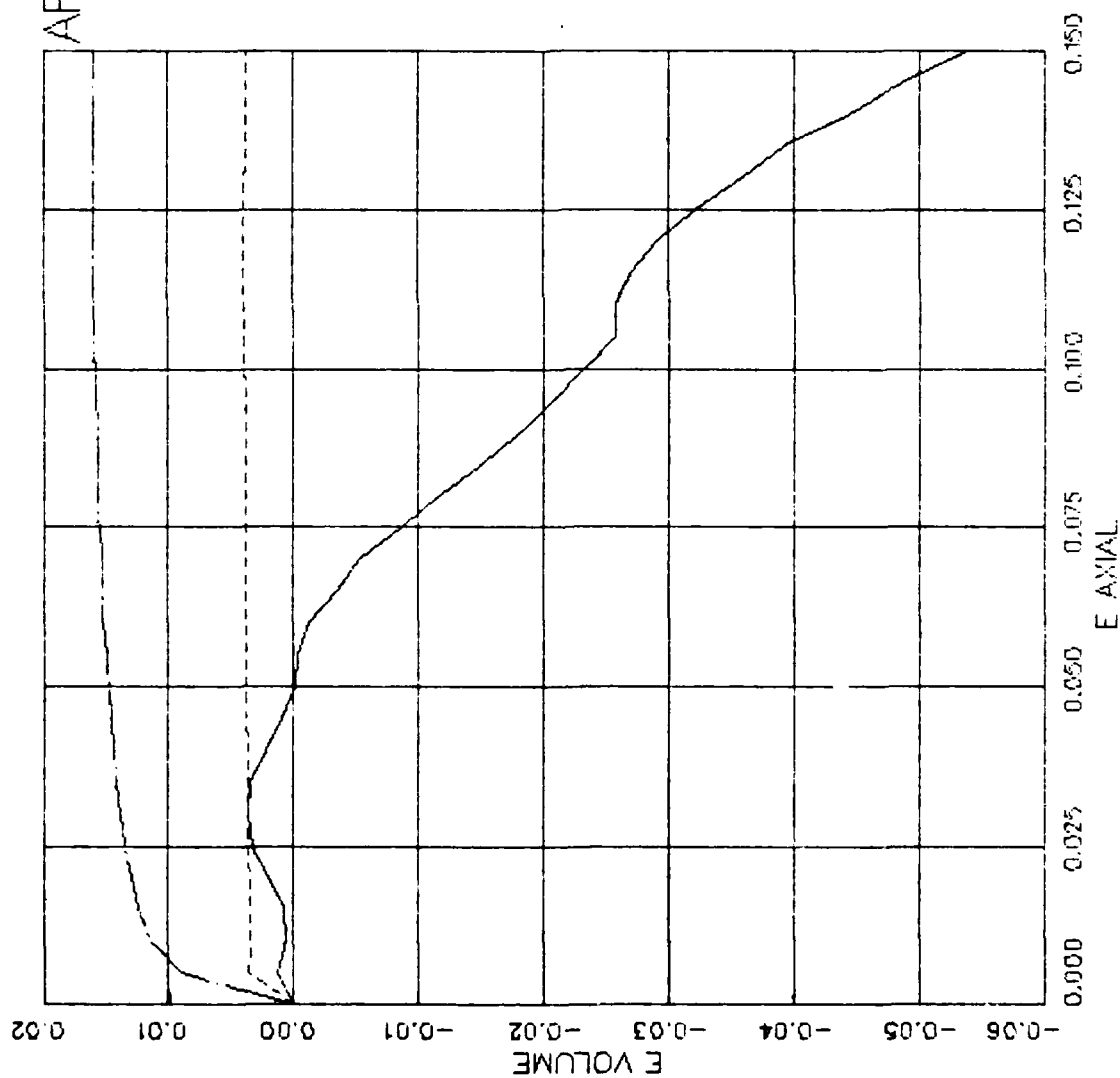
FIGURE W.10   ARA MODEL PARAMETER FIT —   VOLUME STRAIN COMPONENTS

572

AFOSR SOIL ELEMENT MODEL

TEST = PARAMETER FIT
MODEL= ARA1
MATL = DRYCARES-REMOLD
DATA = DRYCARESR/WES/84

LEGEND
TOTAL
ELASTIC
ELAS+COMP

S3C= 3.400*10^8
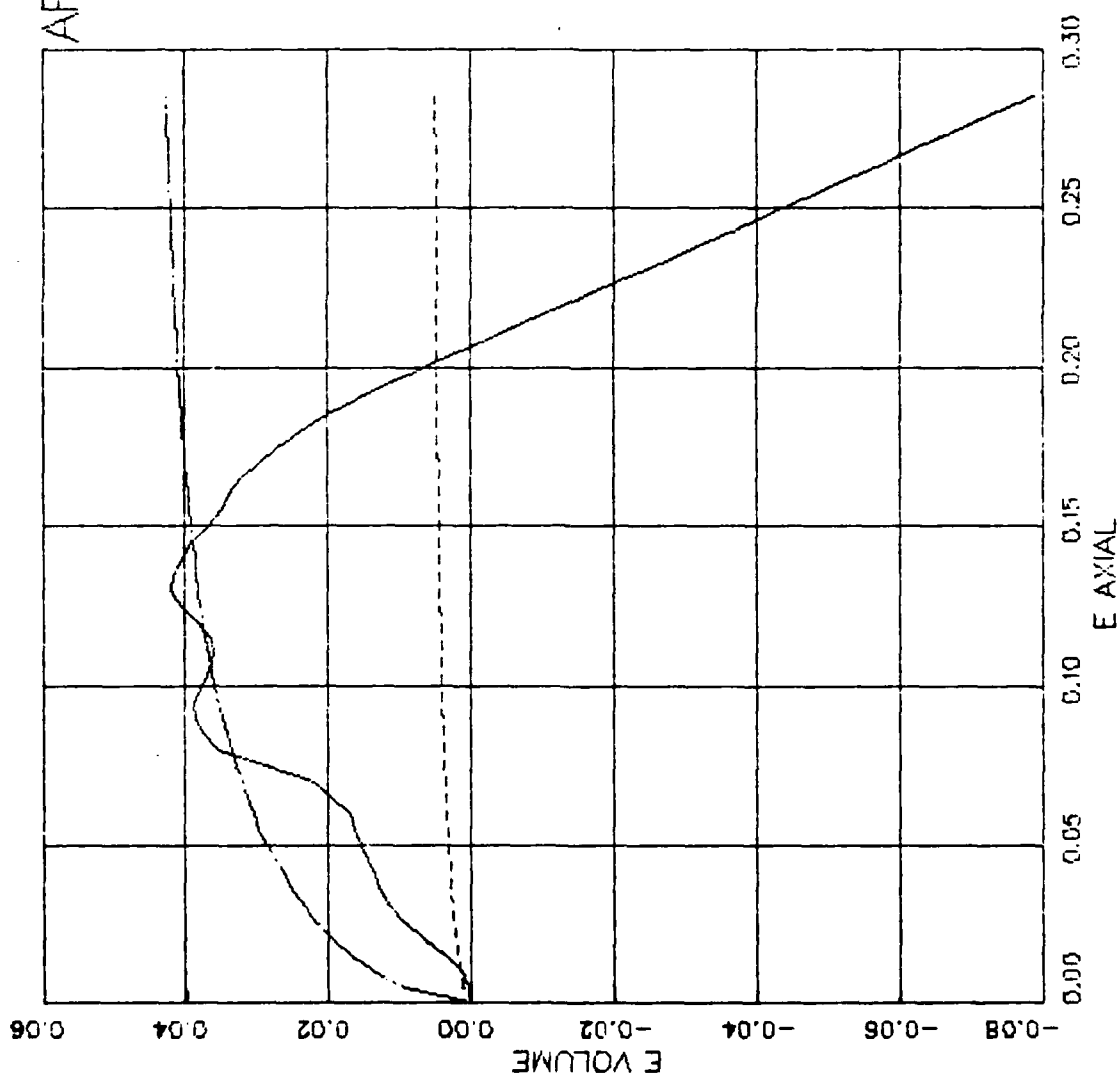
FIGURE W.11 ARA MODEL PARAMETER FIT — VOLUME STRAIN COMPONENTS

573
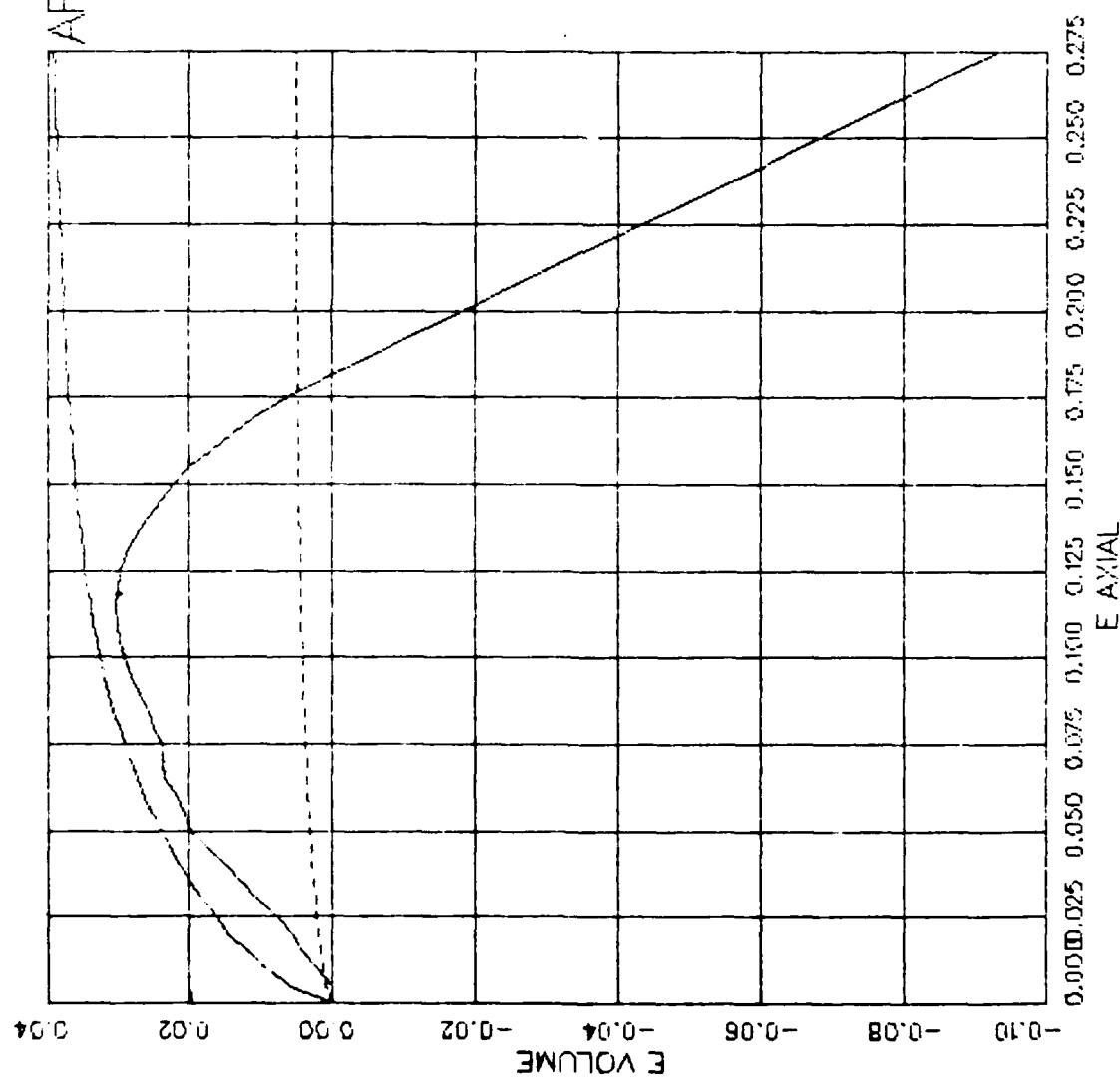
FIGURE W.12 ARA MODEL PARAMETER FIT — VOLUME STRAIN COMPONENTS

574

AFOSR SOIL ELEMENT MODEL

TEST = PARAMETER FIT
MODEL= ARA1
MATL = DRYCARES-REMOLD
DATA = DRYCARESR/WES/84

LEGEND
TOTAL
ELASTIC
ELAS+COMP

S3C= 5.880*10^7
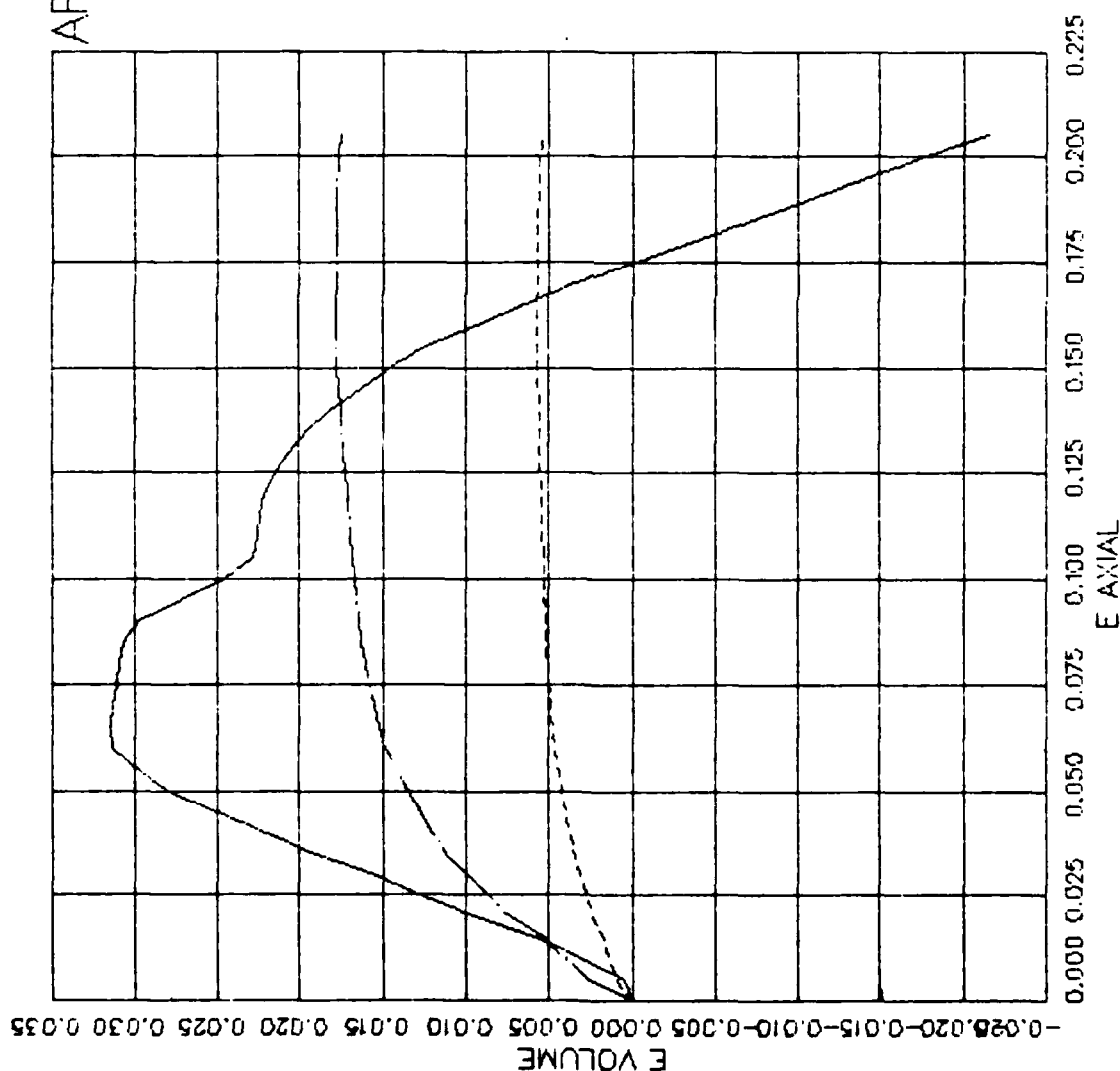
FIGURE W.13 . ARA MODEL PARAMETER FIT — VOLUME STRAIN COMPONENTS

575

AFOSR SOIL ELEMENT MODEL

TEST = PARAMETER FIT
MODEL= ARA1
MATL = DRYCARES-REMOLD
DATA = DRYCARESR/WES/84

LEGEND

TOTAL
ELASTIC
ELAS+COMP

S3C= 1.000*10⁸
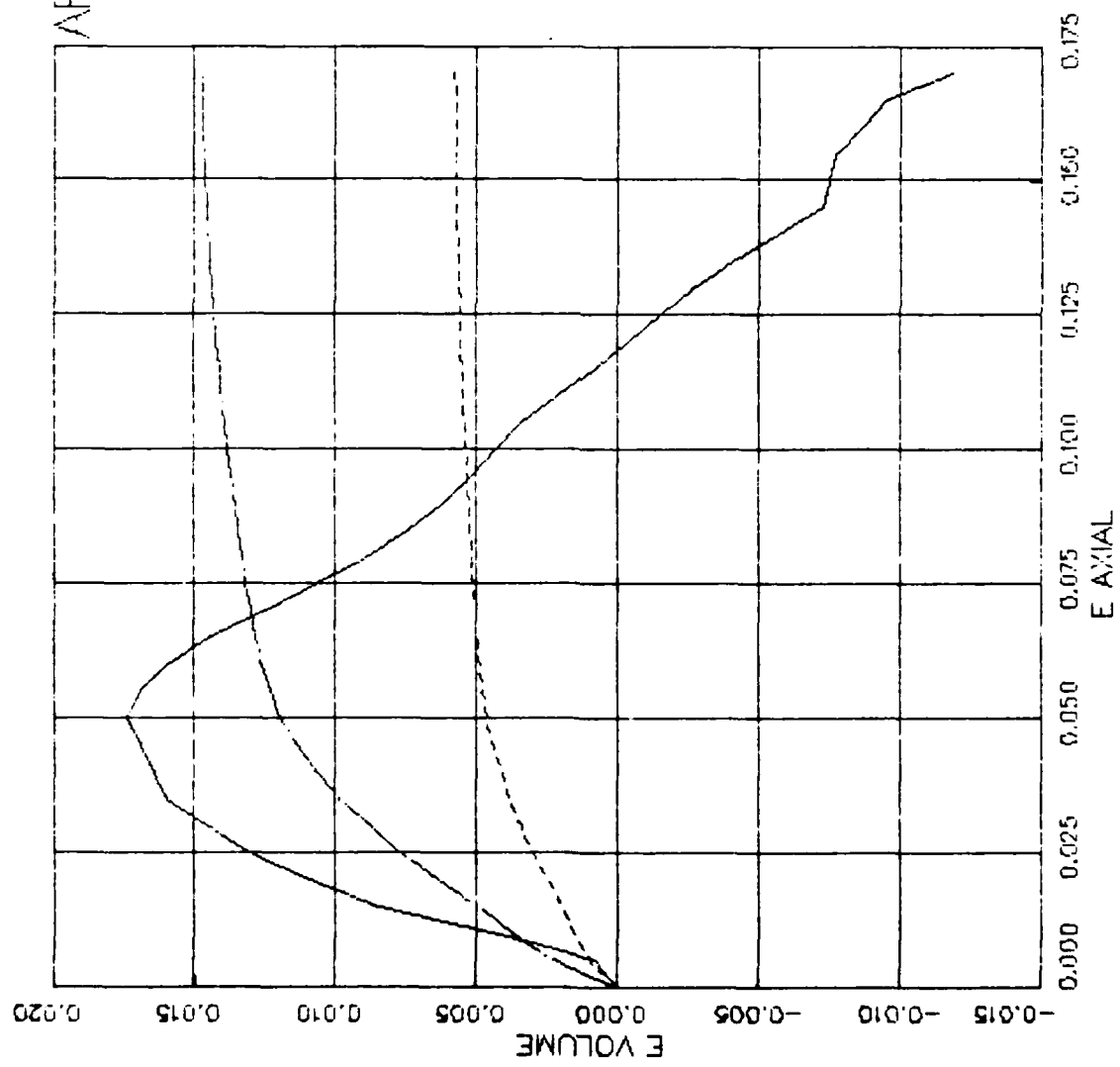
FIGURE W.14 ARA MODEL PARAMETER FIT — VOLUME STRAIN COMPONENTS

576

AFOSR SOIL ELEMENT MODEL

TEST = PARAMETER FIT
MODEL= ARA1
MATL = DRYCARES—REMOLD
DATA = DRYCARESR/WES/84

LEGEND
SIGMA3C 1
SIGMA3C 2
SIGMA3C 3
SIGMA3C 4
SIGMA3C 5
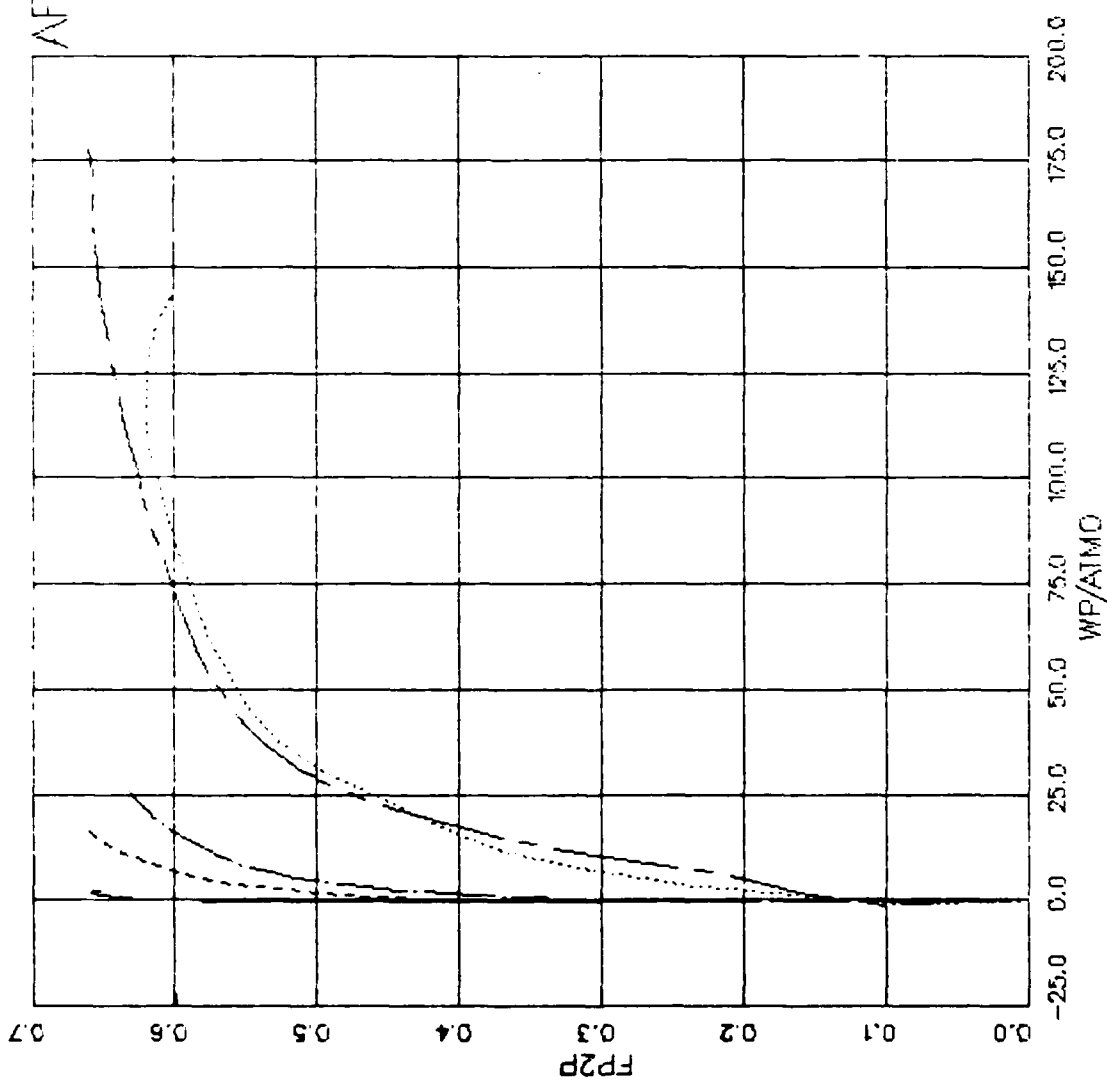
FIGURE N.15   ARA MODEL PARAMETER FIT — EXPANSIVE PLASTIC WORK

AFOSR SOIL ELEMENT MODEL

TEST = PARAMETER FIT
MODEL= ARA1
MATL = DRYCARES—REMOLD
DATA = DRYCARESR/WES/84

APBAR= $5.057*10^{-1}$
AL = $8.691*10^{-1}$
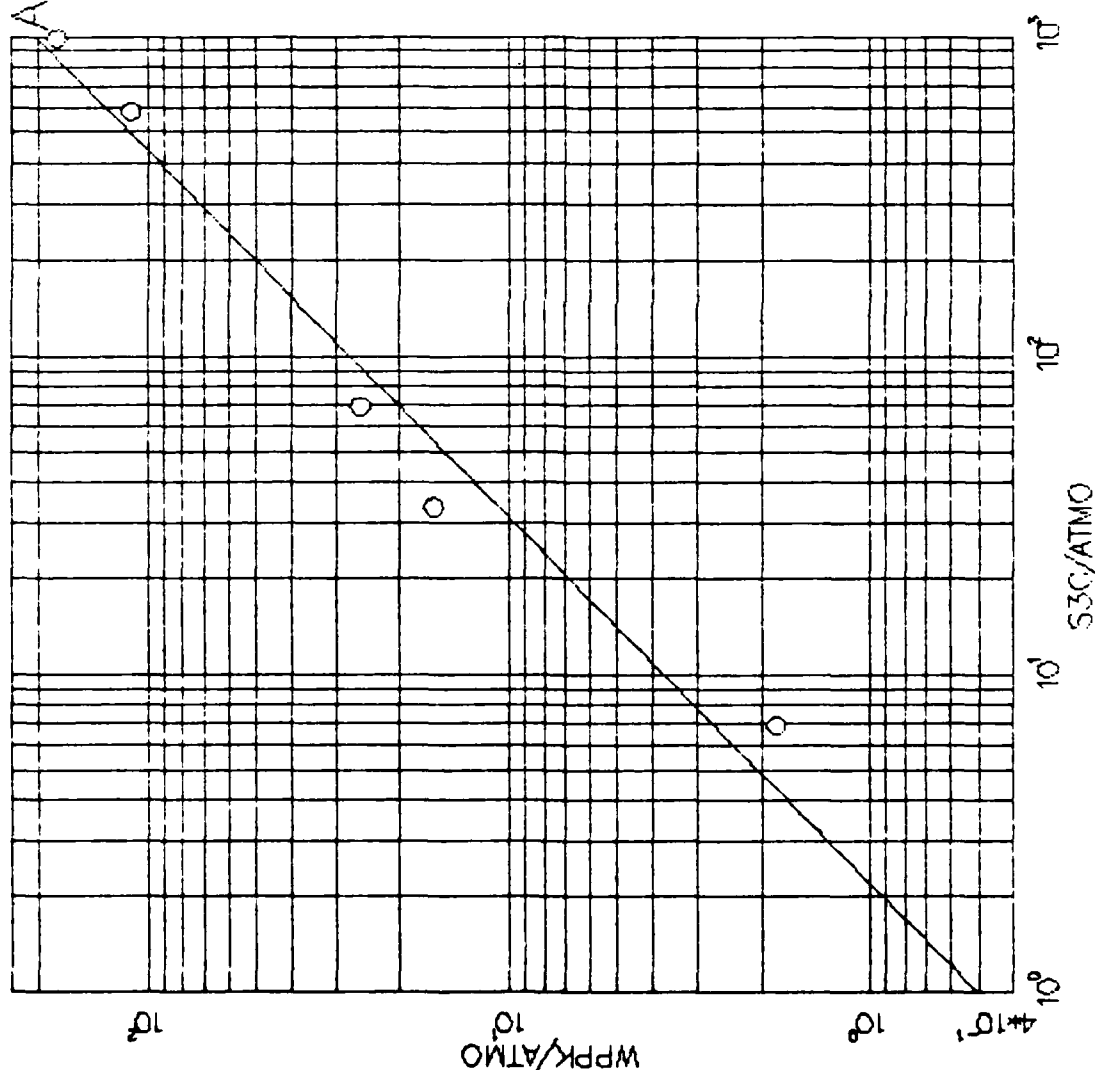
FIGURE W.16   ARA MODEL PARAMETER FIT — WP-PEAK FIT

578
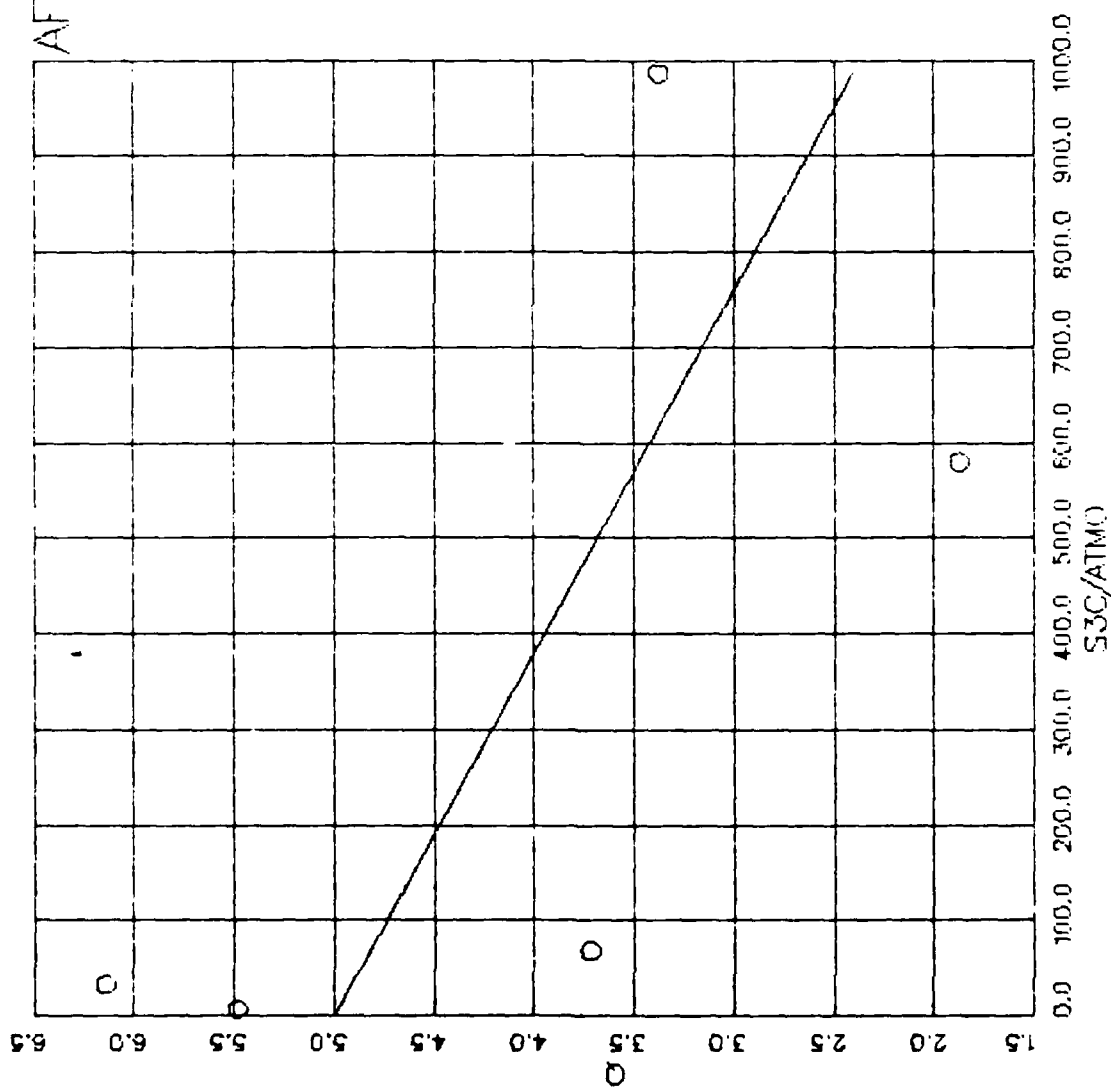
FIGURE W.17 ARA MODEL PARAMETER FIT — Q FIT (HARDENING FUNCTION SHAPE).

AFOSR SOIL ELEMENT MODEL

TEST = PARAMETER FIT
MODEL= ARA1
MATL = DRYCARES-REMOLD
DATA = DRYCARESR/WES/84

LEGEND
SIGMA3C 1
SIGMA3C 2
SIGMA3C 3
SIGMA3C 4
SIGMA3C 5
LSQFIT S3C1
LSQFIT S3C2
LSQFIT S3C3
LSQFIT S3C4
LSQFIT S3C5

$ARG= 2.182*10^{-3}$
$ASG= 1.860*10^{0}$
$ATG=-9.646*10^{-1}$
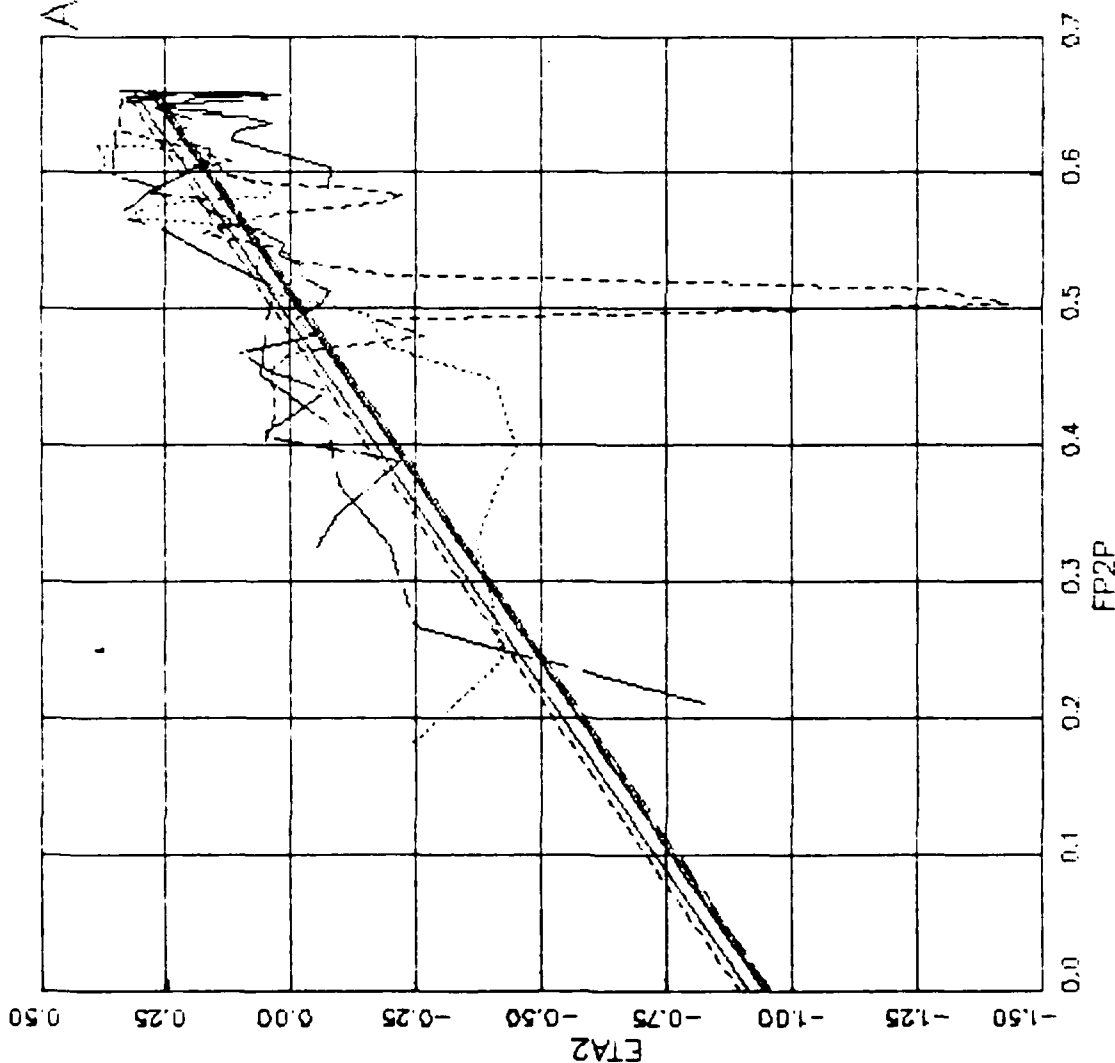
FIGURE W.18   ARA MODEL PARAMETER FIT — ETA2 VS. FP2P

AFOSR SOIL ELEMENT MODEL

TEST = PARAMETER FIT
MODEL= ARA1
MATL = DRYCARES—REMOLD
DATA = DRYCARESR/WES/84

LEGEND

FPP C AT ETA1
GP C AT ETA1
FPP E AT ETA1
GP E AT ETA1
FCP

GRP= 1.000*10^5
AR= 2.500*10^{-1}
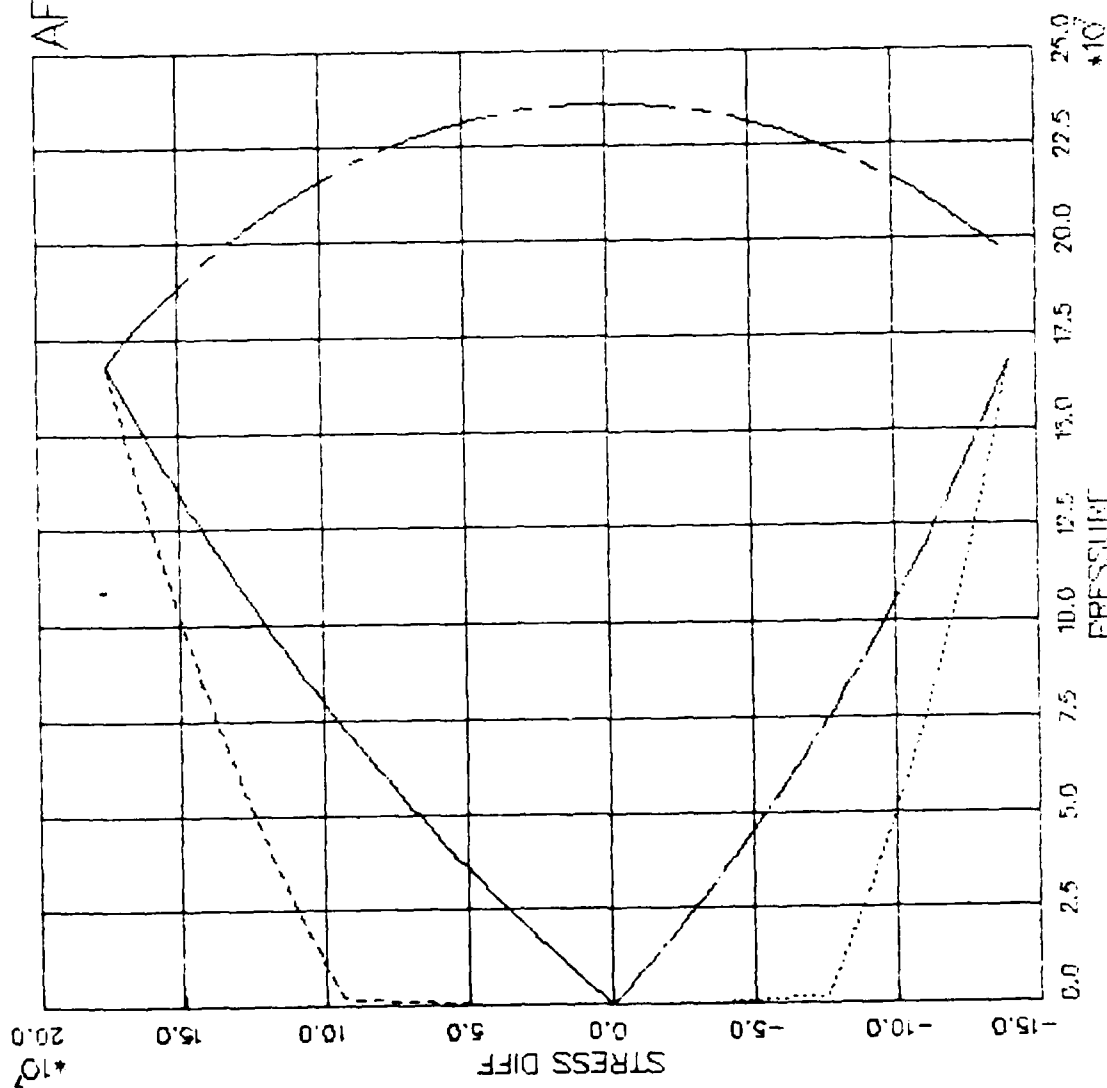
FIGURE W.19   ARA MODEL PARAMETER FIT — YIELD AND PLAS POTENTIAL SURFACE.

581

AFOSR SOIL ELEMENT MODEL

TEST = PARAMETER FIT
MODEL= ARA1
MATL = DRYCARES-REMOLD
DATA = DRYCARESR/WES/84
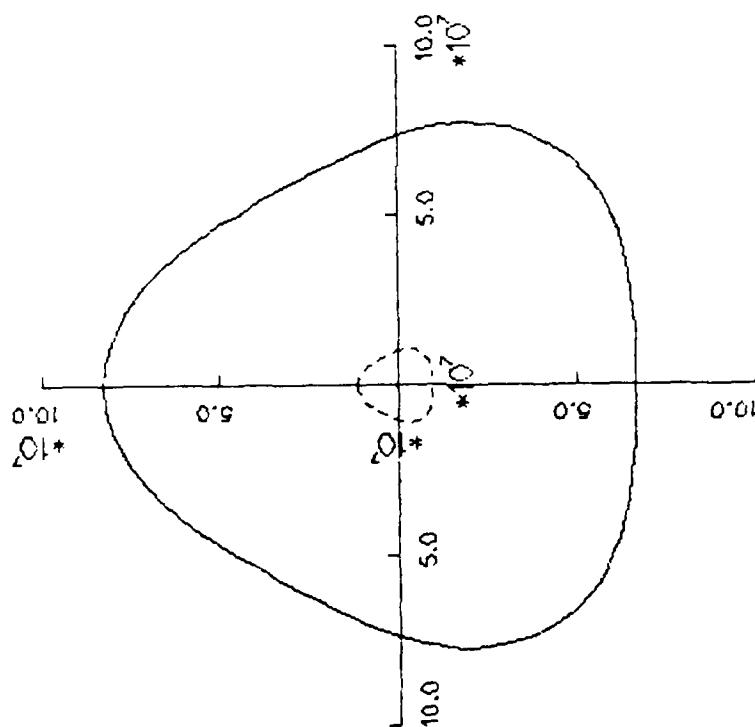
FPPK AT 1.683*10^6
FPPK AT 1.683*10^7

FIGURE W.20   ARA MODEL PARAMETER FIT — OCTAHEDRAL PLANE—FAILURE SURFACE.

FIGURE W.21   ARA MODEL EXERCISE — ISOTROPIC COMP. — PRESSURE VS. VOLUMETRIC STRAIN .

AFOSR SOIL ELEMENT MODEL

TEST = STANDARD TRIAXIAL
MODEL= ARA1
MATL = DRYCARES-REMOLD
DATA = DRYCARESR/WES/84

LEGEND

SIGMA3C= 3.4E6
_____ TEST DATA
SIGMA3C= 7.0E6
_____ TEST DATA
SIGMA3C= 58.8E6
.... TEST DATA
SIGMA3C=100.0E6
_____ TEST DATA

AXIAL STRAIN

STRESS DIFF (PA) *10⁷
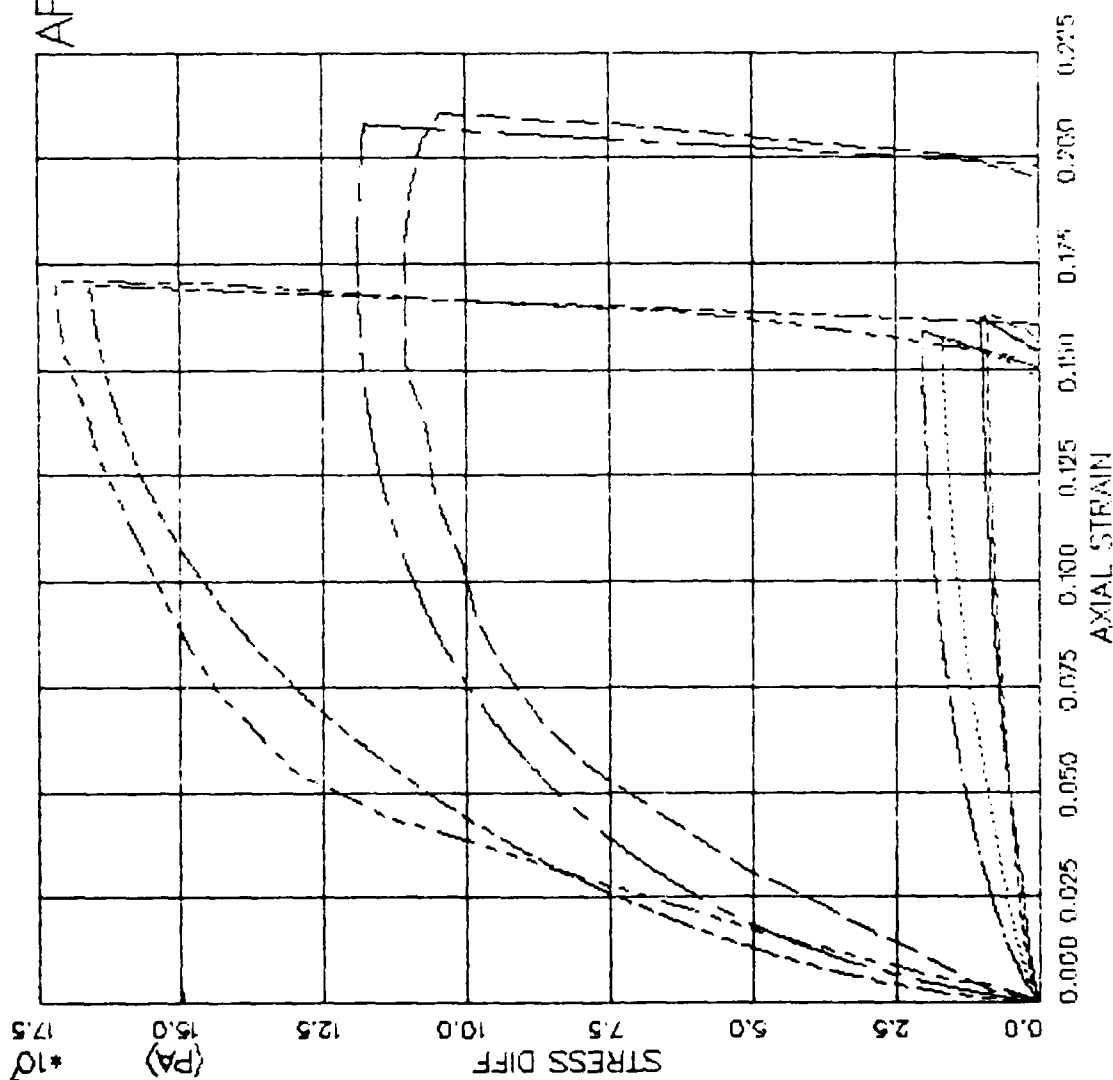
FIGURE W.22   ARA MODEL EXERCISE—TRIAXIAL COMP(UTC) – STRESS DIFF VS. AXIAL STRAIN

584

AFOSR SOIL ELEMENT MODEL

TEST = STANDARD TRIAXIAL
MODEL= ARA1
MATL = DRYCARES-REMOLD
DATA = DRYCARESR/WES/84

LEGEND

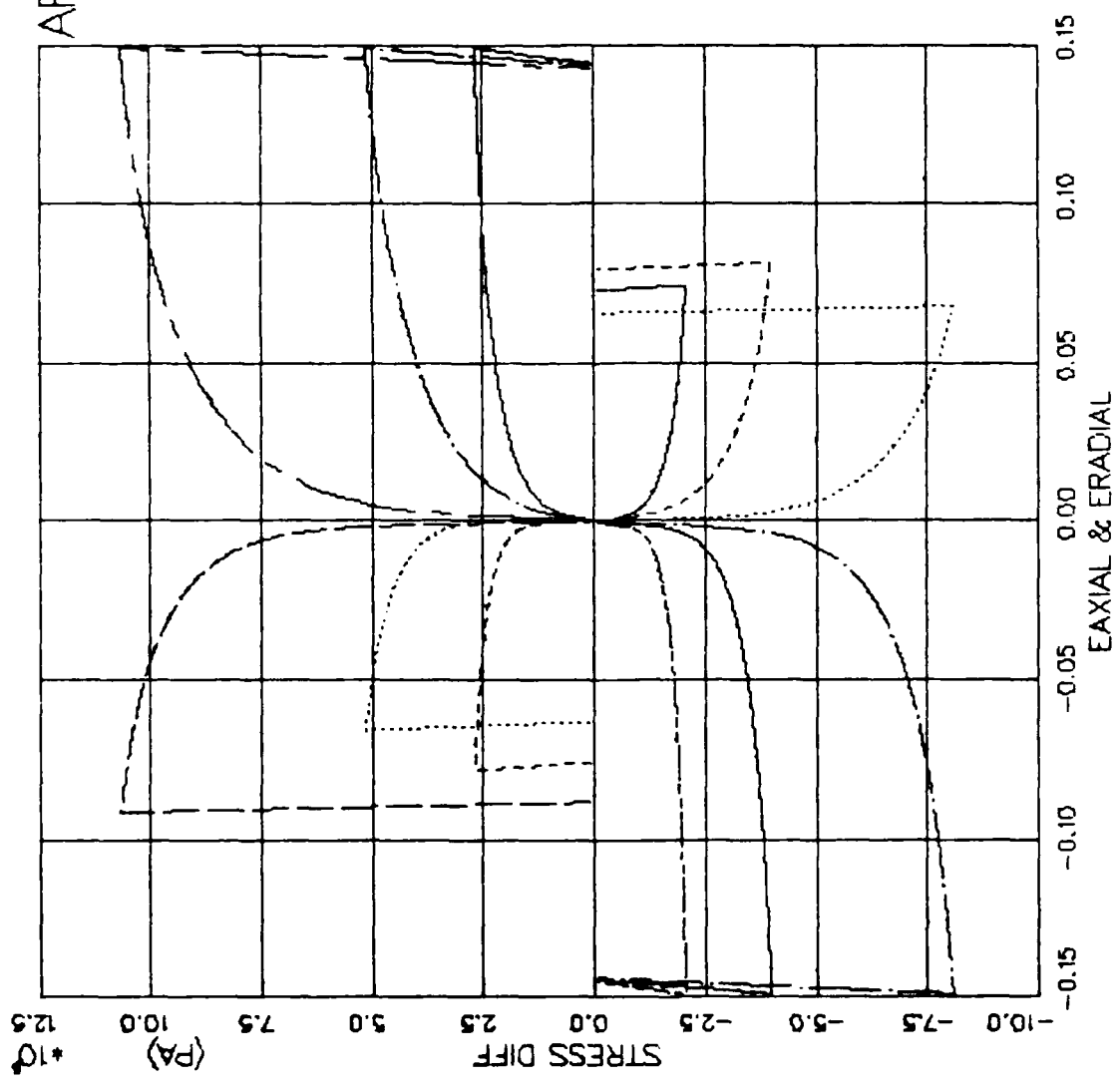SIGMA3C= 3.4E6
SIGMA3C= 7.0E6
SIGMA3C= 58.8E6
SIGMA3C=100.0E6
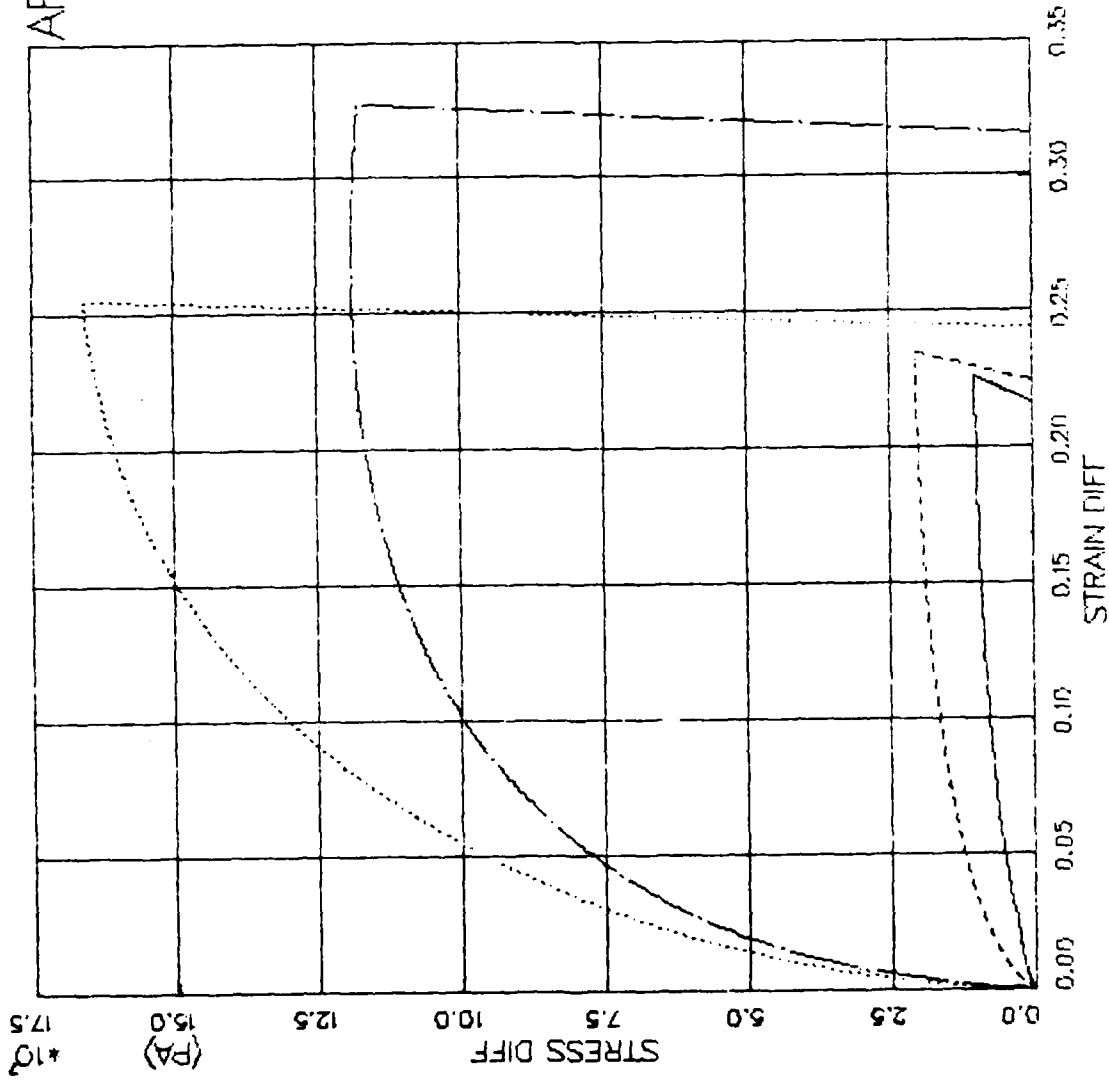
FIGURE W.23   ARA MODEL EXERCISE—TRIAXIAL COMP(CTC) — STRESS DIFF VS. STRAIN DIFF

AFOSR SOIL ELEMENT MODEL

TEST = STANDARD TRIAXIAL
MODEL= ARA1
MATL = DRYCARES—REMOLD
DATA = DRYCARESR/WES/84

LEGEND
SIGMA3C= 3.4E6
TEST DATA
SIGMA3C= 7.0E6
TEST DATA
SIGMA3C= 58.8E6
TEST DATA
SIGMA3C=100.0E6
TEST DATA

AXIAL STRAIN

VOLUME STRAIN

FIGURE W.24 ARA MODEL EXERCISE—TRIAXIAL COMP(QTC) — AXIAL STRAIN VS VOLUME STRAIN

586
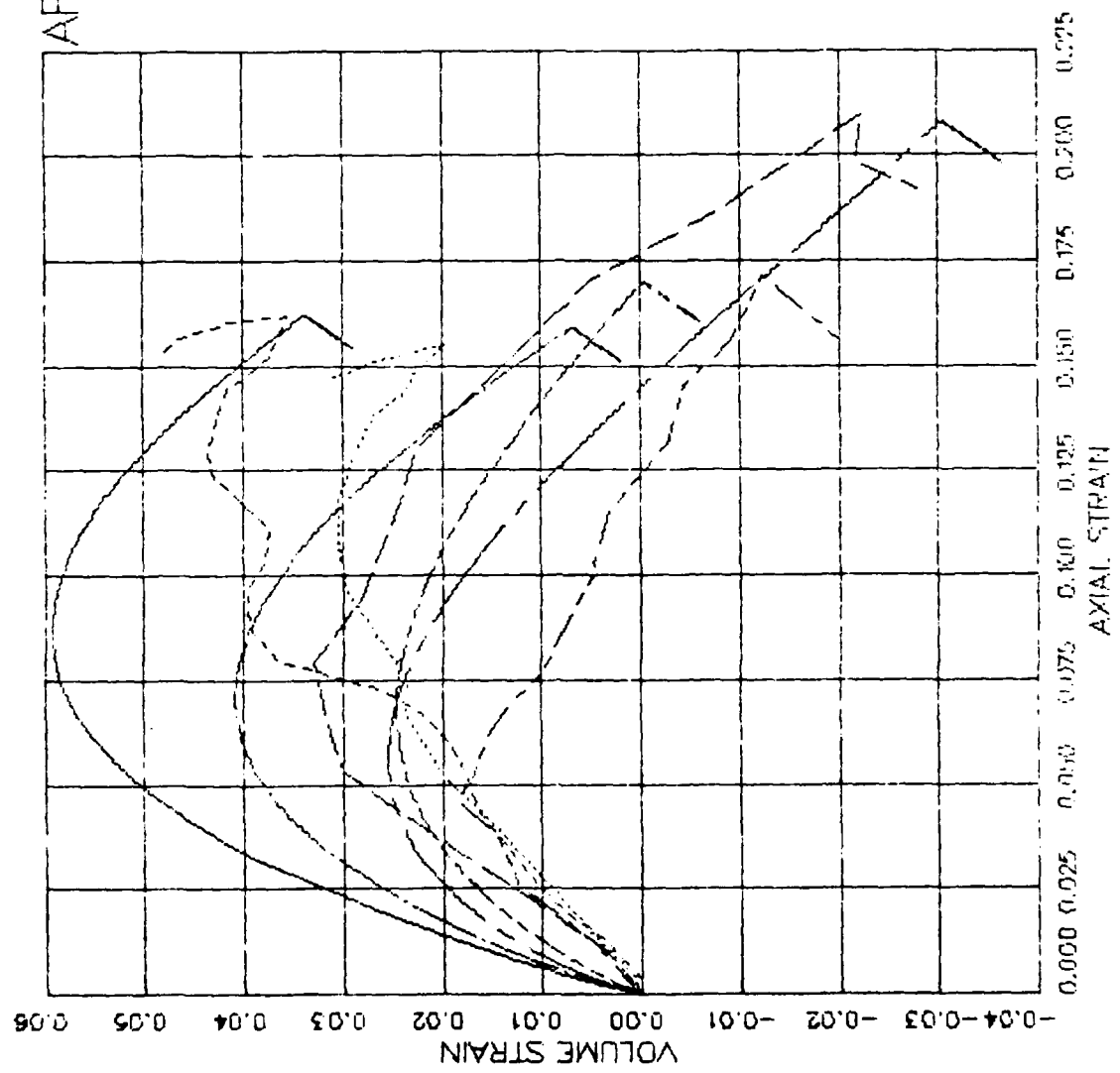
AFOSR SOIL ELEMENT MODEL

TEST = STANDARD TRIAXIAL
MODEL= ARA1
MATL = DRYCARES-REMOLD
DATA = DRYCARESR/WES/84

LEGEND

SIGMA3C= 3.4E6	
TEST DATA	
SIGMA3C= 7.0E6	
TEST DATA	
SIGMA3C= 58.8E6	
TEST DATA	
SIGMA3C=100.0E6	
TEST DATA	

FIGURE W.25   ARA MODEL EXERCISE—TRIAXIAL COMP(CTC) – PRESSURE VS. VOLUMETRIC STRAIN

587

AFOSR SOIL ELEMENT MODEL

TEST = STANDARD TRIAXIAL TEST
MODEL= ARA1
MATL = DRYCARES—REMOLD
DATA = DRYCARESR/WES/84

LEGEND
S3C=1.8E6
TEST DATA
S3C=3.5E6
TEST DATA
S3C=7.1E6
TEST DATA
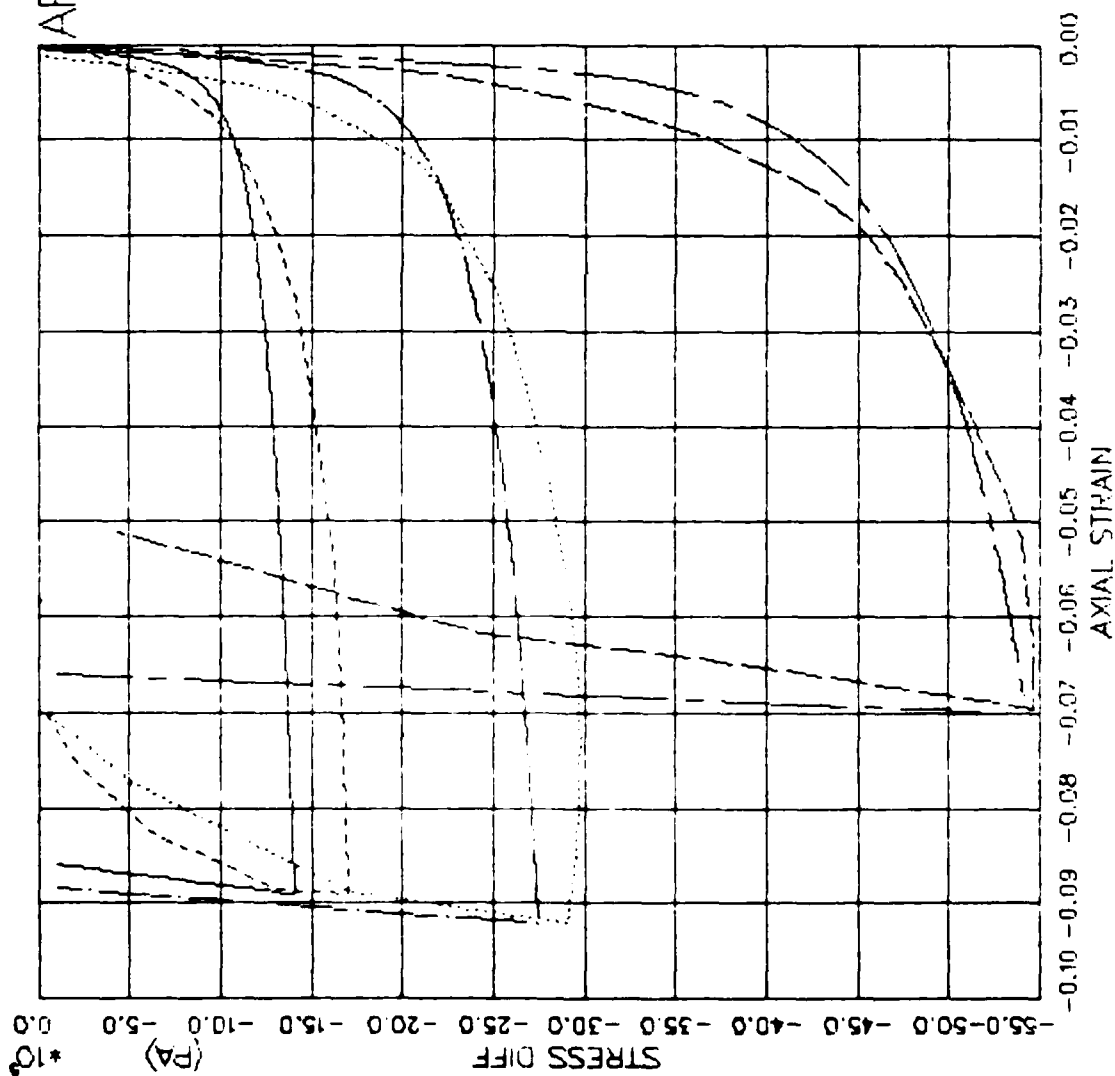
FIGURE W.26   ARA MODEL EXERCISE—TRIAXIAL EXTEN(CTE) — STRESS DIFF VS. AXIAL STRAIN
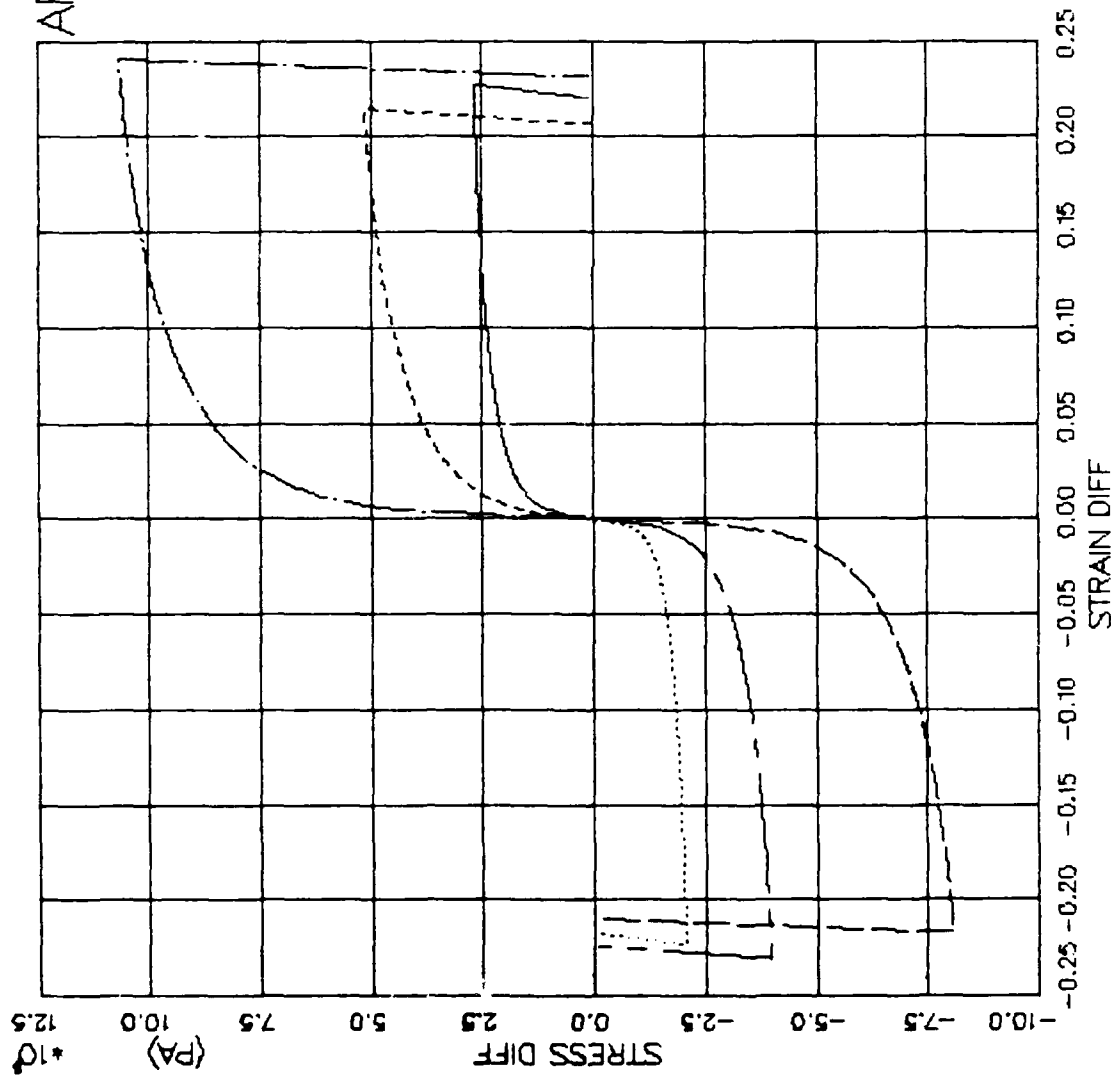
588
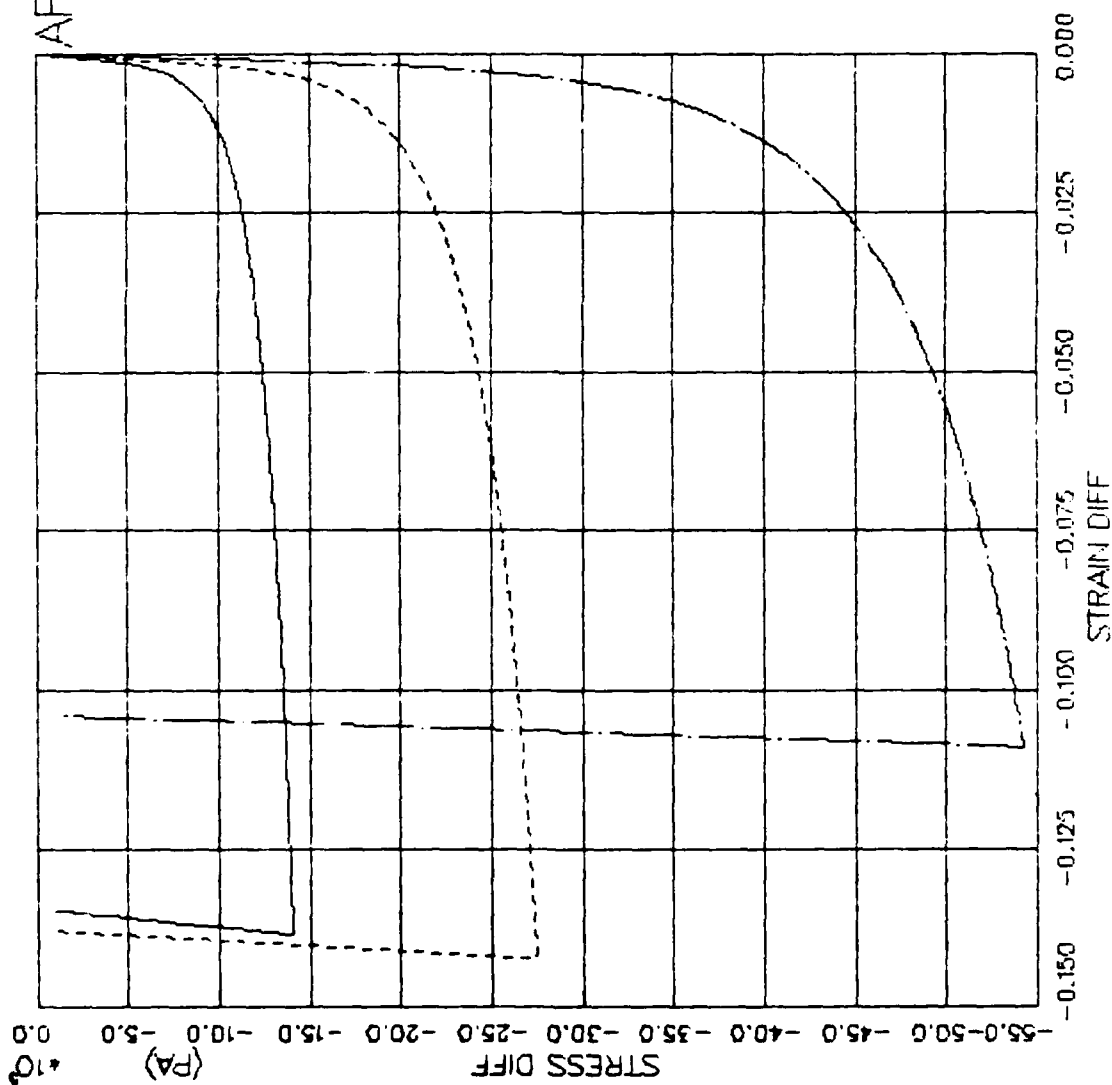
FIGURE W.27 ARA MODEL EXERCISE—TRIAXIAL EXTEN(CTE) — STRESS DIFF VS. STRAIN DIFF

589

AFOSR SOIL ELEMENT MODEL

TEST = STANDARD TRIAXIAL TEST
MODEL= ARA1
MATL = DRYCARES-REMOLD
DATA = DRYCARESR/WES/84

LEGEND
S3C=1.8E6
TEST DATA
S3C=3.5E6
TEST DATA
S3C=7.1E6
TEST DATA
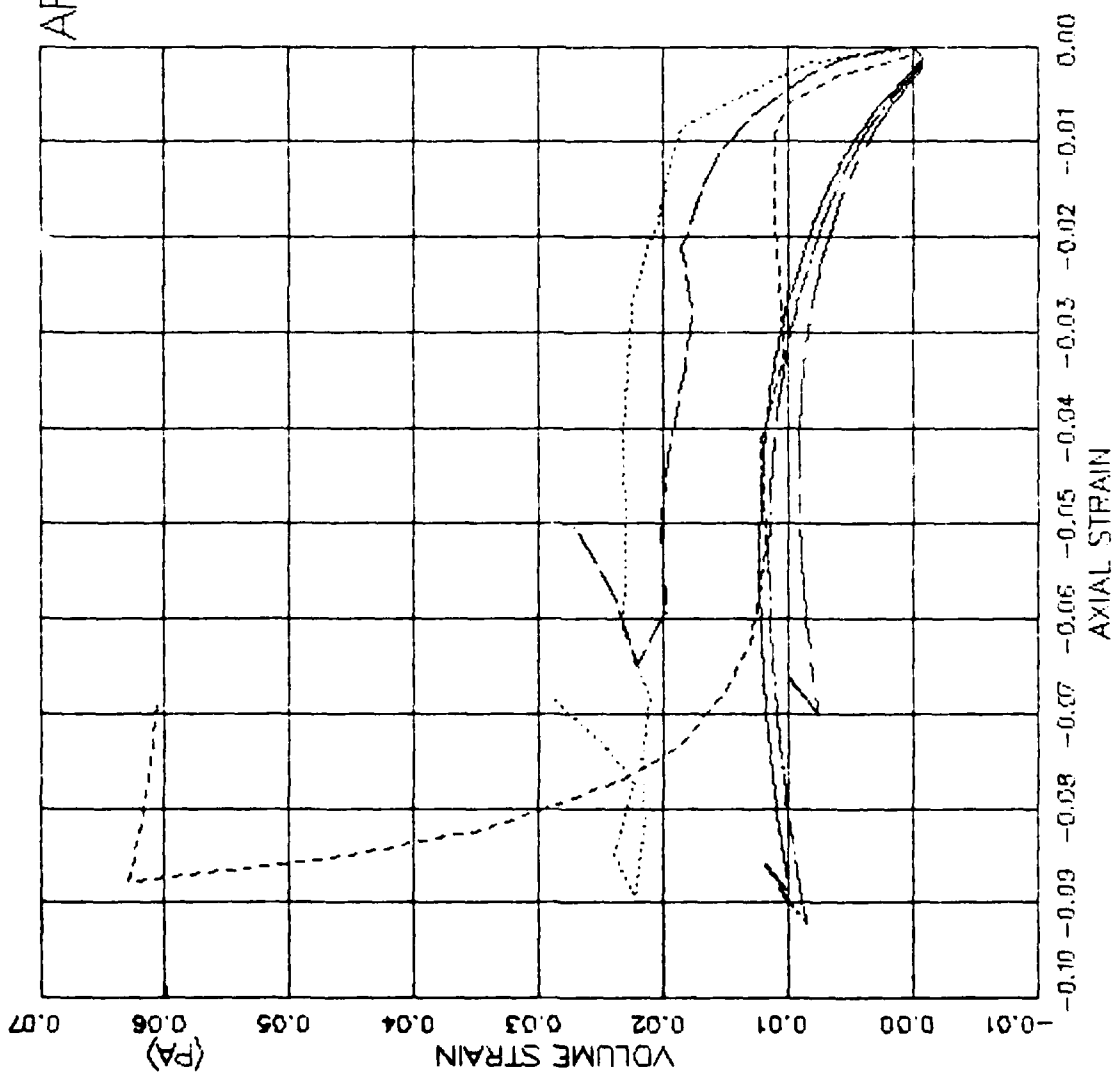
FIGURE W.28   ARA MODEL EXERCISE—TRIAXIAL EXTEN(CTE) — AXIAL STRAIN VS VOLUME STRAIN

AFOSR SOIL ELEMENT MODEL

TEST = STANDARD TRIAXIAL TEST
MODEL= ARA1
MATL = DRYCARES-REMOLD
DATA = DRYCARESR/WES/84

LEGEND
S3C=1.8E6
S3C=3.5E6
S3C=7.1E6
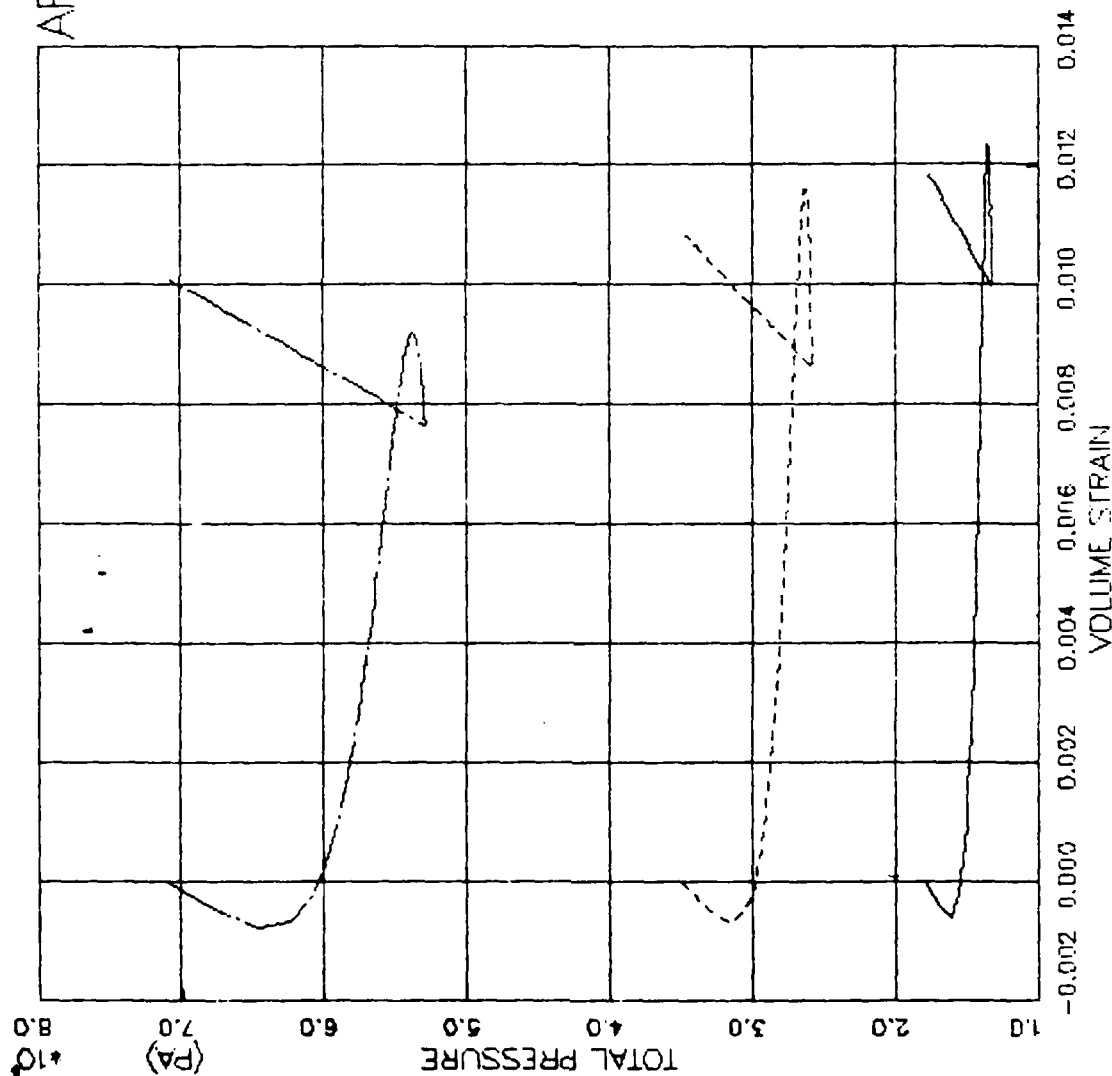
FIGURE W.29 ARA MODEL EXERCISE—TRIAXIAL EXTEN(CTE) — PRESSURE VS. VOLUMETRIC STRAIN .

591
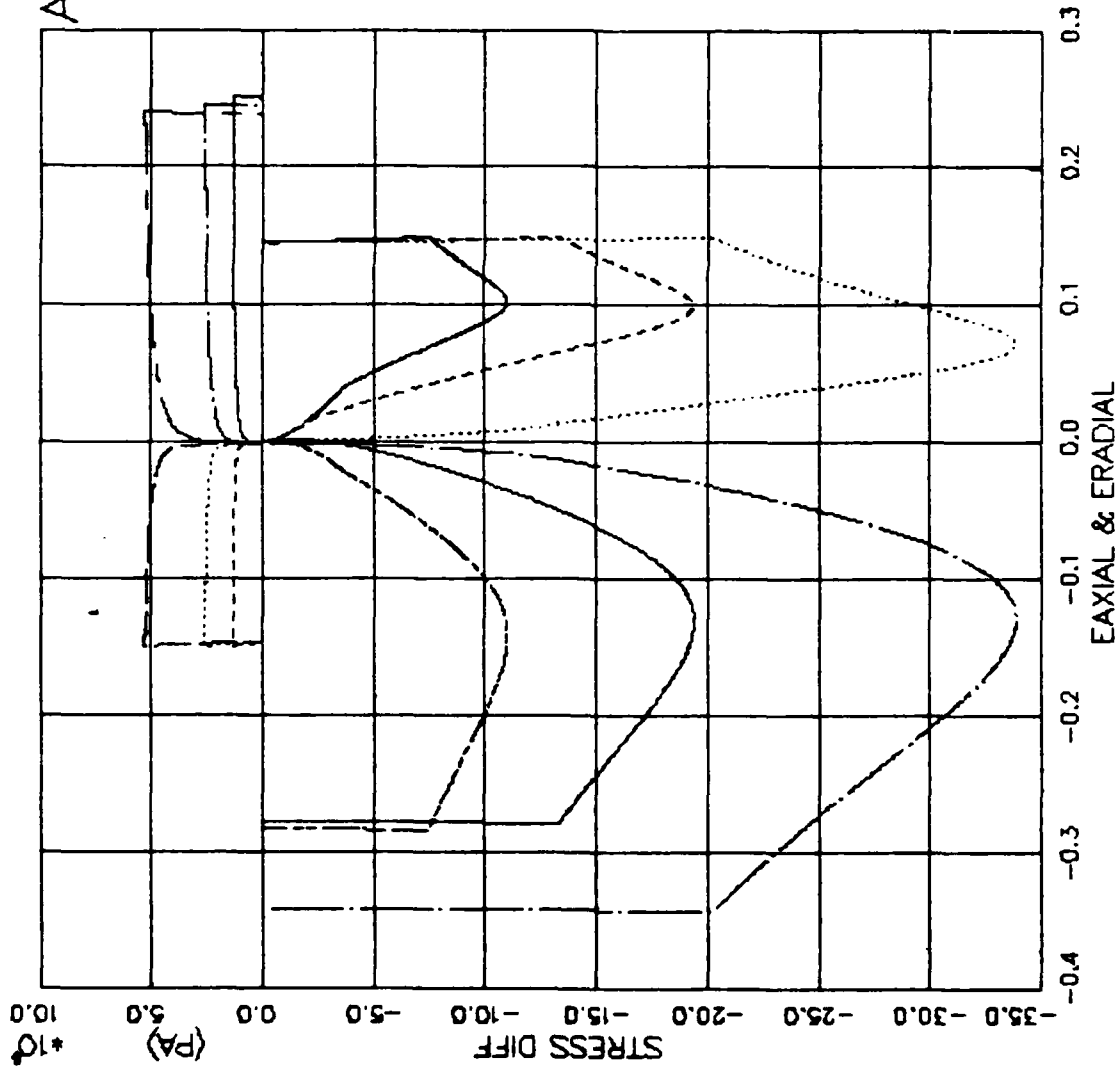
FIGURE W.30 ARA MODEL EXER—REDUCED TRIAX(RTC+RTE) — STRESS DIFF VS. STRAIN
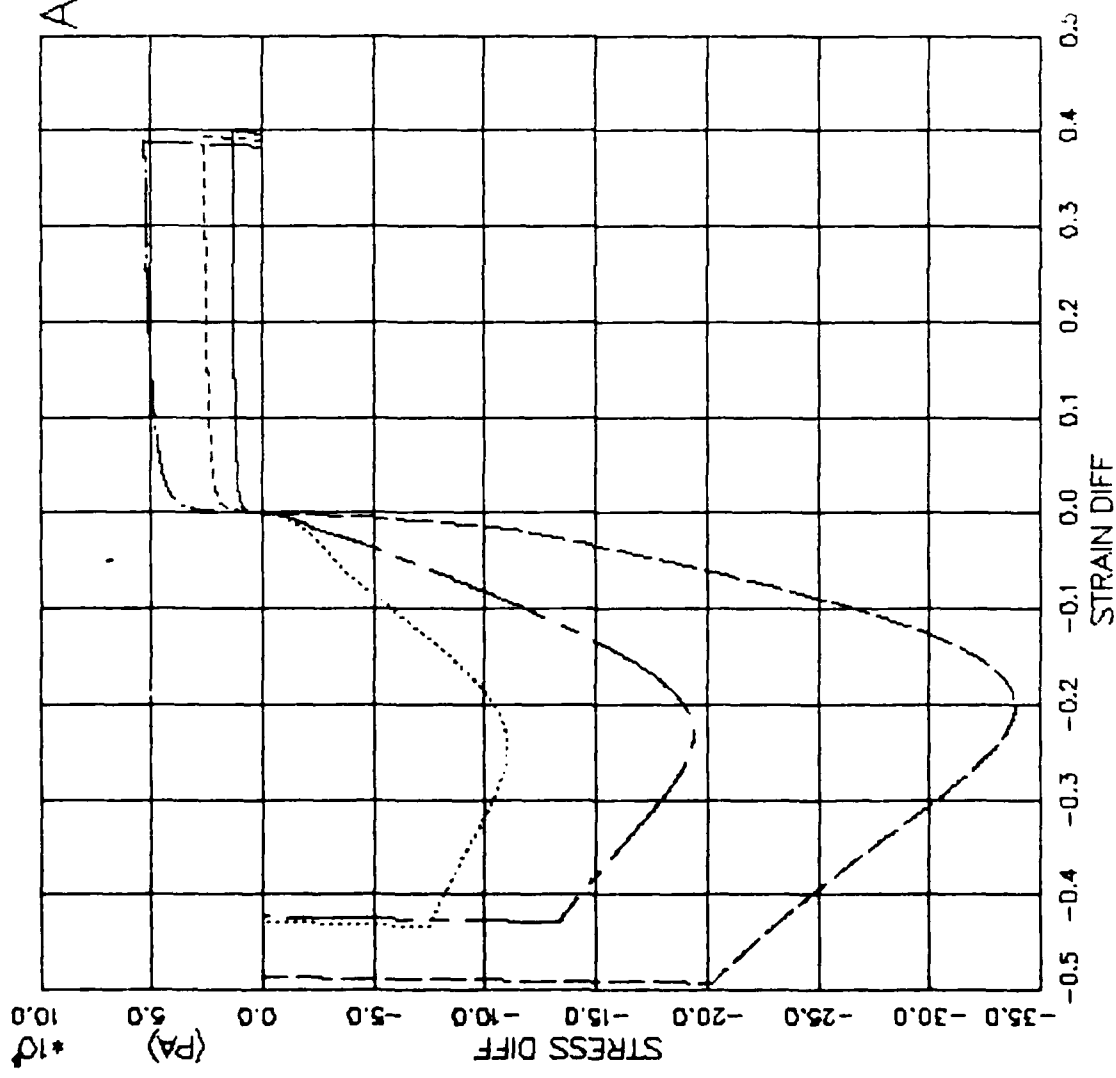
FIGURE W.31 ARA MODEL EXER-REDUCED TRIAX(RTC+RTE) - STRESS DIFF VS. STRAIN DIFF
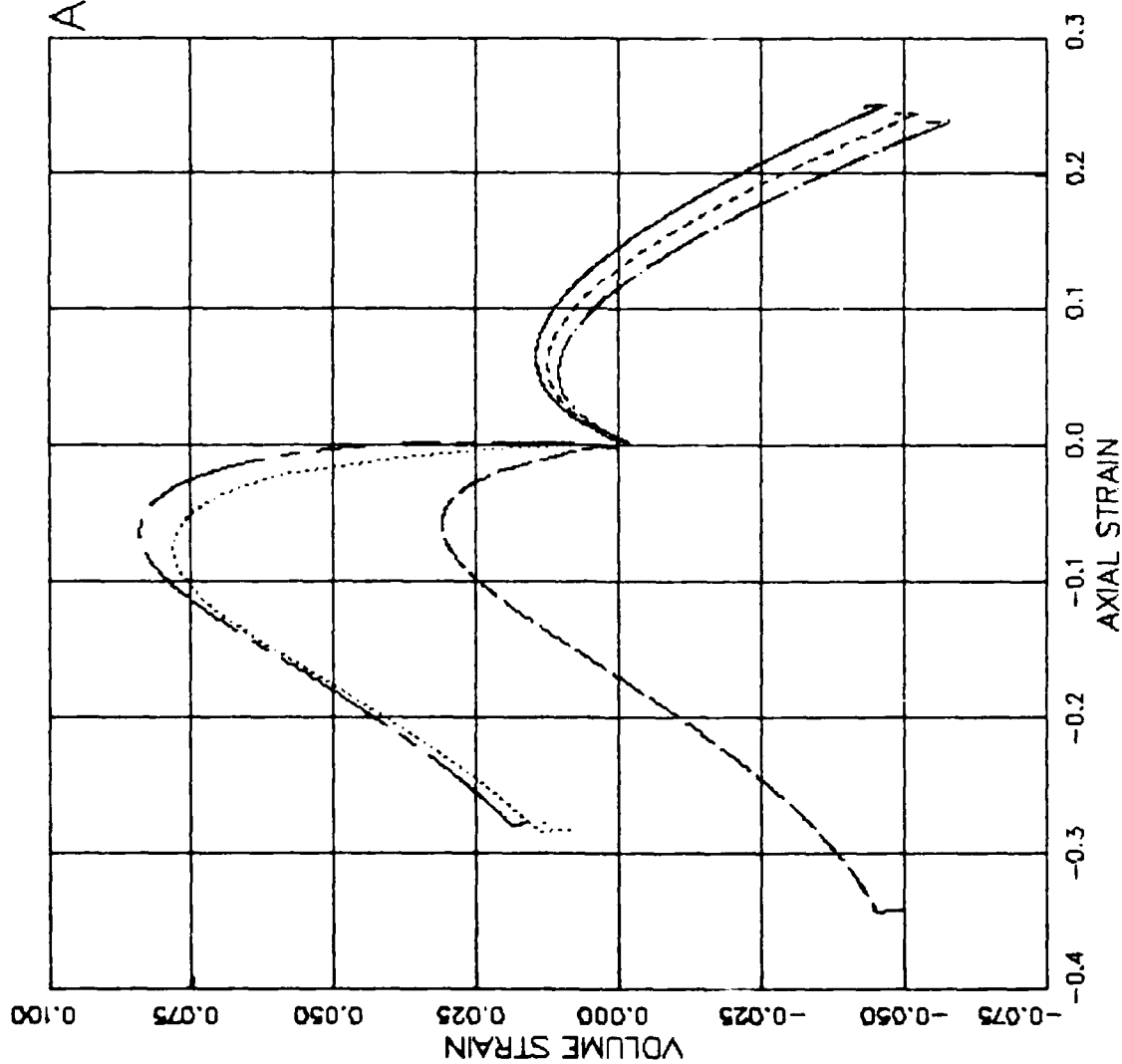
FIGURE W.32 ARA MODEL EXER-REDUCED TRIAX(RTC+RTE) - AXIAL STRAIN VS VOLUME STRAIN

AFOSR SOIL ELEMENT MODEL

TEST = STANDARD TRIAXIAL TEST
MODEL= ARA1
MATL = DRYCARES−REMOLD

LEGEND
RTC/S3C=1.8E6
RTC/S3C=3.5E6
RTC/S3C=7.1E6
RTE/S3C=1.8E6
RTE/S3C=3.5E6
RTE/S3C=7.1E6
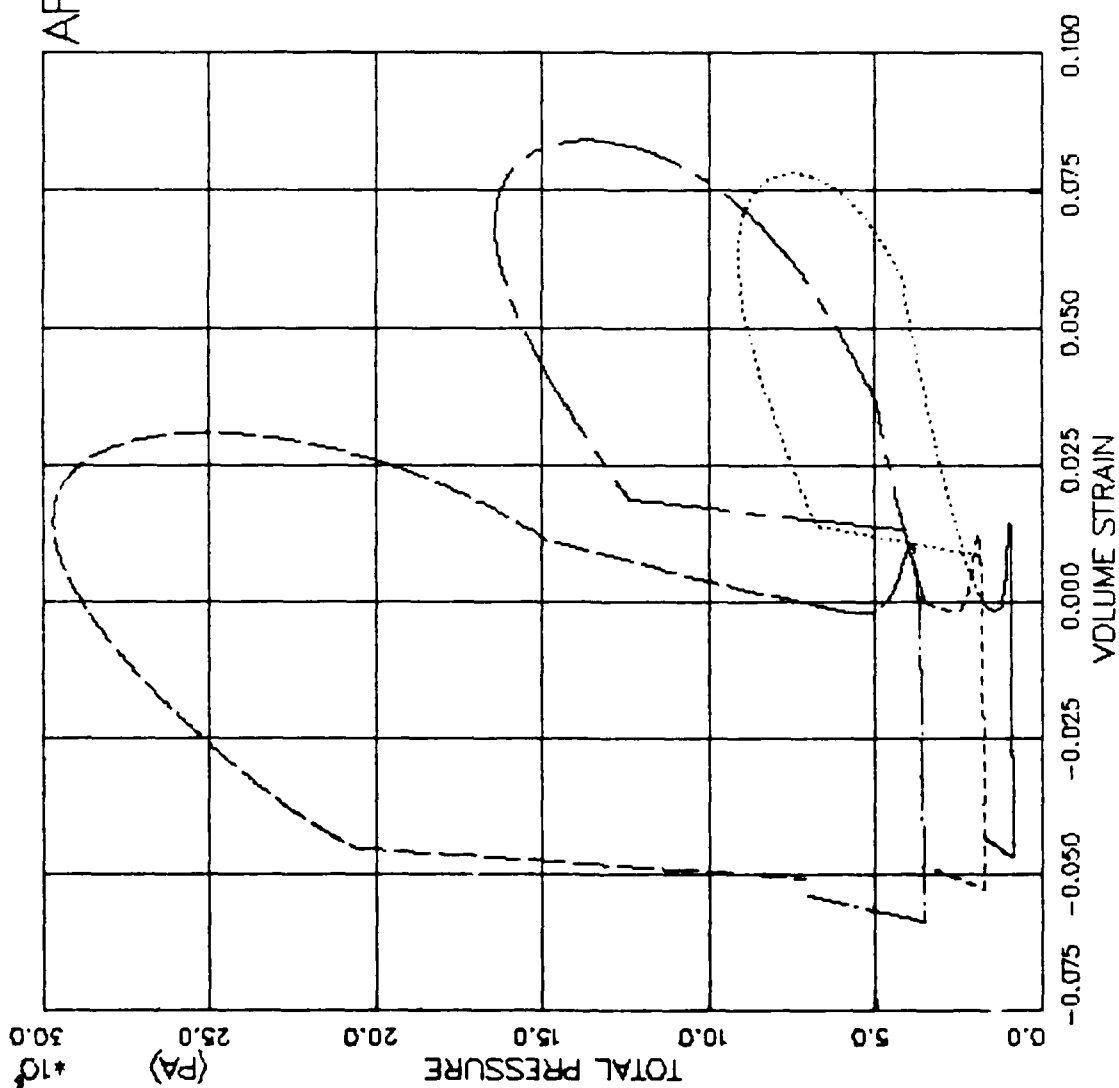
FIGURE M.33 ARA MODEL EXER−REDUCED TRIAX(RTC+RTE) − PRESSURE VS. VOLUMETRIC STRAIN

AFOSR SOIL ELEMENT MODEL

TEST = STANDARD TRIAXIAL TEST
MODEL = ARA1
MATL = DRYCARES—REMOLD

LEGEND
PSC/S3C=1.8E6
PSC/S3C=1.8E6
PSC/S3C=3.5E6
PSC/S3C=3.5E6
PSC/S3C=7.1E6
PSC/S3C=7.1E6
PSE/S3C=1.8E6
PSE/S3C=1.8E6
PSE/S3C=3.5E6
PSE/S3C=3.5E6
PSE/S3C=7.1E6
PSE/S3C=7.1E6

FIGURE W.34 ARA MODEL EXERCISE—PURE SHEAR(PSC+PSE) — STRESS DIFF VS. STRAIN

596

FIGURE W.35 ARA MODEL EXERCISE—PURE SHEAR(PSC+PSE) – STRESS DIFF VS. STRAIN DIFF

AFOSR SOIL ELEMENT MODEL

TEST = STANDARD TRIAXIAL TEST
MODEL= ARA1
MATL = DRYCARES—REMOLD

LEGEND
PSC/S3C=1.8E6
PSC/S3C=3.5E6
PSC/S3C=7.1E6
PSE/S3C=1.8E6
PSE/S3C=3.5E6
PSE/S3C=7.1E6

FIGURE M.36   ARA MODEL EXERCISE—PURE SHEAR(PSC+PSE) — AXIAL STRAIN VS VOLUME STRAIN
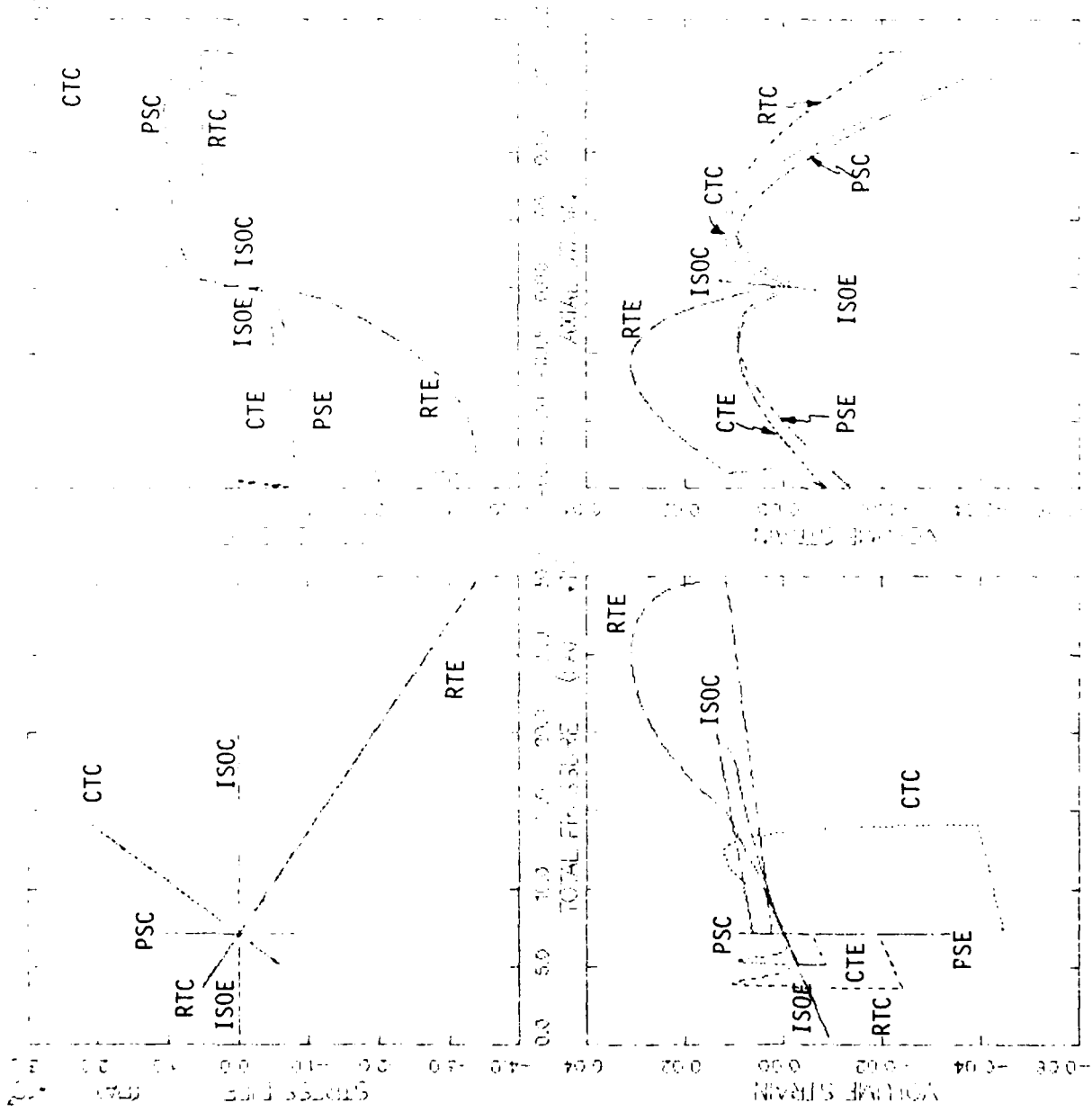
598

FIGURE W.37 . AHA MODEL ...

599
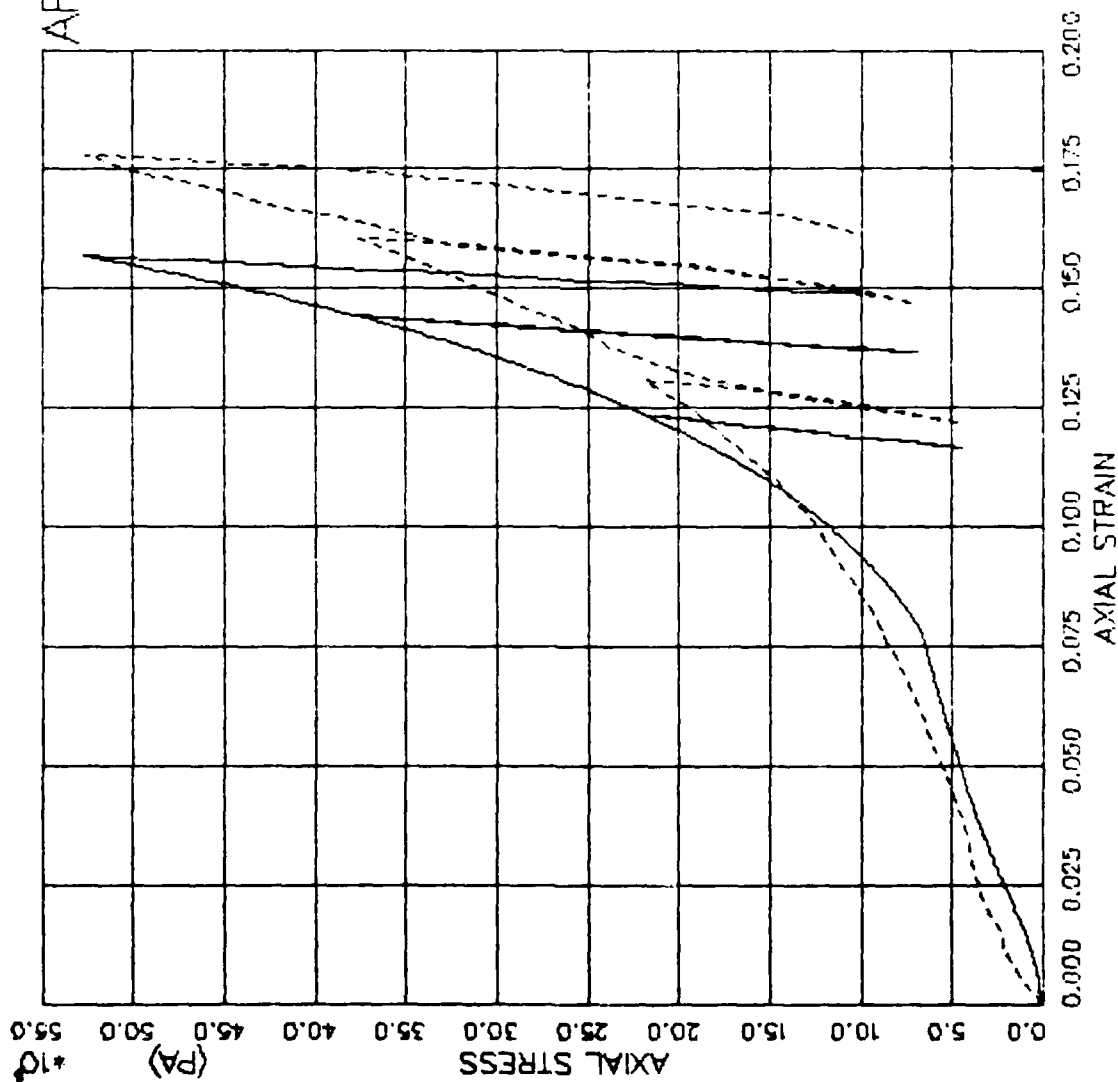
FIGURE M.38 ARA MODEL EXERCISE — UNIAXIAL STRAIN (UX○) — TOT AXL STRESS VS. AXL STRAIN .

AFOSR SOIL ELEMENT MODEL

TEST = UNIAXIAL STRAIN TEST
MODEL= ARA1
MATL = DRYCARES-REMOLD
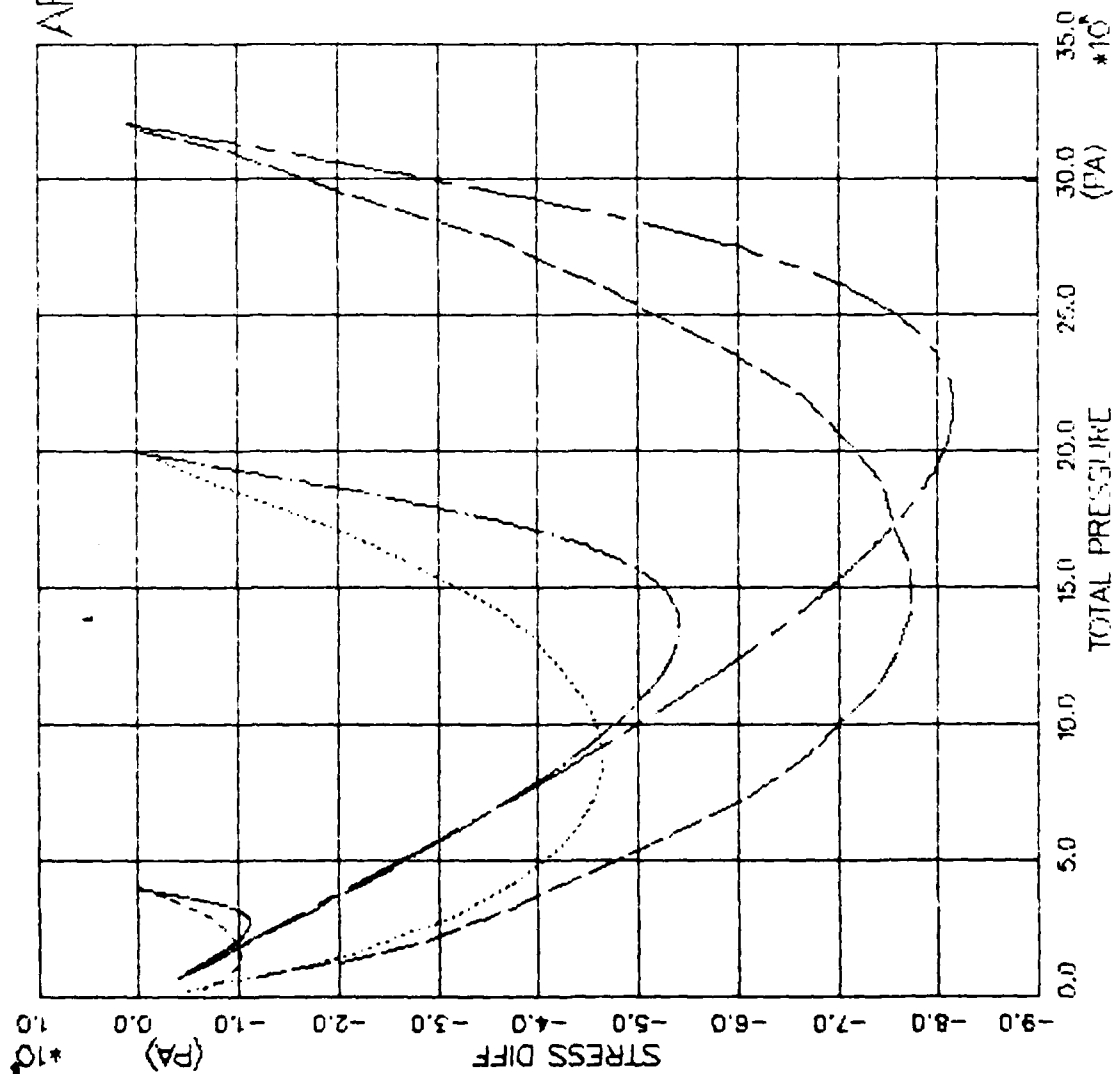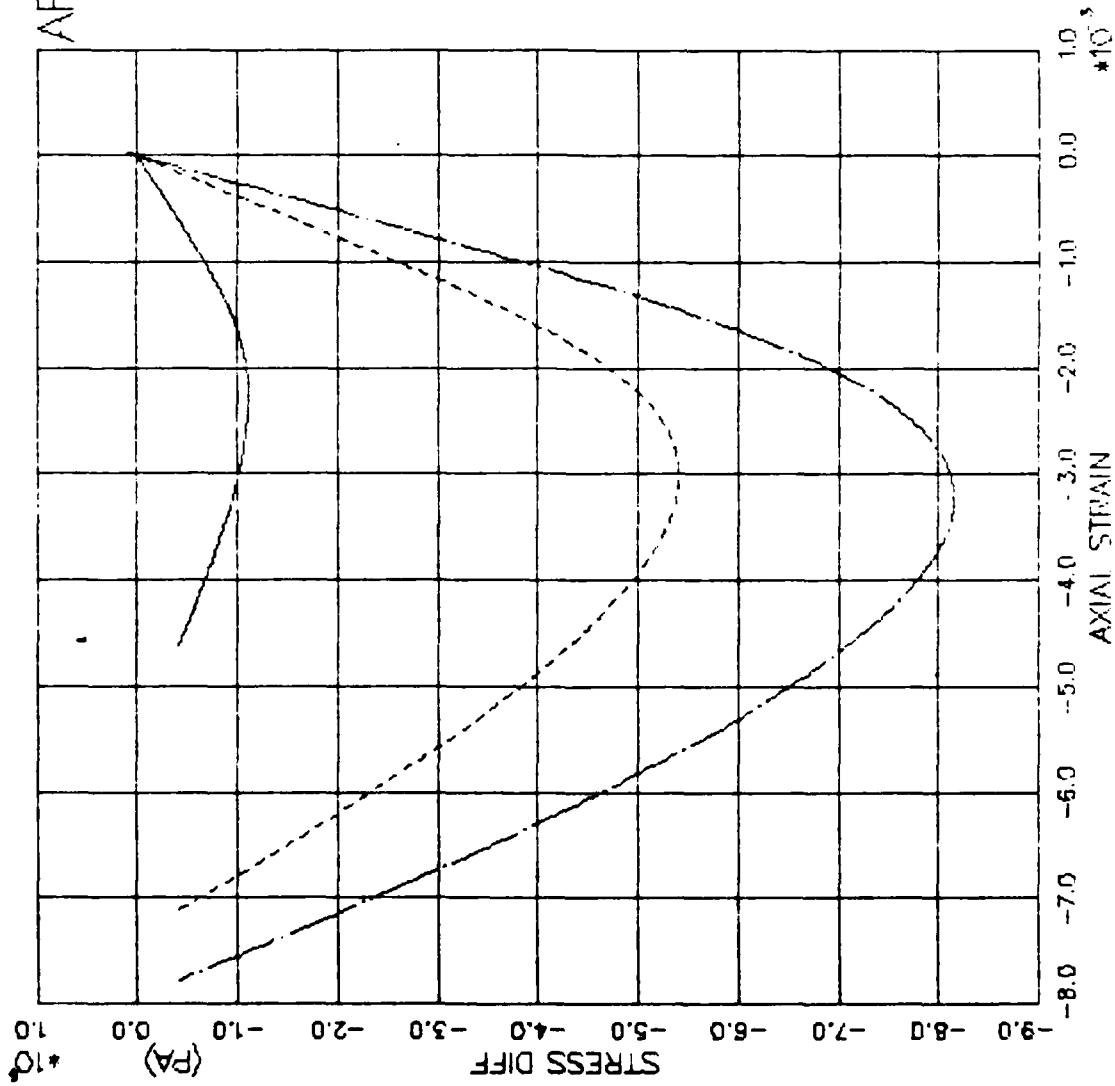DATA = DRYCARESR/WES/84

LEGEND
CALCULATION
TEST DATA

FIGURE W.39   ARA MODEL EXERCISE— UNIAXIAL STRAIN (UXC) — STRESS DIFFERENCE VS. PRESSURE

AFOSR SOIL ELEMENT MODEL

TEST = UNIAXIAL STRAIN TEST
MODEL= ARA1
MATL = DRYCARES—REMOLD
DATA = DRYCARESR/WES/84

LEGEND
CALCULATION
TEST DATA
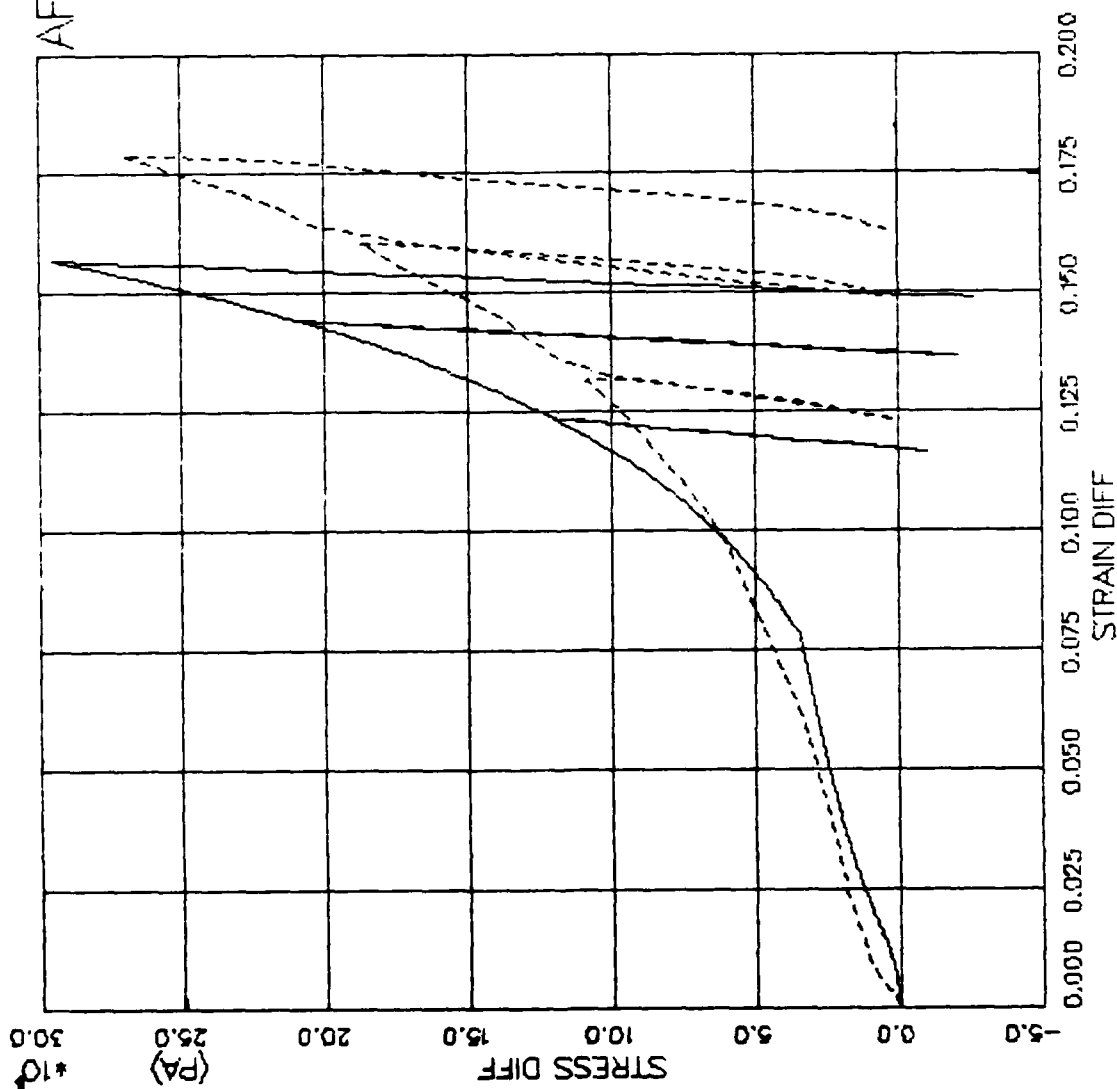
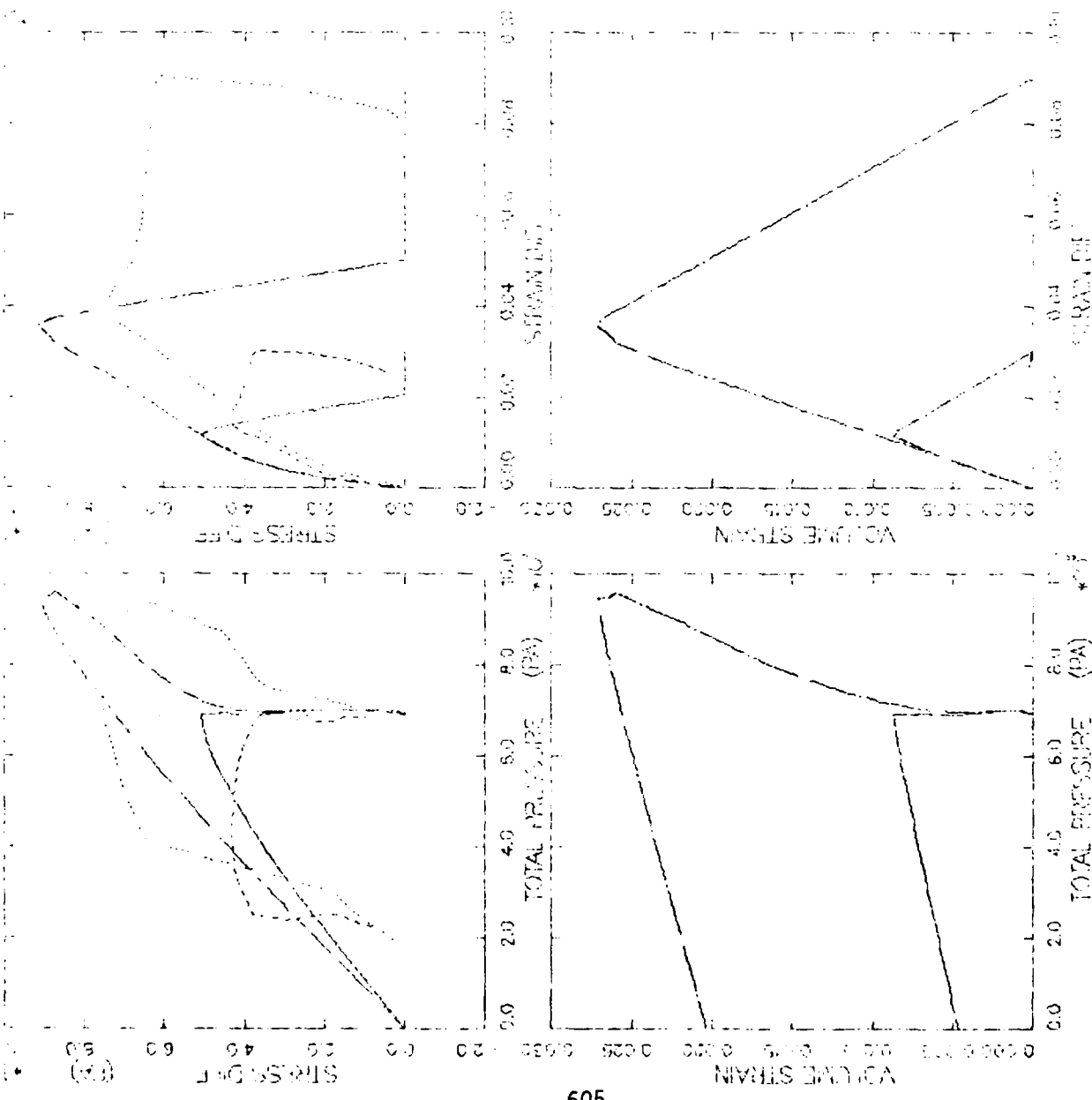FIGURE W.40   ARA MODEL EXERCISE— UNIAXIAL STRAIN (UXC) — STRESS DIFF VS. STRAIN DIFF

602

FIGURE W.41 ARA MODEL EXERCISE—UNIAX STRAIN EXTEN (QCKD) -- STRESS DIFFERENCE VS. PRESSU

AFOSR SOIL ELEMENT MODEL

TEST = UNIAXIAL STRAIN TEST
MODEL= ARA1
MATL = DRYCARES—REMOLD
DATA = DRYCARESR/WES/84

LEGEND
S3C=4.0E6
TEST DATA
S3C=20.E6
TEST DATA
S3C=32.E6
TEST DATA

FIGURE W.42   ARA MODEL EXERCISE--UNIAX STRAIN FXTEN (ICKO) -- STRESS DIFF VS. AXIAL STRAIN

604

FIGURE W.43 ARA MODEL FXER- AMBIENT STANDARD SG — SCR/CAP VS. SR/CAP ANALYSIS

605

AFOSR SOIL ELEMENT MODEL

TEST = STRAIN PATH
MODEL=ARA1
MATL = DRYCARES-REMOLD
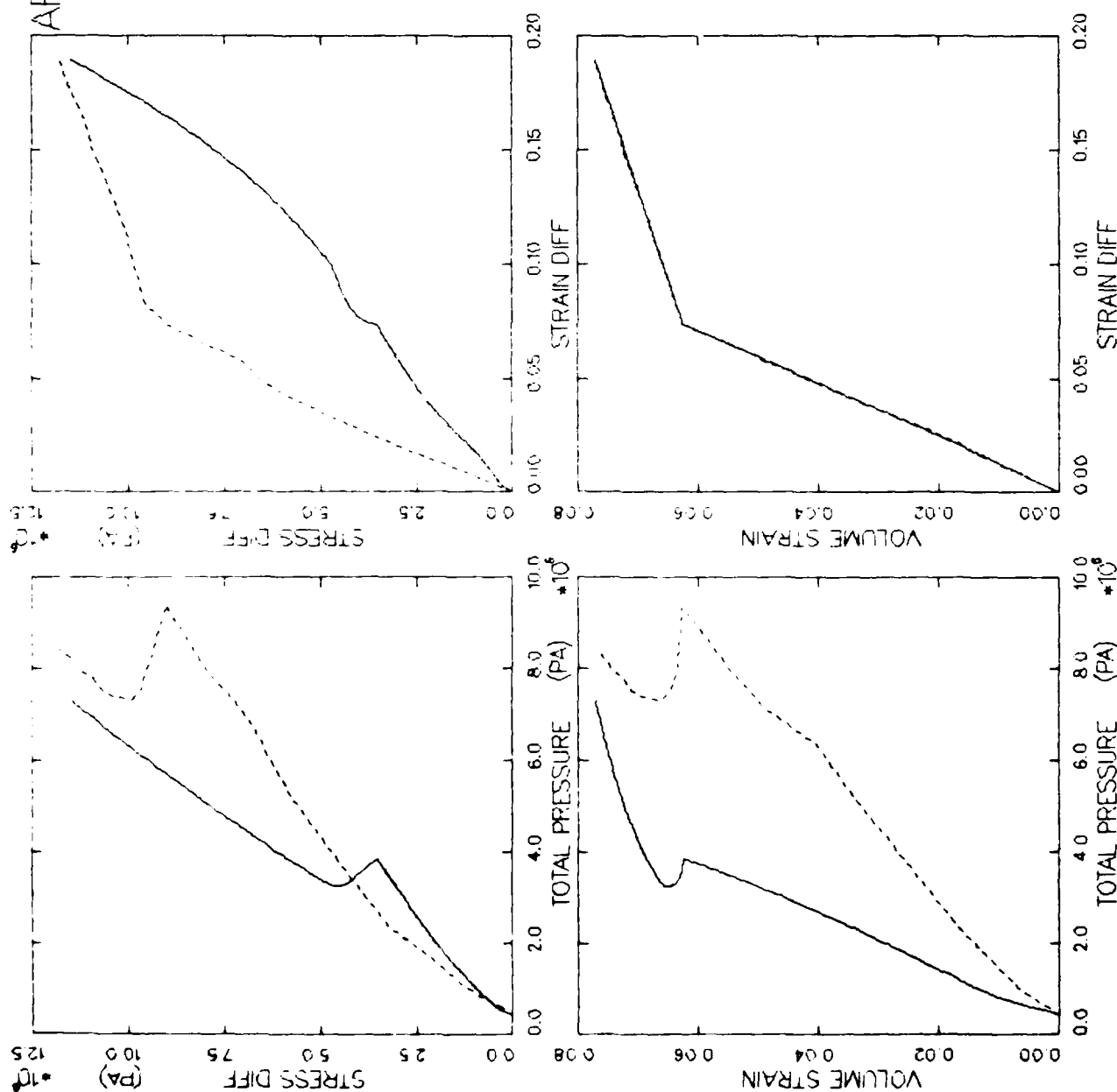DATA = LADE/YUMA/1-5-P1

LEGEND
CALCULATION
TEST DATA

FIGURE W.44 ARA MODEL —LADE AXISYM EPATH1 — SDIFF/P/EV/EDIFF ANALYSIS

AFOSR SOIL ELEMENT MODEL

TEST = STRAIN PATH
MODEL=ARA1
MATL = DRYCARES-REMOLD
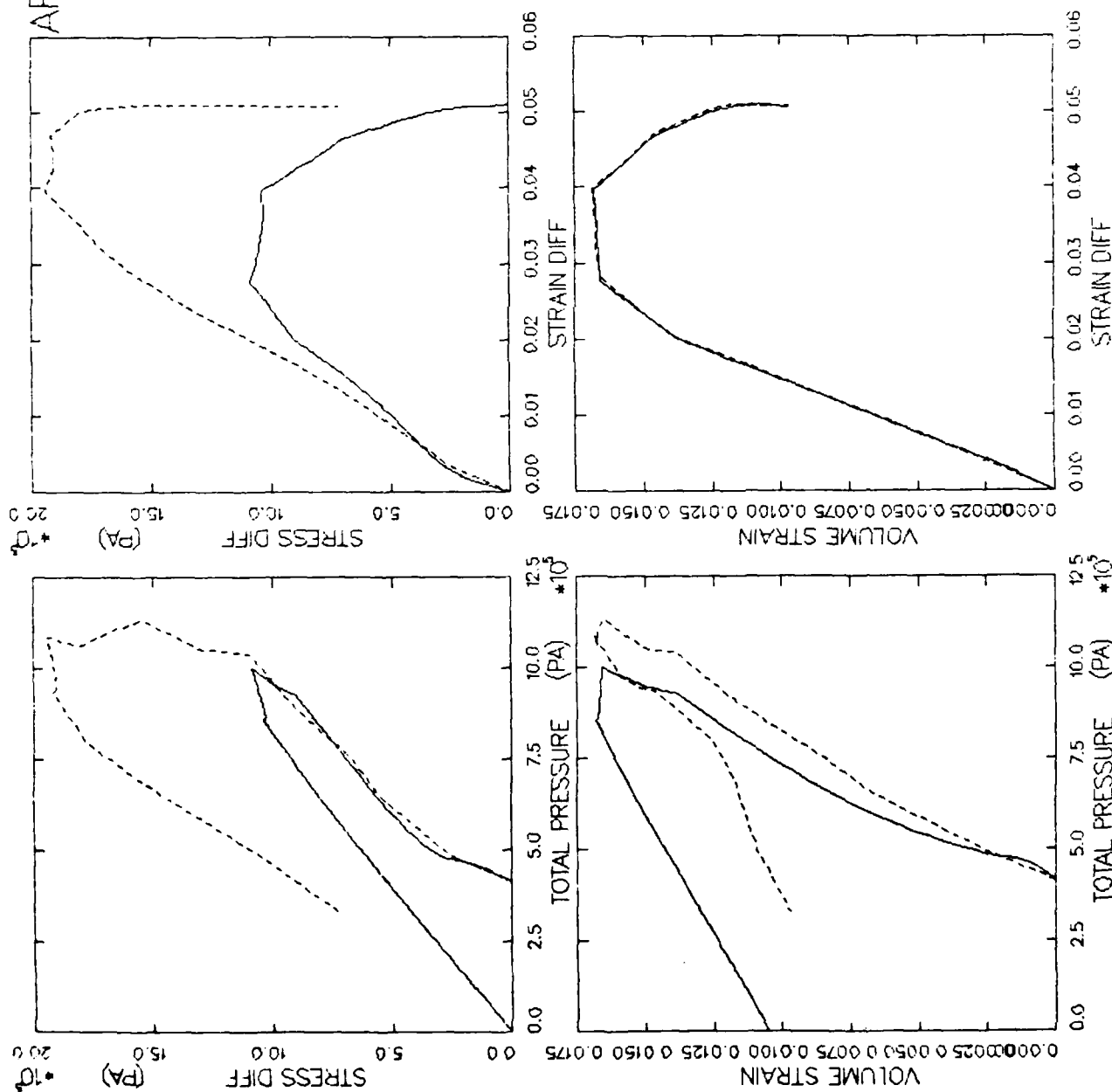DATA = LADE/YUMA/1-3-P2

LEGEND
CALCULATION
TEST DATA

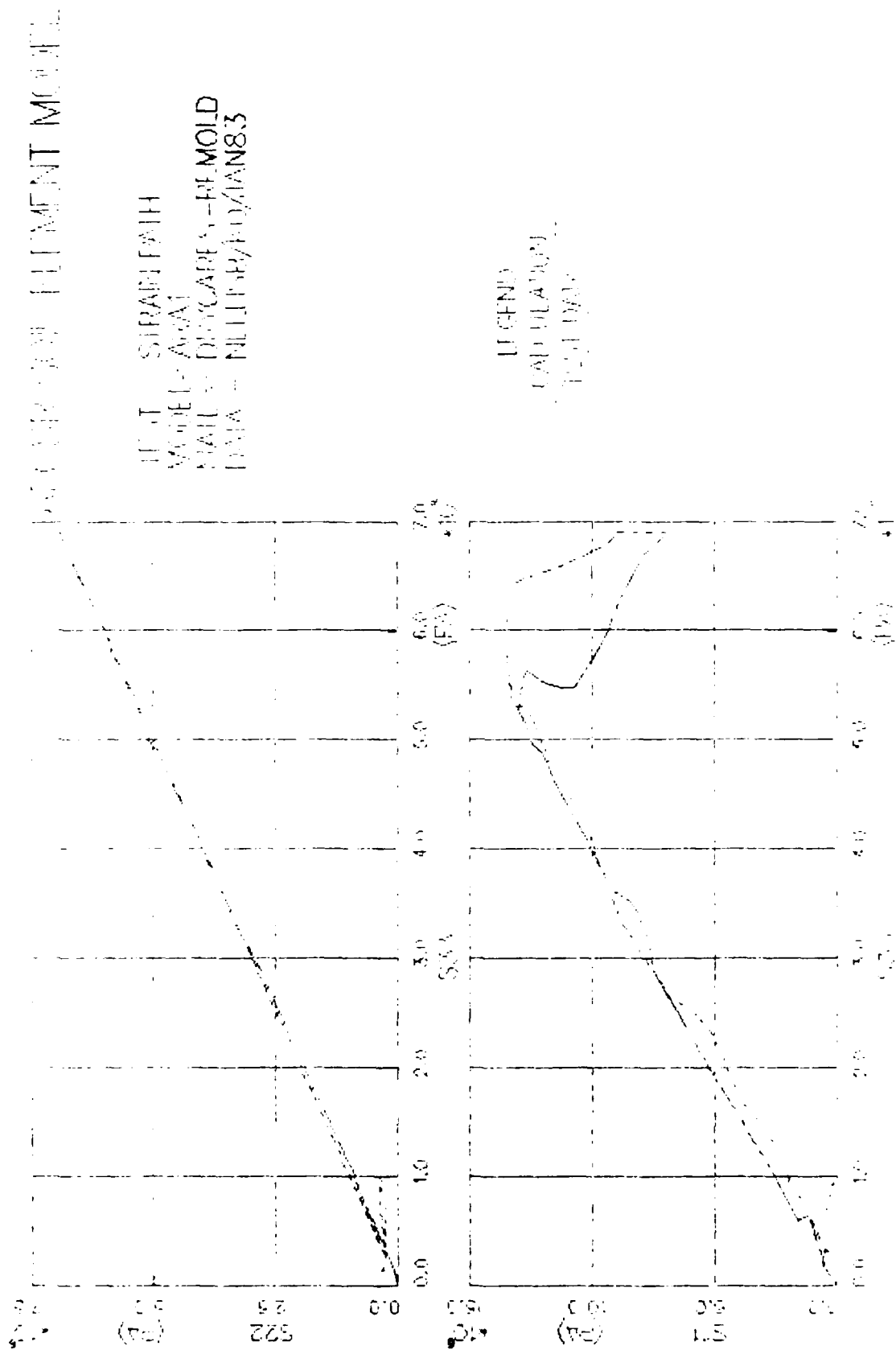FIGURE W.45 ARA MODEL –LADE AXISYM EFATH2 – SDIFF/P/EV/EDIFF ANALYSIS

FIGURE W.46

ARMOUR SOIL ELEMENT MODEL

TEST — STRAIN PATH
MODEL — APA1
MAT'L — DRY/CAPLSS—REMOLD
DATA — NELLIGER/NO/MAN83

LEGEND
CALCULATION
TEST DATA

TOTAL PRESSURE (PA)
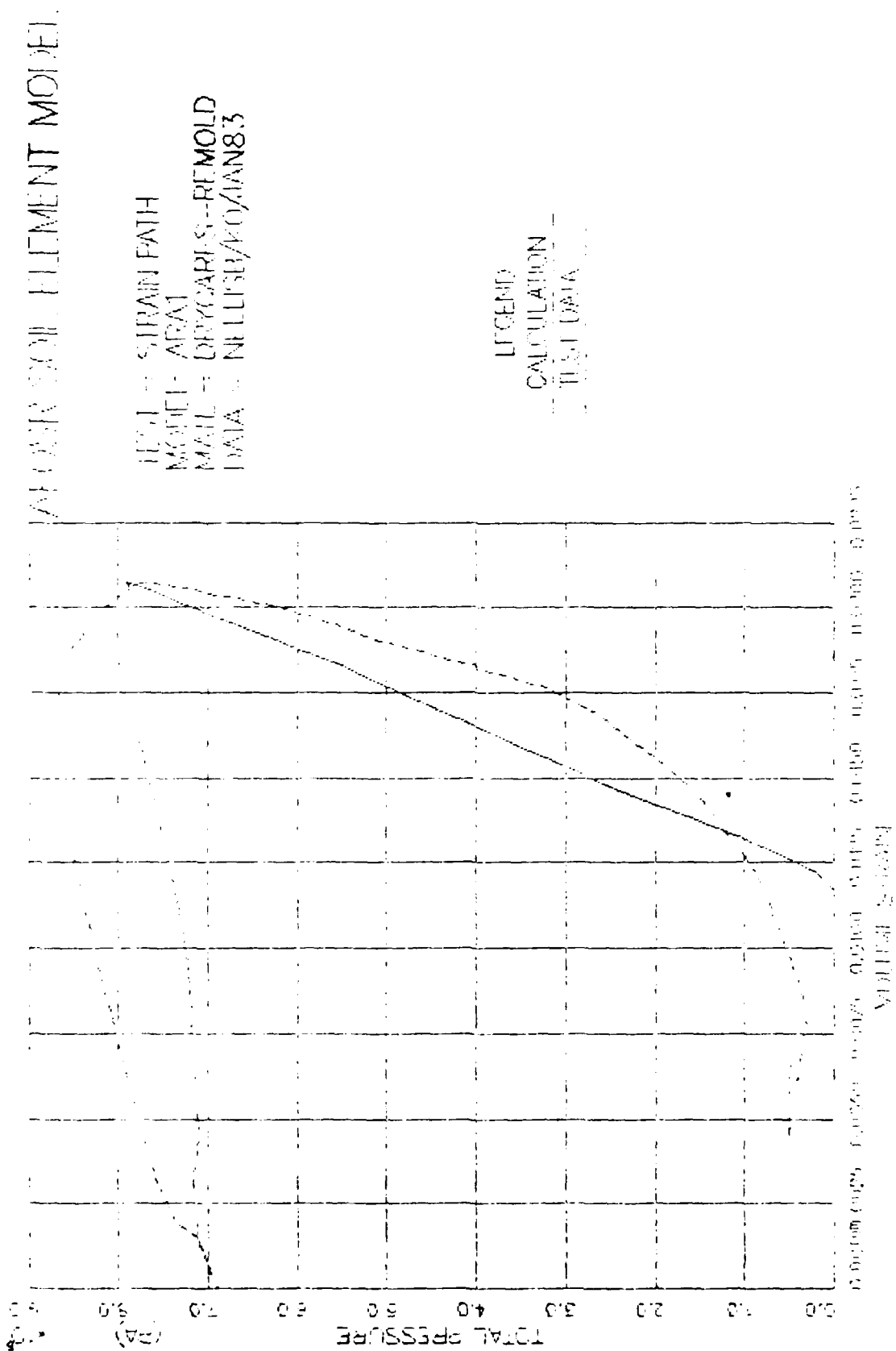
FIGURE N.47 APA MODEL EXAMPLE TEST DATA — PRESSURE VS. VOLUME DEL STRAIN